



University  
of Glasgow

Wildman, Mark (2015) *Reassessing the structural and geomorphic evolution of a 'classic' Atlantic type passive margin: an integrated study of the Namaqualand sector of the South African continental margin.*  
PhD thesis.

<http://theses.gla.ac.uk/6448/>

Copyright and moral rights for this thesis are retained by the author

A copy can be downloaded for personal non-commercial research or study, without prior permission or charge

This thesis cannot be reproduced or quoted extensively from without first obtaining permission in writing from the Author

The content must not be changed in any way or sold commercially in any format or medium without the formal permission of the Author

When referring to this work, full bibliographic details including the author, title, awarding institution and date of the thesis must be given

REASSESSING THE STRUCTURAL AND GEOMORPHIC  
EVOLUTION OF A 'CLASSIC' ATLANTIC TYPE PASSIVE MARGIN:  
AN INTEGRATED STUDY OF THE NAMAQUALAND SECTOR OF  
THE SOUTH AFRICAN CONTINENTAL MARGIN

MARK WILDMAN

B.Sc. (Hons.)

SUBMITTED IN FULFILMENT OF THE REQUIREMENTS FOR THE DEGREE OF DOCTOR  
OF PHILOSOPHY (Ph.D.)



SCHOOL OF GEOGRAPHICAL AND EARTH SCIENCES  
COLLEGE OF SCIENCE AND ENGINEERING  
UNIVERSITY OF GLASGOW

FEBRUARY 2015

SUPERVISORS:

PROF. RODERICK BROWN, DR. CRISTINA PERSANO AND PROF. FINLAY STUART

## Abstract

The origin of high elevation topography at so-called “passive” continental margins and their interior hinterlands has been an outstanding question in geoscience for decades. An important step towards answering this question is to improve our understanding of the response of the landscape to deformation of the lithosphere over different length scales. During continental rifting, elevated rift flanks may develop as a result of lateral extension of the lithosphere combined with vertical movements of the lithosphere driven by isostasy or convection of buoyant mantle flow. However, mechanisms capable of maintaining rift-related topography over geological timescales or driving post-rift rejuvenation of margin topography remain largely speculative and are strongly dependent on theoretical models. By constraining the timing and magnitude of major erosional events that have occurred across a particular margin using suitable empirical data we can begin to unravel the geomorphic development of the margin and identify the forces driving surface uplift. Apatite fission track (AFT) and apatite (U-Th-Sm)/He (AHe) thermochronometry has the unique ability to deliver these constraints by providing information on the cooling of rocks through temperatures of c. 120 - 40°C as they are exhumed from depth (c. 4 - 6 km) by erosion of overlying rock.

Along the western continental margin of South Africa recent insights from thermochronology, structural geology and geomorphology has revealed that the margin may have experienced a more complex post-rift tectonic history than is to be expected for a “passive” margin. In this study, AFT and AHe analysis was performed on samples collected across the high relief escarpment zone along the continental margin (Namaqualand Highlands) and across the continental interior plateau (Bushmanland Plateau) to determine the post-break up cooling history of the continental margin. Sampling was undertaken from a structural perspective by sampling individual fault blocks within the heavily faulted Namaqualand Highlands and by collecting a profile of samples, from the interior plateau, that crosses major structural features at the boundary of the Kaapvaal craton. The approach for AHe analysis was to obtain multiple single grain age measurements (up to 20 grains per sample) for selected samples in order to

investigate and exploit the primary causes of natural dispersion of AHe single grain ages and the influence of this dispersion on thermal history modelling. AFT and AHe data from 56 outcrop samples are jointly inverted using a Bayesian transdimensional approach incorporating the compositional influence on fission track annealing and radiation damage enhanced He retention.

Two major discrete cooling episodes are recorded in thermal history models at c. 150 - 130 Ma and 110 - 90 Ma, respectively. These cooling episodes are broadly coeval with periods of enhanced deposition in the offshore Orange Basin and are therefore linked to discrete periods of enhanced continental erosion. The first phase of erosion is believed to involve the progressive destruction of syn-rift topography which prevailed across the developing continental margin and inland to the SW boundary of the Kaapvaal craton. The second phase of erosion is proposed to have been induced by regional uplift of southern Africa coupled with localised reactivation of basement structures at the continental margin and craton boundary. A vertical thickness of at least c. 3 - 5 km of material was eroded across the continental margin during the Cretaceous with only minor erosion (typically < 0.5km) occurring during the Cenozoic.

There is now considerable support from the low temperature thermochronology record that km-scale denudation has occurred regionally across South Africa during the Mid-Late Cretaceous, long after the end of continental rifting in the South Atlantic. Data from this study reveals a more localised structural component to this regional event and more complexity in the spatial and temporal distribution of denudation during this period. The mechanisms driving this denudation are still uncertain but it is proposed here that regional dynamic uplift of South Africa has occurred due to the presence of an underlying upwelling of buoyant mantle, while in-plane horizontal stresses have triggered reactivation of basement structures. It now seems appropriate to revise the classification of the southwest African continental margin as being “passive” in a tectonic sense and consider the implications this has for our understanding of global plate tectonics.

# Table of Contents

Abstract .....	1
List of Figures.....	7
List of Tables.....	10
Acknowledgements .....	11
Declaration .....	13
<b>CHAPTER 1: INTRODUCTION .....</b>	<b>14</b>
1.1 Project rationale.....	14
1.2 Study Area .....	16
1.3 Thesis outline.....	18
<b>CHAPTER 2: REVIEWING AND REASSESSING PASSIVE MARGINS .....</b>	<b>21</b>
2.1 Introduction: Declassifying rifted margins .....	21
2.2 Rifted margin evolution: Insights from geodynamic modelling.....	23
2.2.1 Rift initiation: active vs. passive rifting .....	25
2.2.2 Lithospheric extension and thinning: pure shear vs. simple shear .....	27
2.2.3 Modern rifted margin modelling: joint physical, thermal and chemical models ...	29
2.3 The influence of structural inheritance .....	32
2.3.1 Pre/syn-rift .....	32
2.3.2 Post-rift .....	34
2.4 The role of regional dynamic uplift .....	36
2.5 Current thinking on the geodynamical setting of the southwest African rifted margin.	38
2.6 Conclusions .....	39
<b>CHAPTER 3: THE TECTONIC GEOMORPHOLOGY OF HIGH ELEVATION CONTINENTAL MARGINS</b>	<b>41</b>
3.1 Introduction .....	41
3.2 Long-term landscape evolution .....	41
3.3 Foundations of modern geomorphology .....	43
3.4 Polycyclic uplift.....	46
3.5 Steady-state landscapes, flexural isostasy and surface process numerical modelling at continental margins. ....	50
3.5.1 Steady-state landscapes and flexural isostasy .....	50
3.5.2 Applications of surface process numerical models .....	52
3.6 Geomorphic response to rifting: Escarpment retreat or plateau downwearing .....	55
3.7 Quantifying surface process models: Insights from low temperature thermochronometry and cosmogenic nuclide analysis.....	57
3.8 Geological factors controlling passive margin evolution .....	62
3.8.1 Regional plate movements.....	62
3.8.2 Surface response to faulting.....	64
3.8.3 Crustal heterogeneity.....	67
3.8.3.1 Rock hardness and rock density.....	67
3.8.3.2 Radiogenic crust .....	69
3.8.3.3 Effective elastic thickness .....	69
3.8.3.4 Igneous bodies .....	70
3.9 Geomorphology of dynamic topography .....	71
3.10 Summary and conclusions .....	74
<b>CHAPTER 4: APATITE FISSION TRACK AND (U-Th-Sm)/He THERMOCHRONOLOGY .....</b>	<b>76</b>
4.1 Introduction .....	76
4.2 Theoretical Background .....	78
4.2.1 Apatite fission track analysis .....	78
4.2.2 Apatite (U-Th-Sm)/He analysis.....	79
4.2.3 Integrating AFT and AHe datasets .....	82
4.3 Uncertainties in apatite fission track analysis.....	83

4.3.1	Chemical composition .....	85
4.3.2	Pressure .....	87
4.3.3	Radiation Enhanced Annealing .....	88
4.3.4	Calibration and reproducibility of track length measurements .....	90
4.4	Uncertainties in apatite (U-Th-Sm)/He analysis .....	91
4.4.1	Alpha ejection.....	92
4.4.2	Implantation.....	94
4.4.3	Inclusions.....	94
4.4.4	Grain radius.....	95
4.4.5	Radiation Damage .....	97
4.4.6	Fragment Length.....	102
4.4.7	Zonation.....	104
4.5	Thermal history modelling: Joint AFT and AHe inversion .....	109
4.5.1	Modelling Approach: QTQt .....	110
4.5.2	Combining AFT and AHe data.....	112
4.5.2.1	Modelling AFT data independently .....	112
4.5.2.2	Modelling AHe data independently: With analytical uncertainty .....	115
4.5.2.3	Modelling AHe data independently: With estimated uncertainty.....	117
4.5.2.4	Modelling AFT and AHe data together .....	119
4.6	Summary and strategy for joint AFT and AHe analysis.....	121

**CHAPTER 5: CONSTRAINING LARGE-SCALE BRITTLE DEFORMATION IN THE NAMAQUALAND HIGHLANDS .....** 123

5.1	Introduction .....	123
5.2	Local Geology .....	124
5.2.1	Study Area .....	124
5.2.2	Morphology.....	124
5.2.3	Namaqua Metamorphic Province.....	126
5.2.4	Neoproterozoic - Palaeozoic: Pan-Africa Orogeny.....	126
5.2.5	Karoo Supergroup.....	128
5.2.6	Syn and post-rift intrusive activity .....	129
5.2.7	Late Cretaceous and Tertiary units .....	130
5.3	AFT Analysis .....	132
5.3.1	Results .....	132
5.3.2	Data quality assessment.....	136
5.3.3	Summary of AFT Data .....	138
5.4	AHe Analysis .....	139
5.4.1	Results .....	139
5.4.2	Data quality assessment.....	139
5.4.3	Summary of AHe Data.....	147
5.5	Thermal History Modelling .....	147
5.5.1	Approach .....	147
5.5.2	Modelling results.....	149
5.5.2.1	150 - 130 Ma: Slow Cooling .....	149
5.5.2.2	150 - 130 Ma: Fast Cooling .....	151
5.5.2.3	110 - 90 Ma: Slow Cooling.....	153
5.5.2.4	110 - 90 Ma: Fast Cooling .....	156
5.5.2.5	80 - 60 Ma .....	156
5.5.3	Alternative scenarios .....	156
5.5.3.1	Profile modelling .....	156
5.5.3.2	Speculative constraints.....	163
5.5.4	Summary of modelling results.....	167
5.6	Temperature-time spatial relationships: Cooling and magnitudes of denudation .....	168
5.6.1	Cooling.....	168
5.6.2	Denudation.....	168
5.6.3	Uncertainties in denudation estimates .....	176
5.7	Discussion .....	178
5.7.1	The Namaqualand continental margin low temperature thermochronology dataset. ....	178
5.7.2	The structural history of the Namaqualand Highlands.....	180
5.8	Summary and Conclusions.....	188

<b>CHAPTER 6: INTRACONTINENTAL DEFORMATION OF THE SOUTH AFRICAN PLATEAU .....</b>	<b>190</b>	
6.1	Introduction .....	190
6.2	Local Geology .....	191
6.2.1	Study Area .....	191
6.2.2	Morphology.....	191
6.2.3	Archean - Palaeoproterozoic craton .....	193
6.2.4	Namaqua Metamorphic Province.....	194
6.2.5	Neoproterozoic - Palaeozoic.....	197
6.2.6	Karoo Supergroup.....	197
6.2.7	Cenozoic.....	198
6.3	AFT Analysis .....	199
6.3.1	Results .....	199
6.3.2	Data quality assessment.....	202
6.3.3	Summary of AFT Data .....	204
6.4	AHe Analysis .....	204
6.4.1	Results .....	204
6.4.2	Data quality assessment.....	208
6.4.3	Summary of AHe Data.....	211
6.5	Thermal History Modelling .....	211
6.5.1	Approach .....	211
6.5.2	Modelling results.....	212
6.5.2.1	Early Cretaceous cooling (150 - 130 Ma) .....	213
6.5.2.2	Mid-Cretaceous cooling (110 - 90 Ma).....	213
6.5.2.3	Late Cretaceous cooling (80 - 60 Ma) .....	217
6.5.3	Alternative scenarios .....	219
6.5.3.1	Profile modelling .....	219
6.5.3.2	Speculative constraints.....	225
6.5.4	Summary of modelling results.....	229
6.6	Temperature-time spatial relationships: Cooling and magnitudes of denudation .....	230
6.6.1	Cooling.....	230
6.6.2	Denudation.....	230
6.7	Discussion .....	234
6.7.1	Low temperature thermochronology across the southwest continental interior .....	234
6.7.2	Intracontinental deformation of the South African plateau .....	237
6.7.2.1	Structural record .....	239
6.7.2.2	Intraplate deformation at the craton boundary .....	242
6.7.2.3	Plume Upwelling: Mantle - Lithosphere interactions.....	243
6.8	Summary and Conclusions.....	245
<b>CHAPTER 7: THE POST-RIFT LANDSCAPE EVOLUTION OF SOUTHWEST AFRICA .....</b>	<b>247</b>	
7.1	Introduction .....	247
7.2	Low temperature thermochronology from SW Africa .....	248
7.2.1	Borehole profiles .....	248
7.2.1.1	AFT data from KC1/70 and QU1/65 .....	248
7.2.1.2	Borehole thermal history models .....	251
7.2.2	South African apatite fission track data .....	252
7.2.3	South African apatite (U-Th-Sm)/He data .....	258
7.3	Denudation of the SW African continental margin and interior plateau .....	262
7.3.1	150 - 130 Ma .....	264
7.3.2	130 - 110 Ma .....	264
7.3.3	110 - 90 Ma .....	265
7.3.4	90 - 70 Ma .....	265
7.3.5	70 - 50 Ma .....	266
7.3.6	50 - 0 Ma .....	266
7.4	Correlating onshore denudation with offshore accumulation: Insights from the Orange Basin .....	266
7.4.1	The Orange Basin .....	266
7.4.2	Stratigraphy of the Orange Basin .....	268
7.4.2.1	Syn-rift sequence (c. 160 - 130 Ma) .....	268
7.4.2.2	Late Hauterivian/Early Barrremian - Early Aptian (c. 130 - 115 Ma).....	270
7.4.2.3	Early Aptian to Late Cenomanian/Early Turonian (115 - 90 Ma) .....	271

7.4.2.4	Early Turonian to Late Maastrichtian (c. 90 - 65 Ma) .....	271
7.4.2.5	Cenozoic sequences (c. 65 - 0 Ma) .....	272
7.4.3	Structural features in the Orange Basin .....	273
7.4.4	Linking onshore denudation with offshore accumulation .....	275
7.5	The Cenozoic evolution of SW Africa .....	279
7.5.1	Volumes and rates of Cenozoic erosion as permitted by low temperature thermochronometry and cosmogenic nuclide analyses .....	279
7.5.2	Late Cretaceous to Cenozoic palaeontology .....	281
7.5.3	The Cenozoic geomorphological development of southwestern Africa .....	284
7.6	Dynamic topography .....	288
7.7	Conclusion .....	292
<b>CHAPTER 8: REASSESSING THE NAMAQUALAND SECTOR OF THE SOUTH AFRICAN CONTINENTAL MARGIN .....</b>		<b>294</b>
8.1	The pre-rift setting of SW Africa: pre-Cretaceous (>150 Ma) .....	294
8.2	Continental rifting and break-up in the Southern Atlantic: Late Jurassic - Hauterivian (150 - 130 Ma) .....	295
8.3	The post rift phase (i): Barremian - Albian (130 - 110 Ma) .....	296
8.4	The post rift phase (ii): Albian - Santonian (c. 110 - 80 Ma) .....	296
8.5	The post rift phase (iii): Campanian to Maastrichtian (80 - 65 Ma) .....	298
8.6	The post rift phase (iv): Paleogene (65 - 25 Ma) .....	298
8.7	The post rift phase (v): Neogene (25 - 0 Ma) .....	299
8.8	Wider implications of this work .....	300
8.9	Future Work .....	303
8.10	Conclusions .....	304
<b>APPENDIX 1: LOW TEMPERATURE THERMOCHRONOLOGY - METHODOLOGY .....</b>		<b>307</b>
A1.1	Sample Preparation .....	307
A1.1.1	Mineral Separation .....	307
A1.1.2	AFT Sample Preparation .....	308
A1.1.3	Apatite (U-Th-Sm)/He Sample Preparation .....	309
A1.2	Apatite Fission Track Analysis .....	310
A1.2.1	Apatite fission track ages - External Detector Method .....	310
A1.2.2	Apatite fission track length data .....	312
A1.2.3	Practical approach to AFT analysis .....	313
A1.3	Apatite (U-Th-Sm)/He Analysis .....	314
A1.3.1	Helium Extraction .....	314
A1.3.2	U, Th and Sm analysis .....	315
A1.3.3	Apatite (U-Th-Sm)/He age calculation .....	315
<b>APPENDIX 2: APATITE FISSION TRACK AND APATITE (U-Th-Sm)/He STANDARDS.....</b>		<b>316</b>
A2.1	Zeta Calibration.....	316
A2.2	Apatite (U-Th-Sm)/He analysis of Durango apatite.....	318
<b>APPENDIX 3: DATA QUALITY ASSESSMENT .....</b>		<b>321</b>
A3.1	AFT single grain ages.....	321
A3.2	AHe single grain ages .....	321
<b>APPENDIX 4: SAMPLE DETAILS.....</b>		<b>325</b>
<b>APPENDIX 5: APATITE FISSION TRACK DATA .....</b>		<b>326</b>
A5.1	Radial plots .....	326
A5.2	Track length distribution .....	333
<b>APPENDIX 6: ADDITIONAL AFT DATA.....</b>		<b>341</b>
<b>APPENDIX 7: ADDITIONAL THERMAL HISTORY MODELS .....</b>		<b>342</b>
<b>REFERENCES.....</b>		<b>343</b>



# List of Figures

Figure 1-1: Topographic map of southwestern Africa .....	17
Figure 1-2: Simplified geological map of southern Africa .....	18
Figure 2-1: Location of major plate boundaries and high elevation continental margins .....	22
Figure 2-2: (a) Generic model of continental rifting (b) Simple schematic diagram of a rifted margin's offshore and continental architecture.....	24
Figure 2-3: Schematic representation of the major differences between Active and Passive rifting styles .....	26
Figure 2-4: Schematic representation of the major differences between simple and pure shear lithosphere extension styles .....	28
Figure 2-5: Illustration of the characteristic features of (a) Type I and (b) Type II rifted continental margins (after Huisman and Beaumont, 2011) .....	31
Figure 2-6: Sketch model of fault migration during lithospheric extension and reactivation of these structures during a post rift phase of extension or compression. ....	33
Figure 2-7: Simple sketch of the influence of mantle convection on the overlying topography... ..	37
Figure 3-1: (a) Illustration of surface uplift ( $U_s$ ), rock uplift ( $U_r$ ) and denudation (D) (b) Illustration of the Airy and Pratt hypotheses of (local) isostasy and flexural (regional) isostasy .	44
Figure 3-2: Illustration of cyclic erosion surfaces .....	48
Figure 3-3: Steady-state and transient landscapes. ....	51
Figure 3-4: Conceptual models of continental margin evolution .....	55
Figure 3-5: Predictions of apatite (U-Th)/He ages across continental margins.....	60
Figure 3-6: Cartoon illustrating the variety of different mechanisms proposed for creating vertical motions at continental margin settings.....	63
Figure 3-7: Drainage system of southern Africa .....	65
Figure 3-8: Illustration showing the potential influence of geological factors on topography .....	68
Figure 4-1: Cartoon showing common thermochronology techniques used in geological investigations .....	77
Figure 4-2: Hypothetical thermal histories and their expected track length distributions .....	80
Figure 4-3: Illustration of the partial annealing and partial retention zone .....	81
Figure 4-4: Relationship between AFT and AHe average ages.. ..	84
Figure 4-5: Relationship between etch pit measurements ( $D_{par}$ ) and AFT age and MTL.....	86
Figure 4-6: Relationship of AFT age and MTL against Uranium content as a proxy for the degree of radiation enhanced annealing experienced by the sample. ....	89
Figure 4-7: Results of interlaboratory AFT length calibration.....	91
Figure 4-8: Cartoon figure representing the effects of implantation, ejection and U and Th rich inclusions caused by long-stopping distances of alpha particles emitted from parent nuclides... ..	93
Figure 4-9: Concept of radial diffusion and spherical equivalent radius.....	96
Figure 4-10: Relationships of AHe age (uncorrected) against spherical equivalent radius .....	96
Figure 4-11: Cartoon diagram of the radiation damage trapping model .....	98
Figure 4-12: Plots of AHe age against effective Uranium .....	98
Figure 4-13: Results for radiation damage forward modelling .....	101
Figure 4-14: The concept of analysing fragmented apatite grains .....	103
Figure 4-15: Relationships of AHe age (uncorrected) against fragment length.....	103
Figure 4-16: Representation of styles of zonation .....	106
Figure 4-17: Evidence of zonation in apatite from fission track mounts.....	107
Figure 4-18: Evidence of zonation in cathodoluminescence images .....	108
Figure 4-19: Thermal history models for four outcrop samples using only AFT data .....	114

Figure 4-20: Thermal history models for four outcrop samples using only AHe data with analytical uncertainty.....	116
Figure 4-21: Thermal history models for four outcrop samples using only AHe data with estimated uncertainty.....	118
Figure 4-22: Thermal history models for four outcrop samples using both AFT data and AHe data with estimated uncertainty .....	120
Figure 4-23: Cartoon illustrating the relative influence on AHe ages by the different factors causing natural AHe single grain age dispersion.....	121
Figure 5-1: Location map of the Namaqualand Highlands study area. ....	125
Figure 5-2: Geological map of the Namaqualand Highlands study area.....	127
Figure 5-3: Plot of AFT and AHe age against elevation .....	133
Figure 5-4: Plot of AFT age against MTL .....	135
Figure 5-5: Plot of AFT age and MTL against MTL standard deviation.....	137
Figure 5-6: Plot of AHe age against spherical equivalent grain radius ( $R^*$ ).....	144
Figure 5-7: Plot of AHe age against effective Uranium (eU). ....	145
Figure 5-8: Thermal history models that represent samples which cooled slowly over the interval 150 - 130 Ma .....	150
Figure 5-9: Thermal history models that represent samples which cooled rapidly over the interval 150 - 130 Ma .....	152
Figure 5-10: Thermal history models that represent samples which cooled slowly over the interval 110 - 90 Ma .....	154
Figure 5-11: Thermal history models that represent samples which rapidly cooled over the interval 110 - 90 Ma .....	155
Figure 5-12: Thermal history model that represents the only sample which rapidly cooled over the interval 80 - 60 Ma.....	157
Figure 5-13: Coastal profile thermal history models .....	158
Figure 5-14: Western NQH profile thermal history models .....	160
Figure 5-15: Kamiesberg profile thermal history models .....	161
Figure 5-16: Western Bushmanland Plateau thermal history models .....	163
Figure 5-17: Thermal history models from the NQ coast with additional constraints .....	164
Figure 5-18: Western Bushmanland plateau profile thermal history models with additional constraints. ....	166
Figure 5-19: Plot represent the expected age and uncertainty of key temperature points in each thermal history .....	169
Figure 5-20(a-e): Sections with predictions on magnitudes of denudation over time intervals since 150 Ma .....	170-174
Figure 5-21: (a) Magnitudes of denudation for Section x-x' with associated uncertainties, (b) Plots showing the effect of geothermal gradient on estimates of denudation. ....	177
Figure 5-22: Major fault lineaments across the Namaqualand Highlands .....	181
Figure 5-23: Structural map of Western Bushmanland plateau region .....	184
Figure 5-24: South African horizontal stress field.....	187
Figure 6-1: Location map of the Bushmanland Plateau study area. ....	192
Figure 6-2: Longitudinal river profile of the Orange River .....	194
Figure 6-3: Geological map of the Bushmanland Plateau study area.....	195
Figure 6-4: Schematic cross section of the Namaqualand Metamorphic Province.....	196
Figure 6-5: Plot of AFT and AHe age against elevation. ....	201
Figure 6-6: Plot of AFT age against mean track length .....	201
Figure 6-7: Plot of AFT age and MTL against MTL standard deviation.....	202
Figure 6-8: Plot of AHe age against spherical equivalent grain radius ( $R^*$ ).....	209
Figure 6-9: Plot of AHe age against effective uranium (eU) .....	210

Figure 6-10: Thermal history models that represent samples which cooled (a) rapidly and (b) slowly, over the interval 150 - 130 Ma .....	214
Figure 6-11: Thermal history models that represent samples which cooled (a) rapidly and (b) slowly, over the interval 110 - 90 Ma .....	215
Figure 6-12: Thermal history models that represent samples with poorly constrained or ambiguous cooling histories.....	216
Figure 6-13: Thermal history models that represent samples which cooled during the interval 80 - 60 Ma .....	218
Figure 6-14: Bushmanland East profile thermal history models .....	220
Figure 6-15: Bushmanland West profile thermal history models. ....	221
Figure 6-16: Bushmanland Central profile thermal history models. ....	223
Figure 6-17: Bushmanland Centre-East profile thermal history models.....	225
Figure 6-18: Bushmanland Centre-East-2 profile thermal history models .....	226
Figure 6-19: Thermal history models testing the influence of imposing an initial constraint on the (a) PRU 106 and (b) BMP Centre-East-2 thermal history models .....	228
Figure 6-20: Plot represent the expected age and uncertainty of key temperature points in each thermal history. ....	231
Figure 6-21: Section with predictions on magnitudes of denudation over discrete time intervals since 150 Ma .....	232
Figure 6-22: Map generalising the trend of regional AFT data from the Bushmanland Plateau ..	236
Figure 6-23: Map illustrating the relationship between the South African structural framework and magnetic anomalies. ....	238
Figure 6-24: Satellite image of the Bushmanland Plateau with structural annotation .....	241
Figure 6-25: Thermo-mechanical models of the interaction between cratonic and non-cratonic lithosphere and plume upwellings and possible models for the deformation of the Bushmanland Plateau, driven by a combination of in-plane and vertical stresses induced by mantle plume upwelling .....	244
Figure 7-1: Map of south west Africa showing location of two sampled boreholes and offshore sediment thicknesses maps .....	249
Figure 7-2: Plots of AFT age and MTL against borehole depth.....	250
Figure 7-3: KC 1/70 and QU 1/65 thermal history models.....	253
Figure 7-4: Database of apatite fission track data.....	254
Figure 7-5: AFT age and MTL interpolation maps .....	256
Figure 7-6: Database of apatite (U-Th)/He data .....	260
Figure 7-7: Interpolation maps based on denudation estimates.....	263
Figure 7-8: Summary of the stratigraphy of the Orange Basin .....	269
Figure 7-9: Histograms summarising offshore sediment accumulation and onshore denudation ..	276
Figure 7-10: Map collating various datasets used to infer Cenozoic the nature of long-term landscape development in SW Africa.....	282
Figure 7-11: Passage of the African plate over hot mantle upwelling.....	291
Figure 7-12: Kimberlite age map. ....	291
Figure A1-1: Illustration of the External Detector Method. ....	311
Figure A2-1: Plot of zeta calibration values over time. ....	318
Figure A5-1: Radial plots of single grain apatite fission track analysis.....	327-333
Figure A5-2: Fission track length distributions for all analysed samples.....	334-333

# List of Tables

Table 5-1: Results of apatite fission track analysis .....	134
Table 5-2: Results of apatite (U-Th-Sm)/He analysis.....	140-143
Table 6-1: Results of apatite fission track analysis .....	200
Table 6-2: Results of apatite (U-Th-Sm)/He analysis.....	205-207
Table 7-1: Denudation rates for southern Africa .....	280
Table A2-1: Results of zeta calibration for apatite fission track analysis .....	317
Table A2-2: Apatite (U-Th-Sm)/He data for Durango apatite standards .....	319-320
Table A3-1: Details of single grain apatite fission track ages excluded from further analysis. ....	323
Table A3-2: Details of single grain apatite (U-Th-Sm)/He ages excluded from further analysis .	324
Table A4-1: Details on sample location and lithology .....	325
Table A6-1: Results of apatite fission track analysis from Brown (1992) .....	341

# Acknowledgements

The completion of this thesis marks the end of an exceptionally demanding, interesting and, at times, frustrating three and a half years of study. While this work has been an extremely personal challenge, I am tremendously grateful to those who have propelled me towards the high points and to those who have dragged me out of the lows. Without their advice, understanding and encouragement I may not have made it to the end.

Firstly, I would like to thank my supervisors Prof. Rod Brown, Dr. Cristina Persano and Prof. Fin Stuart. As a team they have endeavoured to ensure the successful completion of this project and the development of myself as a scientist. I am also grateful to each individually for sharing their unique knowledge and experience. Thanks go to Rod for sharing countless discussions on South African geology and thermochronology and for encouraging me to attend major conferences and engage with researchers from all over the world. Cristina, is thanked for her patience and assistance in preparing samples, checking apatites, counting fission tracks and tackling various other problems that arose during this project. Thanks go to Fin for helping me to understand the workings of the helium line; asking questions of myself and of the project that I was otherwise avoiding and for striving to ensure that I was given the necessary lab time to analyse my many grains.

Undertaking this research has been made all the easier thanks to the help on offer from all members of staff in GES at the University of Glasgow and at SUERC. In particular, thanks goes to Robert McDonald and John Gilleece for help during sample preparation, Peter Chung for assistance with taking CL images, Les Hill for printing many conference posters and Gary Tait for helping to resolve a variety of IT problems. Thanks also go to Luigia Di Nicola at SUERC for her help throughout this project with all aspects of (U-Th-Sm)/He analysis.

A special mention must be made to Romain Beucher (now at University of Bergen) who provided me with a great deal of support and friendship during his time at the University of Glasgow and has been excellent company in the field and at conferences over the past few years.

Prof. Andy Carter, Dr. Martin Rittner, Dr. James Schwanethal, Dr. Yuntao Tian and Dr. Peter Vermeesch are thanked for their assistance during additional (U-Th)/He analysis at University College London. Dr. Marco Andreoli and staff at the South African Nuclear Energy Corporation (NECSA) are acknowledged for assistance during fieldwork and Dr. Andreoli is thanked for many helpful comments and resources throughout the project. Prof. Kerry Gallagher is thanked for his hospitality during my time learning about Bayesian statistics and QTQt quirks. He is also thanked for answering the many questions that were asked in the following months. Thanks also go to Dr. Oliver Dautueil, Prof. Francois Guillocheau, Dr. Tim Redfield, Dr. Delphine Rouby, and Dr. Giulio Viola for giving their time and their expertise on different aspects of the project. Thank you also to Dr. Frederick Roelofse from the Council for Geoscience (CGS) in South Africa (now at the

University of the Free State, Bloemfontein) who kindly provided aliquots of apatite mineral separates from the CGS archive.

I would like to thank my fellow PhD students in GES, particularly those who I have shared an office with. I may have spent most of it with my head down and headphones on but everyone was always willing to give some chat and advice whenever I needed it. An extra thank you goes to those who played in Friday morning football matches which were a welcome stress release; I apologise for any time I left the boot in. I wish everyone success with their own projects especially Kasia, David and Almukhtar as they continue to enjoy the thrills and spills of low temperature thermochronology.

Thanks go to Richard Bett, Kevin Buick, Andrew McDonnel, Paul McFadden, Suraj Ram, Kenny Stevenson and Daniel Winn for their conversation, comedy and competition over the past decade. Their company and friendship has always provided a welcome distraction to my studies and is greatly appreciated.

My family are owed a huge debt of gratitude for their support and encouragement which has been instrumental in all of my academic achievements, and was needed more than ever to help me through this one. An extra thank you goes to my mum for all the sacrifices she has made, hard work she has endured, and the example she has set allowing me to find happiness and success in my life. One day I will explain what it is I have been doing for the last four years.

Finally, I thank Lauren Din for her love, tolerance and understanding since I embarked on this PhD. Knowing that she was always on hand to give a positive outlook on my work when I couldn't see it and provide comfort at the end of long and hard days fuelled my confidence and gave me the motivation to continue. Sitting together with a cup of tea and a caramel log resolved a multitude of troubles. Thank you.

*Funding was provided by a NERC studentship NERC (NE/J500252/1) DTG. Additional financial support was provided by the Jean McCorkell scholarship, GES school conference fund, University of Glasgow mobility scholarship and Edmund Johnson grant from the Geological Society of London. They are all thanked for deeming me and this project worthy of receiving their financial backing.*



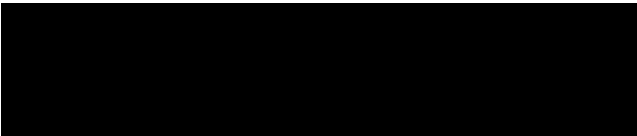
University  
of Glasgow



## Declaration

I declare that, except where explicit reference is made to the contribution of others, this dissertation is the result of my own work and has not been submitted for any other degree at the University of Glasgow or any other institution.

**Signature:**



Mark Wildman

**Date:**

12/02/2015

# CHAPTER 1

## INTRODUCTION

### 1.1 Project rationale

Continental margins that have formed following rifting and break-up of larger supercontinents (e.g. Gondwana) have long been considered “passive” (Lister et al., 1991; Maslanyj et al., 1992; Ziegler and Cloetingh, 2004; Séranne and Anka, 2005). Similarly, ancient geological terrains which dominate the geology of many continental interiors are traditionally described as being “stable” cratons (King, 2005; Foley, 2008; Cocks and Torsvik, 2011). However, insights from geodynamic modelling, structural and geomorphic observations and thermochronology data have questioned how appropriate these terms really are for describing such geological settings. Improving our understanding of the tectonic processes occurring at continental margins and across continental interiors long after rifting and break-up is of major importance to future studies of plate tectonics and to the exploration and exploitation of geo-resources.

One approach to investigating plate tectonics and deep Earth mantle convection is to study the response of the surface to these processes. Geodynamic modelling has provided a new understanding of the different possible styles of lithospheric extension that occur during intracontinental rifting (Huisman and Beaumont, 2011; Lundin and Doré, 2011; Péron-Pinvidic et al., 2013) and the interaction between regional in-plane stresses and vertical stress imposed at the base of the lithosphere by buoyant mantle flow (Burov et al., 2007; Guillou-Frottier et al., 2012; Cloetingh et al., 2013; Braun et al., 2014a). These driving mechanisms have the potential to trigger regional uplift of the Earth’s surface or discrete fault block uplift during reactivation of major structural zones. Such uplift creates elevated landscapes which are progressively destroyed by surface processes (e.g. erosion and weathering) and generate major topographic features. Moreover, it is these surface processes which are responsible for the



removal of significant thicknesses of crustal material (denudation) from the landscape and transportation of this material to adjacent offshore basins. Constraining the timing and magnitude of major episodes of denudation can therefore help improve our understanding of the link between plate tectonics and the evolution of macro-geomorphology over geological timescales. Low temperature thermochronology (LTT) is a well-established technique for constraining the temperature-time history path of rocks in the upper crust, which can in turn be used to infer timing and rates of erosion (Brown et al., 1994; Ehlers and Farley, 2003). This study uses apatite fission track and apatite (U-Th-Sm)/He analysis to generate thermal history information for samples as they cool through temperatures less than  $110\pm 10^\circ\text{C}$  (Lisker et al., 2009) and is the first to explicitly combine these methods in southern Africa.

The southwest African margin is a well-developed continental margin that has long been considered as a type example of a passive margin. Additionally, the presence of a major low seismic velocity anomaly zone in the upper mantle beneath the southern African plate has been interpreted as buoyant mantle upwelling creating dynamic uplift of the continental interior (e.g. Lithgow-Bertelloni and Silver, 1998; Gurnis et al., 2000; Forte et al., 2010a; Fishwick and Bastow, 2011). However, to what extent the post-rift tectonic activity and/or dynamic uplift has influenced the development of the present day topography of Southern Africa is hard to resolve because of the lack of preservation onshore of well-dated post-rift stratigraphy. For this reason, the southwest African margin is an ideal study area to utilise low temperature thermochronology to investigate the erosional and topographic evolution of this interesting area.

This work will provide a fresh perspective on the long-standing debate on the age of the first order topography of South Africa while contributing to our wider understanding of plate tectonics. Specifically this work aims to address the following main hypotheses:

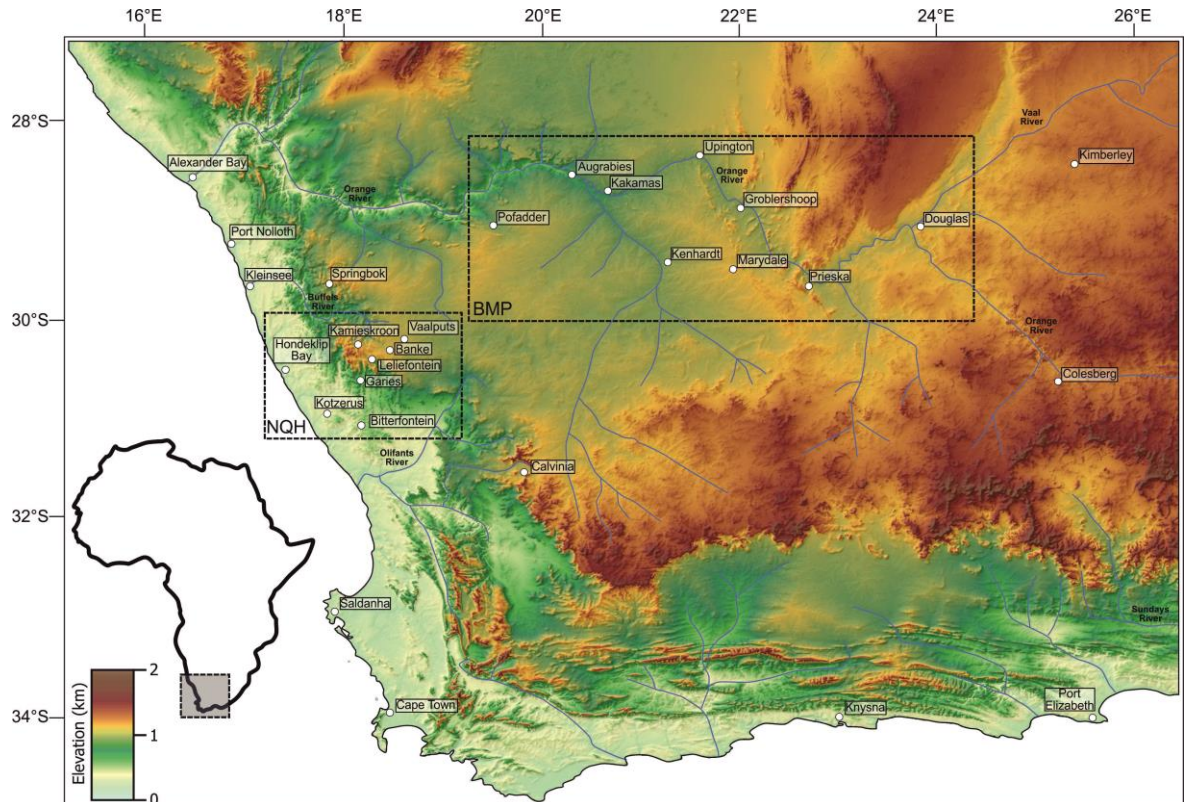
- (i) The present day first-order topography of the southwest African margin is not a rift-related feature.

- (ii) At least one phase of regional km-scale denudation occurred during the post-rift phase and was linked to reactivation of pre-existing basement structures.
- (iii) Dispersion in AHe ages can be used as a proxy for cooling rates and aid thermal history modelling alongside AFT data.

## 1.2 Study Area

The study area comprises the entire western continental margin of South Africa and the elevated continental interior. The margin formed following continental rifting between South America and Africa and opening of the South Atlantic ocean which initiated during the late Jurassic (c. 160-150 Ma). The elevated continental interior and low-lying coastal margin are now characterised by low relief and are separated by a series of escarpments or high relief escarpment zone (Fig. 1-1). Along the southern margin, the Cape Fold Belt forms an additional zone of high relief between the plateau and the coast. New thermochronology data are obtained from two regions within the overarching study area to address two different aspects of the study. The Namaqualand Highland study area (Fig. 1-1) investigates the development of the high relief escarpment zone at the continental margin. The Bushmanland Plateau study area (Fig. 1-1) focusses on the South African interior plateau and tectonic stability of the southwest margin of the Kaapvaal Craton (Fig. 1-2).

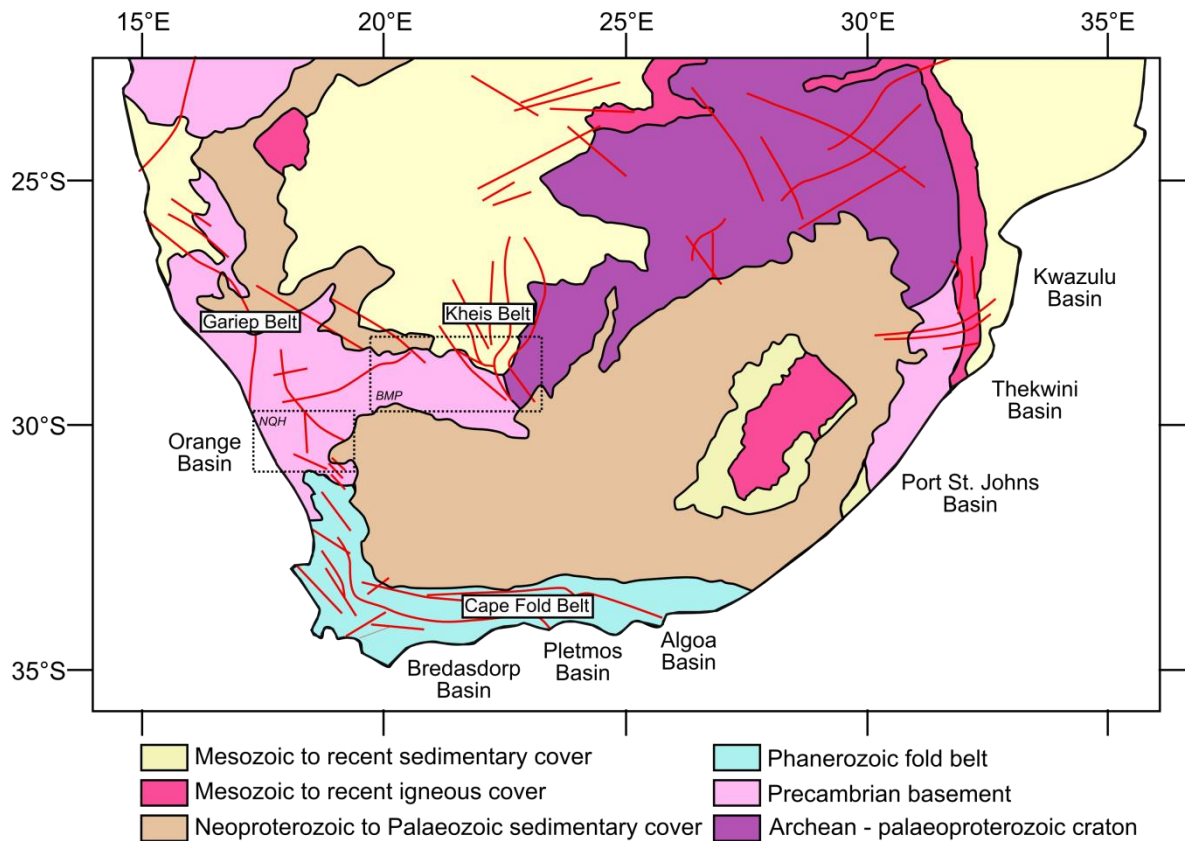
A more detailed description of the morphology and geology of the Namaqualand Highlands and Bushmanland Plateau study areas are provided in Chapter 5 and 6, respectively. A simplified geological map of Southern Africa is shown in Figure 1-2. The Archean - Palaeoproterozoic Kaapvaal craton is a collation of Archean terranes, composed of mainly granitoids and gneiss covered by Palaeoproterozoic basins (Begg et al., 2009; Baptiste et al., 2012). The SW boundary of the Kaapvaal Craton is defined by the prominent structures of the Kheis Belt and marks the transition to the younger, Meso- and Neoproterozoic metamorphic rocks of the Namqua-Natal metamorphic (NMP) province. The basement rocks of the NMP are comprised of intensely deformed, high-grade gneisses with several phases of granitoid intrusion (Groenewald et al., 1991;



**Figure 1-1: Topographic map of southwestern Africa showing major drainage channels and locations of cities, towns and farms referred to throughout the thesis. Study areas are indicated by boxes with dashed outlines, NQH = Namaqualand Highlands; BMP = Bushmanland Plateau.**

Eglington, 2006; Cornell et al., 2006). The NMP is unconformably overlain by shallowly dipping metasedimentary and metavolcanic rocks (Gresse et al., 2006).

The Permo-Triassic Karoo sedimentary basin covers much of central South Africa and is comprised of the glacially dominated Dwyka group and which is stratigraphically overlain by shallow marine sedimentary rocks of the Ecca and fluvial Beaufort Group (Johnson et al., 2006). Sedimentation within the Karoo Basin ended in the Late Jurassic (c. 200 - 175 Ma) with the voluminous and extensive eruption of the Karoo tholeiitic flood basalts and intrusion of numerous coeval dolerite sills and dykes throughout the Karoo basin (Duncan et al., 1997; Jourdan et al., 2007; Moulin et al., 2011; Svensen et al., 2012). Along the southern margin, the geology is dominated by the Cape Supergroup comprised of thick Ordovician-Carboniferous siliciclastic sediments overlying the Pan-African (c. 500 Ma) granites (Tankard et al., 2009). Crustal shortening during the Permo-Triassic intensely folded these rocks and formed the Cape Fold Belt



**Figure 1-2: Simplified geological map of southern Africa (after Schlüter, 2008). Study areas are indicated by boxes with dashed outlines, NQH = Namaqualand Highlands; BMP = Bushmanland Plateau.**

(Newton et al., 2006; Scheepers and Schoch, 2006). Late Mesozoic - Cenozoic sequences are extremely limited across the whole of southwestern Africa. Their occurrence and importance is discussed in detail in subsequent chapters.

### 1.3 Thesis outline

This study presents new low temperature thermochronology data and thermal history models determined for samples collected across the southwest African margin and these are used to infer the timing, rate and magnitude of denudation that has occurred since the onset of rifting. This is interpreted alongside independent geological observations to derive a new model for the development of the southwest African margin over the last c. 150 Ma. To create an appropriate framework for the ensuing discussion, Chapter 2 and Chapter 3 provide a critical review of the historical and modern day approaches to understanding the development of high elevation continental margins.

Chapter 2 addresses the geodynamic aspects of continental rifting, highlighting the uncertainty surrounding the structural and thermal processes which drive lithospheric extension and the importance of pre-existing structure and crustal rheology on the style of rifting.

Chapter 3 then focuses on the geomorphological development of continental margins and their hinterlands including discussions on “classical” geomorphological models of landscape evolution, surface process numerical modelling approaches and the influence of geological factors on the development and preservation of topography.

Chapter 4 moves the discussion towards technical aspects of low temperature thermochronology and, specifically, examines outstanding issues with applying this approach and how to resolve these in a pragmatic and robust manner. The theory of AFT and AHe analysis is briefly outlined; however, the main focus of this chapter is to discuss the present issues and uncertainties associated with integrating AFT and AHe datasets. A subset of the new data obtained for this study is used in this chapter to evaluate the key factors controlling AFT and AHe ages. This chapter also outlines the modelling approach and philosophy used in subsequent chapters.

Chapter 5 and 6 present and discuss the new AFT and AHe data and thermal history modelling results from the Namaqualand Highlands and Bushmanland Plateau study areas, respectively. Thermal history models are then used to derive estimates of crustal denudation responsible for exhuming rocks from depth causing them to cool. The new thermochronology data and thermal histories are discussed alongside previous geological and thermochronological studies from the area to elucidate the post-rift structural and geomorphic history of both areas.

Chapter 7 presents a regional, integrated discussion of the post-rift landscape evolution of southwestern Africa. This discussion summarises the available AFT and AHe dataset and compares the inferences made on regional denudation with the offshore sedimentary record. Key datasets used to investigate Cenozoic

landscape evolution (cosmogenic nuclide data, palaeontology and geomorphic landforms) are also summarised and critically reviewed to provide a robust chronology of landscape development from continental break-up to present day.

*Chapter 8* concludes with a summary of the revised model for the evolution of the southwest African continental margin and presents some final conclusions about both the geological and technical aspects of the study. The wider relevance of this work to similar geological settings and potential significance to industry is also outlined as are directions for further study.

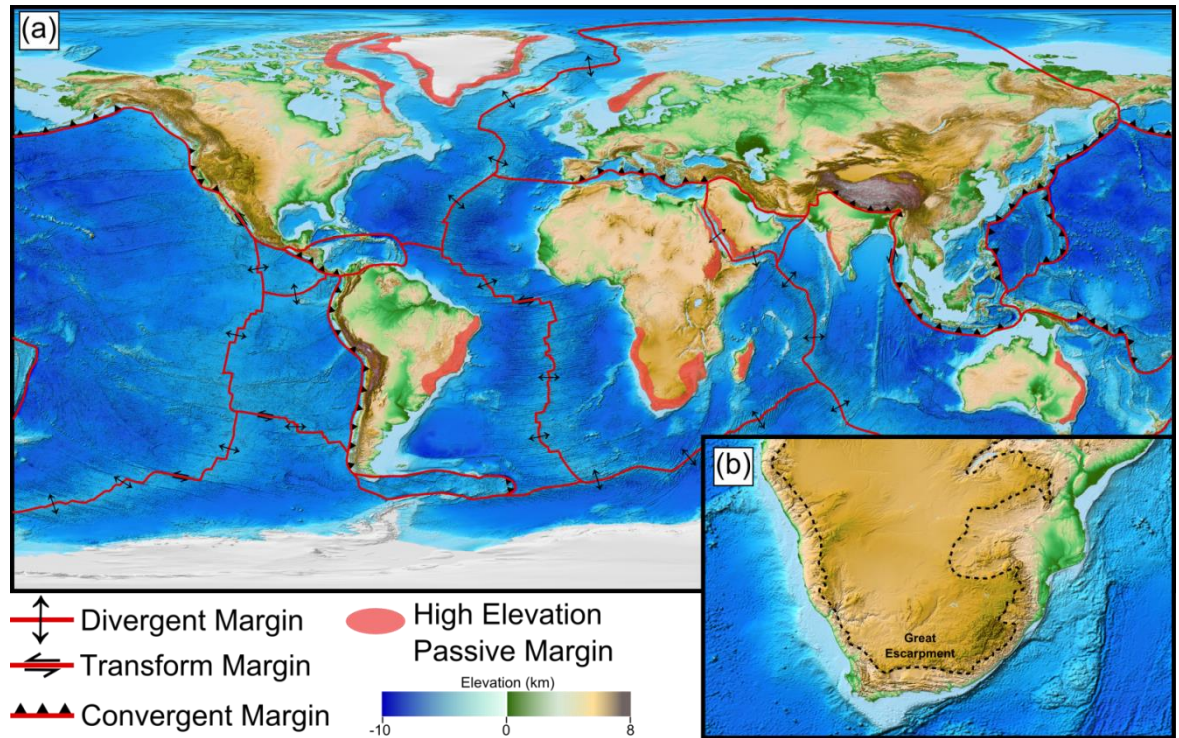
# CHAPTER 2

## REVIEWING AND REASSESSING PASSIVE MARGINS

### 2.1 Introduction: Declassifying rifted margins

The theory of continental drift (Wegener, 1915) and the modern conceptualisation of plate tectonics established a fundamental framework for understanding the Earth as a dynamic system. The theory of plate tectonics provided a means to explain many geological and geomorphological observations that were once at odds with traditional models of landscape evolution. Despite its extraordinary success as a theory, many details of plate tectonics remain poorly understood. A key to enhancing our knowledge of plate tectonics is to reach a better understanding of the local and regional mechanisms that control thermal and structural processes associated with major plate tectonic movements. Manifestations of these processes can be found in the continental lithosphere where deformation causes surface processes (i.e. uplift and erosion) to become enhanced or subdued at different periods in time. Therefore, understanding the long-term development of topography and its geomorphological evolution is central to understanding the complete geological history of a particular continental region; how plate tectonics processes operate globally and processes occurring within the inaccessible interior of the Earth.

A particular plate boundary can be described as being convergent (compressional), divergent (extensional) or translational (strike-slip) (Fig. 2-1). Much of the Earth's prominent morphological features such as orogenic belts (e.g. the Andes in South America or the Himalayas of Asia) and island arcs (e.g. the Caribbean Islands) are found at convergent margins. However, major topographic features such as extensive elevated plateaus (e.g. Southern Africa, Southeastern Australia, North East Brazil) and subsided basins (e.g. Congo Basin, Central Africa; Illinois Basin, North America; Eromanga Basin, Eastern Australia)



**Figure 2-1: Location of major plate boundaries and high elevation continental margins (after Summerfield, 1991). (b) Magnified relief map (same elevation colour scale as Figure 2-1a) of Southern Africa highlighting the Great Escarpment which marks the transition from the low elevation coastal plain to the elevated, low relief continental interior. Topographic map was taken from ETOPO1 Global Relief Model.**

can be found within so called ‘stable’ plate interiors, far from the effects of active plate boundaries (Summerfield, 1991; Moucha et al., 2008). The South African topography is characterised by its extensive high elevation interior plateau and well-developed rifted continental margins surrounding the entire sub-continent. Therefore, Southern Africa provides an excellent case study to investigate the origin of topographic anomalies at rifted margin settings and their persistence over time (Fig. 2-1b).

The term “rifted margin” is often used interchangeably with divergent margin due to the tectonic processes involved during their formation. Rifted margin settings have been studied extensively for over half a century, in no small part due to the hydrocarbon potential locked in their thick offshore sedimentary successions (Summerfield, 1991; Jackson et al., 2000; Szatmari, 2000; Corner et al., 2002; Paton et al., 2006a, 2007; de Vera et al., 2010; Kuhlmann et al., 2010). Much of the analysis of rifted margin formation and evolution has come from geodynamic studies and geomorphology. During early investigations of plate

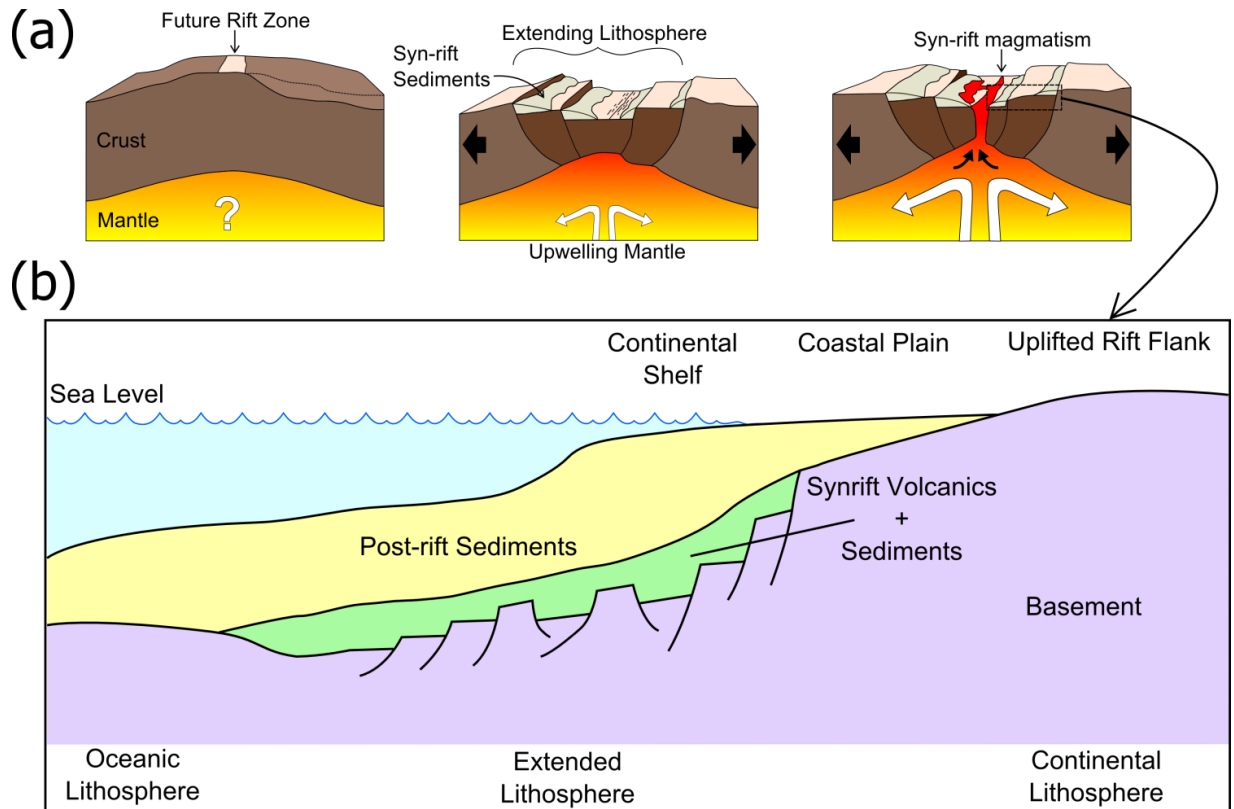


tectonics these disciplines largely tackled margin evolution independently. This resulted in model predictions, particularly of rift related topography, to conflict with one another (King, 1962; McKenzie, 1978; Steckler and Watts, 1982; Ollier, 1985; Braun and Beaumont, 1989; Weissel and Karner, 1989; Gilchrist and Summerfield, 1990).

Despite efforts to integrate the observations from these disciplines, several aspects of rifted margins remain unexplained. A consensus has been reached that divergent margins are produced by continental rifting: a process which involves stretching, thinning and faulting of the lithosphere, with some degree of intra-plate volcanic activity (Fig. 2-2) (Lister et al., 1986; Braun and Beaumont, 1989; White and McKenzie, 1989; Keen and Boutilier, 2000; Whitmarsh et al., 2001; Menzies et al., 2002; Ziegler and Cloetingh, 2004; Lavier and Manatschal, 2006; Reston, 2009; Huismans and Beaumont, 2011; Lundin and Doré, 2011; Franke, 2013). Beyond that, however, traditional methods of further classifying rifted margins (i.e. Volcanic, Non-volcanic, Passive) have arguably not provided a useful generic or globally applicable framework for understanding the true and often complex crustal architecture at a particular margin (Gaina et al., 2013). A critical review of the different approaches and theoretical outcomes of a range of rifted margin analyses from geodynamic and geomorphic perspectives is provided in this chapter and in Chapter 3, respectively. These reviews will be concluded with a summary of the present day perceptions of continental rifted margin evolution and will highlight the necessity for quantitative constraints on surface processes to improve the accuracy of current and future models.

## **2.2 Rifted margin evolution: Insights from geodynamic modelling**

Geodynamic numerical modelling techniques have been used as an approach to understand rifting dynamics since the 1970s. Since then, modelling techniques have grown more sophisticated, partly thanks to the increases in computational power allowing more complex mathematical problems to be solved and more realistic thermal dynamics and structural kinematics to be simulated. In these studies end-member scenarios have typically been put forward to describe the



**Figure 2-2: (a) Generic model of continental rifting involving lithospheric extension with mantle upwelling and some degree of syn-rift magmatism. The timing of mantle upwelling relative to extension of the lithosphere is unresolved and discussed in Section 2.2.1 (after Franke, 2013). (b) Simple schematic diagram of a rifted margin's offshore and continental architecture (after Summerfield, 1991).**

formation and characteristics of one group of margins or another. Over time new information provided from different disciplines investigating rifted margins contradict certain aspects of these end-member scenarios. Frequently, however, these models yield common features strengthening their validity, and become the foundation for more complex models. The following section provides background to these simple end-member models and also to modern day thermo-mechanical models that have enhanced our knowledge of rift margin evolution. Ultimately, these models have brought us from having to rely on simple end-member scenarios to being able to deal with styles of rifting that encompass a more complex evolution over space and/or time (e.g. Kuznir and Karner, 2007; Péron-Pinvidic and Manatschal, 2009; Blaich et al., 2011; Huismans and Beaumont, 2011; Lundin and Doré, 2011; Andersen et al., 2012; Beaumont and Ings, 2012; Armitage et al., 2013).

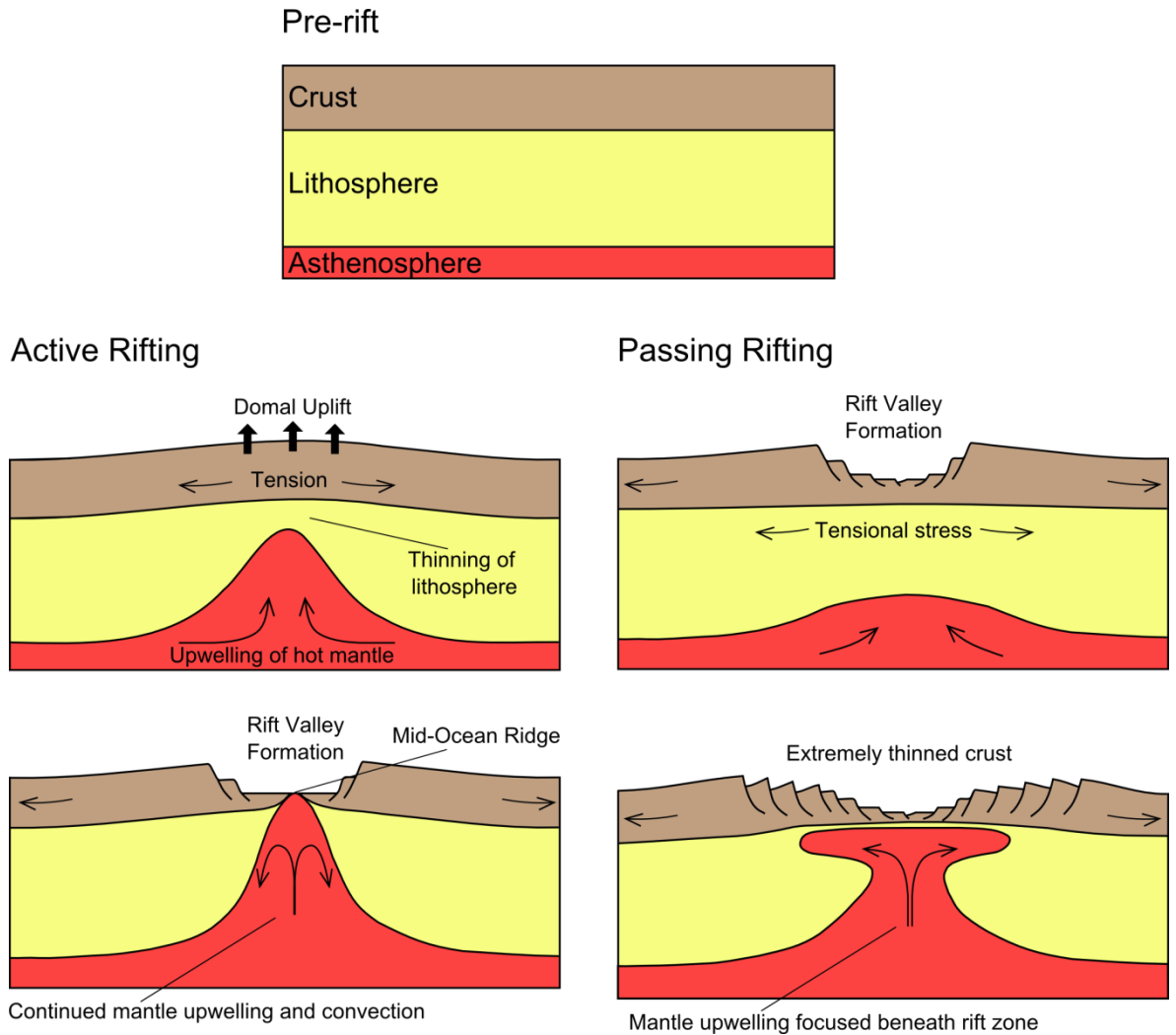
### 2.2.1 Rift initiation: active vs. passive rifting

In early investigations of rift zone initiation a key issue to address, and one that is still not fully understood (e.g. Kuszniir and Karner, 2007; Franke, 2013; Koopmann et al., 2014), was the link between lithospheric extension and mantle upwelling. On one hand, thermally buoyant mantle upwellings are thought to be responsible for triggering lithospheric extension and thinning (active rifting) while on the other, it is suggested that these upwellings are initiated as a result of lithospheric extension focussing the rise of relatively hotter mantle material into the rift (passive rifting) (Fig. 2-3) (Menzies et al., 2002; Ziegler and Cloetingh, 2004; Anderson and Natland, 2005).

The active rifting model involves the presence of an upwelling of hot mantle (c. 150 to 200°C above normal mantle temperatures) beneath the lithosphere. This upwelling mantle plume would cause partial melting of the mantle by decompression and a period of intense volcanism, marking the onset of rifting (White and McKenzie, 1995). Prior to rifting, the lithosphere is uplifted, creating a dome or domes above the underlying mantle plumes. In response to this uplift, the lithosphere ruptures under an extensional stress caused by its higher potential energy, and extends laterally away from the centre of the upwelling region, thinning the crust in the process (Dewey and Burke, 1975; Bott and Kuszniir, 1979; Bott, 1981).

The passive rifting model envisions rifted margins as a consequence of far-field in-plane horizontal lithospheric stresses (e.g. slab pull, basal drag, ridge push) causing extension without the need for an associated plume (McKenzie, 1978; McKenzie and Bickle, 1988). However, during progressive thinning of the lithosphere, upwelling of asthenospheric mantle is suggested to cause partial melting at the base of the lithosphere over a wide area, and potentially result in significant thermal uplift and magmatism following the onset of rifting (White and McKenzie, 1989).

In general, there has been a shift away from the traditional “vertically forced” view of plume driven rifting (Ziegler and Cloetingh, 2004; Foulger, 2007; Torsvik



**Figure 2-3: Schematic representation of the major differences between Active and Passive rifting styles (after Ziegler and Cloetingh, 2004).**

et al., 2009; Franke, 2013). However, the contribution of mantle upwelling to the overall weakening of the lithosphere and its control on the presence and volume of magma exhumed at a particular margin is still significant (Menzies et al., 2002; Ziegler and Cloetingh, 2004). At margins traditionally referred to as “Volcanic Margins” (e.g. Paraná-Etendeka, South Atlantic margin; North Atlantic Igneous Province; Deccan Large Igneous Province, SW India) total volumes of igneous rock added to the continental margin during the rifting phase range from  $1 \times 10^6$  -  $1 \times 10^7$  km<sup>3</sup>. It is suggested that at volcanic margins, igneous material is emplaced over an extensive area (c. 200 km from the rift) over short geological timescales (typically < 5 Myr) (White and McKenzie, 1989). The link between magmatism at rifted margins is further complicated by large volumes of igneous

material being observed at so-called “Non-Volcanic” margins (e.g. Müntener and Manatschal, 2006) and potentially less syn-rift magmatism observed at “Volcanic” margins (e.g. Koopmann et al., 2014). The timing of this volcanism in relation to uplift and rifting therefore has become central to our understanding of the primary forcing driving rift initiation (Summerfield, 1991; Menzies et al., 2002; Franke, 2013; Koopmann et al., 2014).

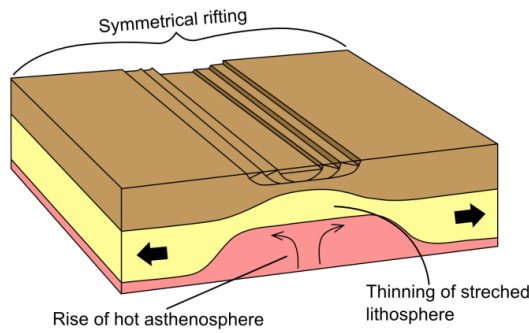
The relationship between lithospheric thinning and mantle upwelling is still a contentious issue within margin studies and it is likely that a particular rifted margin’s evolution will pass through a phase akin to “passive” rifting prior to an “active” phase with associated magmatism (Wilson, 1993; Burov and Cloetingh, 1997; Reemst and Cloetingh, 2000; Huisman et al., 2001). Regardless of the active or passive style, both models highlight the necessity of significant extension and thinning of the crustal lithosphere accompanied by some degree of volcanic activity.

### **2.2.2 Lithospheric extension and thinning: pure shear vs. simple shear**

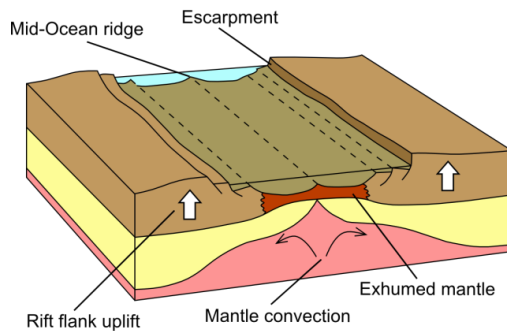
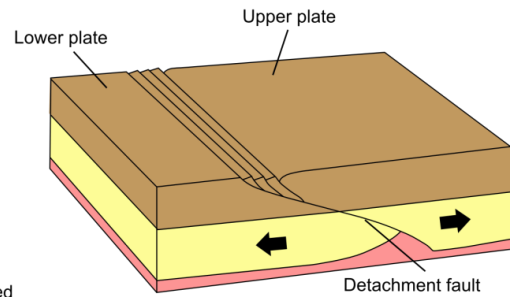
Early models of rifting assumed instantaneous extension, uniform with depth, throughout the entire lithosphere and attributed the primary source of magmatic activity to be the presence of an anomalously hot upwelling from the mantle. However, the style of structural features observed across a margin and the variable morphology of rift flank uplift required to match observations was not reproduced very well by these early models (McKenzie, 1978; White and McKenzie, 1989; Bown and White, 1995; Keen and Boutilier, 2000).

A simple model of pure shear lithospheric extension typically leads to the development of a symmetric rifted margin (Fig. 2-4) (Summerfield, 1991). Thinning of the lithosphere focuses hot mantle asthenosphere beneath the rift axis which becomes the site of extrusive magmatism (McKenzie, 1978; Buck et al., 1988; Latin and White, 1990). A significant flaw in early uniform extension-pure shear models was their inability to generate the uplift required to match observations of the adjacent rift flanks (Summerfield, 1991). To address this issue, non-uniform extension was explored; in these models extension varies

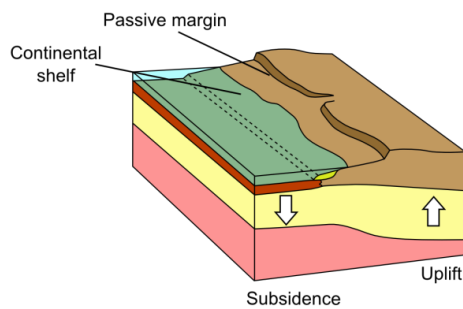
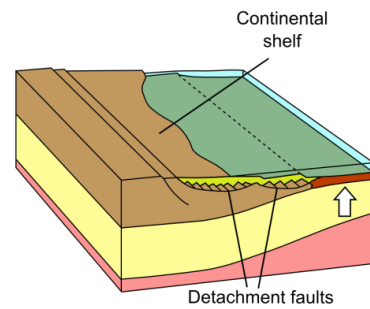
Pure Shear



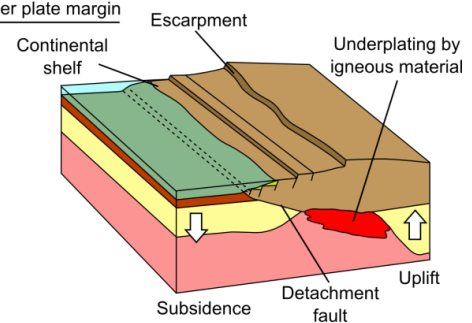
Simple Shear


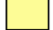






Lower plate margin



Upper plate margin



- |   |                    |  |             |
|---|--------------------|--|-------------|
|  | Continental Crust  |  | Lithosphere |
|  | Oceanic Crust      |  | Mantle      |
|  | Syn-rift Sediments |  | HVLC        |

**Figure 2-4: Schematic representation of the major differences between simple and pure shear lithosphere extension styles (after Summerfield, 1991).**

with depth, location and thermal structure of the lithosphere (Reemst and Cloetingh, 2000; Davis and Kuszniir, 2004; Kuszniir and Karner, 2007; Reston, 2007). Despite this modification, hot mantle still becomes focused beneath the thinned lithosphere but with the addition of ductile deformation occurring within the lower crust, significant uplift of rift flanks could be produced (Kuszniir and Ziegler, 1992).

An alternative view of lithospheric extension is simple shear style deformation controlled by a major detachment fault cutting through the brittle crust into a ductile mantle lithosphere (Wernicke, 1985; Lister et al., 1986; Voorhoeve, 1988; Issler et al., 1989). This style ultimately produces rifted margin settings that are asymmetric both in terms of the distribution of magmatism across the rift and its structural features (Fig. 2-4) (Wernicke, 1981, 1985; Lister et al., 1986). This asymmetry is caused by extension occurring along major detachment faults and results in an upper and lower plate margin (Fig. 2-4) (Lister et al., 1986; Voorhoeve, 1988). Due to the asymmetry of rifted margins produced through simple shear style extension, the uplift and subsidence history of the upper and lower plate during the syn and post rift phases are also predicted to be distinctly different. On the lower plate, unloading of the lithosphere promotes isostatic uplift but thinning of the lithosphere results in overall subsidence of the margin (Issler et al., 1989). On the upper plate, however, the presence of hot upwelling mantle material promotes uplift, while thermal weakening of the lithosphere promotes pure shear in the lower crust and mantle lithosphere (Ziegler and Cloetingh, 2004). Despite the popularity of depth dependant models of lithospheric extension and their ability to explain more features at particular margins than simple uniform extension models, the conditions which control depth dependent extension are still being investigated (e.g. Huisman and Beaumont, 2008).

### **2.2.3 Modern rifted margin modelling: joint physical, thermal and chemical models**

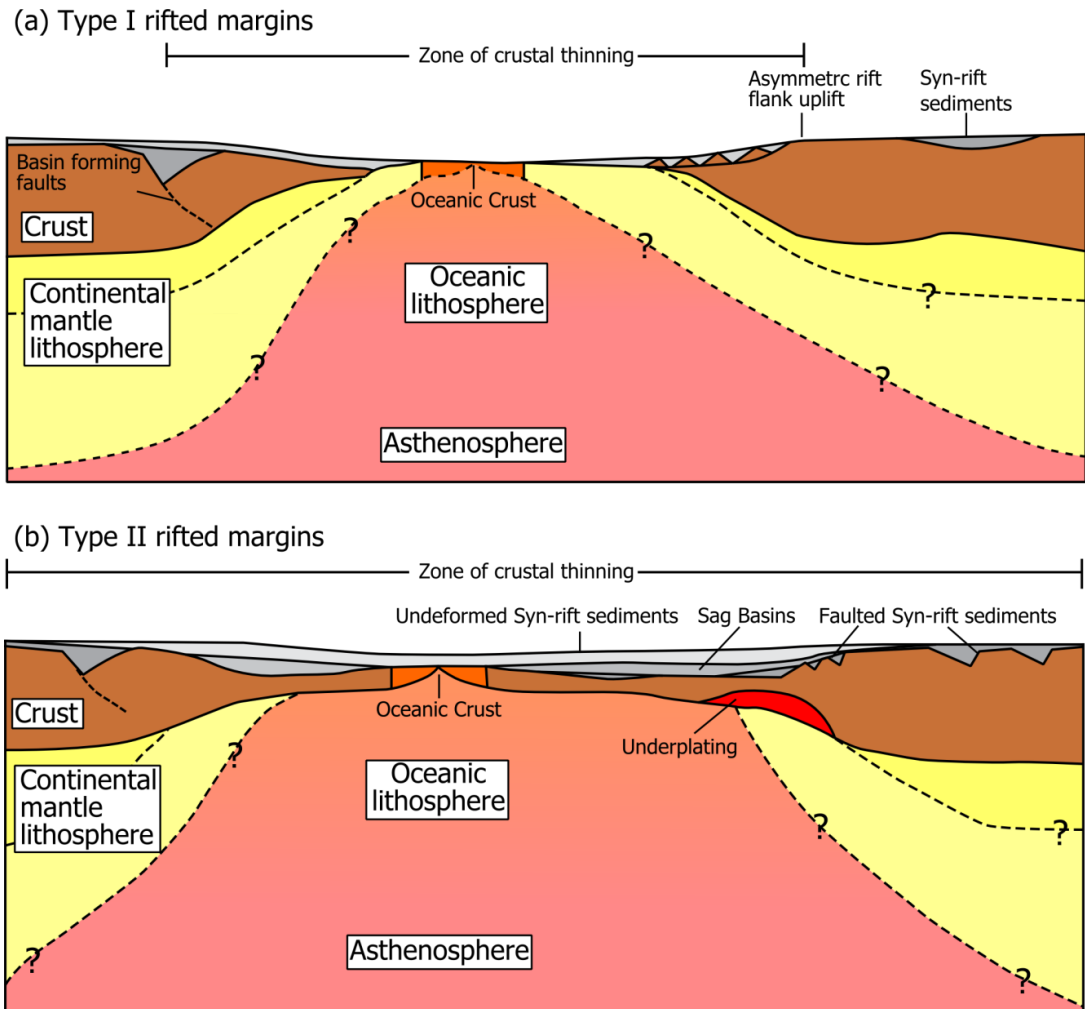
It has long been suggested that a major control on the style of continental rifting and stability of the lithosphere during depth dependant extension is the rheology and composition of the lithosphere (Braun and Beaumont, 1989). However, it is only recently that numerical modelling techniques have been able to incorporate complex rheological structure within the crust and mantle and explore its influence on continental deformation (e.g. Lavier and Manatschal, 2006; Huisman and Beaumont, 2008, 2011; Lundin and Doré, 2011; Beaumont and Ings, 2012; Armitage et al., 2013). Different rheological layers promoting ductile or brittle deformation can act to decouple the crust from the mantle lithosphere

and allow them to thin independently (Lavier and Manatschal, 2006). Modelling by Huisman and Beaumont (2008, 2011) and later Beaumont and Ings (2012) investigated the effects of depth-dependant extension with a decoupled crust/mantle boundary.

This work presented two end member scenarios for depth-dependant extension (Fig. 2-5). At “Type I” margins the crust and mantle are strongly coupled, creating a brittle upper lithosphere and ductile lower lithosphere, whereas at “Type II” margins, a weak crustal rheology causes the crust and upper mantle to decouple. Type I margins can be expected to form after an initial phase of widely distributed extension which propagates inward until a main centre of rifting accommodates the associated stress (Fig. 2-5a). Decoupling the upper and lower lithosphere results in Type II margins where both layers can extend and thin independently of one another (Fig. 2-5b). This style of rifting begins with stretching of the upper and middle crust over a wide region becoming less pronounced with distance from the main rift zone. At the same time, localised mantle necking leads to rupture of the mantle lithosphere prior to crustal breakup.

An additional feature of the Type II scenario is that during rifting of the mantle lithosphere, advection allows hot asthenosphere to be exhumed and cooled, forming a buoyant underplate beneath the crust (Huisman and Beaumont, 2011, Beaumont and Ings, 2012). The presence of this partly metasomised lower continental mantle underplate can result in a reduction of subsidence promoting a shallow marine environment for the developing rift (Huisman and Beaumont, 2011) and/or a two-stage rifting phase. An alternative possibility is that the presence of such low viscosity and density material will create a counterflow back towards the rift axis (Beaumont and Ings, 2012). The inward lateral flow of the lithospheric mantle would result in decompression, melting and emplacement at distal parts of the margin during the rupture of the crust (Beaumont and Ings, 2012). It is suggested that the mechanisms involved in these depth-dependent models are more likely to produce magma poor margins; however, the additional influence of an anomalously hot, ‘active’ upwelling mantle plume has still not been fully explored.





**Figure 2-5: Illustration of the characteristic features of (a) Type I and (b) Type II rifted continental margins (after Huisman and Beaumont, 2011). At Type I margins break-up of the crust occurs before mantle lithosphere causing exhumation and exposure of serpentinized continental mantle lithosphere. Other characteristics include limited magmatism during rifting and delayed establishment of sea-floor spreading and normal ocean crust production. At Type II margins limited syn-rift rift flanks are observed and subsidence is limited due to hot asthenosphere replacing continental mantle lithosphere beneath the rift. Rupture of the continental mantle lithosphere prior to break up of the crust promotes upwelling of hot material and syn-rift magmatism.**

Decoupling of the crust and mantle lithosphere and mantle underplating is predicted to prolong extension of the upper crust and will produce an extremely wide rifted margin (Huisman and Beaumont, 2011). Hyperextension of a rifted margin as described by Lundin and Doré (2011) is a rifted margin that exhibits crustal stretching factors of 3 - 4 or greater. Investigations of the effects of hyperextension across rifted margins largely agree that hyperextension will lead to a severe weakening of the lithosphere by causing the crust to become heavily faulted (Maggi et al., 2000; Burov and Watts, 2006; Lundin and Doré, 2011; Andersen et al., 2012). If these faults are able to cut entirely through the crust,

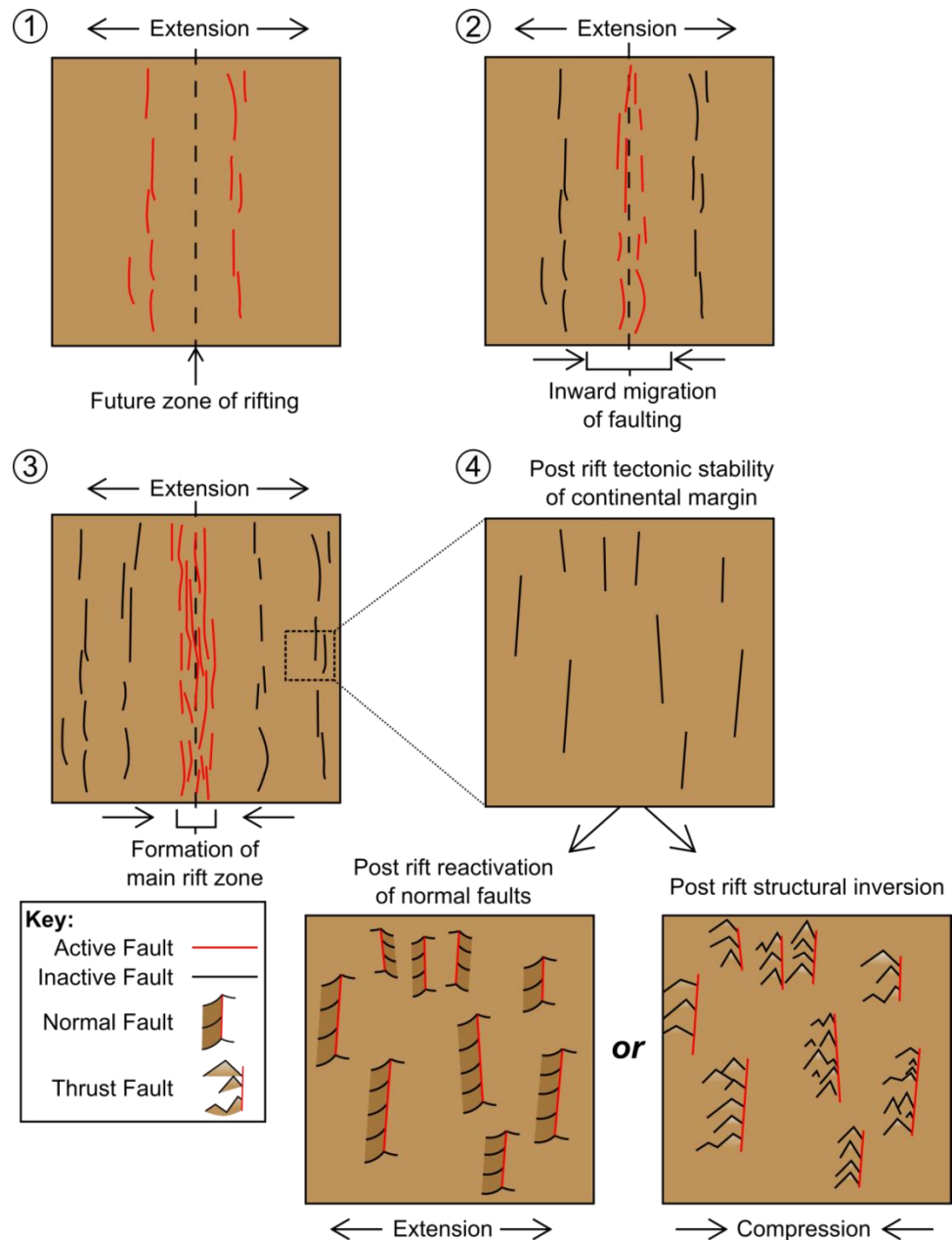
water may infiltrate the mantle causing serpentinization of the upper mantle and create a buoyant, low density “lower crustal body” beneath the rift (White et al., 2008; Lundin and Doré, 2011).

The Northeast Atlantic rifted margin is characterised by widespread magmatism during rifting and yet also exhibits rift basins that can be referred to as being hyperextended (Lundin and Doré, 2011), suggesting hyperextension is not solely a precursor to so-called magma poor margins. The association of hyperextended margins with high-velocity lower crustal bodies suggest that there may be a relationship between a weakening of the lithosphere and serpentinization of the upper mantle. This weakening of the lithosphere prolongs extension and makes the lithosphere more susceptible to future deformation. As stated by Lundin and Doré, (2011), hyperextension models of rifted margin evolution may be appropriate for both magma-rich and magma-poor margins. It is likely that hyperextension is not a special form of the magma-poor end member rifting scenario but instead is another poorly understood mechanism that causes observations at rifted margins to conflict with predictions derived from modelling approaches.

## **2.3 The influence of structural inheritance**

### **2.3.1 Pre/syn-rift**

Pre-existing crustal and mantle-lithospheric discontinuities have long been identified as a major influencing factor on the location of the rift zone (Ziegler and Cloetingh, 2004). In early models, sites of lithospheric weakness that define the location and geometry of rifting were incorporated as an initial condition of the model (White and McKenzie, 1989; Bown and White, 1995; Keen and Boutilier, 2000). The formation of the typical “Atlantic-type” rifted margins involves a phase of widespread tensional stresses where small scale rifts are initiated around the location of future continental break-up and develop complex graben systems (White and McKenzie, 1989, Ziegler and Cloetingh, 2004). Over time the zone of crustal break-up accommodates the majority of stress and becomes the main focus of rifting activity (Fig. 2-6). Syn-rift graben systems become



**Figure 2-6: Steps 1-4 present a sketch model of fault migration during lithospheric extension whereby the main focus of faulting migrates inward and becomes concentrated at the future rift zone, leaving marginal faults inactive. The bottom panels represent reactivation of these structures during a post rift phase of extension or compression.**

progressively less active until break-up ensues and they become tectonically inactive and the margin becomes “passive” (Ziegler and Cloetingh, 2004).

More generally, the orientation of rift initiation relative to the pre-existing structural grain is suggested to be intimately linked to the style of lithospheric deformation (Ziegler and Cloetingh, 2004; Armitage et al., 2010; Autin et al., 2013). Deformation of the lithosphere by pure-shear extension is typical for rifts

cross-cutting the structural grain as the orientation of stress during rifting will not reactivate pre-existing faults (McKenzie, 1978; Govers and Wortel, 1993; Ziegler, 1996). The opposite is the case for rifts that are sub-parallel to the regional basement fabric. Zones of crustal weakness will be reactivated and linked, causing decoupling of the crust and mantle lithosphere promoting simple-shear lithospheric extension (Wernicke, 1981; Lister et al., 1986; Harry and Sawyer, 1992).

Analogue modelling by Corti et al. (2013) has shown that inward focussing of rifting is controlled by (i) the thickness of the brittle and ductile layers of the lithosphere; (ii) the extension rate; (iii) the obliquity of the rift to the orientation of extension and (iv) the width of the weak zone accommodating extension. An increase in (i) and/or a decrease of the remaining factors will promote a greater amount and prolonged phase of slip on the outer faults. Modern day thermo-mechanical rifting models also indicate that extension can be widely distributed throughout the lithosphere promoting hyper- or polyphase extension (e.g. Lavier and Manatschal, 2006; Blaich et al., 2011; Huisman and Beaumont, 2008, 2011; Lundin and Doré, 2011; Reston and McDermott, 2014).

### **2.3.2 Post-rift**

The initiation of the main phase of continental break up is preceded by an inward migration of faulting from the boundaries of the rift zone leaving smaller outer rifts inactive (Ziegler and Cloetingh, 2004). However, the manner in which the crust and mantle evolve during the syn and post-rift phases is still largely uncertain (Fig. 2-6). This is due to uncertainty over whether, during extension, the associated structural processes will strengthen or weaken the lithosphere (Aitken et al., 2013; Kennet and Iaffaldano, 2013). Despite the mechanisms being unresolved, compelling evidence (discussed in subsequent chapters) exists that post-rift reactivation has occurred at many so-called passive continental margins. This raises the possibility that “abandoned” rifts created during the initial stages of rifting are reactivated at some later stage or that pre-existing ancient structures are accommodating post-rift deformation (Ziegler and Cloetingh, 2004).

Post-rift reactivations suggested for many “Passive” margin settings may be triggered by a variety of driving factors. Compression may be induced by the convergence of two plates or far-field effects of active plate boundaries (e.g. Ziegler et al., 1995; Holford et al., 2009; Japsen et al., 2009, 2012; Cloetingh and Burov, 2011; Cogné et al., 2012). Renewed phases of extension may be associated with changes in regional plate movements (Eagles, 2007), changes in the regional stress field generated by lithospheric resistance to plate rotation (Bird et al., 2006) or by a lateral stresses induced by vertical movements of the crust driven by flexural isostasy (e.g. Redfield et al., 2005a, b; Salomon et al., 2014) and/or uplift over hot upwelling mantle plumes (e.g. Guillou-Frottier et al., 2012; Burov and Gerya, 2014).

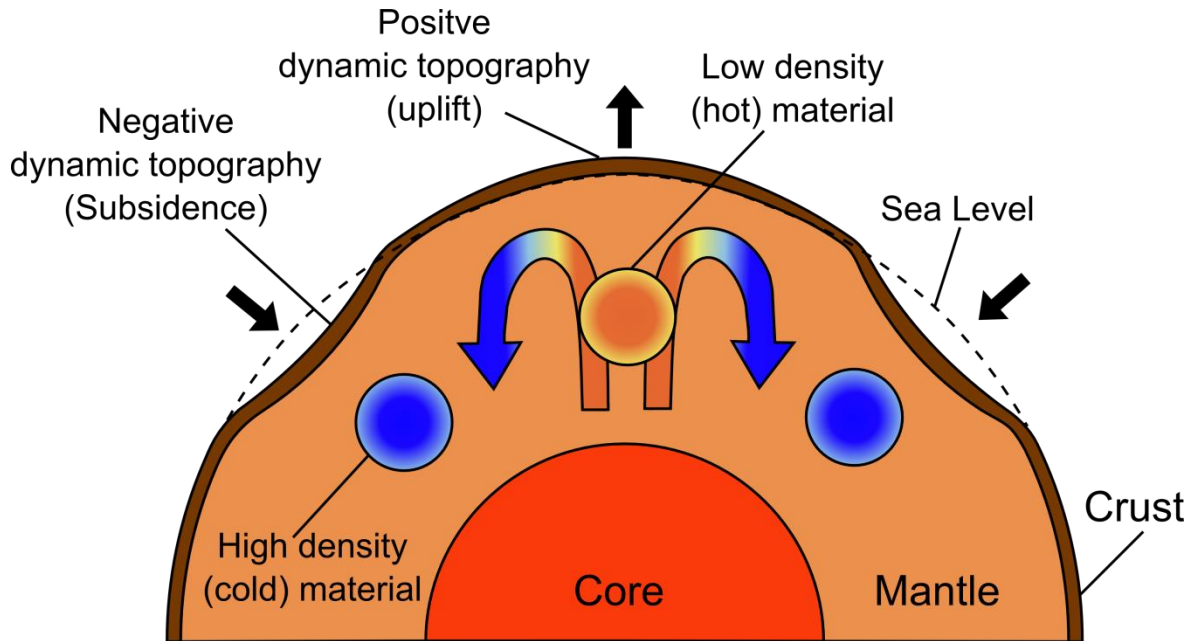
Mantle convection is a well-established mechanism for extending the lithosphere regardless of whether rift initiation is plume driven and has been attributed as the cause of regional post-rift epierogenic uplift episodes (Praeg et al., 2005). However, the importance of heat flow within the crust and upper mantle lithosphere during the post-rift evolution has only recently been evaluated (e.g. Holford et al., 2011; Beaumont and Ings, 2012; Armitage et al., 2013). In the hyperextension model by Lundin and Doré (2011), it is suggested that at magma rich margins the underplated edges of the margin are stronger than the interior that is underlain by serpentized mantle. As a result, during the post-rift phase stresses are focused on this part of the margin which is therefore more prone to deformation. Underplating is a feature common in Huisman and Beaumont, (2011) Type II margins (see also, Beaumont and Ings, 2012) and is thought to be present at many continental margins, manifested as a lower crustal body with high seismic velocity (White et al., 2008; Hirsch et al., 2009). An additional influence may be the presence of a highly radiogenic crustal zone where the consequent elevated heat flow could thermally weaken the crust, perturb the underlying mantle flow or add buoyancy to the overlying lithosphere (Pysklywec and Beaumont, 2004; Holford et al., 2011; Armitage et al., 2013).

## 2.4 The role of regional dynamic uplift

Rifted margin evolution can be thought of in terms of the interaction between lateral processes during rifting (i.e. extension) and a vertical response of the lithosphere (subsidence/uplift). Traditionally, the initial vertical response of the lithosphere at rifted margins was described in terms of doming of over a mantle upwelling, followed by subsidence during thermal relaxation with an associated isostatically driven upwarp of rift flanks (Braun and Beaumont, 1989; White and McKenzie, 1995; Rouby et al., 2013). It is interesting, in this context, that a recent major focus of the geodynamic community is to understand the link between widespread uplift caused by anomalous upwellings of buoyant material from the lower mantle imposing vertical stresses on the base of the lithosphere beneath continental interiors (Simmons et al., 2007; Moucha et al., 2008; Conrad and Husson, 2009; Boschi et al., 2010; Liu and Gurnis, 2010).

The concept of vertical stresses being imposed on the base of the lithosphere from upwelling mantle flow and consequently inducing surface uplift was proposed by (Pekeris, 1935) and termed “Dynamic Uplift” (Fig. 2-7). Over the past two decades investigations of mantle dynamics have provided insights into the origin and structure of mantle thermal and/or chemical anomalies and how they drive mantle flow and interact with the overlying lithosphere (e.g. Nyblade and Robinson, 1994; Burke, 1996; Lithgow-Bertelloni and Silver, 1998; Gurnis et al., 2000). For a review of the geodynamic modelling techniques that have been used in these investigations see Flament et al. (2013).

Dynamic uplift is typically expected to occur over long wavelengths (1000s of kms) with relatively small amplitudes (c. < 2 km), if the lithosphere is treated as a rheologically uniform elastic layer. Mantle flow may also generate small scale, short wavelength and significant amplitude topographic anomalies if more complex lithosphere rheology is incorporated (Moucha et al., 2008; Petersen et al., 2010; Burov, 2011; Cloetingh et al., 2013; Flament et al., 2013) and this is an area that warrants further investigation. In either case, uplift occurs as the lithosphere attempts to gravitationally balance the viscous stresses imposed at the base of the lithosphere induced by mantle upwelling. Models of dynamic



**Figure 2-7: Simple sketch of the influence of mantle convection on the overlying topography. Hot, low density, mantle upwelling promotes uplift, while downward convection of colder, higher density, mantle coupled with isostatic effects, may cause subsidence in areas adjacent to uplifted regions (after Braun, 2010).**

topography are still hindered by several aspects: (i) our poor knowledge of lithospheric structure on a global scale, which is required to understand present day dynamic topography (Moucha et al., 2008); (ii) our poor knowledge of the chemical composition of the upper and lower mantle and the effect this has on the thermochemical circulation (Simmons et al., 2007); (iii) lack of quantitative constraints on the surface response (i.e. erosion) to dynamic topography (iv) contradictory predictions of uplift and subsidence of the lithosphere in different mantle circulation models (Moucha et al., 2008; Müller et al., 2008; Liu and Gurnis, 2010; Van Wijk et al., 2010); (v) the difficulty of identifying short wavelength (c. 100 km) dynamic topography from isostatic vertical motions (Moucha et al., 2008; Flament et al., 2013). So, while dynamic uplift seems to play a significant role in the evolution of regional topography of continental interiors, especially in southern Africa, how this mechanism integrates with thermo-mechanical mechanisms controlling continental margin lithosphere extension and how it ultimately influences rift margin evolution remains elusive.

## 2.5 Current thinking on the geodynamical setting of the southwest African rifted margin

The early models explaining the evolution of continental margins as either active or passive, or evolving by pure or simple shear, are an oversimplification of the reality, but they have nonetheless provided the foundations upon which current and more advanced models are built. Rheological properties of the entire crust-mantle system have been shown to have a major control on the style of depth-dependant extension of the lithosphere (Huisman and Beaumont, 2008, 2011). The pattern and mode of mantle convection and the location of zones of crustal weakness will influence lithospheric extension and govern the evolution of the rifted margin over space and time and influence the volume and distribution of any associated magmatism (Müntener and Manatschal, 2006; Armitage et al., 2010). How these ancient zones of crustal weakness and rift-related structural discontinuities evolve following the major period of rifting is unclear, but they have the potential to change our current thinking on continental margin evolution.

Within the current literature there is evidence that the South Atlantic volcanic passive margin may have significantly less volcanic material than previously thought (Koopmann et al., 2014) and has experienced significant post-rift reactivation (Brandt et al., 2003, 2005; Kounov et al., 2009, Viola et al., 2012). Blaiçh et al. (2011) suggest that the “volcanic” South Atlantic margin and “non-volcanic” Central Atlantic margin have shared similar polyphase rifting styles. Rifting in the South Atlantic is proposed to have initiated during the Late Jurassic - Early Cretaceous and propagated northwards from a position close to the Falkland-Agulhas Fracture Zone (Jackson et al., 2000). This predates the emplacement of the Parana-Etendeka continental flood basalts (c. 135 - 130 Ma) (Hawkesworth et al., 2000; Marsh et al., 2001) which are coeval with break-up (Eagles, 2007; Heine et al., 2013). This suggests that the rifting style may have initially been similar to a developing “non-volcanic” margin before later experiencing volcanism due to the interaction of the rift with an underlying mantle plume prior to complete rupture of the continental crust (Blaiçh et al., 2011, 2013; Franke, 2013; Koopmann et al., 2014). The style of lithospheric



extension in the absence of thermal anomaly was likely depth-dependent (Unternehr et al., 2010; Huisman and Beaumont, 2011), prolonged (e.g. Lundin and Doré, 2011; Péron-Pinvidic et al., 2013) and asymmetric (Jackson et al., 2000; Blaich et al., 2011; Becker et al., 2014). In summary, end-member scenario models do not describe the evolution of the South Atlantic rifted margins, and possibly all rifted margins, in any great detail and further study of the entire margin is required.

Most margin settings are characterised by complex fault systems both in terms of their geometry and timing, and often preserve less or more volcanic material than would be expected for typical end-member volcanic and non-volcanic style margins, respectively (Müntener and Manatschal, 2006; Manatschal and Müntener, 2009; Blaich et al., 2011; Franke, 2013; Koopmann et al., 2014). The classification terms that are assigned to a particular margin are frequently at odds with observations and are therefore inappropriate (Redfield et al., 2005a, b; Péron-Pinvidic and Manatschal, 2009; Blaich et al., 2011; Andersen et al., 2012; Paton, 2012; Gaina et al., 2013; Franke, 2013; Koopmann et al., 2014). Structural inheritance, rift-related structures, thermal weakening of the lithosphere and or an anomalously hot radiogenic crust, may all contribute to weakening the continental lithosphere and prime a “passive” continental margin for a renewed phase or phases of tectonic activity long after the initial rifting event. The driving factors that trigger this reactivation are likely unique to the geological or geodynamical processes acting on the margin and the orientation of the regional stress field relative to the structural fabric. If structural reactivation during the drift phase is a phenomenon that is common across all “passive” margins, then it is necessary to understand whether the trigger for reactivation is due to a combination of processes specific to a particular margin, or if some common influential factor exists that acts across all margins and typically leads to as yet unrecognised phases of post-rift evolution.

## **2.6 Conclusions**

In detail, rifted margins are an enigmatic element of plate tectonics that are more complicated and far more interesting than the traditional classification

terms would lead one to believe. Much of our knowledge of rifted margin evolution is provided by numerical modelling approaches that require independent and quantitative constraints to validate their predictions. Advanced geophysical surveys and improved seismic imaging integrated with offshore well data contribute to this validation by providing new information on the stratigraphy and crustal architecture of the offshore parts of the margin. On the terrestrial sector of many rifted margins, however, this geological record has largely been eroded away and with it the record of major periods of uplift associated with rift and post-rift tectonics. Therefore, other approaches must be employed to investigate the spatial and temporal nature of deformation experienced by the continental lithosphere. This study will employ low temperature thermochronometry to derive cooling histories that can be used to quantify periods of denudation across the margin.

The following chapter explores the approach to understanding passive continental margins from a geomorphological perspective and review the current debate concerning the origin and longevity of high elevation continental margins in particular. The role that thermochronology has played in validating or challenging the results of different surface process models is also discussed. New apatite fission track analysis and apatite (U-Th-Sm)/He data from the Atlantic continental margin of South African and from the continental interior are presented and discussed in subsequent chapters to resolve many outstanding questions on the long-term development of the southwest African continental margin.

# CHAPTER 3

## THE TECTONIC GEOMORPHOLOGY OF HIGH ELEVATION CONTINENTAL MARGINS

### 3.1 Introduction

How the Earth's topography has developed and evolved over geological timescales is a fundamental question for geomorphologists. This question can be addressed to both large scale, regional topography, or to small, local, perturbations in relief. In both cases the topography itself is carved out by surface processes (i.e. erosion and weathering) which in turn are enhanced or subdued over different periods of time due to external forcing such as climate and tectonics. This chapter will present an overview of the historical and present day models and theories used to explain the development of large-scale topography. This overview will first look at classical geomorphological models of long-term landscape evolution and their modern day adaptations and discuss their limitations in explaining long term landscape development. The discussion will then move to a review of some of the numerical modelling approaches to explaining landscape evolution before discussing landscape evolution in the context of continental margins. Through this discussion the need for empirical constraints on the timing and rates of erosion will become apparent and examples of how thermochronology has provided such constraints will be presented. Finally, recent insights into the influence of in-plane regional stresses, vertical mantle driven stresses and compositional and structural heterogeneity in the crust on intraplate deformation is described.

### 3.2 Long-term landscape evolution

Early theoretical models of long-term landscape evolution designed by geomorphologists at the beginning of the twentieth century were formulated without the present day framework of global plate tectonics (e.g. Davis, 1899; Penck, 1924; King, 1953a). Although the concept of continental drift was still in

its infancy, it's relevance to geomorphology was appreciated (e.g. King, 1942, 1953b; Du Toit, 1937, 1954). However, it was not until the general acceptance of plate tectonics in the 1960s that these models could be evaluated as part of the wider Earth's dynamic system.

In the latter half of the twentieth century our increasing understanding of isostatic movements of the Earth's surface (e.g. Gilchrist and Summerfield, 1991; Gilchrist et al., 1994); in-plane stress created by plate movements (e.g. Cloetingh et al., 1985); thermal convection within the mantle (e.g. Conrad and Gurnis, 2003) and the lithological and climatic controls on erosion patterns (e.g. Kooi and Beaumont, 1994) led to a re-evaluation of traditional landscape evolution models. Despite these advances, support for classical models, or at least certain aspects of them, persist and continue to underpin many modern approaches to macro-geomorphology (Ollier and Marker, 1985; Partridge and Maud, 1987, 2000; Ollier and Pain, 1997; Japsen et al., 2012; Green et al., 2013; Lidmar-Bergström et al., 2013; Rabassa and Ollier, 2014; Römer, 2010; Bonow et al., 2014; Twidale, 2014). This has led to two broad schools of thought regarding the generation of the Earth's current topography: that it is generated by repeated cycles of regional uplift and peneplanation to sea level and can therefore be described as young; or, landscapes are slowly eroded remnants of larger topography generated during a major tectonic event or events (e.g. orogenic activity or continental rifting). High elevation continental margins such as those surrounding southern Africa have provided geomorphologists and geophysicists with a suitable laboratory to test competing theories of landscape development. To fully understand the link between the geodynamic processes involved during rifting (see Chapter 2) and the development of continental margin topography, quantitative constraints are needed to resolve the magnitude of onshore erosion in response to surface uplift over space and time.

Prior to discussing models of landscape evolution, it is prudent to define several terms which are fundamental to the large-scale development of topography: surface uplift is the vertical movement of the Earth's surface with respect to the geoid or other specified datum; rock uplift is the vertical movement of a rock column with respect to the geoid or other specified datum; exhumation is the

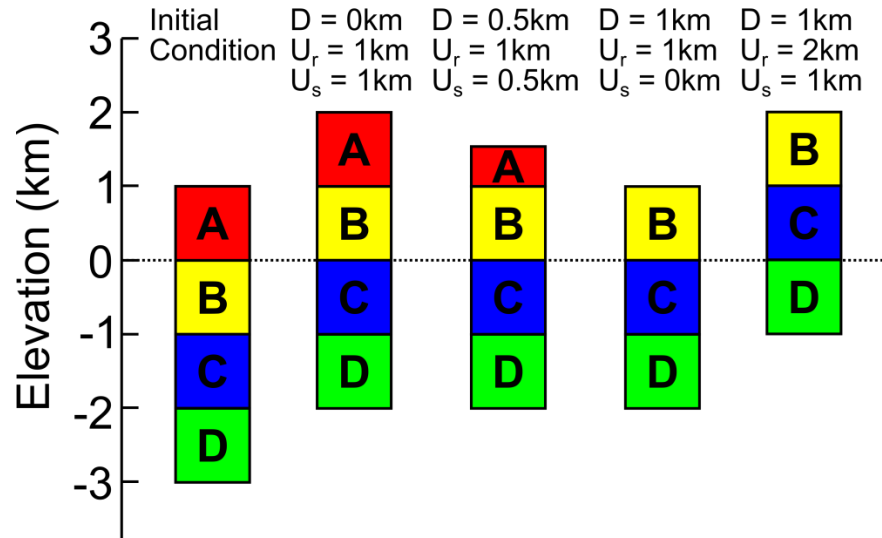
upward movement of a rock toward the surface; and denudation is the removal of material from a rock column. Rock uplift can equal surface uplift only if there is no denudation and, similarly, surface uplift is zero if rock uplift is balanced by denudation (England and Molnar, 1990; Summerfield, 1991; Bishop, 2007) (Fig. 3-1a). Isostasy is the concept that the rigid lithosphere floats on a ductile asthenosphere. Two end-member models of isostasy are proposed for the compensation of blocks of lithosphere. The Pratt model assumes that the lithosphere-asthenosphere boundary is flat and that the lithosphere is comprised of columns, each with uniform density. Elevated regions are therefore proposed to have low crustal density and low lying blocks having high crustal density. The Airy model assumes uniform density throughout the lithosphere and that blocks are compensated at depth by crustal roots (i.e. mountains have thick crustal roots) (Fowler, 2005). In reality both of these models are likely to be operating. Moreover, these models are only applicable over local scales as over regional scales the lithosphere is also supported by its rigidity and flexural isostasy is more significant (Summerfield, 1991) (Fig. 3-1b).

### **3.3 Foundations of modern geomorphology**

Links between the Earth's geological history and the present day topography began to be forged in the late eighteenth century by several workers across Europe (Oldroyd and Grapes, 2008, and references therein). In particular, the work of James Hutton (1788) and later Charles Lyell (1833) established the concept of deep Earth time; providing a framework in which the Earth's topography could be carved out over extremely long timescales. Moreover, and perhaps more significantly for the future of geomorphology, they also pointed to the link between geological structures and surface processes that drive landscape evolution and continually recycle material such as: variable erosion of different rock types and soils by rivers and the sea; transport of sediment from land to sea; and the control exerted on developing drainage patterns by folds, faults and easily erodible substrate.

Geomorphology became particularly popular throughout the mid to late nineteenth century (e.g. Reech, 1858; Cayley, 1859; Maxwell, 1870), paving the

(a) Surface uplift, rock uplift and denudation



(b) Isostasy

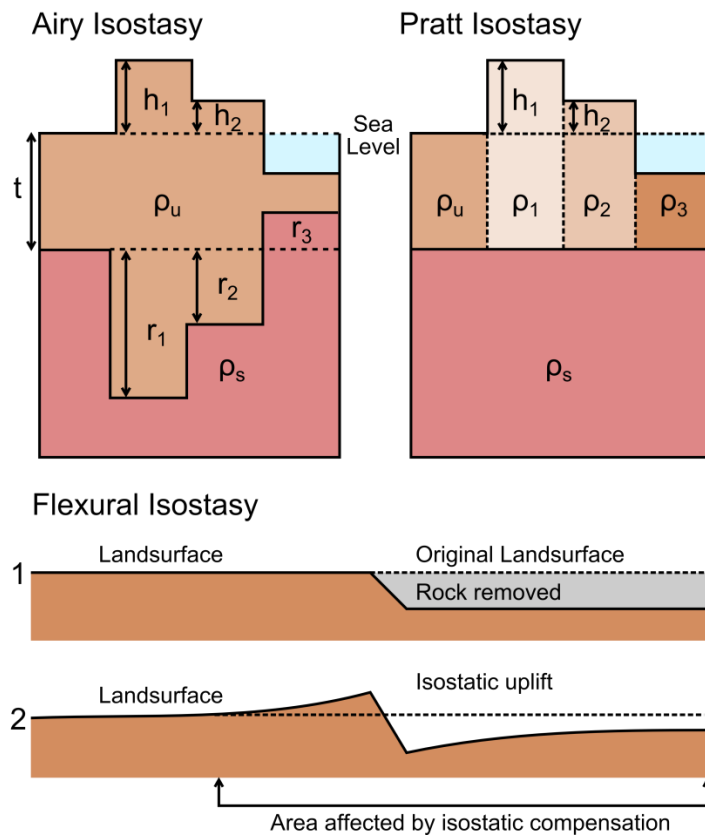


Figure 3-1: (a) Illustration of the distinction between surface uplift ( $U_s$ ) and rock uplift ( $U_r$ ) and the influence of denudation ( $D$ ) on a hypothetical rock column. For this illustration the effects of isostasy are ignored. (b) Illustration of the Airy and Pratt hypotheses of (local) isostasy and flexural (regional) isostasy. For the Airy and Pratt isostasy models  $h_1$  and  $h_2$  are the heights of hypothetical mountains;  $t$  is the thickness of the lithosphere which in the Pratt hypothesis is equal to the isostatic compensation depth.  $r_1$ ,  $r_2$  and  $r_3$  are the roots of thick blocks of lithosphere required to maintain equal density throughout the lithosphere.  $\rho_u$ , is the average density of the lithosphere. In the Pratt hypothesis, an equal isostatic compensation depth is maintained by blocks of lithosphere having different densities where  $\rho_3 > \rho_u > \rho_2 > \rho_1$ . Illustrations redrawn after Summerfield (1991) and Fowler (2005).

way for the first major theoretical concept of long-term landscape evolution. The Davisian model of cyclic erosion (Davis, 1899) envisaged a three-stage evolution of a landscape, initiated by a period of regional tectonic uplift of a low relief surface. The first stage, “youth”, is characterised by rapid river incision, in response to base-level lowering, creating narrow river valleys with flat uplands. The second stage, “maturity”, is characterised by high relief as incision continues, narrowing the previously flat upland. Downwearing of steep slopes causes a decrease in local relief and leads to the final “old age” stage. This stage is characterised by a flat surface at the new base level (i.e. peneplain) with sporadic remnant erosional features.

Criticism of the Davisian model soon followed focusing primarily on the under-appreciated effects of climate, lithology and structure (Summerfield, 1991). Moreover, the lack of specific detail on the surface processes involved in slope degradation and lack of quantitative information on the rates and distribution of uplift were seen as weaknesses in the model (for a review see Summerfield, 2000; Bishop, 2007; Oldroyd and Grapes, 2008). An alternative model, proposed by Penck (1924), differed from the Davisian approach in the manner in which uplift proceeds. Instead of cyclic periods of rapid uplift and long periods of stability, Penck (1924) proposed a period of waxing where rates of uplift increased followed by a period of waning where uplift rates gradually decrease (Summerfield, 1991). With Penck’s contrary view on uplift dynamics came a corresponding alternative model of landscape response involving the development of steep convex river profiles during the waxing phase which were then worn backwards and downward during the waning phase to form concave profiles (Summerfield, 1991; Oldroyd and Grapes, 2008). Like Davis, this model was also criticised for its handling of lithological variations and variable climate.

With a growing appreciation for the importance of continental drift, Lester King devised another landmark model for the long term evolution of landforms. In his view, the step-like topography of southern Africa characterised by low relief surfaces and steep escarpments required a cyclic evolution of uplift and erosion as suggested by Davis; however, the processes involved in generating broad, low-angle, concave pediplains required parallel escarpment retreat in a variation of

Penck's approach (Summerfield, 1991; Blenkinsop and Moore, 2013; Rabassa, 2014). King's model is particularly relevant in the context of this thesis for three reasons: 1) It addresses the long term uplift and denudation of continental interiors; 2) invoked a mechanism for the evolution of major coast parallel escarpments and 3) utilises Southern Africa's well developed continental margin as a case study. This model has provided a useful baseline model for later workers to validate or dispute in either its entirety or particular components. As such the detail and controversy surrounding King's work and later modifications of this model are discussed in subsequent sections and chapters.

"Classical" models as described above are largely based on qualitative dating of geomorphic features and lack empirical data on the timing and rates of the processes which drive their development. For this reason, these models of long term landscape evolution struggle to adequately incorporate the highly variable nature of lithology, structure, climate and weathering, which we now know to play an important role (Summerfield, 2000). Despite this, the link between epeirogenic tectonic movements and the associated surface response is a theme which runs through each of these models and into modern day adaptations (Bishop, 2007). Resolving the uncertainties surrounding the driving mechanisms behind uplift events, the associated rates of uplift and the true nature of continental stability or tectonic quiescence over long timescales remains a major challenge in tectonic geomorphology today.

### **3.4 Polycyclic uplift**

In the original Davisian model of cyclic erosion it was appreciated that any renewed period of uplift prior to complete peneplanation of a previous relief would generate a polycyclic landscape with a 'memory' of previous falls in base-level left behind in the geomorphology record. Despite the criticisms of this model, the notion of alternating periods of uplift and enhanced erosion has persisted to the present day. Part of this endurance can be attributed to the passionate support it gained from Lester King throughout the mid-late twentieth century (see Twidale, 1992, for a review of King's work).

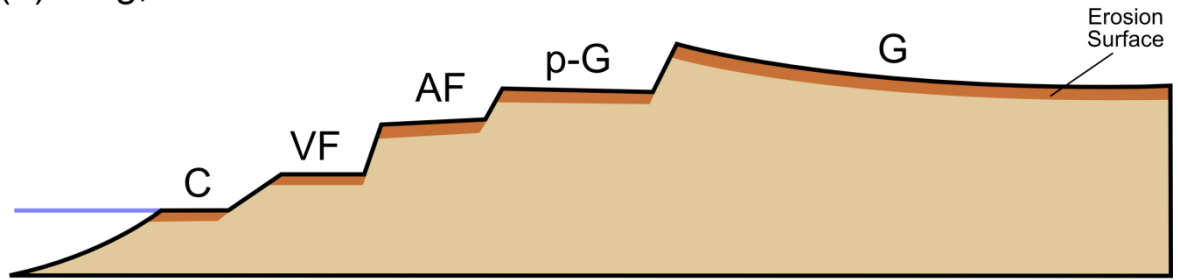


In a series of publications, Lester C. King (e.g. 1942, 1950, 1953a, 1956, 1962 and 1976) discussed the occurrence of prominent “wall-like” scarps and plateaux forming the topography across the South African continent. The regionally distributed plateaux represent preserved erosion surfaces created by a process of pediplanation, driven by river incision to a base-level, following some form of regional uplift. By observing their regional distribution and respective elevations, King assigned relative ages to these six erosion surfaces invoking many periods of uplift and erosion since the Mesozoic (Blenkinsop and Moore, 2013; Fig. 3-2a). The oldest surface was termed the Gondwana surface owing to its pre-break up formation; while the most extensive surface was called the African Surface and was formed in response to rifting in the early Cretaceous (King, 1942, 1953a, 1956).

Two major criticisms surrounded King’s work: 1) the lack of consistent and quantitative dating and correlation of erosion surfaces, particularly over large distances and 2) the under-appreciation or misunderstanding of the isostatic response to removal of overburden (Van der Beek et al., 2002). An isostatic response of the landscape to denudational unloading and offshore sedimentation was, in fact, proposed by King (1955) and Pugh (1955) as the mechanism to drive periods of epierogenic uplift. However, they suggested that this isostatic response occurred only after significant denudation had taken place as opposed to a progressive regional response coeval with denudation (Van der Beek et al., 2002). Because isostatic uplift is a phenomenon acting continuously over time, it cannot be used as a driving mechanism for a discrete regional uplift event as proposed by King.

A comprehensive review and refinement of King’s South African erosion surfaces and their implications for the erosional history of the sub-continent was produced by Partridge and Maud, (1987). Further work in southern Africa by Partridge and Maud (1987, 2000), Partridge (1998), Ollier and Marker (1985), Burke (1996) and Burke and Gunnell (2008) continued the trend of re-evaluating and reassigning the timing and nature of erosion surfaces. In particular, the African Surface has been interpreted as a composite surface which exists above and below the escarpment and was produced through several cycles of erosion

(a) King, 1955 - SW Africa



(b) Green et al., 2013 - S Norway

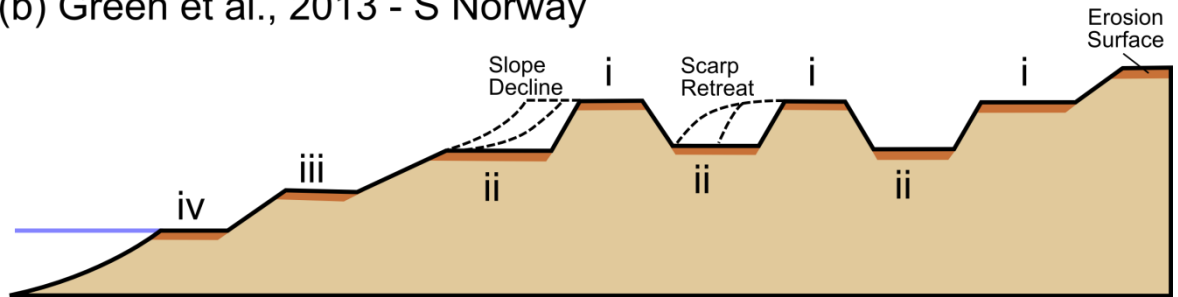


Figure 3-2: (a) Illustration of cyclic erosion surfaces in southern Africa as proposed by King (1955). Based on the classification of King (1955) the erosion surfaces in chronological order are named Gondwana (G); the post-Gondwana (p-G); African (AF), Victoria Falls (VF) and Congo (C). (b) Model of relief development in southern Norway as proposed by Green et al., (2013). Illustration is a simplification of Figure 14 in Green et al., (2013) to highlight the successive nature of erosion surfaces or peneplains (oldest surface = i, youngest surface = iv).

from continental break-up to the Miocene (Partridge and Maud, 1987; Burke and Gunnell, 2008). Alternatively, de Wit (1999) suggested that the African Surface has not experienced major erosion or incision since the Late Cretaceous; while Ollier and Marker, (1985) saw the African Surface as a pre-rift Gondwana palaeoplain which could be correlated with the offshore basal unconformity. Partridge et al. (2006) summarise the Cenozoic South African geomorphology in terms of three major widespread erosion surfaces: 1) African Surface, formed following continental break up; 2) Post-African Surface I, formed following Early Miocene uplift; and 3) the Post-African Surface II, formed during major uplift (c. 700 - 900 Ma) in Pliocene (see Chapter 7 - Section 7.5.3).

Recent work in Scandinavia has attempted to revitalise the study of erosion surfaces to infer cyclic periods of uplift and erosion. This approach termed "Stratigraphic Landscape Analysis (SLA)" by its supporters (e.g. Green et al., 2013; Lidmar-Bergström et al., 2013; Bonow et al., 2014) involves correlating regional planation surfaces based on their form, weathering profile (i.e.

regolith), spatial relationship with other planation surfaces and additional geological constraints (Green et al., 2013) (Fig. 3-2b). In particular, insights from low temperature thermochronology (see below) and identification of sedimentary deposits overlying planation surfaces are used to infer multiple cycles of burial and subsequent denudation. This modern day adaption of the Davis/King-style model of landscape evolution incorporates episodes of burial and exhumation and is suggested to explain many continental margin settings and continental interiors such as: Greenland (Japsen et al., 2006), Norway (Japsen et al., 2009), NE Brazil (Peulvast and de Claudino Sales, 2004; Zalán and Oliveira, 2005), southern South America (Rabassa and Ollier, 2014, and references within), SE Australia (Twidale, 2007) but has been strongly opposed by many other workers (e.g. Chorley, 1965; Inkpen, 2005; Egholm et al., 2013).

Despite the persistence of the Davisian model of cyclic erosion, or modifications of it, for over a century, some of the major criticisms remain unchanged. The main thrust behind the Penck's model was a belief that uplift is not a rapid short lived process but is gradual with the surface experiencing erosion in concert. This view is shared by many supporters of 'steady-state' landscapes (Bishop, 2007) in which a tectonic forcing maintains uplift during erosion. A more fundamental criticism is directed at the formation and correlation of erosion surfaces and therefore their geological significance (Summerfield, 2000; Van der Beek et al., 2002). Alternative explanations for the formation of low relief surfaces have been lowering of interfluves; etch planation; local drainage variations, including interior base levels, controlled by lithology and/or structure; and glacial erosion in glaciated regions (Summerfield, 1991; Thomas, 1995; Phillips, 2002; Mitchell and Montgomery, 2006; Steer et al, 2012; Egholm et al., 2013). As stated by many geomorphologists, and as is evident in Kings own frequent re-evaluation and reclassification of erosion surfaces, correlating and dating planation surfaces can prove difficult primarily due to the tectonic, lithological and climatic variations a region may have experienced over time (Burke and Gunnell, 2008). Correlating these surfaces is based on the assumption that they once formed a single planation surface which has subsequently been dissected. This is unlikely to be the case due to the unstable nature of

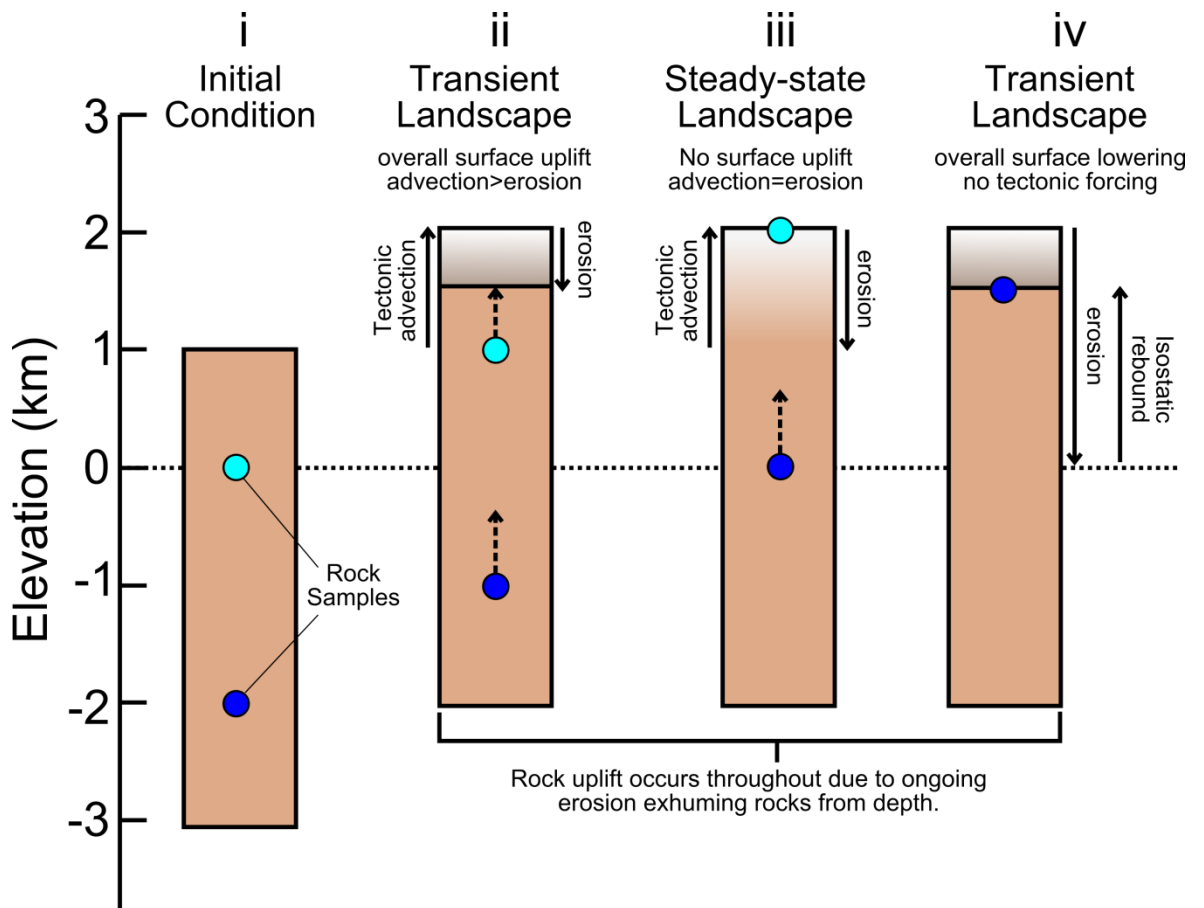
continental platforms over geological timescales (Summerfield, 2000; Moucha et al., 2008).

### **3.5 Steady-state landscapes, flexural isostasy and surface process numerical modelling at continental margins.**

#### **3.5.1 Steady-state landscapes and flexural isostasy**

From the late 1980s through to the present day, numerical modelling of surface process have provided enormous insights into long term landscape development in many geological settings (Beaumont et al., 2000). Integral to these models is the assumption that following tectonic uplift, landscapes develop towards a “steady-state” setting (Kooi and Beaumont, 1994; Willet et al., 2001; Whipple and Meade, 2004). The notion of steady-state landscapes stem from the dynamic equilibrium landscape model of Hack (1960). In a steady-state landscape the rate of tectonically driven rock advection must balance with the surface erosion rate (Willet et al., 2001) (Fig. 3-3). In other words, the relative contributions of climate and tectonics in developing large scale topography are balanced. Willet and Brandon, (2002), define steady state in terms of different component parts including erosional flux, topography, thermal structure and exhumation rate, addressing the uncertainty that surrounds defining landscapes as steady-state. The simplest example of steady-state topography is achieved when rock uplift is driven only by vertical tectonic advection which is balanced by denudation (Bishop, 2007). However, horizontal components of tectonic advection can prolong the time required to achieve steady-state conditions and is only ever achieved for the first-order topography of the entire mountain range (Willet et al., 2001).

In the absence of any additional tectonic forcing, isostatic balance of the lithosphere in response to erosion is the primary means of rock uplift and will reduce the total amount of surface lowering caused by denudation (Gilchrist and Summerfield, 1990). On average, isostasy driven surface uplift is c. 0.8 times the thickness of material removed from the surface by denudation (Bishop, 2007). However, the amount of surface uplift which occurs due to isostasy is a function



**Figure 3-3: Block diagram of the nature of steady-state and transient landscapes. (i) A crustal block with two hypothetical rock samples at depth. (ii) A period of enhanced tectonic uplift raises the surface which is immediately denuded by erosion causing rock uplift. As the rate of tectonic advection exceeds erosion rate there is continuous uplift of the surface. (iii) As advection continues erosion rate may increase due to elevated regions residing in a more erosive climate (Molnar and England, 1990). When advection and erosion are balanced the landscape is in steady-state and there is no surface uplift but rock uplift will continue. (iv) If the tectonic force driving uplift is removed then erosion will lower the surface. This removal of material will induce isostatic rebound of the surface by an amount approximately equal to 80% of the thickness of material removed.**

of the amount of material that has been eroded, the density of erodible material and the elasticity of the lithosphere (Gilchrist and Summerfield, 1991). The elasticity of the lithosphere is quantified in terms of the lithosphere's effective elastic thickness (EET) and characterises the relationship of flexural isostasy with loading/unloading of the lithosphere (Gilchrist and Summerfield, 1991; Watts, 2001; Braun et al., 2013a; Rouby et al., 2013). When the lithosphere possesses a high EET, its flexural rigidity is high and the influence of the imposed load (positive for loading and negative for denudation) over lateral distances is less than for lower values of EET (Bishop, 2007).

The importance of flexural isostasy has been highlighted particularly for high elevation continental margin settings (Karner and Watts, 1982; Braun and Beaumont, 1989; Weissel and Karner, 1989; Gilchrist and Summerfield, 1991; Tucker and Slingerland, 1994; Sacek et al., 2012). The feedback between flexural isostatic uplift and erosion may cause the initial escarpment to retreat and ultimately produce prominent marginal upwarps that persist over time (Gilchrist and Summerfield, 1990, 1991; ten Brink and Stern, 1992; Tucker and Slingerland, 1994). However, the spatial variability of EET across continental margins creates uncertainty in escarpment evolution models that assume uniform flexural rigidity (ten Brink and Stern, 1992; Tucker and Slingerland, 1994). Recent modelling by Braun et al. (2013a) and Rouby et al. (2013) integrated flexure of the lithosphere in response to rifting with surface processes controlling denudation of the continent and deposition in the offshore basin. This modelling has shown that using an uniformly thick EET, which does not vary in space and time, will promote an initially higher rift shoulder, and shallower distal basin but will have a lower amplitude flexural response to denudation, accumulation and thermal subsidence and the converse being the case for a uniformly thin EET.

### **3.5.2 Applications of surface process numerical models**

Using computer-based surface process models (SPM), the development of regional landscapes (c. 1 - 1000 km) have been investigated by integrating the effects of tectonic processes, erosion, isostasy and climatic and lithological variations over 1 - 100 Myr timescales (Bishop, 2007). Applications of SPMs have become increasingly popular particularly in investigating the erosional and structural feedbacks associated with the development of orogenic belts (Willet et al., 2001; Thiede et al., 2005; Koons et al., 2012; Tucker and Van der Beek, 2013; Giachetta et al., 2014) and the intimate relationship between tectonics and climate in mountain building (Whipple et al., 1999; Burbank et al., 2003; Whipple and Meade, 2004). Depending on the parameterisation of SPMs, different and often conflicting outcomes may be achieved from different models investigating the same phenomenon as exemplified by the climate vs. tectonics

debate (Molnar and England, 1990; Raymo and Ruddiman, 1992; Whipple, 2009; Champagnac et al., 2012).

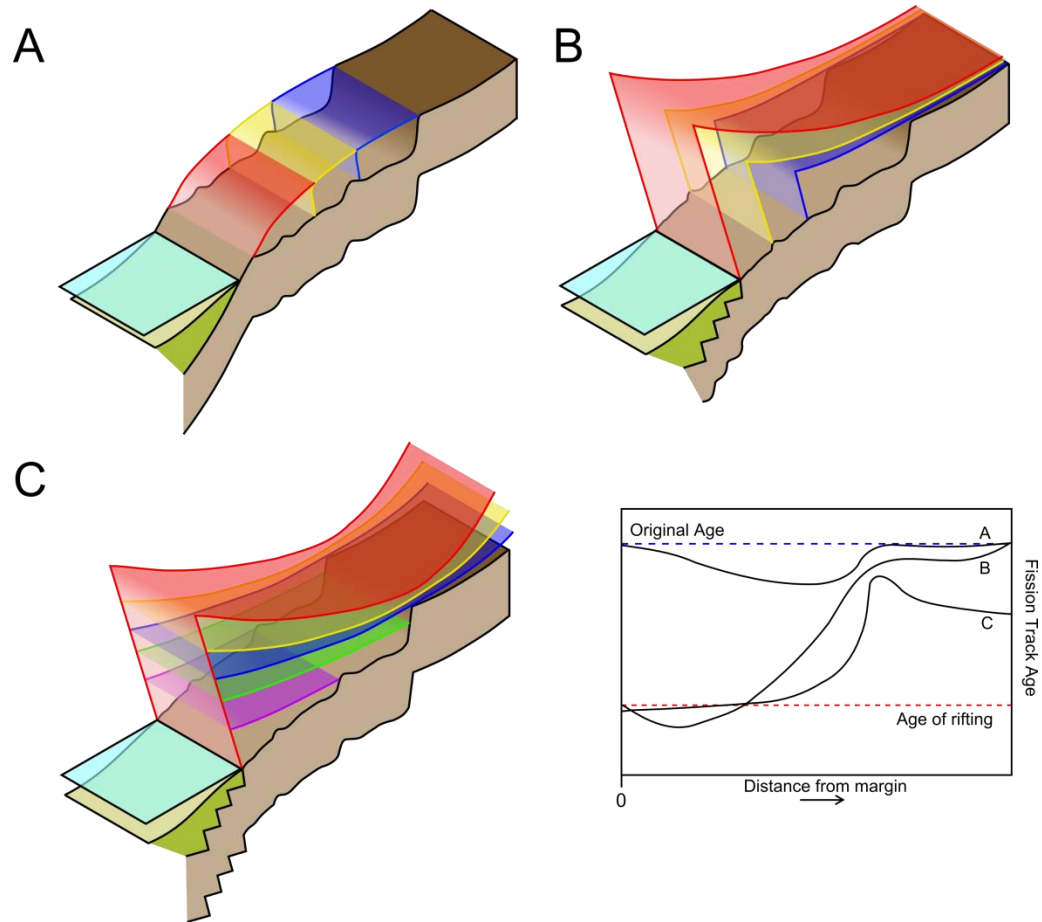
The development of continental margins and the persistence of their marginal escarpments over time have been of particular interest to surface process modellers over the years (Braun and Beaumont, 1989; ten Brink and Stern, 1992; Kooi and Beaumont, 1994; Gilchrist et al., 1994; Tucker and Slingerland, 1994; Van der Beek et al., 2002; Sacek et al., 2012; Braun et al., 2013a). As with other geological settings, without independent quantitative constraints to test their outcomes, the models remain largely conceptual but the information they provide are crucial for understanding the mechanisms involved in forming continental margin topography (Van der Beek and Braun, 1998; Braun and Van der Beek, 2004). Insights from SPMs across the southeast and southwest African margin and the southeast Australian margins have largely rejected the occurrence of a marginal down warping following rifting (e.g. Ollier and Marker, 1985; Seidl et al., 1996) in favour of isostatically induced or fault bounded rift flank upwarps (ten Brink and Stern, 1992; Tucker and Slingerland, 1994; Kooi and Beaumont, 1994; Gilchrist et al., 1994; Van der Beek et al., 2002). A major finding was the occurrence of differential denudation across the margin with much greater amounts of material being removed on the seaward side of the escarpment than inland (Gilchrist and Summerfield, 1990). This observation was supported by comparable sediment thickness volumes in offshore basins (Rust and Summerfield, 1990) and later by extensive LTT work across continental margins (see below). This differential denudation is caused by the response of the pre-rift drainage to a rapid drop in base level. The combination of river erosion and the isostatic response holds a first order control over the development of the margin topography (Gilchrist and Summerfield, 1994). Later SPMs models built on earlier work and identified second order controls such as climate change and lithology (Van der Beek et al., 2002). For example a climate changing from a semi-humid to arid environment will slow denudation across both domains while the exposure of more resistant substrate can cause denudation to decrease as the margin evolves (Gilchrist et al., 1994; Kooi and Beaumont, 1994). Local variations in the lateral and vertical distribution of

resistant rock units can result in steep escarpments and a stepped topography (Gilchrist et al., 1994).

A major limitation of SPMs is that they are somewhat qualitative in that they are not constrained by independent empirical data and observations. Therefore, they are subject to assumptions and subjective parameterisation (Bishop, 2007). Fortunately, this limitation is well-appreciated and the need for independent constraints is acknowledged and typically provided in the form of field-based geomorphic observations, quantitative dating techniques and/or offshore stratigraphic analyses. An additional consideration for interpretation of SPMs is their temporal and spatial resolution (typically 1 - 5km and c. 100 -  $1 \times 10^6$  yr) (Bishop, 2007). This can result in small scale geomorphic features (e.g. knickpoint retreat and river channel width) being unresolved during the modelling process, however, this resolution still provides important information on long-term, large scale landscape evolution (Van der Beek and Braun, 1998; Bishop, 2007; Sacek et al., 2012; Goren et al., 2014).

Another difficulty faced by continental margin SPMs was their ability to include the tectonic processes associated with rifting due to the different timescales over which tectonic and surface processes occur (Beaumont et al., 2000). Recent numerical models have attempted to integrate the newly formulated geodynamic settings (see Chapter 2), such as the parameters that govern lithospheric stretching and thermal dynamics of the underlying mantle with surface processes. In this way, what were uncertainties or assumptions in previous models, such as the value of flexural rigidity of the lithosphere, become parameters; the value and importance of which can be investigated (Braun et al., 2013a; Rouby et al., 2013). These models have been assessed against real-life examples such as the West African margin (Braun et al., 2013a, Rouby et al., 2013), northeast Brazilian margin and southeast Australian margin (Sacek et al., 2012) with reasonable success. However, the influence of precipitation (e.g. Colberg and Anders, 2014), lithological variation (Bishop and Goldrick, 2010) and structural complexity (e.g. Redfield et al., 2005a, b) that a margin may exhibit is yet to be fully resolved and model parameterisation remains challenging.





**Figure 3-4: Conceptual models of continental margin evolution and the expected AFT age trend across the margin for each. Redrawn after Gallagher and Brown (1999a). Red, yellow, blue, etc. =  $t_0$ ,  $t_1$ ,  $t_2$ , etc. A – Parallel escarpment retreat of a downwarped rift flank. B – Escarpment retreat of an elevated rift flank incorporating isostatic readjustments to erosion. C – Downwearing model with a pinned drainage divide inland of the initial rift flank.**

### 3.6 Geomorphic response to rifting: Escarpment retreat or plateau downwearing

Inspired by the dramatic escarpment and plateau landscape of Southern Africa, King's model of landscape evolution envisaged that coast-parallel escarpments evolved towards their present day location and morphology through a process of backwearing (e.g. King, 1953; Fig. 3-4a). This model involves the weathering and erosion of free-facing slopes inducing parallel escarpment retreat (Summerfield, 1991). The initial condition for King's escarpment retreat model was the development of a broad regional monocline (i.e. the Natal monocline) into which fluvial erosion drives the escarpment back towards the warp axis (Ollier and Marker, 1985). King's model involved the generation of pediments (i.e. low relief

surfaces with low slope angles) that become collated to form a pediplain (King, 1955; Summerfield, 1991; Blenkinsop and Moore, 2013).

King and subsequently other workers suggested that this model of escarpment development was applicable to other continental margins, such as the South Australian margin (Ollier, 1982; Seidl et al., 1996). Ollier (1985) attempted to refine and further generalise the combined process involved in the development of high elevation topography of a downwarped continental margin. It was suggested that an uplifted surface becomes downwarped by thermally induced margin subsidence promoting a long wavelength flexing of the lithosphere (Ollier, 1985; Ollier and Marker, 1985; Ollier and Pain, 1997). This produces a warped basal unconformity offshore which Ollier and Pain (1997) suggest is a continuation of the onshore downwarped surface. In this view, sporadic geomorphic features on the coastal plain such as inselbergs and bonhardts (Twidale, 1968) are interpreted to be erosional remnants of a pre-rift surface. One of the main criticisms of parallel escarpment retreat model is focused on the assumptions made regarding the isostatic response of the landscape during the process (Gallagher and Brown, 1999a, b; Van der Beek et al., 2002). Specifically, King's escarpment retreat model suggested an isostatic response only after erosion had caused the escarpment to retreat c. 480 km inland (Blenkinsop and Moore, 2013).

Large scale numerical models (c.  $1 \times 10^3 \text{ km}^2$ ) introduced a different class of model for continental margin evolution by incorporating various parameters including: lithology, climate and, crucially, flexural isostasy of the lithosphere. A variant of the escarpment retreat model was proposed assuming an initially horizontal pre-rift topography and imposing the initial condition that the initial escarpment is produced at by vertical displacement on normal faults at the margin (Gilchrist and Summerfield, 1990; Gilchrist et al., 1994; Tucker and Slingerland, 1994). The highest rates of denudation occur immediately seaward of the initial escarpment lip by intense incision, as river drainage patterns readjust to a rapidly decreasing base level. Erosion of the high-relief escarpment leads to scarp retreat however isostatic adjustments to the removal of material

produces prominent rift flank upwarps (Fig. 3-4b). Denudation is lower seaward of the escarpment and far inland on the continental interior.

The key difference between plateau-downwearing and scarp retreat models is the incorporation of an inland drainage divide (Gilchrist et al., 1994; Kooi and Beaumont, 1994; Van der Beek et al., 2002) (Fig. 3-4c). The initial scarp in both models is a fault bounded rift flank however if the pre-rift topography or lithological variations has produced a drainage divide inland of the initial escarpment, rapid incision will erode the initial escarpment. Progressive removal of interfluves destroys the initial scarp and a new scarp forms at the position of the drainage divide (i.e. pinned-divide) (Gilchrist et al., 1994; Kooi and Beaumont, 1994; Van der Beek et al., 2002).

These models have fundamental differences in both the timing and amount of denudation observed across a margin (Van der Beek et al., 2002; Braun and Van der Beek, 2004). Except from the escarpment retreat of a downwarped margin, the initial elevation of the escarpment and isostatic rebound is greatest towards the coast and as such denudation is predicted to be at a maximum at the coast decreasing to a minimum at the present-day escarpment. If an inland drainage divide is present, denudation is greatest and relatively uniform seaward of the drainage divide. However, if the interior base levels are also lowered during rift flank uplift inland denudation may also be large (Gallagher and Brown, 1998).

### **3.7 Quantifying surface process models: Insights from low temperature thermochronometry and cosmogenic nuclide analysis**

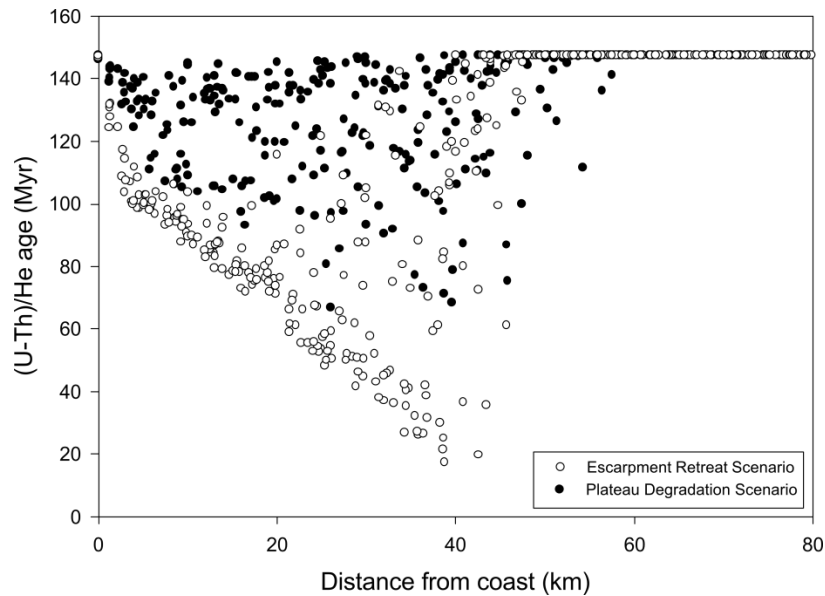
Theoretical models of long term escarpment development are distinguished by their fluvial slope processes which, in turn, produce distinct patterns of erosion over time. Because progressive erosion of the margin will cause rocks, previously at depth, to cool as they are exhumed towards the Earth's surface, low temperature thermochronology (LTT) has been deployed in many studies to validate conceptual landscape evolution models (e.g. Brown et al., 1994, 2002; Gallagher and Brown, 1999a, b; Persano et al., 2002; Reiners et al., 2003; Braun and Van der Beek, 2004; Heimsath and Ehlers, 2005).

Over the past 25 years or so, apatite fission track (AFT) thermochronology has been used at many continental margins to constrain magnitudes of post-rift denudation. Gallagher and Brown (1999a) presented a conceptual relationship between three styles of escarpment evolution and their corresponding expected AFT ages (Fig. 3-4). All models invoke limited erosion on the plateau and therefore AFT ages are significantly older than the age of rifting reflecting much older cooling of a pre-rift land surface. A slight exception to this is model C (Fig. 3-4) where an interior drainage divide causes some denudation of the plateau, but at lower magnitudes required to exhume rocks with completely reset AFT ages following rifting. The major differences in erosion are suggested to occur seaward of the escarpment.

In the downwarp model, remnants of the “palaeoplain” at the coast will yield fission track ages greater than or equal to the age of the palaeoplain; AFT ages progressively young towards the base of the escarpment in response to parallel retreat. The levels of erosion predicted by this model are, however, relatively minor and AFT ages across the coastal plain would usually be older than rifting as denudation was not pronounced enough to bring rocks that were at a depth of more than c. 3 to 4 km before rifting to the surface. In contrast, scarp retreat models accounting for isostatic readjustments and beginning with an initial escarpment formed by km-scale vertical displacement on normal faults produce a fundamentally different style of erosion. Across the margin, denudation is initially highest at the high-relief escarpment. Lesser amounts of denudation are predicted as the escarpment retreats back into an upwarped surface produced by the flexural isostatic response to denudation. In concert with decreasing levels of denudation towards the present day escarpment, AFT ages increase. Where denudation is highest AFT ages may be younger than the age of rifting as they have been exhumed from temperatures higher than c. 110°C. Plateau downwearing is promoted when an inland drainage divide is present. The drainage divide defines the future location of the escarpment as rapid incision occurs on the seaward side. Downwearing is characterised by relatively uniform denudation across the margin and as such does not show a steep gradient in AFT ages towards the escarpment (e.g. Braun and Van der Beek, 2004) (Fig. 3-4).

More recently, AFT analysis has been supplemented with apatite (U-Th)/He analysis in landscape evolution studies to better resolve the timing, magnitude and distribution of erosion (e.g. Persano et al., 2002; Balestrieri et al., 2005; Hansen and Reiners, 2006). The majority of studies at margin settings do not find that thermochronometry data are compatible with the parallel escarpment retreat model of a downwarped surface. Instead the data favour scarp retreat of an uplifted rift flank or plateau downwearing by an interior drainage system. However, resolving which model of escarpment evolution using (U-Th)/He analysis is limited as the margin may not have experienced enough erosion to exhume samples from below the apatite (U-Th)/He closure temperature (Braun and Van der Beek, 2004) (Fig. 3-5). Although the theoretical merits of integrating AFT and apatite (U-Th)/He techniques are clear, in practice several factors influencing the closure temperature of the dating systems, in particular the apatite (U-Th)/He system, can make interpreting such data difficult (see Chapter 4).

Efforts to constrain more recent rates of erosion using cosmogenic nuclide dating are generally in agreement with models of rapid removal of the rift-related escarpment with slower present day erosion rates. This has been shown particularly well for the continental margins of South Africa where cosmogenic studies on the western margin (Cockburn et al., 2000; Bierman and Caffee, 2001; Kounov et al., 2007) and eastern margin (Fleming et al., 1999; Erlanger et al., 2012) have shown dramatically reduced erosion rates during the Cenozoic, relative to those implied by AFT analysis during the Cretaceous (see Chapter 7 - Section 7.5.1). This reduction in erosion rate is suggested to have potentially persisted since the late Eocene (Cockburn et al., 2000) through to the present day on the western margin and has at least been the case over the past c. 1 Myr on both eastern and western margins (Fleming et al., 1999; Bierman and Caffee, 2001; Kounov et al., 2007). Moreover, although rates of denudation on the plateau are greatly reduced compared to Cretaceous levels, local variations in climate and lithology will still cause the removal of supposedly long-lived erosion surfaces (Fleming et al., 1999; Kounov et al., 2007; Erlanger et al., 2012).



**Figure 3-5: Predictions of apatite (U-Th)/He ages with distance from the coast for the escarpment retreat and plateau degradation (downwearing) models of rift flank evolution (after Braun and van der Beek, 2004). The two end member scenarios were modelled over 150 Myr with rifting initiating at 100 Ma. The (U-Th)/He age distribution predicted with a geothermal gradient of 50°C/km and a constant surface temperature of 0°C.**

Use of this approach at other margins such as the southeastern Australian margin has yielded data that suggests rapid erosion occurs at the base of knickpoints and escarpment faces with much lower erosion at the head or crest (Weissel and Seidl, 1998; Heimsath et al., 2006). This pattern of erosion has been used by Wiessel and Seidl (1998) and similarly by Vanacker et al. (2007) to support parallel escarpment retreat across southeastern Australia and southern Sri Lanka, respectively. Conversely, Heimsath et al. (2006) and Jakica et al. (2011) advocate stability of the eastern and western Australia margins, respectively, following rapid removal of an initial escarpment. However, the low temporal resolution (c. <1Myr) limits the insights cosmogenic nuclides can provide into long-term escarpment evolution while proving more sensitive to local escarpment retreat and variations in erosion driven by climate and lithology (Fleming et al., 1999; Persano et al., 2002; Kounov et al., 2007).

Resolving whether escarpment retreat or plateau downwearing are more applicable at one particular margin or another using thermochronology alone has proved to be a particularly difficult and contentious issue. Numerical modelling by Braun and Van der Beek, (2004) investigated the spatial pattern of (U-Th)/He

ages that would occur across a continental margin that had developed to its present morphology by escarpment retreat or plateau downwearing (Fig. 3-5). This work highlighted that simple coast perpendicular age vs. distance transects do not provide enough detail to resolve the manner of escarpment evolution and that coast parallel samples should also be incorporated into surface process models. In order for thermochronometric ages to have significance in terms of the timing and distribution of escarpment erosion additional variables must be considered: (i) the initial height of escarpments; (ii) the geothermal gradient; (iii) the flexural rigidity of the lithosphere and (iv) the rate of escarpment migration (Braun and Van der Beek, 2004). An increase in (i) or (ii) and decrease in (iii) will promote exhumation of deeper or, more accurately, hotter samples which will yield thermochronological ages that correspond to the time of erosion. If rates of escarpment migration are high then LTT ages from different samples may not be distinguishable from one another and provide no insights into the style of escarpment evolution. The data often leaves the style of escarpment evolution largely unresolved when compared to surface process driven numerical models (Van der Beek et al., 2002; Braun and Van der Beek, 2004).

Inferences on the style of escarpment evolution that can be made from simple LTT age vs. distance from coast relationships alone are clearly limited and many margins present a more complex LTT spatial relationship. Green et al. (2013) highlight the western continental margin of South Africa specifically because young (i.e. close to or younger than rifting) AFT ages extend inland beyond the present location of the escarpment. This infers significant denudation occurred on the present day interior plateau following rifting, contrary to the simple conceptual models. This observation of complex and variable ages across the southwest African margin is, in fact, a main impetus behind this thesis. This work follows on from the interpretation of Brown (1992) and Gallagher and Brown (1999a) that anomalous fission track age patterns are produced by post-rift fault reactivation. This explanation is rejected by Green et al. (2013) in favour of alternative scenarios such as heat flow variations during rifting (e.g. Green et al., 2004) or subsequent igneous intrusive activity (Duddy et al., 1998) and/or a more complex evolution involving peneplanation between periods of

uplift and burial (e.g. Green et al., 2013). These scenarios are discussed in detail alongside new LTT data in subsequent chapters.

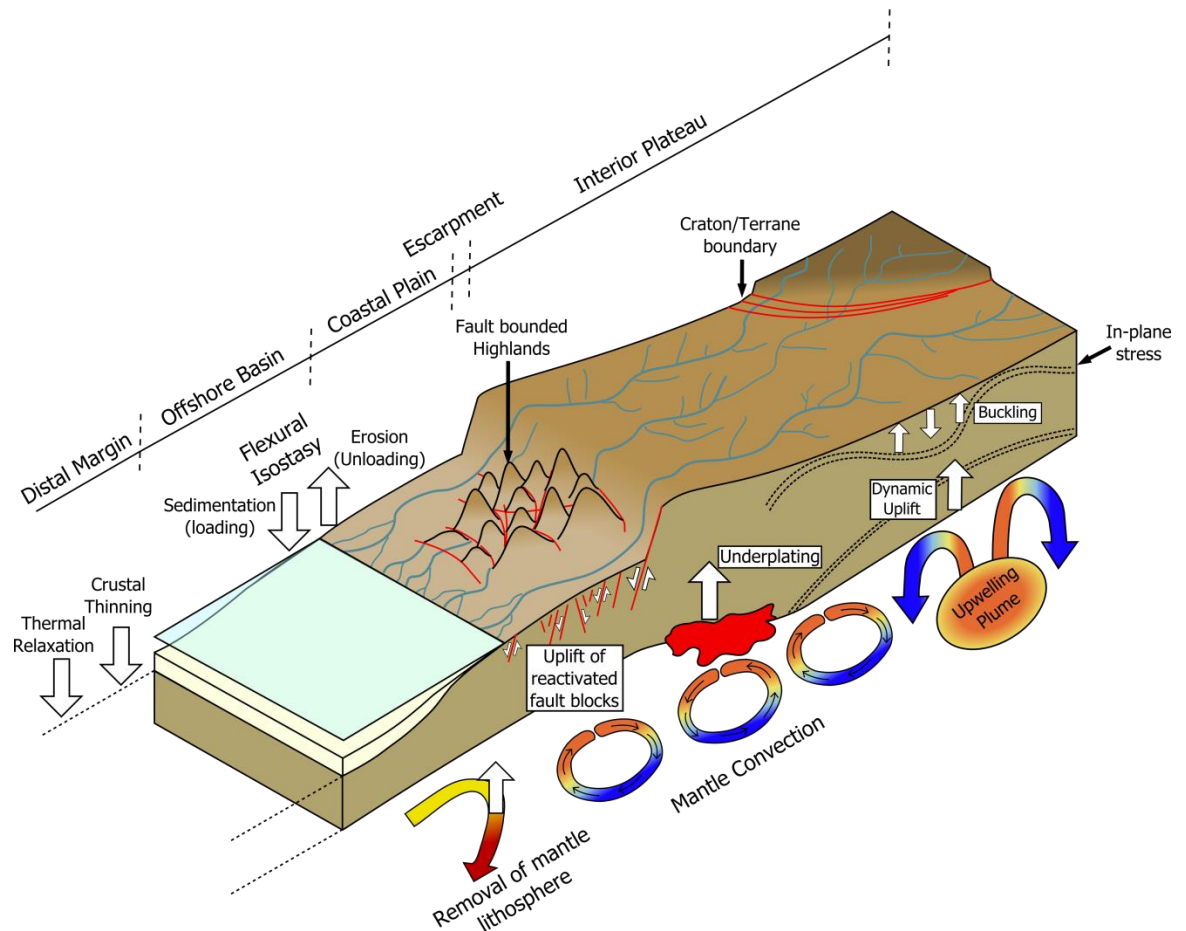
Low temperature thermochronology continues to be a popular method of deriving estimates of denudation from thermal history information. Beyond this, however, resolving the style of escarpment evolution that a margin has experienced is difficult. Braun and Van der Beek, (2004, p. 13) state that “a deeper understanding of the mode of escarpment evolution will not necessarily be attained through more data collection but from a better understanding of the actual processes causing escarpment retreat and how rates of these processes may be affected by climatic variations”. While this is certainly true and is being addressed by recent surface process models (e.g. Sacek et al., 2012; Colberg and Anders, 2014) recent LTT data has been interpreted in the context of regional plate movements (e.g. Holford et al., 2009); local post-rift tectonic reactivation of pre- or syn-rift structures (e.g. Redfield et al., 2005a, b) or dynamic topography (e.g. Flowers et al., 2012). Taking these regional tectonic influences into consideration alongside surface processes is important, particularly in light of the growing appreciation of the complex structural and thermal features rifted margins may exhibit throughout their evolution (Fig. 3-6). Hence, more LTT data should be obtained but the data should have the resolution and regional distribution to investigate post-rift fault reactivation of basement structures along the continental margin and continental interior.

## **3.8 Geological factors controlling passive margin evolution**

### **3.8.1 Regional plate movements**

During continental rifting, in plane stress drives extension and lithospheric thinning. Following continental break-up the margin is traditionally referred to as “passive” due to its relative tectonic quiescence during the drift phase (Ziegler and Cloetingh, 2004). Intraplate settings may then be surrounded by a combination of divergent, convergent and transform margins. Extensive in-plane stress may propagate far from these active plate boundaries (Ziegler and Cloetingh, 2004; Anderson and Natland, 2005; Viola et al., 2005; Foulger, 2007;





**Figure 3-6: Cartoon illustrating the variety of different mechanisms proposed for creating vertical motions at continental margin settings. Crustal thinning during syn-rift extension of the lithosphere can lead to overall subsidence of proximal margin with upwarping occurring at the rift flanks (e.g. Braun and Beaumont, 1989). If a hot thermal anomaly is present during the syn-rift phase initial uplift may occur due to doming over the underlying plume with thermal relaxation leading to subsidence during the post-rift phase (Ziegler and Cloetingh, 2004). The removal of continental mantle lithosphere during rifting (e.g. Huismans and Beaumont, 2011) may produce uplift due to the influx of hot buoyant material. Emplacement of a high density lower crustal body (underplating) beneath the margin can support the margin preventing subsidence or causing uplift due to isostasy or the thermal buoyancy of the underplate material (e.g. Hirsch et al., 2010). In response to uplift of the margin, erosion removes material from the continent which is transported and deposited in offshore basins causing further uplift and subsidence of the on and offshore parts of the margin driven by flexural isostasy (e.g. Rouby et al., 2013). The presence of hot mantle plumes beneath plates can induce long wavelength dynamic uplift (e.g. Gurnis et al., 2000). Mantle convection patterns and in plane stresses created by plate movements or propagated from active plate boundaries can become enhanced by combining with stresses induced by vertical motions and trigger post-rift reactivation of pre-existing faults (e.g. Burov and Cloetingh, 2009).**

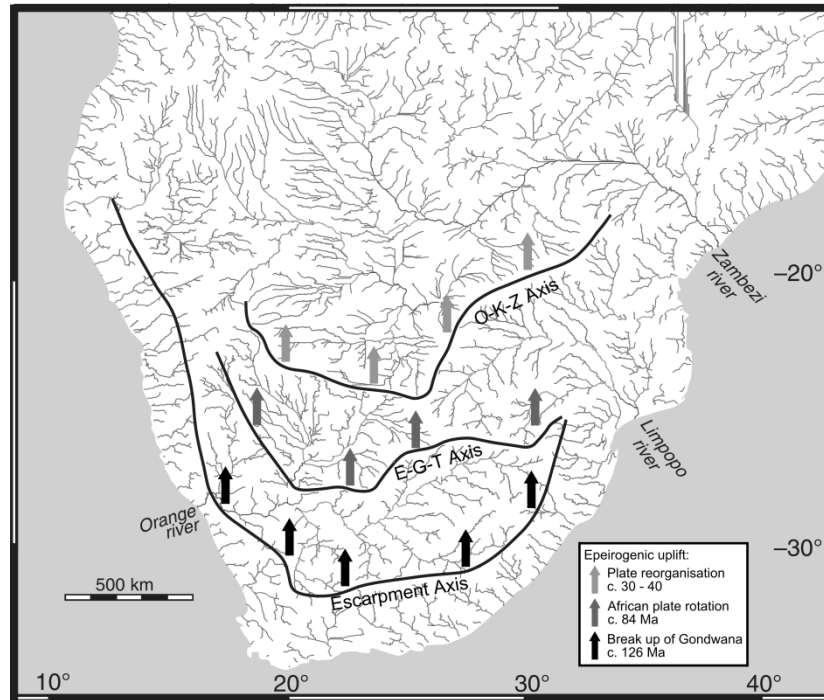
Cloetingh and Burov, 2011) or intraplate stresses may be generated by the relative rotation of plates and microplates of varying lithospheric strength (Nürnberg and Müller, 1991; Schettino and Scotese, 2005; Bird et al., 2006).

Propagation of stresses from subduction zones and mid-ocean spreading centres can occur within plate interiors over distances greater than 1000km away from the active plate boundary (Holford et al., 2009). The stress required to promote deformation may be relatively small and therefore intraplate settings are likely to show such deformation (Cloetingh and Burov, 2011). Large scale compressive stress will induce shortening style structures such as small scale thrusts and folds but may extend to complete buckling of the lithosphere (Ziegler et al., 1995; Bosworth et al., 1999; Holford et al., 2009; Blenkinsop and Moore, 2013). The surface response to compressive deformation will enhance and prolong folding and potentially lead to brittle faulting in the upper crust (Cloetingh and Burov, 2011). Such deformation of the lithosphere has been suggested to have resulted in cycles of uplift and erosion to occur in the post-rift phases of many passive margins, such as the British Isles (Hillis et al., 2008; Holford et al., 2009, 2010), southeastern Australia (Green et al., 2004), southeastern Brazil (Cogné et al., 2011) and Scandinavia (Japsen et al., 2009; Bonow et al., 2014).

In Southern Africa, Moore et al. (2009) explain the causes of the regional episodes of epierogenic uplift and erosion suggested by King (1953) and Partridge and Maud (1987) using far-field horizontal plate forces. Moore et al. (2009) suggest that three coast parallel axes of flexure (Escarpment Axis, Etosha-Griqualand-Transvaal Axis, Ovambo-Kalahari-Zimbabwe Axis) were formed due to the break-up of Gondwana (Gilchrist and Summerfield, 1990), a rotation in the African plate at c. 84 Ma (Nürnberg and Müller, 1991) and a Palaeogene reorganization of spreading geometry in the Indian Ocean (Reeves and de Wit, 2000), respectively (Fig. 3-7). These workers prefer this model of uplift of Southern Africa ahead of plume driven models due to the coherence of drainage patterns to their proposed flexural axes of uplift, occurrence of intrusive activity at the time of proposed uplift and the coeval timing of offshore erosional unconformities.

### **3.8.2 Surface response to faulting**

The influence of a pre-existing structural fabric on the style and location of rifting is well appreciated (e.g. Ziegler and Cloetingh, 2004; Corti et al., 2013;



**Figure 3-7: Drainage system of southern Africa (after Moore et al., 2009). Three major river divides are identified and interpreted to reflect epeirogenic uplift Axes by Moore et al. (2009). E-G-T Axis = Etosha-Griqualand-Transvaal Axis; O-K-Z Axis = Ovambo-Kalahari-Zimbabwe Axes.**

Autin et al., 2013) but the potential of post-rift movement on ancient basement structures or reactivation of failed syn-rift basins is still debated (Ziegler and Cloetingh, 2004). Post-rift inversion structures or extensional tectonic features have previously been identified in offshore rifted margin sequences (Lundin and Doré, 2002; Viola et al., 2005; Paton et al., 2008; de Vera et al., 2010), however, the onshore record of structural deformation is often destroyed by surface processes and is therefore harder to decipher.

In tectonically active regions, the main indication of the presence of brittle deformation is the creation of relief as fluvial incision responds to a change in base level driven by fault block movement (Kirby and Whipple, 2012). Variations in prevailing climate, lithology and pre-existing drainage network can produce distinct patterns of relief over different timescales (Beaumont et al., 1992; ter Voorde et al., 2004; Kirby and Whipple, 2012). In regions where fault movement has occurred in an erosional environment, prominent geomorphic features such as triangular facets, erosional surfaces, and knickpoints may develop and these can be used to evaluate patterns of erosion associated with fault movement (Roe

et al., 2006; Strak et al., 2011). Many geomorphic markers, however, preserve a record over short timescales (<100,000 yrs) and therefore do not provide insights into long-term landscape evolution (Strak et al., 2011). To address this issue, analogue and numerical modelling has been used to investigate the erosional response to thrust (Sinclair et al., 1991; Graveleau and Dominguez, 2008) and normal faulting (Hardy and Gawthorpe, 2002; Cowie et al., 2006; Strak et al., 2011).

In extensional settings the rate of erosion by fluvial incision is positively linked to the steepness of river slopes which are positively related to the timing and growth rate of faults. Moreover, Cowie et al. (2006) suggest that the distribution and interaction of normal faults has a major control on the location of drainage divides and catchment area of drainage on the footwall. For example, for fast rates of fault growth, small drainage basins develop while topographic relief is high and potentially laterally extensive. In compressional environments numerical modelling has pointed to the development of thrust-folds and the dip of major detachment folds as a major control on drainage development and migration of sediments (Tucker and Slingerland, 1996; Van der Beek et al., 2002).

Thermochronology provides another means to assess the magnitude of long-term erosion of uplifted fault blocks. However, the thermal effects associated with fault zones such as lateral heat flow due to fault block juxtaposition; varying geothermal gradients beneath eroding footwalls and buried hanging-walls; and heat flow perturbations beneath the developing relief on the footwall may complicate interpretation of data from such settings (Ehlers et al., 2001). The lag between erosion of the uplifted footwall relative to the timing of fault movement can also have a major influence of the thermal structure over time and therefore on the thermal history an exhumed rock column would experience (ter Voorde et al., 2004, Lock and Willet, 2008). Abrupt variations in fission track ages across basement terrains have been interpreted as evidence for structural reactivation at many margin settings (Raab et al., 2002; Redfield et al., 2004, 2005a, b; Kounov et al., 2009; Cogné et al., 2011, 2012; Danišík et al., 2012; Emmel et al., 2012; Karl et al., 2013; Franco-Magalhaes et al., 2014;

Ksienzyk et al., 2014). Importantly, these interpretations of fission track data are in agreement with recent studies of so-called “passive” margin settings using field-based structural analyses (Paton, 2006b; de Beer, 2012; Bezerra et al., 2014; McPherson et al., 2014), geophysical data (Stankiewicz et al., 2008; Maystrenko et al., 2013), or offshore seismic analysis (Viola et al., 2005; Paton et al., 2008; de Vera et al., 2010; Holford et al., 2014). Combined, these studies support major post-rift and neotectonic structural reactivation at continental margins that induced significant cooling of crustal rocks in the process.

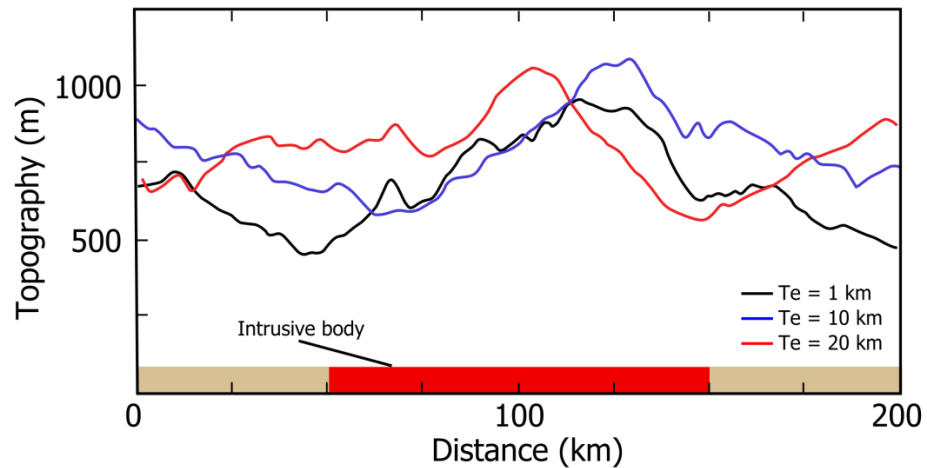
### **3.8.3 Crustal heterogeneity**

#### ***3.8.3.1 Rock hardness and rock density***

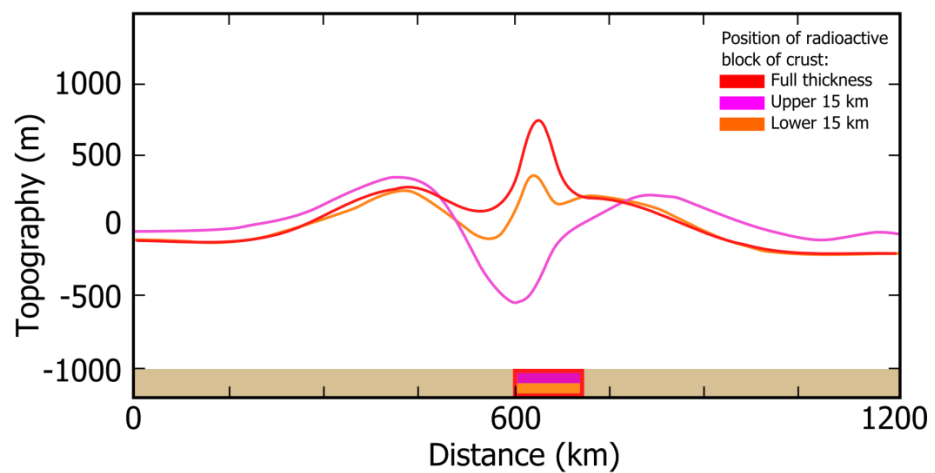
Lithological control in the generation of relief has long been argued by geomorphologists resulting in the formation of bornhardts, knickpoints and even escarpment type morphologies with resistant cap-rocks (e.g. Drakensberg escarpment). This has traditionally been viewed in terms of a rocks hardness, cohesion and particle size, that dictate how easily erodible the lithology will be (Summerfield, 1991). However, recent work has suggested that rock density exerts a greater control over relief generation than rock hardness (Braun et al., 2014b).

Braun et al. (2014b) suggest that the erosion of dense rocks such as granite intrusions will induce an isostatic response greater than when less dense rocks are removed. This results in dense crustal bodies existing as topographic highs in the landscape (Fig. 3-8a). A major source of contention with this model is that it is contradictory to the traditional geomorphic view of difficult to erode granite bodies. Braun et al. (2014a) suggest that isostatic-density driven relief generation will enhance erosion over the dense body creating a faster exhumation rate than the surrounding less dense rock. These effects will be most pronounced at settings where the lithosphere has a low flexural rigidity and has not been affected by a complex structural history (Braun et al., 2014b; Flowers, 2014).

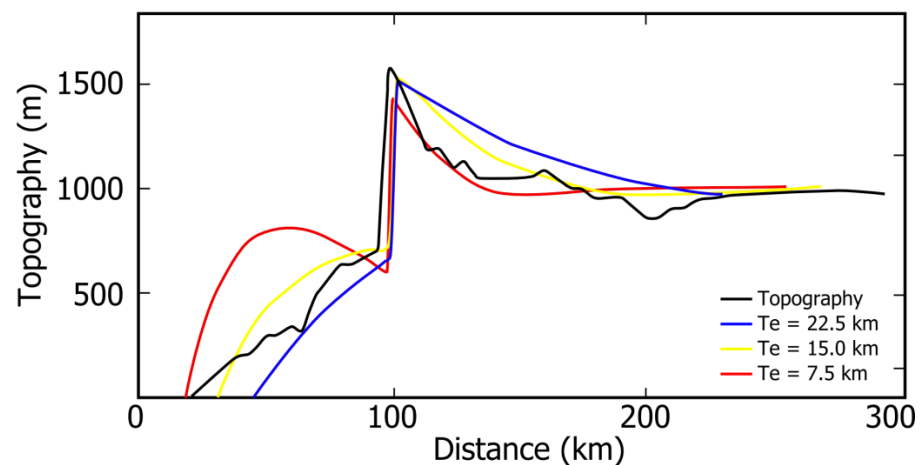
## (a) High density intrusion



## (b) Radiogenic crust



## (c) Lithosphere Elastic Thickness



**Figure 3-8:** Illustration showing the potential effect on topography predicted to occur by introducing (a) a region of dense crust (i.e. high density intrusion into low density sedimentary rock) (after Braun et al., 2014a) and (b) a region of radiogenic crust (after Pysklywec and Beaumont, 2004). (c) Shows the effect of changing the effective elastic thickness of the lithosphere on the development of rift flank topography (after Gilchrist and Summerfield, 1990).

### **3.8.3.2 Radiogenic crust**

The decay of radioactive isotopes (particularly U, Th and K) within the crust produces additional heat energy. Radiogenic heat production is thought to decay exponentially with depth before being dominated by the heat flow imposed on the base of the crust by the upper mantle (Braun et al., 2006). However, lateral variations in radiogenic heat production can be abrupt, dictated by lithology and rock composition (Andreoli et al., 2006). In general terms, the effect of crust with an elevated radiogenic heat production is that in this region the lithosphere will be weaker than the surrounding crust (Holford et al., 2009; Burov, 2011; Cloetingh and Burov, 2011; Armitage et al., 2013; Mareschal and Jaupart, 2013).

Large thermal contrasts can induce instabilities in the lithosphere and promote vertical deformation at major structures at continental margins or supposedly stable interiors (Pysklywec and Beaumont, 2004; Holford et al., 2011; Armitage et al., 2013). Modelling by Pysklywec and Beaumont, (2004) propose feedbacks may be established at regions of radiogenic crust coincident with mantle downwellings (Fig. 3-8b). These feedbacks involve a process of crustal thickening within the radiogenic crust causing heating that further weakens the lithosphere. These effects are most pronounced when the crustal thermal anomaly is distributed uniformly over a region or is buried beneath low radioactivity material. Such a region of radiogenic crust may make the lithosphere inherently prone to deformation as a result of mantle convection or in-plane stresses (Pysklywec and Beaumont, 2004; Holford et al., 2009; Burov, 2011; Cloetingh and Burov, 2011; Armitage et al., 2013; Mareschal and Jaupart, 2013).

### **3.8.3.3 Effective elastic thickness**

The role of flexural isostasy underpins all models investigating vertical movement of the lithosphere as a response to surface processes or mantle dynamics. In general, the regional deformation experienced by rigid lithosphere (high EET) in response to a vertical forcing will be of a smaller magnitude than a less rigid lithosphere (low EET) (Fig. 3-8c). Most models typically explore the effect of various values of EET on whatever process is being investigated.

However, despite being long recognised as a major influence on lithospheric deformation, the impact of laterally variable lithosphere elasticity is underexplored (ten Brink and Stern, 1992; Tucker and Slingerland, 1994).

During the rifting process, isostatic flexure of the lithosphere is initially a consequence of lithospheric thinning and sensitive to the depth of crustal necking (Braun and Beaumont, 1989; Rouby et al., 2013). In the post rift phase, flexing of the lithosphere is driven by unloading of the sub-aerial continental lithosphere and loading of adjacent sedimentary basins (Weissel and Karner, 1989). In this later phase, the efficiency of surface processes and the density of the material being removed have a major impact on the uplift and subsidence history of the margin (Rouby et al., 2013). Recent numerical modelling integrating the dynamics of both the continental and offshore domain has provided insights into the geomorphic evolution of the margin and the corresponding offshore stratigraphic record (e.g. Braun et al., 2013a; Rouby et al., 2013).

Results from this modelling predict that the initial topography, related to flexural uplift during rifting, will be eroded away within 20 Myr and produce an exponential decline in sedimentary volumes in offshore basins over time (Rouby et al., 2013). Moreover, it is suggested that peaks in offshore accumulation during a margin's post-rift history must therefore be driven by separate events such as sea level fall, crustal uplift or a climatically induced increase in erosion rate (Rouby et al., 2013). This model has been supported by field analysis by Dauteuil et al. (2013), using the northern Namibian margin as a type-example.

#### **3.8.3.4 Igneous bodies**

Previous sections have addressed structural deformation or the transfer of mass in the upper crust. However, the addition of crustal material in the form of igneous intrusions can also perturb the thermal and structural stability of the region and influence patterns of uplift. The presence of a lower crustal underplate comprised of igneous material is a feature identified in many rift models and is suggested to support uplifted rift-flanks over time (McKenzie, 1984; Cox, 1993; Gilchrist et al., 1994). Recent seismic imaging has revealed the



presence of lower crustal bodies at many margins in the form of high seismic velocity zones (Hirsch et al., 2010, Reynisson et al., 2010; Thybo and Artemieva, 2013). However, the origin of these zones is not exclusively magmatic and can be related to partial serpentinization of the mantle (e.g. O'Reilly et al., 1996; Lundin and Doré, 2011) or the presence of ancient inherited high grade metamorphic rocks (Ebbing et al., 2006; Gernigon et al., 2006; Reynisson et al., 2010). The uplift associated with the emplacement of a lower crustal body may induce a magnitude of surface uplift up to 10% of the thickness of the underplate (Maclennan and Lovell, 2002). However, depending on the composition, morphology and lateral extent of these crustal bodies, their impact may be spatially variable (Levell et al., 2010).

Local intrusive activity such as the emplacement of dykes and sills and small kimberlite and carbonitite pipes can be significant in terms of the tectonic geomorphology of the area. Their impact on the geomorphology comes either through doming above the intruding material or by creating local variations in lithology and, more importantly, erodability (Summerfield, 1991). This can result in pediment formation with resistant cap rocks atop steep escarpments (Gilchrist et al., 1994; Van der Beek et al., 2002) providing an important geomorphic record. A record of a regions erosional history can also be found in the preservation of crater facies and is discussed with particular relevance to Southern Africa in Chapter 7 - Section 7.5.2. Intrusions may also be closely linked to the structural history of the region. The spatial and temporal relationship of intrusive activity with structural zones and periods of active tectonics, respectively, is well documented (Stracke et al., 1979; White et al., 1995; Jelsma et al., 2004, 2009; Moore et al., 2008; Woolley and Bailey, 2012). However, following intrusion emplacement, these regions may become strengthened and focus later faulting and structural uplift to adjacent regions (Magee et al., 2013).

### **3.9 Geomorphology of dynamic topography**

The King model of landscape evolution ran into criticism partly due to the lack of a mechanism that could produce regional vertical movements of the crust;

lacking any explanation, King named the process of up-warping of the Earth's surface Cymatogeny (Ollier, 2014). Now, we know that such a mechanism may be attributed to vertical stresses being imposed at the base of the crust by upwelling mantle flows (i.e. dynamic uplift). The geomorphic expression of dynamic uplift is termed dynamic topography (Pekeris, 1935; Hager et al., 1985) and is of particular interest within the current literature and this study.

Both the style of uplift and associated topography is described as "Dynamic" as the processes are transient; linked directly to the presence of mantle up or down-welling (Flament et al., 2013). As the plate passes away from its position over the hot upwelling, the associated uplift dissipates and may lead to subsidence adjacent to regions of uplift (Moucha and Forte, 2011). Despite the transient nature, mantle convection cells and zones of anomalous heat flow have been shown to persist over long timescales (up to 10s of millions of years) and, depending on the relative rates of plate motion over the mantle, inducing surface uplift on the order of 10 - 30 m/Myr (Braun, 2010). This uplift is typically expected to occur over long wavelengths (1000s of kms) with relatively small amplitudes (c. < 2000 m) and therefore it should not lead to deep erosion of the uplifted surface (Braun, 2010). However, recent modelling has suggested that dynamic topography can be efficiently eroded due to the strong scaling between the size of the catchments draining the continent and the erosional response of the landscape (Braun et al., 2013b, 2014b).

Geological insights are crucial in understanding the relationship of surface processes with dynamic uplift; yet these can be difficult to obtain and attribute specifically to mantle-flow effects (Braun et al., 2013b). Well-preserved stratigraphic successions in sedimentary basins are often relied upon to provide such geological evidence through the identification of unconformities and marine regressions (Mitrovica et al., 1989; Heine et al., 2008; Petersen et al., 2010). However, any geological expression of dynamic uplift which occurs in sub-aerial environments has the potential to be eroded away. In this situation, understanding the timing, magnitude and distribution of erosion either by investigating geomorphological features (e.g. Burke, 1996; Hartley et al., 2011) or by quantitative dating techniques such as cosmogenic nuclide dating or low

temperature thermochronology is critical. Eroding a dynamic upwelling with consequent deposition in adjacent basins may disrupt the balance between gravitational stress and viscous stress from an upwelling mantle and perturb the underlying mantle flow, potentially driving further uplift (Braun, 2010, Braun et al., 2013b). Braun et al. (2013b) suggest that such a positive feedback could result in a single kilometre of dynamic uplift resulting in several kilometres of erosion.

It is still unclear whether these feedback mechanisms would be efficient over the long wavelengths which are associated with dynamic topography or whether mantle convection may only be affected at small-scales. Mantle convection on a shorter temporal and spatial scale as described above led Moucha et al. (2008) to suggest that continental margins and interiors are never stable over 10 - 100 Myr timescales. Moreover, small-scale mantle convection will likely disrupt eustatic sea level trends and create regional transgressive or regressive phases (Lovell et al., 2010). Consequently, this has implications for the geological record of the margins sedimentary basins and for geomorphic analyses using global sea levels as a stable base level over long timescales.

The signal of dynamic topography is likely modified by deformation of the lithosphere driven by lateral, plate motion driven, effects as discussed in Section 3.8.1. Indeed workers suggest that plume upwellings have a minor influence of lithospheric deformation relative to regional plate motions and intraplate stresses (e.g. Moore et al., 2009). However, a more likely scenario is that mantle upwellings combine with in-plane stresses to deform the brittle upper-lithosphere (e.g. Burov and Cloetingh, 2009; Guillou-Frottier et al., 2012; Cloetingh et al., 2013).

The most likely places to observe the present day and past signal of dynamic topography are low relief areas where dynamic topography may have perturbed drainage and catchment networks, continental interiors that have been tectonically quiet over hundreds of millions of years and the stratigraphic record that has not experienced periods of erosion (Flament et al., 2013). The effects of dynamic uplift have been advocated in a variety of geological settings such as

the Colorado Plateau (Liu and Gurnis, 2010; Karlstrom et al., 2012; Rowley et al., 2013), South America (Shephard et al., 2010; Dávila and Lithgow-Bertelloni, 2013), Eastern Australia (Di Caprio et al., 2011; Matthews et al., 2011), Southern Europe (Boschi et al., 2010) and Southern Africa (Gurnis et al., 2000; Moucha and Forte, 2011; Zhang et al., 2012).

### **3.10 Summary and conclusions**

Classical models of landscape evolution (e.g. Davis, Penck, and King) were developed largely out with the framework of plate tectonics. In the present day view of tectonic geomorphology these models are clearly an oversimplification of a complex problem. In fact, the influx of information from novel modelling techniques combined with new perspectives on geological observations both on and offshore continues to question and challenge established models of landscape development.

Key to resolving this debate will be in understanding if continental settings ever become truly stable and if so, when has this occurred over a regions geological history. Continental stability is crucial for allowing a landscape to evolve to reach its final stage, which, depending on different models, will be either a steady-state relief or planation surface. Regular periods of continental instability, further complicate the morphology of the landscape and, potentially the geological record, as they will drive sea level fluctuations and possibly create local inland base levels for drainage systems. Considering the influence thermal anomalies and regional plate stresses may have in deforming a lithosphere characterised by structural defects and rheological heterogeneity (affecting lithospheric strength) both laterally and vertically, long term stability may be unlikely.

Continental margins, including southwestern Africa, commonly exhibit the following features: a complex structural setting characterised by pre and syn-rift structures; emplacement of syn-rift intrusions of large volumes of mafic material; intense erosion of rift-related topography and offshore deposition; and a poorly understood and likely complex mantle convection throughout margin

development. For this reason, although continental margins may be regarded as “passive” compared to their intense rifting phase, they are likely to be geological settings where vertical and horizontal stresses are accommodated by movement on various scales on pre-existing structures across the entire length of the margin. The notion of a more dynamic post-rift geological setting also extends to continental interiors which have long been considered to be stable platforms. However, the combined effects of mantle driven uplift and regional in plane stress fields may encourage deformation, particularly at weak lithospheric zones such as at the boundaries of thick cratonic regions.

Except for regions where the climate is arid and the lithology is difficult to erode (such as the present day southwestern African margin), erosion efficiently creates relief following uplift. Depending on the flexural rigidity of the lithosphere the isostatic response can contribute to kilometres of overburden being removed from the continental margin following an initial modest uplift. As such thermochronology is a powerful tool for constraining the timing of denudation driven cooling of crustal rocks. While thermochronology may be limited in resolving the specific mechanisms involved in generating the present day topography, the temporal and spatial relationship of the data can be combined with additional geological data to produce an interpretation of the regions geomorphic history. More importantly, thermochronological data should be integrated with future models as key constraints on the crusts thermal history. However, considering the ambiguity in interpreting thermochronological data and uncertainty which persists in these approaches, careful consideration should be given as to how this should be done.

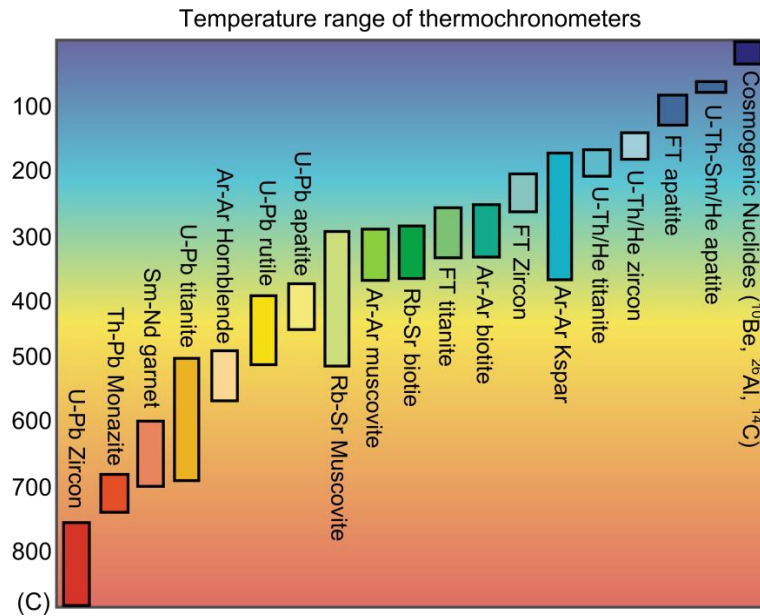
# CHAPTER 4

## APATITE FISSION TRACK AND (U-Th-Sm)/He THERMOCHRONOLOGY

### 4.1 Introduction

Dating techniques that are used to investigate past geological events typically exploit the ability of certain minerals to accumulate and retain daughter products created over time during the natural decay of radiogenic isotopes. The dominant control on the retention of daughter products only within a particular mineral is temperature. In his classic paper on this topic Dodson (1973) demonstrated that for simple monotonic cooling paths the retentivity of individual systems could be described by a specific ‘closure temperature’ that was a function of the cooling rate. In this way different minerals and different radiogenic decay series can be analysed to investigate the cooling history of a rock sample as a response to geological events (Fig. 4-1). In detail, however, the kinetics of diffusion and/or fission track annealing in most thermochronological systems cannot be adequately described using a discrete closure temperature as proposed by Dodson (1973). The sensitivity of these systems typically extends over a wider range of temperature where significant partial loss of daughter products can occur. This behaviour can be exploited to determine and constrain complex cooling paths through a particular temperature zone. It is this behaviour that underpins these methods as powerful thermochronometers rather than simple geochronometers.

Low temperature thermochronometry (LTT), as the name implies, focuses on relatively low temperature cooling within the upper crust of the Earth (c. < 300 to 350°C). For this reason, LTT has become a powerful tool for investigating upper crustal tectonic and geomorphic events where other direct geological evidence is scarce (Ehlers and Farley, 2003). Apatite fission track (AFT) and apatite (U-Th-Sm)/He (AHe) have been widely used in investigations of these



**Figure 4-1: Cartoon showing common thermochronology techniques used in geological investigations. Each technique is characterised by a decay series, a mineral and a range of temperature over which the thermochronometer is sensitive. What defines a *low* temperature thermochronometers is not strictly defined but is here described as thermochronometers sensitive to temperatures less than c. 300 – 350°C.**

types as they have the potential to provide detailed constraints on a rock's thermal history through c. 120 to 35°C. However, limitations inherent in each of these systems and an incomplete understanding of some of the underlying physical properties governing their systematics has, in some cases, led to apparently incompatible AFT and AHe datasets, 'over-dispersion' in observed ages and conflicts in thermal history interpretations derived from each method (Hendriks and Redfield, 2005; Green et al., 2006; Flowers, 2009; Brown et al., 2013).

Theoretical aspects of AFT and AHe analysis are briefly discussed here and in more detail in numerous published literature (e.g. Brown et al., 1994; Gallagher et al., 1998; Farley, 2002; Ehlers and Farley, 2003; Donelick et al., 2005; Lisker et al., 2009). Details of the practical approach to AFT and AHe analysis used in this study are provided in Appendix 1. This chapter will give a brief summary of the analytical techniques before focusing on the present issues and uncertainties associated with integrating data using both of these techniques. Through highlighting and discussing the points of uncertainty surrounding both AFT and AHe analysis, the methodology and interpretive approach used in this thesis will

be justified and described. This approach makes use of multiple single-grain AHe analysis and the use of a Bayesian transdimensional approach (e.g. Gallagher, 2012) to thermal history modelling. It will be demonstrated that this approach is effective for dealing with AFT and AHe data sets which initially appear incompatible or complex but can and do produce reliable and useful thermal history information.

## 4.2 Theoretical Background

### 4.2.1 Apatite fission track analysis

During the spontaneous fission decay of  $^{238}\text{U}$  within apatite, two highly charged fission particles are propelled through the host crystal lattice in opposite directions causing a linear trail of damage, or, a fission track (Fleischer et al., 1975). The number of tracks in a sample increases with time and  $^{238}\text{U}$  content. By counting the number of tracks intersecting a polished grain surface and estimating the concentration of  $^{238}\text{U}$  using the external detector method (EDM) (see Appendix 1.2) an AFT age can be obtained. Prior to analysis, samples undergo a standardised chemical etching treatment allowing fission tracks to be revealed so they are observable under an optical microscope (Donelick et al., 2005).

Fission tracks in apatite form with the same initial etchable track length of  $16 \pm 1 \mu\text{m}$  (Green et al., 1986; Donelick et al., 1990). The effect of thermal annealing is to shorten the maximum etchable length of a fission track. The degree of shortening is a strong function of temperature (Fleischer et al., 1975; Gleadow et al., 1986a; Green et al., 1989). The significance of a samples AFT age can therefore only very rarely be assigned any geological evidence on its own as the measured age is conditional on the distribution of track lengths which is itself a function of the thermal history of the sample (Gleadow et al., 1986a; Green, 1988). Rates of thermal annealing are extremely slow at temperatures below c.  $60^\circ\text{C}$  and rise significantly above this temperature until tracks are effectively instantaneously and completely annealed at temperatures greater than c.  $110^\circ\text{C}$  over geological timescales (Gleadow and Duddy, 1981). The temperature range between  $60$  and  $110 \pm 10^\circ\text{C}$  is known as the Partial Annealing Zone (PAZ)



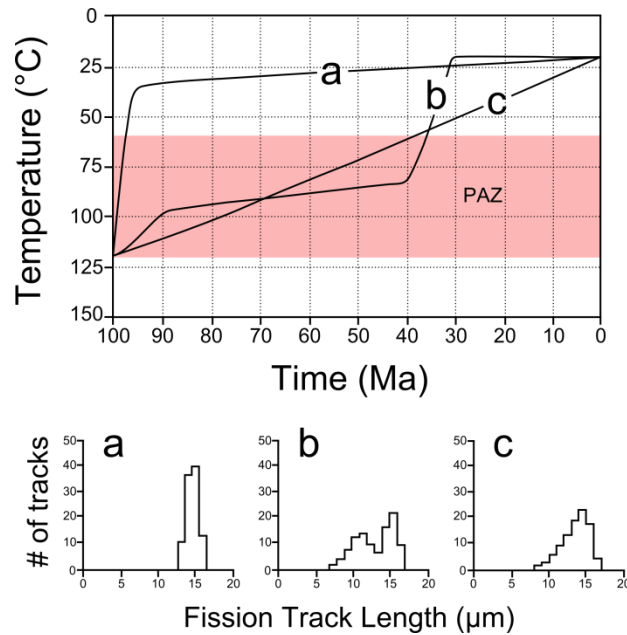
(Gleadow et al., 1986b; Gleadow and Fitzgerald, 1987; Wagner et al., 1989). By measuring horizontal confined track lengths (Appendix 1.2; Gleadow et al., 1986) alongside the AFT age a prediction can be made on the nature of sample cooling through the PAZ (Gleadow et al., 1986) (Fig. 4-2).

As a result of thermal annealing over geological timescales, the measured fission track age of a sample will decrease towards zero with depth as tracks become annealed to a greater degree (Fig. 4-3). Therefore, a “true” apatite fission track age (i.e. one which represents the time a sample last resided at temperatures within the crust  $\geq$  c.  $110\pm 10^\circ\text{C}$ ) will only be recorded if cooling has been sufficiently quick so that a sample is brought to temperatures  $<60^\circ\text{C}$  in a geological instant and consequently thermal annealing is minimal. In all other cases, the track length distribution (TLD) within a sample will represent a mixture of tracks that have been produced at elevated temperatures and have undergone some degree of annealing and tracks produced at temperatures below c.  $60^\circ\text{C}$  which will have not undergone annealing and will therefore be long. Decoding the thermal history information within the TLD is thus the key to robust interpretations of AFT ages.

#### **4.2.2 Apatite (U-Th-Sm)/He analysis**

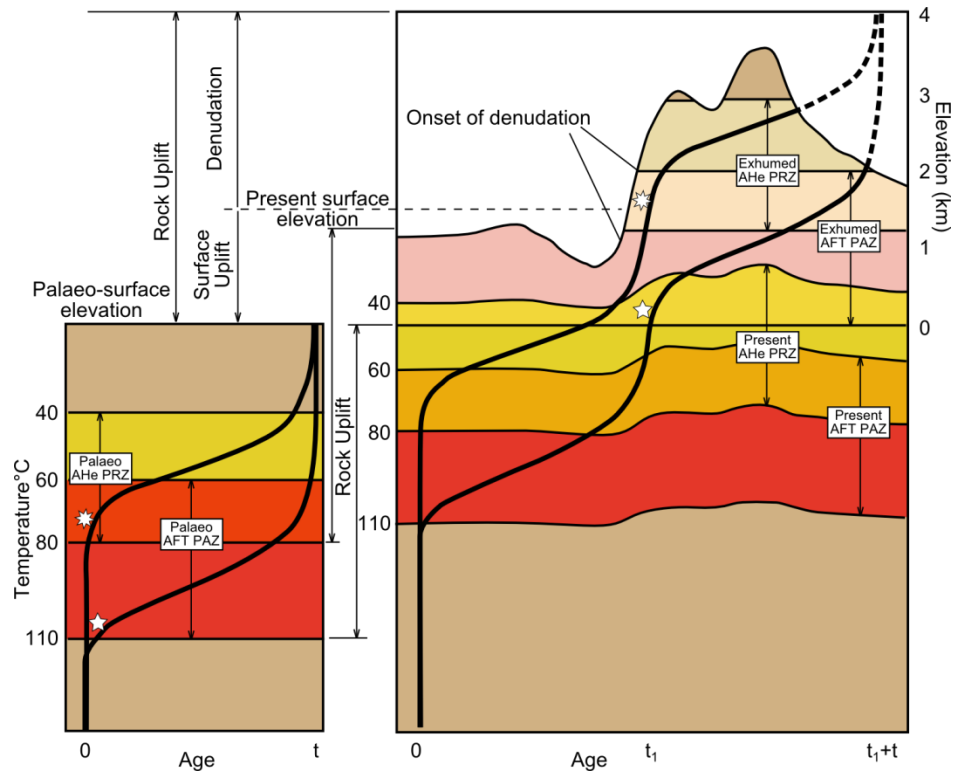
Apatite (U-Th-Sm)/He dating utilises the accumulation of He within the apatite crystal produced by the alpha series decay of U, Th and, to varying degrees of importance, Sm (Zeitler et al., 1987; Farley, 2002; Fitzgerald et al., 2006). Assuming that all of the alpha particles produced and retained within the crystal are from the decay of parent isotopes within the crystal then an AHe age can be obtained by measuring the relative abundances of U, Th and Sm against the amount of He retained in the crystal.

As with other thermochronometers, the measured age reflects the cooling trajectory of the sample through the temperature range that controls He diffusion within apatite. The sensitivity of He diffusion in apatite to temperature defines a theoretical partial retention zone (PRZ) where retention of helium in apatite increases with decreasing temperature. The PRZ influences AHe ages



**Figure 4-2: Upper panel shows three hypothetical thermal histories. Lower panel shows three typical track lengths distributions that are observed for the respective thermal history. For this reason, the track length distribution can be inverted to reveal thermal history information (after Gallagher et al., 1998).**

with depth in a similar manner as the PAZ for AFT ages (Wolf et al., 1998). At temperatures hotter than the maximum temperature of the PRZ, diffusive loss is effectively instantaneous and the AHe age would be zero (Fig. 4-3). At lower temperatures, retention of He progressively increases until at sufficiently low temperatures (c.  $<40^{\circ}\text{C}$ ) diffusion of He is effectively negligible. Early investigations of He diffusion from apatite estimated the PRZ to be a temperature range of c.  $40$  to  $75 \pm 5^{\circ}\text{C}$  (Wolf et al., 1996, 1998; Farley, 2000). However, the concept of defining a single set of kinetic parameters for the AHe system has become increasingly difficult as it has been shown that individual grains begin to retain He at higher temperatures due to variations in crystal size (e.g. Farley, 2000; Reiners and Farley, 2001), composition (e.g. Warnock et al., 1997) and accumulated radiation damage caused by alpha recoil during the decay of U and Th (Shuster et al., 2006; Flowers et al., 2009; Gautheron et al., 2009).



**Figure 4-3:** Left hand figure shows the structure of the theoretical PAZ and PRZ beneath a flat topography and the expected age profile with depth for both AFT and AHe thermochronometers. Asterix and star represent samples currently at depth. Right hand figure shows these samples now exhumed following a period of rapid uplift and denudation producing high relief topography. The high relief topography perturbs the present day PAZ and PRZ at depth. In high relief areas the age profile may have preserved the structure of the profile through the now exhumed palaeo-PAZ and palaeo-PRZ (after Fitzgerald et al., 2006).

Much of our knowledge of Helium diffusion from apatite comes from diffusion experiments using the near gem quality Durango apatite from Cerro de Mercado, Mexico (Farley, 2000). For this reason, Durango apatite is commonly used as a standard for analysis (see Appendix 2.2) and the kinematics of the AHe system incorporated into modelling techniques is based on diffusion experiments using Durango apatite. However, it is now becoming increasingly clear that geologically 'old' samples that contain high concentrations of U, Th and Sm and therefore may have varying degrees of radiation damage and/or zonation of parent isotopes can not be adequately understood using the on Durango apatite based diffusion kinematics is a matter for debate (e.g. Green et al., 2006; Flowers et al., 2009; Gautheron et al., 2009, 2013)

Aside from diffusion of He from the crystal, helium is lost by a process of alpha-ejection (Farley et al., 1996; Hourigan et al., 2005; Spiegel et al., 2009;

Gautheron et al., 2012). This occurs due to alpha particles travelling up to 20  $\mu\text{m}$  before coming to rest after being emitted from their parent isotope (Farley et al., 1996). As such, a proportion of alpha particles produced within 20  $\mu\text{m}$  of the crystal edge are lost from the crystal due to ejection. This phenomenon is commonly corrected for using a correction factor ( $F_t$ ) during the calculation of AHe ages (Farley et al., 1996; Ketcham et al., 2011). However, the justification for making this correction is questionable because it is only ever appropriate if the sample cooled quickly and did not suffer any diffusional loss of He. Consequently, using the  $F_t$  to correct for alpha-ejection will always over-correct ages that have experienced significant diffusive loss of helium during their thermal history (Spiegel et al., 2009; Gautheron et al., 2012). An alternative approach to interpreting AHe ages is to work with the uncorrected, measured ages and use a thermal model to derive constraints on the cooling paths consistent with the measured age and which explicitly accounts for the loss of He by alpha-ejection at each time-step during thermal history (e.g. Meesters and Dunai, 2002a, b). In this way, the necessity of making any assumptions on the thermal history a-priori or to making any geometrical correction for He lost by alpha ejection is circumvented. This latter approach is followed in this thesis.

### 4.2.3 Integrating AFT and AHe datasets

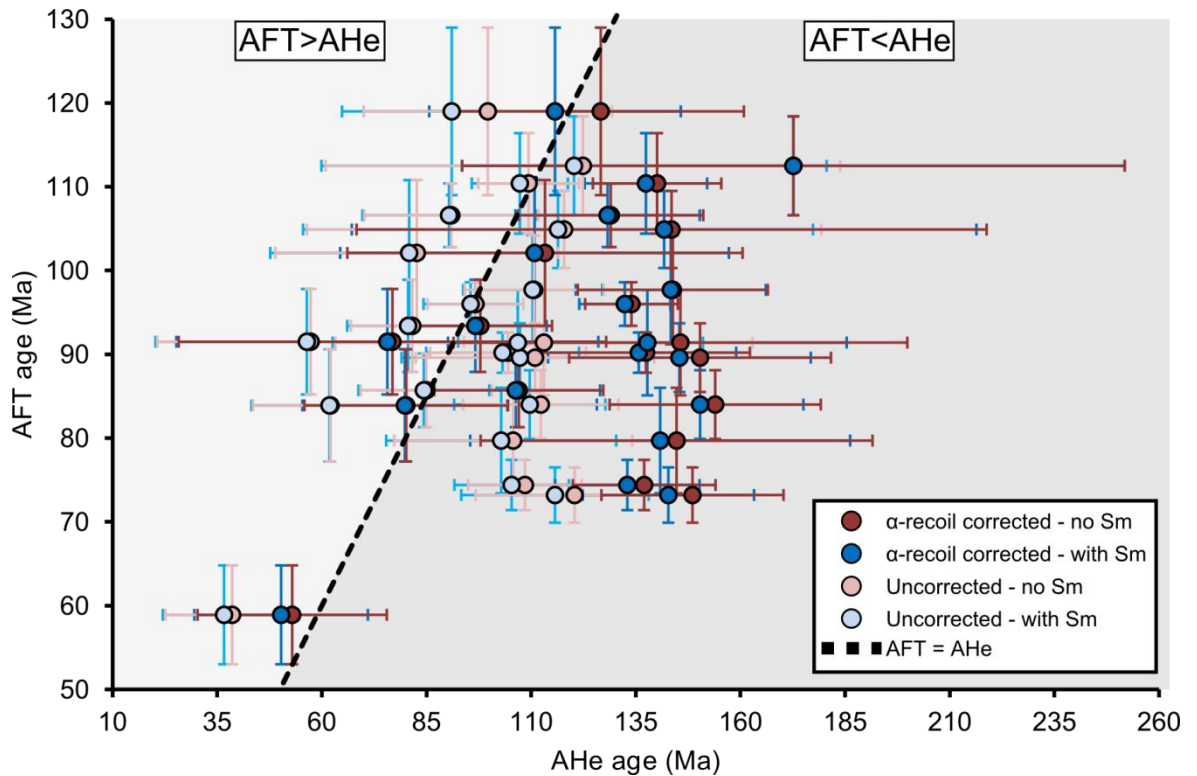
The AFT and AHe thermochronometers are sensitive over different but overlapping temperature ranges. Under normal conditions, combining the AHe technique with AFT analysis should provide two major benefits: (i) AHe analysis augments and enhances the lower temperature portion of the AFT dating domain and (ii) provides new insights into cooling events (denudation driven or otherwise) at temperatures where AFT analysis is no longer sensitive. Combining multiple thermochronometers such as AFT and AHe is therefore a logical step in generating more robust thermal history information. Due to their respective nominal theoretical closure temperatures, a sample would be expected to yield an AHe age that is younger or equal to the complementary AFT age. However, in several studies this relationship is poorly defined either in individual samples or throughout the entire dataset (e.g. Hendriks and Redfield, 2005; Fitzgerald et al., 2006; Green and Duddy, 2006; Flowers and Kelley, 2011; Danišík et al.,

2012; Ksienzyk et al., 2014). In some cases, this relationship improves if the uncorrected age is taken ahead of alpha-recoil corrected AHe ages. This supports suggestions that correcting the raw AHe age using a single  $F_t$  factor will overestimate the degree of helium loss by alpha ejection (Gautheron et al., 2012; Brown et al., 2013).

Many studies also assume that the Sm contribution to the total concentration of radiogenic  $^4\text{He}$  is extremely low relative to that of U and Th (e.g. Hansen and Reiners, 2006; Vermeesch, 2008). Data presented here agrees with previous work that the Sm contribution to the age is small but variable from sample to sample and can have a non-negligible effect on the measured age. For example, three samples have Sm contribution greater than or equal to 5% with sample SA12-35 having a Sm contribution of 8.6%. In most other cases the contribution is less than 2 - 3%. The Sm contribution for Durango standards was less than 0.4% and could therefore be argued as insignificant (see appendix A2.2). However, this is not representative of natural samples. Figure 4-4 shows the relationship between AFT and AHe for new data from SW Africa and highlights the importance of quantifying Sm in AHe analyses and the improvement in the AFT - AHe relationship when uncorrected AHe ages (raw AHe age) are reported. For certain samples, however, the raw AHe age, including the Sm contribution, is still older than the complementary AFT age. Moreover, high levels of single grain AHe age dispersion suggest additional factors are complicating the AFT - AHe relationship and a calculating a single mean AHe age may not be appropriate. The following section looks at aspects of both systems to evaluate the factors decoupling the AFT - AHe relationship and explore whether they present problems or potential for the procurement of thermal history information.

### **4.3 Uncertainties in apatite fission track analysis**

Throughout the 1980s the foundations for the geological application of apatite fission track analysis were laid down in a series of contributions addressing both the theoretical and statistical framework for fission track analysis. A critical outcome of these studies was the identification of the primary control of temperature over track annealing (e.g. Gleadow et al., 1983; Hurford and



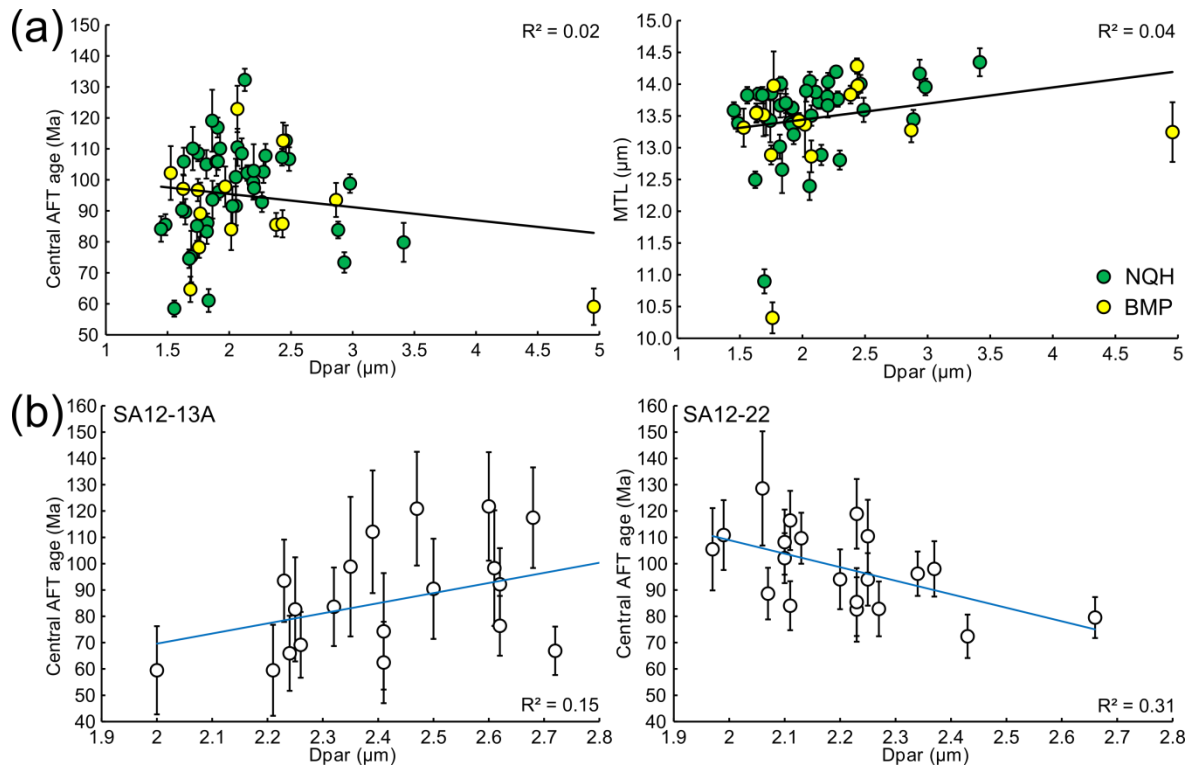
**Figure 4-4: Relationship between AFT and AHe average ages excluding single grains without quantified Sm.** Plot shows the improvement of the expected  $AFT \geq AHe$  relationship when the contribution of Sm is included and a single alpha correction is not applied. The average AHe age used here is calculated using a subset of single grain ages (presented in Chapters 5 and 6) however single grains without quantified Sm have been excluded from the calculation of the mean value to highlight the effect of Sm on the AFT-AHe relationship.

Green, 1983; Green et al., 1986; Laslett et al., 1987; Duddy et al., 1988; Green et al., 1989). Diligent and systematic laboratory calibrations of the annealing behaviour of apatite fission tracks continued throughout the subsequent decades leading to the development of robust numerical models designed to invert track length measurements to extract thermal history information (see section 4.2.1). Through the development of theoretical work, AFT analysis has become a reliable tool for understanding thermally sensitive geological processes with both academic and industry applications. However, certain aspects of fission track annealing have been questioned by several workers suggesting that additional factors may enhance rates of thermal annealing. A few of these factors are briefly explored and discussed as well as the more fundamental issue of how reliable an individual analysts track length measurements may be.

### 4.3.1 Chemical composition

Fluoroapatite is the most common end-member composition of apatite ( $\text{Ca}_{10}(\text{PO}_4)_6\text{F}_2$ ) but it has been shown that compositional heterogeneity between apatite crystals can influence the rate of thermal annealing (Green et al., 1986; O'Sullivan and Parrish, 1995; Carlson et al., 1999). Compositional heterogeneity within apatite can occur by cation or anion substitution of Ca and/or F, respectively (Carlson et al., 1999; Barbarand et al., 2003). Substitution of F typically occurs with OH or Cl. While the potential for the former to increase track resistance to annealing is appreciated by certain workers (e.g. Crowley et al., 1990) the presence of the latter, particularly at concentrations  $> 0.3$  wt% has been shown to be a more common and more dominant cause (Crowley et al., 1991; O'Sullivan and Parrish, 1995; Carlson et al., 1999; Barbarand et al., 2003). REEs, Mn, and Sr can become incorporated into the crystal composition in place of Ca (Ravenhurst et al., 1993; Burtner et al., 1994; Carlson et al., 1999). The influence of REEs is still poorly understood but is likely to exert a significant, though second order, influence on the structure of the fluoroapatite end member crystals (Barbarand et al., 2003).

More recent annealing models have included the compositional effect on thermal annealing by incorporating additional kinetic parameters. Ideally, these kinetic parameters should reflect variations in Cl, REE and all other possible chemical heterogeneities that can influence track annealing. However, as stated by Barbarand et al., (2003), a full compositional characterisation of each analysed grain is analytically challenging. A popular approach is to assume Cl has a dominant control on the resistance of fission tracks to annealing and quantify Cl contents using electron microprobe analysis. Alternatively, the kinetic parameter  $D_{\text{par}}$  (Donelick et al., 1999) can be used in track annealing models as a proxy for the amount of resistance to annealing (Carlson et al., 1999; Barbarand et al., 2003; Ketcham et al., 2007; Sobel and Seward, 2010). This value represents the size of the etch-pit made by the intersection of a fission track with the polished surface of the grain mount and can easily be measured during AFT analysis. For example, small  $D_{\text{par}}$  values imply Fluoroapatite like annealing behaviour while higher  $D_{\text{par}}$  values suggest a higher degree of compositional



**Figure 4-5: Relationship between etch pit measurements ( $D_{par}$ ) and AFT age and MTL. (a) Shows the relationship of average measurements for both parameters for all samples across the region. NQH = Namaqualand Highlands study area; BMP = Bushmanland Plateau study area. (b) Shows the  $D_{par}$  – AFT age relationship for single grain ages from two different samples.**

complexity influencing annealing (Carlson et al., 1999). For a  $10^\circ\text{C}/\text{Myr}$  cooling rate it is suggested that a  $0.1 \mu\text{m}$  change in  $D_{par}$  corresponds to a  $1.5 - 2^\circ\text{C}$  change in AFT closure temperature (Ketcham et al., 2007).

Gautheron et al. (2013) report weak positive correlations between AFT age and  $D_{par}$  and Cl wt% and Barabrand et al. (2003) present a similar correlation between  $D_{par}$  and MTL. Figure 4-5a shows the relationship between  $D_{par}$  and AFT Age/MTL for samples in this study.  $R^2$  values close to zero highlights the lack of correlation between average  $D_{par}$  measurements for samples against central AFT ages and MTLs. Some samples with high  $D_{par}$  values can be treated with caution as they are potentially over etched and therefore will not be representative of the samples compositional effect on annealing. Removing suspiciously large  $D_{par}$  values would encourage a slightly improved positive correlation in the data however as all samples were processed by the same procedure there is no reason to suspect that the majority of these samples with large  $D_{par}$  values are over etched. An exception to this is sample SA12-11 ( $D_{par} = 4.95 \mu\text{m}$ ). Inspection of



this samples fission track mount provides more evidence that this sample is indeed over-etched.

Further investigation on the influence of  $D_{\text{par}}$  is made by plotting Age- $D_{\text{par}}$  relationships for single grain ages. Figure 4-5b shows two samples which show two contrasting correlations. Both positive and negative correlations are identified throughout the dataset and these two samples are the best correlated for each example but the correlation is still statistically poor ( $R^2 \leq 0.31$ ). The complex relationships observed here are not surprising considering the primary influence of temperature on the preservation of track lengths coupled with the possibility of additional compositional complexity, particularly for low Cl samples. Correlations are likely to be absent as many samples have experienced fairly rapid cooling, as implied by their long track lengths and narrow TLDs. If the sample has been rapidly cooled, annealing and any compositional influence over it will have been minimal.

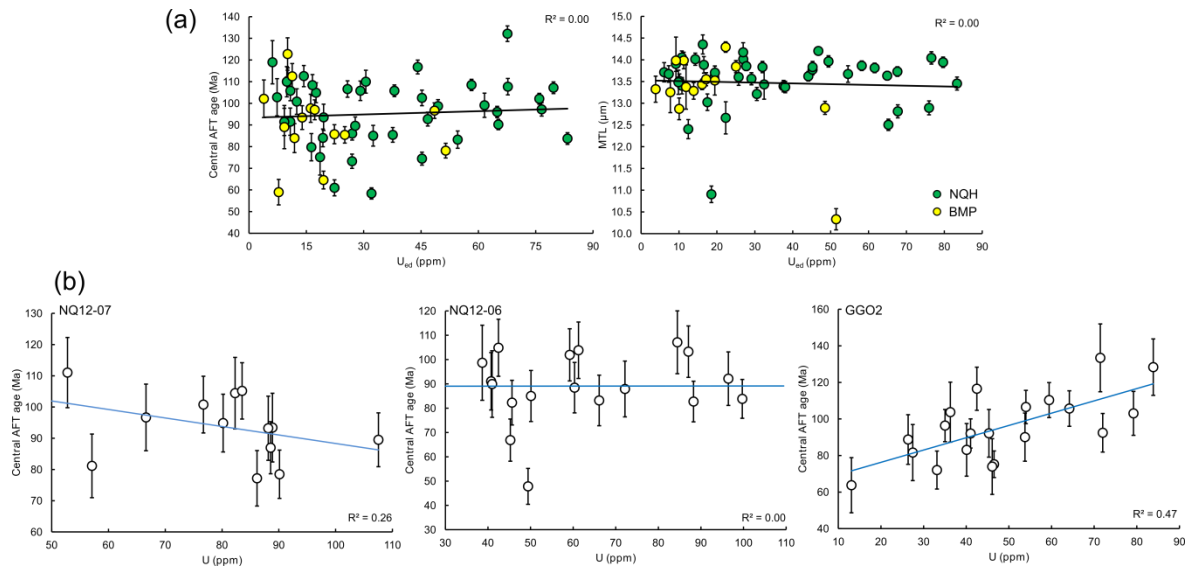
### 4.3.2 Pressure

Contrary to conclusions of early work on fission track annealing (e.g. Fleischer et al., 1965, 1975; Naeser and Faul, 1969), Wendt et al. (2002, 2003) and Vidal et al. (2003) suggest that elevated pressures and stresses can influence fission track annealing kinetics. However, criticism by Kohn et al. (2003) was fuelled mainly by a lack of extrapolation of the pressure dependant annealing model to geological timescales. An additional criticism was aimed at the lack of direct evidence of the effect from, for example, deep borehole profiles in cratonic regions (Kohn et al., 2003; Green et al., 2013). Annealing experiments by Donelick et al. (2003) could not produce results to suggest that pressure has a significant impact on fission track annealing. More recently, Schmidt et al. (2014) performed similar pressure-annealing experiments showing that pressure dependence exists at extreme pressures of 2 - 4 Ga but when extrapolated to pressures more typical of upper crustal temperatures ( $\leq 150^\circ\text{C}$ ) the effect is negligible. It is widely appreciated that current annealing models do not need to be modified to incorporate pressure effects (Green et al., 2013).

### 4.3.3 Radiation Enhanced Annealing

Annealing experiments by Donelick et al. (1990) have shown that fission track annealing can occur even at room temperatures however the kinematics of low temperature annealing is still poorly understood (Gleadow and Duddy, 1981; Hendriks and Redfield, 2005; Spiegel et al., 2007). Hendriks and Redfield (2005) suggest that cratonic rocks that have resided in a geologically stable setting for long periods (i.e. > 100 Myr.) and/or have extremely elevated levels of U and Th may experience enhanced annealing at low temperatures. Radiation enhanced annealing (REA) may occur by (i) elevated temperatures in the sub-surface crust caused by radiogenic decay in basement rocks (i.e. by decay of U, Th, K); (ii) induced defect recovery during alpha-emission (Miro et al., 2005). Supporting this proposition Hendriks and Redfield (2005) present data that appear to show negative correlations between AFT age and MTL with uranium content. It is stated by Hendriks and Redfield (2005) that if such correlations are attributed to REA then the effect will be most pronounced in samples that are geologically old and/or contain high concentrations of U and Th.

Data presented in this study fail to consistently show negative correlations between U content and AFT central age. Figure 4-6a shows a plot of average U content (estimated using the EDM method) versus central AFT age and MTL for all samples analysed. In neither case, nor in either study area investigated in this study, is there a negative correlation with uranium content. However, due to differences in the thermal history experienced by these samples any REA effects may be masked. Figure 4-6b shows single grain data from three different samples that are the “old” (> 90 Ma) and enriched in U (c. 50 - 70 ppm). The correlations observed in these samples are representative of the entire dataset and it can be seen that there exists positive, negative and zero correlation between AFT age/MTL and U content. More accurately, correlations of any sort are suspect because they are statistically very poor with low  $R^2$  values. The samples presented in Figure 4-6b show the best correlation in the dataset. The best fit is, in fact, the *positive* correlation shown by GGO2 ( $R^2 = 0.47$ ,  $N = 20$ ). It is thus concluded that in this study REA cannot be supported as a controlling factor on the observed AFT data.



**Figure 4-6: Relationship of AFT age and MTL against uranium content as a proxy for the degree of radiation enhanced annealing experienced by the sample (Hendriks and Redfield, 2005). (a) Average values for samples across the entire study area. NQH = Namaqualand Highlands study area; BMP = Bushmanland Plateau study area. (b) single grain data correlations for AFT age – uranium content from three samples. The lower plots highlight the lack of consistency in the style and strength of correlations.**

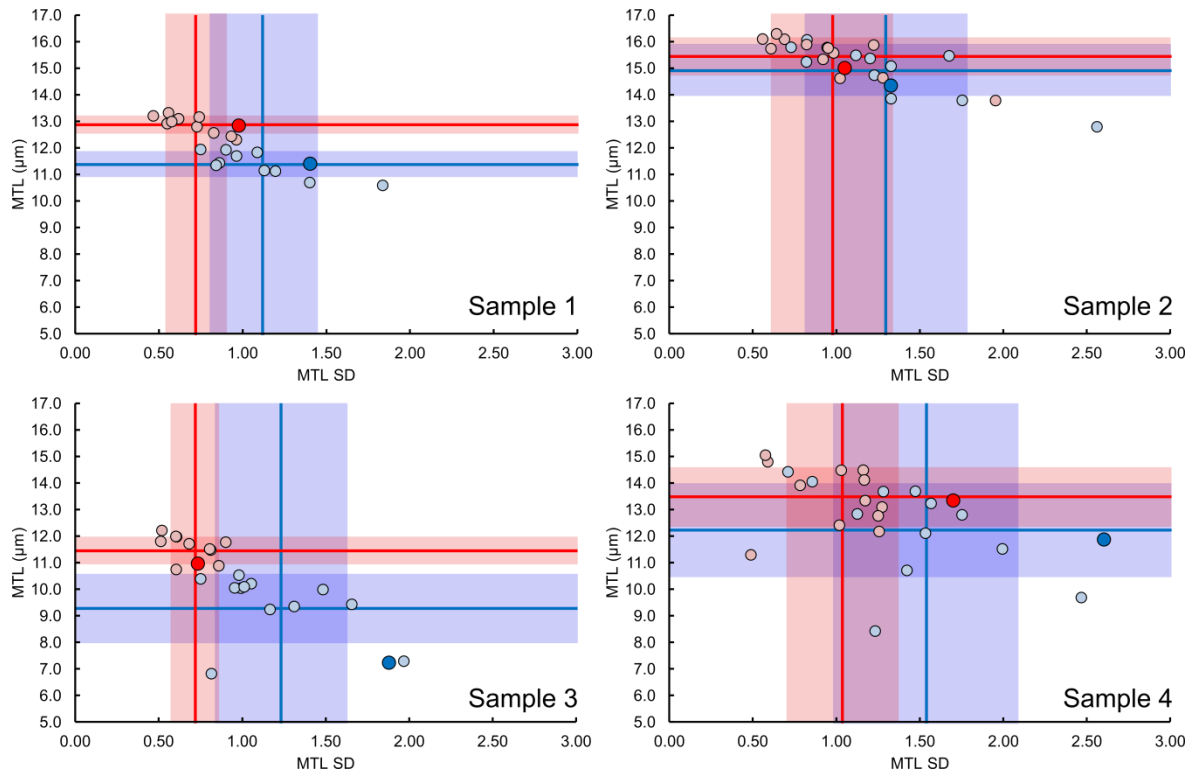
Correlations used to support radiation enhanced annealing were criticised by Green and Duddy (2006) and Green et al. (2006); particularly correlations made in samples with increasing borehole depth which they advocate can be explained in terms of thermal annealing. Their alternative view is that discrepancies between AFT and AHe datasets in cratonic regions are due to radiation damage enhanced retentivity of helium (see section 4.4.5). Larson et al. (2006) direct their criticism at the geological interpretation required by Hendriks and Redfield to justify the need for an improved AFT annealing model. While radiation enhanced annealing is still supported by Hendriks and Redfield (2006), their conclusions were questioned by a subsequent analysis of the same data by Kohn et al. (2009). The debate suggests an unresolved issue in low temperature thermochronology analysis regarding our understanding of old, U and Th rich apatites and the role that radiation damage might play in controlling fission track annealing.

#### 4.3.4 Calibration and reproducibility of track length measurements

While our empirical understanding of fission track annealing is reasonably well developed there still exists a major source of human uncertainty surrounding the measurement of horizontal confined tracks within fission track mounts (Donelick, 2005). Inter-laboratory and multiple analyst experiments of track length measurements (Miller et al., 1993; Barbarand et al., 2003; Ketcham et al., 2009) identified major inconsistencies between track length distributions measured by different analysts. The discrepancy between analysts was initially attributed to differential sampling of long and short track populations and length differences induced by different lab protocols in etching and microscopy technique and, as discussed above, natural sample heterogeneity was another possible source of variation.

Consistency was improved when measured track lengths were normalised for their orientation to the crystallographic c-axis (e.g. Ketcham, 2005). This normalisation is performed to incorporate anisotropic annealing of fission tracks (Green and Durrani, 1977; Donelick, 1991). Another major inconsistency was in measurements of unannealed fission tracks ( $L_0$ ) induced in apatite standards (Ketcham et al., 2009). Knowing the initial track length of a sample is crucial information for thermal history inversion to be successful. The initial track length is suggested to vary with etch pit size and therefore  $D_{par}$  measurements can be used in inversion techniques to calibrate the initial track length (Donelick et al., 1999; Ketcham et al., 2007).

Prior to sample analysis, horizontal confined track (HCT) lengths were measured and compared to MTL, MTL standard deviations and TLDs as measured by previous analysts at the University of Glasgow. The samples were first irradiated and then heated to different degrees to produce different amounts of annealing and consequently produce different TLDs. The results shown in Figure 4-7 show that track length measurements are more reproducible once the orientation of tracks to c-axis is corrected. The mean c-axis corrected track length measured in this study lies within  $1\sigma$  standard deviation the average measured by previous analysts. The standard deviation of the mean track length is reproduced less



**Figure 4-7: Interlaboratory AFT length calibration for analysts at the University of Glasgow. Blue colour represents raw measured track length data. Red colour represents track length data corrected for c-axis orientation. Horizontal line and bar indicates the average and  $1\sigma$  standard deviation of MTL observed for all analysts. Vertical line and bar indicates the average and  $1\sigma$  standard deviation of MTL-SD measurements observed for all analysts. Small circles with faint colour are data from previous analysts following University of Glasgow FT lab protocols. Large circles with intense colour are data measured by M. Wildman prior to sample analysis.**

well but in all cases lies within  $2\sigma$  standard deviation of the average reported MTL-SD from previous analysis. Within uncertainty, track length measurements in this study are comparable with other fission track analysts and any user bias towards longer or shorter tracks should be minimal.

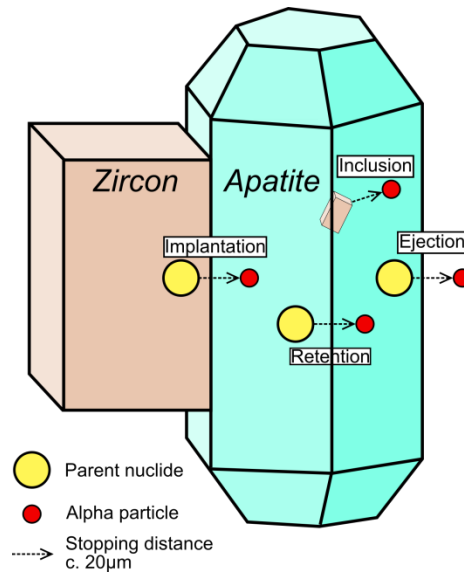
#### 4.4 Uncertainties in apatite (U-Th-Sm)/He analysis

Apatite (U-Th-Sm)/He dating depends on the progressive accumulation of helium within the host crystal lattice. However, to understand the geological significance of AHe data it is necessary to know when and at what temperatures  $^4\text{He}$  begins to become retained within the apatite crystal and by what process He escapes from the crystal over geological timescales (i.e. diffusion or alpha-ejection) (Gautheron et al., 2012). An additional assumption is that all He retained comes from the decay of parent isotopes within the crystal structure

and not from additional sources such as neighbouring grains or mineral or fluid inclusions (Vermeesch et al., 2007). At elevated temperatures  $^4\text{He}$  is lost from the crystal through diffusion but the kinetics of this process are still poorly understood and have been shown to be influenced by grain geometry and the presence of radiation damage defects. This, coupled with the effects of zonation of U, Th and Sm, ejection of alpha particles from the crystal rim and the impact of analysing fragmented grains creates many sources of uncertainty within AHe analysis are often manifested as ‘over-dispersion’ of single grain ages. As diffusion is temperature dependent many of the factors cause dispersion to be highest when cooling is slow or complex. Therefore, enhancing AHe single grain age dispersion may hold crucial thermal history information and is potentially beneficial rather than detrimental to AHe analysis.

#### 4.4.1 Alpha ejection

During the decay of  $^{238}\text{U}$ ,  $^{235}\text{U}$  and  $^{232}\text{Th}$ , alpha particles are emitted and come to rest with a stopping distance of c. 20  $\mu\text{m}$ . As a result of long-stopping distances some alpha particles emitted close to the crystal rim may be ejected (Fig. 4-8) (Farley et al., 1996). The physical size and shape of apatite crystals used in (U-Th-Sm)/He analysis will have a pronounced effect on not only diffusion of He but also the proportional loss of He from apatite through alpha ejection (Gautheron and Tassan-Got, 2010). Farley et al. (1996) produced a model to quantitatively correct for alpha ejection (i.e.  $F_t$  alpha recoil correction) assuming that (i) parent nuclides are homogeneously distributed within the crystal and (ii) that implantation of He to apatite from the surrounding rock matrix is negligible. Since the development of the alpha-correction model there have been suggestions that the correction factor may over estimate true AHe ages due to the interplay of diffusion and alpha ejection (Meesters and Dunai, 2002a, b). However, at elevated temperatures, He is lost predominantly through diffusion which will occur to a greater degree at the crystal rim and should not be effectively replaced by correcting for alpha-ejection. Hence treating diffusive loss and alpha-recoil as independent processes, where first diffusion is corrected using forward modelling and then ejection corrected using  $F_t$ , will over correct sample ages (Dunai, 2005).



**Figure 4-8: Cartoon figure representing the effects of implantation, ejection and U and Th rich inclusions caused by long-stopping distances of alpha particles emitted from parent nuclides.**

Clearly the overcorrection effect will be most pronounced for samples which cool slowly through the PRZ where diffusion has dominated He loss. More recent mathematical models have been developed to generate more accurate correction factors accounting for a better representation of the true crystal geometry, compositional heterogeneity and presence of broken faces (Gautheron and Tassan-Got, 2010; Ketcham et al., 2011; Gautheron et al., 2012). However, adopting the more sophisticated approach outlined by Gautheron et al. (2012) will only improve the accuracy of the correction factor by c. 1 - 5% (Ketcham et al., 2011) and does not address the problem of partially degassed grains at all. In this study an  $F_t$  correction, after Farley et al. (1996) is used to report a 'corrected age'. However, the likelihood of inconsistency between 'corrected' AHe ages and AFT ages (Fig. 4-4) encourages the approach outlined by Meesters and Dunai (2002a, b) where alpha ejection is determined explicitly during thermal history modelling at each time step as appropriate. Moreover, further investigations of AHe age dispersion are made using the raw ages as this removes an added layer of uncertainty that could mask other major dispersion factors (Brown et al., 2013).

#### 4.4.2 Implantation

Just as long stopping distance of alpha particles may result in alpha ejection from the rim of the apatite crystal, it may also result in implantation from adjacent U and/or Th rich minerals (Fig. 4-8) (Farley et al., 1996; Spiegel et al., 2009; Gautheron et al., 2012). This phenomenon will occur if U and Th rich minerals (e.g. zircon, titanite or monazite) are in contact with the apatite crystal, with the effect becoming less potent with increasing distance. Although it has been shown theoretically that  $^4\text{He}$  enrichment could be up to 50%, and in extreme cases >300%, for this to have occurred the apatite would have had to have been entirely surrounded by large, enriched minerals (Gautheron et al., 2012). Spiegel et al. (2009) highlighted the improvement in reproducibility of potentially implanted grains following air abrasion of the grains to remove the outer 20 - 25  $\mu\text{m}$  rim of the crystal. However, this may remove potentially useful information held in the diffusion profile of the grain and for the reasons described above the issue may not require any additional treatment. It should be noted that if significant levels of implantation have occurred in an individual apatite crystal, the probability of selecting that crystal from a mineral separate is relatively low (Brown et al., 2013). This study adopts an approach where many single grain ages (c. 10 - 20 grains) are analysed this allows extreme outliers to be identified. Implantation may be used as a potential explanation for these crystals but in most cases the effect is expected to be small and, if present, is encapsulated in the uncertainty given to the observed age.

#### 4.4.3 Inclusions

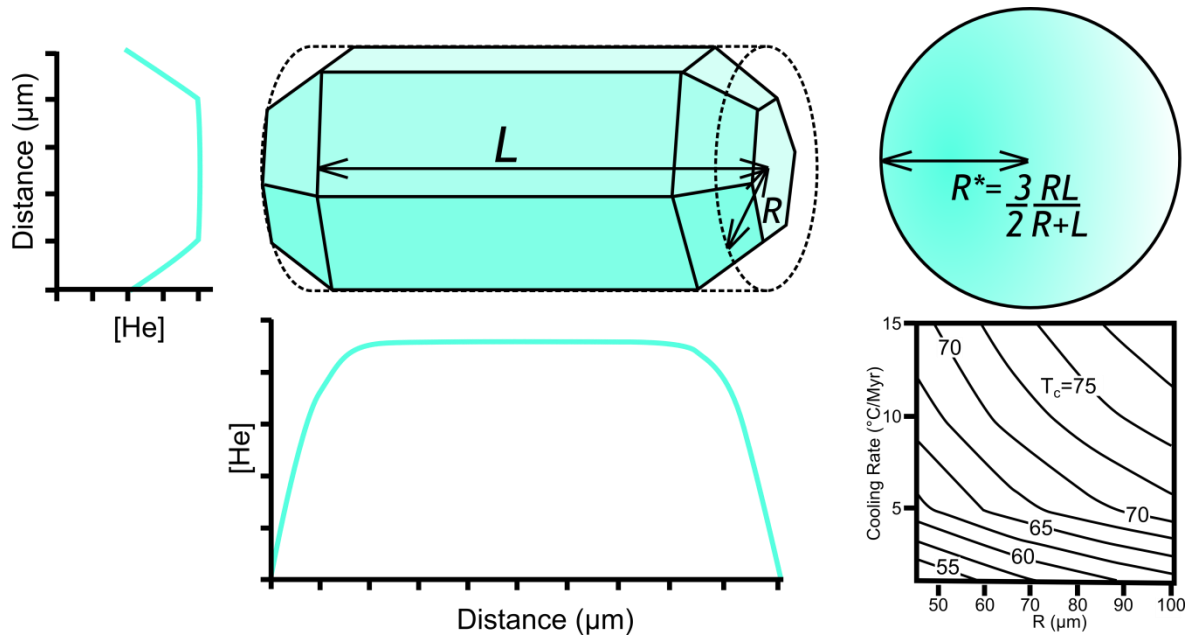
Mineral inclusions, mainly of zircon and monazite, with high concentrations of U and Th can provide an additional source of alpha particles that can become implanted into the crystal lattice. During dissolution of the crystal in  $\text{HNO}_3$  (see Appendix 1.3.2) the apatite will dissolve but the mineral inclusion may not (Vermeesch et al., 2007). Therefore, measured  $^4\text{He}$  that has been implanted into the apatite grain will be parentless and will cause ages that are too old (House et al., 1997; Stockli et al., 2000; Farley, 2002; Fitzgerald et al., 2006). Fluid inclusions can also introduce parentless He as the fluid is typically magmatic or metamorphic and may contain radiogenic material capable of emitting alpha



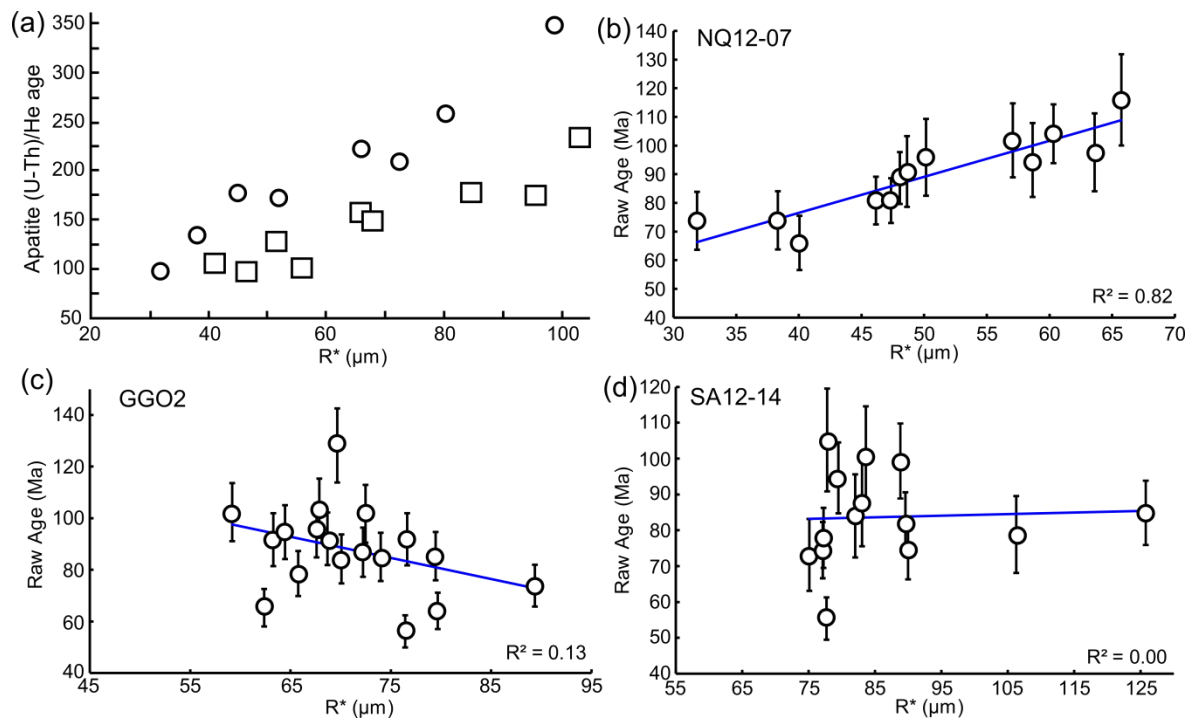
particles (Fitzgerald et al., 2006). However, recent work by Vermeesch et al. (2007) has suggested that unless inclusions are particularly large (e.g. >10% of the apatite volume) and extremely concentrated in U and Th (c. x1000 of host apatite) they will not contribute He concentrations significant enough to seriously impact the age. Only in extreme cases will the closure temperature of the crystal be increased by as much as 5°C but in most cases it will vary by less than 2.5°C. As single grains are routinely screened under both optical and petrographic microscopes to identify and avoid grains with large inclusions, the “extreme” case is unlikely to have been encountered. If smaller inclusions (< few µm) have not been identified they are unlikely to have a major impact on the measured grain age.

#### 4.4.4 Grain radius

The size of the diffusion domain in any thermochronology technique has a major influence over the effective closure temperature of the system (Dodson, 1973; Lovera et al., 2002). Previous experiments of Durango apatite have shown the diffusion domain for apatite is approximated by the size of the crystal (Farley, 2000; Cherniak et al., 2009; van Soest et al., 2011). These studies have highlighted that He diffusion from Durango is crystallographically isotropic and that diffusivity is inversely proportional to the square of the minimum domain dimension for diffusive loss (i.e. grain radius) (Fig. 4-9) (Farley, 2000). This effectively results in an increase in closure temperature of about c. 10°C for grain radii increasing from 50 to 150 µm. This effect is reflected in an increase of AHe age with grain radius, a relationship which becomes more pronounced for slow rates of cooling and can result in single grain age dispersion on the order of 50 - 100% (Reiners and Farley, 2001; Brown et al., 2013). Reiners and Farley (2001) state that for a reproducible age, grains of a similar radius must be analysed. However, (U-Th-Sm)/He analysis of a variety of grain radii can allow interpretations of the samples thermal history to be made on the basis of the relationship between AHe age and grain radius. As most models of He diffusion convert the size of the apatite crystal to a sphere with the same surface to volume ratio, correlations of AHe age and grain size are more accurately made against a spherical equivalent radius (here referred to as  $R^*$ ) (Fig. 4-9).



**Figure 4-9: Illustration of the He diffusion profile along the length and width of a typical apatite crystal. Right hand side shows how the spherical approximation is made for the apatite crystal. Lower right hand side figure shows the influence of grain size and cooling rate on the effective closure temperature of the apatite (U-Th-Sm)/He dating system (after Farley, 2000).**



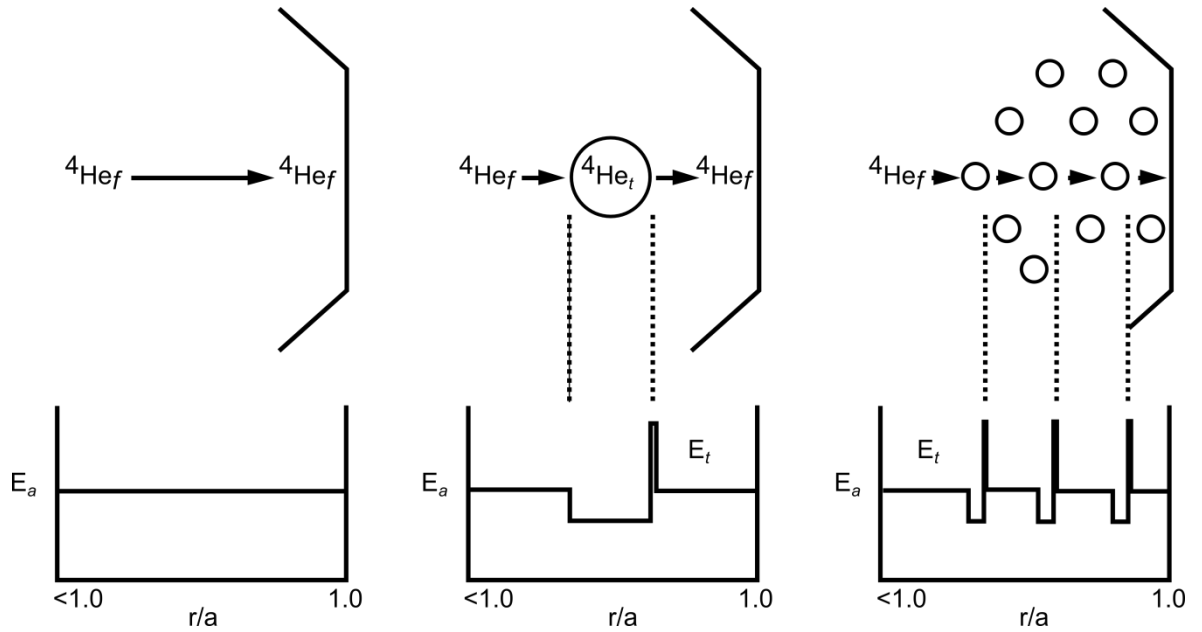
**Figure 4-10: Relationships of AHe age (uncorrected) against spherical equivalent radius. All uncertainties include 1σ analytical uncertainty plus an additional 10% uncertainty observed in the dispersion of Durango standards analysed (see Appendix 2.2). (a) Shows the positive relationship for two samples measured by Reiners and Farley (2001). (b) Strongest positive relationship observed in dataset is from sample NQ12-07. (c) Strongest negative correlation in the dataset recorded by sample GGO2. (d) The common case where the correlation is extremely poorly defined as shown by sample SA12-14.**

Gautheron and Tassan-Got, (2010) outline the importance of reliable crystal measurements and documentation of the crystal shape.

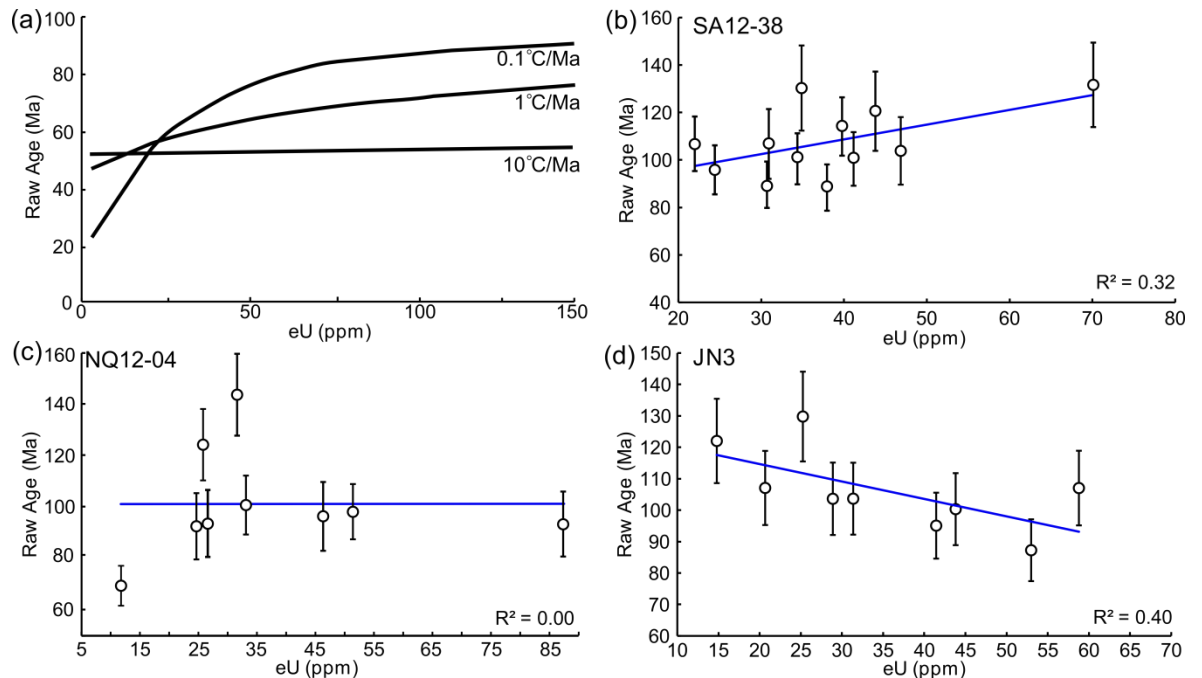
The characteristic positive relationship between AHe age and grain radius reported by Reiners and Farley (2001) is shown in Figure 4-10a. Positive grain age -  $R^*$  relationships were reported in subsequent studies (eg. Hansen and Reiners, 2006) and can be seen for many samples from this study (e.g. Figure 4-10b). In some cases, however, grain age and  $R^*$  is negatively correlated or not correlated. The effect of grain size on the AHe closure temperature and therefore on AHe age is thought to be a fairly well understood relationship if the effects of radiation damage, zonation and fragmentation are small or absent entirely. Another consideration is the rate of cooling the sample has experienced. If cooling has been rapid and, as a result, diffusive loss of helium has been low then the AHe age - radius relationship may not be observed. In almost all of the samples analysed here the effects of radiation damage, zonation and grain fragmentation cannot be ignored and likely disrupt simple age -  $R^*$  relationships.

#### 4.4.5 Radiation Damage

A major focus of recent research in LTT has been towards the influence of radiation damage within U and Th rich minerals (e.g. apatite - Shuster et al., 2006; monazite - Meldrum et al., 1998; titanite - Hawthorne et al., 1991; zircon - Guenther et al., 2013). Radiation damage accumulates due to recoil of parent nuclei during alpha decay which creates defects within the crystal lattice (Nasdala et al., 2001; Shuster et al., 2006). As the volume density of this structural damage increases, the apatite crystal becomes more retentive of  $^4\text{He}$ . The diffusion of a  $^4\text{He}$  atom is governed predominantly by temperature in the absence of radiation damage and diffuses through the crystal lattice with an activation energy ( $E_a$ ). If structural damage and voids produced by radiation damage exist,  $^4\text{He}$  atoms may pass into these vacancies and acquire an energy state lower than the surrounding crystal matrix leaving them trapped (Fig. 4-11).  $^4\text{He}$  atoms then require a greater magnitude of energy ( $E_t$ ) to escape the void (Shuster et al., 2006; Gautheron et al., 2013). Similar to the effect of grain



**Figure 4-11: Cartoon diagram of the radiation damage trapping model (after Shuster et al., 2006).** Free alpha particles ( ${}^4\text{He}_f$ ) travel through the crystal during diffusion with an activation energy ( $E_a$ ). When a damage defect is produced the  ${}^4\text{He}_f$  particle may enter the defect and become trapped ( ${}^4\text{He}_t$ ). Once the alpha particle is trapped it requires a greater energy to diffuse back into the main crystal lattice ( $E_t$ ). The number of potential traps increase with increasing radiation damage and therefore a greater energy is required to successfully diffuse He from the crystal and as such the closure temperature increases.



**Figure 4-12: Plots of AHe age against effective uranium ( $[\text{eU}] = [\text{U}] + [0.235 \cdot \text{Th}]$ ).** (a) The expected AHe age – eU relationship for three different cooling rates as predicted by the RDAAM model of Flowers et al. (2009). (b) SA12-38 shows the strongest positive eU correlation in the dataset. (c) NQ12-04 shows an example of the zero correlation observed in many samples. (d) JN3 shows a good example of a strong negative correlation also observed in some samples in the data set.

radius on AHe ages, the influence of radiation damage is enhanced by slower cooling rates through the PRZ where diffusive loss of He is important (Shuster et al., 2006; Flowers et al., 2009).

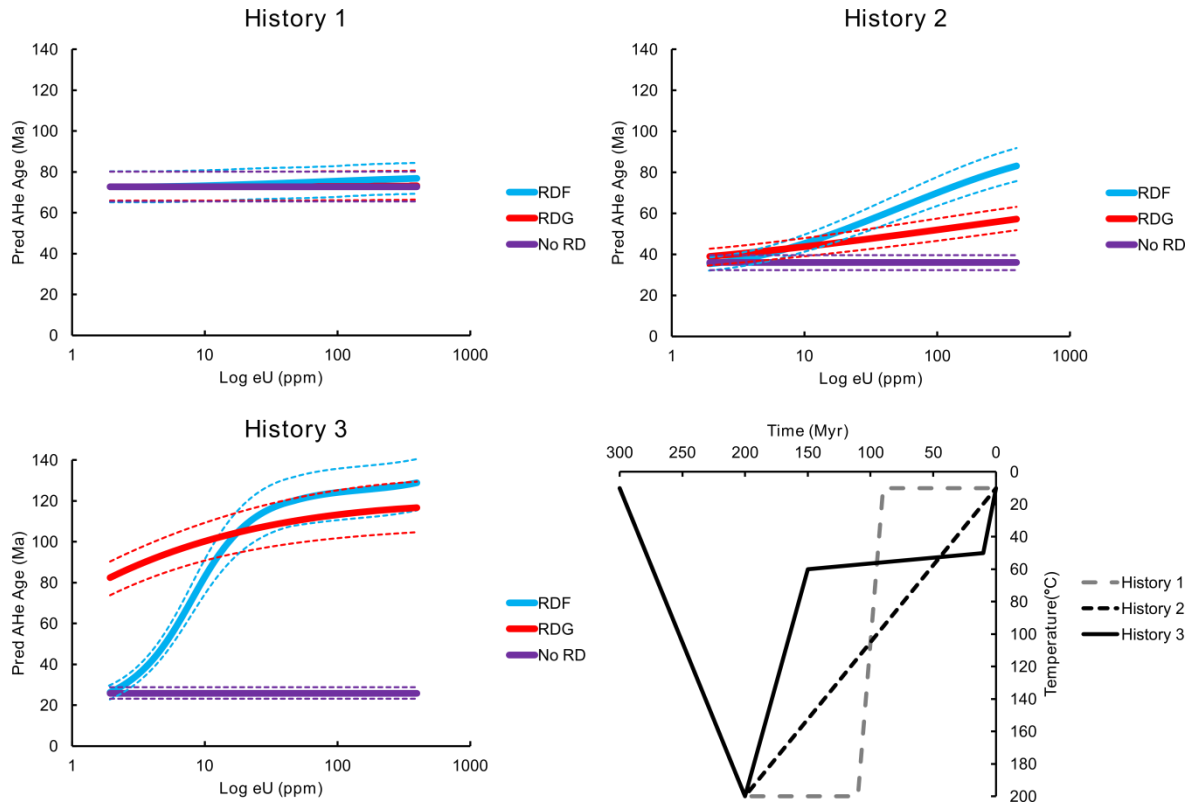
The progressive accumulation of radiation damage defects in an apatite crystal over time will alter the closure temperature of the AHe system in that grain. However, direct empirical evidence for a radiation damage influence on helium diffusion within apatite is currently lacking (Shuster and Farley, 2009). To assess the potential influence of radiation damage on single grain age dispersion, many workers report positive correlations between AHe age and effective uranium ( $eU = U + 0.235 \cdot Th$ ) (Fig. 4-12a) (Ault et al., 2009; Cogné et al., 2011; Flowers and Kelley, 2011; McKeon et al., 2014) and interpret these as a result of slow or complex cooling. While data presented in this study do occasionally show weak positive correlations (e.g. Fig. 4-12b) this is not an observation that persists throughout the entire dataset. In many cases the data can appear irregularly dispersed (Fig. 4-12c) or negatively correlated (Fig. 4-12d). The lack of correlation is likely due, in part at least, to the competing factors influencing AHe ages such as grain radius and fragmentation (Brown et al., 2013).

Numerical models for predicting this behaviour have been suggested (e.g. Flowers et al., 2009; Gautheron et al., 2009; Gautheron et al., 2013) however many unresolved theoretical aspects question both the robustness and appropriateness of using these models. Both the radiation damage model of Flowers et al. (2009) (RDF) and of Gautheron et al. (2009) (RDG) treat sites of alpha-recoil damage as analogous to fission tracks in that at elevated temperatures defects will anneal (e.g. Chaumont et al., 2002). In both models this first-order approximation is treated in a manner similar to the AFT annealing model of Ketcham et al. (2007). The major difference between the two radiation damage models comes from the treatment of the reduction of defects over time and temperature which is inversely proportional to the diffusion coefficient. While the RDG model calculates the reduction of fission track density in a linear manner the RDF model treats it with an empirically determined cubic function and therefore predicts an enhanced reduction in diffusivity with increasing radiation damage. Gautheron et al. (2009) acknowledge that a non-linear

function would improve the model fit to the data but they do not find a physical mechanism to justify such an approach. While the RDF model fits the data better at low levels of radiation damage at higher levels the model fails to match the observed data within uncertainty levels. The difficulty of obtaining a reasonable fit to experimental data is acknowledged by Flowers et al. (2009) and it is stated that parameterisation of their radiation damage accumulation and annealing model was not optimal.

The practical implications for this situation (i.e. significantly different treatments of damage) are illustrated in Figure 4-13 which shows forward modelling results for three different thermal histories. Due to rapid cooling experienced in model 1, there is limited variation in predicted ages regardless what, if any, radiation damage model is used. In model 2, the protracted history through the PRZ causes major discrepancies in predicted ages with increasing eU, particularly at eU concentrations > 10 - 25 ppm. For model 3, where the history experiences a prolonged period in the PRZ, the most severe discrepancy is at low levels at eU. At high concentrations of eU both models predict a gentle increase in age with eU, almost becoming a plateau.

Both RDG and RDF models have, as yet, only been calibrated for F-apatite (Durango) and these have been incorporated into commonly used thermal history inversion packages (e.g. Ketcham et al., 2011; Gallagher et al., 2012). However, as damage zones are believed to behave in a manner similar to fission tracks, then compositional heterogeneity will likewise affect damage annealing. This point remains speculative, however, as it is still not certain to what extent, if any, radiation damage annealing and fission track annealing are comparable. A more recent model developed by Gautheron et al. (2013) has incorporated an additional kinetic parameter ( $D_{\text{par}}$  or Cl wt%) to account for this effect. Interestingly, this new development in our understanding of radiation damage brings us back to issues pertinent to AFT analysis, namely the effect of composition. In order to calibrate radiation damage models and annealing models better understanding is required of the compositional control on both the annealing of radiation damage defects and fission track annealing. Further chemical analysis may point to a more fundamental control on helium diffusion



**Figure 4-13: Results for forward modelling of three thermal histories incorporating: (i) no radiation damage effects; (ii) radiation damage after Flowers et al. (2009); (iii) radiation damage after Gautheron et al. (2009). The grain size for each grain was constant in all models to eliminate this source of dispersion. Dashed lines represent 10% uncertainty levels on synthetic AHe grain ages.**

before considering radiation damage effects (Gautheron et al., 2013) but past studies have identified composition dependent diffusion (Wolf et al., 1996; Warnock et al., 1997; Reiners and Farley, 2001).

Insights from previous AHe studies and recent work on radiation damage in zircon (e.g. Guenther et al., 2013; Ketcham et al., 2013; Pidgeon, 2014) suggests that the phenomenon does have major implications for the reproducibility of age measurements on different grains and for thermal history modelling, but current models still lack an adequate approximation of the physical kinetics of the process. Neither radiation damage model is well calibrated for the complexities inherent in real AHe data sets. However, as supported by many studies reporting highly dispersed (U-Th-Sm)/He ages from either zircon or apatite, radiation damage will likely have an important influence over the closure temperature of the system and, therefore, on the measured AHe age. Because of the current uncertainty in these models in this

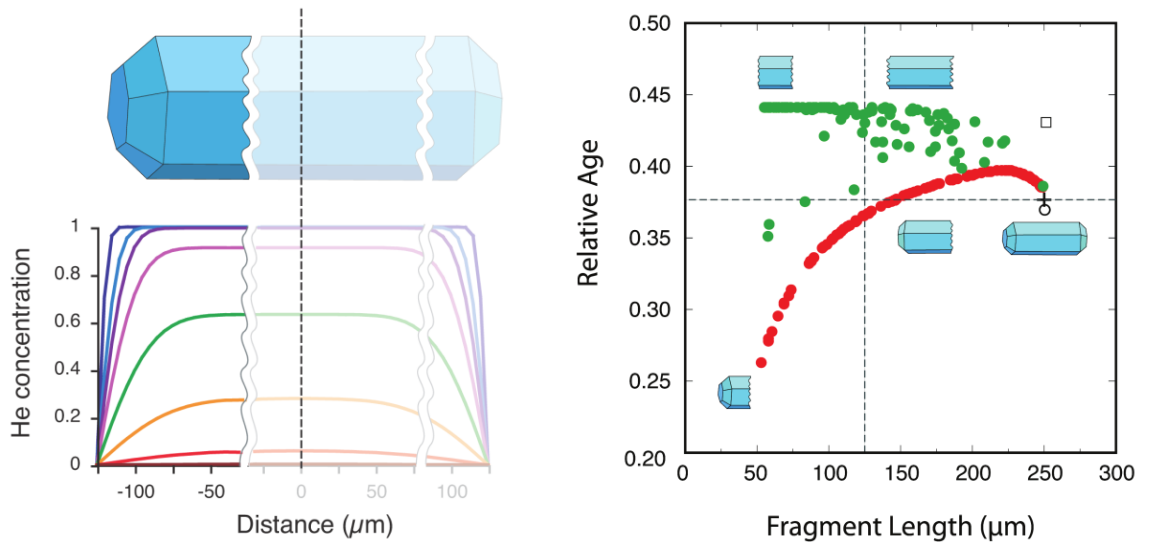
study thermal history inversion was performed using both of these models and the results of these are discussed in the subsequent chapters.

#### 4.4.6 Fragment Length

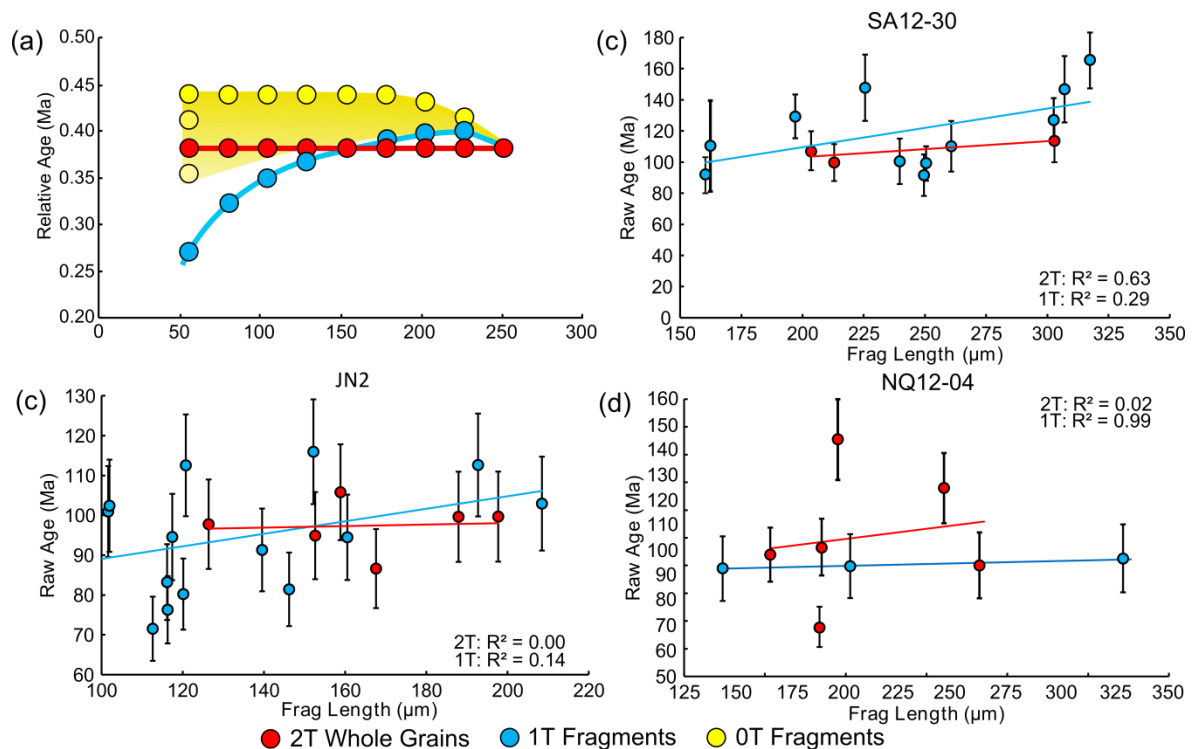
During the mineral separation process, whole apatite crystals (2 termination, or 2T grains) frequently break along their weak basal cleavage and appear with one (1T) or zero (0T) terminations in the mineral separate (Ehlers and Farley, 2003; Beucher et al., 2013; Brown et al., 2013). In past studies, broken crystals have been treated as whole grains during analysis and an additional factor being incorporated into the  $F_t$  correction to account for the altered geometry of alpha ejection from the fragmented grain (Farley et al., 1996; Gautheron and Tassan-Got, 2010). However, recent work has shown that the effect of analysing broken fragments can have a significant effect on AHe age dispersion (Beucher et al., 2013; Brown et al., 2013). Due to inhomogeneous diffusive loss of He, which occurs more readily at the crystal terminations, analysis of fragmented grains will only sample part of the complete helium diffusion profile (Brown et al., 2013). 1T grains that are less than half of the original 2T grain will be younger than the true whole grain age and the fragment age will increase age with increasing length. For 1T grains that are more than half the length of the initial whole grain, an age older than the true age will be obtained. 0T grains will most commonly be older than their corresponding 2T whole grain and reproduce well; except in the case where the 0T fragment was close to the end of the whole grain (Fig. 4-14).

An important observation is that the He diffusion profile is mimicked by the age dispersion - fragment distribution (ADFD) relationship observed from analysing broken crystals (Brown et al., 2013). Depending on how quickly the sample has cooled and how long  $^4\text{He}$  has had to accumulate in the crystal, the shape of the profile will be altered (i.e. slowly cooled samples have a broad  $^4\text{He}$  concentration profile whereas rapidly cooled samples have a very narrow profile). If sufficient 1T fragments are analysed it is suggested that the form of the diffusion profile can be estimated from the pattern of dispersion and the data inverted to extract thermal history information (Beucher et al., 2013).





**Figure 4-14: Cartoon illustrating the influence of analysing fragments of larger apatite crystal. Left hand panel shows the diffusion profile for an apatite crystal that has cooled rapidly (dark purple) through to slowly cooled (red profile). Right hand panel shows the expected age dispersion-fragment distribution (ADFD) plot for synthetic apatite grains. Green circles = 0T grains; red circles = 1T grains; cross = 2T grains age.**



**Figure 4-15: (a) Theoretical Age Dispersion – Fragment Distribution (ADFD) relationship (Brown et al., 2013; Beucher et al., 2013). This is the same plot as shown in Figure 4-14(b) but simplified and recoloured for comparison against sample data plots. (b) Relationships of AHe age (uncorrected) against fragment length. These plots are referred to as ADFD. All uncertainties include 1σ analytical uncertainty plus an additional 10% uncertainty observed in the dispersion of Durango standards analysed (See Appendix 2.2).**

Figure 4-15 shows ADFD plots for data analysed in this study. No plot readily matches the hypothetical ADFD plot as drawn in Figure 4-14. However, this is not unexpected considering these samples are real world samples and as such have a variety of eU and grain width measurements. Moreover, grains may have, on rare occasions, contained an inclusion and/or some degree of parent zonation. So while there is no clear linear increase in 1T grains toward a plateau of 2T ages the plots could be dissected in more detail to look for some control on dispersion due to the presence of fragmented grains. In most cases 1T grains are positively correlated.

While a slower thermal history should increase the fragmentation effect, by broadening the diffusion profile, this will also cause eU and grain size effects to become more pronounced and any correlation may be difficult to observe. Conversely, rapidly cooled samples will have a very narrow diffusion profile and as such there may not be much of an effect caused by analysing 1T grains and again a correlation may be absent. Samples JN2 and SA12-30 show AHe ages that have a positive, albeit fairly weak (0.29 and 0.14, respectively), correlation with fragment length for one termination grains (Fig. 4-15). 2T fragments are fairly coherent with one another. NQ12-04 does not show any correlation for 1T grains. Compared to other samples in the data set this sample has a relatively low MTL implying slower rates of cooling and therefore the fragmentation effect should be more pronounced. 2T grains are more scattered which could be due to eU and grain size effects.

#### **4.4.7 Zonation**

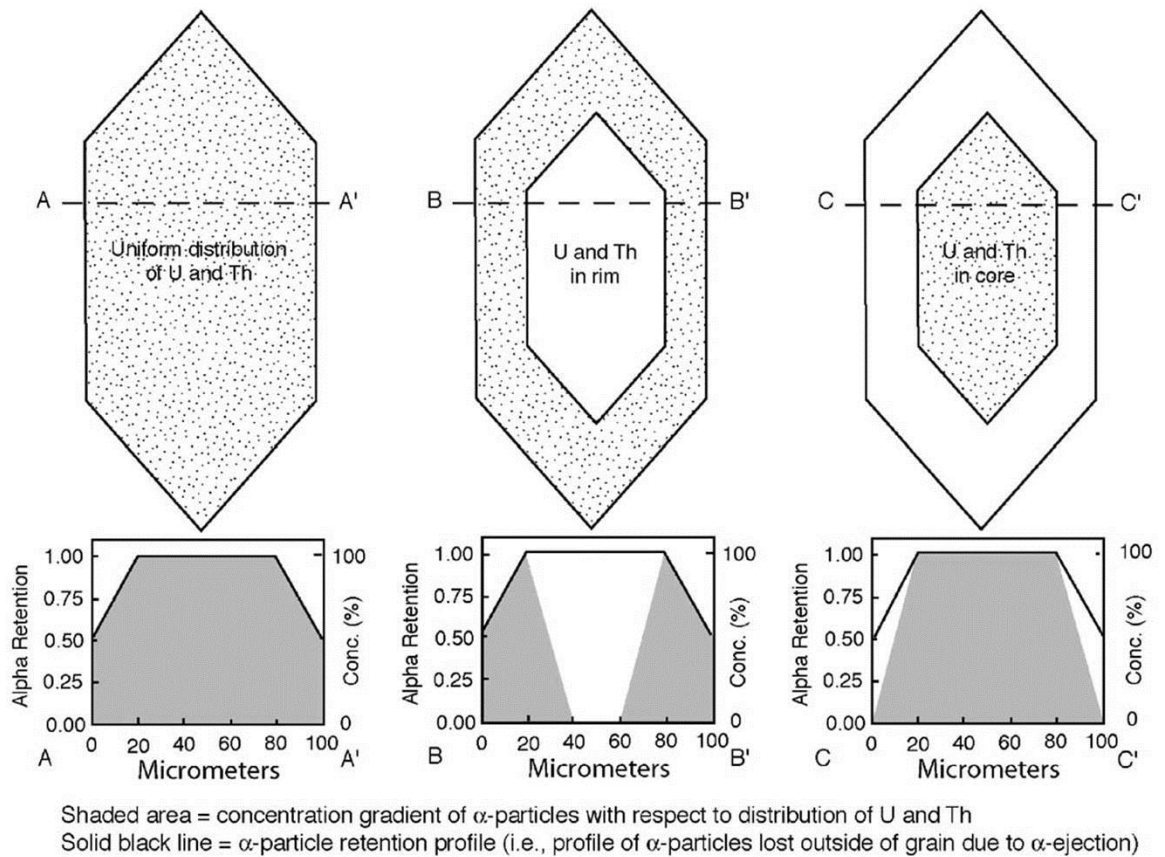
Zonation of parent isotopes (i.e. U and Th) within apatite is rarely measured prior to (U-Th-Sm)/He analysis but has often been cited as a possible source of age variation (Ehlers and Farley, 2003; Fitzgerald et al., 2006; Flowers and Kelley, 2011). Parent nuclide zonation has the potential to influence the measured AHe age in three distinct ways: (i) by altering the spatial extent of alpha ejection and therefore cause an erroneous alpha-recoil correction; (ii) by creating variable fractional He loss due to different He diffusion gradients across zoned apatites compared to un-zoned; and (iii) by creating intra-crystalline

variability of radiation damage, creating zones of higher He retentivity where U and Th concentrations are rich (Farley et al., 2011) (Fig. 4-16).

The combination of these three influences will potentially yield AHe ages that are too old (for apatites with eU enriched cores) or too young (for apatites with eU enriched rims). In a recent study by Ault and Flowers, (2012), prior to analysis, apatite zoning was mapped using LA-ICP-MS (e.g. Farley et al., 2011) to identify apatites exhibiting both enriched cores and enriched rims, as well as apatites with variable spatial zonation. This work observed that age variations between zoned and un-zoned apatites do not typically exceed 10% and reach up to 13% only for thermal histories which involve up to 150 Myr residence times in the PRZ. It is suggested by Ault and Flowers, (2012) that since these age deviations fall within generally accepted levels for (U-Th-Sm)/He analysis and a misinterpretation of AHe data caused by zonation is unlikely and detailed U and Th mapping prior to analysis is not required.

While zonation in zircon is clearly apparent in ion probe analysis and Cathodoluminescence (CL) imaging (Dobson et al., 2008), observing zonation in apatite optically is more difficult due to the relatively low levels of U and Th. Analysis of the fission track distribution, which can act as a proxy for U content, within sample mounts can provide insight to the occurrence and severity of zonation. CL imaging has been suggested as a relatively quick method of screening for zonation of U and Th however an additional outcome of analysis by Ault and Flowers (2012) was that although CL imaging in some cases correlates with the true zonation within the crystal it cannot be trusted entirely due to the potential for other REE to influence the luminescent properties. CL imaging was performed on the sample GGO2 for this study, for two reasons: (i) fission track density suggests strong zonation in U; and (ii) this sample has extremely high levels of average U and Th for an apatite (> 100 ppm).

Fission track mounts clearly show extreme variations in fission track density that can be described as both core enriched and core depleted (Fig. 4-17). However, even within a sample showing such strong zonation there are grains which show no apparent zones of high fission track density (e.g. Fig. 4-17h). The CL images



**Figure 4-16: Representation of two end-member styles of zonation. Not shown is heterogeneous zonation patterns as the influence on the diffusion profile is uncertain due to the uncertainties in how this effects alpha ejection and radiation damage enhanced retention of alpha particles (after Fitzgerald et al., 2006).**

on different individual grains from the same fission track mount clearly shows light and dark portions on the grain showing some degree of compositional control over luminosity (Fig. 4-18). Fission track etch pits can be seen in BSE images to the left of the respective CL images which can be used to correlate regions of low and high track density with luminosity. Areas of high track density correlate with saturated portions of CL image while low track density correlate with illuminated portions. This may only be one example but there appears to be some correlation between the fission track distributions (and by extension U content) and luminosity patterns in CL images and this requires further investigation. The potential effect of variable zonation on AHe ages from a sample set containing fragmented grains is still not yet fully quantified and extra caution should be taken when analysing fragmented grains if strong U zonation has been identified from fission track mounts.

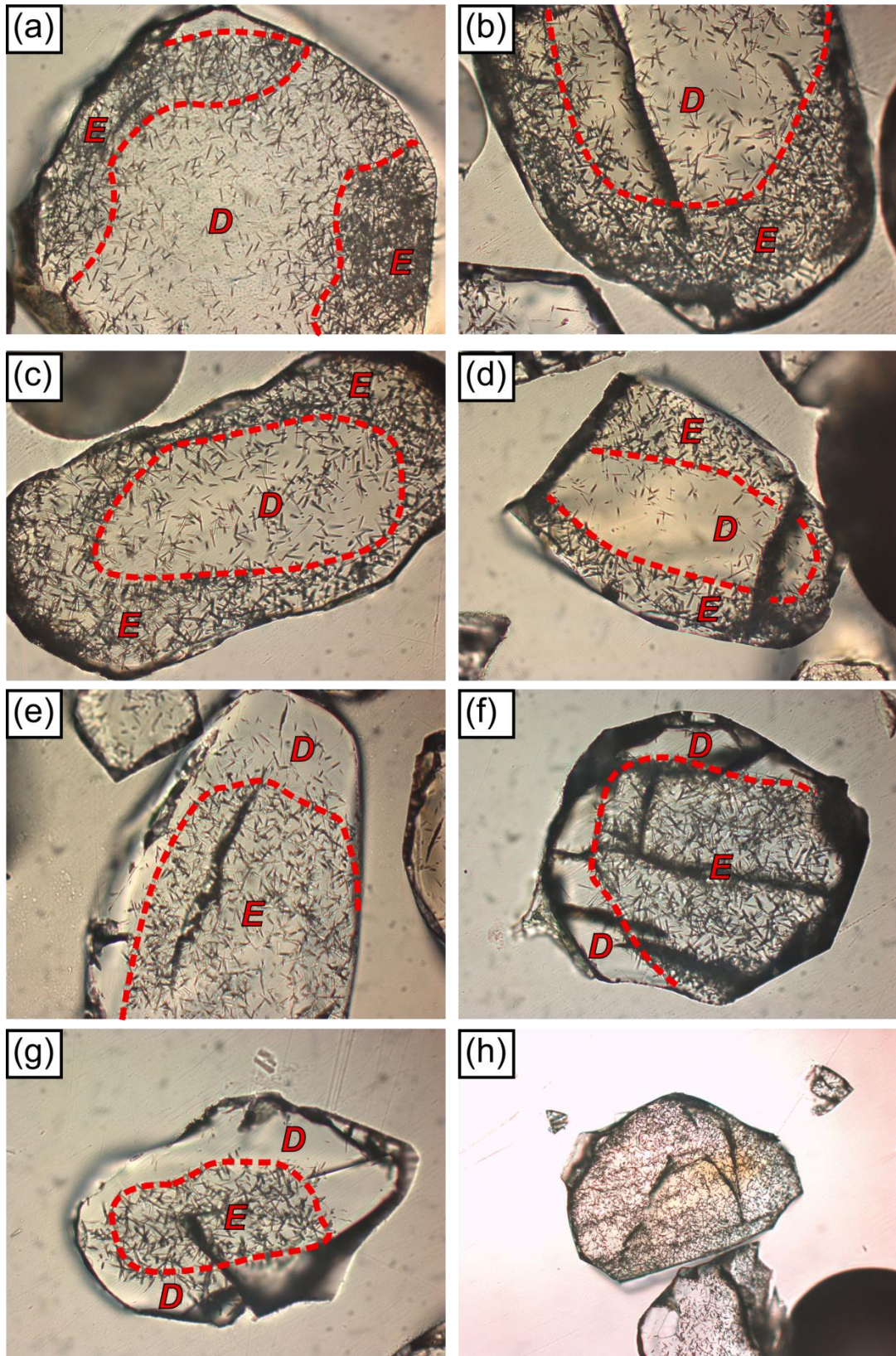
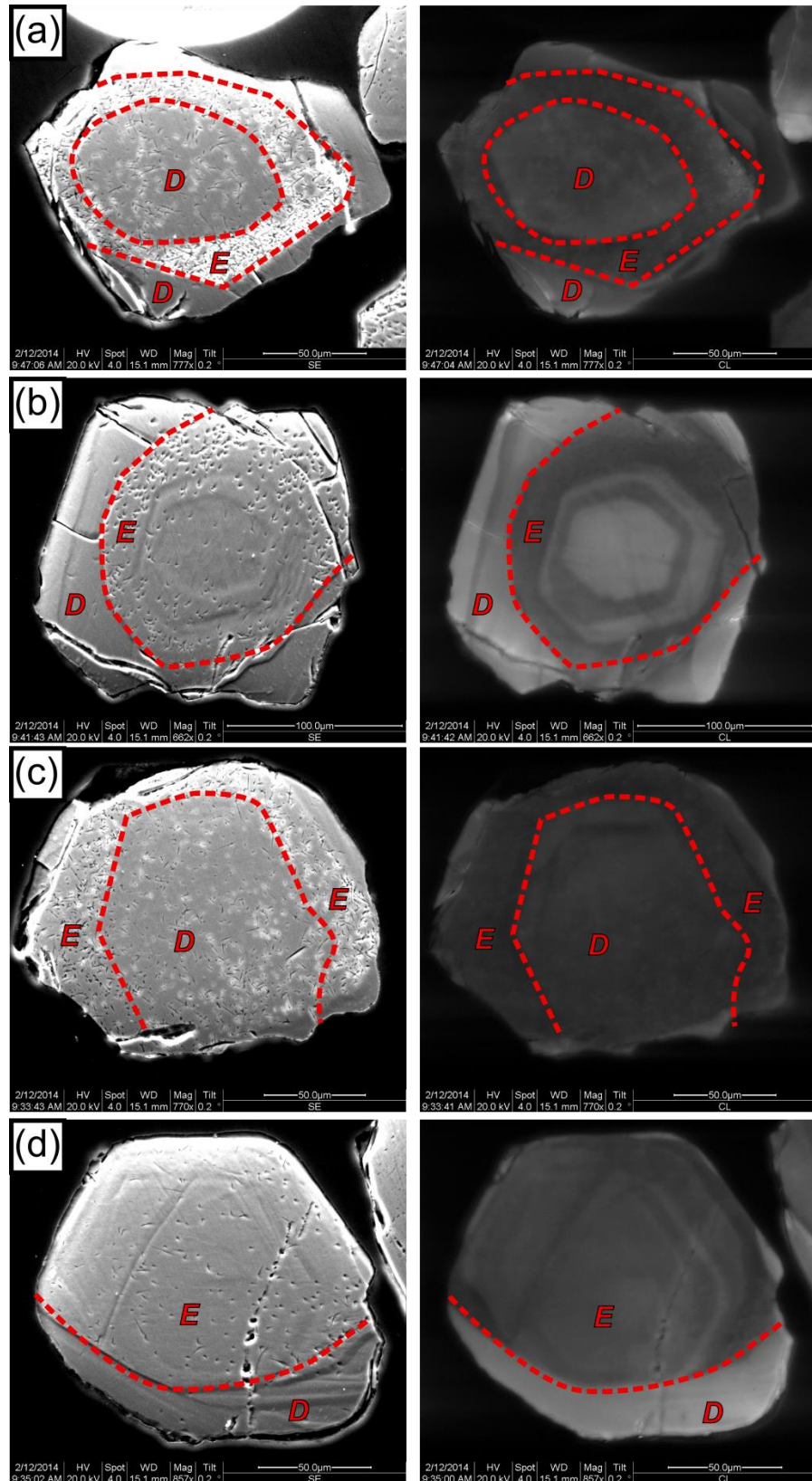


Figure 4-17: Fission track mount photographs for sample GGO2 showing relative enrichment (E) or depletion (D) of uranium. Variation in fission track density across the mount can be used as a proxy for the nature of zonation within the crystal. Pictures a, b, c, d show an example of enriched rim zonation; e, f, g show enriched core zonation. Picture h shows that even within this highly zoned sample some grains do not show a great amount of zonation.



**Figure 4-18: SEM images for sample GGO2 showing relative enrichment (E) or depletion (D). Left hand image shows BSE images of each grain. Right hand images show cathodoluminescence images for each grain. Fission tracks can be observed in BSE images and suggests that where fission track density is higher, there is an enrichment of U. This correlates well with darker bands in CL images, while lighter bands are likely depleted zones.**

## 4.5 Thermal history modelling: Joint AFT and AHe inversion

The ultimate goal of LTT techniques is to derive cooling histories of samples and quantify surface and sub-surface processes that have produced the observed data (e.g. magmatism, uplift and erosion, subsidence and burial). Inverse modelling of LTT data has become a popular method of generating numerical solutions for a rocks temperature-time (T-t) history. Inverse modelling uses the measured data and a forward model, to estimate the behaviour of the system over time, to generate a thermal history from a defined starting T-t condition (ideally obtained from the geological record) and the present day conditions of the sample.

Predicting how the AFT thermochronometer evolves as a function of temperature and time is based on a theoretical annealing model (e.g. Laslett et al., 1987; Ketcham et al., 2007). More recent annealing models require some form of compositional parameter to be assigned to account for the differences in annealing rate in F- (less resistant to annealing) and Cl- rich (more resistant to annealing) apatites (Gleadow and Duddy, 1981, Green et al., 1986). A final consideration for fission track modelling is to account for variations in annealing caused by the angle of tracks to the c-axis of the crystal (e.g. Donelick et al., 2005; Ketcham et al., 2007). It has been shown that fission tracks measured at high angles to the c-axis are shorter than those that are parallel to the c-axis. Normalising track length measurements for their angle to the c-axis (e.g. Ketcham et al., 2007) may provide a better representation of the true track length distribution.

Modelling of the (U-Th-Sm)/He system typically uses a spherical equivalent approximation of the grain shape with the following aspects of the systems behaviour needing to be defined: (i) the activation energy of alpha production from the decay of U, Th and Sm (ii) alpha stopping distances and (iii) thermal diffusivity (e.g. Wolf et al., 1998; Farley et al., 1996; Farley, 2000; Meesters and Dunai, 2002a, b; Ketcham, et al., 2007; Gautheron and Tassan-Got, 2010; Gallagher, 2012). Integrating this information with the dimension of the diffusion

domain (typically effective grain radius is used for a spherical approximation) allows thermal history information to be derived from predicted ages calculated as a function of net daughter product in growth and diffusive loss from the grain (Meesters and Dunai, 2002a, b). As discussed in section 4.4.5 additional calibration models have been developed to account for radiation damage annealing (e.g. Shuster et al., 2006; Gautheron et al., 2009; Flowers et al., 2009) and alpha stopping distances (Farley and Stockli, 2002; Ketcham et al., 2011).

AFT data can be readily modelled jointly with (U-Th-Sm)/He data from the same sample to provide even tighter constraints for possible models to be tested and hence predict a more robust thermal history. Debate still exists however on the fundamental issues of what model should be used to explain the data. Do you use i) a weighted mean thermal history (weighted average of all viable models found) which tends to produce a rather smooth and simpler thermal history which suitably fits the data or ii) a maximum likelihood model (the single model that fits the data the best) which may fit the data better but may be more complex and difficult to justify geologically (e.g. Green et al., 2006). Thermal history models can only be deemed to be successful if they provide information consistent with other geological evidence. Where appropriate geological constraints are available, they can be included in the model explicitly. However, in basement terrains where there are only sparse and limited sedimentary deposits, it is difficult to define reliable additional stratigraphic constraints.

#### **4.5.1 Modelling Approach: QTQt**

In this study, QTQt, a Bayesian transdimensional approach to data inversion, as described in detail by Gallagher (2012), is used for generating thermal history models. Within this approach the multi-kinetic fission track annealing model of Ketcham et al. (2007) and the Durango diffusion model of Farley (2000) is adopted to derive robust thermal history information from the observed AFT and AHe data, respectively. The effects of including the two radiation damage accumulation and annealing models discussed above on thermal history models are also systematically assessed. Prior information on model parameters (i.e.



range of temperature and timescale over which to search) is first provided to define a model space with a prior probability distribution. The model space is then randomly sampled using a Markov Chain Monte Carlo (MCMC) approach (e.g. Gilks, 2005; Sambridge et al., 2006; Gallagher et al., 2009) whereby the current model is perturbed to produce a proposed model which is then accepted or rejected based on the likelihood of the new proposed model fitting the observed data. The novel aspect of this transdimensional approach is that the number of T-t points does not have to be defined explicitly and can be treated as an unknown parameter to be optimised. This allows the data to determine the complexity of the proposed thermal history model. The Bayesian aspect of the modelling technique penalises complex models proposed during sampling in favour of models with fewer T-t points that adequately fit the observed data. This is done by calculating the posterior probability of the model:

$$P(M|D) = P(M).P(D|M)$$

Where  $P(M|D)$  is the posterior probability of obtaining the proposed model given the data;  $P(D|M)$  is the likelihood probability function of obtaining the data given the model and  $P(M)$  is the prior probability density function given to the model. Using this iterative process of exploring the model space, many thermal histories are tested creating an expected thermal history weighted for its posterior probability distribution. A key advantage of this approach is that the outcome defines a range of allowable models and avoids highlighting overly complex thermal histories that may fit the data well but that are unjustified when considered in light of both the model and data uncertainties. Unless otherwise specified, prior information on time was simply the oldest sample age  $\pm$  oldest sample age. The prior information on temperature range was set to  $70 \pm 70^\circ\text{C}$ . Additional prior information, if they are available from geological constraints can be entered in a similar manner.

An additional novel aspect of QTQt is the ability to model samples from vertical and borehole profiles together. This is achieved by optimising an additional model parameter representing the temperature offset between the top and bottom sample. This temperature offset represents the effective geothermal

gradient with temperature information being interpolated linearly through intermittent samples. This approach is utilised in Chapter 5, 6 and 7.

The MCMC algorithm was run for a minimum of c. 200,000 iterations after discarding an initial c. 50,000 iterations deemed to be “burn in” runs (Gallagher et al., 2009). In most cases however, the number of runs far exceeds this as short c. 10,000 iteration runs are performed in order to optimise the MCMC search parameters before performing longer runs. The output of the Bayesian approach is a collation of all thermal history models that have been tested, each with an associated posterior probability of fitting the observed data. From this collection of thermal histories, a summary probability distribution map of temperature at a given time (at intervals of 1 Myr) can be generated. A mean thermal history model (weighted for its posterior probability), termed the expected model, can also be determined with associated 95% credible intervals which provide the uncertainty on the inferred model. The maximum likelihood model is also presented for each sample or profile in subsequent chapters, as this is the model that statistically fits the observed data best. The maximum likelihood model is often overly complicated though, containing structure that is not justified if the uncertainties on the data and model are taken into account, and could lead to over interpretation of the data.

The nature of the expected model is that it will retain well constrained features (i.e. features common to many individual models) while more complex deviations observed in only a small number of viable models are averaged out. The expected model, and its associated probability, provides the most robust insight to the thermal history evolution, and the additional structure indicated by the maximum likelihood model should be always be assessed in light of these constraints as well as other geological information.

## **4.5.2 Combining AFT and AHe data**

### ***4.5.2.1 Modelling AFT data independently***

The dataset presented in this work is a prime example of a complex LTT dataset. The AFT age is often older than the accompanying AHe age and, moreover,

single grain age dispersion in the AHe dataset is large with simple interpretations being hindered further by a lack of correlation with eU or grain radius. A large number of measured single grain ages were retained for interpretation and thermal history modelling (see Appendix 3 for details on excluded single grains). During the modelling process the user is required to make many decisions based on what they know about the geological history of the region and/or the kinematics of a particular dating technique. These decisions are included into the modelling process as constraint boxes for independent thermal history information (i.e. from geological evidence) and as uncertainties on the input data, respectively. The former is discussed in later chapters where and when it is relevant for a particular sample. The following section presents a walkthrough of the decision making process that was used taken in order to reach a consistent modelling procedure.

It is suggested that our theoretical and statistical understanding of fission track analysis is well-developed (Kohn et al., 2006; Green et al., 2013). However, uncertainties still exist in our understanding of fission track annealing and track length measurements as discussed in section 4.3. It is believed here that the  $1\sigma$  uncertainty levels on fission track age measurements via the EDM method (c. 5%) is sufficient to encapsulate the effect these phenomena may have on AFT ages. The uncertainty on track length measurements and crucially their initial track length is addressed by combining a small propagated uncertainty on track length measurements (c. 1%) with an uncertainty on the standard deviation of all measured track lengths (10%) and with the compositional parameter  $D_{\text{par}}$  which has an uncertainty equal to the standard deviation of all  $D_{\text{par}}$  measurements within that sample. Figure 4-19 shows pairs of thermal history models for four different samples. These pairs of models show the results of inverting the fission track data with and without taking into account the tracks orientation to the c-axis after Ketcham et al. (2005).

In samples where the TLD is relatively long and narrow (either corrected or uncorrected for c-axis) the two models do not produce significantly different results (e.g. JN2 and SA12-13A). However, differences in the models are present when there is a broader TLD with a mix of shorter and longer tracks. In both

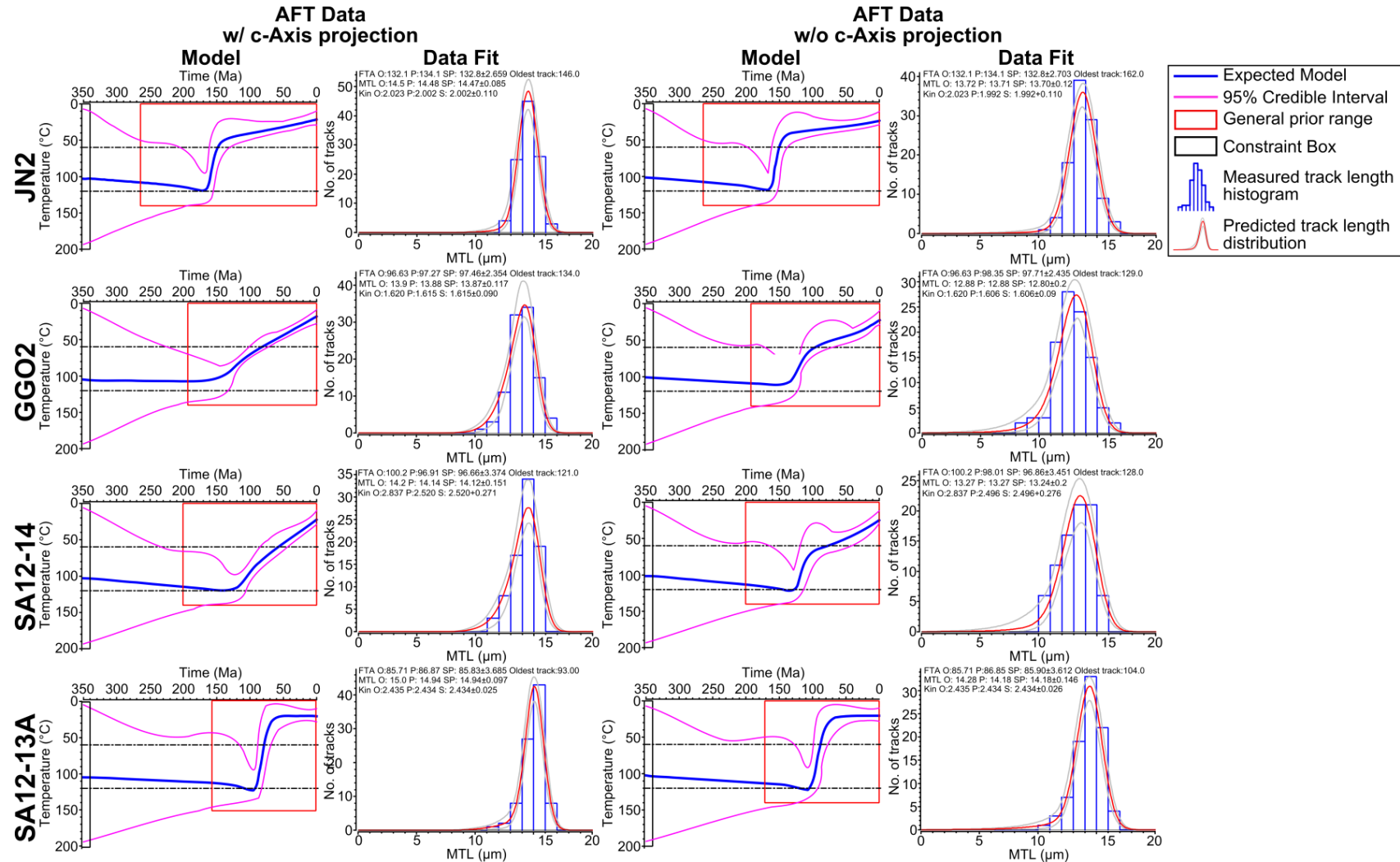


Figure 4-19: Thermal history models for four outcrop samples. The inversion was performed using only fission track data. Models on the left hand side included a correction for the tracks orientation to the crystal c-axis while right hand side models did not. The data fits are presented alongside each model.

cases (SA12-14 and GGO2) the cooling history predicted is more rapid when c-axis projection is not included than when it is. This seems counterintuitive however as correcting for c-axis orientation typically increases the MTL and decreases MTL standard deviation and thus should encourage more rapidly cooled histories. However, prior to c-axis correction the fact that there is a broader TLD means that many different styles of model are able to fit the broad spectrum of track lengths that have been measured. In some cases these histories will be slow similar to the c-axis corrected models but in some cases they may be more rapid or include a rapidly cooled component followed by reheating. This can be seen in the large uncertainty levels in the model at temperatures below c. 60°C. In both models the timing for the onset of cooling is about the same. Anisotropic annealing has been shown to significantly affect the reproducibility of fission track measurements. For this reason, c-axis projection is used routinely in this study.

#### ***4.5.2.2 Modelling AHe data independently: with analytical uncertainty***

The potential complexities of the AHe datasets have already been discussed but in many studies AHe ages are used on their own or with some geological constraint to obtain thermal histories. However, using the Bayesian approach of QTQt in which the data primarily decide the complexity of the thermal history and speculative constraints are kept to a minimum it remains to be seen whether or not AHe on their own can provide useful thermal history information. In the first instance the input AHe ages are assigned an uncertainty which reflects only the analytical uncertainty (typically 1-3%). However, during the modelling process the observed AHe age is resampled from within this uncertainty to help improve the fit of predicted ages while still honouring the observed data (Fig. 4-20).

The thermal histories produced through modelling the AHe data in this way are complicated. Depending on how radiation damage is treated, extremely different thermal histories both in terms of the timing and style of cooling can be produced. In many cases, these thermal histories also contradict the thermal history predicted by AFT data. When radiation damage is not included, the

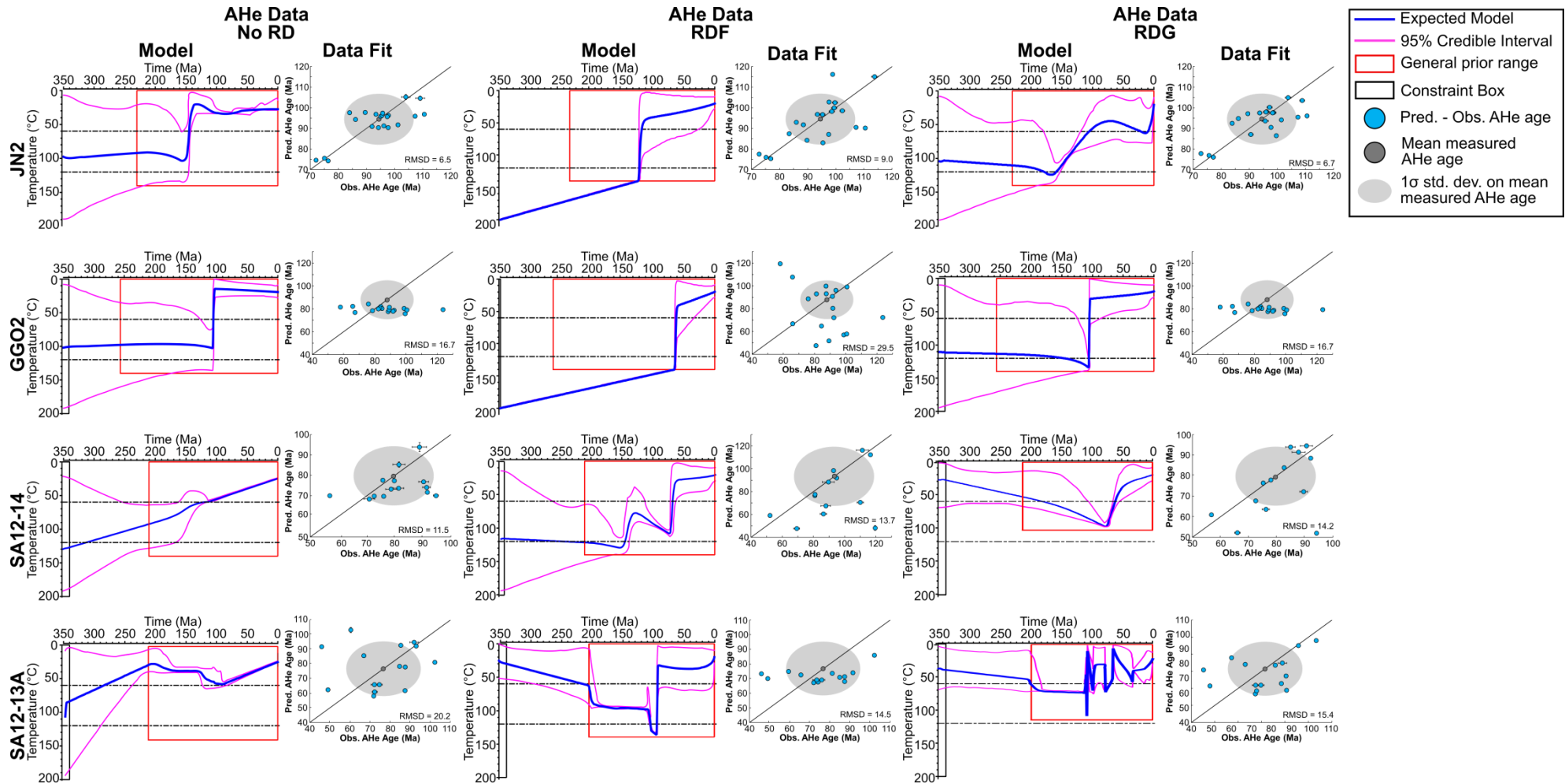


Figure 4-20: Thermal history models for four outcrop samples investigating the effects of modelling only AHe data with a small analytical uncertainty. No RD = No radiation damage model included; RDF = Radiation damage incorporated after Flowers et al. (2009); RDG = Radiation damage incorporated after Gautheron et al. (2009).

thermal histories are well constrained and relatively simple. Cooling is either extremely rapid and then minimal (e.g. JN2, GGO2) or very slow (e.g. SA12-14). The exception to this is SA12-13A which predicts that the sample resided at low temperatures over the last c. 200Ma. Introducing the effects of radiation damage creates larger uncertainty in the low temperature portion of the thermal history (i.e.  $< 60^{\circ}\text{C}$ ) because the measured ages now correspond to a higher closure temperature dependant on the degree of radiation damage experienced. Thermal histories also show additional complexity which can be extreme (e.g. SA12-13A-RDG model) which is required to best fit the complex data. In some cases, there is good agreement with predicted and observed ages but in general the observed data is not reproduced well. The problem is that each AHe age has a very small uncertainty and the model is finding that complex models are required to best fit this data within these data with these tight uncertainty levels.

#### **4.5.2.3 Modelling AHe data independently: with estimated uncertainty**

Modelling AHe data as described above implies that the “true” AHe age that we are trying to measure lies within analytical uncertainty. However, analysis of Durango apatite standards over the course of producing this data has only been able to achieve a standard deviation of 10% (see Appendix 2.2). As such this level of uncertainty should be added on to samples to reflect the natural reproducibility in AHe analysis. In fact, in some cases an additional uncertainty should be added to some apatite grains to account for uncertainties in (i) whether Durango apatite diffusion systematics are applicable to apatites with high concentrations of uranium; (ii) how much Sm is present in apatites that have not been analysed for this study and (iii) unknown compositional influences on diffusion. These uncertainties are difficult to quantify and as such have not been included.

The observed AHe age is now resampled within the *estimated uncertainty* level of c. 9 - 12% of the measured age. This makes it much more likely that less complex models are able to predict AHe ages that are compatible with the observed data. As such, the expected thermal history models may be more

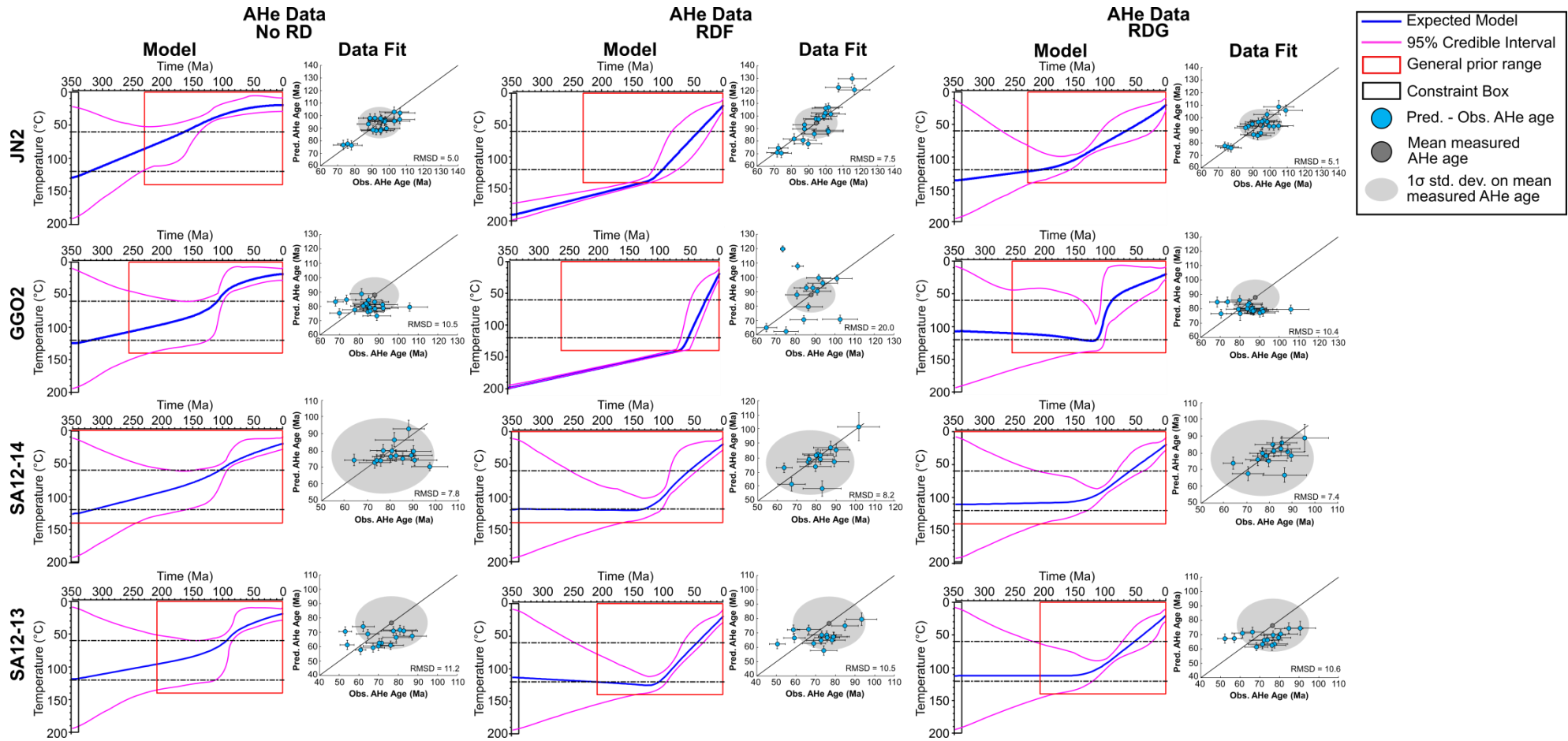


Figure 4-21: Thermal history models for four outcrop samples investigating the effects of modelling only AHe data with a large estimated uncertainty (estimate uncertainty = analytical uncertainty + standard deviation of Durango standards). No RD = No radiation damage model included; RDF = Radiation damage incorporated after Flowers et al. (2009); RDG = Radiation damage incorporated after Gautheron et al. (2009).



poorly constrained over much of their thermal history but complex features which may be unjustified geologically are smoothed out (Fig. 4-21). For most grains the predicted and observed ages agree within uncertainty levels which are now considerably large. Without including the effects of radiation damage, each of the samples have very similar, simple, protracted thermal histories. The effects of the different radiation damage models are best seen in the extremely high eU samples JN2 and GGO2. RDG models for samples SA12-14 and GGO2 are in fairly good agreement with AFT thermal history models while samples JN2 and SA12-13A entirely contradict the rapid cooling predictions of AFT thermal history models. This is because highly dispersed AHe ages are symptomatic of slow cooling histories but JN2 and SA12-13A have long MTLs and narrow TLDs which strongly supports rapid cooling. As such modelling these datasets independently will not produce coherent results. However, it has already been stated that the AHe data have a large uncertainty range which can be modelled alongside fission track data and the uncertainties therein to find a model which is compatible with both datasets.

#### ***4.5.2.4 Modelling AFT and AHe data together***

Integrating both datasets, that is jointly modelling the AFT and AHe data, produces thermal histories which are relatively simple but which are still able to define distinct transitions in cooling style over time (Fig. 4-22). Samples which were predicted to be rapidly cooled based on AFT data alone (e.g. JN2 and SA12-13A) are rapidly cooled when the AHe data are integrated without deterioration in the quality of the data fit. This shows that caution should be taken when modelling AHe independently as the AHe dataset can be reproduced within uncertainty levels both with relatively rapid or slow cooling. The AHe data is still crucially important however as it can help to constrain the cooling history through lower temperatures. In the case of SA12-13A this simply confirms rapid cooling to near surface temperatures. However, the JN2 RDG model predicts that cooling is initially fairly rapid but slows more gradually towards surface temperatures throughout the Mid-Late Cretaceous.

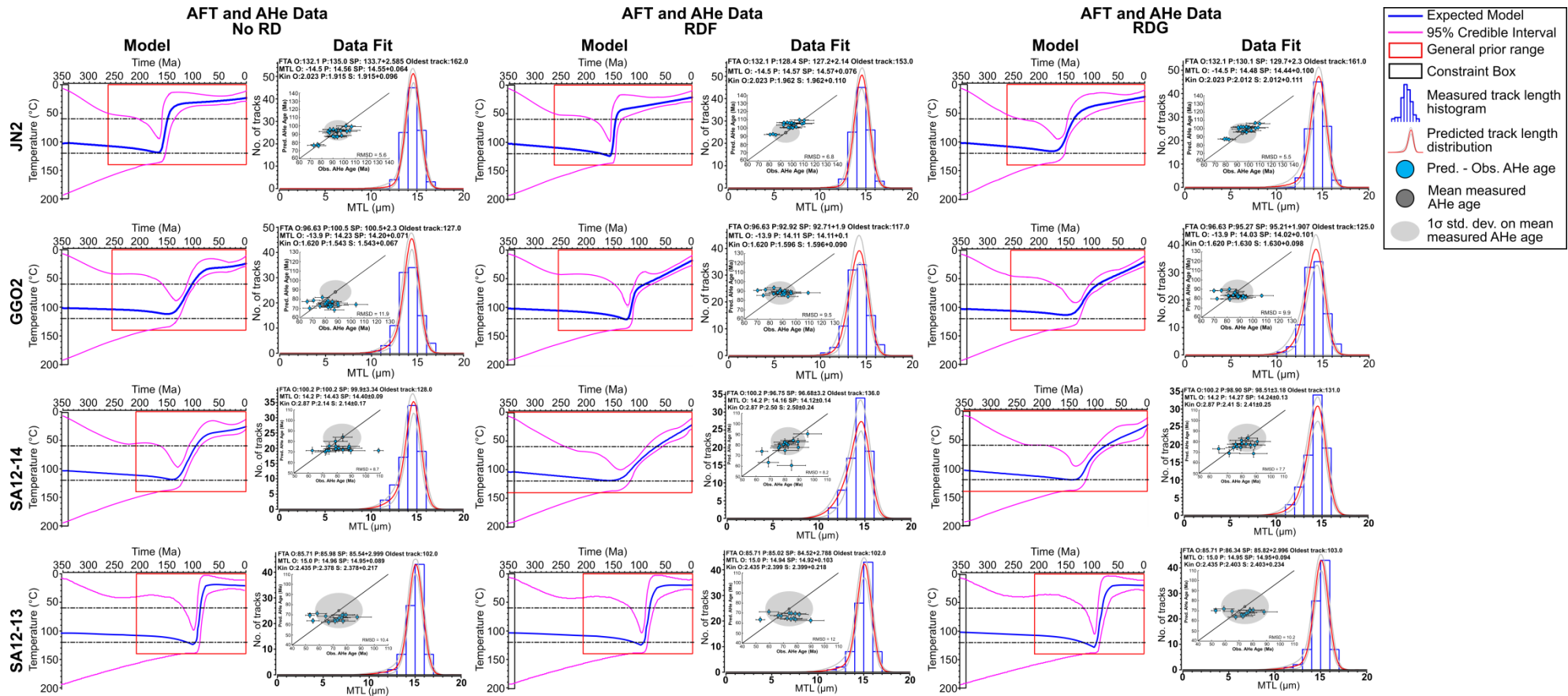
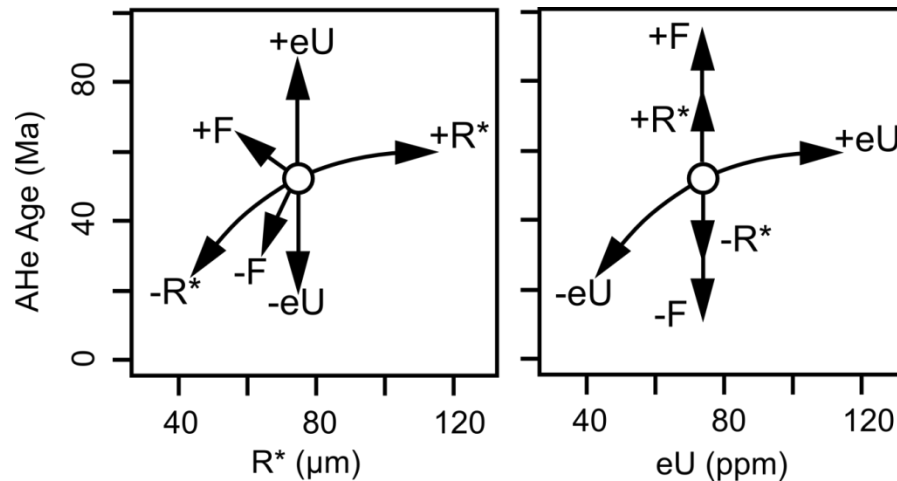


Figure 4-22: Thermal history models for four outcrop samples investigating the effects of modelling both AFT data and AHe data with a large estimated uncertainty (estimate uncertainty = analytical uncertainty + standard deviation of Durango standards). No RD = No radiation damage model included; RDF = Radiation damage incorporated after Flowers et al. (2009); RDG = Radiation damage incorporated after Gautheron et al. (2009).



**Figure 4-23: Cartoon illustrating the relative influence on AHe ages by the different factors causing natural AHe single grain age dispersion (after Brown et al., 2013). (a) shows the expected trajectory for AHe age and  $R^*$  and (b) shows the expected trajectory for AHe age and eU. However, the competing influence of all dispersion contributors perturbs the simple relationship. Age increases with increasing eU and  $R^*$ . Larger fragment lengths of broken crystals are typically older than small fragment lengths.**

Slowly cooled samples highlight the uncertainty in using the current radiation damage models. Major differences can be seen in the style of cooling, however in all models the timing for the onset of cooling is consistent and is considered to be reliable. Certain aspects of the thermal history models are still unresolved but to a large degree this can be attributed to the uncertainties which are inherent in how radiation damage affects AHe ages. By assigning the measured AHe a large uncertainty and resampling the observed age within this uncertainty our poor understanding of radiation damage is dealt with as best as can currently be achieved. Including AFT data is therefore imperative in helping to constrain the AHe data. For the data presented in the subsequent chapters thermal history models will jointly model AFT data alongside resampled AHe data and models using no radiation damage, radiation damage after Flowers et al. (2009) and radiation damage after Gautheron et al. (2009) are systematically determined and discussed.

## 4.6 Summary and strategy for joint AFT and AHe analysis

Low temperature thermochronology has been successfully applied to a variety of geological problems and settings. In settings where cooling has been sufficiently rapid, recent, and/or samples have low concentrations of U and Th, the AFT and

AHe thermochronometers likely behave coherently and conform to closure temperatures that reflect theoretical studies. However, in regions such as South Africa where cooling has been variable and occurred over a long time period (c. 150 Ma) and samples of basement lithologies contain a large variation in U and Th contents problems arise when using low temperature thermochronometers. These problems are common to other studies and have been discussed above in detail, but ultimately the measured AFT or AHe data holds useful temporal information related to upper crustal cooling. In particular, the influence of factors such as radiation damage, grain size and fragmentation of whole grains will induce natural dispersion. This dispersion can be inverted to extract thermal history information but the likelihood of observing simple correlations between AHe age and any of these factors is low as they each act to decouple one another (Fig. 4-23). Therefore, it is suggested that obtaining multi-single grain analysis (c. 10 - 20 grains), maximising the amount of dispersion in AHe ages and integrating the AHe data with robust AFT data will provide the optimum combination which can be inverted to yield thermal histories. By adopting a Bayesian approach to thermal history inversion, which utilises the uncertainties within each of these data sets, a coherent and conservative, thermal history for a sample can be obtained.

# CHAPTER 5

## CONSTRAINING LARGE-SCALE BRITTLE DEFORMATION IN THE NAMAQUALAND HIGHLANDS

### 5.1 Introduction

As discussed in the opening chapters, our understanding of the thermal and structural processes during continental rifting has developed to a point where the traditional models of long term landscape evolution of continental margins are no longer adequate and need to be readdressed. If structural reactivation at so-called “passive” continental margins is common, then it is crucial that quantitative constraints on the timing and magnitude of the major tectonic events are obtained to aid the development of more sophisticated surface process models. Low temperature thermochronology is ideally suited to obtain these constraints by providing information on the temperature-time (T-t) history of samples as they cool through the upper kilometres of the crust.

The Namaqualand sector of the South Atlantic margin has recently been the subject of investigations into the post-rift evolution of the margin and may be a prime example of a passive margin which has experienced many phases of post-rift structural reactivation. However, a lack of post-rift geological evidence and poor age constraints on the timing of deformation means that our understanding of the development of the present day morphology is still unresolved.

This study provides a comprehensive suite of apatite fission track and apatite (U-Th-Sm)/He data which have been inverted using a Bayesian transdimensional Markov Chain Monte Carlo (MCMC) approach to resolve the thermal history of the continental margin. By demonstrating that these cooling episodes relate to crustal denudation, a multi-stage development of the continental margin is proposed.

## 5.2 Local Geology

### 5.2.1 Study Area

The study area extends from the coastal margin at Hondeklip Bay eastward towards Vaalputs, encompassing the low-intermediate nuclear waste disposal site operated by NECSA at Vaalputs. The broad transect cuts through the heart of the Namaqualand basement inlier and through the small towns of Kamieskroon and Leliefontein. The distribution of samples parallel to the coast encroaches on the region just south of Springbok to the north, and extends into the region around the town of Garies in the south (Fig. 5-1).

### 5.2.2 Morphology

The most prominent topographic feature in the study area is the high relief Namaqualand Highlands (NQH) (Fig. 5-1). Seaward of this feature is a coastal plain with a width of c. 40 - 50km which comprises a low relief morphology. This low elevation plain gradually increases in elevation from sea level at the margin to c. 400m at the periphery of the NQH. Inland of the NQH, the Namaqualand Plateau attains an average elevation of approximately 1km. The Namaqualand Plateau is the western extent of a regionally extensive low relief plain spanning across much of the interior of southern Africa. The NQH form a high relief zone rather than a prominent steep escarpment or well-defined escarpments in a stepped topography such as along the SE African margin. Elevations frequently reach up to 1500 m while locally the Kamiesberg Mountains reach up to 1770m. Intervening valley floor elevations are typically 400 - 500 m a.s.l in the western side of the NQH but progressively increase to c. 900 m closer to the plateau. Superficial sandy deposits fill the valley floors and follow a complex network of major and minor structures that predominantly trend NNW-SSE. The nature of valley incision and the origin of the NQH terrain have previously been interpreted as a remnant of Late Jurassic rift shoulders (Partridge and Maud, 1987); a remnant of a post-rift feature uplifted during escarpment retreat (e.g. Gilchrist et al., 1994; Brandt et al., 2005); or an expression of Mid-Late Cretaceous tectonically induced uplift (e.g. Kounov et al., 2009).

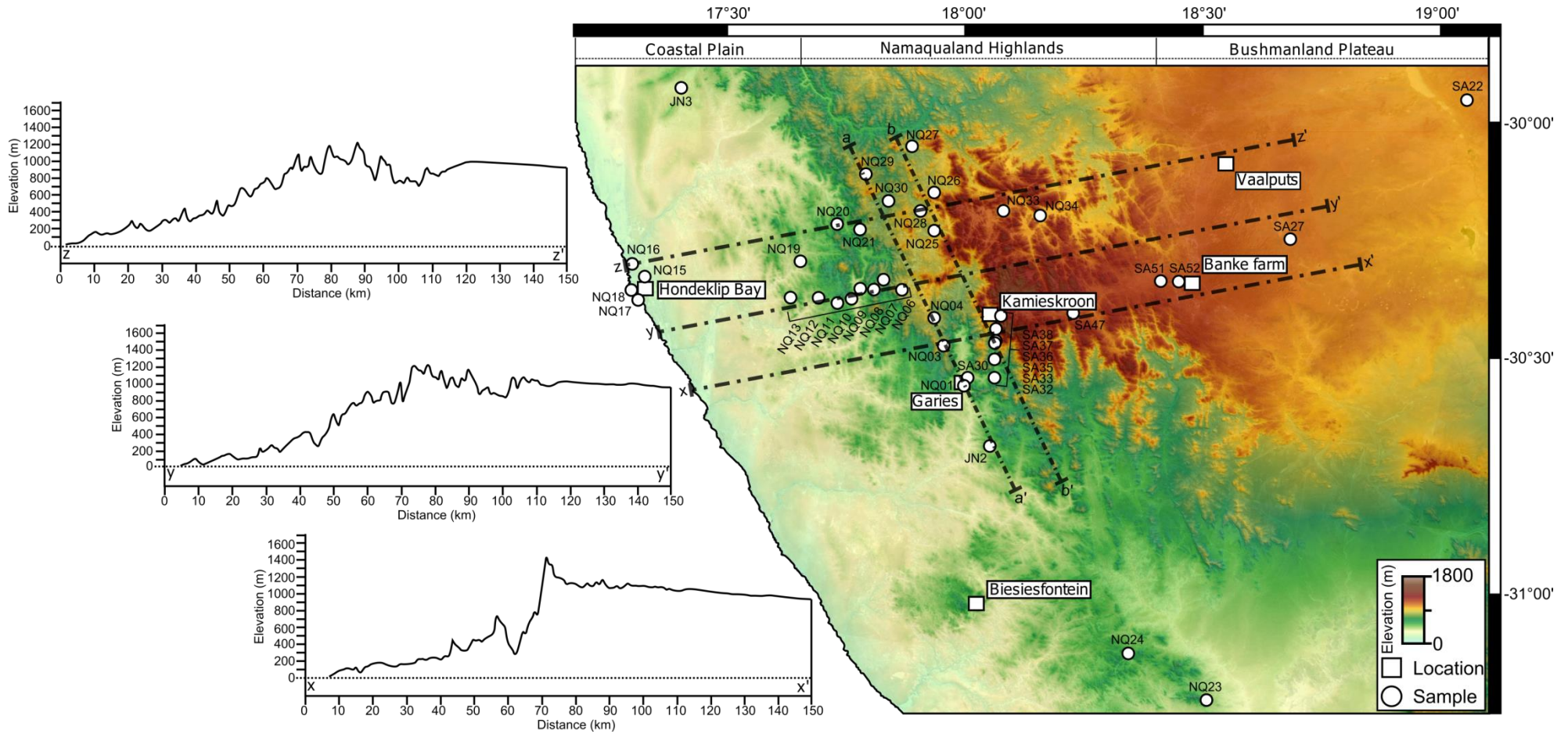


Figure 5-1: Location map of the Namaqualand Highlands study area. DEM created using SRTM90m. Elevation map is draped over Landsat ETM+ RGB:321 satellite images to enhance local relief and geomorphic features. Elevation profiles for three coast perpendicular transects are shown and are used later alongside two coast parallel transects (a-a'; b-b') in Figure 5-20(d) and (e) with projected data.

### 5.2.3 Namaqua Metamorphic Province

Rocks of the Meso-Proterozoic Namaqua Metamorphic Province (NMP) dominate the geology of the study area (Fig. 5-2). The NMP are comprised mainly of granitic gneisses and granite bodies that can be attributed to syn or post tectonic emplacement during multiple periods of orogeny and terrane accumulation (Tankard et al., 1982; Groenewald et al., 1991; Jacobs et al., 1993; Cornell et al., 2006). The NMP therefore records a complicated history of magma emplacement and metamorphism that has produced a variety of supracrustal and intrusive rock types (Thomas et al., 1994a, b; Eglinton, 2006; Voordouw and Rajesh, 2012). A detailed description of these rock types can be found in Eglinton (2006).

What is more pertinent in the context of this study is the tectonic fabric that was established at this time. This basement structure has likely been important in controlling the style of pre, syn and post-rift tectonics (e.g. Ziegler and Cloetingh, 2004). At least four compressional deformation events have been documented in gneissic foliations and folding of the crust and are thought to have been driven by processes coeval with the regional Kibaran Orogeny (c. 1200 - 1000 Ma) and global Grenville Orogeny (c. 1300 - 950 Ma) (Jacobs et al., 1993; Clifford et al., 2004; Eglinton, 2006; Viola et al., 2012; Colliston et al., 2014). Following these phases of crustal shortening, a phase of extension followed in western Namaqualand, and has been attributed to the collapse of the Namaqualand orogenic belt (Dewey et al., 2006). Dykes, folds and lineations ascribed to these deformation events typically strike NW-SE or NE-SW and occasionally E-W (Cornell et al., 2006). The main phase of metamorphism of the NMP was largely granulite-facies metamorphism (T: 800-860°C and P: ~5-6 kbar/15-18km) and was completed by c. 1000 - 800 Ma (Waters, 1989; Eglinton, 2006).

### 5.2.4 Neoproterozoic – Palaeozoic: Pan-Africa Orogeny

Neoproterozoic-Palaeozoic units are rare within the study area and outcrop only in the south towards the town of Bitterfontein (Fig. 5-2). These units consist of sedimentary rocks that have experienced very low-grade metamorphism and are



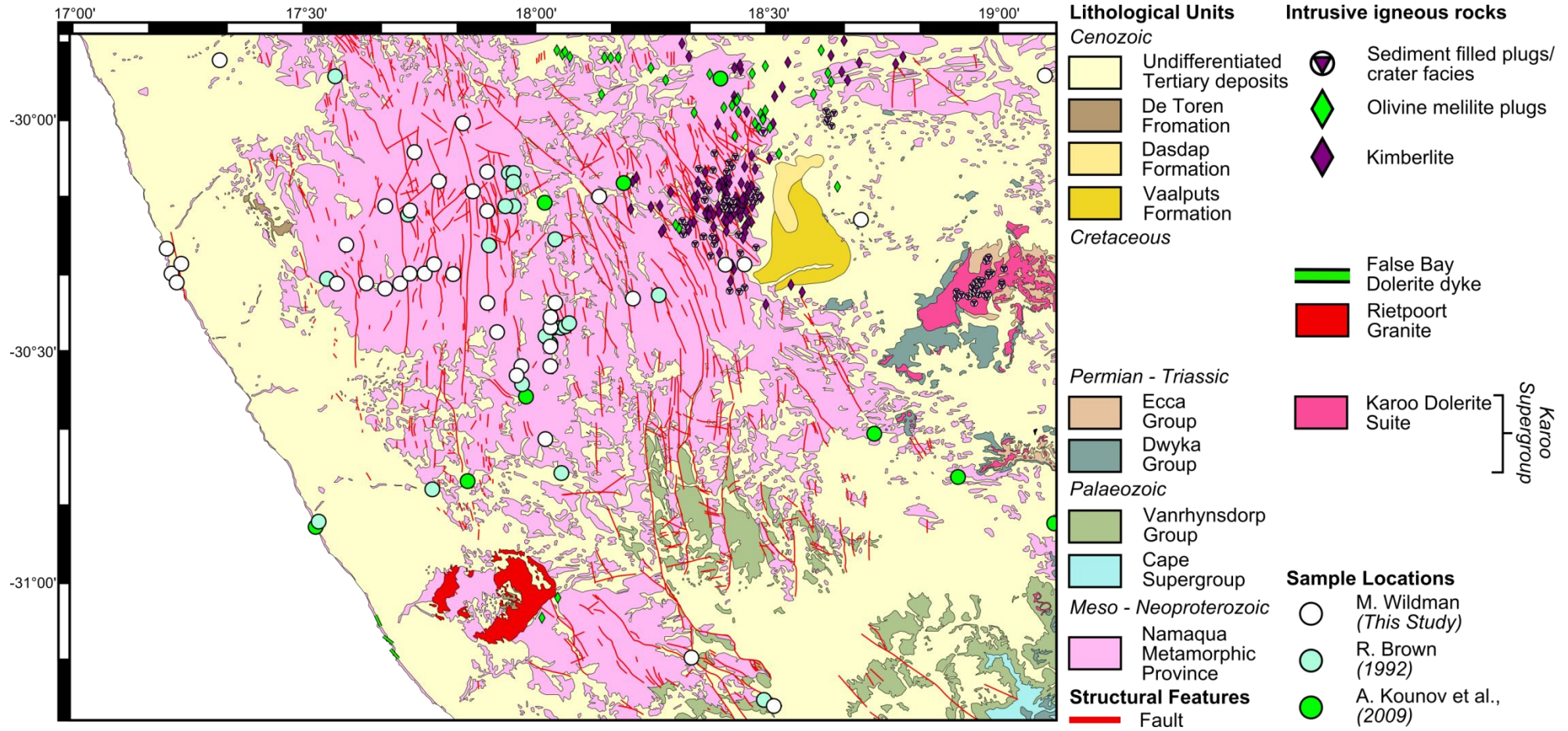


Figure 5-2: Geological map of the Namaqualand Highlands study area. Geological map was redrawn to highlight the major geological units, structures and features relevant to this study, using 1:250,000 maps produced by the Council for Geoscience, South Africa. (Garies, sheet 3017: de Beer, 2010; Loriesfontein, sheet 3018: Macey et al., 2011; Springbok, sheet 2916: Marais et al., 2001).

part of the Vanrhynsdorp Group. The Vanrhynsdorp group was deposited during the latter stages of the Pan-African orogeny (c. 700 - 500 Ma) in a foreland basin setting (Gresse and Germs, 1993). In the study area, the Vanrhynsdorp Group outcrop in half-graben structures trending N-S and as gently folded, fault parallel synclines, that overly an easterly dipping unconformity across the NMP basement (Gresse et al., 2006; Macey et al., 2011). The main Vanrhynsdorp Basin in the southeast of the study area is characterised by a fold-and-thrust belt with NW-SE trending faults. The influence of the pan-African orogeny is observed in the NMP as brittle overprint structures produced during dextral and sinistral movement along shear zone and thrusting towards NE and SW depending on the orientation and geometry of the fault (Viola et al., 2012).

### **5.2.5 Karoo Supergroup**

Rocks of the Karoo Supergroup were deposited in a sub-continental foreland basin during the Carboniferous - Triassic (Tankard et al., 2009). The Karoo Basin covers an area of approximately  $7 \times 10^5 \text{ km}^2$  across central South Africa but only outcrops in the most easterly extent of the study area (Fig. 5-2). The Karoo Supergroup deposits in this region include the lowermost Permian Dwyka and Ecca Group rocks (Johnson et al., 2006) which are intruded by Late Triassic-Early Jurassic Karoo dolerite sills and dykes. Dwyka glacial diamictites were unconformably deposited on the NMP basement and Vanrhynsdorp units during Late Carboniferous to Early Permian glaciations of southern Africa (Visser, 1990). The thickness and lithofacies of the Dwyka Group are highly variable and are attributed to erosion of an irregular pre-Karoo relief (Johnson et al., 2006). Clasts within the diamictite can be variable in size and are typically derived from the surrounding NMP or Palaeozoic bedrock (Macey et al., 2011). Glacial pavements are preserved on many basement exposures (Macey et al., 2011) and show striations indicating a SW direction of ice movement. Conformably overlying the Dwyka Group glacial deposits is the Permian Ecca Group consisting of shale units that are thinly laminated and fossiliferous (Johnson et al., 2006). These rocks were deposited in a shallow-marine environment and are the dominant sedimentary unit in the north-west Karoo Basin. Their exposure in the study area is limited and is typically observed beneath extensive dolerite sills.

The intrusion of Karoo dolerite sills and dykes (c.  $180\pm 5$  Ma) was coeval with the eruption of thick continental flood basalts ( $> c. 1.5 - 2$  km) and marks the termination of Karoo deposition and the onset of continental rifting in eastern Gondwana (Duncan et al., 1997; Jourdan et al., 2005, 2007; Moulin et al., 2011; Svenson et al., 2012). Karoo dolerite intrusions are widely preserved in the eastern part of the study area as prominent isolated summits (koppies) above the flat lying plateau.

### **5.2.6 Syn and post-rift intrusive activity**

The Karoo dolerite intrusions have been dated at c. 180 Ma (Duncan et al., 1997; Jourdan et al., 2005; 2007) and are thought to be linked to the break-up of eastern Gondwana during the Late Jurassic. Igneous activity coeval with Atlantic rifting can be found in the most southern region of the study area (Fig. 5-2). The Koegel Fontein complex near the towns of Kotzesrus and Biesiesfontein is comprised of a variety of intrusive bodies including tholeiitic basalt plugs, syenite and granite plutons and dykes of varying composition (de Beer et al., 2002; Curtis et al., 2011). The Reitpoort Granite is the largest of these and is described as a homogenous, medium-coarse grained alkali-feldspar granite forming prominent dome-like hills (de Beer, 2010). A suite of NNW-SSE trending dolerite dykes cross cut the Koegel Fontein complex. These dykes are named the False Bay dolerite suite after the dolerite dykes of similar age and composition observed in the Southern Cape (Day, 1987; Reid, 1990; Reid et al., 1991; Trumbull et al., 2007; de Beer, 2010).

Later Cretaceous intrusions are commonly olivine melilitite plugs and alkali and carbonitite dykes. Olivine melilitite plugs are poorly exposed and are inferred by the identification of low hills or depressions covered in boulders and rubble. The Biesiesfontein plugs intrude into the Reitpoort Granite and have been dated at c. 55 Ma (Moore and Verwoerd, 1985). The Sandkopsdrif Complex north of Rietpoort is made up of numerous alkaline and carbonitite dykes (de Beer, 2010; Curtis et al., 2013) and is thought to post-date olivine melilitites in Biesiesfontein (Moore and Verwoerd, 1985). An important observation that can be made from these intrusions is their coherent trend along a N to NNW striking fracture zone

suggesting a link between reactivation of major structures during the Early Cretaceous and the Early Cenozoic creating pathways for intrusive rock (e.g. Jelsma et al., 2009).

The Gamoep suite consisting of olivine melilitite plugs and possible kimberlite intrusions is found inland on the interior plateau north of Banke farm close to the Vaalputs nuclear repository site. Preservation of up to 260m of carbonaceous shales and tuff bands within the diatremes of pipe-bodies are commonly topped with conglomerates and arenites. These are interpreted as crater-lake deposits and indicate limited erosion has taken place since the emplacement of these igneous intrusives (Cornelissen and Verwoerd, 1975; Moore and Verwoerd, 1985). The intrusions have been radiometrically dated at 54 - 77 Ma (Moore and Verwoerd, 1985). Fossil frogs discovered in the sediment infill have been used to infer a Late Cretaceous to Tertiary (Haughton, 1931) or Eocene age for the sediments (Estes, 1977). Palynological evidence presented by Scholtz (1985) however suggests a Palaeocene age for the sediments (64 - 54 Ma).

### **5.2.7 Late Cretaceous and Tertiary units**

The preservation of crater-lake sedimentary successions is highly significant as they provide insights into a period of the margins geological history which is otherwise absent. The other major Late Cretaceous - Early Cenozoic sedimentary units of note are the Dasdap and Vaalputs formation which are exposed immediately eastward of the NQH on the plateau near Banke Farm, south of Vaalputs (Fig. 5-2). These sequences are observed as silicified and kaolinitised conglomerates and coarse grained, cross-bedded sandstones forming prominent mesas and inliers (Brandt et al., 2003). Rounded pebbles of various compositions within the conglomerate horizons and the occurrence of widespread cross laminations in the Dasdap sediments suggest that these sediments were deposited in a fluvial environment. The dominant presence of granitoid and blue-vein quartz pebbles in conglomerate units suggests a metamorphic basement source. However, occasional pebbles of Dwyka tillite composition, confined to the Vaalputs sequence, were also described by Brandt et al. (2005). The composition of conglomerate clasts, palaeocurrent indicators and grain size

characteristics indicate a westerly provenance and easterly directed palaeocurrents for the Dasdap and Vaalputs sediments (Brandt et al., 2003, 2005). The volcanic pipes in the region discussed above are overlain by these units in places and therefore provide an upper age limit of c. 67 Ma for the Dasdap sequence (Brandt et al., 2003, 2005; Viola et al., 2012).

The Vaalputs formation and adjacent Santab-se-Vloer Basin overly the Dasdap sequence and are intersected and bounded, respectively, by prominent NNW - SSW trending faults. One particular group of outcrops of Dasdap sediments at Kookoppe form a fault bounded north-northwest linear chain. This is in keeping with the predominantly NNW - SSE structural trend observed within the wider region (Viola et al., 2012). These observations have two main implications in the context of this study: i) erosion of basement and some Karoo Supergroup Dwyka units occurred during the Late Cretaceous, possibly related to tectonically steepened river gradients and increased rainfall associated with the humid Late Cretaceous climate (Partridge and Maud, 1987; Brandt et al., 2005), and ii) tectonic activity across the margin, including significant displacement and differential uplift across faults, extends far inland of the escarpment zone, and has been episodically significant long after the initial phase of rift related lithospheric thinning.

A variety of Cenozoic sedimentary deposits are present over a narrow zone along the low coastal plain extending along almost the entire length of the margin (e.g. Roberts et al., 2006, de Beer, 2012). These Cenozoic deposits are typically preserved in the form of elevated marine terraces, semi- and unconsolidated aeolian sands and as inliers preserved in localised depressions in basement lithologies. The strata comprising coastal marine terraces are best represented by the Alexander Bay Formation which records Miocene and younger cycles of erosion and weathering; attributed to sea-level fluctuations driven by both tectonic and eustatic processes (Roberts et al., 2006). Three distinct packages have been defined within the Alexander Bay Formation at 90 m, 50 m and 30 m above sea level. Late Oligocene to Early Miocene terrestrial sediments are rarely preserved; typically thin c. 10 m; and are poorly understood both in terms of their depositional environment and age (de Beer, 2010, 2012). The Oligocene De

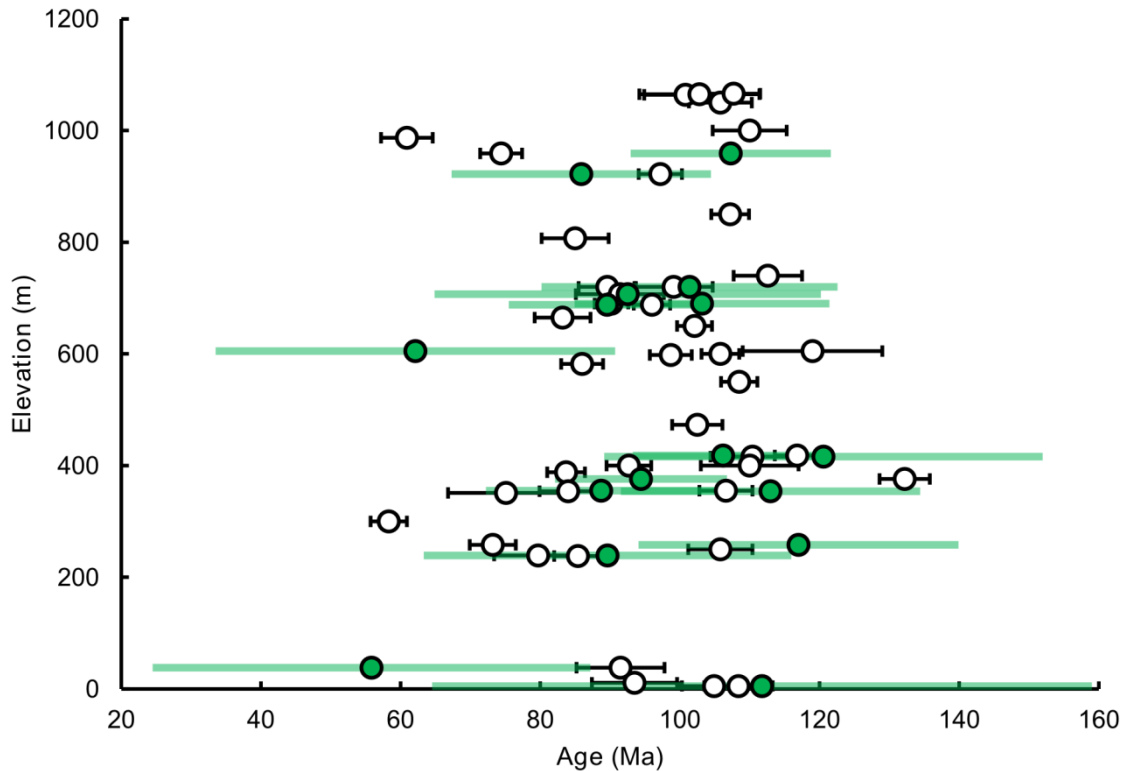
Toren Formation is present on the Koegel Fontein intrusive complex and on the periphery of the NQH at Quaggafontein farm. The sediments are proposed to have been deposited in a similar environment to the Dasdap Formation. The Koiingnaas Formation overlies strongly weathered basement along the margin at Hondeklip Bay and were deposited in channels formed during regression during the Oligocene (de Beer, 2010).

## 5.3 AFT Analysis

### 5.3.1 Results

Apatite fission track (AFT) analysis was performed on samples using the external detector method (EDM) as outlined in Appendix 1.2. All uncertainties for AFT data reported here and in Chapter 6 are  $1\sigma$  standard error. A zeta value of  $316.7 \pm 10.5$  was used in age calculations for all samples except JN2 and JN3 for which a zeta value of  $317.3 \pm 11.1$  was used (see Appendix 2.1). Central AFT ages range from  $58.3 \pm 2.6$  to  $132.2 \pm 3.6$  Ma with c. 35% falling between 100 and 110 Ma. AFT ages do not show any correlation with elevation and, in fact, some of the youngest measured AFT ages can be found at the highest elevations (Fig. 5-3). Horizontal confined track (HCT) lengths were measured to investigate the thermal history of the samples. Mean track lengths (MTL) range between  $10.9 \pm 0.19$  and  $14.35 \pm 0.22$   $\mu\text{m}$  with the majority being greater than 13  $\mu\text{m}$ . The width of track length distribution (TLD) of these samples is reflected using the standard deviation of length measurements (MTL-SD) which are between 0.97 and 2.50, the majority of these however are less than two (see Appendix 5.2 for all TLD plots).

The data are summarised in Table 5-1 and Figure 5-4. In settings where there has been more than one thermal event, AFT age - MTL plots may show a 'Boomerang' style relationship (e.g. Green, 1986; Gallagher and Brown, 1997). This relationship is produced by a proportion of samples having long MTLs and ages coeval with the initial thermal event and a proportion of the samples having long MTLs and ages coeval with the second, younger, thermal event. The intervening samples represent samples which remained at depth following the



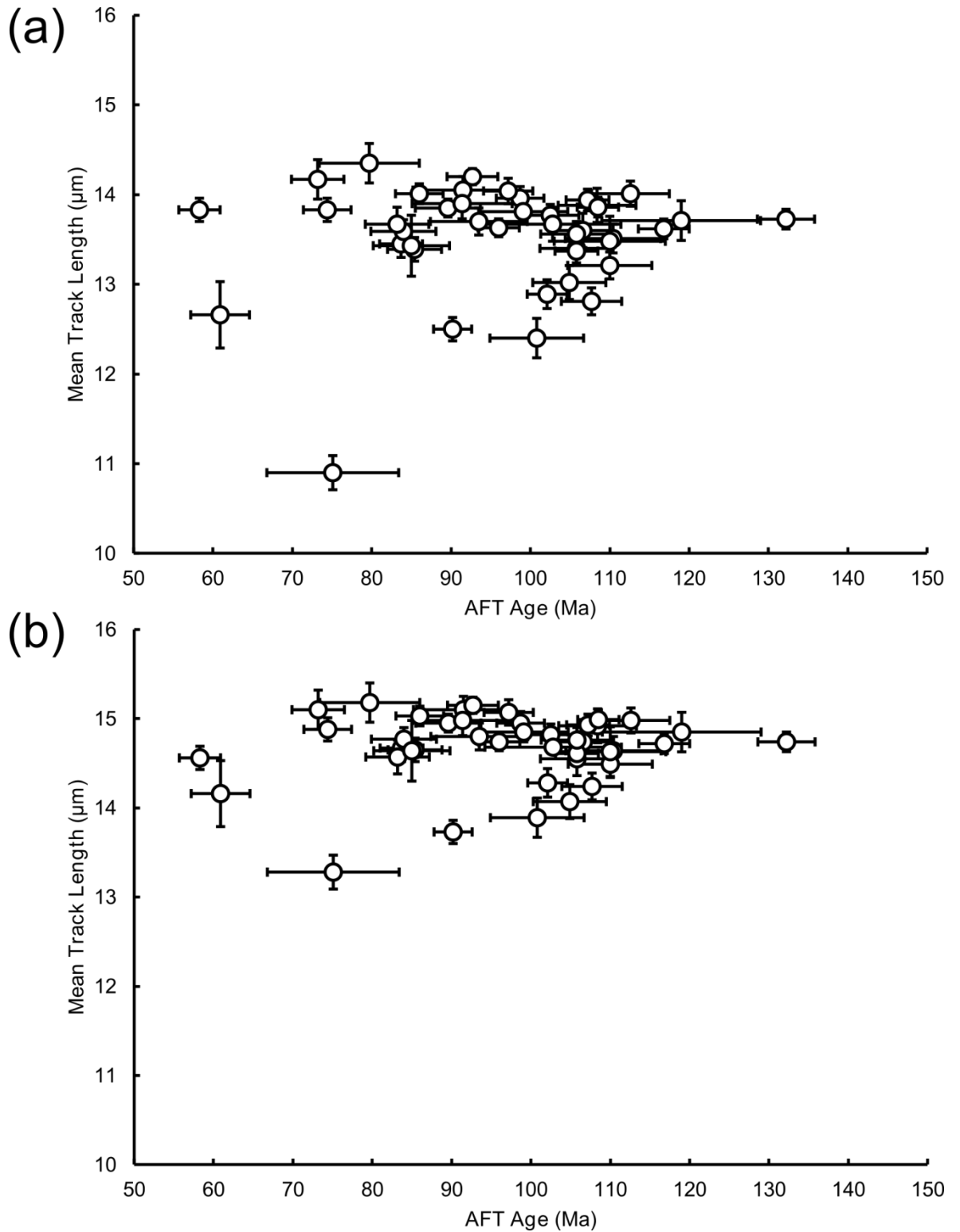
**Figure 5-3: Plot of AFT and AHe age against elevation. White circles are Central AFT ages with uncertainty bars representing  $1\sigma$  standard error on the central age. Green circles are uncorrected mean AHe ages with uncertainty bars representing  $1\sigma$  standard deviation. The standard deviation is used in this instance to highlight the dispersion in single grain AHe ages.**

initial cooling event and so were partially annealed prior to the second phase of cooling (Gallagher and Brown, 1997). Observing a boomerang style plot is difficult for this dataset as almost all MTLs are similar in value and are predominantly greater than  $13 \mu\text{m}$ . Therefore, it is likely that most samples resided at elevated temperatures and were almost completely reset prior to cooling and did not reside in the PAZ for extremely long periods. Despite the range in MTL being small for the majority of samples, the shorter (i.e. c.  $13 - 13.5 \mu\text{m}$ ) MTLs are associated with the older (c.  $100 - 110 \text{ Ma}$ ) AFT ages. This amount of thermal annealing may simply be due to relatively slow rates of cooling and will be resolved during thermal history modelling. Distinguishing a clear trend in the main cluster of data is difficult because of the low spread of MTLs. However, there are several samples which fall away from the main cluster of data due to their short (i.e.  $< 13 \mu\text{m}$ ) MTL and/or young age (c.  $< 80 \text{ Ma}$ ). A boomerang relationship could be argued for as there appears to be a decrease in

Sample	Long. (°)	Lat. (°)	Elev. (m)	$\rho_s^a$ ( $10^6\text{cm}^{-2}$ )	$N_s^b$	$\rho_i^a$ ( $10^6\text{cm}^{-2}$ )	$N_i^b$	$\rho_d^a$ ( $10^6\text{cm}^{-2}$ )	$N_d^b$	$P(\chi^2)^c$ (%)	$D_{par}^d$ ( $\mu\text{m}$ )	$[U]^e$ (ppm)	C. AFT Age (Ma) $\pm 1\sigma$	#Xtls	Measured		c-axis correction <sup>h</sup>		#HCT <sup>i</sup>			
															MTL ( $\mu\text{m}$ ) $\pm 1\sigma$	SD <sup>g</sup>	MTL ( $\mu\text{m}$ ) $\pm 1\sigma$	SD <sup>g</sup>				
JN2	18.05	-30.68	376	42.7	3605	100.2	8451	19.8	14137	0.01	2.13	67.6	132.2	3.6	20	13.73	0.11	1.08	14.74	0.12	0.79	103
JN3	17.38	-29.90	418	24.2	1790	64.7	4796	19.9	14137	0.81	1.91	44.1	116.8	3.2	20	13.62	0.11	1.10	14.72	0.12	0.78	103
NQ12-01	17.99	-30.55	238	15.0	1365	40.4	3675	14.6	16086	0.04	1.49	37.6	85.4	3.4	20	13.39	0.13	1.32	14.65	0.14	0.80	100
NQ12-03	17.95	-30.46	582	11.1	1163	29.8	3127	14.7	16086	0.57	1.83	27.0	86.0	3.0	20	14.01	0.11	1.10	15.03	0.12	0.76	101
NQ12-04	17.93	-30.40	720	7.2	1324	21.2	3898	16.6	16348	0.00	1.65	27.8	89.6	4.1	19	13.85	0.10	0.98	14.95	0.11	0.63	100
NQ12-06	17.86	-30.34	690	26.7	2080	76.9	5989	16.5	16348	0.32	1.62	65.3	90.2	2.4	19	12.50	0.13	1.39	13.73	0.14	1.04	115
NQ12-07	17.82	-30.32	688	29.6	2511	72.0	6095	14.8	16086	0.12	1.92	65.0	96.0	2.6	20	13.63	0.10	1.23	14.74	0.11	0.82	151
NQ12-08	17.80	-30.34	598	23.1	2283	60.9	6012	16.5	16348	0.06	2.98	49.5	98.7	3.0	19	13.96	0.13	1.23	14.95	0.14	0.90	73
NQ12-09	17.77	-30.34	355	12.6	1153	31.8	2906	17.1	16086	0.49	2.49	25.8	106.6	3.8	20	13.60	0.19	1.92	14.74	0.21	1.20	101
NQ12-10	17.75	-30.36	239	5.9	208	19.2	678	16.5	16348	0.50	3.42	16.3	79.7	6.3	9	14.35	0.22	1.05	15.18	0.23	0.83	22
NQ12-11	17.72	-30.37	416	4.6	477	11.2	1167	17.2	16086	0.82	2.07	10.1	110.4	6.0	20	13.51	0.16	1.43	14.64	0.17	0.90	38
NQ12-12	17.68	-30.36	388	31.2	1649	96.3	5096	16.5	16348	0.10	2.89	83.4	83.7	2.7	18	13.45	0.15	1.50	14.67	0.16	0.97	106
NQ12-13	17.62	-30.36	354	7.8	747	21.8	2082	14.9	16086	0.28	1.45	19.3	84.0	4.1	20	13.59	0.13	1.27	14.77	0.14	0.91	100
NQ12-15	17.30	-30.32	38	4.5	373	11.7	966	15.0	16086	0.17	2.06	10.8	91.5	6.3	20	14.05	0.15	1.45	15.10	0.16	0.91	94
NQ12-16	17.27	-30.29	11	8.5	643	22.0	1654	15.2	16086	0.01	1.87	19.5	93.5	6.1	20	13.70	0.15	1.22	14.80	0.16	0.83	65
NQ12-17	17.29	-30.36	5	8.6	914	21.7	2316	16.8	16086	0.14	1.82	17.5	104.9	4.6	20	13.02	0.19	1.91	14.07	0.21	1.33	100
NQ12-18	17.28	-30.34	5	8.9	1161	21.8	2846	16.9	16086	0.02	2.11	16.6	108.4	4.9	20	13.88	0.19	1.30	14.92	0.20	0.88	100
NQ12-19	17.64	-30.28	250	5.2	754	11.8	1723	15.4	16086	0.64	1.90	10.8	105.8	4.6	20	13.40	0.19	1.48	14.55	0.20	1.06	82
NQ12-20	17.72	-30.20	473	22.3	1556	53.5	3723	15.6	16086	0.18	2.28	45.3	102.5	3.6	19	13.77	0.12	1.28	14.82	0.13	0.87	108
NQ12-21	17.77	-30.21	665	24.6	1468	80.9	4831	17.3	16086	0.00	1.82	54.6	83.2	4.0	17	13.67	0.19	1.41	14.57	0.20	0.98	102
NQ12-23	18.52	-31.23	300	9.0	779	40.3	3474	16.5	16348	0.18	1.56	32.0	58.3	2.6	20	13.83	0.13	1.31	14.56	0.14	0.90	103
NQ12-24	18.35	-31.13	400	20.8	1164	58.3	3259	16.5	16348	0.93	2.27	46.8	92.7	3.2	20	14.20	0.09	0.97	15.15	0.10	0.66	108
NQ12-25	17.93	-30.21	740	7.1	772	15.6	1700	15.8	16086	0.64	2.46	14.3	112.6	4.9	20	14.01	0.14	1.45	14.98	0.15	0.96	112
NQ12-26	17.93	-30.13	850	37.4	2822	90.4	6823	16.5	16348	0.17	2.43	79.7	107.2	2.7	20	13.94	0.12	1.21	14.93	0.13	0.80	103
NQ12-27	17.88	-30.03	600	18.5	2167	44.5	5213	16.2	16086	0.43	1.91	38.0	105.8	2.7	23	13.37	0.13	1.35	14.61	0.14	0.85	104
NQ12-28	17.90	-30.17	650	35.6	2282	95.2	6107	17.4	16086	0.35	2.15	76.0	102.1	2.5	20	12.89	0.16	1.83	14.28	0.18	1.11	128
NQ12-29	17.78	-30.09	720	28.7	586	74.8	1527	16.5	16348	0.17	2.20	61.6	99.1	5.6	10	13.81	0.11	1.15	14.85	0.12	0.80	111
NQ12-30	17.83	-30.15	550	31.6	2426	74.9	5758	16.4	16348	0.40	1.75	58.2	108.5	2.6	20	13.86	0.11	1.13	14.99	0.12	0.75	110
NQ12-33	18.08	-30.17	1050	13.9	1319	33.4	3174	16.3	16086	0.03	1.64	29.1	105.8	4.5	20	13.56	0.14	1.40	14.76	0.15	0.97	100
NQ12-34	18.16	-30.18	1000	15.0	949	34.8	2203	16.3	16438	0.05	1.93	30.6	110.0	5.3	20	13.21	0.15	1.49	14.49	0.16	0.98	106
SA12-22	19.08	-29.93	922	35.9	2565	81.3	5812	14.0	16086	0.01	2.20	76.6	97.2	3.1	20	14.04	0.14	1.48	15.07	0.15	0.97	108
SA12-27	18.70	-30.23	987	5.6	334	24.1	1434	16.6	16348	0.71	1.84	22.4	60.9	3.7	18	12.66	0.37	1.95	14.16	0.41	1.38	27
SA12-30	18.00	-30.53	258	9.4	1012	33.4	3600	16.6	16348	0.06	2.94	27.0	73.2	3.3	20	14.17	0.22	1.20	15.10	0.23	0.80	100
SA12-32	18.06	-30.53	351	6.0	106	20.4	360	16.2	16348	0.85	1.70	18.6	75.1	8.3	3	10.90	0.19	1.54	13.28	0.23	0.95	2
SA12-33	18.06	-30.49	400	5.2	353	12.3	836	16.6	16348	0.75	1.71	9.9	110.0	7.0	23	13.48	0.28	1.33	14.63	0.30	0.95	23
SA12-35	18.06	-30.45	605	3.4	232	6.5	442	14.1	16086	0.62	1.87	6.1	119.0	10.0	17	13.71	0.22	1.31	14.85	0.24	0.86	35
SA12-36	18.06	-30.45	707	3.6	288	10.4	822	16.6	16348	0.57	2.03	9.2	91.4	6.3	21	13.90	0.17	1.58	14.98	0.18	0.93	82
SA12-37	18.06	-30.43	807	12.4	409	38.0	1256	16.6	16348	0.61	1.74	32.5	85.0	4.8	12	13.43	0.34	1.68	14.64	0.37	1.13	24
SA12-38	18.07	-30.40	959	15.3	808	53.9	2839	16.6	16348	0.61	1.68	45.3	74.4	3.0	20	13.83	0.13	1.31	14.88	0.14	0.89	100
SA12-47	18.23	-30.39	1064	5.0	484	11.2	1086	14.3	16086	0.22	2.06	12.5	100.8	5.9	21	12.40	0.22	1.80	13.89	0.25	1.22	74
SA12-51	18.42	-30.32	1066	34.9	3341	75.0	7183	14.4	16086	0.00	2.30	67.7	107.7	3.8	20	12.81	0.15	1.19	14.24	0.17	1.19	139
SA12-52	18.46	-30.32	1065	3.2	208	7.1	461	14.5	16086	0.99	2.20	7.3	102.8	8.6	16	13.67	0.19	1.42	14.68	0.20	1.01	55

**Table 5-1: Results of apatite fission track analysis.** a:  $\rho_{i,s,d}$  are track density of induced, spontaneous, dosimeter tracks. b:  $N_{i,s,d}$  are the number of induced, spontaneous and dosimeter tracks counted. c: p-value of the chi-sq age homogeneity test (Galbraith, 2010; see appendix 3.1). d:  $D_{par}$  measurements are etch pit diameters used as a proxy for the influence of chemical composition on track annealing (Donelick et al., 2005). Between three to five  $D_{par}$  measurements were measured for each dated single grain. e: Uranium content estimated using EDM. f: Central AFT ages calculated with TrackKey (Dunkl, 2002) with  $1\sigma$  standard error. Ages were calculated using a  $\zeta = 316.7 \pm 10.5$  ( $317.3 \pm 11.1$  for samples JN2 and JN3) for a standard IRMM540 glass g: SD is the standard deviation of measured horizontal confined track lengths. h: mean track length after individual track length measurements are corrected for their orientation to the c-axis after Ketcham et al., (2005). i: HCT = Horizontal Confined Track. Analysis details can be found in Appendix 1. For details on sample lithology see Appendix 4.





**Figure 5-4: Plot of AFT age against mean track length. AFT ages are Central AFT ages with  $1\sigma$  standard error. Plot (a) shows AFT age against MTLs uncorrected for their c-axis orientation; (b) shows AFT age against MTLs corrected for their c-axis orientation after Ketcham et al., (2005). For both plots MTLs have uncertainty bars with  $1\sigma$  standard error.**

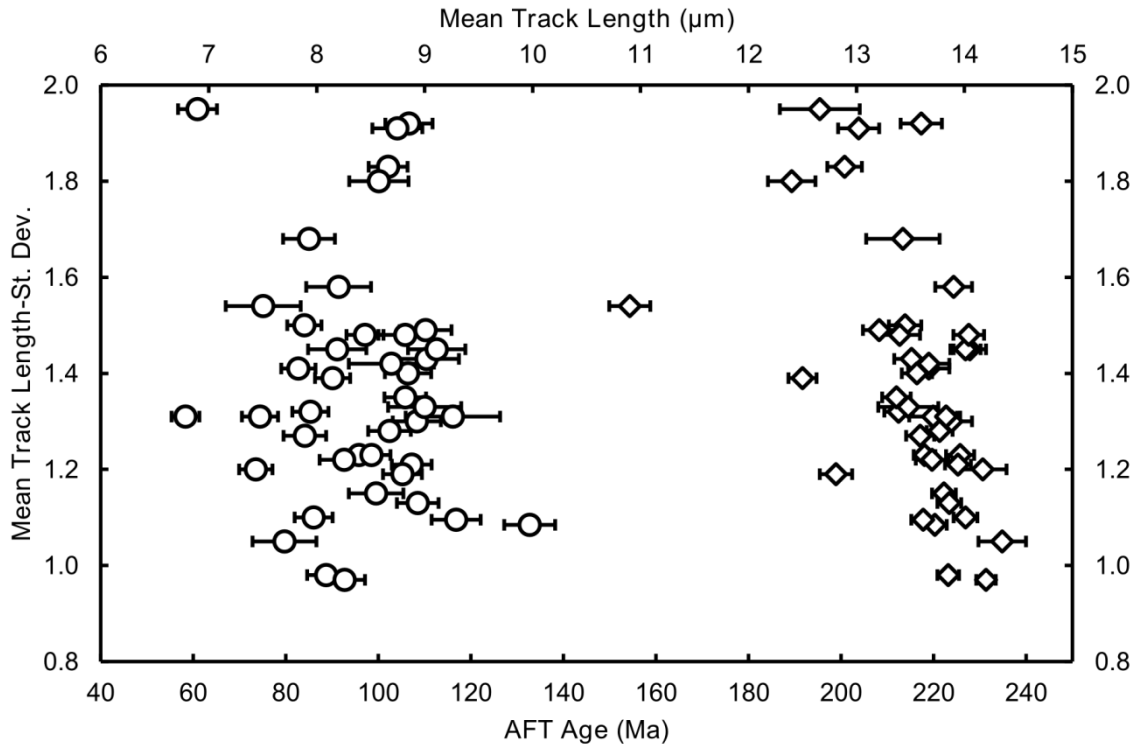
MTL with age from a starting point defined by relatively long track lengths at c. 100 - 120 Ma. The ending point for the boomerang curve is defined by a single sample which has a long MTL and age of 58.3 Ma. Although this trend could be described, in actuality its existence is tenuous. Very few points define its structure, particularly towards the younger end of the plot. Moreover, the sample which defines the base of the boomerang has limited AFT data (2 lengths and 3 single grain ages) due to the poor quality of the sample and therefore must be treated with caution. Finally, the samples which comprise this proposed boomerang are from the Namaqualand plateau, the Namaqualand highland terrain and from the Bitterfontein area close to the Koegelfontein complex. Each of these areas is characterised by a different structural, thermal and geomorphic setting and may have responded to discrete geological events or processes.

Figure 5-5 illustrates the relationship between AFT age and MTL against MTL-SD. A high MTL-SD indicates a broad TLD and a low MTL-SD represents a narrow TLD. There is no correlation between AFT age and MTL-SD suggesting that there are samples with similar ages but with distinct track length distributions and therefore different cooling histories. There is a general negative correlation between MTL and MTL-SD. This is the expected relationship for track length distributions with samples with a long mean track length typically having a narrow TLD, indicative of fairly rapid cooling.

### 5.3.2 Data quality assessment

The quality of the data was assessed following the steps outlined in Appendix 3 and outlier single grain ages were removed only when appropriate. The number of single grains counted for each sample ranges from 3 to 23 with more than 90% of samples yielding more than 15 grains with sufficient quality suitable for counting. Dispersion (Galbraith, 2010) on single grain ages is generally low, with an average of 6% across the entire sample set and not exceeding 20%. Radial plots visually illustrating single grain dispersion are found in Appendix 5.1.

9 samples yielded  $P(\chi^2)$  equal to or less than 0.05 (and dispersion of 8-19%). These samples yielded 17 grains or above suitable for counting with the number



**Figure 5-5: Plot of AFT age (left hand side; lower x-axis) and mean track length (right hand side; upper x-axis) against mean track length standard deviation. AFT ages are Central AFT ages with  $1\sigma$  standard error. MTLs are uncorrected for their c-axis orientation; with  $1\sigma$  standard error.**

of spontaneous tracks ranging from 643 to 3341. Therefore the issue of a low  $P(\chi^2)$  value being attained due to a ‘lack of evidence’ is avoided as plenty of tracks have been counted. A mixture model (Galbraith and Green, 1990; Appendix 5.1) was used to investigate whether the single grain age distributions better represent more than one population of ages. No sample produces a clear distinction of two or more populations but the mixture model does suggest that two or, in the case of SA12-51, three, populations could be present in some sample data sets. However, there is always a large uncertainty on the percentage of grains that can be assigned to each population and this blurs the distinction of individual populations.

The number of track lengths found within each sample varies from 2 to 151 with more than 80% containing at least 50 HCTs. In cases where, MTLs are relatively short or TLDs are relatively broad; the shape of the TLD is either normally

distributed around the mean value or is negatively skewed with a large proportion of longer tracks and tail of shorter tracks.

$D_{\text{par}}$  values for the Namaqualand area range between 1.45 to 3.42  $\mu\text{m}$  with most values (76% of samples) falling between 1.7 and 2.3  $\mu\text{m}$ . This range of values is comparable with Durango apatite which has been quoted as having a  $D_{\text{par}}$  range of  $2.05 \pm 0.16 \mu\text{m}$  (Sobel and Seward, 2010). It is suggested that the majority of samples have compositional controlled annealing properties similar to the Durango standard. There is no clear relationship between  $D_{\text{par}}$  values and MTLs, MTL-SDs or AFT ages (see Chapter 4 - Figure 4-5) suggesting that compositional variations cannot be solely responsible for the observed AFT data. Estimated uranium values range from 6.11 to 83.36 ppm with a widespread variation across all samples and no correlation with age, MTL or MTL-SD (c.f. Chapter 4 - Figure 4-6).

### 5.3.3 Summary of AFT Data

The AFT data presented here for the NQH study area can be described as having ages that range from the Early Cretaceous to Early Tertiary with moderate to long MTLs. TLDs are generally narrow to moderately broad. A lack of correlation observed in plots of  $D_{\text{par}}$  and uranium content against MTL, MTL-SD and AFT age suggest that there is no dominant compositional control on the data observed. It is reinforced here that the majority of samples have relatively long MTLs and therefore they have not experienced significant partial annealing and the effect of varying apatite composition will be small. The relationship between track length and AFT age indicates that major cooling of the crust occurred throughout the Cretaceous, continuing into the Early Tertiary. This cooling may have been spatially and temporally variable across the study area with individual samples potentially recording both a rapid and protracted response to multiple cooling events.

## 5.4 AHe Analysis

### 5.4.1 Results

A subset of samples were selected for AHe analysis based on their quality and sample location. 16 samples were chosen and multiple single grain AHe analysis was performed (Table 5-2). Apatite (U-Th-Sm)/He analysis was performed as outlined in Appendix 1.3. For AHe data reported here and in Chapter 6 uncertainty on mean AHe ages is reported as  $1\sigma$  standard deviation and uncertainty on single grains is  $1\sigma$  standard error, propagated from analytical errors, plus  $1\sigma$  standard deviation of Durango apatite age standards (see Chapter 4, section 4.5.2.3). Mean AHe ages, uncorrected for alpha recoil, range from 55.8 to 120.6 Ma and alpha-recoil corrected ages (after Farley et al., 1996) range from 74.3 to 156.9 Ma. However, there are two problems with quoting ages in this way. (i) mean ages are associated with large degrees of single grain age dispersion ranging from 12 - 56% (dispersion = standard deviation of age/mean age) (ii) corrected ages do not take into account the abundance of alpha particles produced in the outer 20  $\mu\text{m}$  of the crystal that are lost due to diffusive loss at high temperatures and not alpha ejection. That being said, the mean age does provide a useful frame of reference to compare against AFT ages and the wider geological context but should not be quoted without some indication of the single grain age dispersion. The oldest single grain age of  $181.4 \pm 24.7$  Ma is obtained from sample NQ12-11 while the youngest of  $22.4 \pm 3.4$  Ma is from NQ12-15. As explained in Chapter 4 - Section 4.4, AHe ages are subject to extreme variation due to their eU content, grain size and whether or not they are fragments of larger crystals and so AHe ages alone cannot be interpreted easily.

### 5.4.2 Data quality assessment

In theory, AFT ages should be greater than or equal to their equivalent AHe age. Samples from the NQH show that 44% of average AHe ages are indeed younger than AFT ages and only three samples that are older, do not overlap within the uncertainty given to the average age (i.e. sample standard deviation) (Fig. 5-3). The uncertainty levels on AHe ages are representative of the dispersion of single

Sample	Grain #	<sup>4</sup> He (cc)	<sup>238</sup> U (ng)	<sup>235</sup> U (ppm)	<sup>235</sup> U (ng)	<sup>235</sup> U (ppm)	<sup>232</sup> Th (ng)	<sup>232</sup> Th (ppm)	<sup>147</sup> Sm (ng)	<sup>147</sup> Sm (ppm)	eU <sup>a</sup> (ppm)	T <sup>b</sup>	L <sup>c</sup> (µm)	W <sup>c</sup> (µm)	R <sup>d</sup> (µm)	F <sub>i</sub> <sup>e</sup>	Raw Age ±Est. UC <sup>f</sup> (Ma)	Cor. Age <sup>g</sup> ±Est. UC <sup>f</sup> (Ma)	Raw Age (Ma) Average	Raw Age (Ma) St. Dev	Cor. Age (Ma) Average	Cor. Age (Ma) St. Dev
JN2	1	1.8E-09	0.10	69.3	7.2E-04	0.50	0.42	291.4	138.3	1	116.3	70.5	40.6	0.62		74.6 8.4	121.2 13.7	94.4	12.3	138.5	14.4	
	2	2.0E-09	0.05	36.9	3.6E-04	0.27	0.77	567.3	170.4	1	112.6	69.4	39.8	0.59		70.1 8.1	118.5 13.6					
	3	1.8E-09	0.07	52.3	5.2E-04	0.38	0.51	367.7	139.0	1	120.1	67.9	39.7	0.60		78.3 8.9	130.7 14.9					
	4	8.9E-09	0.27	73.5	1.9E-03	0.53	1.98	545.7	202.3	2	187.9	87.7	53.3	0.70		99.2 11.3	141.4 16.1					
	5	9.3E-09	0.25	69.0	1.8E-03	0.50	2.21	613.6	213.7	2	197.7	85.2	52.6	0.70		98.9 11.3	142.3 16.3					
	6	8.9E-09	0.14	66.1	1.0E-03	0.48	2.57	1170.7	341.7	2	126.4	83.2	46.9	0.65		97.2 11.2	149.0 17.2					
	7	8.7E-09	0.27	102.8	1.9E-03	0.75	1.74	663.5	259.5	2	158.8	81.1	48.5	0.67		105.3 12.0	156.5 17.9					
	8	5.9E-09	0.12	32.4	8.6E-04	0.24	1.87	507.2	151.8	2	167.6	93.6	54.9	0.70		86.0 9.9	122.2 14.1					
	9	9.8E-09	0.25	83.7	1.8E-03	0.61	2.57	866.0	287.8	1	117.4	100.3	52.7	0.69		94.2 10.8	135.6 15.6					
	10	5.7E-09	0.14	53.6	1.0E-03	0.39	1.80	667.3	210.8	1	116.1	96.1	51.0	0.68		82.6 9.5	121.0 13.9					
	12	1.5E-08	0.23	71.2	1.7E-03	0.52	4.47	1372.7	394.3	2	152.6	92.2	53.1	0.69		94.6 10.9	136.7 15.8					
	16	5.2E-09	0.11	48.1	8.3E-04	0.35	0.63	263.0	110.3	1	116.8	90.4	48.9	0.68		160.8 18.3	237.2 27.0					
	17	1.9E-08	0.46	99.9	3.3E-03	0.72	4.02	864.1	303.7	1	192.7	98.1	58.6	0.73		112.5 12.9	154.2 17.7					
	18	2.2E-08	0.62	125.1	4.5E-03	0.91	4.82	959.4	351.4	1	208.5	97.9	59.5	0.73		102.9 11.8	140.6 16.1					
	19	7.1E-09	0.20	66.6	1.4E-03	0.48	1.35	446.0	171.9	1	120.7	99.8	53.0	0.70		111.8 12.8	159.6 18.2					
	20	7.8E-09	0.27	83.5	2.0E-03	0.61	1.82	548.3	213.0	1	139.5	97.3	54.1	0.71		90.9 10.4	128.6 14.7					
	21	8.2E-09	0.32	87.8	2.3E-03	0.64	1.68	463.9	197.5	1	160.5	94.7	54.9	0.71		94.1 10.7	132.0 15.0					
	22	1.2E-08	0.26	66.0	1.9E-03	0.48	1.03	259.1	127.4	1	193.2	90.5	55.0	0.72		193.0 21.9	269.1 30.5					
	23	3.9E-09	0.11	49.5	7.7E-04	0.36	1.01	464.8	159.1	1	96.2	94.6	47.6	0.66		93.1 10.7	140.4 16.1					
	24	7.2E-09	0.21	62.6	1.5E-03	0.45	1.28	373.8	150.9	1	152.2	94.6	54.1	0.71		115.2 13.1	162.7 18.6					
	25	3.7E-09	0.10	47.6	7.6E-04	0.35	0.86	389.7	139.6	1	101.6	93.2	47.9	0.67		99.5 11.4	149.4 17.1					
	26	4.1E-09	0.15	43.2	1.1E-03	0.31	1.13	321.3	119.0	1	146.2	97.8	55.0	0.71		80.6 9.2	113.5 13.0					
	27	5.1E-09	0.17	81.7	1.2E-03	0.59	1.02	480.0	195.1	1	101.9	91.0	47.2	0.67		101.5 11.6	152.5 17.4					
JN3	1	2.6E-09	0.16	24.2	1.1E-03	0.18	0.20	29.9	31.4	1	170.4	124.1	68.2	0.78		103.6 11.4	132.5 14.6	106.2	12.9	140.6	18.7	
	2	3.0E-09	0.17	12.7	1.3E-03	0.09	0.12	8.6	14.8	1	187.7	171.4	88.2	0.83		122.0 13.4	146.2 16.1					
	3	2.2E-09	0.15	32.3	1.1E-03	0.23	0.17	38.0	41.4	2	187.6	98.2	58.4	0.75		95.1 10.5	127.4 14.1					
	4	3.9E-09	0.22	42.8	1.6E-03	0.31	0.34	66.9	58.8	1	157.9	113.5	62.6	0.76		107.0 11.9	140.7 15.6					
	5	2.7E-09	0.16	16.5	1.2E-03	0.12	0.17	17.1	20.7	1	184.4	146.2	78.5	0.81		107.1 11.8	131.8 14.5					
	6	1.9E-09	0.11	20.3	7.7E-04	0.15	0.19	36.0	28.9	1	160.9	113.9	63.1	0.76		103.6 11.5	136.1 15.1					
	7	2.5E-09	0.08	18.0	6.1E-04	0.13	0.51	109.2	43.8	2	191.3	99.0	59.0	0.73		100.3 11.5	144.3 16.5					
	8	2.4E-09	0.13	30.9	9.4E-04	0.22	0.39	93.0	53.0	1	120.4	118.3	59.5	0.74		87.2 9.8	120.9 13.6					
	9	2.5E-09	0.13	20.9	9.4E-04	0.15	0.11	17.7	25.3	1	210.8	108.6	64.8	0.77		129.8 14.3	185.7 20.4					
NQ12-04	1	5.1E-09	0.40	42.77	2.9E-03	0.31	0.13	13.8	46.3	1	328.6	106.1	68.5	0.79		96.4 13.5	122.0 17.0	101.4	21.2	134.8	25.6	
	2	4.5E-09	0.29	63.33	2.1E-03	0.46	0.45	100.2	87.3	1	202.1	94.5	57.4	0.74		93.4 12.7	126.4 17.2					
	3	3.4E-10	0.28	31.43	2.0E-03	0.23	0.11	12.9	34.7	1	194.1	134.4	74.9	0.81		9.3 1.3	11.5 1.6					
	4	1.2E-09	0.08	30.30	6.2E-04	0.22	0.03	10.9	0.36	129.1	33.1	2	188.7	76.8	47.9	0.70	101.0 11.3	144.3 16.2				
	5	4.3E-09	0.22	29.71	1.6E-03	0.22	0.06	7.4	0.92	124.0	31.7	2	196.2	123.0	70.2	0.80	143.8 16.0	180.6 20.1				
	6	1.4E-09	0.12	23.07	8.6E-04	0.17	0.03	5.9	24.6	1	142.7	119.9	63.3	0.77		92.4 13.0	119.4 16.9					
	7	3.3E-10	0.03	9.70	2.2E-04	0.07	0.03	8.7	0.30	96.6	11.8	2	187.8	80.6	49.8	0.70	69.3 7.8	98.3 11.1				
	8	2.5E-09	0.20	24.72	1.5E-03	0.18	0.06	7.2	26.6	2	261.9	111.5	68.9	0.79		93.6 13.1	118.2 16.6					
	12	2.0E-09	0.12	38.85	8.9E-04	0.28	0.16	52.1	0.34	109.4	51.4	2	164.8	87.2	51.7	0.71	98.1 10.8	137.8 15.2				
	22	2.1E-09	0.12	23.27	8.6E-04	0.17	0.05	10.0	0.53	104.7	25.8	2	245.4	90.9	57.5	0.75	124.4 13.9	166.1 18.6				
NQ12-06	3	4.4E-09	0.21	33.3	1.5E-03	0.24	1.46	230.01	0.69	108.7	87.58	1	176.6	119.6	67.0	0.76	64.7 7.3	86.5 9.7	103.2	18.3	135.7	23.3
	4	3.6E-09	0.17	37.8	1.3E-03	0.27	0.53	115.71	0.35	74.9	65.22	1	165.4	105.3	59.9	0.74	96.7 10.9	129.3 14.6				
	5	7.9E-09	0.49	64.2	3.5E-03	0.47	0.45	60.10	1.50	198.7	78.74	1	191.3	125.4	70.8	0.79	105.9 11.9	141.5 15.9				
	6	1.5E-08	0.88	128.9	6.4E-03	0.93	0.95	138.30	1.23	179.4	162.34	2	247.9	104.8	64.9	0.77	110.0 12.1	142.5 15.6				
	8	1.0E-08	0.51	60.5	3.7E-03	0.44	1.24	147.70	1.04	124.6	95.64	1	176.6	137.4	74.2	0.79	105.1 11.6	132.3 14.6				
	9	1.2E-09	0.05	14.1	3.5E-04	0.10	0.17	50.83	0.13	37.9	26.11	1	176.0	88.1	52.9	0.71	109.2 12.3	145.9 16.4				
	10	5.6E-09										2	276.5	78.0	51.3							
	11	8.7E-10	0.21	26.5	1.5E-03	0.19	1.08	135.07	0.80	100.8	58.39	1	185.9	130.6	72.5	0.78	15.1 1.7	20.2 2.3				
	14	4.7E-09	0.13	19.3	9.4E-04	0.14	0.68	100.70	0.54	80.4	43.08	2	191.7	118.3	67.8	0.77	130.0 14.5	169.2 18.9				
	16	5.7E-09	0.11	17.0	8.1E-04	0.12	1.40	213.17	0.76	115.8	67.19	2	241.0	104.3	64.3	0.75	103.7 11.7	138.5 15.6				

Table 5-2: Results of apatite (U-Th-Sm)/He analysis. a: eU (effective uranium) is calculated as  $eU_{ppm} = [U_{ppm}] + (0.235 * [Th_{ppm}])$ . b: T = Number of terminations identified on crystal. c: L & W = Length and Width of crystal or crystal fragment. d:  $R^* = \text{spherical equivalent radius calculated as } R^* = (3 * (RL)) / (2 * (R + L))$  where  $R = W/2$ . e: correction factor after Farley et al. (1996), assuming homogeneous distribution U and Th. f: Estimate Uncertainty is equal to  $1\sigma$  analytical uncertainty, which include error propagated from U, Th, Sm and He measurement uncertainties, plus an additional 10% which is the standard deviation (reproducibility) of repeat analysis of Durango apatite standards. g: Corrected AHe age = Raw AHe age/ $F_i$ . Analysis details can be found in Appendix 1. Shaded data has been excluded from mean value calculations and further interpretation (see Appendix 3.2). For details on sample lithology see Appendix 4.

Sample	Grain #	<sup>4</sup> He	<sup>238</sup> U		<sup>235</sup> U		<sup>232</sup> Th		<sup>147</sup> Sm		eU <sup>a</sup>	T <sup>b</sup>	L <sup>c</sup>	W <sup>c</sup>	R <sup>d</sup>	F <sup>e</sup>	Raw Age ±Est. UC <sup>f</sup>		Cor. Age <sup>g</sup> ±Est. UC <sup>f</sup>		Raw Age (Ma)		Cor. Age (Ma)						
		(cc)	(ng)	(ppm)	(ng)	(ppm)	(ng)	(ppm)	(ng)	(ppm)							(ppm)	(μm)	(μm)	(μm)	(Ma)	(Ma)	Average	St. Dev	Average	St. Dev			
NQ12-07	2	1.9E-09	0.12	51.0	8.9E-04	0.37	0.29	121.0	0.19	77.5	79.8	2	168.3	75.3	46.2	0.67	80.7	8.9	119.0	13.1	<b>89.6</b>	<b>14.1</b>	<b>122.5</b>	<b>19.1</b>					
	4	2.9E-09	0.21	46.9	1.5E-03	0.34	0.17	37.4	0.24	53.9	56.1	1	175.6	100.6	58.7	0.75	94.2	12.8	128.5	17.4									
	7	4.0E-10	0.02	14.8	1.5E-04	0.11	0.12	84.0			34.6	2	123.9	68.1	40.1	0.61	66.0	9.0	86.8	11.8									
	8	4.3E-09	0.23	35.7	1.6E-03	0.26	0.30	47.2	0.42	65.3	47.0	1	202.2	111.9	65.7	0.77	115.9	15.7	152.3	20.7									
	9	5.8E-10	0.04	47.5	3.2E-04	0.34	0.08	89.7			69.0	2	153.3	49.4	31.9	0.53	73.8	10.0	97.0	13.2									
	13	3.2E-09	0.15	27.7	1.1E-03	0.20	0.40	72.6	0.33	59.7	44.9	2	228.4	97.6	60.3	0.75	104.0	11.5	138.3	15.3									
	15	1.7E-09	0.10	38.5	7.1E-04	0.28	0.18	69.5	0.17	67.4	55.1	1	112.9	95.0	50.2	0.70	95.9	13.1	139.6	19.1									
	16	5.5E-10	0.04	17.7	3.0E-04	0.13	0.06	24.5	0.11	46.2	23.6	2	140.8	81.4	47.4	0.69	80.9	8.9	117.8	13.0									
	17	1.8E-09	0.13	49.3	9.7E-04	0.36	0.10	37.6			58.4	2	166.5	80.5	48.6	0.70	91.0	12.3	119.6	16.2									
	23	5.0E-11	0.05	17.1	3.4E-04	0.12	0.14	51.1			29.2	2	171.5	79.8	48.6	0.68	5.2	0.7	6.8	0.9									
	25	2.0E-09	0.12	22.5	8.7E-04	0.16	0.20	37.7	0.29	53.8	31.6	1	154.0	117.0	63.6	0.76	97.6	13.3	129.5	17.7									
	26	1.6E-09	0.12	49.3	8.5E-04	0.36	0.14	57.0	0.18	74.5	63.1	2	134.0	84.2	48.1	0.69	88.8	9.7	128.5	14.1									
	28	1.2E-09	0.12	89.2	8.6E-04	0.65	0.06	44.3			100.3	2	131.5	63.4	38.3	0.62	73.9	10.0	97.2	13.2									
	33	1.2E-09	0.07	16.5	5.3E-04	0.12	0.07	15.9	0.24	55.1	20.4	2	200.4	93.9	57.1	0.82	101.8	11.2	137.9	15.2									
	NQ12-09	1	1.2E-09	0.04	32.2	3.1E-04	0.23	0.39	293.8	0.09	70.0	101.4	2	146.3	60.3	37.5	0.57	70.3	7.9	122.7					13.8	<b>88.7</b>	<b>16.5</b>	<b>125.2</b>	<b>17.5</b>
		2	1.9E-09	0.06	21.0	4.4E-04	0.15	0.63	215.1	0.11	36.3	71.7	2	177.4	80.9	49.4	0.67	73.9	8.3	109.7					12.3				
		3	2.4E-09	0.08	21.8	5.5E-04	0.16	0.59	169.2			61.7	0	128.4	103.7	55.4	0.71	90.1	13.0	126.5					18.3				
4			0.00	0.6	1.6E-05	0.00	0.03	6.9			2.2	1	164.7	96.6	56.0	0.71													
5		7.5E-09	0.18	18.2	1.3E-03	0.13	1.94	197.3			64.6	0	191.2	143.2	78.1	0.79	96.2	14.0	121.2	17.7									
6		5.1E-09	0.10	17.0	7.6E-04	0.12	0.89	144.3	0.19	30.8	51.0	2	158.9	124.3	67.0	0.76	132.9	14.9	174.6	19.6									
7		2.6E-09	0.10	18.5	7.0E-04	0.13	0.64	121.7			47.3	0	192.8	103.8	61.3	0.74	84.7	12.2	114.2	16.4									
8		2.0E-09	0.06	10.3	4.0E-04	0.07	0.54	99.7	0.24	44.1	33.8	1	157.2	117.1	64.0	0.75	86.7	9.7	115.8	13.0									
9		1.2E-09	0.04	11.6	2.6E-04	0.08	0.34	108.4	0.14	43.6	37.2	1	142.3	93.5	52.8	0.70	85.7	9.4	123.2	13.5									
11		1.0E-09	0.04	22.0	2.7E-04	0.16	0.31	181.9			64.9	1	111.5	77.8	43.3	0.63	77.4	11.2	122.8	17.8									
12		3.2E-09	0.10	23.1	7.0E-04	0.17	0.88	211.4	0.19	45.5	73.0	1	150.3	105.0	58.4	0.73	86.8	12.6	119.7	17.4									
13		3.6E-12	0.08	27.4	5.9E-04	0.20	0.53	181.3			70.2	1	164.1	84.6	50.4	0.69	0.1	0.0	0.2	0.0									
15		9.7E-10	0.03	7.8	1.9E-04	0.06	0.30	88.2			28.5	1	133.6	100.8	54.9	0.71	82.0	11.9	116.1	16.9									
16		4.2E-09	0.10	20.2	7.5E-04	0.15	0.88	171.6	0.20	39.4	60.7	2	206.9	99.5	60.1	0.73	108.4	12.2	147.6	16.6									
17		2.8E-09	0.10	31.0	6.9E-04	0.22	0.86	279.3	0.08	27.2	96.8	1	143.2	92.3	52.4	0.71	78.3	11.4	112.8	16.4									
NQ12-10		2	6.7E-10	0.06	19.4	4.4E-04	0.14	0.02	6.6	0.23	72.9	21.1	1	103.1	109.8	53.7	0.73	81.7	9.5	111.6	12.9	<b>89.6</b>	<b>26.3</b>	<b>122.8</b>	<b>40.3</b>				
		3	9.5E-10	0.08	17.7	5.6E-04	0.13	0.02	5.0	0.28	64.6	19.0	1	178.6	98.5	57.9	0.75	91.8	10.6	122.0	14.0								
	4	7.2E-10	0.04	18.6	2.8E-04	0.13	0.02	7.8	0.10	49.2	20.5	1	152.8	73.5	44.4	0.68	136.4	17.9	202.0	26.6									
	5	3.1E-10	0.04	9.3	2.7E-04	0.07	0.01	2.6			10.0	1	108.1	121.1	58.2	0.75	63.8	9.0	84.6	11.9									
	6	1.1E-09	0.08	25.6	5.9E-04	0.19	0.02	5.5	0.26	82.7	27.1	1	163.2	87.7	51.9	0.72	101.4	12.9	140.0	17.8									
	8	5.5E-10	0.06	20.4	4.5E-04	0.15	0.03	8.6			22.6	1	172.7	83.3	50.3	0.71	66.3	9.2	92.9	12.8									
	9	1.5E-09	0.12	27.3	8.8E-04	0.20	0.03	7.2	0.34	75.8	29.2	1	146.6	109.7	59.9	0.76	90.3	10.0	118.7	13.1									
	10	1.4E-09	0.12	24.4	8.9E-04	0.18	0.02	3.4			25.4	1	176.4	106.7	61.4	0.77	90.2	13.0	117.4	16.9									
	12	7.1E-10	0.08	16.8	5.6E-04	0.12	0.03	7.2	0.28	60.9	18.6	2	179.4	101.2	59.2	0.76	65.8	7.4	87.1	9.8									
	13	3.9E-10	0.04	23.4	3.2E-04	0.17	0.02	8.8			25.6	1	105.0	84.5	45.2	0.68	66.3	9.2	97.3	13.5									
	14	4.7E-09	0.30	19.6	2.2E-03	0.14	0.19	12.1	1.59	104.0	22.6	1	194.9	176.8	91.2	0.84	107.2	11.9	127.6	14.2									
	15	5.8E-10	0.06	13.3	4.3E-04	0.10	0.02	5.0			14.6	1	155.1	107.3	59.8	0.76	72.8	10.1	95.8	13.3									
	17	5.8E-10	0.06	18.2	4.0E-04	0.13	0.04	13.1			21.4	1	143.2	92.3	52.4	0.72	72.9	7.9	104.6	11.4									
	18	5.2E-10	0.02	11.8	1.8E-04	0.09	0.01	6.1	0.13	60.6	13.3	2	138.4	77.1	45.2	0.68	148.0	19.9	217.7	29.3									
	19	1.9E-08	0.00	0.8	3.3E-05	0.01	0.03	4.9	0.00	0.8	2.0	2	199.0	106.9	63.2	0.75	8649.6	174096.6	11536.7	232207.8									
	NQ12-11	1	5.2E-10	0.03	5.7	2.5E-04	0.04	0.41	67.6	1.06	176.1	21.6	1	219.2	104.6	63.3	0.74	32.4	3.6	43.5	4.8					<b>120.6</b>	<b>31.4</b>	<b>156.9</b>	<b>40.9</b>
		2	1.2E-11	0.03	8.4	2.1E-04	0.06	0.05	13.8			11.7	1	166.6	90.2	53.3	0.72	2.5	0.3	3.4	0.4								
3		8.6E-11	0.02	4.6	1.3E-04	0.03	0.02	4.8	0.39	95.8	5.7	1	165.1	99.0	57.1	0.74	28.4	3.2	38.4	4.3									
4		6.7E-11	0.01	2.0	1.1E-04	0.01	0.01	2.0			2.5	1	192.7	122.2	69.6	0.79	30.7	4.3	39.0	5.5									
5		5.9E-10	0.04	6.4	3.0E-04	0.05	0.03	4.9	0.16	25.8	7.6	1	185.1	116.8	66.6	0.78	99.2	10.9	127.1	13.9									
6		4.7E-10	0.03	3.7	1.9E-04	0.03	0.02	3.3	0.14	19.7	4.5	1	227.6	111.4	67.1	0.78	115.4	12.8	147.8	16.4									
7		3.4E-10	0.02	3.6	1.3E-04	0.03	0.03	6.1			5.1	1	234.6	93.1	58.3	0.74	109.4	11.9	147.4	16.0									
8		8.7E-10	0.04	9.8	2.9E-04	0.07	0.03	6.8			11.5	0	155.8	101.5	57.4	0.75	153.6	20.9	205.9	28.0									

Table 5-2: Continued

Sample	Grain #	<sup>4</sup> He	<sup>238</sup> U		<sup>235</sup> U		<sup>232</sup> Th		<sup>147</sup> Sm		eU <sup>a</sup>	T <sup>b</sup>	L <sup>c</sup>	W <sup>c</sup>	R <sup>d</sup>	F <sup>e</sup>	Raw Age ±Est. UC <sup>f</sup>		Cor. Age <sup>g</sup> ±Est. UC <sup>f</sup>		Raw Age (Ma)		Cor. Age (Ma)	
		(cc)	(ng)	(ppm)	(ng)	(ppm)	(ng)	(ppm)	(ng)	(ppm)							(ppm)	(Ma)	(Ma)	Average	St. Dev	Average	St. Dev	
NQ12-13	9	7.3E-10	0.22	47.3	1.6E-03	0.34	0.47	103.0	1.54	336.0	71.9	1	188.8	98.2	58.4	0.74	18.0	1.9	24.3	2.6				
	10	1.7E-10	0.01	2.8	8.8E-05	0.02	0.01	1.7			3.2	1	122.4	119.2	60.1	0.76	101.1	24.8	133.4	32.7				
	11	3.5E-10	0.01	2.0	1.0E-04	0.01	0.01	1.2			2.2	0	202.8	117.7	68.4	0.79	181.4	24.7	230.3	31.4				
	12	4.4E-10	0.03	5.3	1.9E-04	0.04	0.02	3.8			6.3	1	180.2	104.6	60.8	0.76	117.1	14.5	154.1	19.1				
	13	3.8E-10	0.03	4.1	2.4E-04	0.03	0.01	1.4			4.4	1	194.5	128.0	72.2	0.80	87.3	12.2	109.0	15.2				
	1	8.7E-10	0.06	7.2	4.6E-04	0.05	0.04	4.3			8.3	1	186.5	136.7	75.0	0.81	98.9	13.5	122.6	16.7	<b>113.0</b>	<b>21.4</b>	<b>148.7</b>	<b>27.2</b>
	3	2.1E-09	0.14	19.3	1.0E-03	0.14	0.10	14.0			22.8	1	177.6	127.1	70.2	0.79	107.3	14.6	135.5	18.4				
	4	7.7E-10	0.05	15.6	3.7E-04	0.11	0.05	14.7	0.21	64.2	19.2	2	202.1	80.0	50.1	0.71	98.1	10.9	138.9	15.5				
	5	1.6E-09	0.07	9.6	5.2E-04	0.07	0.04	5.0			10.9	1	206.8	120.1	69.8	0.79	161.0	22.1	203.2	27.9				
	7	1.0E-09	0.07	15.2	5.0E-04	0.11	0.03	7.4			17.1	1	209.7	93.1	57.1	0.75	104.8	14.4	140.3	19.3				
	8	2.0E-09	0.14	42.4	1.0E-03	0.31	0.05	16.3	0.14	40.8	46.6	2	180.1	85.5	51.8	0.72	104.9	11.8	145.3	16.4				
	10	8.1E-10	0.04	11.5	2.9E-04	0.08	0.03	8.6	0.15	44.4	13.6	2	149.7	96.1	54.5	0.73	136.4	16.2	186.3	22.1				
	12	1.7E-09	0.11	15.0	7.8E-04	0.11	0.09	12.1			17.9	1	202.5	118.9	68.9	0.79	106.1	14.4	134.7	18.3				
	15	8.2E-10	0.05	10.2	3.9E-04	0.07	0.05	8.6	0.29	54.7	12.3	2	213.4	99.7	60.6	0.76	99.3	11.2	131.0	14.8				
	17	1.5E-09	0.04	6.2	2.9E-04	0.05	0.03	4.7	0.22	34.9	7.4	2	197.7	113.0	65.9	0.78	254.5	29.4	327.0	37.8				
1	1.5E-10	0.16	7.0	1.1E-03	0.05	0.62	27.7			13.6	0	299.7	172.4	100.4	0.85	4.0	0.4	4.8	0.5	<b>55.8</b>	<b>31.3</b>	<b>74.3</b>	<b>43.8</b>	
2	4.1E-11	0.01	1.1	6.0E-05	0.01	0.03	3.6	0.03	4.6	2.0	1	219.2	116.1	68.9	0.78	22.4	3.4	28.9	4.4					
3	2.0E-10	0.02	2.1	1.5E-04	0.02	0.12	12.3	0.12	12.5	5.0	2	260.4	121.9	74.1	0.79	32.1	3.5	40.8	4.5					
4	2.3E-11	0.01	1.2	7.2E-05	0.01	0.03	3.2	0.07	8.8	2.0	2	265.3	111.5	69.1	0.78	11.4	1.5	14.6	1.9					
5	7.6E-11	0.67	65.4	4.9E-03	0.47	0.12	11.4			68.5	0	191.2	143.2	78.1	0.82	0.9	0.1	1.2	0.1					
6	2.7E-10	0.01	2.3	9.5E-05	0.02	0.07	13.2	0.06	10.0	5.4	2	255.2	94.1	59.6	0.74	70.1	8.8	95.4	11.9					
7	1.1E-10	0.01	1.1	5.8E-05	0.01	0.03	4.6			2.1	0	192.8	103.8	61.3	0.75	53.5	5.8	68.8	7.5					
8	2.9E-10	0.01	2.4	8.6E-05	0.02	0.05	9.5	0.04	8.5	4.7	2	212.3	95.6	58.5	0.73	101.0	16.4	137.5	22.3					
NQ12-17	2	1.3E-09	0.092	9.0	6.7E-04	0.07	0.03	2.8	0.13	12.8	9.7	1	170.6	154.6	79.8	0.82	104.5	13.8	127.4	16.8	<b>111.8</b>	<b>47.3</b>	<b>136.4</b>	<b>57.5</b>
3	7.3E-10										2	218.2	133.4	76.6										
4	3.4E-10	0.028	6.8	2.0E-04	0.05	0.01	3.5			7.7	2	180.9	94.9	56.4	0.74	88.7	12.2	119.4	16.4					
6	2.9E-09	0.151	6.9	1.1E-03	0.05	0.11	5.1	0.22	10.3	8.1	1	229.8	194.9	102.6	0.86	132.9	14.2	155.0	16.5					
7	1.2E-09	0.075	5.7	5.4E-04	0.04	0.07	5.1			0.0	6.9	2	227.9	151.9	85.4	0.83	111.1	15.1	133.7	18.1				
8	3.1E-10	0.064	5.3	4.6E-04	0.04	0.03	2.3	0.25	20.7	5.9	2	211.5	149.5	82.8	0.83	34.9	4.0	42.2	4.8					
9	3.9E-09	0.194	8.0	1.4E-03	0.06	0.38	15.7			11.7	2	243.6	199.2	106.0	0.86	112.6	15.4	130.2	17.9					
10	5.8E-10	0.055	5.3	4.0E-04	0.04	0.10	9.3	0.19	17.8	7.5	2	206.7	141.4	79.0	0.81	59.9	6.6	74.0	8.1					
11	6.8E-10	0.048	4.8	3.5E-04	0.03	0.02	2.4			5.4	2	169.6	153.1	79.1	0.82	102.7	14.1	126.0	17.3					
12	2.2E-09	0.090	13.1	6.5E-04	0.10	0.03	4.1	0.08	12.3	14.2	1	178.9	123.6	68.9	0.79	181.3	22.0	229.1	27.7					
13	5.4E-10	0.065	8.3	4.7E-04	0.06	0.03	3.6	0.12	15.7	9.2	2	182.7	130.5	72.1	0.80	60.4	7.0	75.6	8.8					
14	4.2E-10	0.470	51.7	3.4E-03	0.38	0.22	24.6	1.38	151.9	57.9	2	219.6	128.3	74.5	0.81	6.5	0.8	8.1	1.0					
16	4.4E-09	0.187	10.9	1.4E-03	0.08	0.13	7.6	0.31	17.8	12.8	1	217.0	177.5	94.5	0.85	161.3	17.2	190.7	20.3					
18	2.5E-09	0.090	8.8	6.5E-04	0.06	0.05	5.1	0.21	20.2	10.0	2	190.4	146.1	79.2	0.82	196.2	21.5	240.2	26.4					
19	8.3E-10	0.058	5.5	4.2E-04	0.04	0.02	2.2			6.1	2	181.5	151.5	80.2	0.82	106.4	14.7	129.9	18.0					
SA12-22	1	4.5E-09	0.52	37.3	3.8E-03	0.27	0.26	19.0			42.0	2	295.9	136.6	83.2	0.83	63.5	7.1	76.9	8.6	<b>85.9</b>	<b>18.6</b>	<b>108.4</b>	<b>26.6</b>
2	3.4E-09	0.28	37.0	2.0E-03	0.27	0.15	19.1			41.7	1	201.0	122.8	70.6	0.79	89.0	10.0	112.0	12.6					
3	3.1E-09	0.29	25.5	2.1E-03	0.18	0.30	26.1			31.8	2	237.4	139.2	80.7	0.82	70.0	7.8	85.7	9.5					
4	5.6E-09	0.36	84.5	2.6E-03	0.61	0.35	82.3			104.5	2	156.3	104.3	58.7	0.75	102.4	11.3	136.7	15.1					
7	1.1E-08	0.74	86.0	5.3E-03	0.62	0.64	74.2			104.1	2	214.7	126.0	73.1	0.80	104.5	11.5	130.7	14.4					
SA12-30	1	5.0E-09	0.30	13.7	2.2E-03	0.10	0.06	3.0	1.19	54.5	14.5	1	302.6	169.1	99.1	0.86	127.0	13.8	148.4	16.1	<b>117.0</b>	<b>22.9</b>	<b>144.0</b>	<b>23.6</b>
2	9.0E-10	0.07	20.0	5.4E-04	0.15	0.01	3.8	0.37	98.9	21.1	1	160.3	95.9	55.3	0.74	91.4	11.6	123.1	15.6					
3	1.1E-09	0.08	11.5	5.9E-04	0.08	0.02	3.2	0.40	56.4	12.3	1	250.5	106.0	65.6	0.78	98.8	11.1	126.4	14.2					
4	3.9E-09	0.04	2.1	2.7E-04	0.02	0.01	0.6	0.17	9.8	2.2	1	269.1	162.0	93.4	0.85	574.9	161.6	735.6	206.7					
5	4.2E-09	0.31	15.2	2.2E-03	0.11	0.02	0.8			15.5	1	260.8	175.5	98.5	0.86	110.1	16.2	128.6	19.0					
6	1.7E-09	0.09	8.6	6.7E-04	0.06	0.01	1.0			8.9	1	307.0	117.9	74.2	0.81	146.8	21.3	181.6	26.4					
8	1.9E-09	0.15	13.1	1.1E-03	0.09	0.02	1.5			13.5	1	239.7	138.1	80.4	0.82	100.5	14.6	122.0	17.7					
9	9.7E-09	0.44	13.0	3.2E-03	0.09	0.06	1.8	2.67	79.3	13.6	1	317.4	205.6	116.5	0.88	165.2	18.1	188.2	20.6					
10	2.3E-09	0.12	11.9	8.8E-04	0.09	0.07	7.1	0.86	84.6	13.6	1	197.0	143.3	78.8	0.82	129.1	14.1	158.3	17.3					

Table 5-2: Continued



Sample	Grain #	<sup>4</sup> He	<sup>238</sup> U		<sup>235</sup> U		<sup>232</sup> Th		<sup>147</sup> Sm		eU <sup>a</sup>	T <sup>b</sup>	L <sup>c</sup>	W <sup>c</sup>	R <sup>d</sup>	F <sup>e</sup>	Raw Age ± Est. UC <sup>f</sup>		Cor. Age <sup>g</sup> ± Est. UC <sup>f</sup>		Raw Age (Ma)		Cor. Age (Ma)	
		(cc)	(ng)	(ppm)	(ng)	(ppm)	(ng)	(ppm)	(ng)	(ppm)							(ppm)	(μm)	(μm)	(μm)	(Ma)	(Ma)	Average	St. Dev
11		1.5E-09	0.13	23.8	9.5E-04	0.17	0.01	2.5			24.5	1	249.6	93.8	59.2	0.76	91.5	13.3			120.4	17.5		
12		2.7E-09	0.18	11.7	1.3E-03	0.09	0.02	1.1	0.85	55.6	12.1	2	302.9	141.8	86.2	0.84	113.5	13.7			135.9	16.4		
14		4.9E-09	0.26	21.0	1.9E-03	0.15	0.04	3.0			21.9	1	225.6	147.9	83.5	0.83	147.7	21.3			178.1	25.7		
16		9.3E-10	0.07	9.9	5.0E-04	0.07	0.01	2.1	0.43	61.5	10.4	2	212.9	114.2	67.6	0.79	99.4	12.0			126.1	15.2		
17		1.2E-09	0.08	17.3	5.9E-04	0.13	0.02	4.3	0.36	77.4	18.4	2	203.5	95.6	58.1	0.75	107.0	12.5			142.1	16.5		
19		1.5E-09	0.10	13.6	7.6E-04	0.10	0.01	0.7	0.52	67.8	13.9	1	162.4	137.4	72.4	0.80	109.9	29.5			136.6	36.6		
SA12-35	1	5.9E-10	0.01	1.0	7.9E-05	0.01	0.02	1.3	0.15	13.4	1.3	1	214.1	145.7	81.5	0.82	300.2	50.6			367.4	61.9		
	3	7.0E-11	0.08	15.4	5.9E-04	0.11	0.26	49.3			27.1	2	242.4	93.1	58.6	0.74	4.0	0.6			5.5	0.8		
	4	4.2E-10	0.02	2.7	1.4E-04	0.02	0.04	5.8	0.37	51.9	4.1	1	174.3	127.5	70.0	0.78	107.8	14.9			137.6	19.0		
	5	1.7E-10	0.02	3.5	1.2E-04	0.03	0.03	5.4			4.8	1	216.5	94.1	58.0	0.74	60.0	8.2			80.9	11.0		
	6	4.9E-11	0.01	1.2	6.0E-05	0.01	0.03	4.6	0.37		2.2	2	234.5	110.5	67.1	0.77	20.9	2.4			27.3	3.1		
	7	8.9E-10	0.01	1.1	1.1E-04	0.01	0.21	15.1	0.76	55.3	4.6	1	157.6	186.5	87.9	0.82	104.4	15.3			128.1	18.8		
	8	2.2E-10	0.22	55.4	1.6E-03	0.40	1.12	277.9	1.42	352.7	121.1	1	144.0	105.6	58.0	0.73	3.6	0.5			5.0	0.7		
	10	2.3E-10	0.01	2.5	1.0E-04	0.02	0.07	11.9	0.28	49.9	5.3	1	207.4	103.1	61.9	0.75	60.8	8.7			81.4	11.6		
	11	8.3E-11	0.01	2.2	8.2E-05	0.02	0.06	12.2			5.1	2	237.5	93.1	58.4	0.73	26.0	3.7			35.7	5.1		
	13	5.0E-10	0.08		5.8E-04		0.19					2	248.0	132.9	78.6	0.81	32.6	4.5			40.4	5.6		
	14	2.2E-10	0.02	3.5	1.2E-04	0.03	0.06	13.8			6.7	1	143.9	112.3	60.6	0.74	59.4	8.4			79.9	11.3		
	15	2.9E-10	0.02	2.6	1.5E-04	0.02	0.05	5.8			4.0	1	199.3	127.7	72.5	0.79	73.7	10.2			93.2	12.9		
	16	2.6E-10	0.02	3.8	1.4E-04	0.03	0.03	5.8			5.2	1	219.0	96.4	59.3	0.75	78.8	10.7			105.4	14.3		
	17	2.0E-10	0.01	2.4	8.3E-05	0.02	0.07	15.3			6.1	2	245.0	87.6	55.7	0.72	58.8	8.4			82.1	11.8		
SA12-36	1	1.3E-09	0.03	4.2	1.9E-04	0.03	0.43	68.5			20.2	2	245.2	101.0	62.8	0.74	81.0	11.9			109.3	16.1		
	2	0.01	3.8	6.4E-05	0.03	0.03	13.8	0.26	113.8		6.9	2	193.9	68.7	43.7	0.65					92.5	27.7		
	3	8.5E-10	0.03	5.0	2.2E-04	0.03	0.20	32.7			11.5	1	217.5	106.1	64.0	0.73	88.8	9.7			118.0	12.9		
	4	9.8E-10	0.02	4.2	1.7E-04	0.02	0.37	67.1			18.9	1	167.5	114.2	63.9	0.77	73.0	8.0			97.9	10.7		
	5	1.5E-09	0.06	7.8	4.4E-04	0.06	0.36	46.8			18.8	2	203.2	123.4	71.0	0.78	86.2	12.4			110.9	15.9		
	6	4.4E-09	0.07	5.9	4.8E-04	0.04	1.35	121.4			34.5	1	189.8	152.5	81.6	0.80	93.8	13.8			117.2	17.3		
	7	1.1E-09	0.02	3.2	1.1E-04	0.02	0.29	59.7	0.65	134.5	17.3	1	173.6	105.2	60.6	0.73	98.5	10.6			134.9	14.6		
	8	1.2E-10	0.02	3.1	1.4E-04	0.03	0.07	10.5			6.5	2	204.9	111.0	65.5	0.76	26.8	3.0			35.1	3.9		
	9	1.4E-09	0.06	4.3	4.7E-04	0.03	0.25	16.5			7.6	1	169.5	187.8	90.6	0.83	95.1	13.4			114.8	16.2		
	10	7.1E-10	0.02	5.5	1.2E-04	0.03	0.27	92.2			25.5	1	171.4	82.6	49.9	0.67	72.7	10.7			107.9	15.9		
	11	4.2E-09	0.08	4.2	5.6E-04	0.02	0.45	24.3	1.90	103.2	8.9	1	275.9	163.1	94.4	0.83	170.9	18.6			205.2	22.3		
	12	1.6E-10	0.01	3.7	1.0E-04	0.03	0.19	50.5	0.56	145.6	15.6	2	189.7	89.5	54.3	0.70	20.7	2.3			29.5	3.3		
	13	4.2E-09	0.05	7.4	3.8E-04	0.05	1.26	179.0	0.98	138.9	49.5	1	193.7	120.4	68.9	0.76	87.1	9.3			114.3	12.3		
	14	1.1E-10	0.22	23.6	1.6E-03	0.17	0.64	69.3			40.0	2	226.3	127.3	74.5	0.75	2.4	0.3			3.0	0.3		
	16	1.8E-09	0.03	5.1	2.0E-04	0.04	0.75	134.9	0.85	153.5	36.8	2	212.9	114.2	67.6	0.76	70.7	7.8			96.6	10.6		
SA12-38	1	2.4E-09	0.16	19.0	1.1E-03	0.14	0.10	11.9	0.91	110.3	22.0	1	169.2	139.0	73.9	0.80	106.8	11.5			133.0	14.4		
	2	3.3E-09	0.20	25.6	1.4E-03	0.19	0.28	36.5	1.20	156.9	34.4	1	154.1	140.7	72.4	0.79	100.3	10.8			126.3	13.6		
	3	1.4E-09	0.09	21.9	6.3E-04	0.16	0.15	36.7	0.57	142.6	30.7	2	142.1	105.6	57.7	0.74	89.5	9.8			120.9	13.3		
	4	6.3E-09	0.07	6.0	5.4E-04	0.04	1.84	149.3	0.86	69.7	41.2	2	277.1	133.0	80.5	0.80	100.2	11.3			125.9	14.2		
	5	8.1E-09	0.51	26.1	3.7E-03	0.19	0.39	19.8	2.10	107.4	30.9	1	237.1	181.0	98.2	0.85	106.6	14.5			125.2	17.0		
	6	5.4E-09	0.21	26.0	1.5E-03	0.19	0.61	75.0	1.01	124.2	43.8	1	156.3	143.9	73.9	0.79	120.4	16.8			152.0	21.2		
	7	2.6E-09	0.16	18.7	1.2E-03	0.14	0.20	23.8	1.33	155.9	24.4	2	230.2	121.6	72.1	0.79	95.6	10.5			120.4	13.2		
	8	3.8E-09	0.21	31.3	1.5E-03	0.23	0.10	14.4			34.9	0	160.5	129.7	69.3	0.79	130.3	17.9			164.6	22.7		
	9	7.5E-09	0.53	41.5	3.8E-03	0.30	0.27	21.5			46.9	0	223.6	150.5	84.4	0.83	103.8	14.2			125.3	17.2		
	10	2.5E-09	0.19	31.1	1.3E-03	0.23	0.17	28.3	0.74	123.6	37.9	2	210.2	106.2	63.6	0.77	88.4	9.7			115.0	12.6		
	11	6.3E-09	0.38	34.3	2.7E-03	0.25	0.24	22.1	1.63	148.0	39.8	2	233.7	137.0	79.4	0.82	114.0	12.5			139.6	15.3		
	12	6.3E-09	0.27	48.8	1.9E-03	0.35	0.49	89.2	0.91	165.9	70.1	1	145.7	122.5	64.7	0.77	131.6	18.0			171.6	23.5		

Table 5-2: Continued

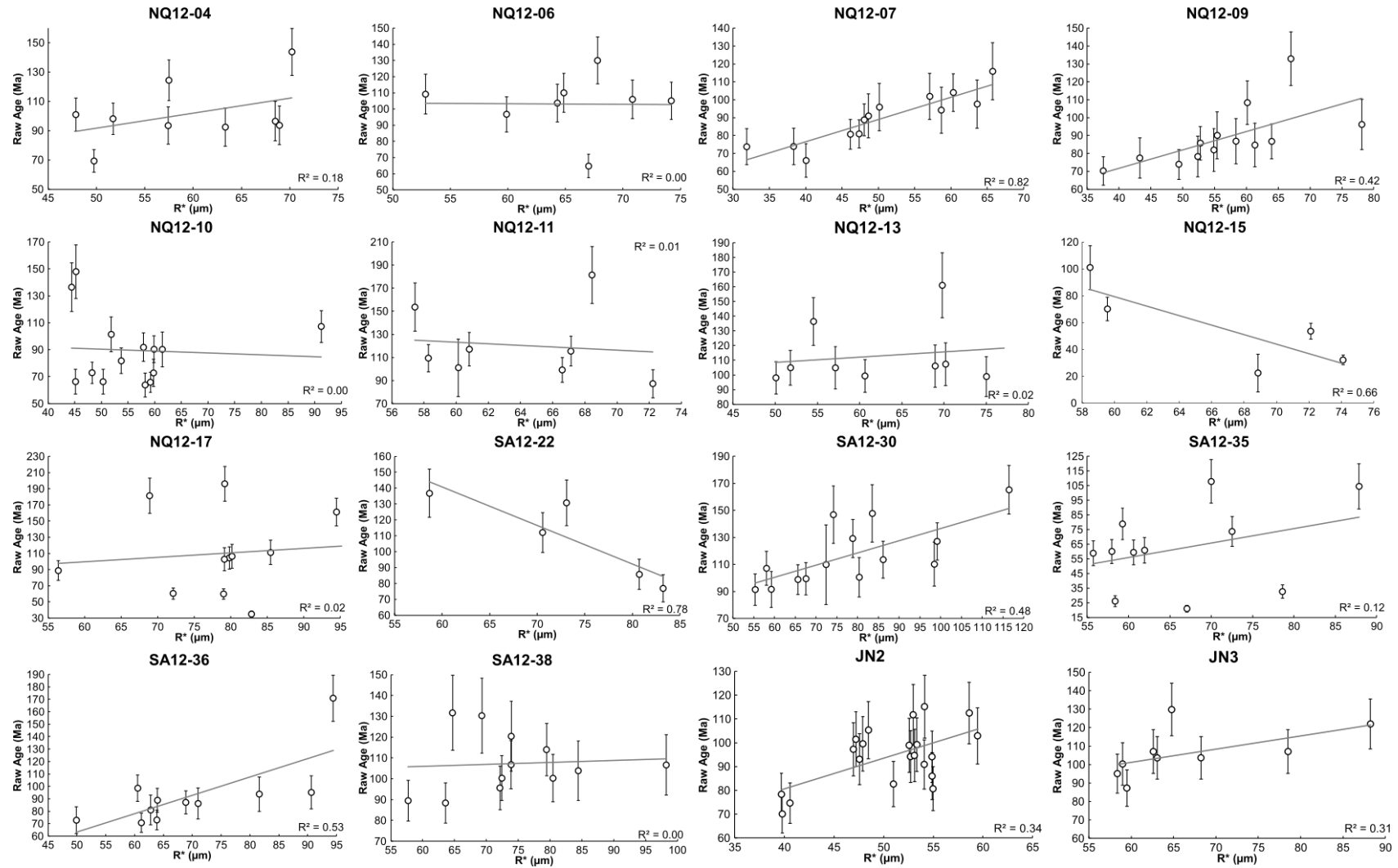


Figure 5-6: Plot of AHe age against spherical equivalent grain radius ( $R^*$ ). AHe ages are mean AHe ages uncorrected for alpha-ejection. Uncertainties on AHe ages are  $1\sigma$  analytical uncertainty (typically 1-3%) +  $1\sigma$  standard deviation of Durango standards (10%).  $R^*$  is calculated using the formula  $(3*(RL))/(2*(R+L))$  where R = the measured radius of the apatite crystal and L = measured length of the apatite crystal.

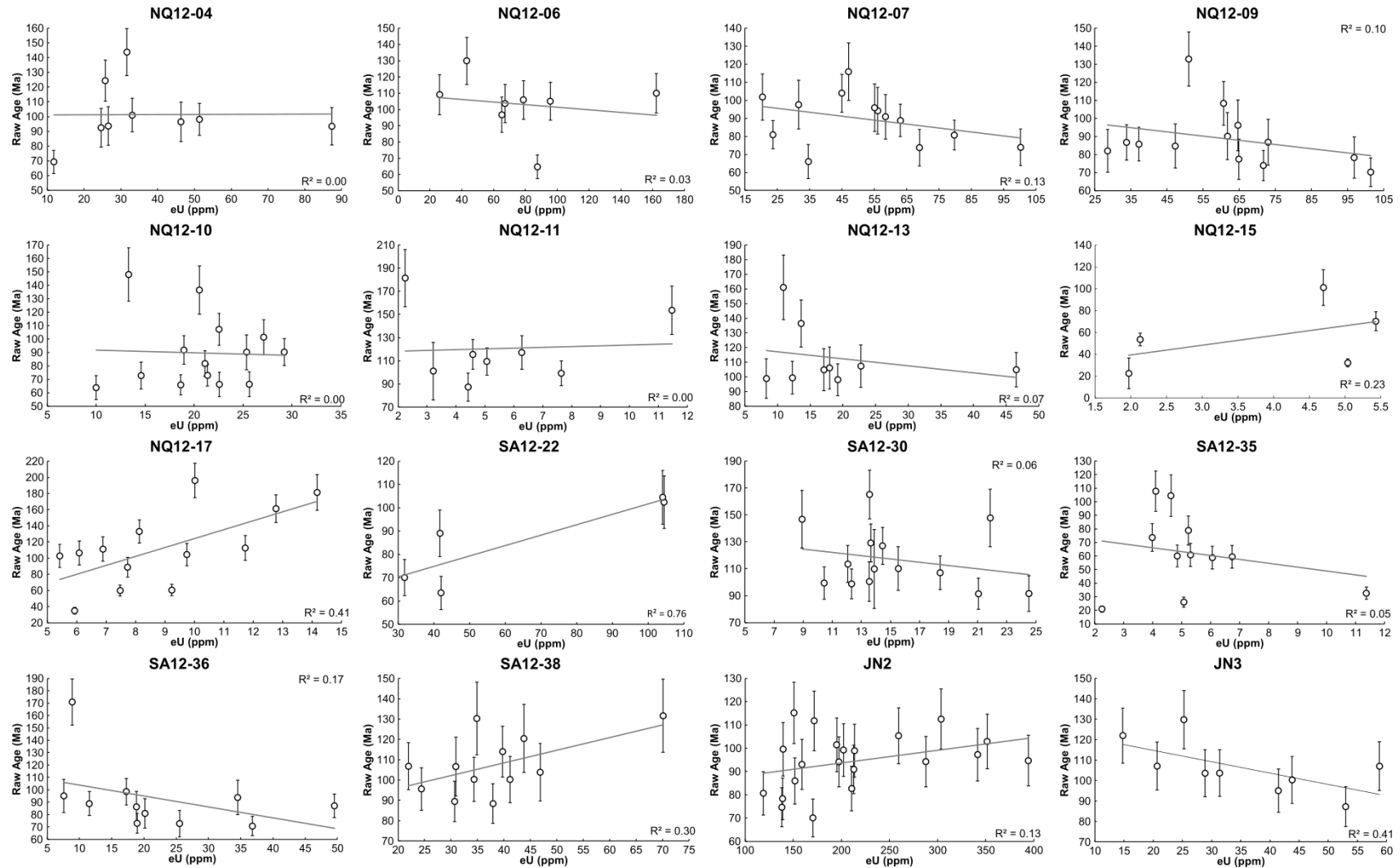


Figure 5-7: Plot of AHe age against effective Uranium (eU). AHe ages are mean AHe ages uncorrected for alpha-ejection. Uncertainties on AHe ages are  $1\sigma$  analytical uncertainty (typically 1-3%) +  $1\sigma$  standard deviation of Durango standards (10%). eU is calculated using the formula  $[U_{ppm}] + (0.235 * [Th_{ppm}])$  and is used as a proxy for accumulated radiation damage.

grain ages. Under normal circumstances an AHe age that was approximately the same as the AFT age would be indicative of a sample that was rapidly cooled. However, because these samples have a variety of grain sizes and variable uranium and thorium concentrations, the exact closure temperature of the AHe system for each grain is different and such a simple approximation of the samples thermal history cannot be made.

If a sample has experienced relatively slow cooling then correlations of spherical equivalent grain radius ( $R^*$ )/eU with AHe age may be evident. However, as suggested by Brown et al. (2013) the combined effects of these influences may decouple the expected correlation. Moreover, a large number of grains analysed were 1T or, in some cases, 0T fragments of larger grains. Despite this many samples still adhere to an apparent positive age- $R^*$  correlation (Fig. 5-6). Sample NQ12-15 is the only sample in which we can observe a negative age- $R^*$  correlation however this sample has the fewest number of grains and it is poorly defined. eU relationships are more complex as samples show a mix of correlations that are positive, negative or entirely absent (Fig. 5-7). A linear fit may not be representative of the expected age-eU relationship. For example, Flowers et al. (2009) report that for relatively slow cooling rates (c. 0.1 - 1°C/Myr) the age-eU relationship will first be positively correlated but will then plateau above eU concentrations of c. 50 ppm. Guenthner et al. (2014) have reported eU-age correlations in zircon are strongly negative at high eU concentrations but at lower eU correlations may be positively correlated. More complex correlations could be estimated from the plots presented in Figure 5-7. For example, JN2 could be described as having a positive correlation until eU = c. 250 ppm and there is then a plateau of ages; or NQ12-09 could be described as having a plateau of ages until c. 50 ppm and are then negatively correlated. However, attempting to fit such correlations on eU dispersion plots may be premature as our understanding of how the accumulation and annealing of radiation defects occurs and the impact this has on alpha-trapping is still developing. Expecting to observe correlations in age and eU may also be ambitious considering grain radius and the presence of fragmented grains will be influencing the closure temperature and preservation of the He diffusion profile, respectively. Other factors must also be considered such as the possible

presence of zonation, unidentified inclusions, implantation and the contribution of Sm which is not quantified in certain grains. Key to single grain age dispersion is the sensitivity of He diffusion when the sample (or grain) is residing at elevated temperatures.

### **5.4.3 Summary of AHe Data**

The AHe data presented here is consistent with the general interpretation made based on AFT data: that major cooling has occurred during the Early - Late Cretaceous and possibly into the Tertiary. Single grain AHe ages are associated with a large amount of dispersion and as such come under severe scrutiny regarding the quality of the data and the implications they have for our understanding of the AHe dating approach. The competing influences that typically cause single grain age dispersion act in tandem to disrupt simple correlations and mask any dominating influence.

However, the former comment regarding quality can be addressed directly. Standard lab procedures were followed and analysis of Durango apatite standards produced results consistent with previous studies (see Appendix 2.2). When AHe ages appeared to be outliers, samples were carefully scrutinised and rejected only if there was not any other independent evidence to support the reliability of the data. Therefore, the measured AHe age, plus analytical uncertainty, plus an uncertainty reflecting the reproducibility of the Durango apatite standard should contain the true AHe age that is directly linked to the thermal history experienced by the sample. Because of this assumption, AHe and AFT data and their respective uncertainties can be treated in terms of probability functions that can be used in thermal history modelling techniques.

## **5.5 Thermal History Modelling**

### **5.5.1 Approach**

The general modelling approach has been outlined in Chapter 4 - Section 4.5. All samples from this region are outcrop samples taken from basement lithologies apart from SA12-27 which has been collected from a boulder clast of basement

origin from within the glacial tillite of the Permian Dwyka Group. During modelling, SA12-27 was assigned a specific initial constraint of  $300 \pm 10$  Ma,  $20 \pm 10^\circ\text{C}$  to represent the fact that the sample must have been at the surface at this time to be deposited within the Permian unit. For basement samples, where an appropriate/effective stratigraphic age was unknown, a single constraint point was used with a time and temperature range  $350 \pm 10$  Ma and  $100 \pm 100^\circ\text{C}$ , respectively. This constraint ensures that the thermal history is constrained at least as far back as the approximate age of Karoo deposition covering NMP basement rocks, but allows a large temperature range to be explored to allow the model to start at depth or at the surface if the data so requires it. In most cases, palaeo-temperatures were significantly high to reset the AFT record during the Late Jurassic/Early Cretaceous and as such the early part of the history is unconstrained. Assigning a more specific constraint box would be an assumption that has no influence on the model outcome. Where there is the possibility that complete resetting has not occurred alternative models with different initial constraints are investigated. For all samples the present-day temperature value is assumed to be  $20 \pm 10^\circ\text{C}$ .

A lack of geological information limits the amount of post-rift constraints that can be added to the models however the implications of sporadic fossil evidence, sedimentary deposits and igneous intrusions across the region on nearby samples is also investigated below (Section 5.5.3.2). In an attempt to increase the amount of information used during modelling and with the aim of finding thermal histories consistent with many samples, multiple outcrops were treated as vertical profiles with a small temperature offset both at present day and in the geological past (see Section 5.5.3.1). Normally this functionality would be employed on a steep vertical profile covering a relatively large elevation range or down a borehole profile (examples of these are given in Chapter 7 - Section 7.2.1). However, if samples, even over a small elevation range, have shared a similar thermal history then the combined information from the data will help us obtain a model that is consistent with all the data in a region. The criteria for grouping samples together was based on their close proximity to one another ( $< 10$  km, and typically less than this) and the similar nature of their thermal histories when modelled as individual samples. In order

to model samples as profiles an additional parameter known as the Vertical Offset is specified in order to define the temperature difference between the top and bottom sample in the profile. This is calculated, assuming a geothermal gradient of  $25 \pm 10^\circ \text{C/km}$ , as:

$$\text{Vertical Offset} = (E_{\text{top}} - E_{\text{bottom}}) * G_{\text{mean}} [\pm (E_{\text{top}} - E_{\text{bottom}}) * G_{\text{max/min}}]$$

Where  $E_{\text{top}}$  and  $E_{\text{bottom}}$  is the elevation of the top and bottom sample of the vertical profile;  $G_{\text{mean}}$  is the assumed geothermal gradient;  $G_{\text{max/min}}$  is the upper and lower estimates of the geothermal gradient used to calculate the uncertainty on the vertical offset.

## 5.5.2 Modelling results

Data from all 42 outcrop samples were inverted using the procedure outlined above and in Chapter 4 - Section 4.5. Many samples yield models with similar thermal histories and can be grouped into the same class of models. The following report of modelling results will describe examples from each of these model classes; in most cases, an outcrop sample with only AFT data is presented alongside a sample with AFT and AHe data. In general, the onset of cooling for thermal histories recorded by the expected model occurs within one of three time periods: 150 - 130 Ma, 110 - 90 Ma, 80 - 60 Ma. In rare models cooling is recorded in between these intervals but could belong to one class or another once you account for the uncertainty on those models. Within these time intervals models show varying cooling rates and these define the different classes of models discussed here. In addition to the T-t history, the spatial relationship of these models is also important and is discussed in detail in section 5.6.

### 5.5.2.1 150 – 130 Ma: Slow Cooling

The majority of models that record cooling beginning during the Early Cretaceous are characterised by relatively slow cooling rates. Figure 5-8a shows two examples of this thermal history with cooling initiating at c. 150 Myr and continuing in an almost linear manner until the present day. Due to the

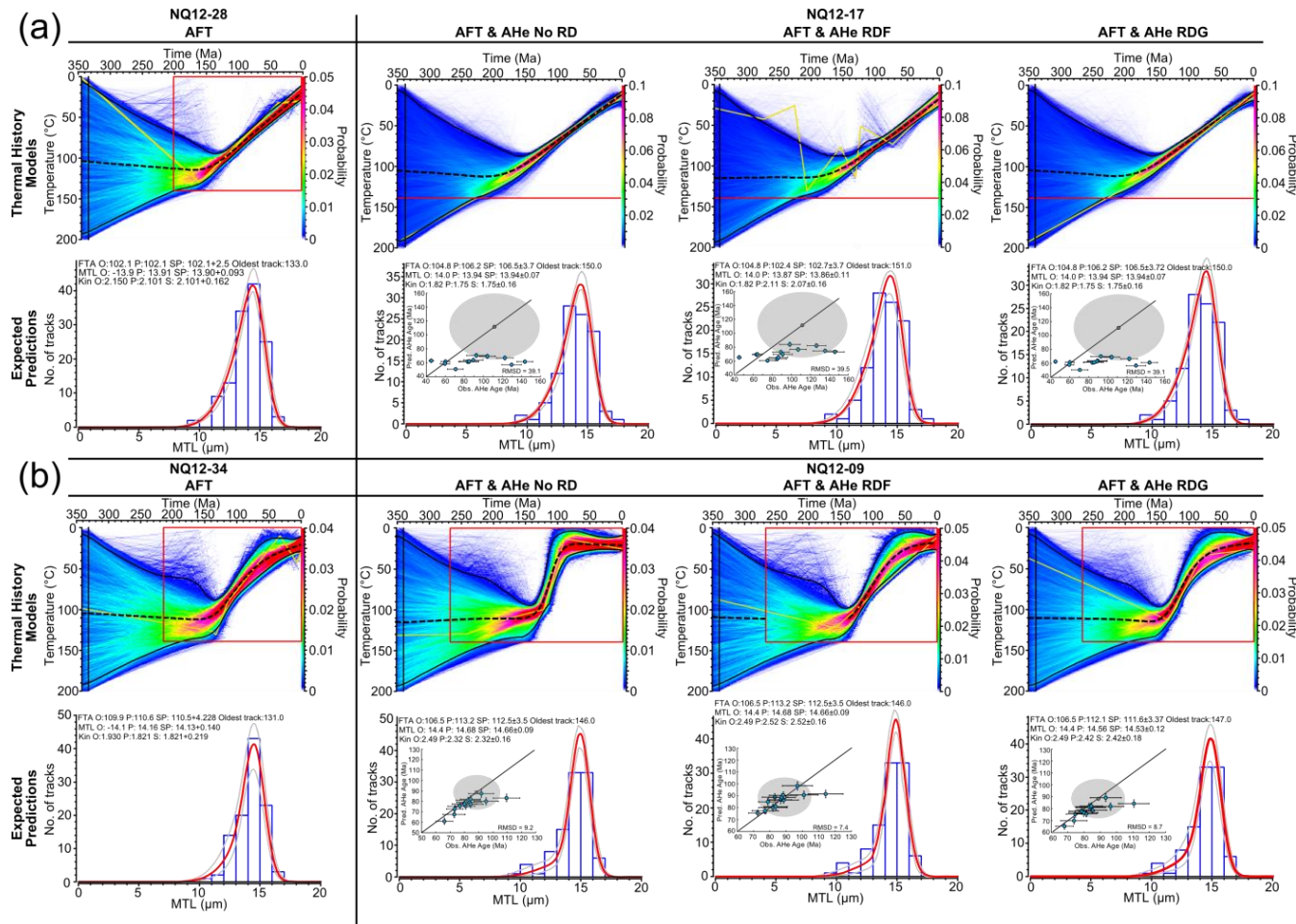


Figure 5-8: Thermal history models that represent samples which cooled slowly over the interval 150 – 130 Ma. The expected model is represented by a dashed black line with 95% credible intervals (solid black lines). The maximum likelihood model is also presented (yellow line). The black box represents initial constraint on the model. The red box represents general ranges for prior (see Chapter 4 - Section 4.5.1). The colour map represents the probability distribution of the thermal history. The blue histograms represent the measured TLD; red line represents the predicted TLD from the expected model with 95% credible intervals (grey curves). The blue circles illustrate the relationship between the observed and predicted AHe age. The dark grey circle represents the mean measured AHe age (uncorrected for alpha-ejection). The light grey circle represents the  $1\sigma$  standard deviation on the mean AHe age.



unconstrained initial conditions of the model and the protracted nature of cooling, defining a maximum temperature at a given time is difficult. The timing is estimated when the space between the 95% credible intervals narrows and the model begins to become well constrained (i.e. c. 150 Myr). The maximum temperature is estimated as that being recorded by the expected model at this time and is typically  $110 \pm 10^\circ\text{C}$ . Subtle differences in thermal histories, largely in the maximum temperature, can be observed between NQ12-28 and NQ12-17 and subtle differences can be observed for NQ12-17 itself depending on the radiation damage model used. However, these are insignificant and all models suggest a cooling rate of c.  $0.6^\circ\text{C}/\text{Myr}$ . Figure 5-8(b) shows models that are also used as examples of slow cooling; however, cooling is slightly faster than those described above. The product is a two-stage thermal history where cooling initiates at c. 150 - 130 Ma and reaches near surface temperatures by c. 50 - 30 Ma. Without incorporating any radiation damage model, the thermal history for NQ12-09 shows a more rapid cooling rate of c.  $1.8^\circ\text{C}/\text{Myr}$ . However, including either radiation damage model both improves the data fit for AHe data and reduces the cooling rate to c.  $0.8 - 1^\circ\text{C}/\text{Myr}$ . A special mention has to be given to sample NQ12-06 (see Appendix 7) as the thermal history changes significantly when radiation damage is incorporated; transforming the thermal history from one that is predominantly rapidly cooled to one where cooling is more protracted. In the models incorporating radiation damage an initial short lived, rapid episode of cooling is observed from 130 - 110 Ma at a cooling rate of c.  $1.5^\circ\text{C}/\text{Myr}$ . Following this period of enhanced cooling, rates are reduced to c.  $0.6 - 0.7^\circ\text{C}/\text{Myr}$  which is comparable with other samples assigned to this class of models.

#### **5.5.2.2 150 – 130 Ma: Fast Cooling**

The most rapid cooling at this time is recorded in four samples across the study area. NQ12-25 and NQ12-33 which are in the southern most region of the study area and on the eastern edge of the NQH, respectively, have cooling rates of c.  $1.6 - 1.80^\circ\text{C}/\text{Myr}$  (Fig. 5-9). This cooling initiates at c. 130 Ma and following rapid cooling, progressively rolls over towards surface temperatures by 70 - 50 Ma. JN3 and JN2 record faster cooling which initiates at a slightly earlier time

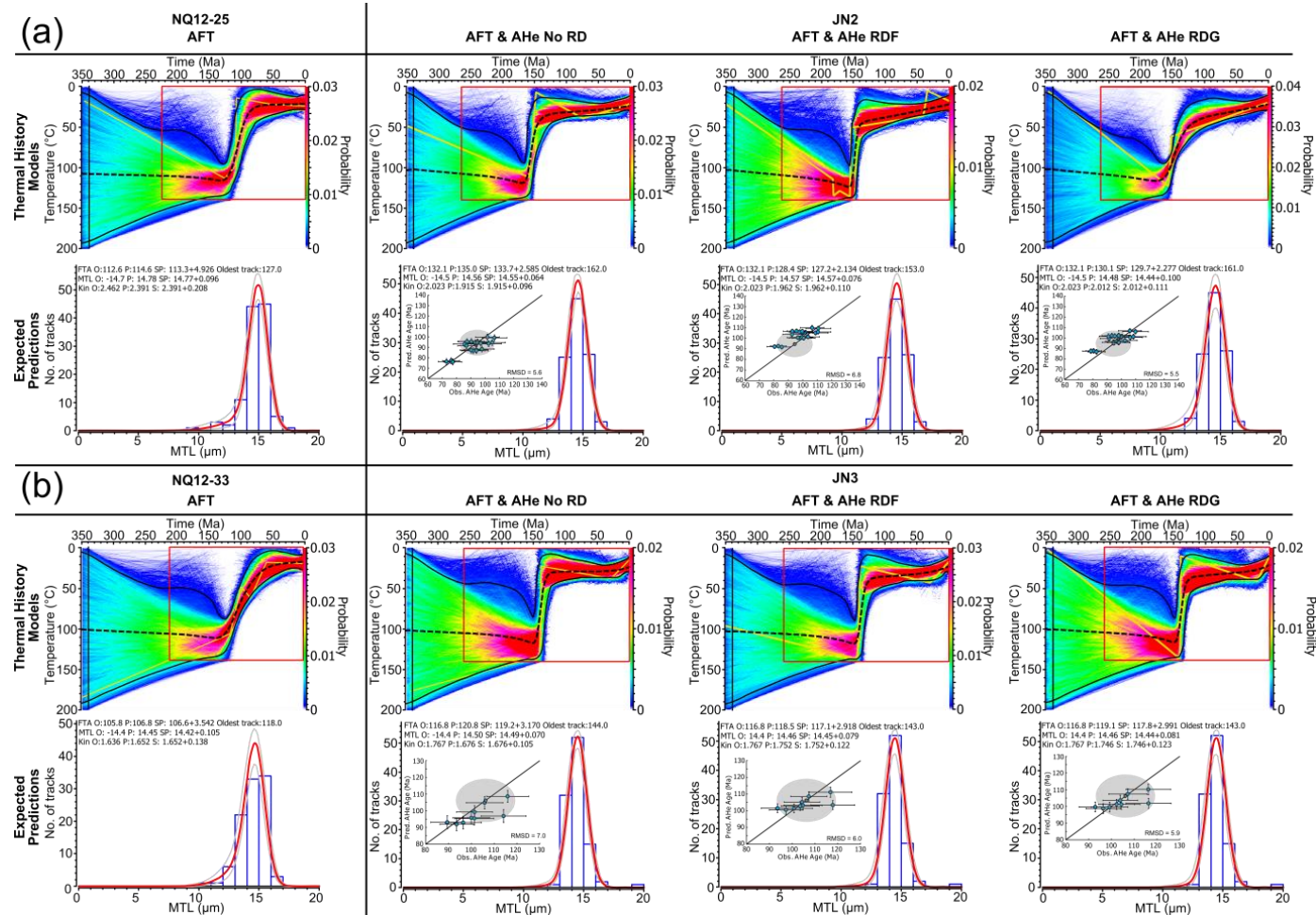
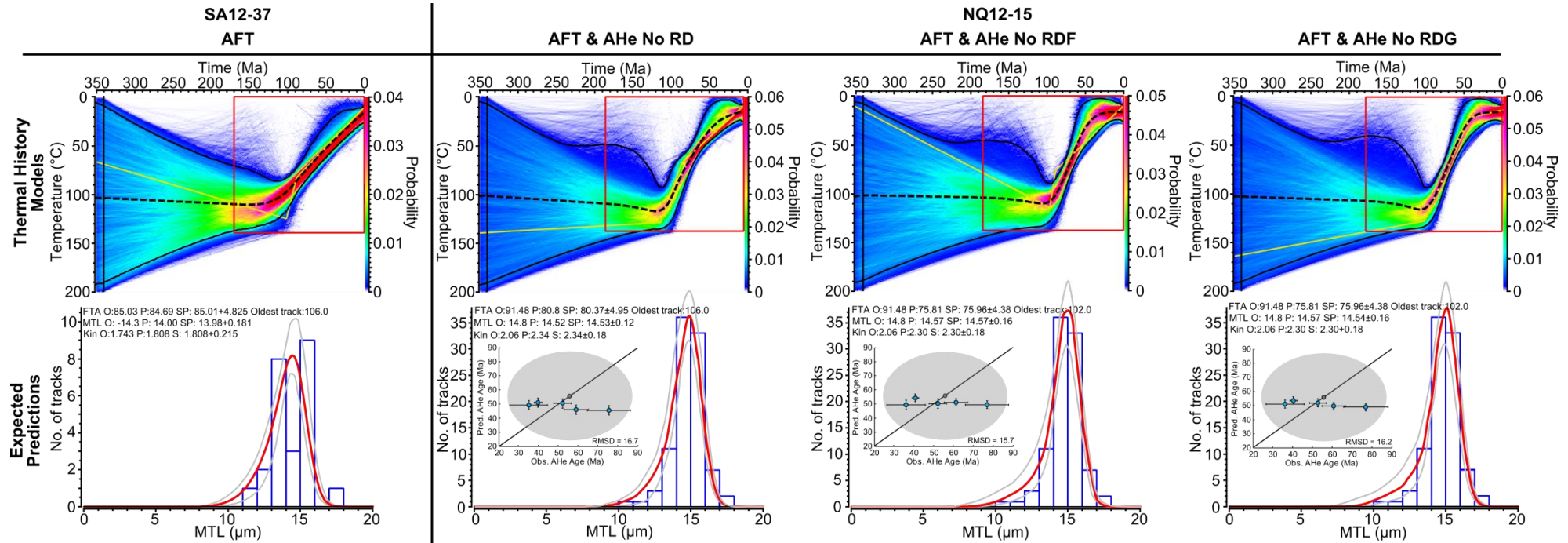


Figure 5-9: Thermal history models that represent samples which cooled rapidly over the interval 150 – 130 Ma. The expected model is represented by a dashed black line with 95% credible intervals (solid black lines). The maximum likelihood model is also presented (yellow line). The black box represents initial constraint on the model. The red box represents general ranges for prior (see Chapter 4 - Section 4.5.1). The colour map represents the probability distribution of the thermal history. The blue histograms represent the measured TLD; red line represents the predicted TLD from the expected model with 95% credible intervals (grey curves). The blue circles illustrate the relationship between the observed and predicted AHe age. The dark grey circle represents the mean measured AHe age (uncorrected for alpha-ejection). The light grey circle represents the 1 $\sigma$  standard deviation on the mean AHe age.

(c. 150 Ma). Cooling rates are between 2 and 4.25°C/Myr depending on which radiation damage model is used. The models also imply that near surface temperatures were reached shortly after this rapid cooling event and have been maintained for at least 100 Ma. The maximum likelihood model shows a period of rapid cooling at c. 150 - 130 Ma for all models. The structure in the NQ12-33 maximum likelihood model matches that of SA12-33 but is absent in other models of this class. Some structure is shown in the latter part of the thermal history models for both JN2 and JN3. While this structure varies in style for JN2 depending on the radiation damage model used; JN3 consistently shows a period of late Cenozoic cooling (c. 30 - 20 Ma) following minor reheating, regardless of the radiation damage model used. It should be remembered, however, that this portion of the thermal history is at the very bottom of the AFT and AHe temperature sensitivity and therefore is less tightly constrained.

### **5.5.2.3 110 – 90 Ma: Slow Cooling**

Thermal history models that show cooling beginning during the 110 - 90 Ma time interval and are characterised by slow cooling profiles are very rare, with only four samples fitting this description (Fig. 5-10). Cooling rates for these samples are comparable to slow cooling recorded during the earlier interval ranging between 0.7 and 0.95°C/Myr. Each of the models for these samples should be treated with extreme caution however due to the quality of the data on which they are based. SA12-32 only has 2 HCTs and 3 single grain ages and SA12-37, while better, only has 24 HCTs and 12 single grain ages which is far less than is typically measured for fission track analysis. SA12-27 has a large number of single grains ages but a low number of HCTs (n=27) and therefore there is a lot of uncertainty in the observed TLD. NQ12-15 on the other hand has strong AFT data with plenty of lengths and single grain ages but the AHe data is limited extremely complex. This AHe data has large degrees of dispersion that cannot easily be explained in terms of grain size or radiation damage. The data fit for NQ12-15 is poor with the expected model compromising on both the accuracy of predicted AFT and AHe data in order to produce a model which best satisfies the complex data set.



**Figure 5-10: Thermal history models that represent samples which cooled slowly over the interval 110 – 90 Ma. The expected model is represented by a dashed black line with 95% credible intervals (solid black lines). The maximum likelihood model is also presented (yellow line). The black box represents initial constraint on the model. The red box represents general ranges for prior (see Chapter 4 - Section 4.5.1). The colour map represents the probability distribution of the thermal history. The blue histograms represent the measured TLD; red line represents the predicted TLD from the expected model with 95% credible intervals (grey curves). The blue circles illustrate the relationship between the observed and predicted AHe age. The dark grey circle represents the mean measured AHe age (uncorrected for alpha-ejection). The light grey circle represents the  $1\sigma$  standard deviation on the mean AHe age.**

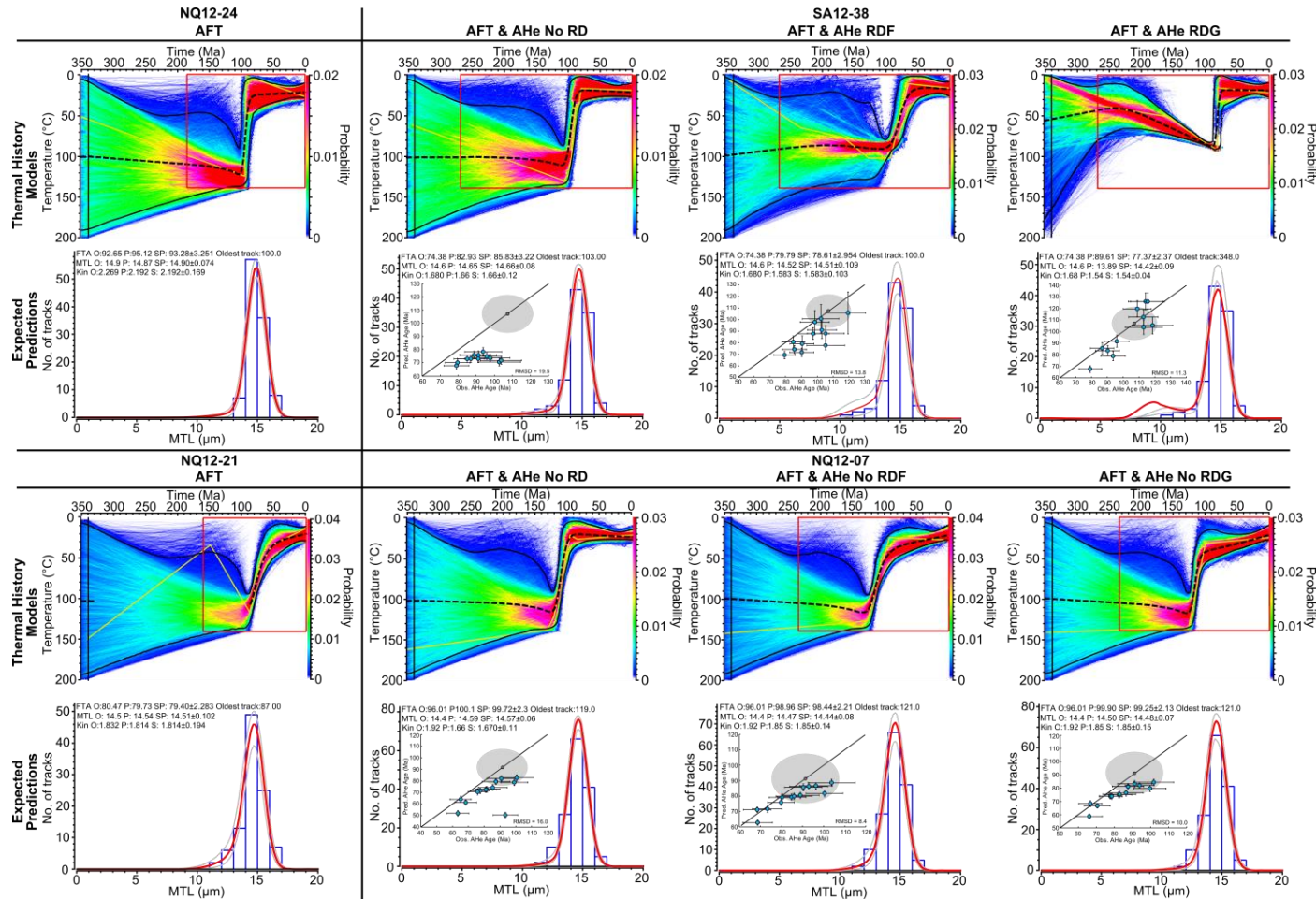


Figure 5-11: Thermal history models that represent samples which rapidly cooled over the interval 110 – 90 Ma. The expected model is represented by a dashed black line with 95% credible intervals (solid black lines). The maximum likelihood model is also presented (yellow line). The black box represents initial constraint on the model. The red box represents general ranges for prior (see Chapter 4 - Section 4.5.1). The colour map represents the probability distribution of the thermal history. The blue histograms represent the measured TLD; red line represents the predicted TLD from the expected model with 95% credible intervals (grey curves). The blue circles illustrate the relationship between the observed and predicted AHe age. The dark grey circle represents the mean measured AHe age (uncorrected for alpha-ejection). The light grey circle represents the 1 $\sigma$  standard deviation on the mean AHe age.

#### **5.5.2.4 110 – 90 Ma: Fast Cooling**

By far the most common and strongest class of thermal history is characterised by rapid cooling rates that begin between 110 and 90 Ma (Fig. 5-11). 50% of the outcrop samples modelled can be included in this class of models highlighting its regional importance. A major control on the style of thermal history observed is the fission track length data which, in this case, is characterised by long MTLs with unimodal and narrow track length distributions. As such radiation damage effects do not have a major influence on the overall cooling rate and this is reflected in the temperature at which the period of rapid cooling terminates and becomes more protracted towards the surface. Cooling rates generally range from c. 1.5 - 5°C/Myr (Fig. 5-11a) but in certain samples can be higher at 7.4 - 8.1°C/Myr (Fig. 5-11b).

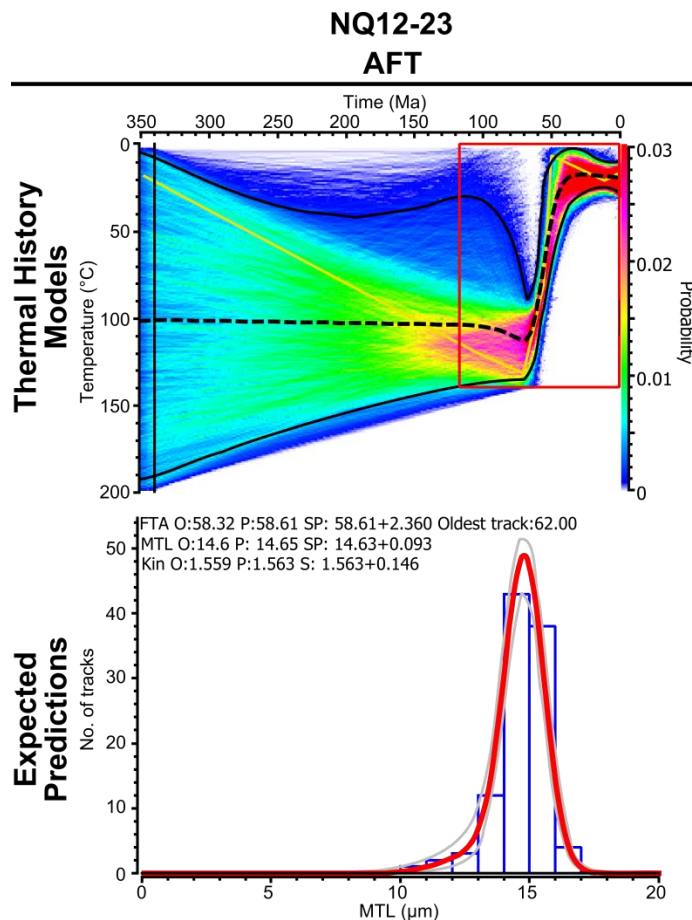
#### **5.5.2.5 80 – 60 Ma**

A third cooling episode is poorly preserved across the study area. However, the thermal history for one sample clearly shows cooling initiating between at c 70 - 65 Ma (Fig. 5-12). The style of cooling for NQ12-23 is very rapid occurring at a rate of 10°C/Myr. This sample resides in a complex structural setting and is c. 50 km SW of the Koegel fontein igneous complex which has intrusive bodies dated to c. 70 - 50 Ma (de Beer, 2002). Fission track data for this sample is robust with plenty of track lengths and single grain ages. This cooling episode, although only recorded in one sample throughout the entire study area, is likely to be a distinct thermal history from the previously discussed cooling events.

### **5.5.3 Alternative scenarios**

#### **5.5.3.1 Profile modelling**

Modelling vertical profiles will be most effective for borehole profiles where there is a clear temperature offset between the samples both at the present day and geological past and the samples represent a true rock column. However, outcrop samples taken from a steep vertical profile can also be inverted assuming they have been exhumed as a single rock column (i.e. the profile is not dissected by a fault). Where samples are in close proximity to one another (c.



**Figure 5-12: Thermal history model that represents the only sample which rapidly cooled over the interval 80 – 60 Ma. The expected model is represented by a dashed black line with 95% credible intervals (solid black lines). The maximum likelihood model is also presented (yellow line). The black box represents initial constraint on the model. The red box represents general ranges for prior (see Chapter 4 - Section 4.5.1). The colour map represents the probability distribution of the thermal history. The blue histograms represent the measured TLD; red line represents the predicted TLD from the expected model with 95% credible intervals (grey curves). The blue circles illustrate the relationship between the observed and predicted AHe age. The dark grey circle represents the mean measured AHe age (uncorrected for alpha-ejection). The light grey circle represents the  $1\sigma$  standard deviation on the mean AHe age.**

<10 km) and/or are not separated by clear structural features they may have shared a similar thermal history and therefore can be modelled together with a small temperature offset or a temperature offset that reflects their difference in elevation (or depth) over time. To further enhance the dataset, additional data from Brown (1992) is also included where appropriate (see Appendix 6).

The cluster of samples at Hondeklip Bay are modelled together incorporating all AFT data and AHe data where available (Fig. 5-13). Individually, NQ12-15 and NQ12-17 are slowly cooled thermal histories beginning at c. 150 Ma while NQ12-

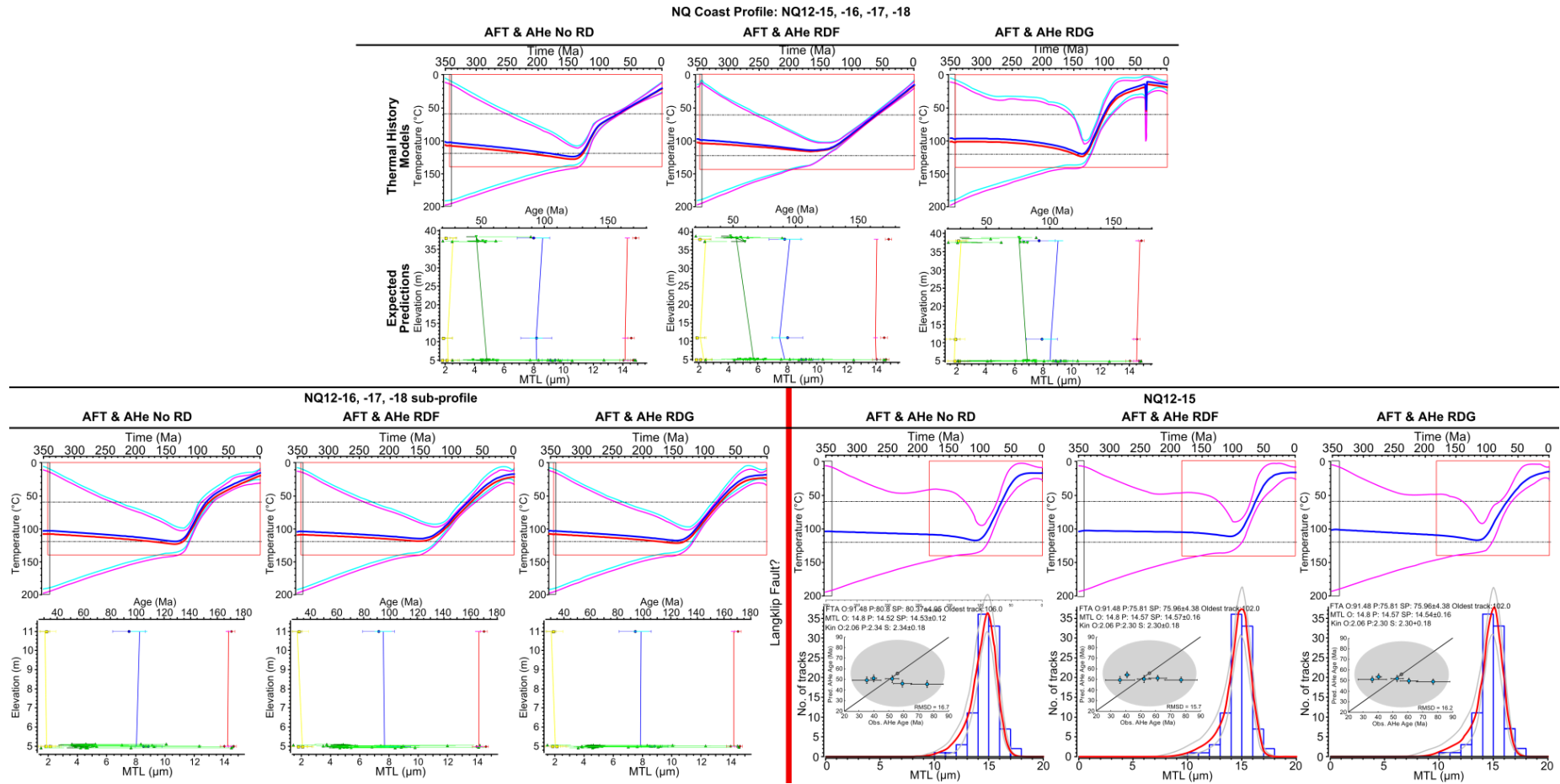
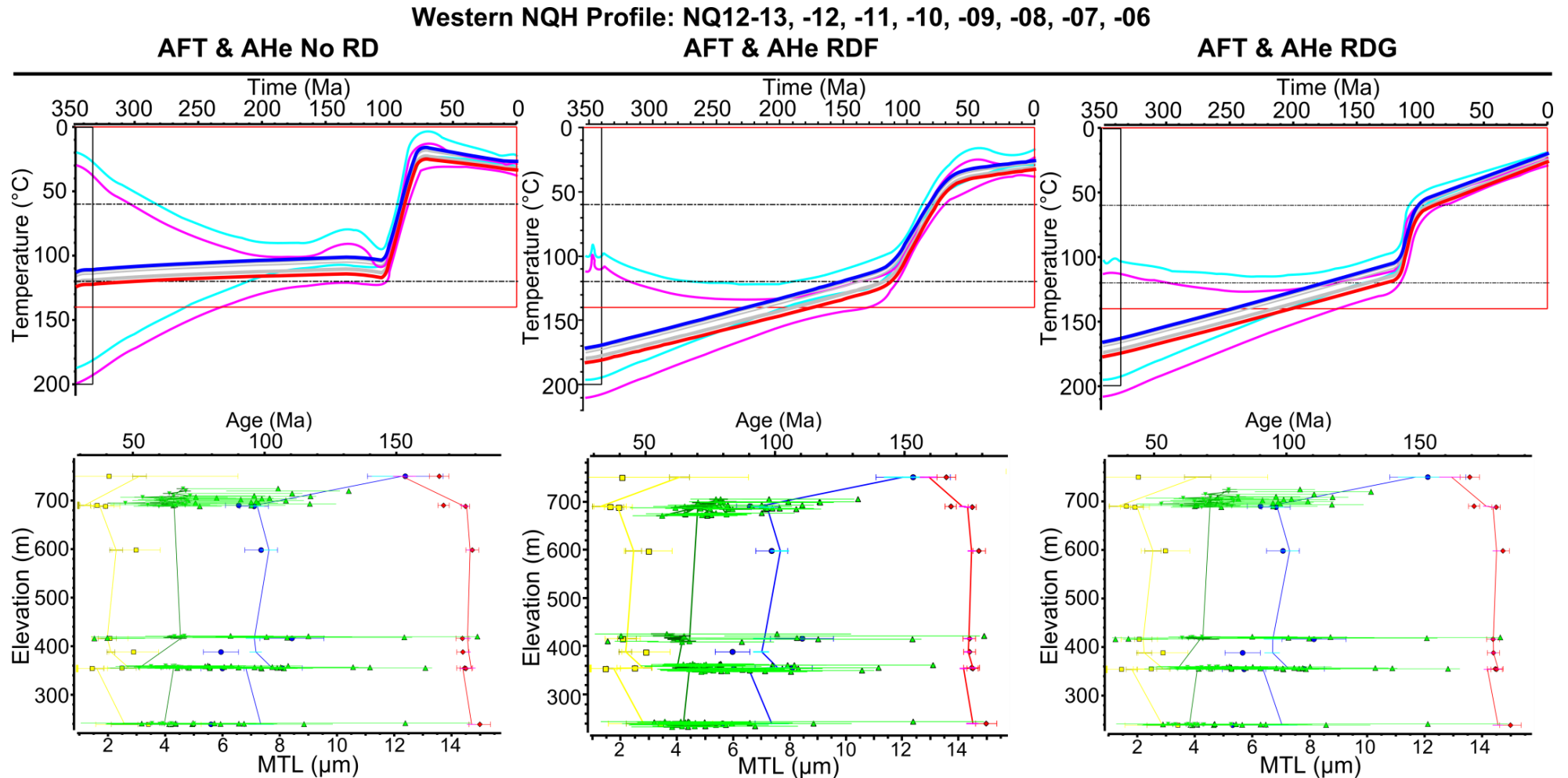


Figure 5-13: Coastal profile thermal history models. Expected model of the top and bottom sample is represented by a thick blue and red line, respectively, with 95% credible intervals (cyan and magenta lines). Black box represents initial constraint on the model. Red box represents general ranges for prior (see Chapter 4 - Section 4.5.1). Yellow square/bar = Measured/predicted  $D_{par}$ ; blue circle/light blue bar = Measured/predicted AFT age; red diamond/magenta bar = measured/predicted MTL; green triangle/light green bar/dark green bar = measured/resampled observed/predicted AHe age. Histograms represent the measured TLD; red line represents the predicted TLD with 95% credible intervals (grey curves). The blue circles illustrate the relationship between the observed and predicted AHe age. The dark grey circle represents the mean measured AHe age (uncorrected for alpha-ejection). The light grey circle represents the  $1\sigma$  standard deviation on the mean AHe age.



16 and NQ12-18 are characterised by more rapid cooling slightly later at c. 130 -120 Ma. Together, the model becomes dominated by the earlier, slowly cooled history. This is to be expected as NQ12-15 and NQ12-17 contain complex AHe datasets that are best reproduced through a slow cooling history, particularly once radiation damage effects are included. Despite this, the composite model still honours the data of NQ12-16 and NQ12-18 well. The poorest data fit is for NQ12-15 as the No RD and RDF model poorly reproduce the AFT MTL and RDG model fails to reproduce the AFT age and AHe ages with great success. Profile modelling was then performed without NQ12-15. The sample was removed not only due to the poor data fit in places but because the Langklip Fault (de Beer, 2012) cuts through this cluster of samples; separating NQ12-15 from the other samples. These samples may have experienced subtle or major differences in their thermal history due to post-rift fault movement. Profile modelling of the three remaining coastal samples again produces a slowly cooled thermal history from c. 150 Ma with a good data fit (Fig. 5-13). A subtle but potentially important difference is that the cooling rate is slightly faster than the previous profile model and reaches near surface temperatures in the Mid - Late Cenozoic; consistent with fossil evidence from the region (see Chapter 7 - Section 7.5.2).

A short, c. 30 km, transect of 8 samples from Weltevreden farm to Twee fontein farm, northwest of Garies, span an elevation range of 239 - 750m and were modelled as a single profile (Fig. 5-14). The fit of AFT data is poor for certain samples in the profile but is, in many cases, quite good. The AHe data fit is worse but by resampling the observed age most AHe ages overlap with predicted ages. The expected thermal history from this composite dataset suggests fairly rapid cooling at c. 110 - 100 Ma. In either model, including radiation damage effects the thermal history is confined to high temperatures in the Permian in order to fully reset the AFT and AHe LTT's prior to the onset of rapid cooling at c. 115 Ma. The assumption that this transect has not been affected by any structural displacement and therefore influenced the thermal history of individual samples is questioned by the presence of major structural lineaments and recent work supporting structural reactivation across the SW margin (Kounov et al., 2009; Viola et al., 2012; Salomon et al., 2014).



**Figure 5-14: Western NQH profile thermal history models. Expected model of the top and bottom sample is represented by a thick blue and red line, respectively, with 95% credible intervals (cyan and magenta lines). Black box represents initial constraint on the model. Red box represents general ranges for prior (see Chapter 4 - Section 4.5.1). Yellow square/bar = Measured/predicted  $D_{par}$ ; blue circle/light blue bar = Measured/predicted AFT age; red diamond/magenta bar = measured/predicted MTL; green triangle/light green bar/dark green bar = measured/resampled observed/predicted AHe age.**

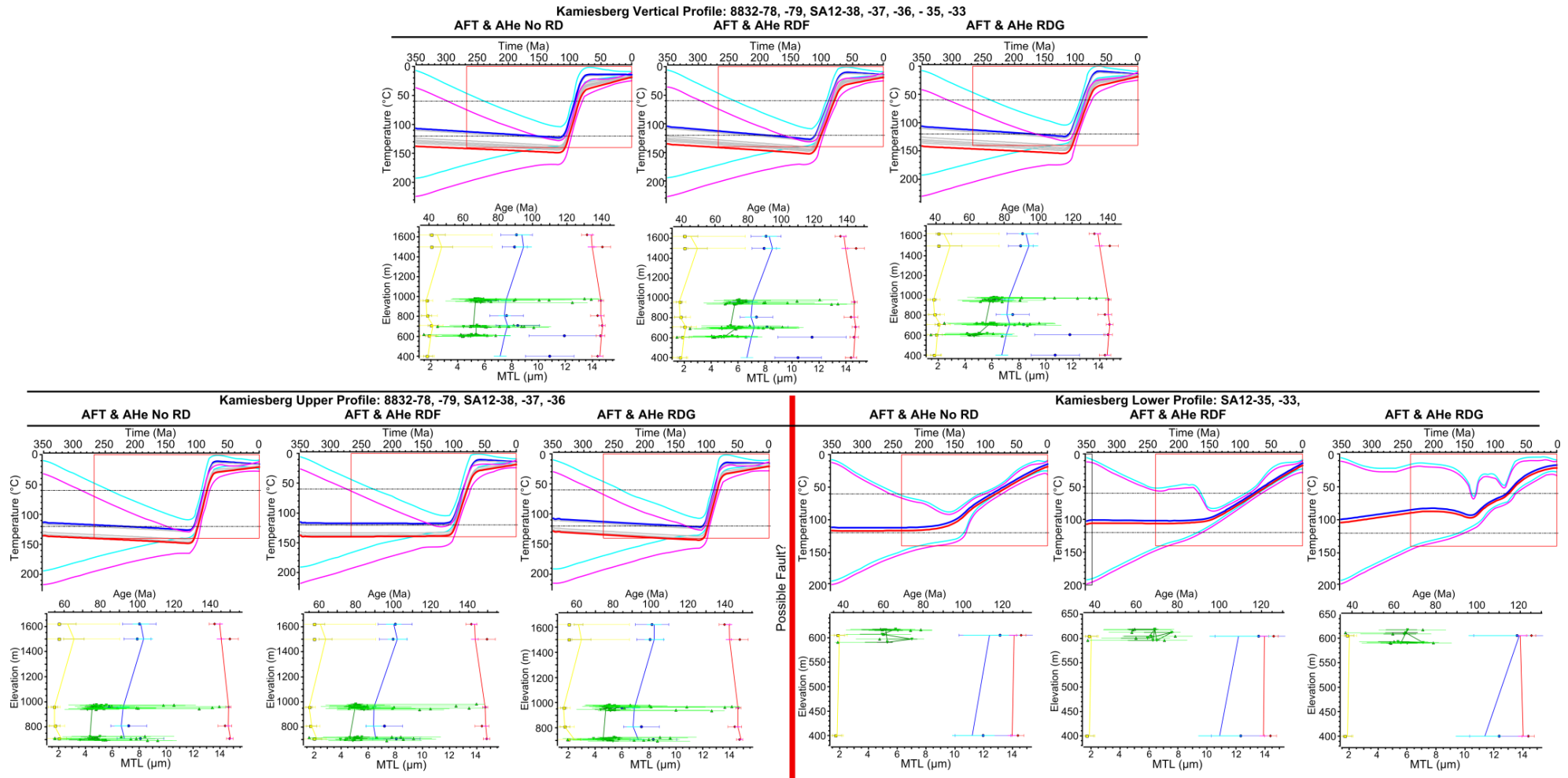
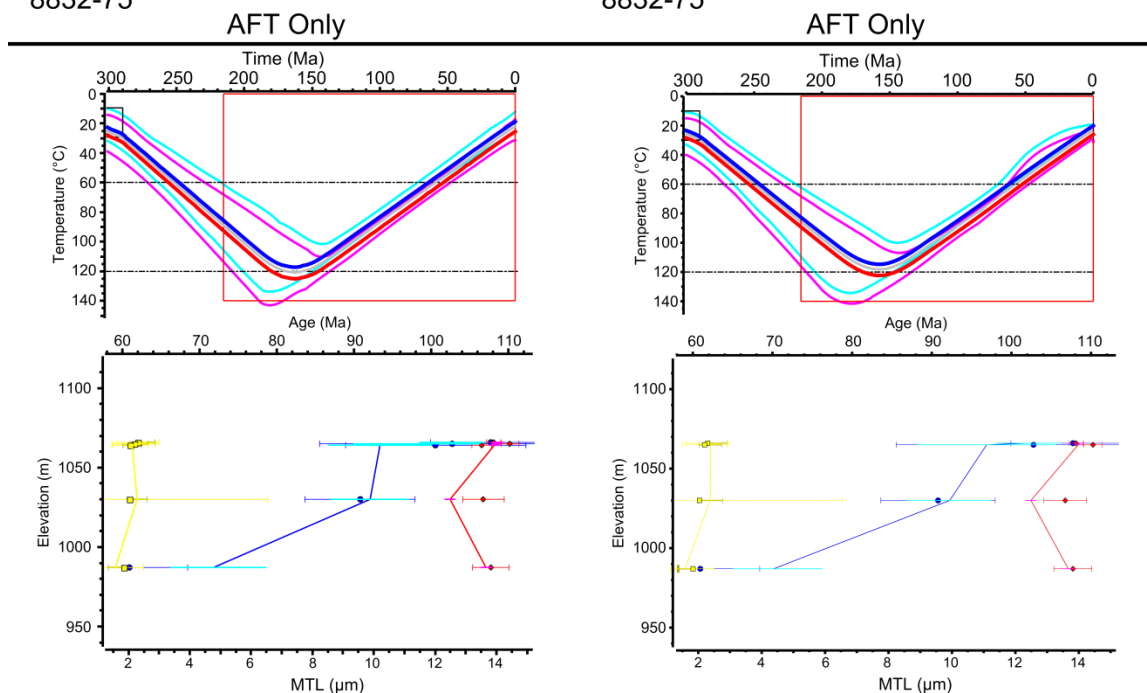


Figure 5-15: Kamiesberg profile thermal history models. Expected model of the top and bottom sample is represented by a thick blue and red line, respectively, with 95% credible intervals (cyan and magenta lines). Black box represents initial constraint on the model. Red box represents general ranges for prior (see Chapter 4 - Section 4.5.1). Yellow square/bar = Measured/predicted  $D_{par}$ ; blue circle/light blue bar = Measured/predicted AFT age; red diamond/magenta bar = measured/predicted MTL; green triangle/light green bar/dark green bar = measured/resampled observed/predicted AHe age.

A more appropriate vertical profile is available up the Kamiesberg Mountain along the eastern valley wall of Wilterhouts River, south of the town of Kamieskroon. This profile initially comprised of 7 outcrop samples covering 1220 m of elevation and separated by distances less than 10 km (N to S) and 5 km (E to W). Contrary to the expected relationship of AFT age and elevation, the oldest AFT ages in this profile are at the base. As expected these samples have the poorest data fit when all samples in the profile are modelled together (Fig. 5-15). To resolve this, the profile is split into (i) an upper profile consisting of AFT ages that are c. 90 Ma and (ii) a lower profile consisting of two samples with AFT ages of c. 115 Ma. A rapidly cooled, tightly constrained cooling event at c. 110 - 90 Ma is defined for the first profile while a slower cooling history initiating at c. 150 - 130 Ma is defined for the second. Modelling the second profile with radiation damage, after Gautheron et al. (2009), shows interesting differences to previous models of a similar type. In this model, maximum temperatures are predicted to be lower at the onset of cooling and two cooling events may be present: slow cooling from 130 - 80 Ma and then a slight increase in cooling rate from then until the Late Cenozoic.

An ENE-WSW transect from SA12-47 to SA12-27 covers close to 50 km and an elevation range of 987 - 1066 m (Fig. 5-16). SA12-47, -51 and -52 share similar AFT data and similar thermal histories: relatively slow cooling from c. 150 - 130 Ma. Samples 8832-75 and SA12-27 show cooling initiating at c. 100 Ma which is rapid and protracted, respectively. These two samples, however, have the lowest number of HCTs and therefore their TLD is poorly constrained. All samples were modelled together to test whether a common thermal history could satisfy the data set. A definitive constraint is imposed on this profile at  $300 \pm 10$  Ma,  $20 \pm 10$  C as SA12-27 is taken from a basement clast within the Permian dwyka group unit. A simple monotonic cooling history from elevated temperatures at c. 150 Ma to surface temperatures at present day is predicted. AFT age predictions are in good agreement with observed data. The data fit for the youngest AFT age (SA12-27) is poorest but still overlaps considerably within uncertainty levels. The MTLs are reproduced well by the model except for sample 8832-75. This sample however has relatively few HCTs ( $n = 39$ ) and no

NQ Plateau Profile: SA12-47, -51, -52, -27,  
8832-75NQ Plateau Sub-profile: SA12-51, -52, -27  
8832-75

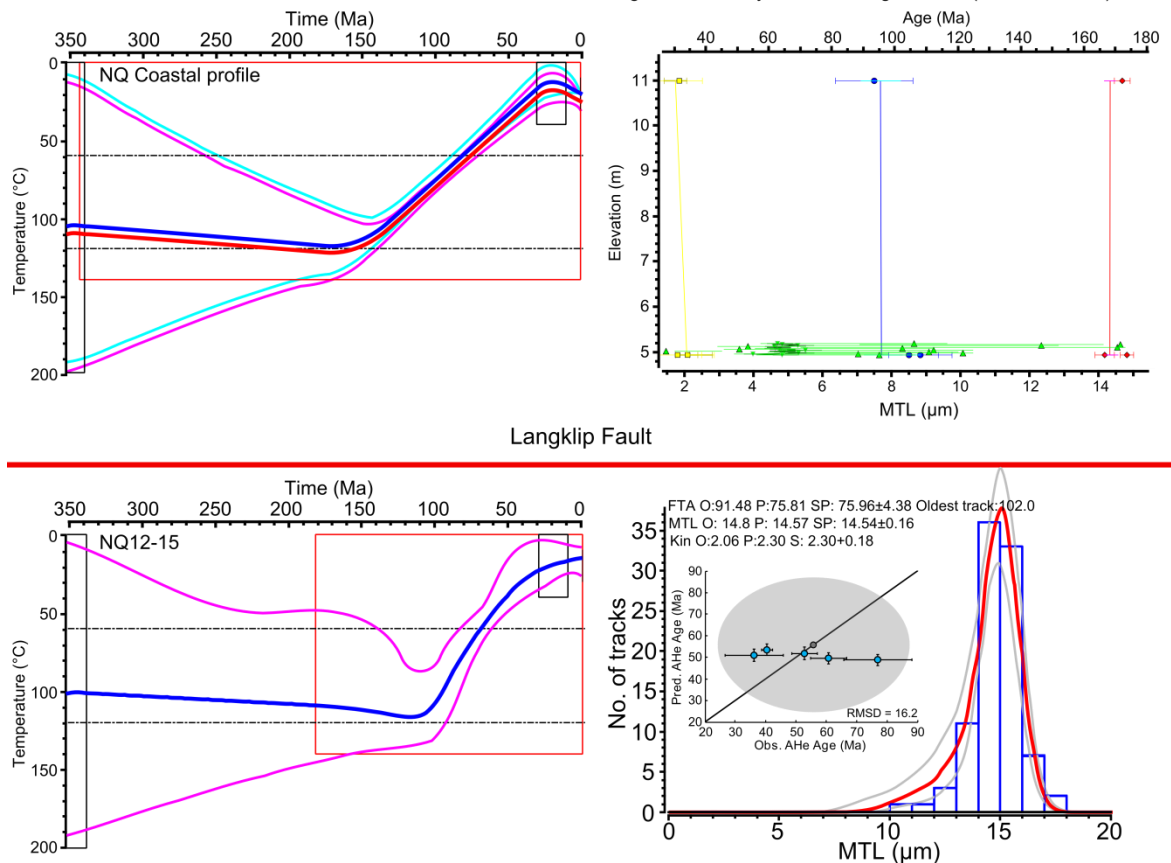
**Figure 5-16: Namaqualand Plateau thermal history models. Expected model of the top and bottom sample is represented by a thick blue and red line, respectively, with 95% credible intervals (cyan and magenta lines) Black box represents initial constraint on the model. Red box represents general ranges for prior (see Chapter 4 - Section 4.5.1). Yellow square/bar = Measured/predicted  $D_{par}$ ; blue circle/light blue bar = Measured/predicted AFT age; red diamond/magenta bar = measured/predicted MTL; green triangle/light green bar/dark green bar = measured/resampled observed/predicted AHe age.**

measured compositional parameter and therefore the measure MTL may not be a true representation of the true value. A sub-profile which excludes samples 8832-75 and SA12-47 is tested as these two samples are considerably further away from the other samples of the profile (c. 20 km) and are well in to the heavily faulted NQH. Excluding these samples does not have any great effect on the thermal history.

### 5.5.3.2 Speculative constraints

Independent geological constraints are limited across the study area. Across the NQH the only post-rift deposits are unconsolidated Neogene - Quaternary sands. More useful deposits are found along the coastal plain and coastal margin on the western side of the NQH and sedimentary deposits and crater-lake deposits on the plateau on the eastern side of the NQH. As such, there are few samples

NQ Coastal models with near surface constraint at  $20 \pm 10$  Ma: Fossil Miocene hominoid teeth - Alexander Bay fm. (Senut et al., 1997)  
Late Oligocene to Early Miocene Koignass fm. (De Beer, 2010).



**Figure 5-17: Thermal history models from the NQ coast with additional constraints. Upper model is the composite profile model from three coastal samples (NQ12-16,-17 & -18). Lower model is sample NQ12-15 which is also from the coastal region but separated from the main profile by the Langklip fault. Expected model is represented by a thick blue line with 95% credible intervals (magenta lines). Black box represents T-t constraints on the model. Red box represents general ranges for prior (see Chapter 4 - Section 4.5.1). Yellow square/bar = Measured/predicted  $D_{par}$ ; blue circle/light blue bar = Measured/predicted AFT age; red diamond/magenta bar = measured/predicted MTL; green triangle/light green bar/dark green bar = measured/resampled observed/predicted AHe age. Histograms represent the measured TLD; red line represents the predicted TLD with 95% credible intervals (grey curves).**

whose models can be independently constrained using direct lithological information.

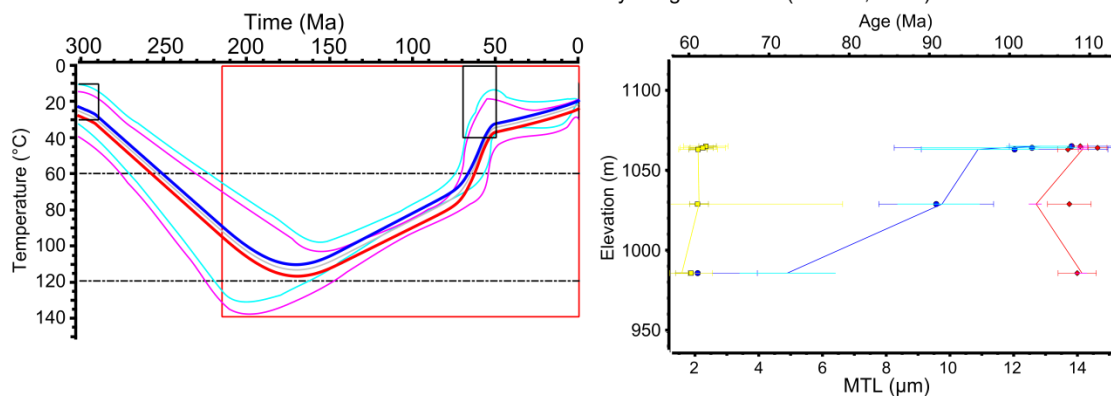
The cluster of samples collected at Hondeklip Bay can be constrained using fossil evidence in thin sedimentary formations which overlie the NMP rocks across the coastal plain (Fig. 5-17). Fossil hominoid teeth from the marine sand Alexander Bay formation assign an early Miocene age to the deposit (Senut et al., 1997). These overlie the calcified and silicified gravels and sandstones of the Koignass Formation which is presumed to have been deposited in a fluvial environment

during a Late Oligocene to Early Miocene marine regression (de Beer, 2010). Coastal samples can then be assigned an additional constraint of  $20\pm 10$  Ma,  $20\pm 20^\circ\text{C}$  to reflect near surface temperatures of the basement rock prior to deposition of these Cenozoic deposits. Although more speculative, as the outcrop is c. 20 km NE of the coastal samples, the De Toren formation is also presumed to be of Late Oligocene age due to the formation overlying the Early Cenozoic intrusions of the Biesiesfontein suite in the southern part of the study area (de Beer, 2010). Thermal models are tested, using this constraint, for the profile of coastal samples excluding NQ12-15 (Fig. 5-17).

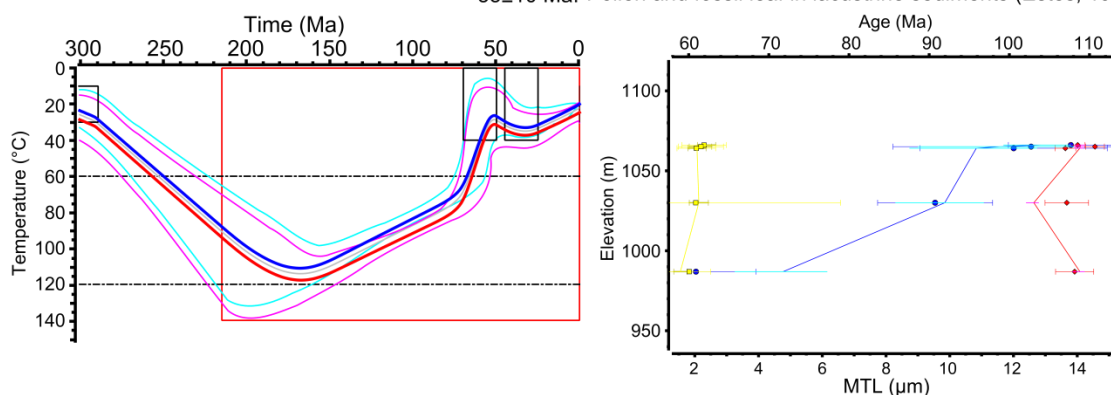
Bamford and Corbett (1994, 1995) and Bamford and Stevenson (2002) report the presence of fossilised wood discovered on the offshore continental shelf and onshore continental margin. The species of these woods are described as Lower Cretaceous in age and are suggested to have been initially deposited in continental clastic sediments and where then subject to rapid burial and silicification. Considerable reworking of the material prior to deposition on the continental shelf is attributed to Late Cretaceous erosion. Bamford and Stevenson (2002) argue for an extensive forested area over a low-lying coastal region in the Upper Cretaceous. Fossil hominoid teeth and fossil fish bones, also of Lower Miocene age, are found at Buffels Bank mine of the Buffels River (Senut et al., 1997). The sample JN3 is located in this region, however, the models currently satisfy near surface temperatures at this time and so forcing a constraint box is not required.

It has already been established that the NQ plateau profile has to begin with a surface constraint at c. 300 Ma. Late Mesozoic and Cenozoic constraints come from the sediments in and around the Vaalputs area and fossiliferous crater-lake sediments preserved in the Gamoep intrusive suite and in particular the Arnot pipe at Banke farm (Fig. 5-18). The Dasdap and Vaalputs sediments are proposed to be Late Cretaceous to Early Palaeocene in age. This is supported by palynological evidence dated at 71 to 64 Ma (Scholtz, 1985) and preservation of fossilised frogs and wood in clay deposits (Adamson, 1931; Haughton, 1931). A constraint box of  $60\pm 10$  Ma,  $20\pm 20^\circ\text{C}$  was therefore included for individual and profile models. The thermal histories show gentle cooling at near surface

NQ Plateau Profile with near surface constraint at  $60 \pm 10$  Ma: Dasdap and Vaalputs Sediments (Brandt et al., 2003; 2005)  
 Fossil frogs and wood in Arnot pipe crater lake sediments (Haughton, 1931; Adamson, 1931)  
 Palynological record (Scholtz, 1985)



NQ Plateau Profile with near surface constraint at  $60 \pm 10$  Ma: As above  
 $35 \pm 10$  Ma: Pollen and fossil leaf in lacustrine sediments (Estes, 1977)



**Figure 5-18: Namaqualand plateau profile thermal history models with additional constraints. Expected model is represented by a thick blue line with 95% credible intervals (magenta lines). Black box represents T-t constraints on the model. Red box represents general ranges for prior (see Chapter 4 - Section 4.5.1). Yellow square/bar = Measured/predicted  $D_{par}$ ; blue circle/light blue bar = Measured/predicted AFT age; red diamond/magenta bar = measured/predicted MTL; green triangle/light green bar/dark green bar = measured/resampled observed/predicted AHe age. Histograms represent the measured TLD; red line represents the predicted TLD with 95% credible intervals (grey curves).**

temperatures during the Cenozoic when the Cretaceous-Paleocene constraint is used.

Estes (1977) reported younger pollen and fossil leaf evidence from the same lacustrine sediments aged from the late Eocene to early Oligocene. A second constraint box of  $35 \pm 10$  Ma,  $20 \pm 20^\circ\text{C}$  is also included to reflect this. The profile thermal history shows progressive heating from surface temperatures to a maximum temperature just above c.  $110^\circ\text{C}$  at 160 - 170 Ma. By 150 Ma cooling has begun at a rate of c.  $0.45^\circ\text{C}/\text{Myr}$ . At c. 80 - 75 Ma cooling becomes enhanced and continues at a rate of c.  $8.25^\circ\text{C}/\text{Myr}$  until c. 55 Ma taking the thermal



history to near surface temperatures by the Late Cretaceous - Early Palaeocene. The thermal history passes through the later constraint box with the model showing minor reheating beforehand and progressive cooling after. The structure in the model at this time should be treated with caution because there is quite a lot of uncertainty in the models at this stage, the thermochronology data has very limited resolution at these low temperatures and the temperature variation since the Early Palaeocene is at most 15°C and therefore is relatively minor and may either not be real or may not be directly related to denudation. The most important aspect is how well this composite model fits the data. The fission track ages, kinetic parameter and most of the track length data are predicted very well. The poorest fit is with the MTL of sample 8832-75 where the MTL is predicted to be younger than observed. As stated above, this sample had a relatively small number of HCTs and therefore the true MTL could change with more measurements. A more conservative approach would be to exclude both this sample and SA12-47 from the profile as they are furthest away from the proposed constraints and reside in a valley in the NQH. Modelling only the samples adjacent to the Vaalputs basin, reproduces the same style of thermal history described above with a very good data fit.

#### **5.5.4 Summary of modelling results**

From the modelling performed three broad cooling episodes are identified: (i) 150 - 130 Ma; (ii) 110 - 90 Ma and (iii) 80 - 60 Ma. The first cooling episode is predominantly characterised by slow cooling. The second cooling episode however is recorded as a much more rapid event and is the dominant thermal history observed across the study area. Both of these cooling episodes are present in samples from the margin through the plateau and therefore suggest a more complex, multi-stage evolution of the margin as opposed to a simple retreat or degradation of a rifted margin escarpment. The third cooling event is harder to see in the study area and appears in an outcrop sample only once, in a location further south from the main dataset. The only other occurrence is a period of rapid cooling recorded when multiple samples from the interior plateau are modelled together and constrained by local geological information. Based on previous AFT studies in the region and recent structural investigations

(discussed below) it is suggested here that each of these time intervals represents enhanced denudation driven cooling with a spatial-temporal relationship controlled by reactivation of basement structures. The spatial relationship of this data and the implications for the timing and magnitude of denudation are discussed in the following section and for simplicity and consistency, “preferred” models will be chosen for samples or collections of samples. For all samples containing AHe data, the expected model including radiation damage after Gautheron et al. (2009) is chosen and where profile models have produced a thermal history consistent all the data from individual samples, this is preferred to single outcrop sample models. Where models have geological constraints, these are preferred to models without.

## **5.6 Temperature-time spatial relationships: Cooling and magnitudes of denudation**

### **5.6.1 Cooling**

The major phase of cooling recorded by each individual sample varies across the study area. The majority of samples ( $n = 33$ ) can be split into roughly equal groups that record cooling during either 150 - 130 Ma or 110 - 90 Ma (Fig. 5-19). 6 samples have an expected model which fall somewhere between these cooling episodes. However, the uncertainty on the timing of the onset of cooling usually results in these samples overlapping with the proposed cooling episodes. Moreover, many of these ambiguous samples are constrained only with AFT data and therefore the true nature of the thermal history may not be fully resolved. By c. 60 Ma thermal histories predict that most samples were residing at temperatures of c. 40 - 60°C or less implying that throughout the Cenozoic the amount denudation has been lower than c. 2 - 3 km for normal geothermal gradients.

### **5.6.2 Denudation**

The study area has been dissected into five transects: three which are approximately perpendicular to the coast and two which are approximately parallel to the coast. Coast perpendicular transects are 150 km in length and

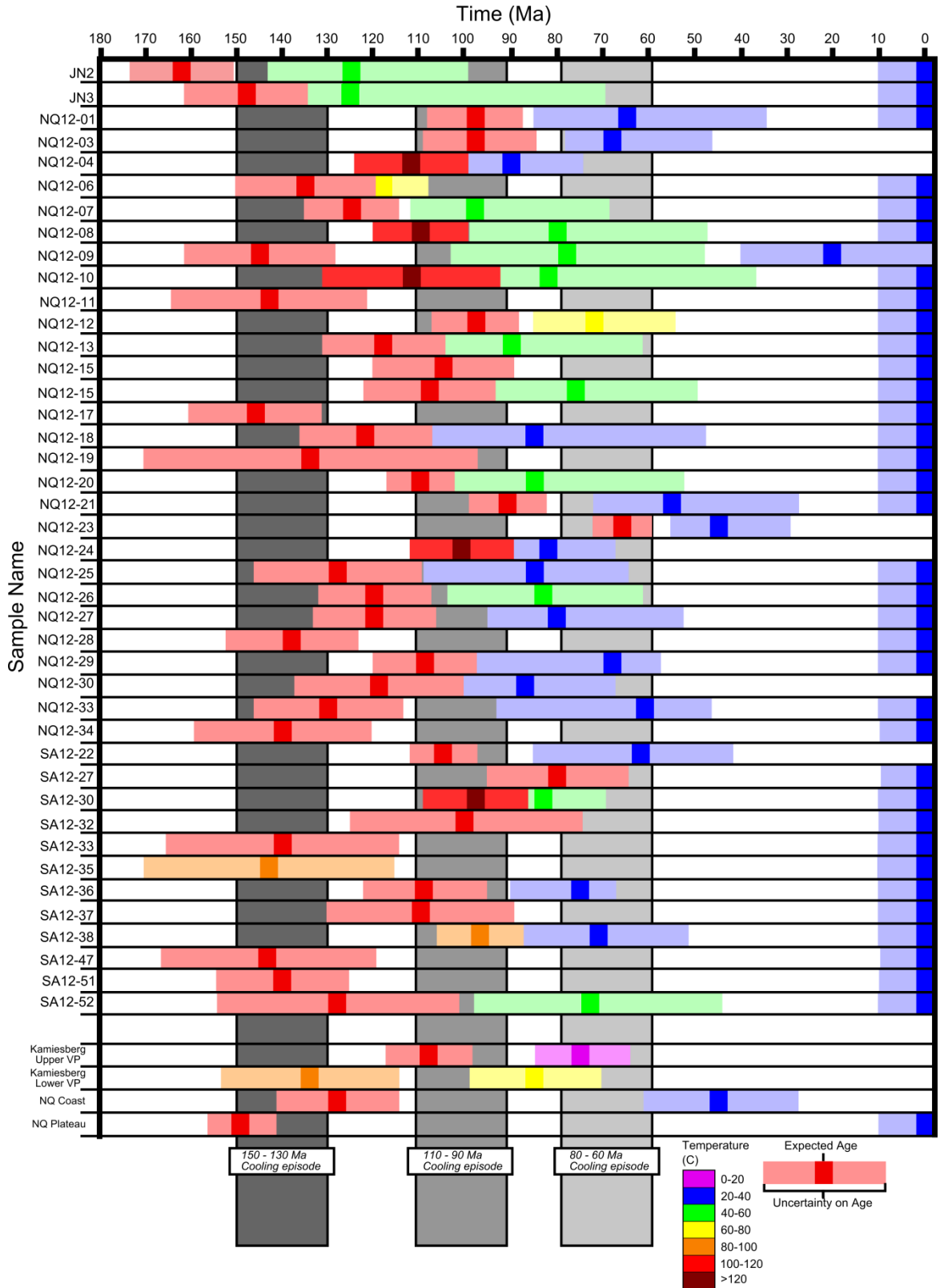
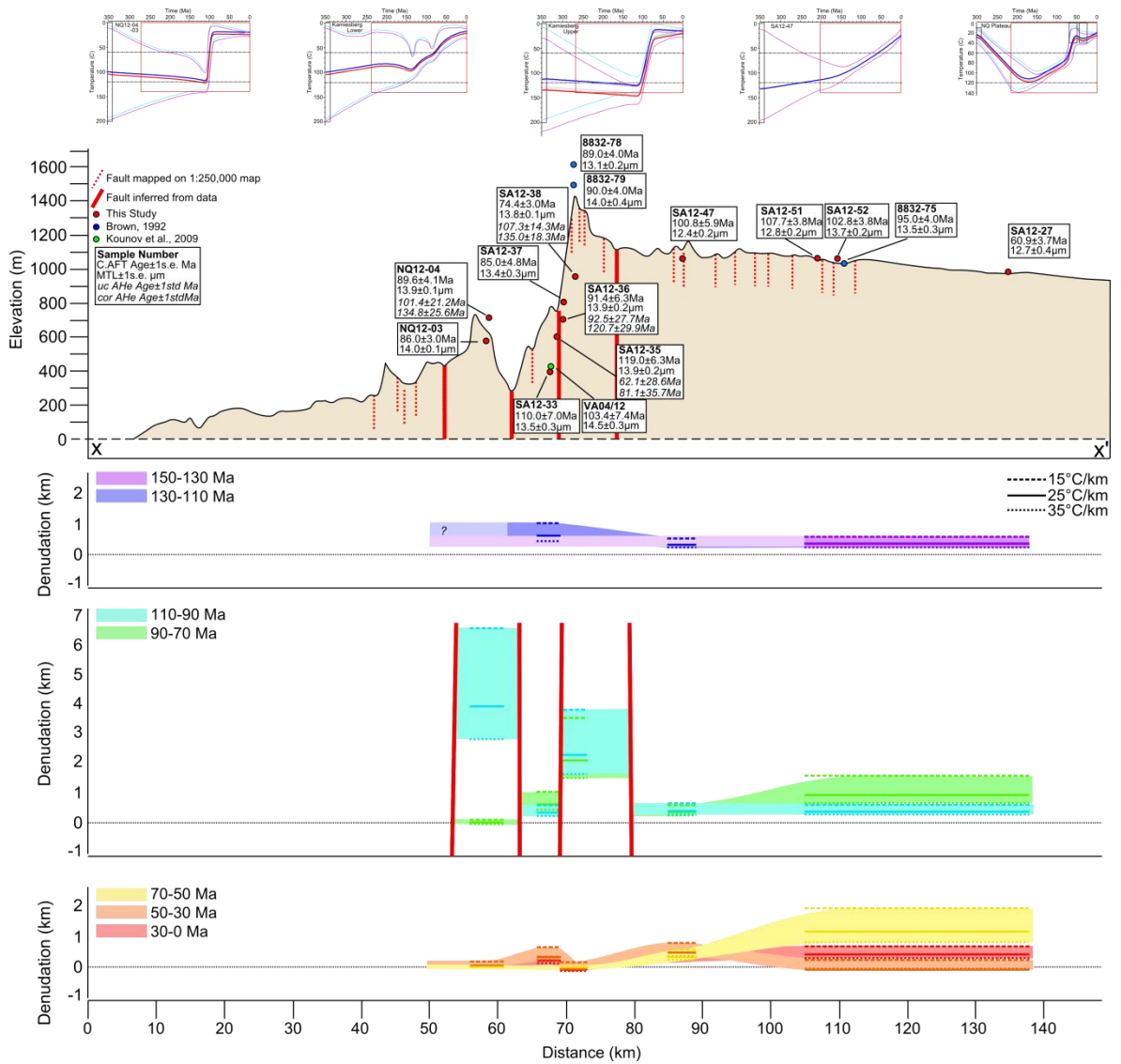


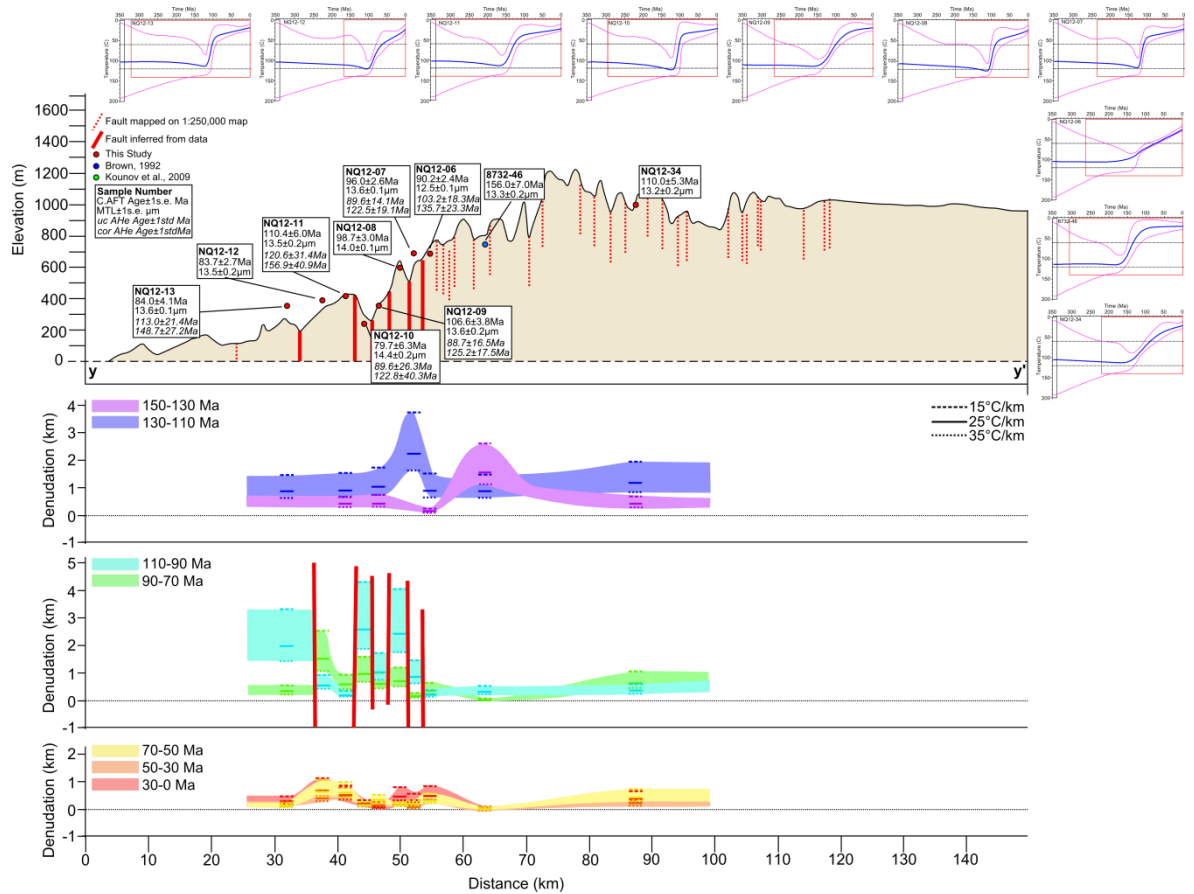
Figure 5-19: Plot represent the expected age and uncertainty (coloured bars) of key temperature points in each thermal history. These “key” points include the onset of cooling; changes in cooling rate causing inflections in the T-t path and the time when surface temperatures were reached. The colour of the bars is representative of the temperature of the thermal history at that time.



**Figure 5-20(a):** Section x-x' with predictions on magnitudes of denudation over time intervals since 150 Ma. Data within 7.5km either side of the section trace was projected at 90° onto the line of section. Denudation estimates are made directly from thermal history models generated by inverting data from this study and from Brown (1992). Denudation is estimate using three estimates of the geothermal gradient (15, 25, 35°C/km) with 25°C/km being the preferred estimate.

extend from the margin, through the NQH, to the interior plateau. Coast parallel transects are 90 km in length and cut through the high relief basement rocks of the NQH. For both transects data within 7.5 km either side of the line of section is projected at 90°. Simple calculations were made to calculate the amount of denudation required to drive cooling over distinct time intervals (Fig. 5-20):

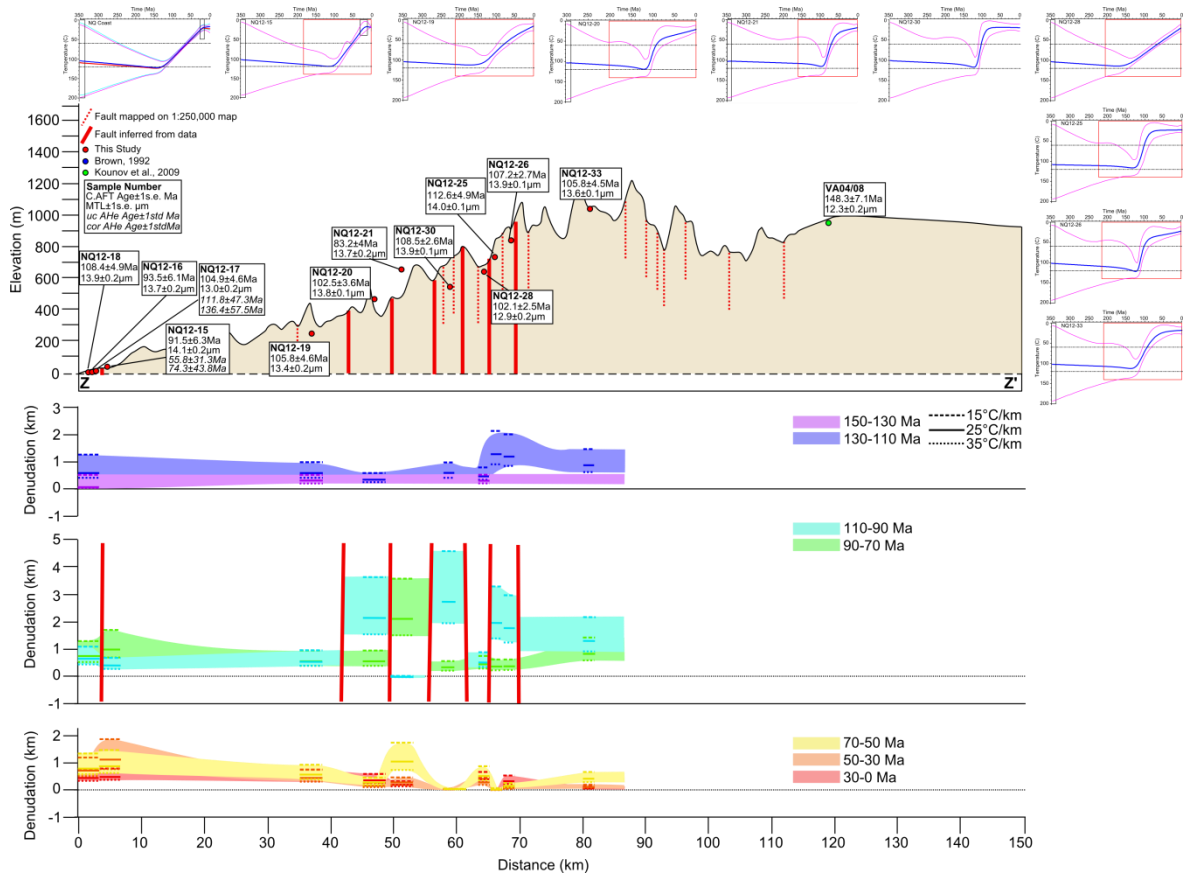
$$D_{t_0-t_1} = \frac{\Delta T_{t_0-t_1}}{G}$$



**Figure 5-20(b): Section y-y' with predictions on magnitudes of denudation over time intervals since 150 Ma.**

Where  $t_0$  and  $t_1$  = the beginning and end of the time interval;  $D$  = denudation (km);  $\Delta T$  = change in temperature over the time interval ( $^{\circ}\text{C}$ );  $G$  = geothermal gradient ( $^{\circ}\text{C}/\text{km}$ ).  $\Delta T$  is obtained graphically from the expected thermal history to avoid any assumptions of a specific closure temperature. The amount of denudation required to cool the sample from elevated temperatures to surface temperatures depends on the geothermal gradient of the region. Present day gradients across much of Southern Africa are c. 20 - 25  $^{\circ}\text{C}/\text{km}$  (Ballard and Pollack, 1987; Jones, 1987). Maintaining the conservative approach adopted during modelling, the upper limit of this temperature range (i.e. 25  $^{\circ}\text{C}/\text{km}$ ) was assumed to best represent the palaeogeothermal gradient. To reflect the uncertainty on the palaeogeothermal gradient, the amount of denudation for a particularly low (15  $^{\circ}\text{C}/\text{km}$ ) and high (35  $^{\circ}\text{C}/\text{km}$ ) gradient was also calculated.

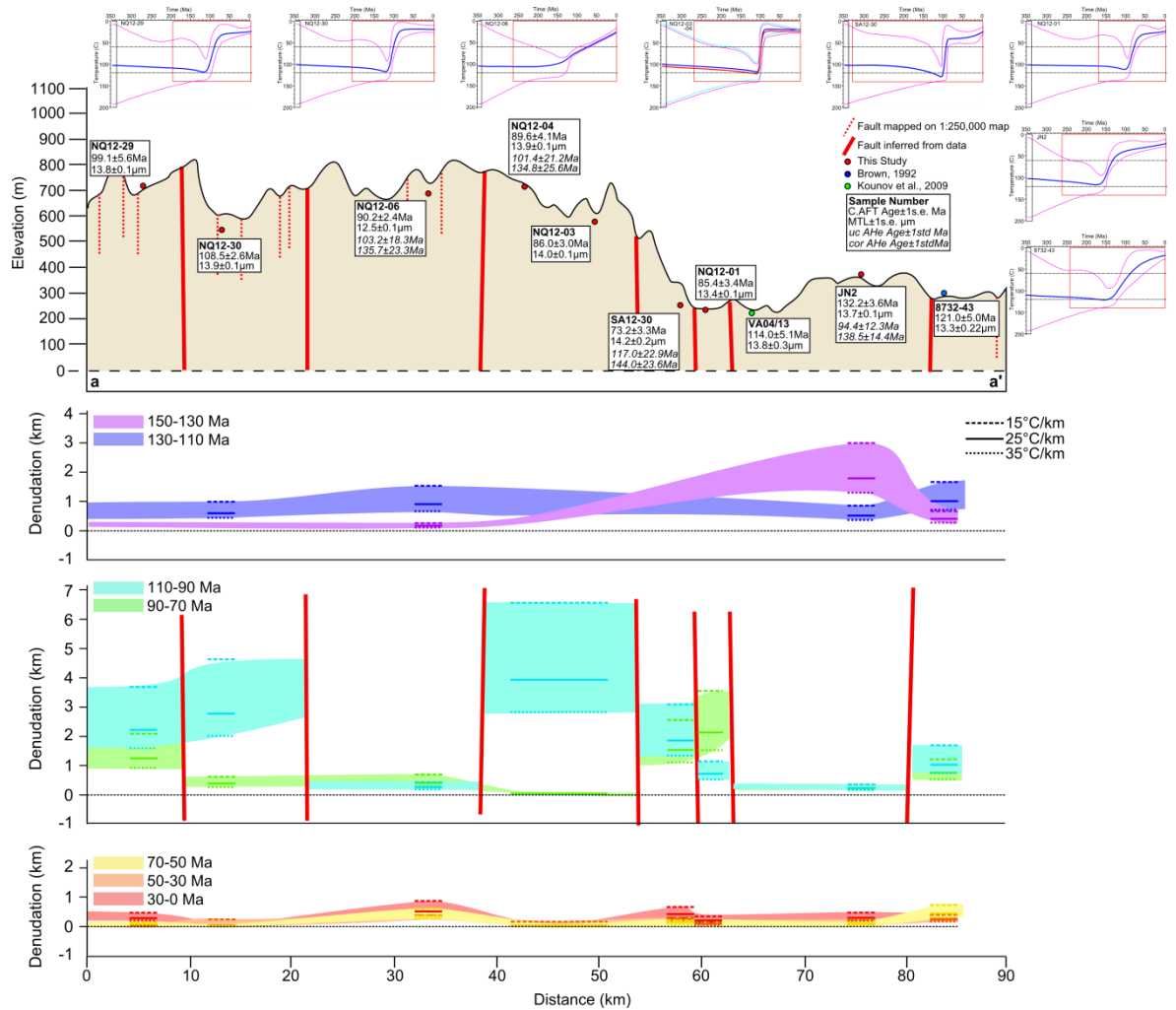
Cooling for many samples began during the 150 - 130 Ma interval, however, due to greater uncertainty towards the start of this interval, when temperatures



**Figure 5-20(c): Section z-z' with predictions on magnitudes of denudation over time intervals since 150 Ma.**

were at, or greater than, the base of the PAZ, the expected model may not truly represent the maximum temperature at 150 Ma. For samples which record major cooling during the 110 - 90 or 80 - 60 Ma cooling episodes, no estimate is made on earlier palaeotemperatures. Partly because of this, denudation during 150 - 130 Ma is a minimum estimate, typically up to 1 km or less. 8732-46 and JN2 however show greater denudation on the order of 1 - 3 km (Fig. 20b and 20d). These higher magnitudes of denudation may be a truer estimate on the amount of denudation at this time as there are tighter constraints on temperature or these samples may have been located in a region where denudation was more focused such as an up-thrown fault block or rift shoulder.

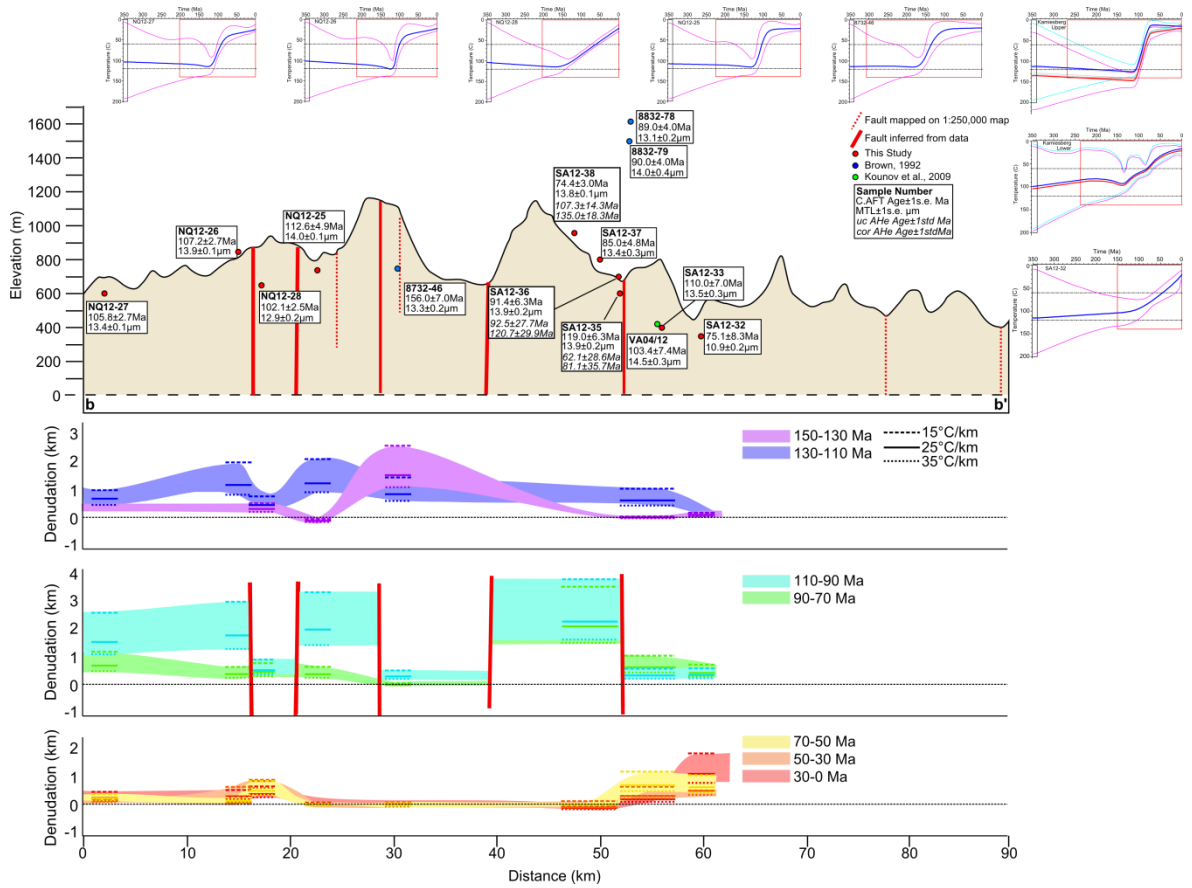
Through 130 - 110 Ma denudation of the margin is relatively uniform at with c. 1 - 3 km of material being removed with only minor regional variations. During this period it is proposed that much of the elevated topography and relief created during rifting was eroded away. During this period the margin resides in a period



**Figure 5-20(d): Section a-a' with predictions on magnitudes of denudation over time intervals since 150 Ma.**

of relative tectonic quiescence but may still have been experiencing minor local tectonic displacements and isostatic adjustments. Enhanced periods of denudation throughout the early Cretaceous are recorded from the margin well into the interior plateau.

The greatest levels of denudation are recorded during 110 - 90 Ma and are largely localised to the NQH region and, specifically, localised to individual fault blocks in the NQH. Locally in the NQH, the total denudation is 2 - 4 km over this time period. Major structural features appear to separate samples which record enhanced denudation from those which have cooled in response to the removal of minor (<1km) amounts of crustal section. It is suggested here that the differences in denudation observed across the NQH is the result of vertical



**Figure 5-20(e): Section b-b' with predictions on magnitudes of denudation over time intervals since 150 Ma.**

motion of discrete fault blocks driven by a combination of regional vertical uplift and an extensional stress regime. Samples recording enhanced denudation are up-thrown blocks being eroded more rapidly than the surrounding rock. Along the coastal plain, denudation recorded by samples is between 0.5 and 1 km (Fig. 20c) which is similar to that recorded in the down thrown blocks within the NQH. These lower levels of denudation are also recorded in samples from the low elevation, low relief, region south of the NQH (Fig. 20d) as well as low relief interior plateau. Although 0.5 - 1 km of denudation is comparatively low, over a 20 Myr timescale it is not negligible and reflects on going erosion of the entire margin. Variations in geothermal gradient may lessen the discrepancy in denudation recorded in samples from NQH. However, even if the higher estimate of the geothermal gradient (i.e. 35°C/km) is used for the samples recording enhanced denudation and the lower estimate of the geotherm (i.e. 15°C/km) is used for the lower denudation samples; there is still a significant discrepancy of c. 1 km in most circumstances.



The nature of the change in denudation as you move from the 110 - 90 Ma into the 90 - 70 Ma interval is difficult to resolve as the latter interval records denudation which is either higher, lower or approximately the same as the former interval. Sample NQ12-21 for example suggests c. 2 - 3km of denudation during this time whereas the NQ12-03 and NQ12-04 composite thermal history suggests that nearly 4km of section were removed during 110 - 90 Ma and then almost nothing since then. The reason for the ambiguity in the 90 - 70 Ma is likely due to one of, or a combination of, the following: (i) the initial denudation during 110 - 90 Ma cooled the sample sufficiently so that it cannot document later cooling the LTT record; (ii) structural reactivation combined with a pre-existing relief and variable lithology promotes a different erosion rates to occur across the margin prolonging the removal of 110 - 90 Ma topography; or (iii) Late Cretaceous compression reactivates appropriately orientated structures and drives another phase of uplift and denudation of fault blocks. If inversion has occurred in the Late Cretaceous it has not driven denudation to such an extent that rocks have been exhumed from beneath the PAZ. Instead inversion may have uplifted both blocks that were either heavily denuded or preserved during the 110 - 90 Ma cooling event and enhanced denudation persisted until the end of the Cretaceous. It is over this and the following time interval that the geological constraints imposed on the samples which reside on the plateau by the Dsdap and Vaalputs sediments and preserved crater-lake facies at Banke farm are particularly important. Without this constraint directing the thermal history to the surface at this time the composite thermal history would predict denudation amounts comparable with SA12-47; c. 0.5 km during each time interval throughout its entire history (c. 0.03 km/Myr). Including these constraints suggests that the plateau experienced just over 2 km of denudation from 90 - 50 Ma which is comparable with denudation occurring across certain fault blocks within the NQH.

In general, by 70 - 50 Ma, denudation has dramatically reduced across both the coastal plain and NQH. Apart from the example above and for sample NQ12-21, the amount of denudation predicted by thermal history models is less than 1 km and in many cases less than 500 m. As stated above by c. 60 - 50 Ma most of the samples are predicted to have resided at temperatures of 60°C or lower.

Therefore, there is limited resolution on the amount and nature of cooling through the Cenozoic, particularly if AHe data is absent or the available AHe data has high levels of eU and as such have high closure temperatures. Through 50 - 30 Ma and 30 - 0 Ma denudation is predicted to be less than c. 500 m. Local variations persist where denudation is predicted to be higher than this up to c. 1.1 km. If real these local variations may be caused by local river networks and the erosion of remnant Karoo or younger lithologies on an irregular relief however it should again be reinforced that this portion of the thermal history is poorly constrained.

### 5.6.3 Uncertainties in denudation estimates

Denudation models presented in Figure 5-20 are calculated using the expected thermal history model for three different geothermal gradients. The expected model lies within 95% credible intervals which can be treated as an uncertainty on the expected model. The uncertainty on the denudation calculation for Figure 5-20a is determined using the temperature of the upper 95% credible interval ( $T_{\text{Min}}$ ) and lower 95% credible interval ( $T_{\text{Max}}$ ) (Fig. 5-21). However, it must be remembered that the expected model and 95% credible intervals should be interpreted as a probability density function. As such, uncertainties which propagate into calculations of denudation should similarly be viewed in terms of probability centred on the amount of denudation calculated using the temperature estimated from the expected model ( $T_{\text{expected}}$ ). The upper uncertainty for each time interval was calculated using  $T_{\text{Max}}$  at the beginning of the designated time interval and  $T_{\text{Min}}$  at the end of the designated time interval reflecting the maximum temperature difference over the time interval. Similarly, the lower uncertainty was calculated using  $T_{\text{Min}}$  at the beginning of the designated time interval and  $T_{\text{Max}}$  at the end of the designated time interval reflecting the minimum temperature difference over the time interval. In certain occasions the minimum temperature difference is negative and suggests burial of the sample. The maximum temperature difference results in upper uncertainties which imply c. 5 km denudation recorded locally. The upper and lower extremes of these uncertainty levels are unlikely scenarios. As the uncertainty is calculated using the 95% limits the value of  $T_{\text{Max}}$  and  $T_{\text{min}}$  at a given

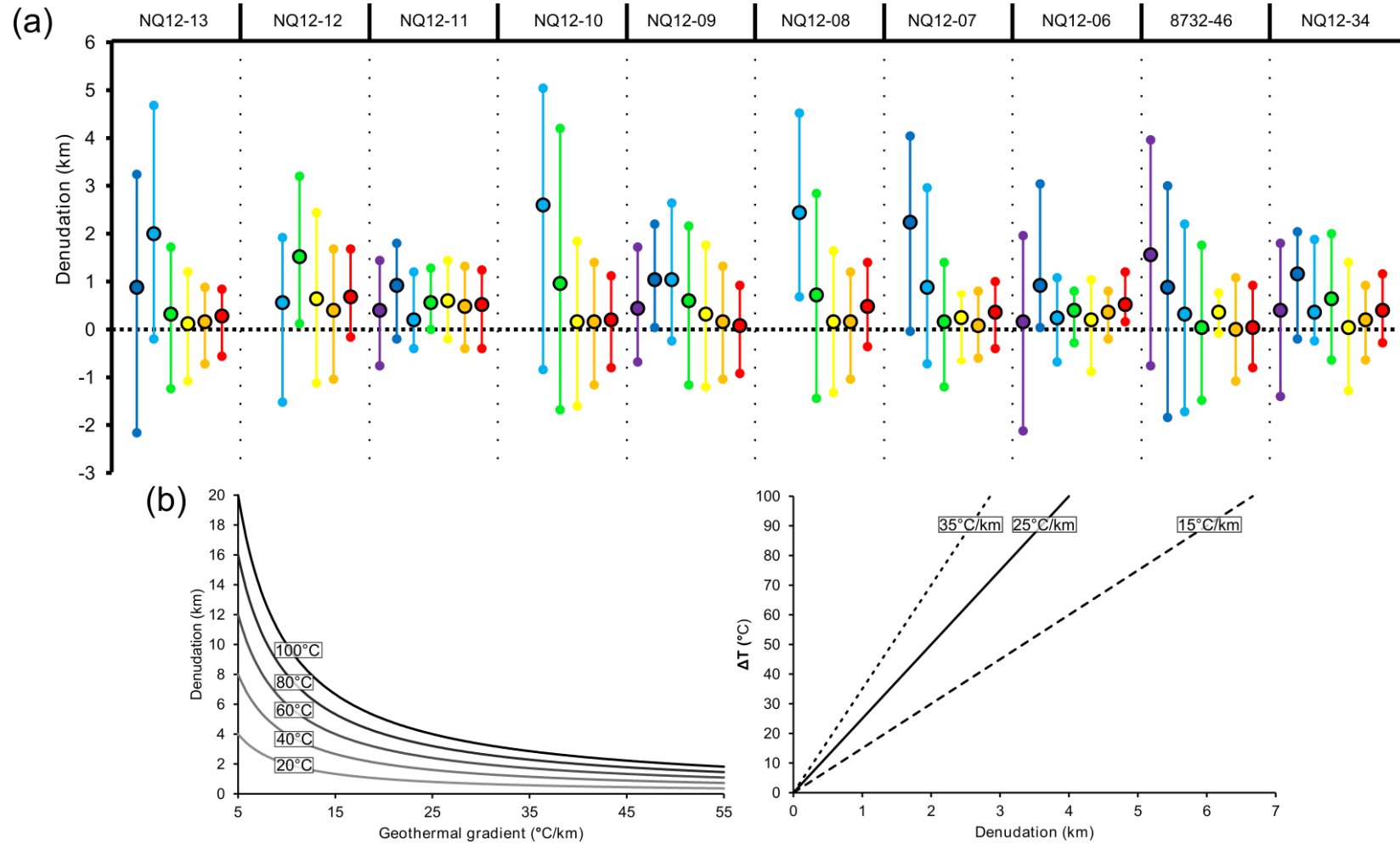


Figure 5-21: (a) Magnitudes of denudation for Section x-x' (see Figure 5-20a) with associated uncertainties for an assumed geothermal gradient of 25 °C/km. The colours of symbols and uncertainty bars represent the same time intervals used in Figure 5-20 and the same colour scheme is used here. (b) Plots showing the effect of geothermal gradient on estimates of denudation. Temperature values in left hand plot represent the change in temperature over a specific time interval in the samples thermal history. The manner of the transformation (non-linear) made for denudation estimates assuming an alternative geothermal gradient will also apply to the uncertainty derived from the expected thermal history.

time have a probability of 2.5%. Propagating these uncertainties through denudation calculations will result in the upper and lower denudation limits having a probability of <1%. Estimates of denudation are extremely sensitive to the geothermal gradient assumed (Fig. 5-21b). The influence of geothermal gradient on denudation estimates is non-linear and most significant for low geothermal gradients. This is unlikely to be the case in the study area as the basement rocks are particularly enriched in heat providing radiogenic elements (U, Th and K) (Andreoli et al., 2006). This has helped maintain moderate-high heat flow values across the Namaqualand Highlands (Jones, 1987; Andreoli et al., 2006). Propagating these uncertainties into the estimates of denudation will clearly result in a much larger range of possible denudation values. However, as stated above, these uncertainty ranges should be viewed in terms of their probability and therefore the upper and lower uncertainty for denudation amounts predicted using the 15°C/km and 35°C/km geothermal gradients will also c. 1%.

## **5.7 Discussion**

### **5.7.1 The Namaqualand continental margin low temperature thermochronology dataset**

Previous low temperature thermochronology studies in the Namaqualand region have been limited with only two studies generating AFT from outcrop samples (Brown, 1992; Kounov et al., 2009). Samples analysed by Brown (1992) were collected somewhat sporadically across the margin but have also been collected at a variety of elevations. Data from Kounov et al. (2009) consists of two transects across the margin extending onto the inland plateau. The contribution of data from this study helps to create an extremely detailed LTT database across this sector of the margin by improving the regional and local sample coverage as well as improving the temporal resolution by including AHe analysis.

The trend of data can be compared with the conceptual models of Gallagher and Brown (1999a) (see Chapter 3 - Section 3.6). The observed data does not agree with any of these models because young post rift ages extend far inland from the margin and abrupt age variation across the NQH region obscures any progressive

increase in ages with increasing distance across the margin. However, as discussed previously, the LTT age trend alone is not a good representation of the thermal history of the region. Looking at the trend in thermal history models across coast perpendicular transects (Fig. 5-20) it can be seen that there appear to be two general classes of models: (i) protracted to moderately quick cooling at c. 150 - 130 Ma and (ii) fairly rapid to very rapid cooling at c. 110 - 90 Ma. Interestingly the transition from one style of models to another is abrupt and coincides with prominent structural lineaments. The former event coincides nicely with the initiation of rifting between S. America and S. Africa (c. 165 - 130 Ma) and so is ascribed to the erosion of pre-existing topography due to incising rivers adjusting the new base level of the evolving Atlantic Ocean. The regional distribution of the younger event coupled with its apparent structural control and fast nature of the cooling recorded and lack of any other thermal influence (e.g. intrusions) supports a regional denudation event confined to uplifting fault blocks at this time.

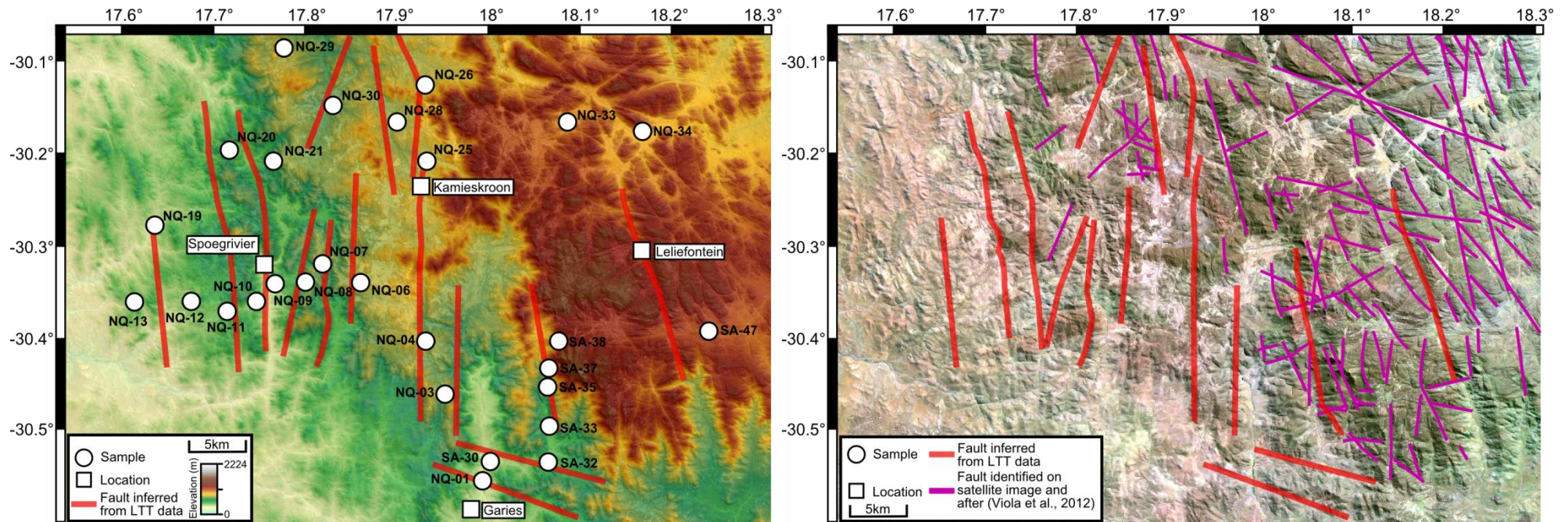
Data from earlier studies is largely consistent with the data presented here. AFT ages are generally Early - Late Cretaceous with moderate to long MTLs. The exceptions to this are one sample of Late Jurassic age recorded by Brown (1992) (8732-46) in the heart of the NQH and an Early Jurassic age recorded by Kounov et al. (2009) from their southern transect near to the town Calvinia. Kounov et al. (2009), propose that inverse modelling of their data supports a two stage thermal history across the margin. The major phase of cooling is ascribed to the Mid-Cretaceous (115 - 90 Ma) and is attributed to a tectonically induced period of enhanced denudation. Moreover, they suggest that discrete fault block reactivation during this time results in differential denudation to have occurred over major structures. The earlier event is driven by either rift-related tectonic denudation or thermal relaxation of the surface following widespread Karoo magmatism at c. 180 Ma (Jourdan et al., 2005). Kounov et al. (2009) give precedence to the latter mechanism as this cooling episode is only recorded in samples from the plateau region of the southern transect which were collected in the Karoo basin. However, data from Brown (1992), and data presented here clearly have preserved a record of Early Cretaceous cooling. The different datasets therefore do not contradict each other and in fact help to validate and

refine one another. The latest Jurassic - Early Cretaceous cooling at c. 160 - 130 Ma is recorded regionally but preserved only locally. The discrete, structurally controlled, nature of the second cooling event from 115 - 90 Ma across the margin is somewhat poorly constrained by Kounov et al. (2009), due to the uncertainty in their fission track data and uncertainties in models. However, the preservation of the older cooling event across the margin adjacent to samples recording younger, rapid cooling helps to support this hypothesis.

Kounov et al. (2009), limit Cenozoic denudation to less than 2 - 3 km however acknowledge that the AFT analysis does not have the temperature sensitivity to resolve this part of the thermal history. Under normal circumstances AHe would provide constraints over this unresolved temperature range. However, due to the effects of radiation damage and grain size, particularly in old, U and Th rich samples, the temperature sensitivity of the AHe system (i.e. PRZ) may be elevated above normal conditions. Despite this the modelling presented here does not support any Cenozoic cooling greater than 2 - 3 km and in many models limit denudation to less than 1km. This observation agrees with cosmogenic nuclide analysis in Calvinia (Kounov et al., 2007) which reports a decrease in denudation rate by an order of magnitude during the Cenozoic relative to the Cretaceous.

### **5.7.2 The structural history of the Namaqualand Highlands**

The structural evolution of the Namaqualand sector of the South Atlantic continental is complex and poorly understood (Andreoli et al., 2009). Understanding the structural evolution of the margin from the initiation of lithospheric extension during rifting to the present day is crucial in further developing our understanding of the geomorphic evolution of continental margins. Major pre-rift tectonic events include the Kibran Orogeny (c. 1000 Ma) and the Pan-African Orogeny (c. 600 - 480 Ma) (Tankard et al., 2009). Deformation associated with these events helped to install much of the pre-existing structural grain in both Namaqualand and in the Cape Fold Belt (Viola et al., 2012). These ancient fractures will likely provide sites of pre-existing weakness in the lithosphere that accommodate deformation during later



**Figure 5-22:** Left panel shows a DEM of the NQH draped over a Landsat ETM+ RGB:321 satellite image. Faults marked on this map are directly related to faults drawn on transects from Figure 5-20 and mark the abrupt transition between regions of enhanced and subdued denudation during the Mid-Late Cretaceous. Right panel shows a Landsat ETM+ RGB:742 satellite image which highlights the relief variation of the region, location of sediment filled valley floors and subtle changes in basement lithology. The same faults from the left panel are drawn on this map as well as fault lineaments identified on the satellite image and after Viola et al., (2012).

tectonic events with or without the creation of new fractures (e.g. Sykes, 1978; Daly et al., 1989; Saintot et al., 2011; Viola et al., 2012). Unfortunately, due to the longevity of the margin and lack of stratigraphic information preserved unravelling the structural history has proved difficult.

Recent work by Viola et al. (2012) has attempted to piece together the fragmented structural history recorded in the Namaqualand basement terrain by utilising remote sensing techniques to identify major structural lineaments combined with a detailed field based analysis of brittle fault structures (Fig. 5-22). In this way, Viola et al. (2012), advocate that evidence for ten distinct structural deformation events can be found in the Namaqualand basement. However, some of these deformation events are tentative and their age poorly constrained. In some cases cross-cutting relationships, used to constrain the relative age of deformation, implies active structures which are sub-parallel to the orientation of maximum stress at that time.

The earliest post-rift (or syn-rift) palaeo-stress tensor identified in the Namaqualand basement is suggested to have been produced by sub-horizontal extension orientated NE-SW and causing reactivation of older vertical faults (Viola et al., 2012). This phase of extension is assigned to the initiation of rifting and opening of the Atlantic due to the coherence of the orientation of extension and the perpendicular orientation of major Early Cretaceous dyke swarms (Reid and Rex, 1994; Will and Frimmel, 2013). Activation of pre-existing lines of structural weakness is in agreement with models of fault propagation during rifting (e.g. Ziegler and Cloetingh, 2004; Autin et al., 2013; Corti et al., 2013) with the majority of extension being accommodated on faults in the offshore domain (Lundin and Doré, 2002; Paton et al., 2007; de Vera et al., 2010). Major extensional deformation across this sector of the margin at this time may have been limited due to its distant position relative to the rift zone, however recent geodynamic models have shown that deformation may occur at large distances away from the main rift zone (Huisman and Beaumont, 2008, 2011).

The second post-rift palaeo tensor is again relatively poorly constrained but indicates E-W extension (Viola et al., 2012). It is this extension that is proposed



to coincide with the major period of mid-Cretaceous tectonic denudation as advocated by Kounov et al. (2009), this work and in other published work (e.g. Brown et al., 1990; Tinker et al., 2008a; Flowers and Schone, 2010; Stanley et al., 2013). These two periods of extension are supported by palaeo-stress analysis in NW Namibia where ENE-WSW and SW-NE extension is suggested to have prevailed during rifting and Mid - Late Cretaceous, respectively (Salomon et al., 2014). Thermal histories presented here are consistent with considerable denudation driven unloading of the continental margin which may have induced considerable flexure of the margin (e.g. Redfield et al., 2005; Dautheil et al., 2013) and contributed to coast perpendicular extension (Salomon et al., 2014).

Although post-rift lithologies across the Namaqualand margin are extremely rare their occurrence in the Vaalputs region inland of the Namaqualand Highlands provides important constraints for the structural history over Late Cretaceous and Cenozoic (Fig. 5-23). Fault-slip structures extend into the silicified and Kaolinitised weathering profiles of the Late Cretaceous Dasdap alluvial fan sediments meaning that they post-date rift related deformation (Brandt et al., 2003, 2005; Viola et al., 2012). These structural data record both compression and extension and can be correlated with palaeo stress tensors from the wider basement terrain which did not correlate with previous deformation events (Viola et al., 2012). This is suggested to be evidence of post-rift fault reactivation of ancient or syn-rift structures (Brandt et al., 2003, 2005; Viola et al., 2012). Late Cretaceous - Cenozoic compression is thought to have occurred regionally in two short lived episodes at c. 85 - 83 Ma and 69 - 65 Ma with an intervening period of renewed extension (Viola et al., 2012). The compressional episodes are recorded in the silicified weathering profiles that cap the Dasdap sediments as well as in the volcanic breccias preserved at the Gamoep melilite pipe (77 - 54 Ma; Phillips et al., 2000).

Identifying cooling episodes coincident with late and post-Cretaceous structural events is difficult but certain samples with young fission track ages and moderately long track lengths could have thermal histories that were affected by Late Cretaceous - Cenozoic cooling. However, since the earlier Mid-Cretaceous episode appears to have been regionally extensive with large

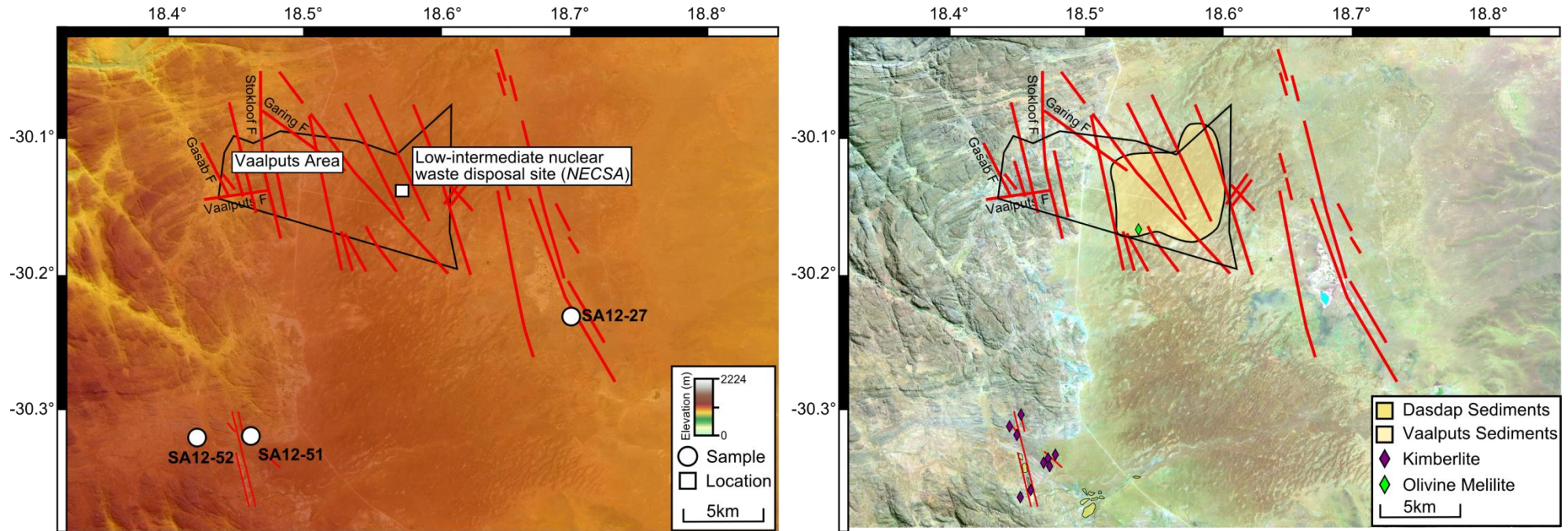


Figure 5-23: Left panel shows a DEM of the Namaqualand plateau region draped over a Landsat ETM+ RGB:321 satellite image. Faults marked on this map are drawn after Brandt et al., (2003 and 2005) The black polygon defines the region of the Vaalputs area owned by the South African Nuclear Energy Corporation (NECSA) for the disposal of low-intermediate nuclear waste disposal. Right panel shows a Landsat ETM+ RGB:742 satellite image which highlights the relief variation of the region, location of sediment filled valley floors and changes in lithology. The Dasdap sediments are identified as bluish-white sediments at the periphery of the NQH on the satellite image (Brandt et al., 2005).

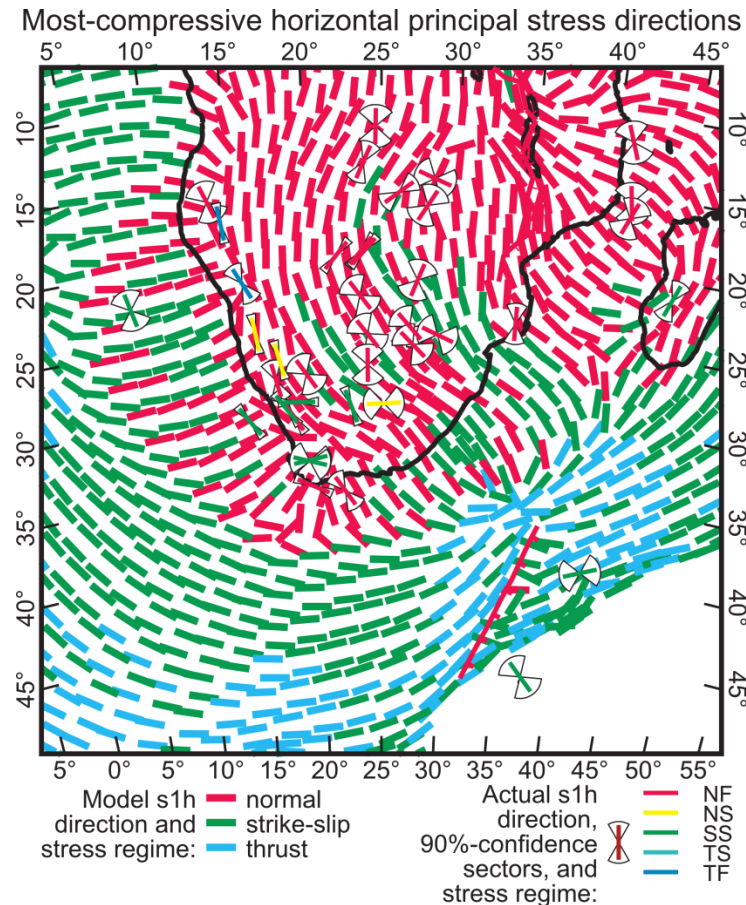
magnitudes of denudation, younger events may be beyond the resolution of the AFT and AHe approaches. The orientation of  $\sigma_1$  during the first post-rift compression event is believed to be NW to SE rotating through to E-W. Subsequent extension and the second phase of compression are orientated NE-SW causing NW-SE orientated normal faults to become reactivated and/or inverted. Santonian - Maastrichtian events are linked to continent wide episodes of compression and extension. The former is recorded along the Tethyan margin in North Africa where sedimentary basins have been folded and inverted (Guiraud and Bosworth, 1997). Extension is associated with rifting along the northern Atlantic and Indian Ocean margins recorded in renewed subsidence of sedimentary basins and the occurrence of magmatism at this time (Guiraud and Bosworth, 1997). The Late Maastrichtian - early Cenozoic episode of compression is observed in thrusting along Pan-African shear zones along the Damara Belt in central Namibia. This is recorded in fission track data across the region (e.g. Raab et al., 2002) and is discussed more in Chapter 6. The expression of Late Cretaceous - Cenozoic compression is still somewhat enigmatic as palaeostress data from NW Namibia fails to document any clear evidence (Salomon et al., 2014). This is contrary to the conclusions of Viola et al. (2012), Andreoli et al. (2009) and Raab et al. (2002) that relate compression during the Santonian and Late Maastrichtian to far-field compression tectonics in North and Central Africa. Local variations may therefore exist within the wider regional, or continental, stress regime; the deformation experienced across the margin will then be significantly controlled by the orientation of basement structures relative to this stress field. Moreover, the interplay between the flexural response of the lithosphere to unloading of the margin during erosion and loading during sedimentation may enhance extensional stresses during the post-rift phase.

Evidence for neotectonic activity has been identified along the Namibian margin, (White et al., 2009) southwest African margin (Andreoli et al., 1996; Brandt et al., 2005; de Beer, 2012) and in the adjacent offshore Atlantic basins (Viola et al., 2005). The alignment of offshore mud volcanoes and interpretation of seismic profiles through the Orange Basin identified NNW-SSE steep faults that propagated downwards to older (syn-rift) listric faults. Palaeoseismic investigations have identified neotectonic activity in across the Vaalputs region

(Andreoli et al., 1996) which has subsequently been supported by field based observations in mine trenches both at Vaalputs (Brandt et al., 2005) and across the Langklip Fault at Hondeklip Bay (de Beer, 2012). Moreover, it is suggested that under the present day stress regime the frequency of seismic events is increasing over time (Andreoli et al., 2009). While neotectonic events may not have induced the levels of denudation during the Late Cenozoic required to become recorded in LTT data they are significant as they may induce local variations in the geomorphic development of the margin and allow us to understand the current stress field and how this has changed over time.

The present day stress field across the Namaqualand region is referred to in literature as the Wegener Stress Anomaly (WSA) (Andreoli et al., 1996, 2006; Viola et al., 2005, 2012; Brandt et al., 2005; Bird et al., 2006; Kounov et al., 2009). This large regional stress field ( $\geq 2 \times 10^6 \text{ km}^2$ ) is characterised by a NW-SE/NNW-SSE orientation of horizontal principal compressive stress which has been attributed to by the resistance of the strong lithosphere of the African plate against the rotation of the Somalia plate at the opening East African rift (Bird et al., 2006). Alternative explanations include ridge-push from the developing South West Indian Ridge (Viola et al., 2005). Andreoli et al. (2009) propose a model where by the WSA was established during the Mid-Cretaceous but rotated to a NNE-SSW orientation throughout most of the Cenozoic before becoming established in its current orientation in the Pliocene-Pleistocene. Spatially and temporally complex uplift events during the rotation of the stress field are proposed; with different styles of faulting occurring on steep, sub-vertical, structures, forming small highland terrains (Andreoli et al., 2009).

Finite element modelling by Bird et al. (2006) incorporating rheological and density moment (density moment = the integral of density, over the thickness of the lithosphere, multiplied by elevation; Turcotte and Schubert, 2002) variations across Africa characterised the continental stress field and reproduced the WSA anomaly along the western margin. Through this process they observe that the NW-SE orientation of compressive horizontal stress is, in many places, actually induced by NE-SW extension (Fig. 5-24). The establishment of the WSA stress field in the Mid-Cretaceous would contribute to the period of discrete fault block



**Figure 5-24: Most compressive horizontal principal stress directions from as predicted by Bird et al. (2006). Stress field if dominated by effects of relative plate rotation where there is a strong resistance to the relative rotation between the Somalia and Africa plates. NF = Normal faulting; NS = Normal – strike-slip faulting; SS = Strike-slip faulting; TS = Strike-slip – Thrust faulting; TF = Thrust faulting. Intraplate indicators of stress regime and azimuth of the most compressive horizontal principal stress (Actual s1h) are from the World Stress Map (Reinecker et al., 2004).**

displacement during regional margin uplift proposed here. Later compression during the rotation of the regional stress field in the Late Cretaceous/Cenozoic may have failed to invert major structures due to their orientation to the stress field or induce only minor reverse movement on steep vertical faults with overall net-extension still prevailing (e.g. Holford et al., 2014). The development of post-rift relief during the Mid - Late Cretaceous due to structural processes associated with the WSA is referred to as the Wegener-Type Orogeny by Andreoli et al. (2009). However, the exact structural processes responsible and the location of faults which accommodated major deformation are still unknown.

## 5.8 Summary and Conclusions

The data presented here does not conform to previous conceptual models of escarpment evolution at Atlantic or “passive” continental margins. It contradicts traditional models as (i) there is no trend in AFT ages across the coastal region reflecting the progressive retreat or downwearing of a rift related escarpment and (ii) exceedingly young AFT ages which post-date rifting by as much as 70 Ma persist across the high relief escarpment zone and, crucially, onto the elevated plateau. By integrating AFT age and track length data with a complex but plentiful AHe data set robust thermal histories are produced and estimates of denudation can be made. In this way a major period of enhanced denudation during the post-rift phase is identified and attributed to an episode or episodes of structural reactivation.

A more appropriate model for the evolution of the continental margin at Namaqualand is required. It is proposed here that regional uplift during lithospheric extension at the beginning of rifting was associated with prolonged faulting far from major zone of rifting. This resulted in an elevated landscape with a series of escarpments or fault scarps which were progressively eroded away during the Early Cretaceous. In the Mid - Late Cretaceous (c. 110 - 90 Ma), a combination of long-wavelength uplift and horizontal extensional stresses induced a regional period of uplift which was manifested across Namaqualand as a series of vertical motions across reactivated basement structures. This differential uplift resulted in some samples being exhumed rapidly from temperatures hotter than the base of the PAZ while others continued to cool through lower temperatures and thus retained a record of the earlier denudation event. The mechanism behind this deformation event could be a combination of lateral flow of the upper mantle and flexure of the margin due to sediment loading inducing or enhancing regional horizontal extension of a brittle crust. Mantle driven dynamic uplift and isostatic adjustments responding to erosion may have provided an additional vertical component to the evolution of the margin during the Cretaceous. A period of compression during the Late Cretaceous is less well-defined across Namaqualand but has been advocated by previous structural analysis. If there has been uplift driven by compression it has

been relatively minor so that denudation has not exhumed more rock from elevated temperatures. However, compression may have helped to maintain enhanced denudation through to the end of the Cretaceous. This model agrees with previous work which supports minor denudation through the Cenozoic however it leaves several hundreds of metres and possibly 1 km of crust that could have been removed, at least locally, during the Cenozoic.

# CHAPTER 6

## INTRACONTINENTAL DEFORMATION OF THE SOUTH AFRICAN PLATEAU

### 6.1 Introduction

A defining morphological feature of high elevation continental margins is an elevated, low relief interior plateau. These continental plateaus have long been considered as “stable” geological regions that have experienced limited deformation over long periods of time. Recent insights from geodynamical models, however, imply that vertical stresses imposed at the base of the lithosphere by the vertical component of mantle flow may induce dynamic uplift (or subsidence for down-welling mantle) of the interior plateau (e.g. Gurnis et al., 2000; Moucha et al., 2008; Braun, 2010; Forte et al., 2010a; Flament et al., 2013). In addition to this, thermo-mechanical models simulating the interaction between mantle convection and the overlying lithosphere suggest that brittle deformation of the upper crust at short-wavelength scales may occur during long wavelength, plume induced uplift of the lithosphere (e.g. Burov and Cloetingh, 2009; Guillou-Frottier et al., 2012; Cloetingh et al., 2013).

The geology of continental interiors is often dominated by old Archean - Palaeoproterozoic cratons surrounded by younger basement rocks, and this is certainly the case in southern Africa (Tankard et al., 2009). These younger regions are characterised by a strong tectonic fabric which developed during early accretion of older cratons (Jacobs et al., 1993; Karlstrom and Humphreys, 1998; Zhao et al., 2001). The southwest corner of the Kaapvaal craton and its boundary with the Namaqua mobile belt represents such a tectonic setting with prominent NW-SE trending thrust faults and shear zones defining the craton boundary. Recent work has shown that due to thermal, compositional and structural contrasts across the craton margin, regional stresses and/or mantle



instabilities may become focused at the craton margin and induce intraplate deformation (Lenardic et al., 2000, 2003; Guillou-Frottier et al., 2012).

This study provides a new suite of apatite fission track and apatite (U-Th-Sm)/He data from the Bushmanland Plateau across the structural zone defining the margin of the Archean Kaapvaal craton. Using the Bayesian transdimensional approach to thermal history inversion, as described previously (see Chapter 4 - Section 4.5), temperature-time (T-t) cooling paths are obtained for each of the analysed samples. The spatial and temporal relationship of the thermal histories is used to derive magnitudes of denudation and assess the timing and nature of intracontinental deformation across this region of the South African plateau.

## **6.2 Local Geology**

### **6.2.1 Study Area**

The Bushmanland Plateau (BMP) study area extends from the town of Pofadder in the west to the town of Douglas in the East (c. 400 km) (Fig. 6-1). The northern extent continues just across the Namibian border with two samples coming from Namibia on the northern side of the Orange River valley. To the south the study area extends just south of the town of Prieska. The study area is much larger than the NQH study area and the data are sparser. This is due to the lack of basement exposure across this very low relief region of the plateau.

### **6.2.2 Morphology**

The continental interior of southern Africa is typically referred to as a plateau due to its extensive low-relief plains. This description is generally consistent with the study area here where elevations vary only gradually between 900 - 1100m, and rarely reach elevations above 1200m (Fig. 6-1). In the northwest of the study area the Asbestos Hills achieve elevations up to 1600 m and mark the transition into the Kaapvaal craton. The main South African drainage conduit, the Orange River, enters the study area from the southeast and exits in the northwest before continuing westward towards the Atlantic Ocean. At the town of Douglas, the NW trending Orange River converges with the southwest flowing

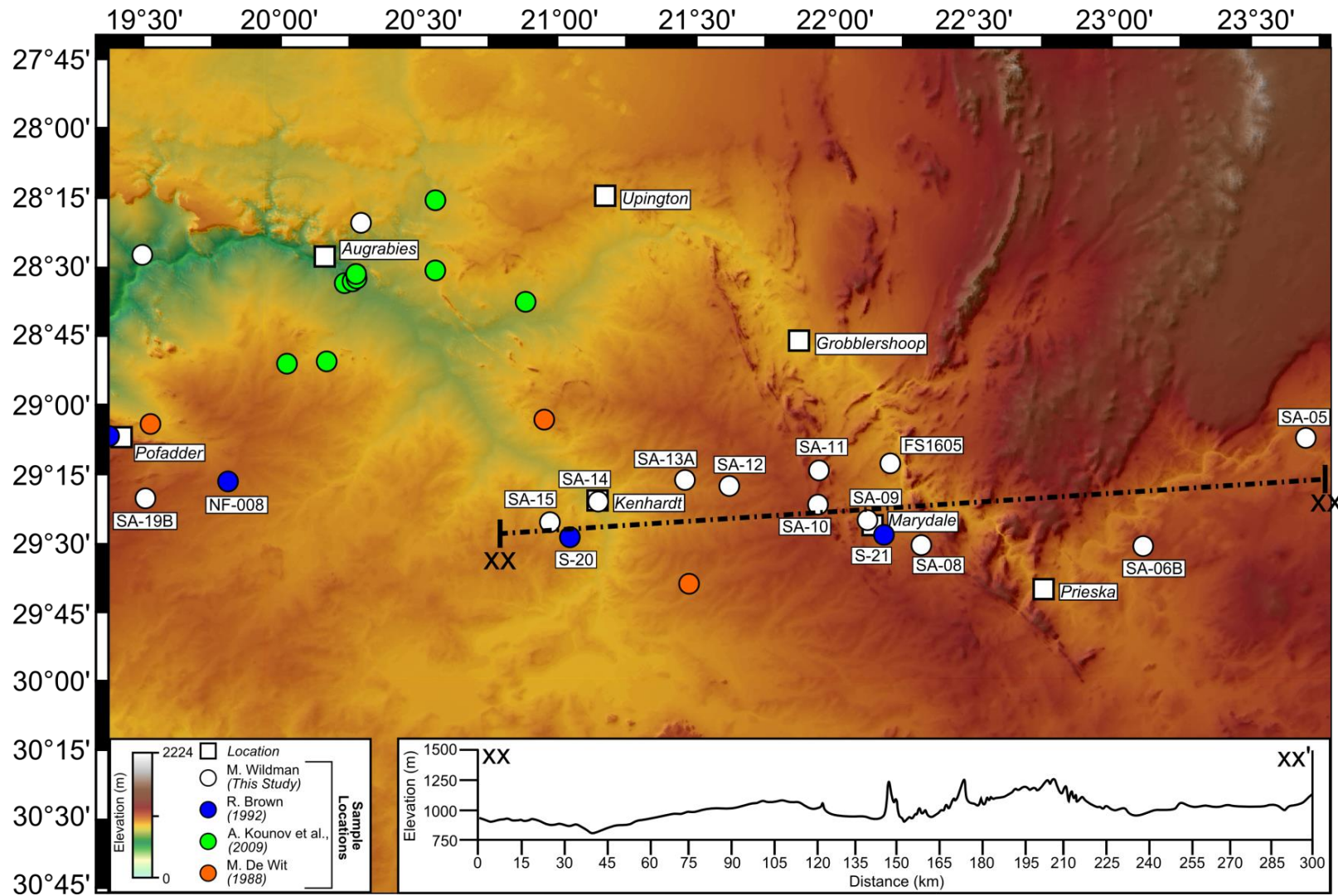
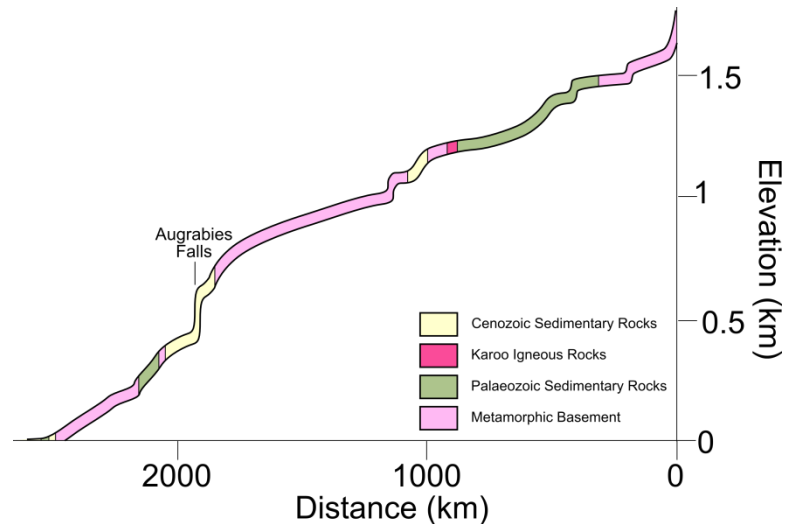


Figure 6-1: Location map of the Bushmanland Plateau study area. DEM created using SRTM 90m. Elevation profile for a transect across the plateau is shown and is used below in Figure 6-21 with data projected onto the line of section.

Vaal River which drains the northeast of South Africa. The Orange River deviates southeast along the trend of the Asbestos Hills before becoming deflected towards the northwest at Prieska. At this point the Orange River follows the major structural trend of the Kheis Front and specifically the Doringberg Lineament. After continuing in this trend for c. 170 km, the Orange River meanders as it flows west through the towns of Upington and Kakamas. The main Orange River channel progressively decreases in elevation through the study area but includes several significant knickpoints along its course, particularly at the Augrabies Falls (Fig. 6-2).

### **6.2.3 Archean – Palaeoproterozoic craton**

The Archean - Palaeoproterozoic Transvaal Supergroup rocks can be found in three structural basins on the Kaapvaal craton in South Africa and Botswana (Eriksson et al., 2006). In the north east of the study area the Transvaal Supergroup is preserved in the Griqualand West Basin (Fig. 6-3). A well preserved stratigraphy is observed in the Transvaal Supergroup which was deposited in a shallow marine environment during periods of transgression and regression on the Kaapvaal craton (Altermann and Nelson, 1998; Eriksson et al., 2006). The base of the stratigraphic section is characterised by limestone, dolomite and shale units which are capped by banded iron formations of the Asbestos Hills Subgroup (Beukes and Gutzmer, 2008; Schröder et al., 2011). The Transvaal Supergroup in this region has experienced multiple deformation phases over c. 2500 - 1000 Ma involving extensive thrusting and stacking of stratigraphic sequences during continental amalgamation (Altermann and Hälbich, 1990, 1991; Eriksson et al., 2006). However, the sequence has only experienced limited (sub-greenschist) metamorphism (Kendall et al., 2013). The boundary between the Transvaal Supergroup, and the Kaapvaal craton, and the rocks of the Namaqualand metamorphic province (NMP) is marked by the prominent NW-SE to N-S striking Doringberg Lineament and Blackridge Thrust (Altermann and Hälbich, 1991) (Fig. 6-3; c.f. Chapter 1 - Figure 1-2).



**Figure 6-2: West-east longitudinal river profile of the Orange River with underlying lithology (after Paul et al., 2014).**

### 6.2.4 Namaqua Metamorphic Province

The NMP rocks exposed in the study area are granites and granitic gneisses and are subtly different from those present in the NQH. The entire NMP has experienced significant metamorphism over c. 2000 - 1000 Ma, the differences can be found in minor variations in the timing and P-T conditions of metamorphism, variations in the original unmetamorphosed material and composition and extent of intrusive activity (Cornell et al., 2006). Lithostratigraphic variations in the NMP define terrane subprovinces which are bounded by major structural discontinuities (Fig. 6-4). While the NQH region is dominated by the Bushmanland Terrane, major shear zones and thrust belts define numerous terrane boundaries along the Orange River which extend into southern Namibia.

Along the Orange River the NMP can be subdivided into three zones (Western, Central and Eastern marginal zones) characterised by variations in structural style and metamorphic grade by major tectonic discontinuities (Tankard et al., 1982). The Eastern Marginal Zone (EMZ) is characterised by an array of NNW trending, steeply dipping, en echelon faults. These faults, particularly the Doringberg and Brakbos faults, define the structurally complex transition from the Kaapvaal craton to the younger NMP (Tankard et al., 1982, 1995, 2009; Altermann and Hälbig, 1991; Eriksson et al., 2006). The NW structural trend

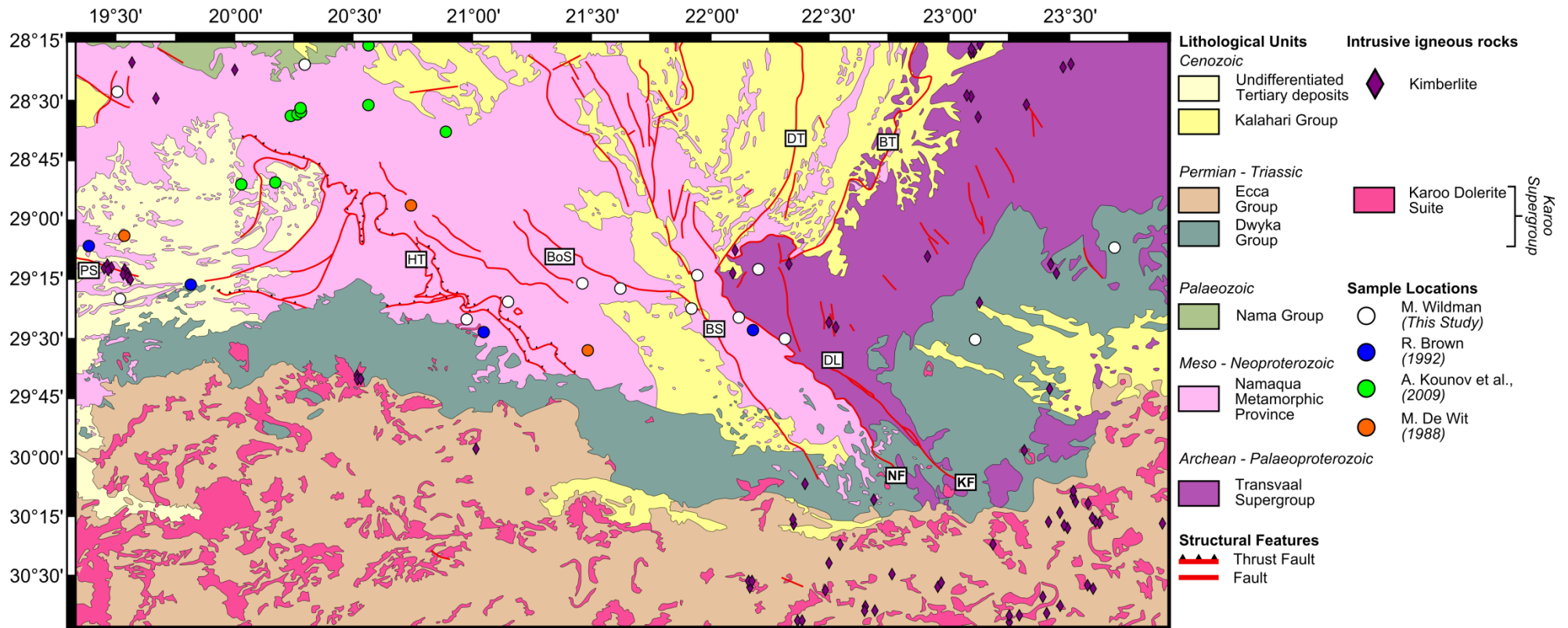
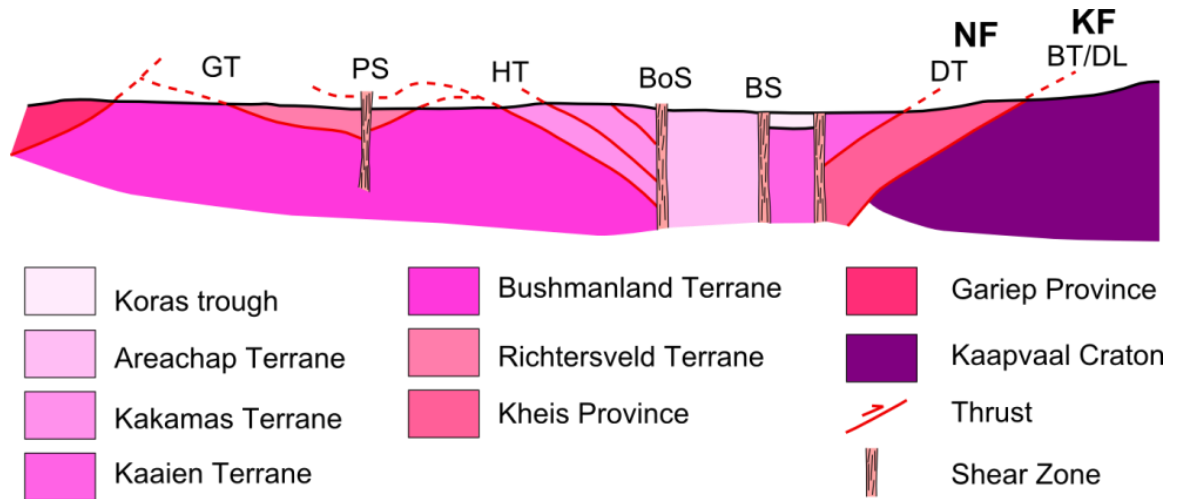


Figure 6-3: Geological map of the Bushmanland Plateau study area. Geological map was redrawn to highlight the major geological units, structures and features relevant to this study, using 1:1,000,000 scale maps produced by the Council for Geoscience, South Africa. (Fourie and Cole, 1997). For sample names, refer to Figure 6-1. Fault names: PS = Poffader Shear Zone; HT = Hartbees Thrust; BoS = Bouzen River Shear Zone; BS = Brakbos Shear Zone; DT = Dadep Thrust; BT = Blackridge Thrust; DL = Doringberg Lineament; NF = Namaqua Front; KF = Kheis Front (after Tankard et al., 2009 and Thomas et al., 1994a).



**Figure 6-4: Schematic cross section of the Namaqualand Metamorphic Province (after Thomas et al., 1994a). Fault names are the same as in Figure 6-3 (GT = Goothoek Thrust).**

associated with the EMZ extends through Southern Namibia and into South Africa where post-Karoo displacement is suggested by the presence of basement inliers in contact with Karoo sediments (Tankard et al., 2009).

The NW structural trend continues throughout the Central Zone of the NMP which comprises the Areachap and Kakamas Terrane. The Hartbees River Thrust bounds the western extent of this region and trends initially NW-SE before deviating E-W and running parallel to the trend of the Orange River. The generally E-W structural trend of the Western Zone is best represented by the Tantalite Valley shear zone, Goothoek Thrust and, further south, Buffels river shear zone. Within the Tantalite Valley shear zone, NNE to NE trending normal structures associated with transtensional stresses juxtapose basement gneisses against late Proterozoic sediments of the overlying Nama Group (Gresse and Germs, 1993; Gresse et al., 2006). These structural trends appear to have a control over the course of the Orange River which alternates between a northwest direction to southwest direction several times as it flows westward from the Kaapval craton. This typical trellis pattern of the main channel suggests that the river channel geometry is being strongly controlled by separate structural directions defined by the NW trend of the EMZ and E-W trend within the Tantalite Valley shear zone.

### **6.2.5 Neoproterozoic – Palaeozoic**

The Nama Group unit is believed to have been deposited in a similar geological setting and at a similar time to the Vanrhynsdorp Group, discussed in Chapter 5 - Section 5.2.4 (Gresse et al., 2006). This depositional environment is proposed to be a foreland basin which formed on the craton edge due to flexure of the lithosphere during Pan-African thrusting (Gresse and Germs, 1993; Tankard et al., 1995; Gresse et al., 2006). Exposure of the Nama Group in the study area is limited, occurring only in the northwest where it extends into southern most Namibia. Specifically, the Nama group in the study area is represented by the sub-horizontal Kuibis Subgroup succession of sandstone and shale cycles (Fig. 6-3).

### **6.2.6 Karoo Supergroup**

The glacially dominated Dwyka Group was deposited unconformably on the Precambrian basement in the study area during the Late Carboniferous to Early Permian (Johnson et al., 2006). Its preservation is more extensive here than in the NQH study area, forming the outer extent of the main Karoo basin which covers much of the interior of South Africa (Fig. 6-3). The diamictite facies within the Dwyka Group can appear massive or well stratified and clast rich. Clasts are variable in size and form and their origin is commonly attributed to the surrounding bedrock which has been dislodged from the surrounding outcrops (Visser, 1989, 1990). Stratified diamictites contain bedding planes and alternating successions of mudrock, conglomerate and sandstone beds produced by sediment gravity flows and rain-out debris flows (Visser and Young, 1990; Johnson et al., 2006).

The Ecca group is represented mainly by the Prince Albert Formation which attains a thickness up to c. 300 m (Johnson et al., 2006) (Fig. 6-3). The Prince Albert Formation predominantly comprises sandstones, siltstones, and silty shales which fine upwards from the boundary above the Dwyka Group glacial deposits (Scheffler et al., 2006; Herbert and Compton, 2007). The presence of mudrocks and marine fossils suggest a shallow marine depositional environment

with sandstones and siltstones possibly deposited in a deltaic environment (Catuneanu et al., 1998).

Intrusive dolerite dykes, sills and sheets heavily punctuate the Karoo Basin across the study area (Fig. 6-3). Dolerite sheets can form resistant caps up to 200m thick on small hills which rise above the extensive flat lying plateau (Duncan and Marsh, 2006). The intrusion of the Karoo Dolerite Suite is thought to have occurred fairly rapidly at c. 180 - 185 Ma (Duncan et al., 1997; Jourdan et al., 2005, 2007; Moulin et al., 2011; Svensen et al., 2012). Similarly aged mafic rocks are found in Namibia and the Lebombo Mountains in Swaziland and collectively they are suggested to be coeval with continental flood basalt emplacement associated with continental rifting and break up of Eastern Gondwana at this time (Cox, 1992; Duncan et al., 1997).

### **6.2.7 Cenozoic**

The Kalahari Group sedimentary unit fills palaeovalleys within the Karoo Supergroup and older basement rocks and can reach a thickness up to c. 210 m (Fig. 6-3). However, in the study area their thickness is typically < 60 m (Partridge et al., 2006). The Kalahari Group unit is mainly comprised of poorly sorted and poorly consolidated gravels and sands which have been accumulated during the Cenozoic (Thomas and Shaw, 1990). However, the timing of the development of the Kalahari Basin and subsequent sediment infill remains uncertain due to the absence of direct dating of the sediments (Haddon and McCarthy, 2005). The evolution of the basin has largely been inferred from proposed models of regional tectonic and drainage evolution involving Cenozoic epirogenic uplift which has proved to be a source of much controversy (e.g. Partridge and Maud, 1987; Burke, 1996; Brown et al., 2002; Doucouré and de Wit, 2003; Moore et al., 2009).



## 6.3 AFT Analysis

### 6.3.1 Results

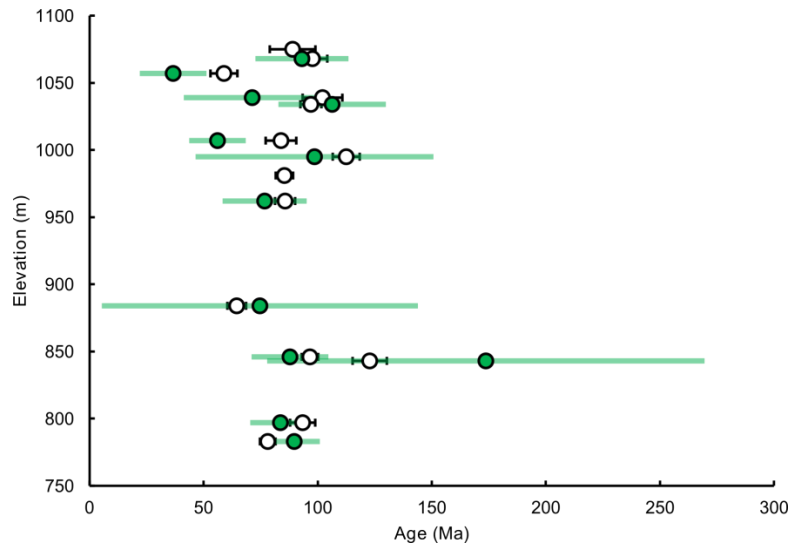
The external detector method, as outlined in Appendix 1.2, was used to obtain AFT ages from 14 samples from a transect across the interior plateau of southwestern Africa (Table 6-1). The transect extends west from Douglas to Pofadder cutting across the major Doringberg and Hartbees fault lineaments, as well as the Orange River. Table 6-1 summarises the data obtained for these samples. A zeta value of  $317.3 \pm 11.1$  was used to calculate AFT ages for samples FS1605, GGO2 and PRU106 and a value of  $316.7 \pm 10.5$  used for the remaining samples (see Appendix 2.1). Central AFT ages range from  $58.9 \pm 5.9$  to  $122.8 \pm 7.5$  Ma with half of the ages falling between c. 85 and 100 Ma. There is no apparent correlation between AFT age and elevation (Fig. 6-5).

Each sample contained at least 9, and in most cases more than 50, horizontal confined track (HCT) lengths which were measured to constrain thermal history information. Mean track lengths (MTL) within samples range from  $10.33 \pm 0.24$  to  $14.29 \pm 0.12$   $\mu\text{m}$ . The standard deviation of track length measurements (MTL-SD) range from 1.17 to 2.19 and the majority are  $< 2$ . This is representative of the fact that most samples have a fairly narrow to moderately broad track length distribution (see Appendix 5.2 for TLDs).

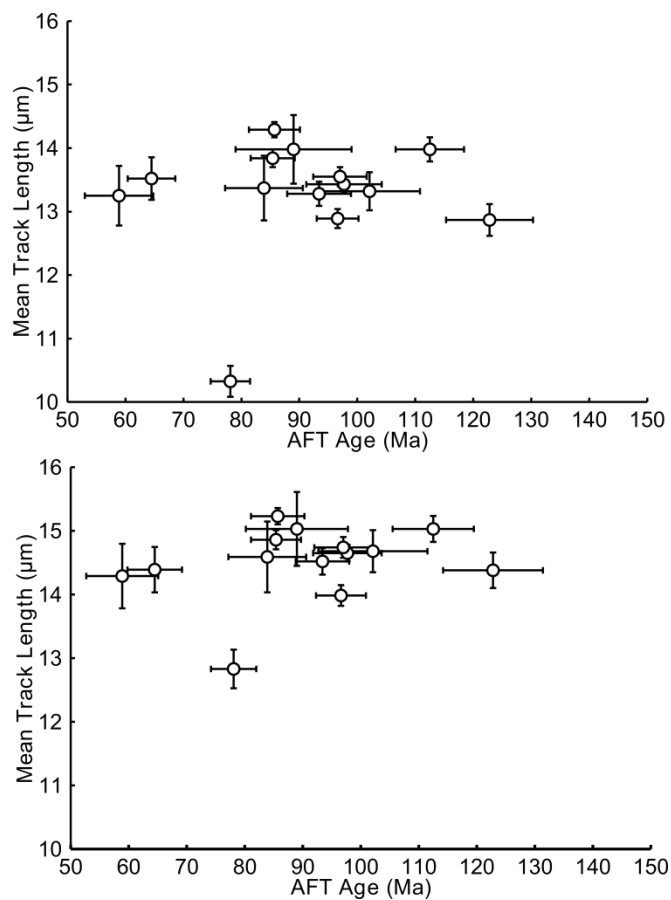
Figure 6-6 does not show a clear relationship between AFT Age and MTL. However, there appears to be a similarity in the spread of the data to the Age-MTL plot for the NQH region further west that was presented in Chapter 5. A cluster of longer MTLs exist for ages that are between c. 80 and 100 Ma which could be tenuously linked to the younger peak of a boomerang plot (Fig. 6-6). Additionally, the sample PRU 106 which has a low MTL and Late Cretaceous age could represent the partially annealed record of cooling from an Early Cretaceous event. The overall negative correlation between MTL and MTL-SD is an indication that when track lengths are long the distribution is narrow, further supporting a record of rapid cooling in a particular sample (Fig. 6-7).

Sample	Long. (°)	Lat. (°)	Elev. (m)	$\rho_s^a$		$\rho_i^a$		$\rho_d^a$		$P(\chi^2)^c$ (%)	$D_{par}^d$ ( $\mu m$ )	[U] <sup>e</sup> (ppm)	C. AFT Age (Ma) <sup>f</sup> $\pm 1\sigma$	#Xtls	Measured		c-axis correction <sup>h</sup>		#HCT <sup>i</sup>
				$(10^6 cm^{-2})$	$N_s^b$	$(10^6 cm^{-2})$	$N_i^b$	$(10^6 cm^{-2})$	$N_d^b$						MTL ( $\mu m$ ) $\pm 1\sigma$	SD <sup>g</sup>	MTL ( $\mu m$ ) $\pm 1\sigma$	SD <sup>g</sup>	
FS1605	22.20	-29.22	843	5.7	400	12.1	845	16.5	13142	0.99	2.07	10.1	122.8 7.5	20	12.87 0.25	2.00	14.38 0.28	1.35	63
GGO2	20.30	-28.36	846	21.3	2174	68.8	7023	20.0	13142	0.00	1.75	48.5	96.6 3.6	20	12.89 0.15	1.55	13.98 0.16	1.12	100
PRU 106	19.52	-28.48	783	19.2	1092	82.3	4672	21.7	13142	0.06	1.76	51.5	78.1 3.4	19	10.33 0.24	2.19	12.83 0.30	1.17	80
SA12-05	23.70	-29.15	1007	4.3	249	13.5	777	16.7	16348	0.46	2.02	11.9	83.9 6.7	20	13.37 0.51	2.10	14.59 0.56	1.44	17
SA12-06b	23.14	-29.54	1068	7.4	537	18.7	1362	15.6	16348	0.03	1.97	16.1	97.7 6.5	18	13.43 0.12	1.26	14.65 0.13	0.85	51
SA12-08	22.31	-29.52	1039	1.9	195	4.4	465	15.5	16348	1.00	1.53	3.9	102.1 8.7	20	13.32 0.30	1.85	14.68 0.33	0.96	39
SA12-09	22.12	-29.40	995	5.8	535	12.4	1150	15.4	16348	0.94	2.44	11.3	112.5 5.9	22	13.98 0.19	1.44	15.03 0.20	0.92	57
SA12-10	21.94	-29.36	1075	4.0	151	12.0	449	16.6	16438	0.22	1.77	9.2	89.0 10.0	12	13.98 0.54	1.61	15.03 0.58	1.09	9
SA12-11	21.94	-29.24	1057	2.2	122	9.4	526	16.1	16348	0.63	4.96	7.7	58.9 5.9	16	13.25 0.47	1.83	14.29 0.51	1.23	15
SA12-12	21.63	-29.30	981	10.3	930	29.1	2631	15.2	16348	0.13	2.38	25.1	85.4 3.8	22	13.84 0.14	1.23	14.86 0.15	0.91	78
SA12-13a	21.47	-29.28	962	9.1	787	25.3	2190	15.1	16348	0.08	2.44	22.3	85.7 4.4	20	14.29 0.12	1.17	15.23 0.13	0.77	89
SA12-14	21.15	-29.35	797	6.2	1013	15.5	2553	14.9	16348	0.00	2.87	13.9	93.4 5.5	20	13.28 0.19	1.33	14.52 0.21	0.94	81
SA12-15	20.98	-29.42	884	5.7	305	23.1	1237	16.6	16348	0.50	1.69	19.5	64.5 4.1	22	13.52 0.34	1.38	14.39 0.36	1.03	17
SA12-19b	19.53	-29.34	1034	7.7	994	16.9	2183	13.8	16086	0.10	1.63	17.2	97.0 4.6	21	13.55 0.15	1.38	14.74 0.16	0.89	126

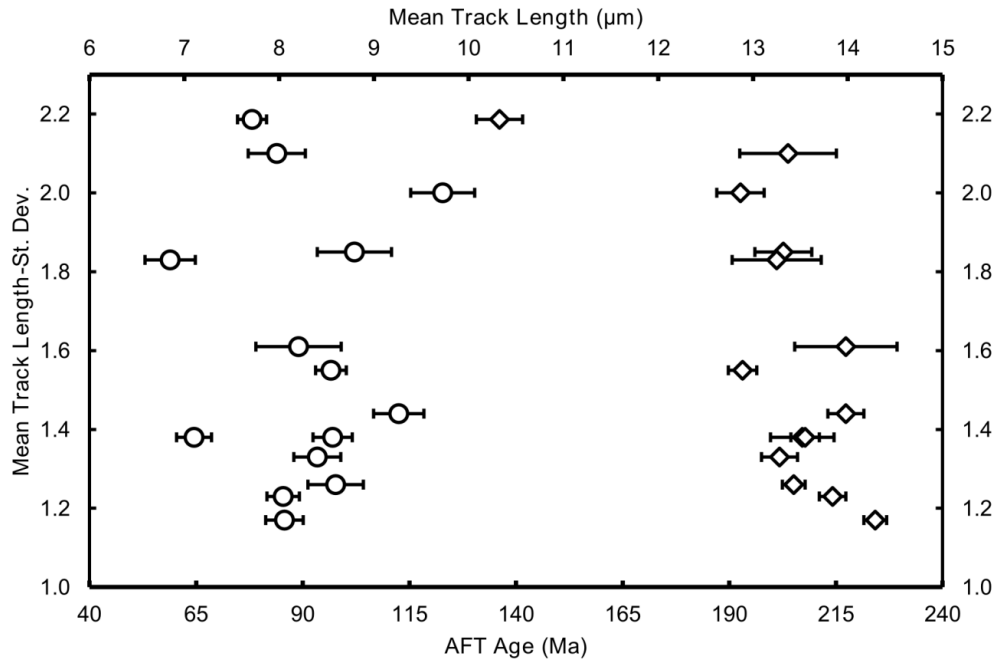
**Table 6-1: Results of apatite fission track analysis. a:  $\rho_{i,s,d}$  are track density of induced, spontaneous, dosimeter tracks. b:  $N_{i,s,d}$  are the number of induced, spontaneous and dosimeter tracks counted. c: p-value of the chi-sq age homogeneity test (Galbraith, 2010; see Appendix 3.1). d:  $D_{par}$  measurements are etch pit diameters used as a proxy for the influence of chemical composition on track annealing (Donelick et al., 2005). Between three to five  $D_{par}$  measurements were measured for each dated single grain. e: Uranium content estimated using EDM. f: Central AFT ages calculated with TrackKey (Dunkl, 2002) with  $1\sigma$  standard error. Ages were calculated using a  $\zeta = 316.7 \pm 10.3$  ( $317.4 \pm 11.1$  for samples GGO2, FS1605 and PRU106) for a standard IRMM540 standard glass g: SD is the standard deviation of measured horizontal confined track lengths. h: mean track length after individual track length measurements are corrected for their orientation to the c-axis after Ketcham et al., (2005). i: HCT = Horizontal Confined Track. Analysis details can be found in Appendix 1. For details on sample lithology see Appendix 4.**



**Figure 6-5: Plot of AFT and AHe age against elevation. White circles are Central AFT ages with uncertainty bars representing  $1\sigma$  standard error on the central age. Green circles are uncorrected mean AHe ages with uncertainty bars representing  $1\sigma$  standard deviation. The standard deviation is used in this instance to highlight the dispersion in single grain AHe ages.**



**Figure 6-6: Plot of AFT age against mean track length. AFT ages are Central AFT ages with  $1\sigma$  standard error. Plot (a) shows AFT age against MTLs uncorrected for their c-axis orientation; (b) shows AFT age against MTLs corrected for their c-axis orientation after Ketcham et al. (2005). For both plots MTLs have uncertainty bars with  $1\sigma$  standard error.**



**Figure 6-7: Plot of AFT age (left hand side; lower x-axis) and mean track length (right hand side; upper x-axis) against mean track length standard deviation. AFT ages are Central AFT ages with  $1\sigma$  standard error. MTLs are uncorrected for their c-axis orientation; with  $1\sigma$  standard error.**

### 6.3.2 Data quality assessment

The 14 samples analysed across the study area provided a good number of grains suitable for AFT dating ( $n > 17$  for 12 samples) each with a moderate to high track density. Outlier grains were once again removed following the protocol described in Appendix 3.1. Radial plots for all 14 samples can be found in Appendix 5.1 and highlight the dispersion on single grain ages which for all samples is less than 21%.

Only 3 samples produced a  $P(\chi^2)$  value equal to or less than 0.05. These samples yielded 18 grains or above suitable for counting with the number of spontaneous tracks ranging from 537 to 2174. This means that there should be sufficient evidence for the  $P(\chi^2)$  value to be an indication of whether or not the spread in age is consistent with a single discrete population of single grain ages. The mixture model of Galbraith and Green, (1990) suggests that two of these samples potentially have two populations of ages (see Appendix 5.1). GGO2, although having an extremely low  $P(\chi^2)$ , has a low dispersion and therefore does

not require two populations to explain the single grain age distribution. For the other two samples, two populations are possible but their existence is only weakly supported. The single grain ages from SA12-06B and SA12-14 could be separated into two populations with mean ages at  $79.7 \pm 9.2$  and  $117 \pm 14$  Ma and  $76.9 \pm 5.4$  and  $117.6 \pm 9$  Ma, respectively. As observed for samples in the Namaqualand region, single grain ages within a given sample can be assigned to either of these two populations. In this case, almost 50% of grains could belong to one population or the other. However, the large uncertainty on the percentage of grains that can be assigned to a population significantly weakens the justification for two discrete populations. The timing of the two populations seen in these two samples does agree with the central AFT ages from both this study area and in Namaqualand as well as the individual populations of single grain ages of Namaqualand samples with low  $P(\chi^2)$  values. It is important to note that the AFT age of any grain is a function of both the grain composition and the sample thermal history, and so the single grain ages can only be interpreted robustly with reference to the TLD measurements in conjunction with the compositional kinetic parameters for the sample.

The quality of track length data is poorer than for samples from Namaqualand due to a lower number of horizontal confined tracks available. However, 9 samples yielded 50 HCTs suitable for measurement. Even the sample with 9 HCTs (i.e. SA12-10) will provide some thermal history information for the sample. When MTLs are relatively short or TLDs are relatively broad, the shape of the TLD is either normally distributed around the mean value or is negatively skewed with a proportionally large number of longer tracks and tail of shorter tracks.

The maximum  $D_{\text{par}}$  value from the BMP region is  $4.96 \mu\text{m}$  (SA12-11). This  $D_{\text{par}}$  value is anomalous with the range of other  $D_{\text{par}}$  values in the area ( $1.53$  and  $2.87 \mu\text{m}$ ) and has likely been over-etched during sample preparation. As a result of over-etching track lengths may overestimate the true track length. The range in  $D_{\text{par}}$  values is larger than the NQH data set and may reflect a larger degree of heterogeneity in apatite composition. Despite this, there is no correlation between AFT age or MTL with  $D_{\text{par}}$  suggesting it does not exert a dominant influence on the observed AFT data (see Chapter 4 - Figure 4.5).

Estimated uranium contents range from 3.9 to 51.5 ppm with most samples having U contents towards the moderate to low end of this range. There is a lack of correlation of uranium content with MTL and a weak negative correlation with age (see Chapter 4 - Figure 4.6). This apparent correlation is not sufficient to justify radiation enhanced annealing as a control over AFT ages (e.g. Hendriks and Redfield, 2005) as there is no complimentary influence on MTL; different thermal events may have been recorded by individual samples; and the largest U concentrations do not fall into the negative correlation created by the remaining data (see Chapter 4 - Figure 4.6).

### **6.3.3 Summary of AFT Data**

The AFT ages presented here for the Bushmanland plateau region are predominantly Mid-Cretaceous (80 - 100 Ma) with two samples yielding Early Cenozoic ages and two samples Early Cretaceous ages. Moderate to long MTLs suggest cooling at these times was fairly rapid but moderate in some places. TLDs indicate that periods of rapid or slow cooling cannot be assigned solely to one time period. This data is in good agreement with data from the Namaqualand region that suggests major cooling of the crust occurred throughout the Cretaceous and possibly extending into the Early Tertiary. Overall, however, this dataset strongly supports a Mid-Cretaceous pulse of rejuvenated erosion of the South African plateau. This data also highlights complex spatial-temporal cooling across the study area with samples potentially recording both a rapid and protracted response to multiple cooling events.

## **6.4 AHe Analysis**

### **6.4.1 Results**

Twelve samples were dated using AHe analysis (Table 6-2). The approach of obtaining multiple single grain analyses was employed here following Appendix 3.2. However, due to sample quality three samples currently have less than 5 single grains analysed. Three samples however yielded AHe ages of 14 or more grains. The range of mean AHe ages (uncorrected: 25.5 - 173.7 Ma; alpha-recoil corrected: 35 - 221.8 Ma) and the dispersion associated with these samples

Sample	Grain #	<sup>4</sup> He	<sup>238</sup> U		<sup>235</sup> U		<sup>232</sup> Th		<sup>147</sup> Sm		eU <sup>a</sup>	T <sup>b</sup>	L <sup>c</sup>	W <sup>c</sup>	R <sup>*d</sup>	F <sub>t</sub> <sup>e</sup>	Raw Age ±Est. UC <sup>f</sup>		Cor. Age <sup>g</sup> ±Est. UC <sup>f</sup>		Raw Age (Ma)		Cor. Age (Ma)	
		(cc)	(ng)	(ppm)	(ng)	(ppm)	(ng)	(ppm)	(ng)	(ppm)	(ppm)		(μm)	(μm)	(μm)		(Ma)	(Ma)	Average	St. Dev	Average	St. Dev	Average	St. Dev
SA12-05	1	1.4E-10	0.02	2.69	1.2E-04	0.02	0.02	3.9	0.02	3.1	3.6	1	173.5	120.9	67.2	0.78	48.6	29.5	62.5	37.9	<b>56.1</b>	<b>12.4</b>	<b>72.8</b>	<b>15.8</b>
	2	6.5E-10	0.06	11.35	4.5E-04	0.08	0.03	6.2	0.02	3.5	12.9	1	175.0	112.1	63.7	0.77	75.0	19.3	97.1	24.9				
	3	2.3E-08	0.05	2.02	3.5E-04	0.01	0.32	13.2			5.1	0	308.5	176.4	102.9	0.85	1458.3	163.1	1723.9	192.8				
	4	1.9E-10	0.13	26.05	9.6E-04	0.19	2.18	428.9	0.44	87.3	127.0	1	218.8	96.1	59.1	0.72	2.4	0.3	3.4	0.4				
	5	3.6E-10	0.01	2.44	1.0E-04	0.02	0.09	15.5			6.1	0	159.8	120.3	65.5	0.76	44.6	4.9	58.8	6.4				
SA12-06B	3	8.9E-10	0.05	8.8	3.6E-04	0.06	0.03	5.4	0.02	3.5	10.1	2	232.8	98.2	60.8	0.76	128.0	15.1	168.2	19.9	<b>93.1</b>	<b>20.4</b>	<b>122.0</b>	<b>26.5</b>
	7	7.9E-10	0.06	10.4	4.1E-04	0.08	0.05	8.4	0.03	5.8	12.5	2	174.4	111.3	63.3	0.77	95.0	10.6	123.6	13.8				
	8	1.1E-09	0.07	16.6	5.2E-04	0.12	0.05	12.3			19.6	1	145.0	108.7	59.3	0.75	110.7	15.0	146.9	19.9				
	9	6.9E-10	0.05	7.3	3.7E-04	0.05	0.05	7.3			9.1	1	151.8	135.2	70.2	0.79	88.9	12.0	112.6	15.2				
	10		0.05	12.9	3.7E-04	0.09	0.04	10.6			15.5	1	191.0	90.1	54.7	0.73								
	11	1.1E-09	0.07	8.5	4.8E-04	0.06	0.06	7.8	0.04	4.7	10.4	2	264.1	108.1	67.3	0.78	108.1	11.9	138.3	15.2				
	12	5.3E-10	0.05	7.5	3.5E-04	0.05	0.04	6.5			9.1	1	231.4	105.2	64.3	0.77	74.2	10.1	96.2	13.0				
	13	3.8E-10	0.03	5.9	2.5E-04	0.04	0.07	12.4			8.9	2	263.3	94.4	60.1	0.75	60.2	6.5	80.6	8.7				
	14	5.3E-10	0.04	8.9	3.0E-04	0.06	0.04	9.6			11.2	2	204.9	95.1	57.9	0.74	82.6	8.9	110.9	12.0				
	15	1.4E-09	0.11	23.1	7.7E-04	0.17	0.07	16.1			27.1	1	200.7	95.3	57.8	0.75	90.0	12.2	120.5	16.4				
SA12-08	1	3.6E-10	0.05	18.3	3.7E-04	0.13	0.11	41.0	0.19	69.1	41.00	1	198.1	74.5	47.0	0.68	37.9	5.2	52.3	7.2	<b>71.3</b>	<b>30.0</b>	<b>94.6</b>	<b>44.2</b>
	2	1.7E-10	0.01	4.9	8.8E-05	0.04	0.03	11.2	0.07	29.7	11.22	0	97.6	100.5	49.7	0.69	71.7	10.3	94.8	13.7				
	3	2.2E-10	0.01	2.3	7.8E-05	0.02	0.02	5.0	0.05	10.5	5.03	1	183.1	101.6	59.7	0.75	109.3	15.3	146.6	20.5				
	4	1.2E-09	0.08	31.4	5.9E-04	0.23	0.04	14.7	0.17	66.3	14.76	2	158.8	80.3	48.1	0.70	104.6	14.6	149.6	20.9				
	5a	2.0E-10	0.02	2.6	1.8E-04	0.02	0.05	4.9			4.91	1	195.1	139.1	60.7	0.80	45.4	4.9	54.0	5.8				
5b	2.0E-10	0.02	4.3	1.4E-04	0.03	0.03	7.1			6.0	1	99.5	136.4	60.7	0.75	59.0	6.4	70.2	7.6					
SA12-09	1	4.3E-10	0.02	5.9	4.3E-02	0.04	0.01	3.8	0.64	211.1	6.9	1	137.6	93.9	52.5	0.72	164.1	38.2	232.6	54.2	<b>98.6</b>	<b>52.1</b>	<b>143.9</b>	<b>68.9</b>
	2	6.9E-10	0.03	7.8	5.7E-02	0.06	0.04	12.6	0.40	114.0	10.8	2	164.0	92.8	54.2	0.72	145.2	16.1	202.4	22.4				
	3	1.6E-10	0.01	6.8	4.9E-02	0.05	0.05	25.2	0.62	321.2	12.7	1	169.5	67.5	42.2	0.63	51.4	5.7	82.9	9.3				
	4	8.2E-11	0.01	2.1	1.5E-02	0.01	0.02	6.2			3.5	2	192.7	80.9	50.2	0.67	60.1	6.7	89.2	10.0				
	5	1.1E-10	0.01	5.6	4.1E-02	0.04	0.01	7.1			7.4	1	144.3	68.8	41.7	0.64	72.1	10.8	112.1	16.8				
SA12-11	1	2.1E-10	0.01	2.2	7.7E-05	0.02	0.07	13.6	0.23	46.1	5.4	0	204.2	97.6	59.1	0.73	60.6	6.8	82.9	9.3	<b>36.6</b>	<b>14.6</b>	<b>50.3</b>	<b>20.7</b>
	2	1.0E-10	0.01	4.9	9.0E-05	0.04	0.06	24.8	0.12	48.7	10.8	0	115.2	93.2	49.8	0.68	30.7	3.5	44.9	5.0				
	3	9.4E-11	0.01	2.2	5.2E-05	0.02	0.05	15.0	0.13	40.1	5.8	0	115.6	105.1	54.2	0.71	39.2	4.4	55.4	6.2				
	4	2.1E-10	0.02	5.2	1.8E-04	0.04	0.13	28.1	0.24	51.0	11.8	0	155.7	109.7	60.8	0.74	29.8	3.2	40.1	4.4				
	5	3.5E-10	0.04	3.1	3.0E-04	0.02	0.34	25.6	0.65	48.9	9.2	1	202.6	161.9	86.7	0.82	22.9	2.5	28.0	3.1				
SA12-13A	2	1.2E-09	0.18	13.7	1.3E-03	0.10	0.01	0.9	0.24	17.8	14.0	2	250.6	145.4	84.5	0.83	51.8	8.1	62.2	9.8	<b>76.7</b>	<b>18.4</b>	<b>98.4</b>	<b>23.8</b>
	4	1.4E-09	0.11	19.6	8.2E-04	0.14	0.13	22.0			24.9	2	238.7	98.3	61.1	0.76	77.2	10.4	101.8	13.8				
	5	1.0E-09	0.12	27.5	8.8E-04	0.20	0.22	48.9			39.2	1	169.0	101.9	58.7	0.74	48.0	5.2	64.6	6.9				
	8	1.4E-09	0.12	18.1	8.4E-04	0.13	0.12	18.3			22.6	2	281.6	95.1	61.0	0.76	81.2	11.0	107.1	14.5				

**Table 6-2: Results of apatite (U-Th-Sm)/He analysis. a: eU (effective uranium) is calculated as  $eU_{ppm} = [U_{ppm}] + (0.235 * [Th_{ppm}])$ . b: T = Number of terminations identified on crystal. c: L & W = Length and Width of crystal or crystal fragment. d:  $R^* = \text{spherical equivalent radius calculated as } R^* = (3 * (RL)) / (2 * (R + L))$  where  $R = W/2$ . e: correction factor after Farley et al., (1996), assuming homogeneous distribution U and Th. f: Estimate Uncertainty is equal to  $1\sigma$  analytical uncertainty, which include error propagated from U, Th, Sm and He measurement uncertainties, plus an additional 10% which is the standard deviation (reproducibility) of repeat analysis of Durango apatite standards. g: Corrected AHe age = Raw AHe age/ $F_t$ ). Analysis details can be found in appendix 1. Shaded data has been excluded from mean value calculations and further interpretation (see Appendix 3). For details on sample lithology see Appendix 4.**

Sample	Grain #	$^4\text{He}$	$^{238}\text{U}$		$^{235}\text{U}$		$^{232}\text{Th}$		$^{147}\text{Sm}$		eU <sup>a</sup>	T <sup>b</sup>	L <sup>c</sup>	W <sup>c</sup>	R <sup>nd</sup>	F <sub>t</sub> <sup>e</sup>	Raw Age ±Est. UC <sup>f</sup>		Cor. Age <sup>g</sup> ±Est. UC <sup>f</sup>		Raw Age (Ma)		Cor. Age (Ma)	
		(cc)	(ng)	(ppm)	(ng)	(ppm)	(ng)	(ppm)	(ng)	(ppm)							(ppm)	(Ma)	(Ma)	Average	St. Dev	Average	St. Dev	
	9	1.6E-09	0.11	12.8	8.2E-04	0.09	0.15	16.7	0.13	14.4	16.8	2	316.1	105.6	67.9	0.78	89.6	9.7	114.8	12.5				
	10	1.2E-09	0.09	18.0	6.5E-04	0.13	0.08	16.6			22.1	1	218.3	94.8	58.4	0.75	89.4	9.6	119.4	12.8				
	11	8.2E-10	0.07	16.9	5.2E-04	0.12	0.07	17.7	0.07	15.9	21.2	2	200.4	91.6	55.9	0.74	74.5	8.4	101.2	11.4				
	12	2.0E-09	0.17	17.0	1.2E-03	0.12	0.03	3.1	0.14	13.8	17.8	1	193.3	144.4	78.8	0.82	89.4	12.0	109.1	14.7				
	14	3.9E-09	0.27	36.2	2.0E-03	0.26	0.14	18.5	0.18	24.4	40.8	1	203.8	121.0	70.0	0.79	104.2	11.1	131.4	14.0				
	15	1.0E-09	0.09	19.8	6.3E-04	0.14	0.08	19.3			24.5	2	182.5	97.6	57.7	0.74	79.2	10.7	106.3	14.4				
	16	1.7E-09	0.18	21.6	1.3E-03	0.16	0.16	19.3			26.3	1	220.2	124.4	72.7	0.80	60.9	8.2	76.3	10.3				
	17	6.1E-10	0.12	13.1	8.9E-04	0.09	0.01	1.0			13.4	1	187.0	141.1	76.8	0.82	40.4	5.9	49.6	7.3				
	20	3.2E-09	0.22	18.4	1.6E-03	0.13	0.26	22.3	0.22	18.5	23.8	2	311.3	122.9	77.0	0.81	93.7	10.1	116.1	12.5				
	21	1.7E-09	0.16	13.2	1.1E-03	0.10	0.05	4.0	0.15	12.5	14.2	1	304.3	124.4	77.5	0.81	83.3	9.1	102.2	11.1				
	24	8.1E-10	0.06	8.8	4.4E-04	0.06	0.06	8.6	0.08	11.5	10.9	2	220.8	111.5	66.8	0.78	88.4	10.1	113.4	12.9				
SA12-14	2	2.0E-09	0.18	17.8	1.3E-03	0.13	0.13	12.8			20.9	1	224.9	133.6	77.2	0.81	77.9	8.4	96.0	10.3	<b>83.7</b>	<b>13.2</b>	<b>101.0</b>	<b>16.1</b>
	3	4.0E-09	0.36	8.9	2.6E-03	0.06	0.11	2.8	0.73	18.3	9.7	1	260.3	247.4	125.8	0.89	84.7	9.1	95.6	10.3				
	6	3.1E-09	0.23	16.7	1.7E-03	0.12	0.14	10.3	0.40	28.5	19.2	2	357.3	124.4	79.5	0.82	94.4	10.3	115.6	12.6				
	7	2.0E-09	0.19	12.6	1.4E-03	0.09	0.13	8.8	0.26	17.4	14.8	2	224.1	163.8	90.0	0.84	74.4	8.1	88.8	9.6				
	8	2.4E-09	0.18	11.7	1.3E-03	0.08	0.08	5.5	0.23	15.0	13.1	1	254.7	154.3	88.8	0.84	99.3	10.6	118.6	12.7				
	12	2.5E-08	0.78	15.8	5.7E-03	0.11	0.54	10.8	1.56	31.5	18.4	1	197.6	316.0	131.7	0.89	222.2	23.7	249.8	26.7				
	13	1.2E-09	0.18	14.3	1.3E-03	0.10	1.67	135.2			46.2	1	186.1	162.5	84.8	0.81	16.8	1.8	20.7	2.3				
	18	2.7E-09	0.23	14.2	1.7E-03	0.10	0.14	8.9	0.45	28.1	16.4	2	271.1	153.2	89.6	0.84	81.7	8.9	97.6	10.6				
	19	1.5E-09	0.11	11.3	8.1E-04	0.08	0.21	21.0	0.27	27.6	16.4	2	214.8	135.2	77.1	0.80	74.3	7.9	92.4	9.9				
	21	8.8E-10	0.11	9.8	8.2E-04	0.07	0.07	5.8	0.21	18.0	11.3	2	282.8	126.8	77.7	0.81	55.4	6.0	68.1	7.3				
	22	6.2E-10	0.04	4.4	3.0E-04	0.03	0.03	2.7			5.0	2	179.1	146.0	77.8	0.81	105.2	14.3	129.4	17.6				
	23	3.3E-09	0.27	20.2	1.9E-03	0.15	0.16	12.3			23.2	1	270.4	139.2	83.0	0.82	87.5	11.9	106.0	14.5				
	26	5.1E-10	0.05	5.2	3.7E-04	0.04	0.03	2.6			5.9	2	245.3	125.8	75.1	0.81	73.1	10.0	90.6	12.4				
	27		0.15	17.9	1.1E-03	0.13	0.04	5.5			19.3	2	203.7	126.1	72.2	0.80								
	30	3.4E-09	0.33	12.8	2.4E-03	0.09	0.11	4.0			13.8	2	301.6	185.2	106.3	0.86	78.6	11.0	90.8	12.7				
	34	6.3E-09	0.45	36.8	3.3E-03	0.27	0.25	20.0			41.8	2	218.6	149.7	83.6	0.83	100.8	13.8	121.9	16.7				
	37	1.5E-09	0.13	11.1	9.6E-04	0.08	0.06	4.9			12.3	2	228.2	143.8	82.0	0.82	84.0	11.6	102.0	14.1				
SA12-15	1	1.7E-09	0.07	6.5	5.0E-04	0.05	0.19	18.3			10.9	1	165.6	159.8	47.0	0.81	123.6	17.2	152.6	21.2	<b>74.7</b>	<b>69.3</b>	<b>93.3</b>	<b>83.8</b>
	2	3.8E-09	1.07	176.0	7.7E-03	1.28	0.61	100.5			200.9	0	290.7	91.1	49.7	0.75	25.7	3.5	34.0	4.7				
SA12-19B	1	2.4E-09	0.17	12.4	1.2E-03	0.09	0.06	4.0			13.4	2	295.9	136.6	83.2	0.83	104.8	12.4	126.7	15.0	<b>106.3</b>	<b>23.5</b>	<b>133.7</b>	<b>26.3</b>
	3	1.9E-09	0.10	8.5	7.1E-04	0.06	0.03	2.7			9.2	2	237.4	139.2	80.7	0.82	144.7	19.2	176.0	23.3				
	4	9.4E-10	0.09	20.1	6.2E-04	0.15	0.04	8.7			22.3	2	156.3	104.3	58.7	0.75	81.2	10.1	107.7	13.5				
	5	2.0E-09	0.17	19.3	1.2E-03	0.14	0.04	4.2			20.4	1	214.7	126.0	73.1	0.80	95.6	12.4	118.8	15.4				
	6	3.0E-09	0.22	49.5	1.6E-03	0.36	0.06	14.3			53.2	2	171.7	101.5	58.8	0.76	105.4	12.4	139.4	16.5				

Table 6-2: Continued.



Sample	Grain #	<sup>4</sup> He	<sup>238</sup> U		<sup>235</sup> U		<sup>232</sup> Th		<sup>147</sup> Sm		eU <sup>a</sup>	T <sup>b</sup>	L <sup>c</sup>	W <sup>c</sup>	R <sup>a,d</sup>	F <sub>t</sub> <sup>e</sup>	Raw Age ±Est. UC <sup>f</sup>		Cor. Age <sup>g</sup> ±Est. UC <sup>f</sup>		Raw Age (Ma)		Cor. Age (Ma)	
		(cc)	(ng)	(ppm)	(ng)	(ppm)	(ng)	(ppm)	(ng)	(ppm)	(ppm)		(μm)	(μm)	(μm)		(Ma)	(Ma)	Average	St. Dev	Average	St. Dev		
GGO2	5	1.2E-08	0.77	101.0	5.6E-03	0.73	0.70	91.4			123.2	1	149.9	142.6	72.5	0.80	101.7	11.2	127.6	14.0	<b>87.8</b>	<b>16.8</b>	<b>111.2</b>	<b>22.2</b>
	6	4.6E-09	1.08	91.1	7.9E-03	0.66	1.00	83.6			111.4	1	153.6	176.3	84.0	0.82	28.3	3.1	34.3	3.8				
	8	2.3E-08	1.52	323.4	1.1E-02	2.35	1.30	273.0			389.9	1	190.9	99.5	59.2	0.75	102.4	11.2	136.1	15.0				
	9	2.0E-08	0.14	18.5	1.0E-03	0.13	0.66	84.6			38.5	2	205.0	122.7	70.8	0.78	528.9	60.1	679.0	77.2				
	11	2.2E-08	1.30	236.4	9.4E-03	1.71	2.69	487.0			352.6	2	182.8	109.7	63.3	0.76	91.7	10.2	120.5	13.5				
	12	2.2E-08	1.36	161.8	9.8E-03	1.17	0.08	9.5			165.2	2	264.5	112.7	69.7	0.80	128.2	14.3	160.9	18.0				
	13	4.4E-09	2.28	376.9	1.7E-02	2.73	2.32	381.7			469.4	1	158.8	123.5	66.7	0.78	12.9	1.4	16.6	1.8				
	14	7.7E-09	0.94	183.3	6.8E-03	1.33	0.11	21.0			189.6	1	170.5	110.0	62.4	0.77	65.3	7.3	84.6	9.4				
	15		0.00	0.5	2.6E-05	0.00	0.02	2.0			0.9	1	156.1	140.4	72.6	0.79								
	16	2.9E-08	3.08	268.6	2.2E-02	1.95	2.75	238.1			326.5	1	255.5	134.1	79.7	0.82	64.1	7.0	78.6	8.6				
	17	1.5E-08	1.23	199.3	8.9E-03	1.45	0.26	41.0			210.4	1	141.0	132.5	67.6	0.79	95.3	10.5	120.9	13.3				
	18		0.00	0.3	1.3E-05	0.00	0.01	1.2			0.5	1	192.4	120.1	68.6	0.77								
	19	2.9E-08	3.19	319.5	2.3E-02	2.32	4.58	455.2			428.8	1	238.3	129.6	76.4	0.80	56.2	6.2	69.8	7.7				
	20	2.9E-08	2.88	169.6	2.1E-02	1.23	1.47	85.9			191.0	2	316.4	146.8	89.4	0.84	73.9	8.1	88.2	9.7				
	21	1.1E-08	0.69	110.0	5.0E-03	0.80	0.70	110.6			136.7	1	124.3	142.3	67.9	0.78	103.9	11.4	132.8	14.6				
	22	2.9E-08	2.58	235.4	1.9E-02	1.71	0.91	82.4			256.4	1	234.5	136.9	79.5	0.82	85.3	9.4	104.2	11.4				
	23	1.9E-08	1.43	244.5	1.0E-02	1.77	2.20	373.5			334.0	1	109.8	146.0	65.8	0.77	78.6	8.7	101.7	11.3				
	24		1.25	150.1	9.1E-03	1.09	2.30	274.2			215.6	1	231.3	120.1	71.5	0.79								
	25	1.3E-08	1.02	134.9	7.4E-03	0.98	0.78	102.3			159.9	1	156.4	139.2	72.2	0.80	86.8	9.5	108.9	11.9				
	26	2.9E-08	2.28	264.0	1.7E-02	1.91	2.12	243.5			323.2	1	204.9	129.9	74.0	0.80	85.0	9.4	106.1	11.7				
	27	3.4E-09	0.20	28.8	1.4E-03	0.21	0.57	81.8			48.2	1	139.7	140.4	70.1	0.78	84.2	9.5	107.9	12.1				
	28	2.3E-08	1.54	234.7	1.1E-02	1.70	2.03	307.9			308.7	1	157.7	129.1	68.7	0.78	92.0	10.2	117.5	13.0				
	29	8.9E-09	0.73	77.9	5.3E-03	0.57	0.25	26.0			84.6	1	201.3	136.9	76.6	0.81	91.9	10.1	113.1	12.4				
	30	1.7E-08	1.14	213.3	8.3E-03	1.55	1.24	230.0			268.9	1	127.4	129.7	64.5	0.77	94.6	10.4	122.8	13.5				
FS1605	1	1.7E-09	0.03	4.3	2.0E-04	0.03	0.05	8.0			6.2	1	143.6	134.2	68.6	0.78	333.2	37.7	427.1	48.3	<b>173.7</b>	<b>95.9</b>	<b>221.8</b>	<b>120.9</b>
	2	4.7E-10	0.05	5.1	3.3E-04	0.04	0.04	4.3			6.2	2	238.3	121.7	72.7	0.80	70.8	7.9	88.7	9.8				
	3	2.9E-09	0.08	9.4	5.6E-04	0.07	0.07	8.2			11.4	2	202.0	128.3	73.0	0.80	248.7	27.4	311.2	34.3				
	5	1.3E-09	0.06	9.4	4.3E-04	0.07	0.02	3.0			10.1	1	142.5	133.5	68.2	0.79	171.1	22.1	216.7	28.1				
	7	7.7E-10	0.03	4.9	2.3E-04	0.04	0.01	1.2			5.2	1	170.6	122.0	67.4	0.79	188.6	45.7	239.4	58.1				
	9	5.1E-10	0.03	4.7	1.9E-04	0.03	0.02	3.2			5.5	0	132.5	128.1	64.8	0.77	139.9	17.8	180.5	23.0				
	10	2.0E-10	0.02	6.0	1.4E-04	0.04	0.03	7.9			7.8	0	167.2	89.2	52.8	0.72	63.7	7.3	88.7	10.1				
PRU106	4	9.8E-09	0.74	62.0	3.3E-01	0.45	0.33	27.7			68.9	1	153.6	176.3	84.0	0.83	97.7	10.7	117.9	12.9	<b>89.7</b>	<b>11.2</b>	<b>111.5</b>	<b>9.1</b>
	5	4.2E-09	0.33	49.1	3.9E-01	0.36	0.39	57.6			63.0	1	205.2	114.1	67.0	0.78	81.8	9.0	105.0	11.6				

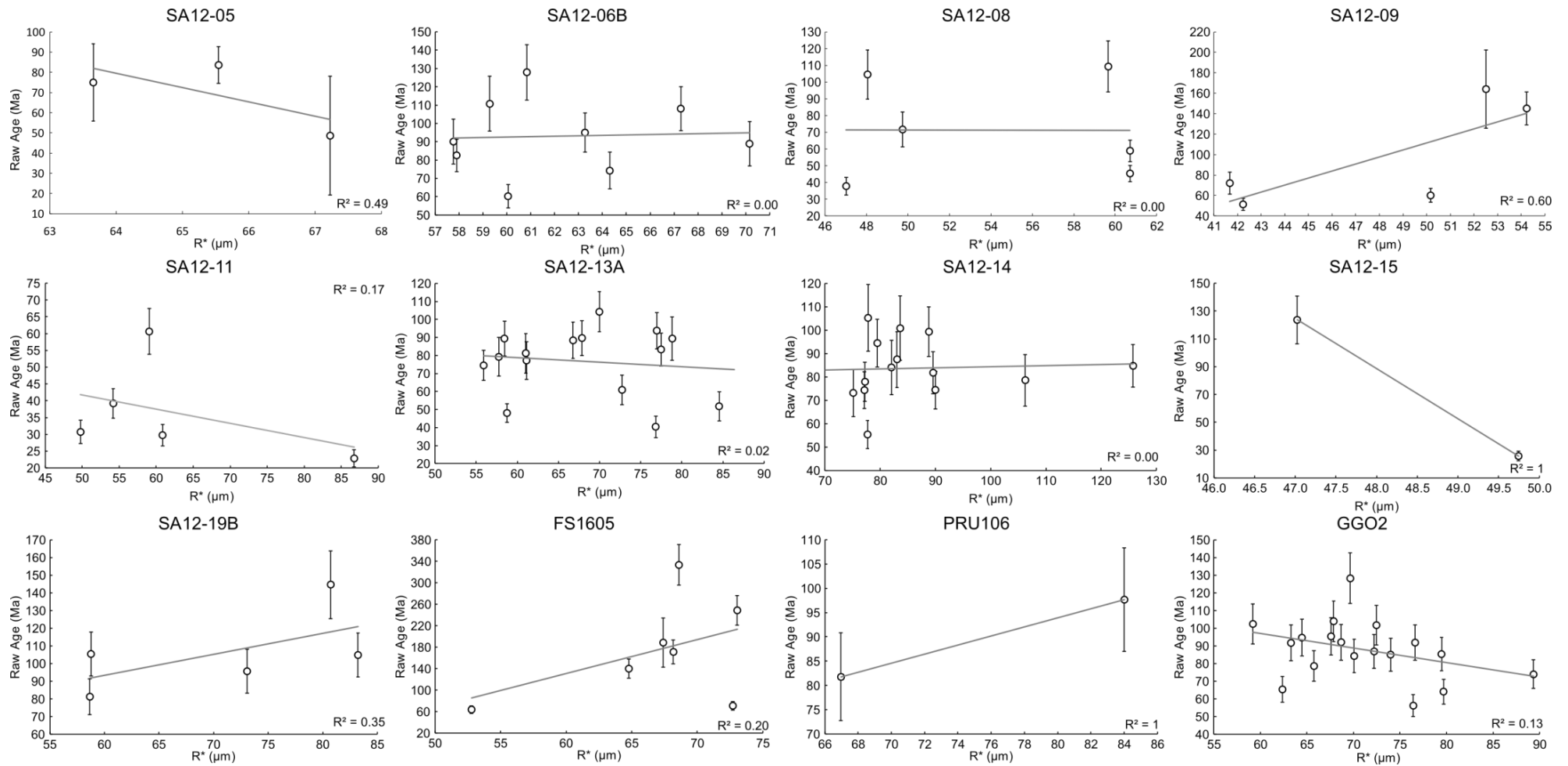
Table 6-2: Continued.

(c. 19% and 55%) is large. That being said, the mean age does provide a useful frame of reference to compare against AFT ages and the wider geological context. The oldest single grain age of  $333.2 \pm 37.7$  Ma is obtained from sample FS1605 while the youngest of  $16.6 \pm 1.8$  Ma is from SA12-11. AHe ages are subject to extreme variation due to their eU content, grain size and crystal fragmentation. Therefore the AHe ages alone cannot be interpreted based only on the observed ages (see Chapter 4 - Section 4.4).

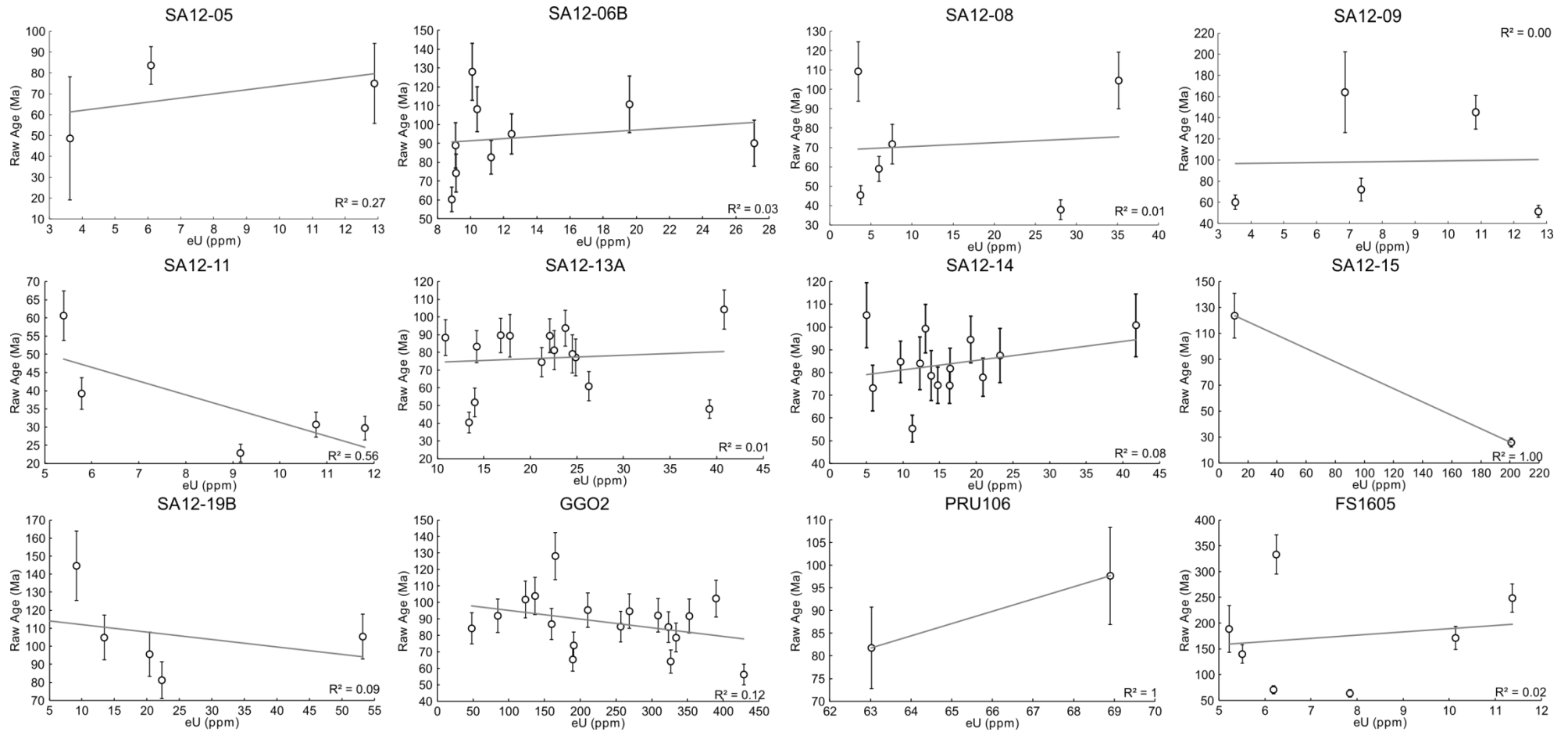
### 6.4.2 Data quality assessment

67% of AFT ages are older than their corresponding mean AHe ages and are within error of all mean AHe ages (Fig. 6-5). However, a significant number of single grain analyses are older than their respective fission track age. The most extreme sample is FS1605 where the oldest single grain age is more than twice the AFT age. Although a major discrepancy exists here between the AHe and AFT data, this old age cannot be easily discarded. There were no analytical problems during the analysis of these samples; the sample itself was selected and screened carefully for inclusions; and the dispersion of the remaining single grain analysis in the sample data set are not so reproducible that this old age can be excluded statistically. There is a positive correlation between age and grain radius and none with eU. The eU values are also quite low ( $< 12$  ppm) and this is validated by an average U content of 10 ppm from AFT analysis. It should be noted that this sample has a relatively short track length and broad TLD. These old ages may have been caused by long residence times at relatively hot temperatures combined with slow cooling or partial resetting of helium ages following an initial cooling event. In short, although the data look incompatible with AFT data they should not be dismissed immediately.

In general, samples do not show any strong positive age- $R^*$  relationships (Fig. 6-8). Considering the discussion in Chapter 4 and the data presented in Chapter 5, caution is required when looking for correlations in data sets with relatively few data points. As such only SA12-06B; SA12-13A; SA12-14 and GGO2 can be interrogated properly. Only SA12-06B shows any correlation between AHe age and  $R^*$ , and this is a negative one. Correlations are also absent in plots of eU



**Figure 6-8: Plot of AHe age against spherical equivalent grain radius (R\*). AHe ages are mean AHe ages uncorrected for alpha-ejection. Uncertainties on AHe ages are 1σ analytical uncertainty (typically 1-3%) + 1σ standard deviation of Durango standards (10%). R\* is calculated using the formula  $(3*(RL))/(2*(R+L))$  where R = the measured radius of the apatite crystal and L = measured length of the apatite crystal.**



**Figure 6-9: Plot of AHe age against effective uranium (eU). AHe ages are mean AHe ages uncorrected for alpha-ejection. Uncertainties on AHe ages are  $1\sigma$  analytical uncertainty (typically 1-3%) +  $1\sigma$  standard deviation of Durango standards (10%). eU is calculated using the formula  $[U_{ppm}] + (0.235 * [Th_{ppm}])$  and is used as a proxy for accumulated radiation damage.**

against AHe age (Fig. 6-9). This is not to suggest that grain size and radiation damage are not having an effect on measured AHe age but instead that there is no clear signal that one is dominating over the other.

### 6.4.3 Summary of AHe Data

The AHe ages presented here range between Mid Jurassic to Late Oligocene. This does not dictate that major cooling occurred during either of these time periods but instead highlights the complex nature of AHe dating in geologically old regions. Ultimately, AHe ages alone only provide an estimate on the timing of cooling. In order to understand the thermal history in a more quantitative manner, thermal histories consistent with the measured ages need to be derived while taking into account the effects of radiation damage and grain size. Quantitative thermal history modelling including these data is the focus of the following section. Qualitatively, the helium data appears consistent with major cooling occurring across southwest Africa during the Cretaceous. However, there appears to be some evidence that Cenozoic cooling may be expressed locally. These data further highlight the problems that arise with analysing only a small number of grains (i.e. <10). If dispersion is high within a sample, then only a large number of single grain analyses will confirm this. Moreover, if samples are dispersed and an outlier still exists then a large number of single grain analysis will be required to confidently and statistically exclude this outlier from the data. Multiple single grain analysis not only provides more information on the samples AHe age but also on the influence of radiation damage and grain size on that age.

## 6.5 Thermal History Modelling

### 6.5.1 Approach

The modelling approach adopted here is described in detail in Chapter 4 - Section 4.5. Two of the samples collected were clasts from within the Dwyka glacial tillite. SA12-05 was a granite dropstone and SA12-06B was a gneissic boulder within a fine grained, weathered, cream coloured matrix. As such these samples, when modelled are assigned a specific initial constraint of  $300 \pm 10$  Ma,

$20\pm 10^{\circ}\text{C}$  (stratigraphic age consistent with the Dwyka formation). As described for samples from the NQH study area, basement rocks were assigned an initial constraint of  $350\pm 10$  Ma and  $100\pm 100^{\circ}\text{C}$  to allow freedom for the initial model conditions. For many samples, maximum palaeo-temperatures are significantly elevated so that the AFT and AHe thermochronometers were almost completely reset and this is reflected in samples which have long MTLs and narrow TLDs. There are, however, samples with low MTLs and high MTL-SD. These samples possess a significant number of partially annealed tracks arising from partial resetting of the AFT system at palaeo-temperatures  $<110\pm 10^{\circ}\text{C}$ . Therefore, different initial constraints will be tested to allow for the preservation and annealing of very old tracks. For all samples the present-day temperature value is assumed to be  $20\pm 10^{\circ}\text{C}$ . The lack of any further independent geological stratigraphic evidence prevents the use of additional constraints being placed on the thermal histories. Where sporadic Cretaceous and Cenozoic geological features are present, the influence of speculative constraints on the thermal history can be tested. In the same manner as described in Chapter 5 - Section 5.5.1, thermal history profiles are modelled for samples which yield similar age and track length parameters and thermal histories and do not appear to be separated by major structures. This approach is employed to increase the amount of information used to generate thermal history models which may satisfy the observed data of many samples.

### **6.5.2 Modelling results**

Thermal histories were obtained for all 14 outcrop samples along the BMP transect. While many samples across the NQH study area could be grouped and discussed together based on their common thermal history styles, but for samples from the BMP transect, this is more difficult. Heterogeneous thermal histories across the study area may arise because of a combination of factors such as the presence of known and unknown structures; complex and spatially variable surface processes caused by migration of the Orange River which dissects the study area; or local thermal perturbations by intrusive bodies sufficiently close to samples so that they are thermally reset. Although the style of cooling may be variable across the BMP study area the timing of major cooling

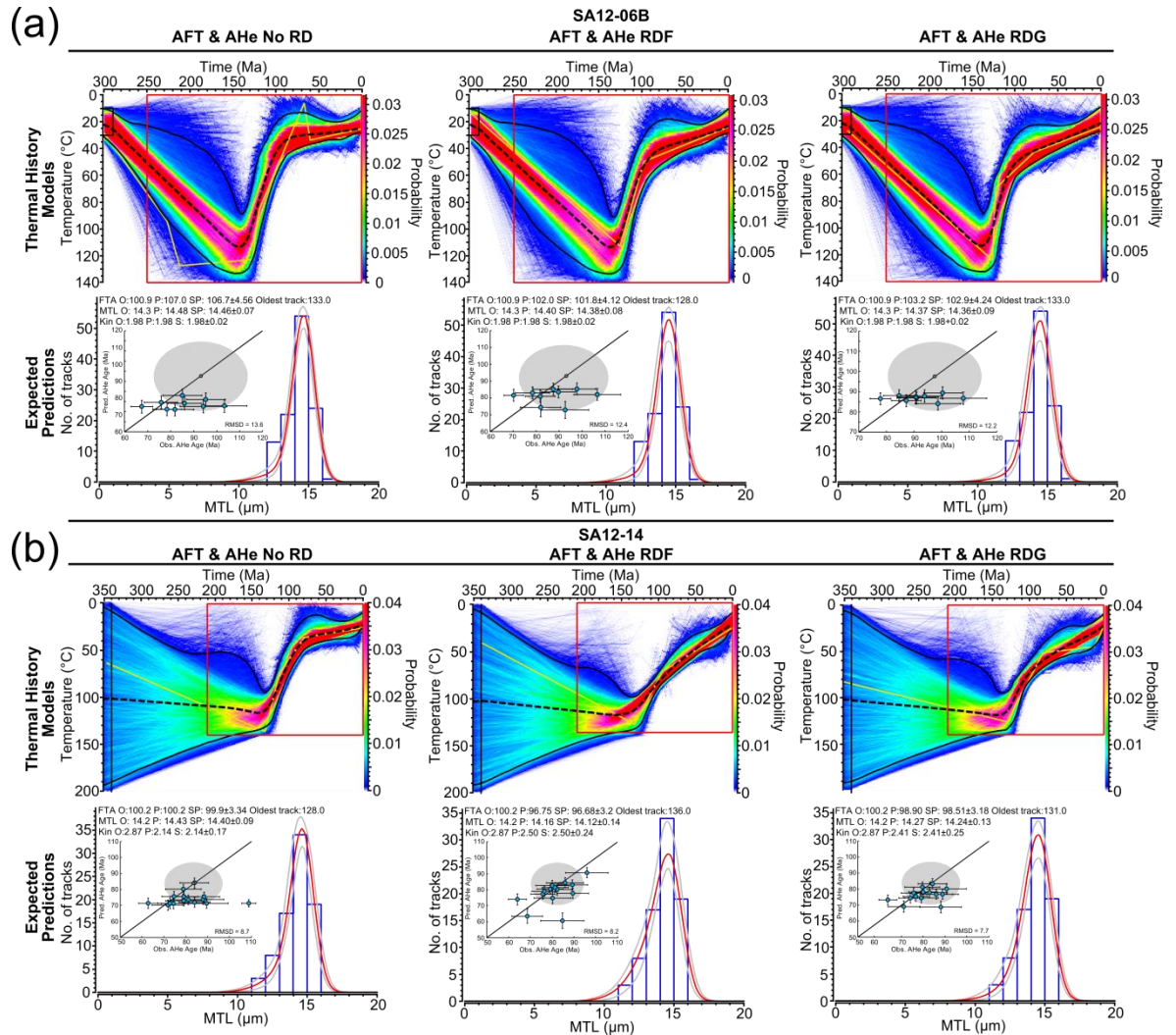
events is consistent with what has been recorded in the NQH. Each of the major cooling intervals: (i) 150 - 130 Ma; (ii) 110 - 90 Ma and (iii) 80 - 60 Ma, are also recorded here to some extent.

### **6.5.2.1 Early Cretaceous cooling (150 – 130 Ma)**

At the eastern boundary of the BMP study area, near the town of Douglas, two samples were collected from granitic gneiss boulder clasts within the Dwyka group glacial tillite. These models are constrained to be at the surface in the Permian. In both thermal histories the samples are heated to temperatures of c. 110 - 115°C by the Late Jurassic - Early Cretaceous before cooling initiates. SA12-05 cools slowly at a rate of c. 0.78°C/Myr until present day. However, SA12-06B cools more rapidly at c. 130 Ma until c. 95 Ma at a rate of c. 1.86°C/Myr (Fig. 6-10a). Following this period of enhanced cooling the rate drops to 0.21°C/Myr until present day. The style of cooling history shown by SA12-06B is mimicked by SA12-09 (see Appendix 7). Further west and northwest SA12-14 and GGO2 show the onset of cooling at this time with an initial rapid pulse of cooling at rates of c. 1 to 1.6°C/Myr followed by slower cooling rates of c. 0.2 to 0.6°C/Myr (Fig. 6-10b). The initial pulse of cooling is replaced by a slower cooling phase by c. 100 - 80 Ma, depending on which radiation damage model is used. The data fit for Early Cretaceous cooling models is generally good, particularly for the AFT data. AHe data is more complex but shows a good data fit when the resampled observed age is compared with the predicted age rather than the actual measured age.

### **6.5.2.2 Mid-Cretaceous cooling (110 – 90 Ma)**

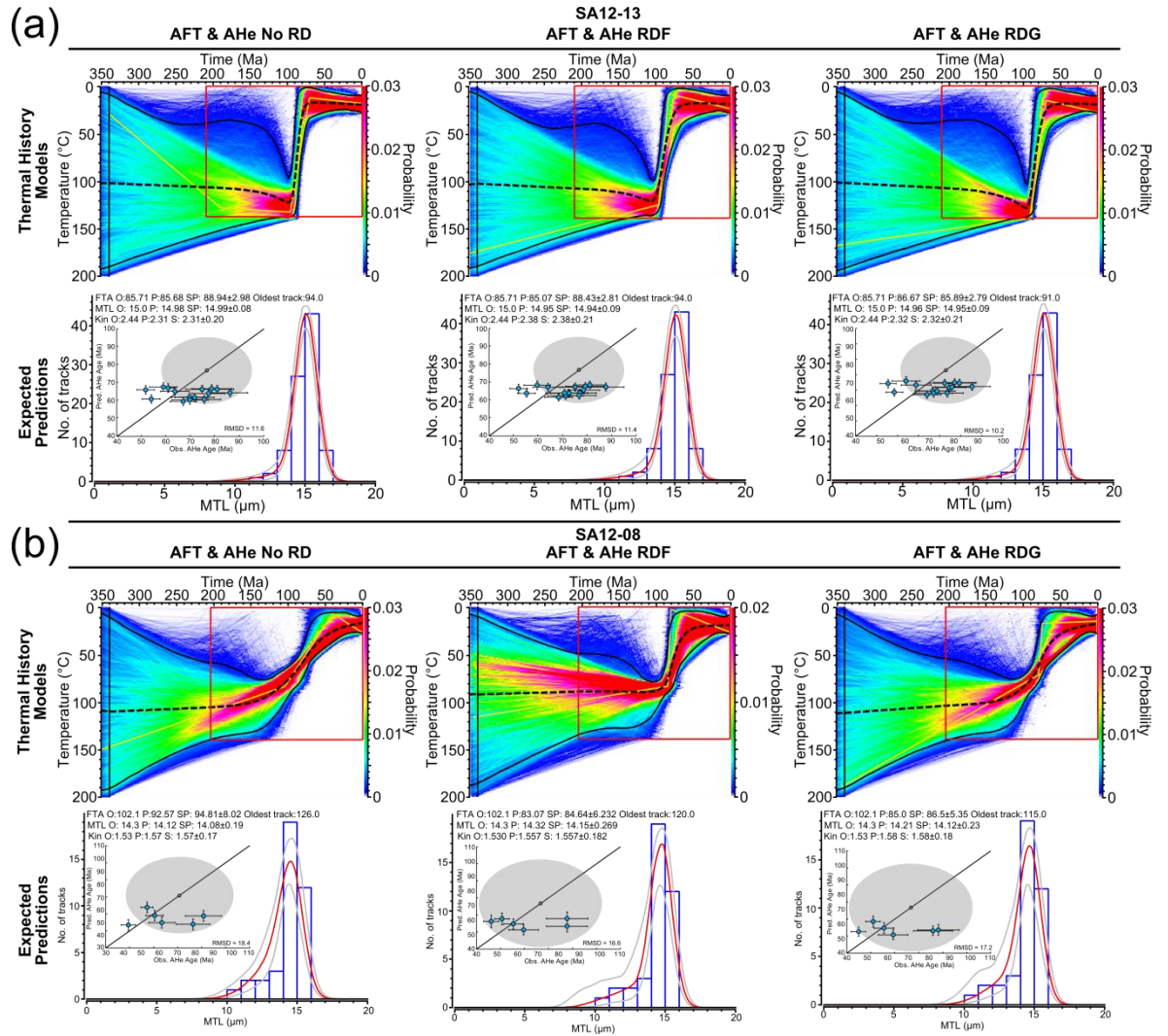
Almost half of the samples from the BMP transect record the onset of cooling during the Mid-Cretaceous from c. 110 to 90 Ma. Four samples are characterised by rapid cooling at this time at rates of c. 1.5 to 2.5°C/Myr. SA12-13A shows the most rapid cooling at this time with cooling rates at almost 5°C/Myr for a period of 20 Myr (Fig. 6-11a). SA12-08 however is slightly more ambiguous (Fig. 6-11b). Without including radiation damage effects, the model shows relatively slow cooling of c. 0.74°C/Myr with a timing of onset difficult to pin down but appears c. 20 Myr earlier than the time interval discussed here. Incorporating radiation



**Figure 6-10: Thermal history models that represent samples which cooled (a) rapidly and (b) slowly, over the interval 150 – 130 Ma. The expected model is represented by a dashed black line with 95% credible intervals (solid black lines). The maximum likelihood model is also presented (yellow line). The black box represents the initial constraint on the model. The red box represents general ranges for the prior (see Chapter 4 – Section 4.5.1). The colour scale represents the probability distribution of the thermal history. The blue histograms represent the measured TLD; red line represents the predicted TLD from the expected model with 95% credible intervals (grey curves). The blue circles illustrate the relationship between the observed and predicted AHe age. The dark grey circle represents the mean measured AHe age (uncorrected for alpha-ejection). The light grey circle represents the  $1\sigma$  standard deviation on the mean AHe age.**

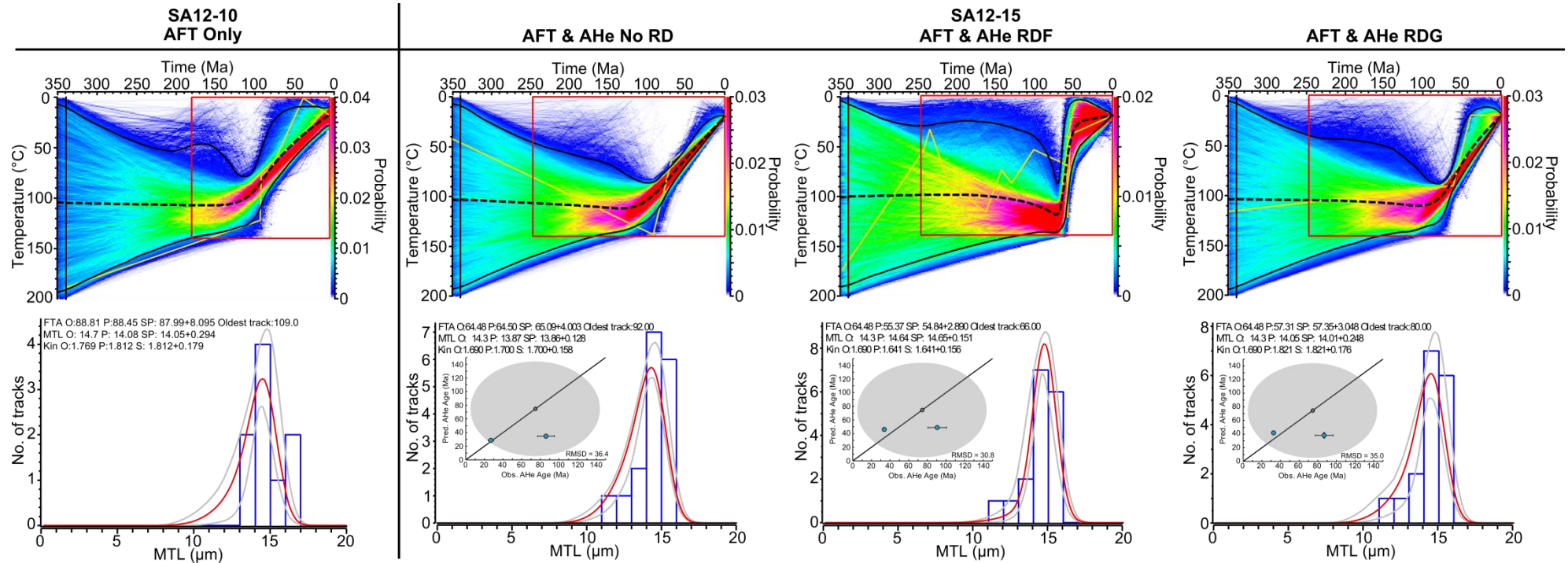
damage into the models steepens the cooling profile and brings the onset of cooling forward to c. 100 Ma. The episode of cooling is best constrained as the sample passes through temperatures cooler than 80 - 90°C. The model is poorly constrained before this time and no comment can be made as to whether the sample was at sufficiently elevated temperatures to reset the AFT data. This is not likely to be the case as the TLDs show a distinct tail of old, partially annealed, HCT lengths. The track length data is fitted reasonably well in all





**Figure 6-11: Thermal history models that represent samples which cooled (a) rapidly and (b) slowly, over the interval 110 – 90 Ma. The expected model is represented by a dashed black line with 95% credible intervals (solid black lines). The maximum likelihood model is also presented (yellow line). The black box represents the initial constraint on the model. The red box represents general ranges for the prior (see Chapter 4 – Section 4.5.1). The colour scale represents the probability distribution of the thermal history. The blue histograms represent the measured TLD; red line represents the predicted TLD from the expected model with 95% credible intervals (grey curves). The blue circles illustrate the relationship between the observed and predicted AHe age. The dark grey circle represents the mean measured AHe age (uncorrected for alpha-ejection). The light grey circle represents the  $1\sigma$  standard deviation on the mean AHe age.**

models however the AFT age and AHe ages are fitted less well. The AHe ages are fitted best when radiation damage is incorporated but the AFT data is fitted better without including the effects of radiation damage. For all other samples the data fit is generally good. Maximum likelihood models either followed the general shape of the expected model or minor perturbations are within the 95% credible intervals of the expected models. SA12-08 is again the exception to this as the maximum likelihood model when the RDAAM radiation damage model



**Figure 6-12: Thermal history models that represent samples with poorly constrained or ambiguous cooling histories. The expected model is represented by a dashed black line with 95% credible intervals (solid black lines). The maximum likelihood model is also presented (yellow line). The black box represents the initial constraint on the model. The red box represents general ranges for the prior (see Chapter 4 – Section 4.5.1). The colour scale represents the probability distribution of the thermal history. The blue histograms represent the measured TLD; red line represents the predicted TLD from the expected model with 95% credible intervals (grey curves). The blue circles illustrate the relationship between the observed and predicted AHe age. The dark grey circle represents the mean measured AHe age (uncorrected for alpha-ejection). The light grey circle represents the  $1\sigma$  standard deviation on the mean AHe age.**

after Flowers et al. (2009) is incorporated suggests two enhanced cooling episodes; one at c. 150 Ma and a second at 80 Ma. While the maximum likelihood model will not be taken as the preferred model for further discussion it is important to appreciate the possible complexity that a model may exhibit despite having no independent geological constraints to validate it.

Slower cooling initiating at this time is recorded by SA12-10 and for SA12-15 when no radiation damage effects are considered (Fig. 6-12). However, for both of these samples limited track length data was obtained (9 and 17, respectively) and for SA12-10, limited single grain FT ages were obtained (12 crystals). SA12-15 is supplemented with two AHe ages although these are wildly incoherent spanning a range of 100 Ma. However, inverting SA12-15 with these irregular AHe ages and including either radiation damage model changes the implied thermal history dramatically. Instead of protracted cooling from c. 110 Ma the thermal history becomes rapidly cooled at c. 70 Ma. In short, the data for both of these samples is relatively poor and the models are poorly constrained. The dominant cooling style over 110 - 90 Ma at this time is still suggested to be fairly rapid.

### **6.5.2.3 Late Cretaceous cooling (80 – 60 Ma)**

Much like its presence in the NQH, a Late Cretaceous cooling episode is poorly recorded in samples from the BMP transect. SA12-11, however, regardless of how radiation damage is treated in the modelling approach, consistently shows cooling beginning at 75 Ma at quite a fast rate of 1.4 °C/Myr to the present day (Fig. 6-13). On one hand the reliability of the model is questioned by the quality of the SA12-11 AFT dataset which consists of only 15 HCTs and 16 single grain ages and therefore leaves the TLD poorly defined. On the other hand a young cooling episode is supported by young AHe single grain ages from SA12-11 ranging from c. 16 - 38 Ma. Both the FT age and AHe ages are reproduced fairly well by the model. The only other occurrence of an 80 - 60 Ma cooling episode is in a thermal history model for SA12-15 using the radiation damage model of Flowers et al. (2009) where cooling initiates at 70 Ma and is more rapid than observed for SA12-11 (Fig. 6-12). However, as discussed above this sample also has limited track length information and the AHe ages available add additional

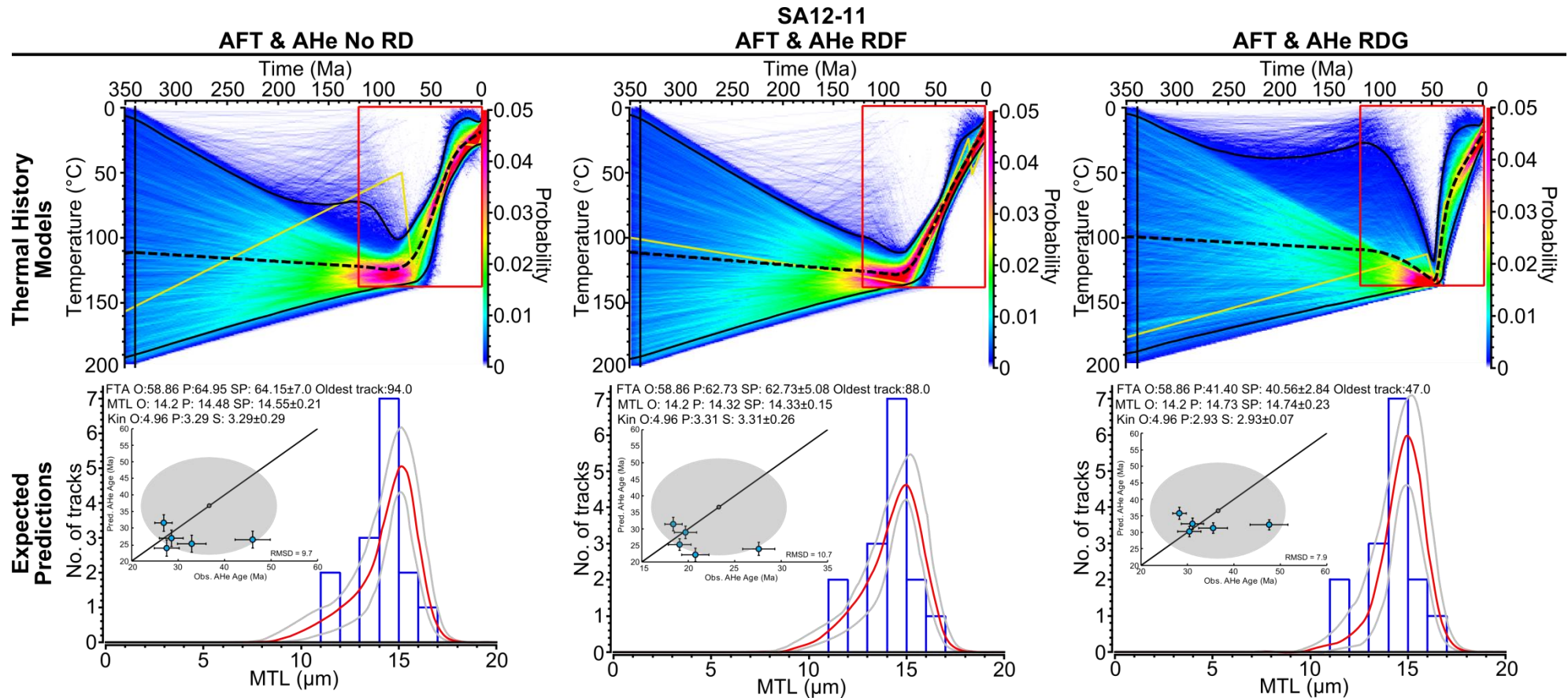


Figure 6-13: Thermal history models that represent samples which cooled during the interval 80 – 60 Ma. The expected model is represented by a dashed line with 95% credible intervals (solid black lines). The maximum likelihood model is also presented (yellow line). The black box represents the initial constraint on the model. The red box represents general ranges for the prior (see Chapter 4 – Section 4.5.1). The colour scale represents the probability distribution of the thermal history. The blue histograms represent the measured TLD; red line represents the predicted TLD from the expected model with 95% credible intervals (grey curves). The blue circles illustrate the relationship between the observed and predicted AHe age. The dark grey circle represents the mean measured AHe age (uncorrected for alpha-ejection). The light grey circle represents the 1 $\sigma$  standard deviation on the mean AHe age.

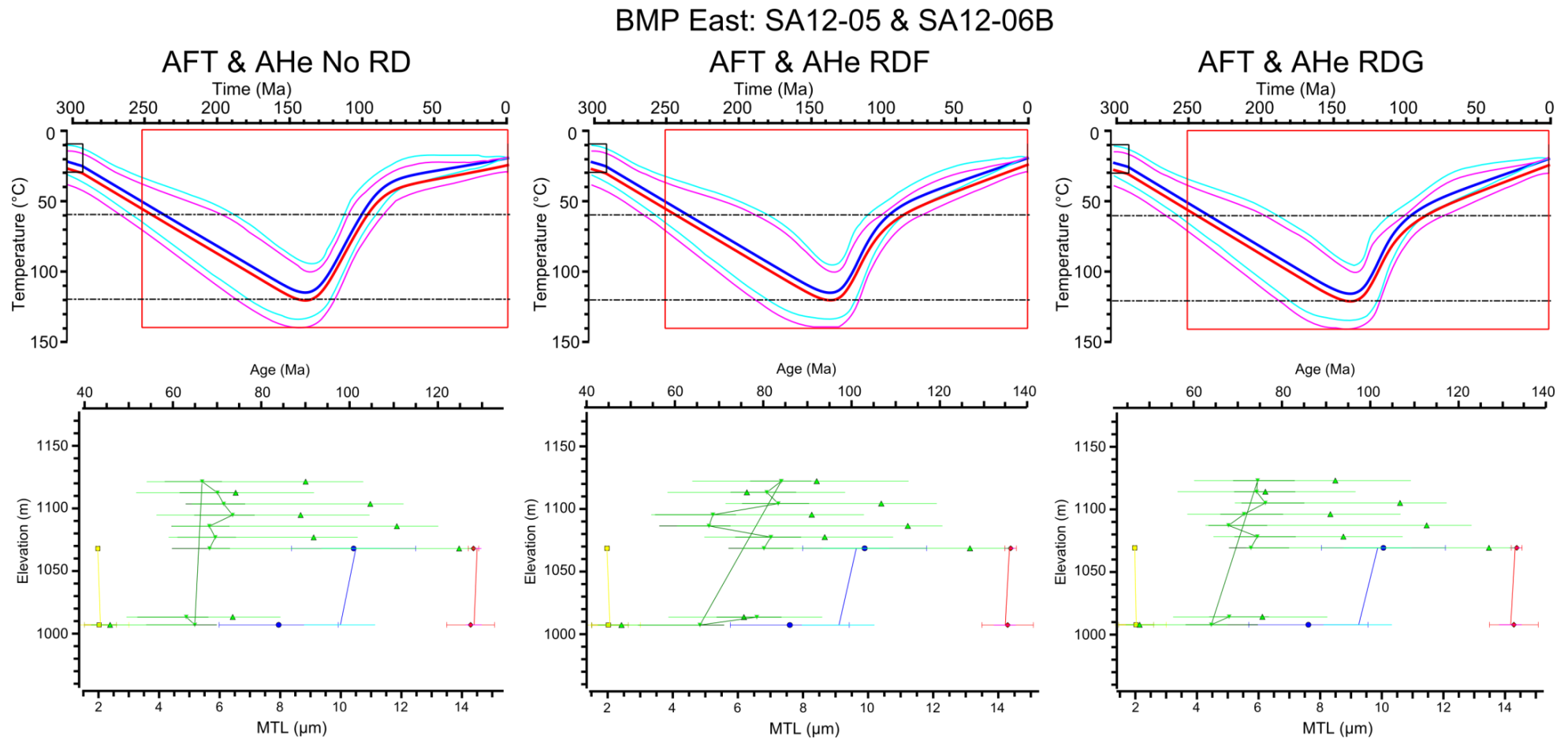
complexity to the dataset rather than help to resolve it. As such, the true nature of Late Cretaceous - Early Cenozoic cooling remains uncertain.

### 6.5.3 Alternative scenarios

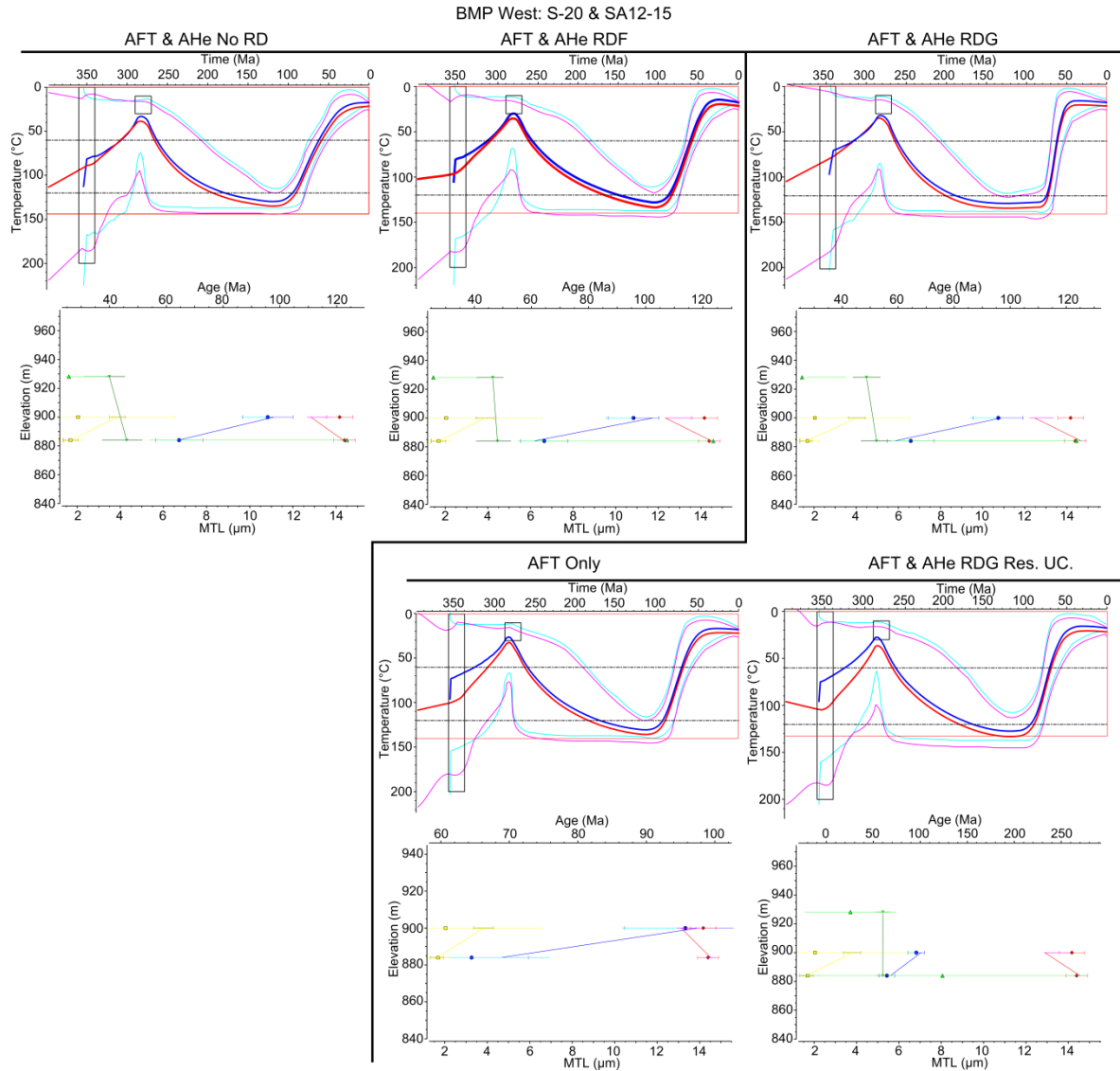
#### 6.5.3.1 Profile modelling

SA12-05 and SA12-06B, located near to the town of Douglas, are separated by a distance of c. 70 km and elevation range of only 60m. The surrounding region is relatively free of major structures. More importantly, the samples share common thermal history features, namely near surface temperatures at c. 300 Ma, heating until c. 150 - 130 Ma before the onset of protracted cooling. These samples are treated as a profile and modelled together to investigate whether a common thermal history can satisfy both data sets (Fig. 6-14). The composite thermal history is similar to the individual model for SA12-06B, however, the model still fits the data for SA12-05 well. The data fit is poorest for the AHe data from SA12-06B but predicted AHe ages still overlap with the resampled observed AHe age. The thermal history suggests cooling at a rate of c. 2.4°C/Myr beginning in the Early Cretaceous before gradually slowing down from c. 105 - 70 Ma to a rate of 0.4°C/Myr until the present day.

On the western side of the transect SA12-15 is less than 10km NW from sample S-20 obtained by Brown (1992). Moreover, both of these samples lie to the west of the Hartbees River Thrust fault and may, together, represent the exhumation of a block of crust (BMP West profile; Fig. 6-15). An additional consideration is how to deal with S-20 being a sample from the Permian Ecca Group and SA12-15 being from the NMP basement. Individual temperature time constraints are specified for each sample which allows them to cool independently during the early part of the thermal history ( $S-20_{\text{constraint}} = 280 \pm 10 \text{ Ma}, 20 \pm 10^\circ \text{ C}$ ;  $SA12-15_{\text{constraint}} = 350 \pm 10 \text{ Ma}, 100 \pm 100^\circ \text{ C}$ ). Care must be taken with modelling this data because sample S-20 is characterised by a broad TLD with a significant number of short track lengths. As such a variety of thermal histories, some simple, some complex, may satisfy the observed data. The approach adopted here of modelling multiple samples as one, should help to resolve the uncertainties in such samples. Unfortunately in this case, sample SA12-15 contains limited AFT



**Figure 6-14: Bushmanland East profile (SA12-05 and SA12-06B) thermal history models. Expected model of the top and bottom sample is represented by a thick blue and red line, respectively, with 95% credible intervals (cyan and magenta lines). Black box represents initial constraint on the model. Red box represents general ranges for prior (see Chapter 4 – Section 4.5.1). Yellow square/bar = Measured/predicted  $D_{par}$ ; blue circle/light blue bar = Measured/predicted AFT age; red diamond/magenta bar = measured/predicted MTL; green triangle/light green bar/dark green bar = measured/resampled observed/predicted AHe age. Histograms represent the measured TLD; red line represents the predicted TLD with 95% credible intervals (grey curves).**



**Figure 6-15: Bushmanland West profile (S-20 and SA12-15) thermal history models. Expected model of the top and bottom sample is represented by a thick blue and red line, respectively, with 95% credible intervals (cyan and magenta lines). Black box represents constraints on the model. Red box represents general ranges for prior (see Chapter 4 – Section 4.5.1). Yellow square/bar = Measured/predicted  $D_{par}$ ; blue circle/light blue bar = Measured/predicted AFT age; red diamond/magenta bar = measured/predicted MTL; green triangle/light green bar/dark green bar = measured/resampled observed/predicted AHe age. Histograms represent the measured TLD; red line represents the predicted TLD with 95% credible intervals (grey curves). Res. UC. = Resampled uncertainty model.**

single grain ages and HCT lengths as well as only two, highly dispersed AHe ages. Including all AFT and AHe data available for both of these samples produces models which reach temperatures greater than  $120^{\circ}\text{C}$  during the Early Cretaceous.

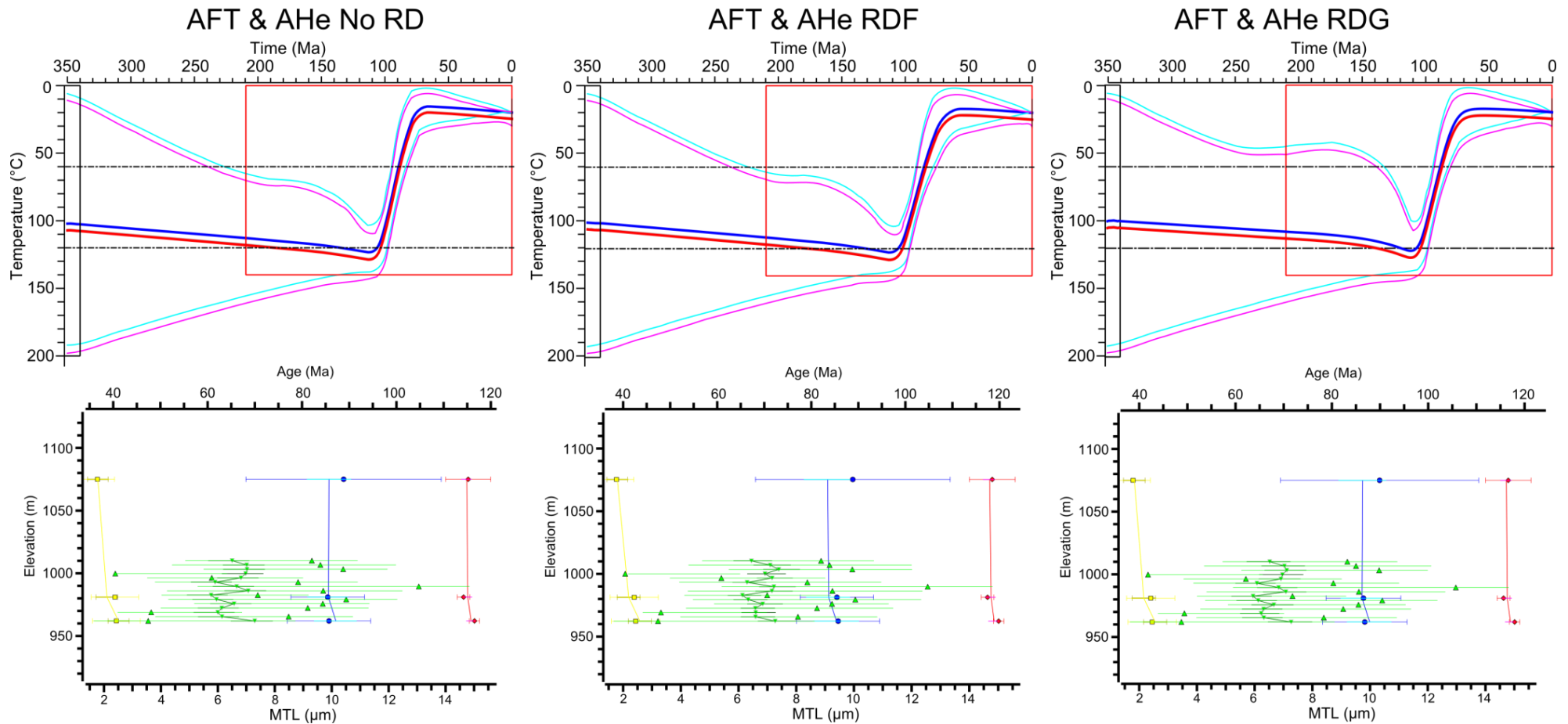
Modelling the BMP West profile using the radiation damage model of Flowers et al. (2009) and modelling without radiation damage predicts cooling to have initiated at c. 100 Ma with the former model cooling faster than the latter. The thermal history

obtained using radiation damage after Gautheron et al. (2009) implies that rapid cooling initiates closer to 80 Ma. The previous discussion regarding the uncertainty surrounding radiation damage models should be noted here and the highly dispersed but limited AHe data should be acknowledged. Moreover, although the AFT data is reproduced during the modelling reasonably well, the poorest fit is the MTL for S-20 using the RDG (Gautheron et al., 2009) model. The AHe data may be incorrect due to a combination of analytical error, poorly understood radiation damage effects or some other factor as discussed in Chapter 4 and yet exert a significant influence on the thermal history. The influence of the AHe data on the thermal history is also explored (Fig. 6-15). By removing the AHe ages completely, the AFT data is well reproduced and the thermal history is rapidly cooled at c. 100 Ma, similar to the No RD and RDF models. So that AHe data is not being discarded purely on the basis that it doesn't look right, the data are included once more but in this scenario the uncertainty on the AHe age is treated as an unknown and rescaled during the modelling process. In this scenario the thermal history model is again rapidly cooled at c. 100 Ma with an improved data fit than that of the original RDG model. This model is the preferred model for the BMP East profile.

Three samples separated by nearly 50 km were taken from basement rock types within a block bounded by the Hartbees River Thrust fault to the west and the Brakbos fault to the east (BMP Central profile). The dataset of these samples is variable with SA12-13A having high quality AFT data and many single grain AHe ages, SA12-12 having a quality AFT dataset and no AHe ages and SA12-10 having limited HCTs and no AHe data. Each of these samples, however, is characterised by the same style of thermal history. This thermal history is one which is rapidly cooled at c. 100 Ma. It is no surprise then that integrating these samples together and inverting the data produces a rapidly cooled thermal history at c. 100 Ma (Fig. 6-16). This cooling history appears fairly robust across this fault bounded block and is distinct from the cooling episodes recorded by the two previous composite models discussed above.



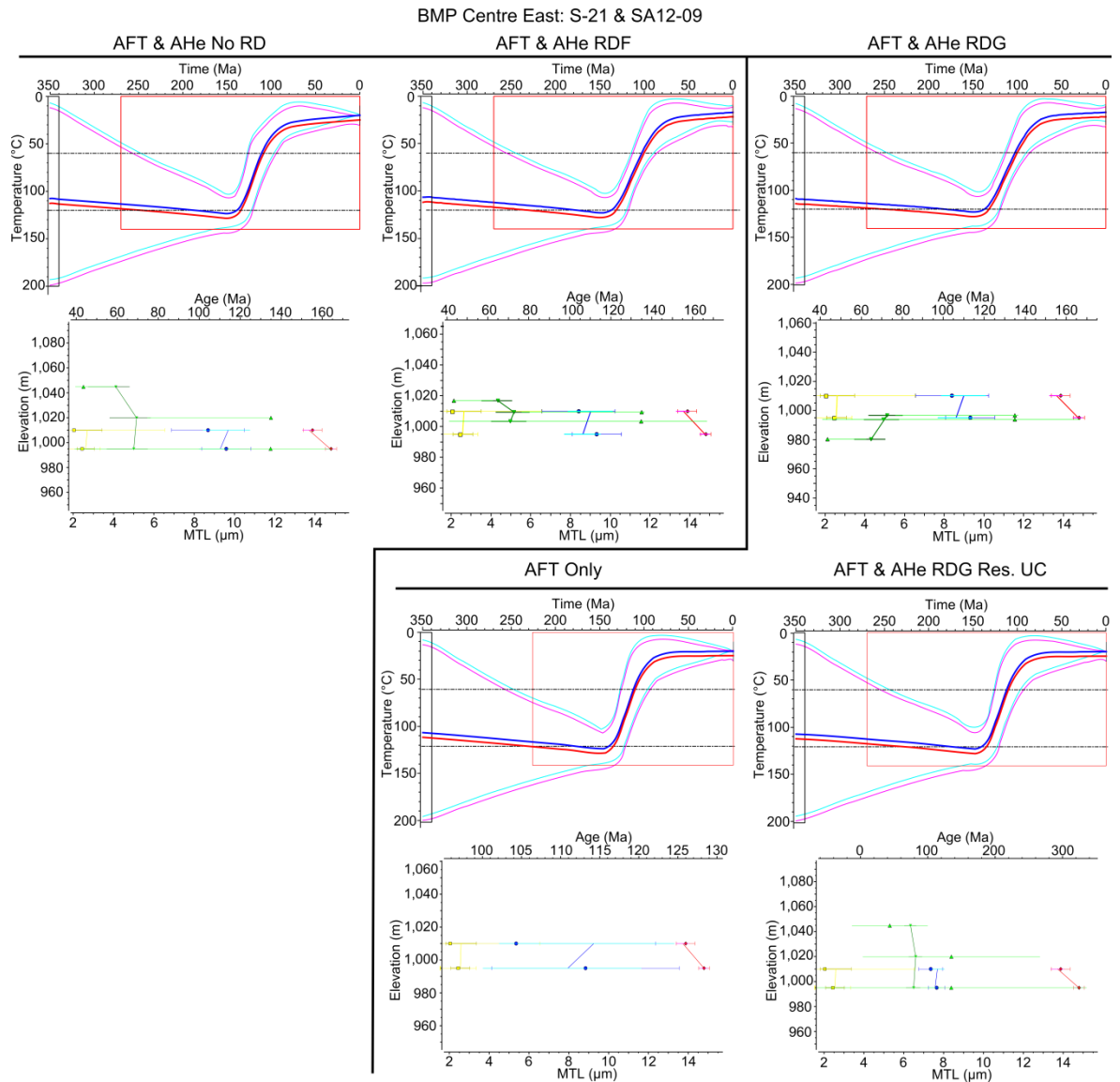
## BMP Central: SA12-13A, SA12-12, SA12-10



**Figure 6-16: Bushmanland Central profile (SA12-13A, SA12-12 and SA12-10) thermal history models. Expected model of the top and bottom sample is represented by a thick blue and red line, respectively, with 95% credible intervals (cyan and magenta lines). Black box represents initial constraint on the model. Red box represents general ranges for prior (see Chapter 4 – Section 4.5.1). Yellow square/bar = Measured/predicted  $D_{par}$ ; blue circle/light blue bar = Measured/predicted AFT age; red diamond/magenta bar = measured/predicted MTL; green triangle/light green bar/dark green bar = measured/resampled observed/predicted AHe age. Histograms represent the measured TLD; red line represents the predicted TLD with 95% credible intervals (grey curves).**

In the region between the eastern BMP profile samples and the central BMP profile samples are five samples that are within 50 km or less of each other and have distinct thermal histories. As the region is dissected by numerous large and small scale faults defining the boundary between the Archean Kaapvaal craton and Neoproterozoic NMP, caution is taken when grouping samples together in one crustal block. Sample SA12-09 and S-21 are 10km apart and reside in a region between the Brakbos Fault and Dadep Thrust (BMP Centre-East profile). The results from inverse modelling are very consistent regardless of how radiation damage effects are treated (Fig. 6-17). The cooling history is one which begins at temperatures  $> 120^{\circ}\text{C}$  at c. 150 Ma and cools reasonably quickly to below  $40^{\circ}\text{C}$  by 80 Ma. Once again the AHe data of SA12-09 is limited and dispersed and the influence of AHe ages on the thermal history is investigated in the same manner as for the BMP West profile. However, there is no major modification to the thermal history when the AHe data is removed or when the error is rescaled. This is likely due to there being enough AFT single grain ages and HCTs from both samples to constrain the model with or without the AHe data.

SA12-08 and FS1605 are further apart geographically (c. 35 km), but a profile scenario is tested for these samples as they appear, at the  $1 \times 10^6$  scale, to be within a tectonic block bounded by the Dadep Thrust and Blackridge Thrust/Doringberg Lineament (BMP Centre-East-2). Because FS1605 has an AHe age of  $333.2 \pm 37.7$  Ma a Dwyka aged constraint with a relatively low temperature range (i.e.  $100 \pm 100^{\circ}\text{C}$ ) may not be appropriate. To allow for partial resetting of AHe ages since the Permian, an initial constraint which reflects post-peak metamorphic conditions during the Proterozoic ( $900 \pm 100$  Ma,  $300 \pm 300^{\circ}\text{C}$ ) was tested (Fig. 6-18). Long residence times within the PAZ are predicted so that older tracks can be generated and partially annealed as required by the TLD. At c. 110 - 90 Ma there is an increase in the rate of cooling which is gentle or abrupt depending on the radiation damage model used. However, the AHe data is still as poorly reproduced for FS1605 as for the individual sample model. This influence of the complex AHe data set is assessed as before by (i) removing it entirely and (ii) by rescaling the error. The resultant thermal histories predict cooling to be fairly protracted from c. 200 Ma to 120 - 110 Ma before a gentle

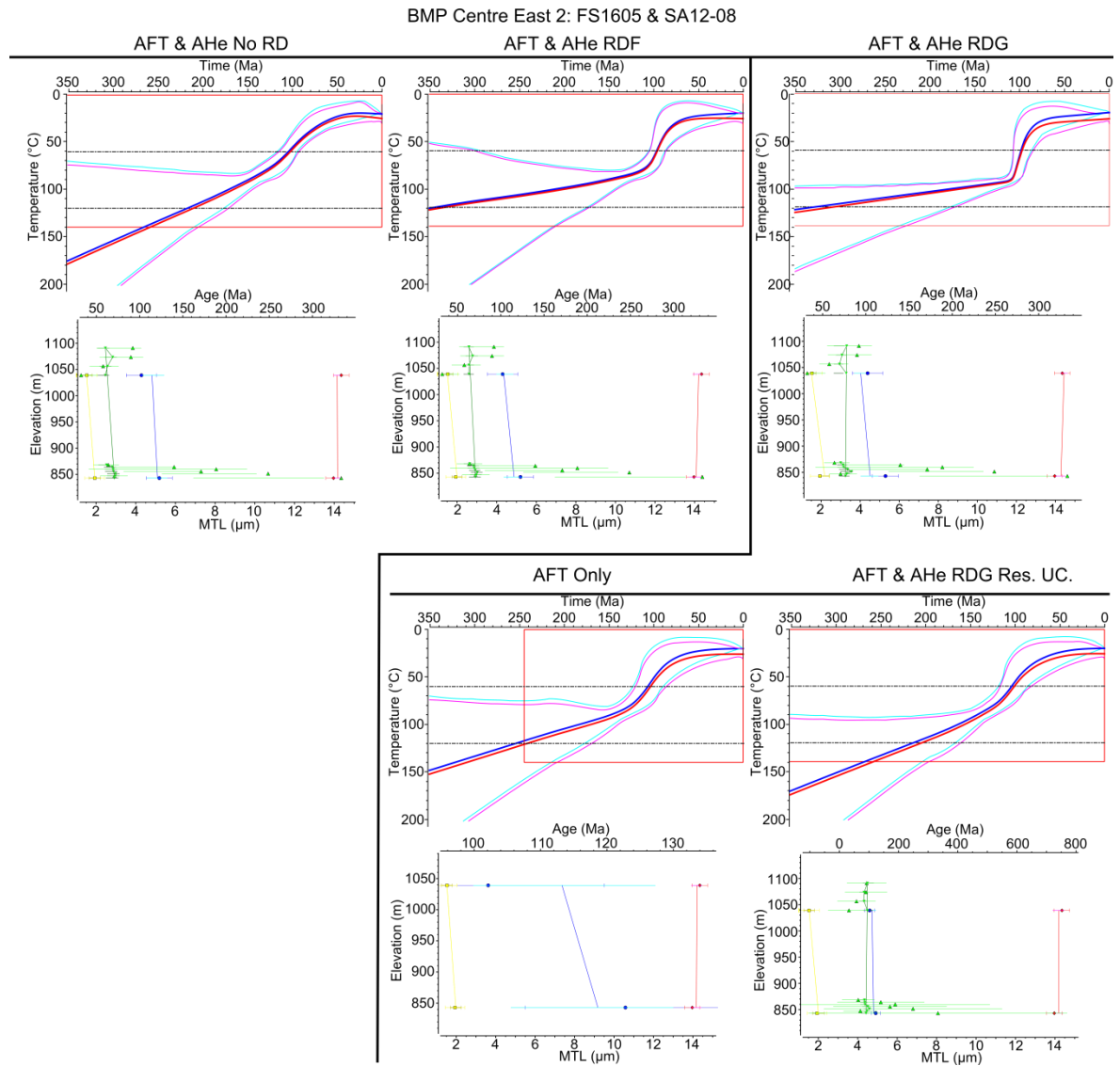


**Figure 6-17: Bushmanland Centre-East profile (S-21 and SA12-09) thermal history models.** Expected model of the top and bottom sample is represented by a thick blue and red line, respectively, with 95% credible intervals (cyan and magenta lines). Black box represents constraints on the model. Red box represents general ranges for prior (see Chapter 4 – Section 4.5.1). Yellow square/bar = Measured/predicted  $D_{par}$ ; blue circle/light blue bar = Measured/predicted AFT age; red diamond/magenta bar = measured/predicted MTL; green triangle/light green bar/dark green bar = measured/resampled observed/predicted AHe age. Histograms represent the measured TLD; red line represents the predicted TLD with 95% credible intervals (grey curves). Res. UC. = Resampled uncertainty model.

increase in the cooling rate until near surface temperatures are reached at c. 80 Ma.

### 6.5.3.2 Speculative constraints

Well dated geological features which can be used to independently constrain the thermal histories are rare. Samples SA12-05 and SA12-06B are constrained at the



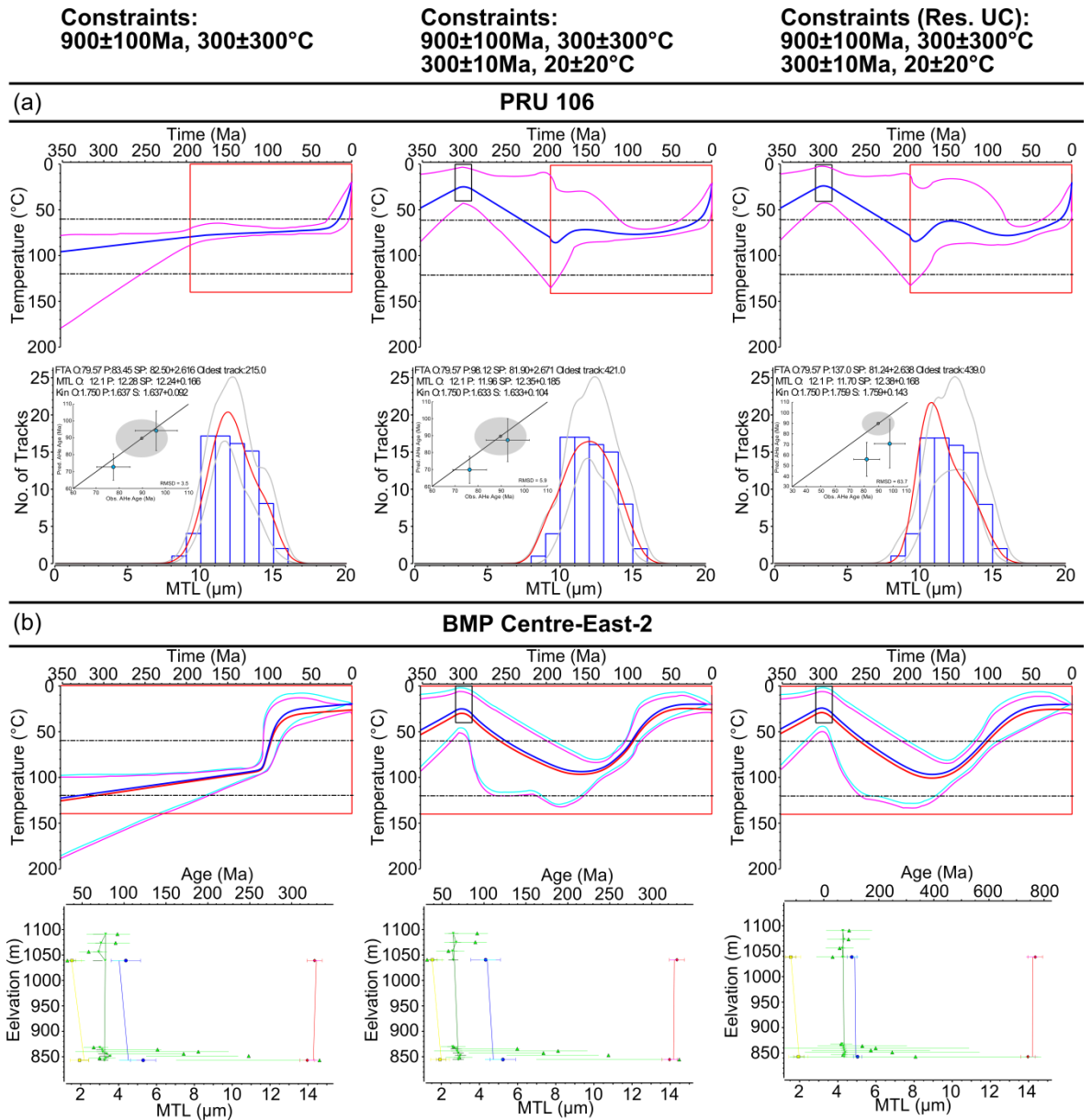
**Figure 6-18: Bushmanland Centre-East-2 profile (FS1605 and SA12-08) thermal history models.** Expected model of the top and bottom sample is represented by a thick blue and red line, respectively, with 95% credible intervals (cyan and magenta lines). Black box represents constraints on the model. Red box represents general ranges for prior (see Chapter 4 – Section 4.5.1). Yellow square/bar = Measured/predicted  $D_{par}$ ; blue circle/light blue bar = Measured/predicted AFT age; red diamond/magenta bar = measured/predicted MTL; green triangle/light green bar/dark green bar = measured/resampled observed/predicted AHe age. Histograms represent the measured TLD; red line represents the predicted TLD with 95% credible intervals (grey curves). Res. UC. = Resampled uncertainty model.

surface during the Permian as the samples were taken from basement clasts within the glacial diamictite Dwyka unit. This unit forms the base of the extensive Karoo Supergroup lithological unit which dominates much of central South Africa. It is known that the thickness of these sediments, which were deposited in a foreland basin setting, decreases to the north. However, their maximum distribution and thickness in the past is unknown. It can be speculated

that samples from basement lithologies were at or close to the surface during Dwyka glaciations and prior to the deposition of the Karoo Supergroup sedimentary units deposited during the Permian - Late Triassic. For most samples this constraint is largely insignificant as the AFT and AHe data requires that the sample reach temperatures of c. 100 - 120°C prior to cooling and therefore both thermochronometers will have been completely or almost completely reset.

Examples where the initial T-t constraint may significantly impact the thermal history are for sample PRU106 and the BMP Centre-East-2 profile model. Each of these samples have track length distributions which are negatively skewed or very broad with a low MTL. This suggests that there is an appreciable portion of short partially annealed tracks alongside more recent, less annealed, long track lengths. For simplicity the influence of changing the initial starting condition of PRU106 and the BMP Centre-East-2 model is assessed using only the radiation damage model after Gautheron et al. (2009).

PRU106 is one of the most interesting thermal histories in the entire dataset as it has features that are not observed in any other sample. There is no evidence to suggest that the data themselves are unreliable so the features in the model should be interpreted as being real. However, such interpretations should be made with caution as the thermal history is anomalous relative to the surrounding samples; AHe data is limited; and, although a large number of HCTs have been measured, TLD are broad and may have ambiguous interpretations. The interesting and unique features observed in the original “unconstrained” model are a period of modest heating from 150 - 100 Ma, long residence times at temperatures c. 70 - 80°C and a period of rapid cooling to surface temperatures at c. 30 - 20 Ma. This structure remains if the sample is simply given an initial constraint reflecting post-intrusion/metamorphism of the sample ( $900 \pm 100$  Ma,  $300 \pm 300$ °C) (Fig. 6-19a). This implies that zero net exhumation or burial occurred while the Karoo supergroup was being deposited through the Permian and Triassic. Forcing the sample to be near surface temperatures during the Permian does not greatly change the thermal history of the sample from the Early Cretaceous. While there is no apparent analytical reason to discredit the



**Figure 6-19: Thermal history models testing the influence of imposing an initial constraint on the (a) PRU 106 and (b) BMP Centre-East-2 thermal history models (see text for details). Expected model of the top and bottom sample is represented by a thick blue and red line, respectively, with 95% credible intervals (cyan and magenta lines). Black box represents constraints on the model. Red box represents general ranges for prior (see Chapter 4 – Section 4.5.1). Yellow square/bar = Measured/predicted  $D_{par}$ ; blue circle/light blue bar = Measured/predicted AFT age; red diamond/magenta bar = measured/predicted MTL; green triangle/light green bar/dark green bar = measured/resampled observed/predicted AHe age. Histograms represent the measured TLD; red line represents the predicted TLD with 95% credible intervals (grey curves). Res. UC. = Resampled uncertainty model.**

AHe ages for PRU106, they do seem largely incompatible with the AFT data and modelled thermal history. For this reason, the uncertainty on each single grain AHe age is rescaled and the sample modelled again with the same thermal history constraints. However, this does not impact the overall structure of the

model. The current thermal histories imply that PRU106 may have been buried under a relatively thin (c. 2 - 3 km) Karoo sedimentary cover and then experienced zero exhumation during the Cretaceous. The main exhumation phase occurred during minor uplift during the Miocene. The BMP Centre-East-2 profile is also forced to the surface prior to the deposition of the Karoo Supergroup (Fig. 6-19b). Heating then occurred until c. 150 Ma which equates to burial of the sample under c. 2 - 3 km of overburden. The thermal history predicts protracted cooling over the next 100 Myr until the sample has again reached near surface temperatures.

Post-rift constraints are found as preserved crater-lake deposits in the Marydale region. The Strompoor intrusive suite has crater facies with fossil evidence which is comparable in age with the fossil record found in crater-lake deposits at Banke in Namaqualand (Smith, 1986; de Wit et al., 2009). Hence, the fossil frogs and flora found at Strompoor is suggested to be Late Cretaceous - Earliest Tertiary in age. The preservation of these deposits suggests that erosion over the region has been limited since the Late Cretaceous and that the basement was close to or at the surface at this time. This constraint could only be applied to the samples which are closest to the evidence (i.e. central BMP samples). However, the unconstrained thermal history models for these samples predict that major cooling was completed prior to the Late Cretaceous and therefore incorporating this tentative constraint explicitly does not significantly influence the expected thermal history.

#### **6.5.4 Summary of modelling results**

The presence of extensive outcrops of Dwyka and Ecca group rocks suggests that the Karoo sedimentary sequence progressively covered the entire study area during the Permian and Triassic. Models which suggest burial to or residence at elevated temperatures is preferred to models which suggest cooling during the Permian and Triassic. However, for samples which have been completely reset, the Permian-Triassic history does not have an influence on the later portion of the thermal history. For the following discussion on the timing of cooling

episodes and magnitudes of denudation the models implementing the radiation damage model of Gautheron et al. (2009) are used as the primary reference.

## **6.6 Temperature-time spatial relationships: Cooling and magnitudes of denudation**

### **6.6.1 Cooling**

Three cooling episodes were proposed in the previous chapter: 150 - 130 Ma; 110 - 90 Ma; and 80 - 60 Ma. These three cooling episodes can be used in this study area to group samples that share similar timings for the onset of cooling (Fig. 6-20). Five samples record cooling during the first cooling event in the Early Cretaceous as do two “profiles” that were modelled (e.g. BMP East and BMP Centre-East). The second cooling episode is recorded by five individual samples, three of which have been modelled simultaneously to highlight their common thermal history (BMP Central). Samples which began cooling in the Early Cretaceous have reached relatively low palaeotemperatures of c. 40 - 70°C by c. 110 - 90 Ma and cooling rates begin to decrease. This highlights the local enhancement of cooling across the transect which is not recorded by some samples. The third cooling episode, is tentative with only two samples showing significant cooling from temperatures >100°C and one showing a slight increase in cooling rate following prolonged residence in the PAZ (PRU 106). Both SA12-11 and SA12-15 are interpreted with caution and further data should be acquired for both. Neither sample has robust fission track length data; SA12-11 has an anomalously high  $D_{\text{par}}$  value and SA12-15 has limited and extremely dispersed AHe data. SA12-11 however does reside in a zone of significant structural complexity and therefore the measured data may be a true reflection of the thermal history experienced by the sample.

### **6.6.2 Denudation**

Magnitudes of denudation are calculated using the T-t history predicted by the expected thermal history model and assuming geothermal gradients of 15, 25 and 35°C/km as described in Chapter 5 (Fig. 6-21). The plateau transect is 300 km in length and cuts through the basement rocks of the NMP and across major



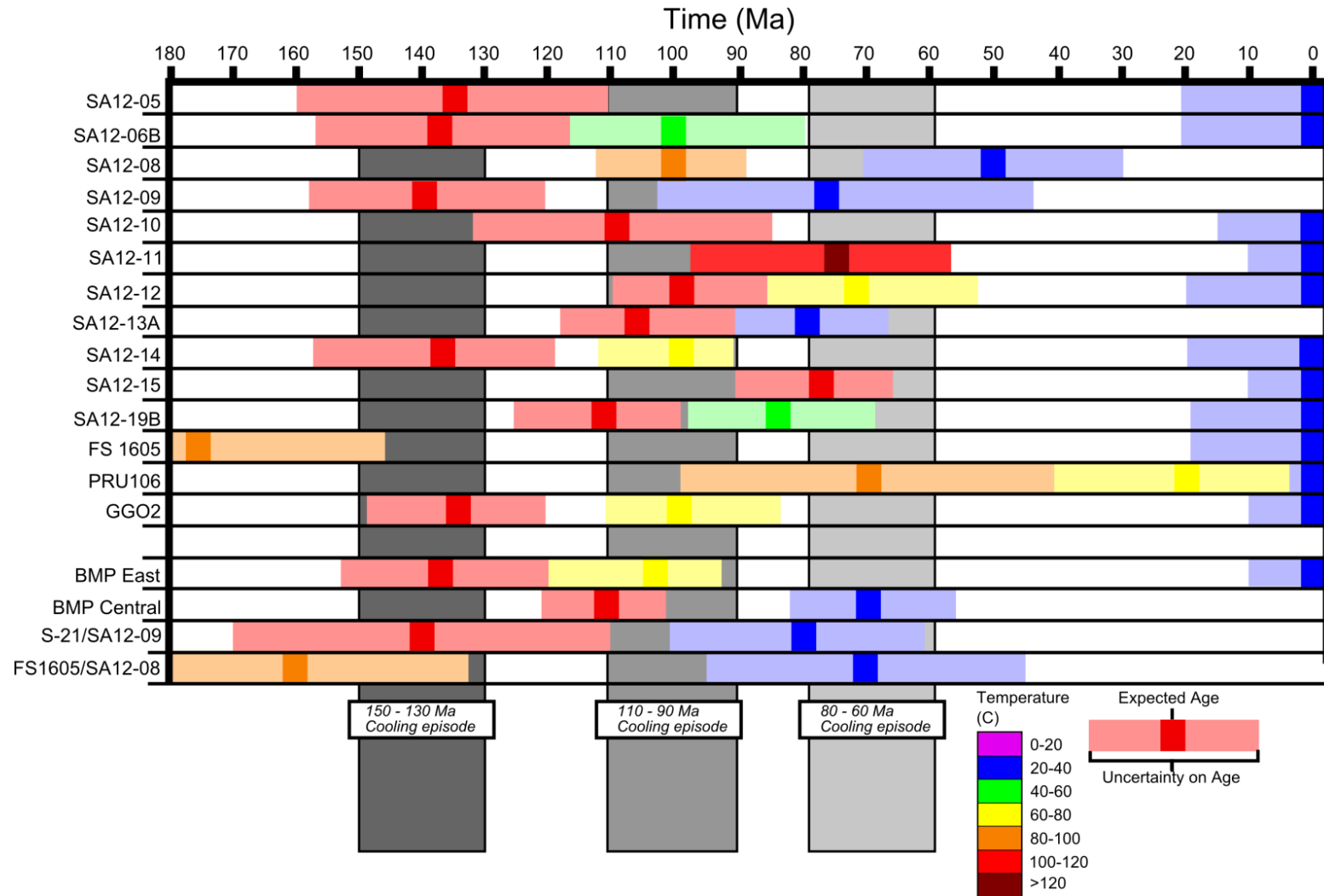
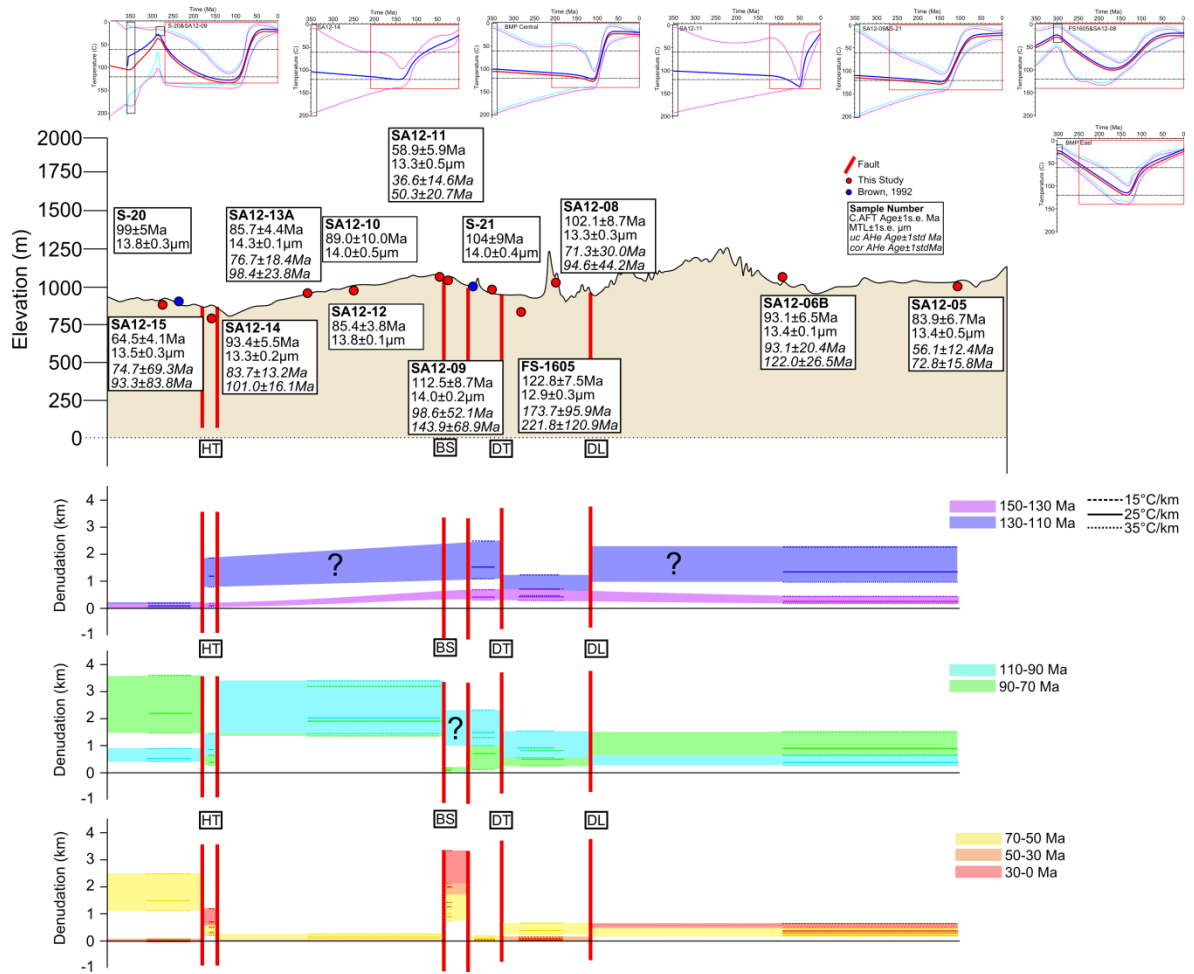


Figure 6-20: Plot represent the expected age and uncertainty (coloured bars) of key temperature points in each thermal history. These “key” points include the onset of cooling; changes in cooling rate causing inflections in the T-t path and the time when surface temperatures were reached. The colour of the bars is representative of the temperature of the thermal history at that time.



**Figure 6-21: Section xx-xx' with predictions on magnitudes of denudation over discrete time intervals since 150 Ma. Data within 7.5km either side of the section trace was projected at 90° onto the line of section. Denudation estimates are made directly from thermal history models generated by inverting data from this study and from Brown (1992). Denudation is estimated using three estimates of the geothermal gradient (15, 25, 35°C/km) with 25°C/km being the preferred estimate.**

NW-SE trending structures. Data within 20km either side of the line of section is projected at 90°.

Interpolating predictions of denudation across the section is difficult during the Early Cretaceous because many samples do not record cooling over this time. During the 150 - 130 Ma interval, the amount of denudation recorded in sample thermal histories is predicted to be less than 1 km and appears to be fairly constant across the entire transect, however, only a few samples record cooling at this time. For some models cooling initiates closer to c. 130 Ma and therefore there is a lot of uncertainty on palaeotemperatures before this time. In many samples, the removal of overburden may have cooled samples through

temperatures higher than c.  $110\pm 10^{\circ}\text{C}$  for much of this time interval and therefore it has not been recorded. From 130 - 110 Ma, denudation is predicted to be c. 1 - 1.5km by four thermal history models across the entire transect. Denudation is predicted to be less than 1km in the region between the Dabep Thrust and Doringberg Lineament at the craton edge.

A more complete record is preserved during the Mid - Late Cretaceous (110 - 70 Ma) which highlights the heterogeneity of denudation across the margin. On the western craton margin denudation is predicted to be less than 1km with denudation being greater during the 90 - 70 Ma time interval. The largest magnitudes of denudation are recorded by three samples taken from a block between the Hartbees and Brakbos faults. Here denudation is predicted to have occurred at an average rate of 0.05 km/Myr for both the 110 - 90 and 90 - 70 Ma interval equating to a total thickness of 2km.

The Doringberg Lineament is a convenient structural boundary for the eastern section of the margin, characterised by low denudation rates during the Mid-Late Cretaceous. Similarly, the Brakbos Fault provides a western boundary for the heavily denuded central block of the transect. Between these structural boundaries are five samples which are spread over an area of c. 35 km<sup>2</sup> and dissected by the Dabep Thrust. From these five samples two pairs of samples were modelled as profiles (i.e. BMP Centre-East; and BMP Centre-East-2). Smaller normal faults are observed west of Grobershoop but more faults between the BF and KF are not identified at the  $1:1\times 10^6$  map scale. The lack of rock exposure and hence stratigraphic constraints in this region inhibits identification of such structures. The incompatible nature of thermal histories obtained from the samples suggests distinct denudation histories have occurred in individual fault blocks. West of the BMP Central block a single sample residing between two mapped thrust faults that are part of the Hartbees Thrust belt, predicts denudation to be as low as that observed on the eastern section. The most westerly samples S-20 and SA12-15 have been modelled together and produce a composite thermal history that predicts enhanced denudation beginning at c. 110 Ma and exceeding 2km of denudation through 90 - 70 Ma. Enhanced denudation during the Mid to Late Cretaceous is also predicted by two

samples to the west that are off section including SA12-22 which is the most easterly sample in the NQH study area.

For most samples, Cenozoic (< 70 Ma) denudation is predicted to be on the order of a few hundred metres. From 70 - 50 Ma, three samples suggest that denudation was closer to or greater than 1km. High denudation predicted by SA12-08 and the BMP West profile is likely a continuation of enhanced denudation rates which initiated in the Mid-Late Cretaceous. In contrast, SA12-11 however suggests that this time interval is when the sample last cooled below c.  $110 \pm 10^\circ\text{C}$  and therefore implying several kilometres of denudation since this time. In fact, the estimates of denudation for this sample suggest that denudation continues at a rate of 50 - 70m/Myr until present day. It should be remembered that while both AFT and AHe age data suggest a young cooling event, the lack of track length data makes constraining the nature of cooling difficult and the current thermal history is a very simple model which best fits the available data.

## 6.7 Discussion

### 6.7.1 Low temperature thermochronology across the southwest African continental interior

The new data presented here forms the first thermochronology study to specifically investigate the influence of major tectonic fault zones on the long term evolution of the South African interior plateau. Previous work in the region has included data from the Augrabies Falls area (Kounov et al., 2013) and from sporadic data from along the Orange River valley (de Wit, 1988; Brown, 1992). AFT and AHe data from Augrabies Falls and from the Fish River Canyon in southern Namibia records enhanced cooling from c. 100 to 65 Ma (Kounov et al., 2013). This is in good agreement with the age range presented here and is interpreted by Kounov et al. (2013) as representing the effects of regional uplift increasing river gradients and hence erosion rates. Comprehensive modelling of all data presented by Kounov et al., (2013) from this area is not possible due to the lack of track length measurements for many samples and is made more difficult due to “incompatible” AHe ages that are greater than their

corresponding AFT ages; although in most cases overlap within  $2\sigma$ . Kounov et al. (2013) do not invoke regional tectonic reworking as the dominant mechanism enhancing denudation at this time but do suggest that a record of localised fault reactivation is preserved in their study areas. In the Fish River Canyon an AFT age of  $67\pm 26$  Ma in the hangingwall is adjacent to AFT ages of  $81\pm 12$  -  $84\pm 17$  Ma in the footwall of a major thrust fault and is used to invoke almost 1km of offset around c. 70 Ma. This interpretation on this data alone has to be treated with caution as the AFT ages have a large uncertainty which could allow them to be part of the same cooling event. These data also do not have track length information and therefore there is no indication whether these younger samples represent rapid cooling following major tectonic uplift or thermal event or whether they represent slower rates of erosion in response to an earlier uplift event.

No such observation is made for data from the Augrabies Falls region which is interpreted as representing a single block that has experienced enhanced denudation in the Mid-Late Cretaceous. The cluster of AFT ages with Mid to Late Cretaceous ages combines with data presented in this study to form a strong NW-SE trend of c. 80 - 100 Ma AFT ages which falls between the prominent Hartbees and Brakbos faults (Fig. 6-22). New data and models presented here however show that east and west of this fault zone, older syn-rift cooling is preserved suggesting this large block may have experienced discrete uplift and erosion relative to surrounding areas during the Mid-Late Cretaceous. Although the limited data from Kounov et al. (2013) does not provide strong evidence for structural reactivation at c. 70 Ma, data from Raab et al. (2002) and Brown et al. (2014) in northwestern Namibia lends support to this as a regionally significant tectonic event at this time. These authors infer from their data and complimentary forward thermal history modelling that c. 2km of vertical displacement has occurred across the Omaruru-Waterberg Lineament since the Early Cretaceous with a major period of enhanced denudation occurring at c. 70 Ma.

A transect of samples from the coast (near Kleinsee) to Kenhardt was collected by de Wit (1988). The majority of the samples collected in this transect yield

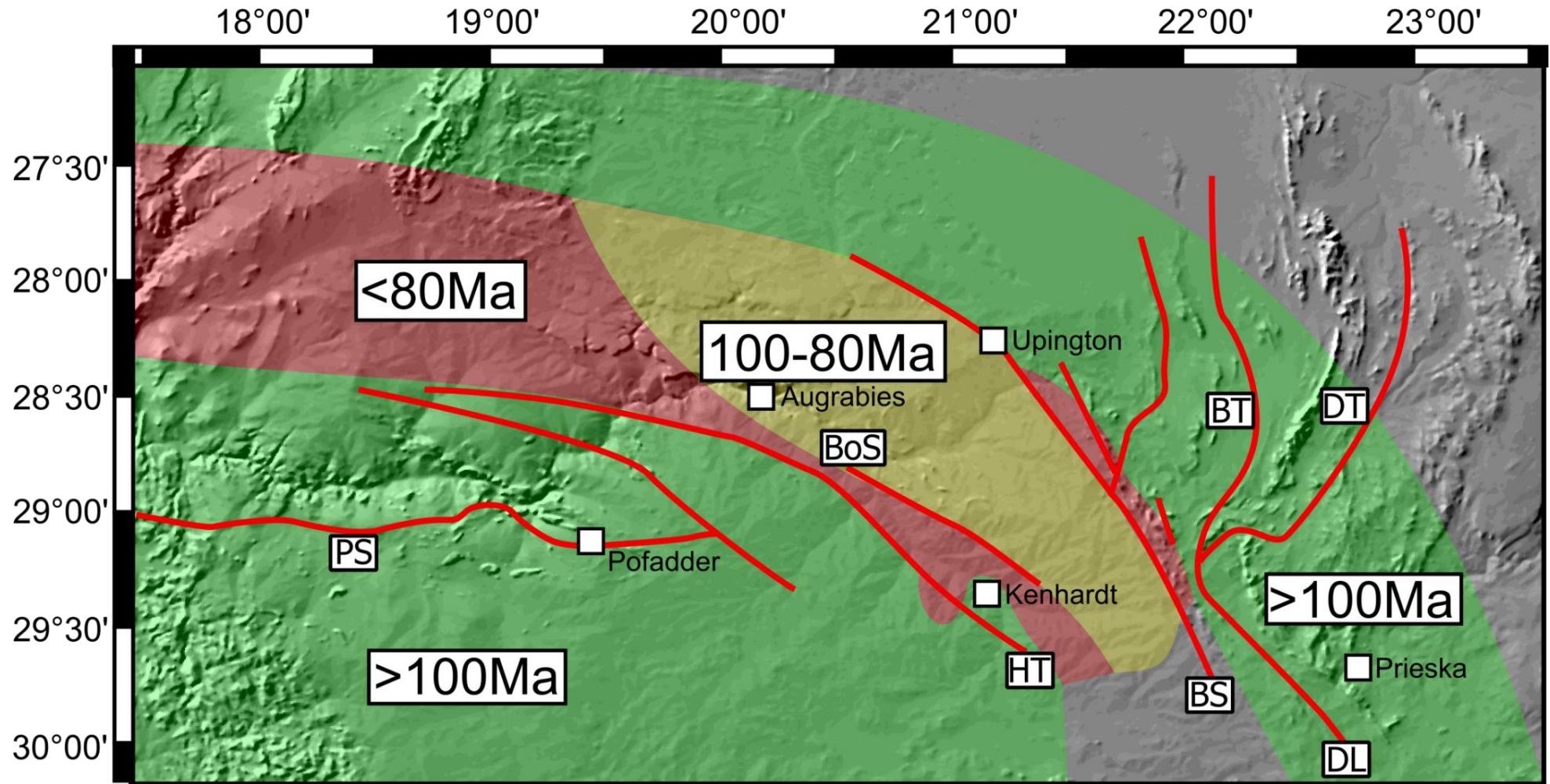


Figure 6-22: Map generalising the trend of regional AFT data from the Bushmanland Plateau based on the data of de Wit (1988), Brown, (1992) and Kounov et al., (2009) and this study. Fault names are the same as in Figure 6-3. A more detailed contour map of AFT data from SW Africa is presented in the Chapter 7 – Figure 7.5.

ages between 108 and 129 Ma with MTLs ranging from 13.3 - 14.0  $\mu\text{m}$ . This data is comparable with other data from the continental margin and plateau (e.g. Brown, 1992; Kounov et al., 2009; this study) and it is discussed in a regional context in Chapter 7. Two samples from the de Wit (1988) study are from Kakamas and Kenhardt and have yielded AFT ages of  $70\pm 5$  Ma and  $73\pm 4$  Ma and MTL of  $13.98\pm 0.1$   $\mu\text{m}$  and  $14.23\pm 0.1$   $\mu\text{m}$ , respectively. The MTL-SD for these samples is low and therefore it can be assumed that the TLD is narrow, however, no track length histograms are presented. de Wit, (1988) interpret these AFT data as evidence for thermal overprinting due to Late Cretaceous magmatism. The Stompoor intrusion discussed previously has been described as being Late Cretaceous in age (Smith, 1986) but other intrusive bodies of this age in this study area are relatively rare; the Stompoor intrusion itself is c. 30 - 40 km SW of the young AFT ages of de Wit (1988).

The vast majority of other intrusive bodies in the region are considerably older than the Stompoor intrusion (c. 115 - 130 Ma). Moreover, the regional data surrounding these samples do not agree with a widespread thermal event at c. 70 Ma; either the thermal event was extremely localised (i.e. an intrusion) or another mechanism is required. It is proposed that the data of de Wit (1988) can also be explained by rapid cooling driven by compression related uplift along the Hartbees River Thrust at during c. 80 - 60 Ma. This cooling episode is weakly observed in the data presented here (e.g. SA12-15) but the c. 70 Ma ages can be traced to follow the trend of the Hartbees Thrust into southern Namibia and then west, following the Groothoek Thrust, to match up with ages <80 Ma observed by Brown (1992).

### **6.7.2 Intracontinental deformation of the South African plateau**

The regional tectonic setting of the Bushmanland Plateau study area is dominated by major structural discontinuities which mark the boundary between the Archean Kaapvaal craton terrane and Namaqua-Natal mobile belt (Altermann and Hälbich, 1991; Nguuri et al., 2001; Griffin et al., 2003; Sodoudi et al., 2013). These tectonic lineaments are clearly visible on aeromagnetic images of South Africa (Fig. 6-23). Ancient cratonic terranes and adjacent mobile belts

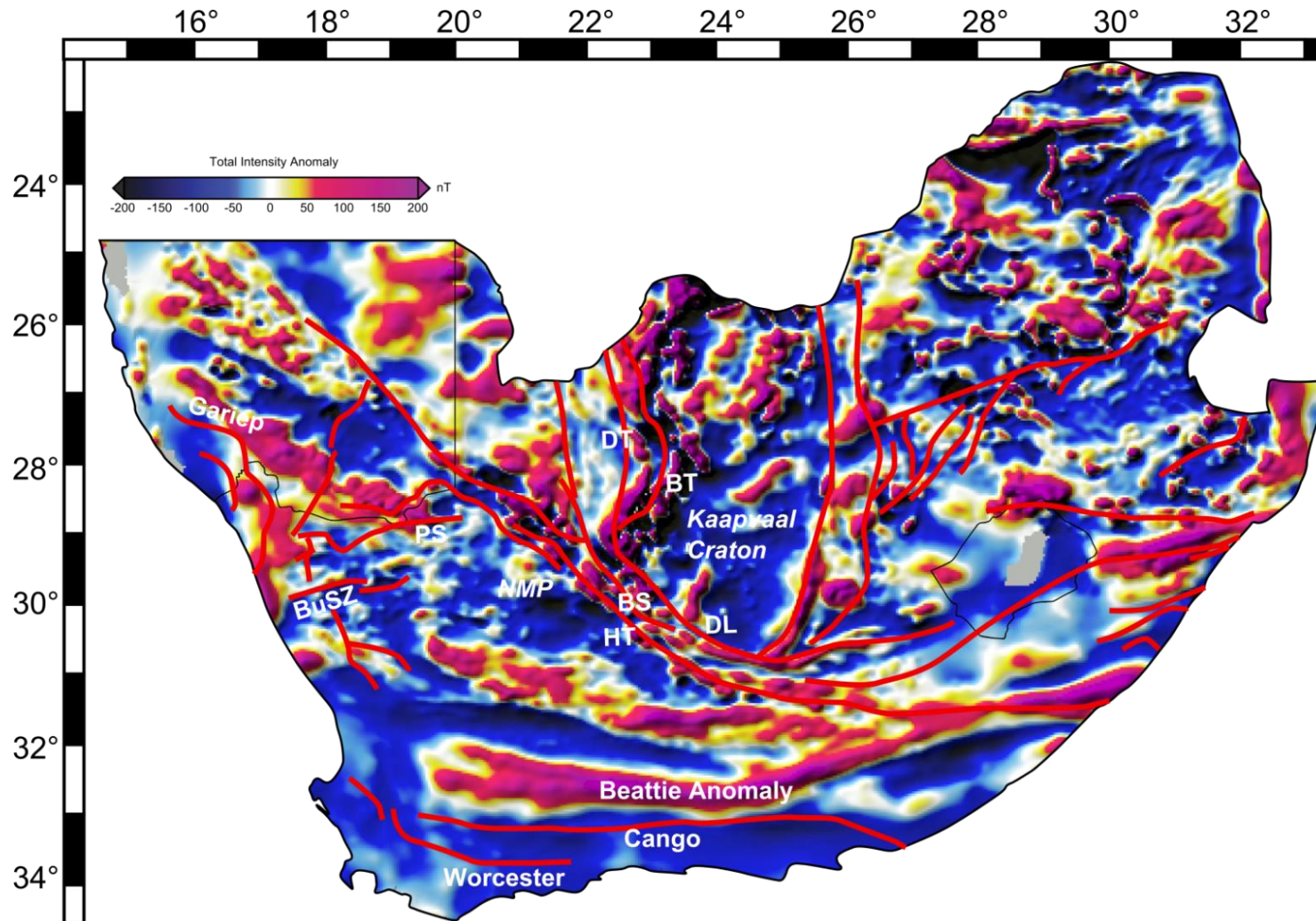


Figure 6-23: Map illustrating the relationship between the South African structural framework and magnetic anomalies. Strong positive magnetic anomalies mark the boundary between the Kaapvaal Craton and adjacent NMP. Labelling and positioning of major features was done after Tankard et al., (2009). Abbreviations of fault names are the same as Figure 6-3 and 6-4 (above), Magnetic data was taken from global EMAG2 2-arc min resolution Earth Magnetic Anomaly Grid (Maus et al., 2009).



have recently been the subject of much study regarding their formation (Shirey et al., 2001; Lee et al., 2008; Cooper and Miller, 2014) accretion (Eriksson et al., 2009; Zeh et al., 2009), internal structure (Fishwick et al., 2005; Müller et al., 2012) and long-term stability (Peslier et al., 2010; Wang et al., 2014).

These studies have largely been undertaken using geophysical methods to image the lithosphere and underlying mantle; geochemical analysis of basement lithologies and intrusive igneous bodies to investigate the composition, rheology and metamorphic history of the region; and geodynamical models designed to integrate these observations and predict the nature and interaction of mantle flow and lithospheric deformation (e.g. Guillou-Frottier et al., 2012; Cloetingh et al., 2013; Burov et al., 2014). A growing number of these studies are concluding that, ultimately, the concept of continental interiors being tectonically “stable” over long geological periods is no longer universally appropriate (e.g. Moucha et al., 2008). Understanding how the topography of continental interiors has evolved in response to thermal and structural perturbations will help to constrain thermo-mechanical models which advocate major topographic undulations in cratonic regions. The thermochronology data and thermal history inversions presented support enhanced denudation driven by intracontinental deformation during the Mid-Late Cretaceous.

#### **6.7.2.1 Structural record**

The BMP study area is dominated by metamorphic basement lithologies and entirely lacking Mesozoic and early Cenozoic units. The lack of stratigraphic information severely inhibits constraining recent tectonic displacements on major faults which dissect the area. An additional problem is the lack of exposure across the flat lying plateau which creates uncertainty about cross cutting relationships of lithological and structural boundaries. The majority of structures mapped at the  $1:1 \times 10^6$  scale are confined to the NMP where they define terrane boundaries and lithological discontinuities (Fig. 6-3). Exceptions to this are the southern extents of the Brakbos and Doringberg faults which displace NMP basement against Dwyka Group rocks. SW of the town of Bucklands, a fault is also mapped which displaces Archean Transvaal Group rocks

against Dwyka Group rocks. It is clear that some degree of fault reactivation occurred post-Permian and is therefore unrelated to terrane accretion or Pan-African Orogenic activity. High angle reverse faults and tight folding has also been identified within the Dwyka Group unit near the town of Douglas (Andreoli, 2014, pers. Comm.).

Geological evidence for Mesozoic tectonic activity is also rare in southern Namibia but sporadic examples of Karoo dolerite suite rocks with a faulted contact with Dwyka Group, Nama Group and/or NMP rocks exist. Fault dissected Karoo dolerites suggest tectonic activity less than c. 180 Ma. Cenozoic faulting is suggested to have been instrumental in carving out the Fish River Canyon, South Namibia (Mvondo et al., 2011). Two phases of extension are advocated by Mvondo et al. (2011) with N-S grabens shaping the lower Fish River Canyon due to E-W extension in the Late Eocene and NE-SW grabens shaping the upper Fish River Canyon due to younger NW-SE extension in the Plio-Pleistocene. However, the constraints used to determine the timing of such faulting (e.g. displacements of the African surface) are highly qualitative and uncertain. In Northwest Namibia, late Mesozoic tectonism is constrained by the preservation of Etendeka volcanic rocks, associated with Early Cretaceous rifting in the southern Atlantic, in coast-parallel, half grabens (Raab et al., 2002; Brown et al., 2014). These grabens are bounded by NNW-SSE trending normal faults which displace Etendeka lavas against NMP basement (Brown et al., 2014). Further evidence is provided by syn-tectonic conglomerate units comprised of Etendeka volcanic material which dip to the east into a westerly dipping normal fault (Ward and Martin, 1987).

These examples from NW Namibia indicate tectonic activity occurred c.  $\leq 130$ Ma however, as with the previously described examples no younger constraint is available. Due to these limited constraints, the possibility of an episode or episodes of tectonic activity following the major phase of continental extension cannot be ruled out. Moreover, seismic data has suggested that the tectonic boundary between the Kaapvaal craton and NMP mobile belt is still active (Tankard et al., 2009). Offshore seismic reflection data from the Orange, Luderitz and Walvis Basins adjacent to the South African and Namibian

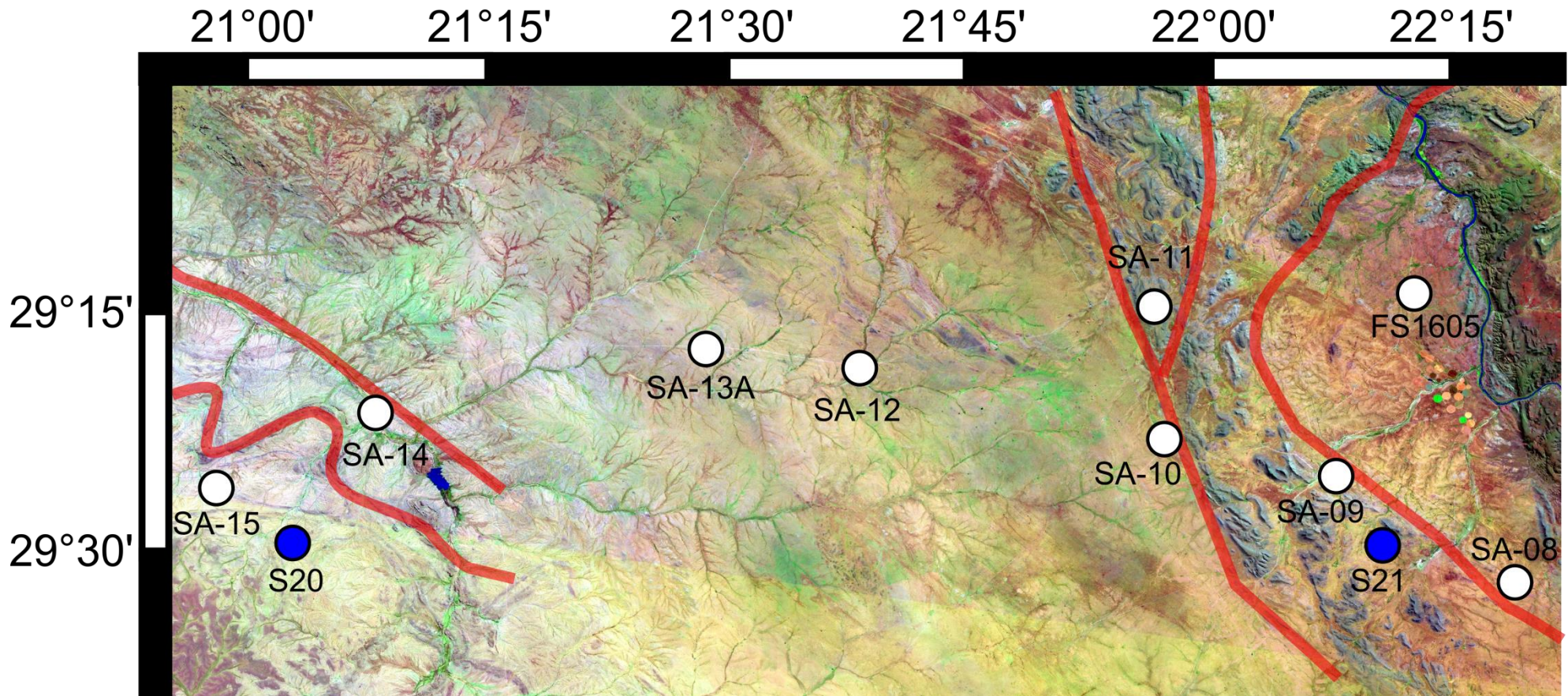


Figure 6-24: Landsat ETM+ RGB:742 satellite image which highlights the relief variation of the region as well as several drainage pattern features. Red lines represents faults which may have experienced significant displacement during the Mid – Late Cretaceous and induced differential fault block uplift and subsequent erosion.

continental margins have shown regional deformation in the Upper Cretaceous sequences and segmentation of the margin by faults which can be traced onshore (Dingle et al., 1983; Clemson et al., 1997; Viola et al., 2005; de Vera et al., 2010). The structures that may have accommodated large amounts of displacement during the Mid - Late Cretaceous, inferred from the thermochronological data and limited structural information, are highlighted in Figure 6-24.

### **6.7.2.2 *Intraplate deformation at the craton boundary***

Models that attempt to reconstruct the western Gondwana continental block prior to the opening of the South Atlantic identify gaps and overlaps between the African and South American plates (e.g. Vink 1982; Unternehr et al. 1988; Nürnberg & Müller, 1991; Eagles, 2007; Torsvik et al., 2009). These misfits have been used to invoke crustal thinning, basin formation and importantly, in the context of this study, intraplate deformation (Eagles, 2007; Aslanian et al., 2009; Torsvik et al., 2009; Aslanian and Moulin, 2013).

Intraplate deformation of the continental crust is poorly understood and may be accommodated by local and regional tectonic events (Cloetingh and Burov, 2011; Gaina et al., 2013). As discussed in Chapter 3 - Section 3.8, intraplate deformation is controlled by mantle-lithosphere interactions and how they respond to the propagation of far-field stress within the lithosphere and/or thermal perturbations in the convecting mantle (Heine et al., 2008, Burov and Cloetingh, 2009). The BMP transect cuts across the tectonic boundary between the Archean craton and Namaqualand mobile belt. It has been suggested that the large crustal thickness and high strength of the cratonic lithosphere adjacent to thinner, weaker crust of the neighbouring mobile belt will focus deformation at the craton boundary (Lenardic et al., 2003; Burov et al., 2007; Baptiste et al., 2012). Seismic data indicate that the NMP lithospheric mantle is indeed thinner and warmer than that underlying Kaapvaal craton (Baptiste and Tommassi, 2013; Sodoudi et al., 2013). Geochemical studies of intrusive igneous material provide insights into the thermal and compositional structure of the mantle lithosphere over time. These investigations have suggested that prior to the Mesozoic the

thermal state and thickness of the off and on-craton lithosphere was roughly the same with subsequent erosion of the off-craton lithosphere causing thinning by c. 30 km (Janney et al., 2010).

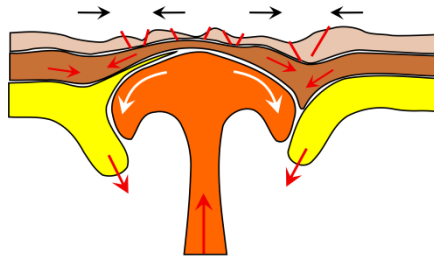
If regional stresses have become focused along the craton boundary then faults may become reactivated. However, the reactivation of faults and magnitude of displacement will be dependent on the steepness of the original fault structure; the relative orientation of the fault and regional stress field and the frictional resistance along the fault plane (Sibson, 1985; Turner and Williams, 2004). In a structural setting such as is observed in the BMP study area which includes both steep normal and reverse faults of differing orientations as well as major shear zone faults, the crust may have deformed extremely heterogeneously in response to a regional stress field (e.g. Janssen et al., 1995; Ziegler et al., 1995; Bonini et al., 2012; Salomon et al., 2014). If there has been a change in the regional stress field from an extensional regime during 110 - 90 Ma to a compressional regime from 80 - 60 Ma (Viola et al., 2012; Gaina et al., 2013) then resolving the surface response to this deformation will prove incredibly difficult. However, it is proposed that while the data presented here may not have the resolution to define multiple tectonic events with great precision the data do support that tectonically induced uplift and erosion occurred in discrete fault bounded blocks during the Mid - Late Cretaceous.

### ***6.7.2.3 Plume Upwelling: Mantle – Lithosphere interactions***

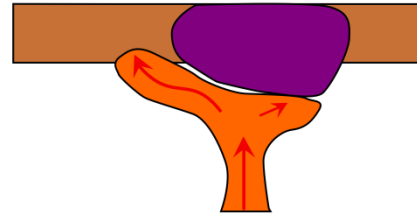
The longevity of high elevation continental interiors is frequently ascribed to dynamic uplift related to vertical stresses induced by mantle upwelling (e.g. Australia: Czarnota et al., 2013, Antarctica: Anderson et al., 2012, North America: Forte et al., 2010b, Southern Europe: Boschi et al., 2010, South America: Shephard et al., 2012). The South African continental interior is frequently used as the archetypal example of dynamically supported topography with the presence of a well-imaged zone of low seismic velocity beneath the African plate being cited as evidence for an African Superplume (Nyblade and Robinson, 1994; Lithgow-Bertelloni and Silver, 1998; Brandt et al., 2012). Recent thermo-mechanical modelling has investigated the impact of plume upwelling on

(a) Thermo-mechanical models: Craton - lithosphere - plume interactions

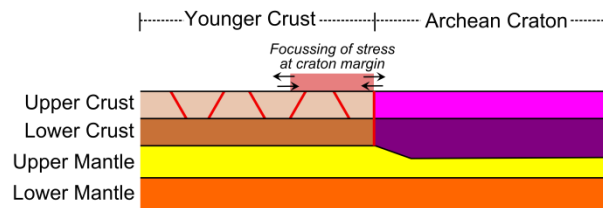
(i) *Mantle - Lithosphere interactions stratified VEP model* (Cloetingh et al., 2013)



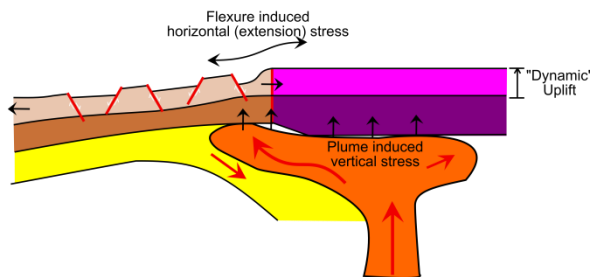
(ii) *Plume head - cratonic block interactions* (Guillo-Frottier et al., 2012)



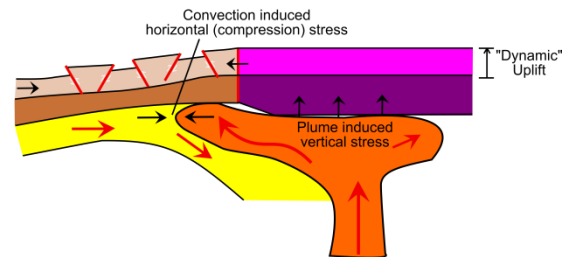
(b) SW African intraplate deformation



(i) *Intraplate Deformation: Extension*



(ii) *Intraplate Deformation: Compression*



**Figure 6-25: (a) Thermo-mechanical models of the interaction between cratonic and non-cratonic lithosphere and plume upwellings (i) Illustration of the Visco-Elastic-Plastic (VEP) thermo-mechanical model (Cloetingh et al., 2013). Model investigates the effect of a stratified lithosphere, defined by different rheological properties, deforming over an upwelling plume. Lower crust can deform under ductile conditions causing long wavelength deformation while the upper crust deforms over shorter wavelengths in a brittle manner. Due to the presence of the upwelling plume mantle lithosphere may become down-thrusted. (ii) Model for plume head–cratonic blocks interactions (after Guillou-Frottier et al., 2012). In this model continuous plume activity can result in partial erosion of the base of cratonic blocks which can focus plume pathways along the base of the craton. (b) Possible models for the deformation of the Bushmanland Plateau, driven by a combination of in-plane and vertical stresses induced by mantle plume upwelling. Prior to the impingement of any mantle plume, regional stresses are already focused at the craton margin. Plume upwelling imposes vertical stresses at the base of the lithosphere inducing dynamic uplift. The strong craton uplifts as a single block however the adjacent crust is prone to rupture due to a combination of regional in-plane stresses and pre-existing structure. (i) Uplift of the continental interior promotes flexure induced in-plane extension due to doming of the lithosphere focused over the mantle plume. (ii) Mantle plume upwelling becomes focused at the craton margin and induce subduction of colder mantle lithosphere creating horizontal stresses along the base of the lithosphere back towards the craton.**

a mechanically decoupled upper crust and lithospheric mantle (Cloetingh et al., 2013). This modelling suggests that for a stratified viscous-elastic-plastic continental lithosphere, vertical motions of the surface do not directly mimic

the long wavelength undulation of the lithosphere-mantle boundary (Burov and Guillou-Frottier, 2005; Burov et al., 2007; Guillou-Frottier et al., 2012). Instead, during mantle upwelling, bending of the brittle crust induces lateral stresses and instabilities which may promote short-wavelength topographic features (i.e. fault block movement) (Fig. 6-25a) (Chen et al., 2013, Burov and Guillou-Frottier, 2005). As described above, craton edges and in particular the southwestern edge of the Kaapvaal craton are characterised by abrupt variations in lithospheric thickness which may induce edge-driven convection or focus upwellings in the mantle around the craton (Fig. 6-25b; Guillou-Frottier et al., 2012). This, in turn, can influence surface topography over different length scales (King and Ritsema, 2000; Priestley et al., 2008; Reusch et al., 2010; Fishwick and Bastow, 2011).

The interaction between mantle convection and the continental lithosphere at a cratonic boundary setting has been investigated at the present day active rift zone in East Africa. Structural features have become preferentially focused in the weak Proterozoic lithosphere adjacent to the Archean Tanzanian craton (Petit and Ebinger, 2000; Corti et al., 2007; Guillou-Frottier et al., 2012). The location and magnitude of vertical motions of the lithosphere in craton boundary settings will be influenced by a combination of rheology, tectonic inheritance, contrasts in lithospheric thickness but also thermal perturbations (Guillou-Frottier et al., 2012). Despite this it seems apparent that vertical motions are focused at cratonic margins while the cratons themselves may remain relatively flat and undeformed (Burov and Guillou-Frottier, 2005; Wallner and Schmelting, 2010).

## 6.8 Summary and Conclusions

The occurrence of intraplate deformation is required by plate reconstruction models attempting to refit South American and African plates and thermo-mechanical models have suggested that craton edges may be suitable sites for deformation. Key to resolving this is understanding how an upwelling plume interacts with cratonic regions and their inherently weak neighbouring crust that is currently residing in a regional stress field. The data presented here is taken

from such a tectonic setting and suggests that significant denudation occurred during the Mid and Late Cretaceous.

The data also has implications for the development of the rift-related topography of the continental margin. The presence of samples which record major cooling during 150 - 130 Ma suggest that significant magnitudes of denudation persisted far inland during the time of rifting. The sporadic preservation of the Early Cretaceous record of cooling supports the hypothesis that later Cretaceous denudation was confined to reactivated tectonic blocks. In short, intraplate deformation induced periods of enhanced denudation during the 110 - 90 Ma and, possibly, 80 - 60 Ma. The type of intraplate deformation (i.e. extension/compression) (Fig. 6-25c) is not resolved in this study due to the uncertainty surrounding the timing of plume upwelling beneath Southern Africa; the overall form (i.e. extension/compression) of the regional Mid - Late Cretaceous stress field prior to and after plume impingement; and the orientation of this stress field relative to pre-existing structures and hence their probability of becoming reactivated.

Further sampling could be undertaken to improve the resolution of the thermochronological data set in the region. However, further structural observations and identification of post-Karoo geological evidence will help to constrain thermal history models and the interpretation of them. In the absence of such geological constraints the present data set can be used to help constrain surface processes acting in response to intraplate deformation and therefore help to resolve the dominant mechanisms driving deformation.

The conclusions from this study are that rift-related denudation (c. 150 - 130 Ma) extended from the margin to well inland, at least to the craton boundary. Subsequent intracontinental deformation induced fault block uplift and a renewed phase or phases of denudation over the intervals 110 - 90 Ma and 80 - 60 Ma. Cenozoic denudation is generally low, however, locally it is observed to be greater than 1km. Based on the current data this appears to be rare and requires further investigation.



# CHAPTER 7

## THE POST-RIFT LANDSCAPE EVOLUTION OF SOUTHWEST AFRICA

### 7.1 Introduction

Understanding South Africa's topographic development has been a major challenge for geologists and geomorphologists for over a century (King, 1942; Du Toit, 1954; Partridge and Maud, 1987; Burke and Gunnel, 2008). A major hindrance in this effort has been the paucity of reliably dated onshore post-rift lithologies combined with a poor understanding of the tectonic and surface process that control the creation and destruction of relief over time. Over the past thirty years or so, low temperature thermochronology has provided insights into the nature of crustal cooling in South Africa, pointing to the Cretaceous as a time that is characterised by major regional denudation of the landscape.

However, the limited resolution of low temperature thermochronology techniques and the scope for alternative interpretations of the data has permitted other workers to advocate that South Africa's topography is a "young" mid-late Cenozoic feature (Partridge and Maud, 1987; Ollier and Pain, 1997; Burke and Gunnel, 2008; Paul et al., 2014). This chapter provides a regional summary of all available AFT and AHe data across South Africa to highlight the dominance of a Cretaceous cooling signal but also to address the spatial complexity of these data. Thermal histories obtained from inverting data collected in this study and from Brown (1992) are then converted to estimates of denudation of the western South African margin over time, and compared with sedimentation rates and total accumulated volume in the adjacent Orange Basin. Both data sets invoke large-scale mass transfer from the onshore to offshore domain throughout the Cretaceous with a dramatic decrease in denudation and accumulation in the Cenozoic. The Cenozoic therefore remains a contentious period in southern Africa's geomorphic history largely due to the

lack of accessible and well-dated material that can be used to infer the regional tectonic or geomorphic environment. A summary of the available cosmogenic nuclide, paleontological, geological and geomorphic studies that have been used to investigate South Africa's Cenozoic development is provided and discussed in the context of the LTT data presented in this thesis.

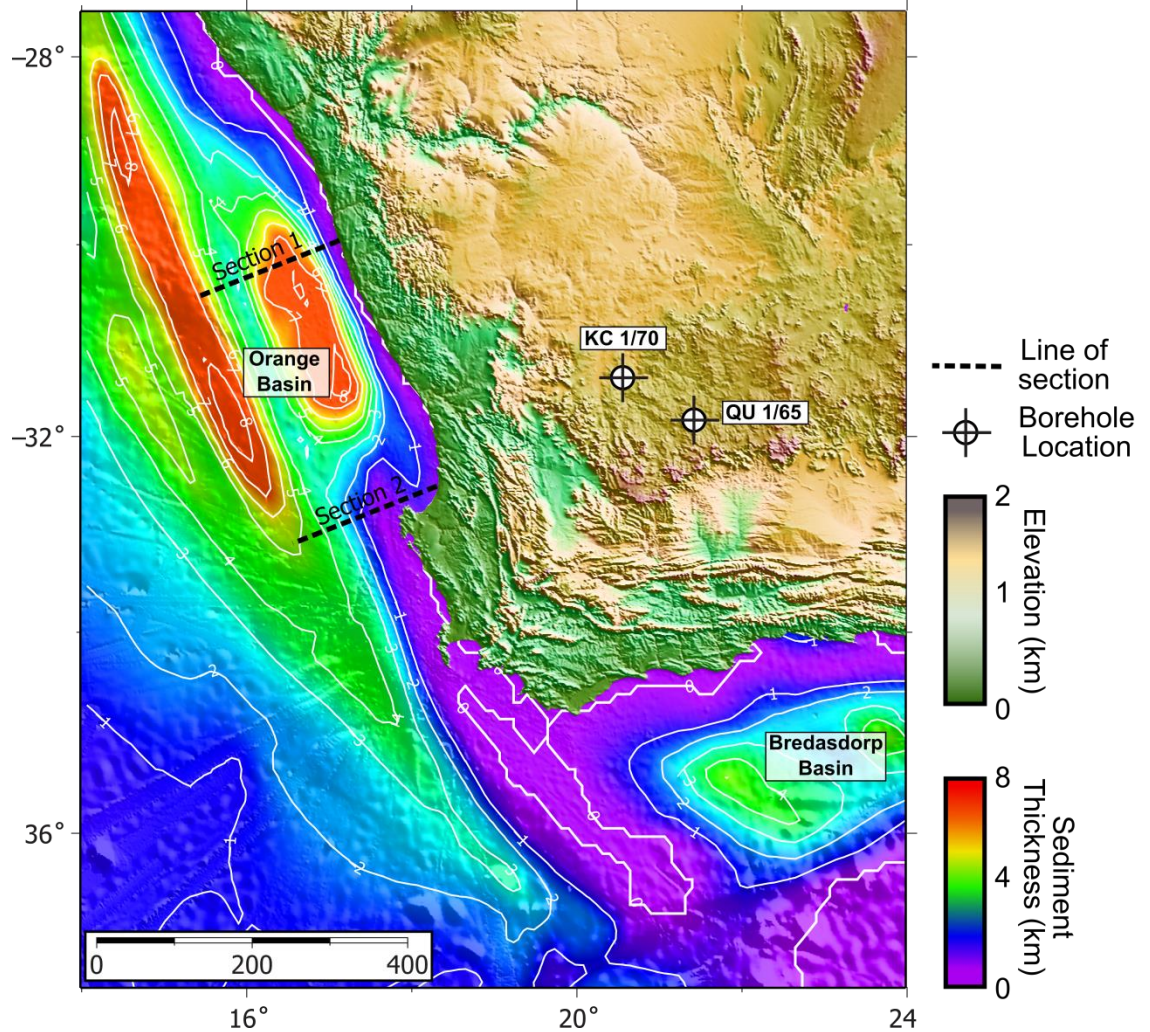
## **7.2 Low temperature thermochronology data from SW Africa**

Apatite fission track (AFT) and apatite (U-Th-Sm)/He (AHe) data presented in Chapter 5 and Chapter 6 is crucial as it covers regions where data were previously sporadic or absent entirely. More than this, in the case of the NQH study area, the data were obtained at a higher spatial resolution than previous studies to target and investigate fault reactivation within the margin escarpment zone. The new AFT data contribute to and enhance what is now an extensive regional AFT dataset. AHe data, by comparison, is still severely lacking in southern Africa. As such the AHe data, obtained through multiple single-grain analysis, provides much needed independent, empirical evidence to augment and to corroborate insights obtained from the AFT analysis. The following section will review the regional AFT and AHe datasets and discuss them in the context of conclusions drawn from the previous chapters. Prior to this discussion two final thermal history models are presented. Both of these models are produced through the joint inversion of multiple samples collected from their deep borehole profiles.

### **7.2.1 Borehole profiles**

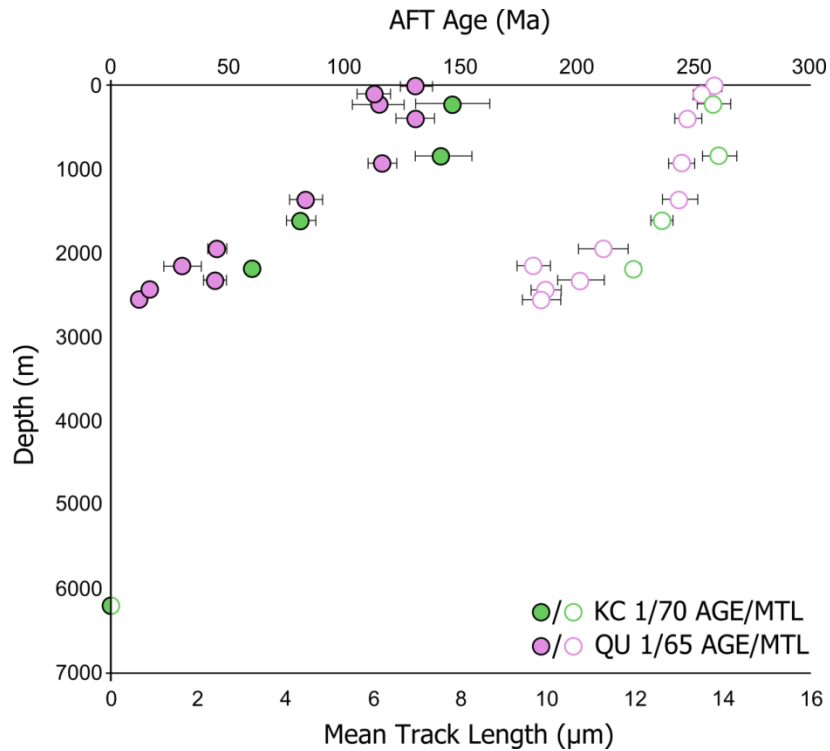
#### ***7.2.1.1 AFT data from KC1/70 and QU1/65***

Two borehole sample profiles from KC 1/70 and QU 1/65 (Fig. 7-1) are an important addition to the current dataset as they provide information on the present day thermal structure of the upper crust; can provide insights into how quickly a vertical column of rock has cooled, and due to their location on the inland plateau can constrain the amount of crustal cooling that has occurred far



**Figure 7-1: Map of southwestern Africa showing the location of two borehole locations from which samples were dated using AFT analysis. Offshore sediment thicknesses are shown (after Rouby et al., 2009). The two lines of section correspond to the cross sections drawn in Figure 7-8 (after Guillocheau et al., 2012).**

from the continental margin. The data were collected by Brown, (1992) but have not, before now, been modelled in a manner where each sample is inverted simultaneously and all aspects of the data relating to the samples thermal history are taken into account. These data include AFT parameters (AFT age, MTL and TLD), the stratigraphic age of (i.e. initial condition) of each sample, present day temperature of the sample and vertical temperature offset between the samples. The latter two parameters are based on the geothermal gradient of the upper crust. Uncertainty limits accounting for the uncertainty on the geothermal gradient are also incorporated into calculations of the vertical offset and present day sample temperature.



**Figure 7-2: Plots of AFT age (filled circles) and MTL (open circles) against borehole depth for KC 1/70 (green symbols) and QU 1/65 (purple symbols). AFT ages are central AFT ages with  $1\sigma$  standard error. MTL are uncorrected for their orientation to c-axis and have  $1\sigma$  standard error.**

The data are summarised in Figure 7-2 and are documented fully in Appendix 6. Eleven samples from QU 1/65 were collected over a vertical range of 2534 m and show a clear negative relationship between depth and both AFT age and MTL at depths > 1000 m; the bottom sample has an AFT age of  $11\pm 1$  Ma and MTL of  $9.83 \pm 0.42 \mu\text{m}$ . At depths shallower than c. 1000 m, there is no correlation between depth and AFT and or MTL with five samples having AFT ages within the range of 112 - 130 Ma and MTLs between 13 and 14  $\mu\text{m}$ . A qualitative interpretation of this data would be that the rock column cooled reasonably quickly during or just prior to the 110 - 130 Ma interval recorded by AFT ages. Prolonged residence of the deeper samples at elevated temperatures has caused track lengths to become partially annealed creating the negative correlation with depth (and temperature).

Fewer samples ( $n = 5$ ) were obtained from the KC 1/70 borehole profile. Independently, the data do appear to be negatively correlated with depth; however, defining the structure of the correlations for KC 1/70 is more difficult

due to the limited number of data points. When plotted on the same axes as QU1/65 a remarkable similarity in the data sets is evident. At depths greater than c. 1000 m AFT ages and MTLs progressively decrease with depth. At depths shallower than c. 1000 m the KC 1/70 AFT ages are consistent with one another (KC-1 -  $142 \pm 12$  Ma and KC-3 -  $142 \pm 16$  Ma) and overlap with the oldest ages from QU1/65. Track lengths in the upper section of the KC1/70 profile are also reasonably long with MTL of  $13.77 \pm 0.38$   $\mu\text{m}$  and  $13.90 \pm 0.39$   $\mu\text{m}$ , respectively. It is therefore likely that both KC 1/70 and QU 1/65 experienced similar cooling histories. An additional piece of information unique to KC1/70 is obtained due to the bottom sample in the profile having a zero age and zero mean track length. From this it can be surmised that the temperature at the sample depth (6190 m) is  $> c. 110 - 120^\circ\text{C}$  and therefore tracks are not being preserved in the sample.

### **7.2.1.2 Borehole thermal history models**

Modelling the borehole profile data follows the same procedure adopted for modelling pseudo-vertical profiles in previous chapters (see Chapter 5 - Section 5.5.3.1). As the profiles cover a large vertical range it is important to make an initial estimate on the temperature difference between samples both at the present day and over geological time. For this purpose, an estimated geothermal gradient of  $25^\circ\text{C}/\text{km}$  was used to determine an initial offset and present day temperature value. Using an upper and lower estimate of  $35$  and  $15^\circ\text{C}/\text{km}$ , respectively, upper and lower limits on the temperature offset and present day temperature were obtained. As there is a large degree of uncertainty on the estimates of the geothermal gradient, particularly in the geological past, the temperature offset value was allowed to vary over the model run (i.e. the offset was resampled from within the uncertainty limits). A limitation to the borehole datasets is the lack of any compositional parameter used to constrain the compositional influence on annealing (i.e.  $D_{\text{par}}$ ). This information was not collected by Brown (1992) as it was not common procedure to do so. To ensure that the compositional aspect of annealing was incorporated into the t-T models an initial 'standard'  $D_{\text{par}}$  value of  $2.04 \pm 1.5$   $\mu\text{m}$  was assigned (approximate  $D_{\text{par}}$  value of Durango apatite, Sobel and Seward, 2010) and the MCMC inversion was

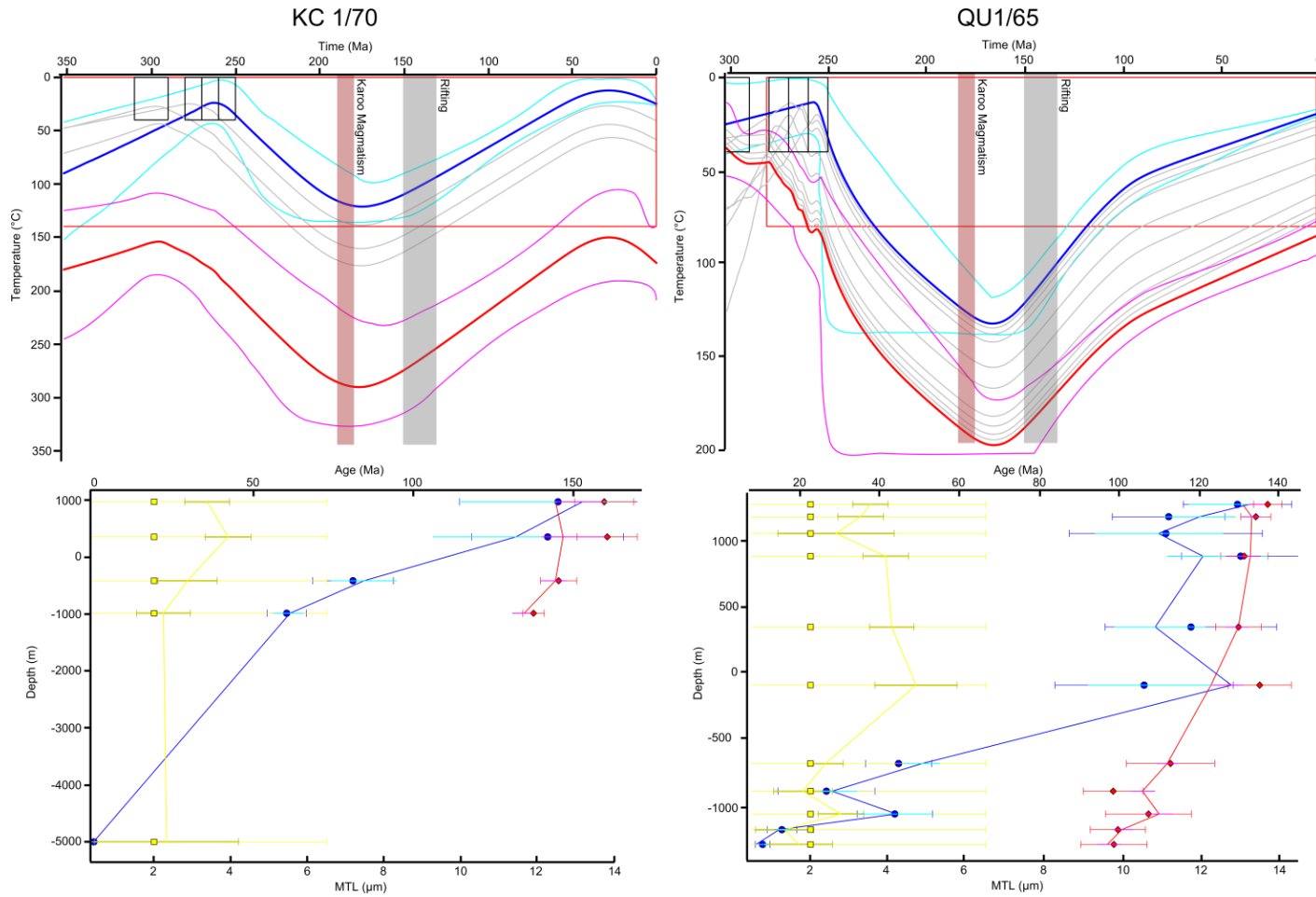
allowed to search for viable  $D_{\text{par}}$  values within this range that were consistent with all the other observed parameters and stratigraphic constraints.

Both boreholes are located within the Karoo basin and therefore penetrate through the major lithologies of the Karoo Supergroup. For this reason stratigraphic ages can be incorporated into the model as an added constraint. Each sample was assigned two constraint points (with bounds) reflecting their stratigraphic age and present day downhole temperature. The deepest samples from QU1/65 and KC1/70 are Cambrian granites and Proterozoic basement, respectively. For this reason, the thermal history model begins a significant time before the age of sedimentary units and therefore allows for the possibility of old, inherited, tracks to be preserved in detrital apatites within the sedimentary rocks. For display purposes, the thermal history shown and discussed (Fig. 7-3) is illustrated only from the Carboniferous to present day; prior to this time, the model is essentially unconstrained.

As predicted from the initial inspection of the AFT age/MTL vs. depth plot, there are similarities in the thermal histories obtained for KC 1/70 and QU 1/65. These include burial heating from surface temperatures initiating at c. 260 - 270 Ma with the top sample in the profile reaching temperatures  $> 120^{\circ}\text{C}$  by c. 170 Ma. Monotonic cooling from this time is predicted by the KC 1/70 model with near surface temperatures being reached by c. 50 Ma. The QU 1/65 model predicts an initial phase of rapid cooling between 170 and 100 Ma at a rate of  $1^{\circ}\text{C}.\text{Myr}$  reaching temperatures of c.  $60^{\circ}\text{C}$ . Subsequent cooling through the Tertiary until present day then proceeded at a slower rate of c.  $0.4^{\circ}\text{C}.\text{Myr}$ .

### **7.2.2 South African apatite fission track data**

An extensive database of apatite fission track data is now available across southern Africa. Much of this data has been collected from the Namibian and South African continental margins with fewer data available from the South African interior and border areas between South Africa, Botswana and Zimbabwe. The regional database presented here includes all AFT data from outcrop samples (number of samples = 655) collected south of  $18^{\circ}\text{S}$  (Fig. 7-4).



**Figure 7-3: KC 1/70 and QU 1/65 thermal history models. Expected model of the top and bottom sample is represented by a thick blue and red line, respectively, with 95% credible intervals (cyan and magenta lines). Black box represents initial constraint on the model. Red box represents general ranges for prior (see Chapter 4 – Section 4.5.1). Yellow square/bar = Measured/predicted  $D_{par}$ ; blue circle/light blue bar = Measured/predicted AFT age; red diamond/magenta bar = measured/predicted MTL; green triangle/light green bar/dark green bar = measured/resampled observed/predicted AHe age. Histograms represent the measured TLD; red line represents the predicted TLD with 95% credible intervals (grey curves).**

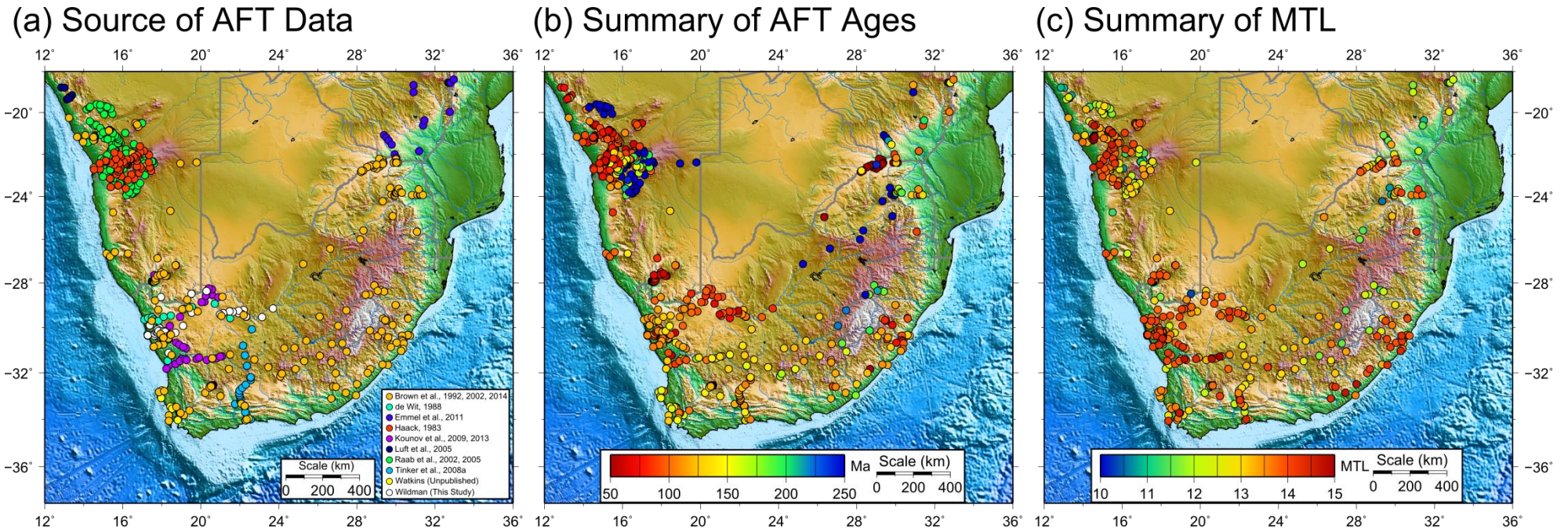


Figure 7-4: Database of apatite fission track data which shows (a) Sources of AFT data (b) Mean AFT age and (c) MTL where available. DEM data is a combination of STRM30plus (1km data derived from the SRTM 3 arc sec (90m) global data) and the ETOPO2 global data (for ocean areas).

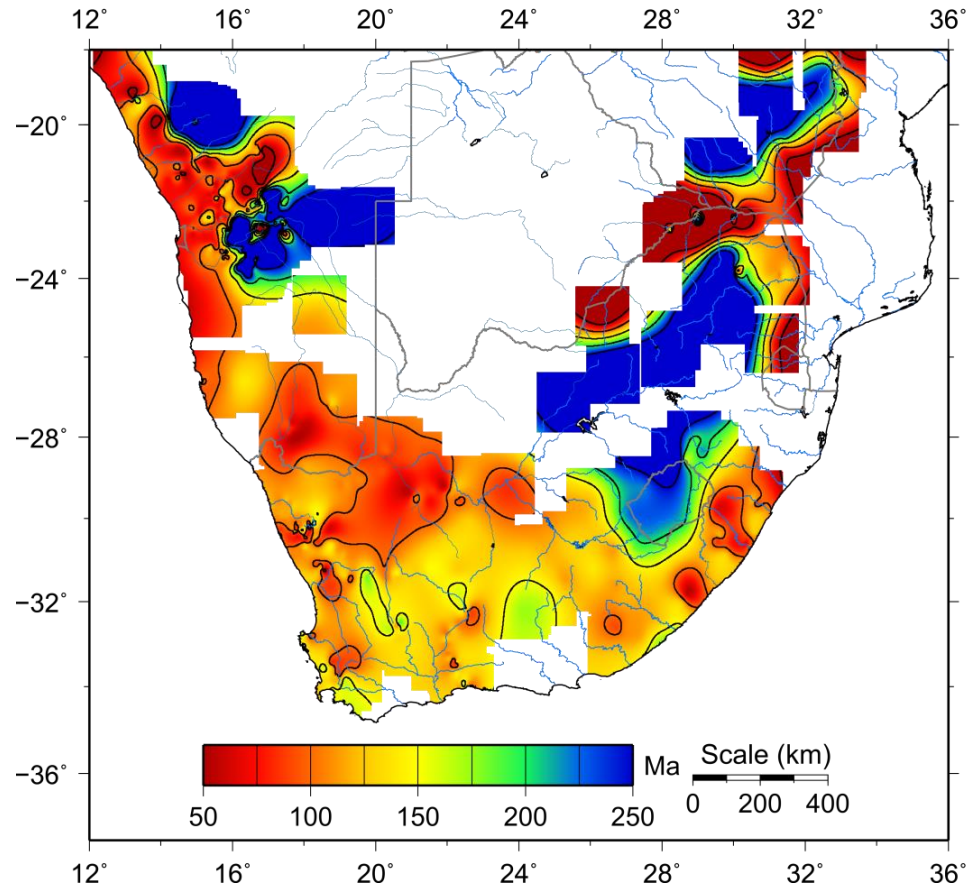


The sources of this data are listed in the caption to Figure 7-4a with most of the data being fully published. AFT ages range from  $38 \pm 3$  to  $547 \pm 95$  Ma (Fig. 7-4b) with younger ages typically found at the continental margins and older ages in the interior. However, as can be seen in the SW corner of Figure 7-4b, younger ages exist far inland and, on a more local scale (10s of km), abrupt variations in AFT age can be observed.

A smaller number of outcrop samples with reliable MTLs are available ( $n = 572$ ) due to track length measurements not being routine in earlier studies (e.g. Haack, 1983) or occasional samples being devoid of tracks suitable for measuring (Fig. 7-4c). As this data was generated over several decades additional parameters which are now routinely measured to help constrain fission track annealing (e.g. angle of track to c-axis and kinetic parameters like Cl content and  $D_{\text{par}}$ ) are occasionally absent. For this reason, the database consists of the raw measured MTL which was reported (i.e. not corrected for orientation). MTLs range from  $9.8 \pm 0.3 \mu\text{m}$  to  $18.1 \pm 0.4 \mu\text{m}$ . This maximum value seems overly long considering the maximum etchable length of a fission track under experimental conditions is  $16 \pm 1 \mu\text{m}$ ; it is not a volcanic rock (i.e. it has not cooled instantly); and there are only 8 measured track lengths with a large MTL-SD. In this sample, if only a few tracks were over-measured or features within the crustal were incorrectly measured as long tracks, then the MTL would be overestimated. Similar to the distribution of AFT ages, there is quite a lot of spatial variation in MTLs. In general, however, MTLs which are long ( $> 14 \mu\text{m}$ ) are found along the coastal margins. Shorter track lengths are spread across both the margins and continental interior.

To better visualise the spatial distribution of AFT ages and MTLs interpolation maps were produced using a natural neighbour interpolation technique (Fig. 7-5). AFT ages older than c. 250 Ma, indicated by blue to dark blue parts of the colour map, are entirely confined to the continental interior, landward of the coast parallel escarpment zone. In places, high resolution clusters of data points have recorded the transition from older Permo-Carboniferous ages to younger syn or post-rift ages (e.g. northern Namibia, south eastern South Africa, north eastern South Africa, and southern Zimbabwe). Based on the distribution of the

(a) AFT age



(b) MTL

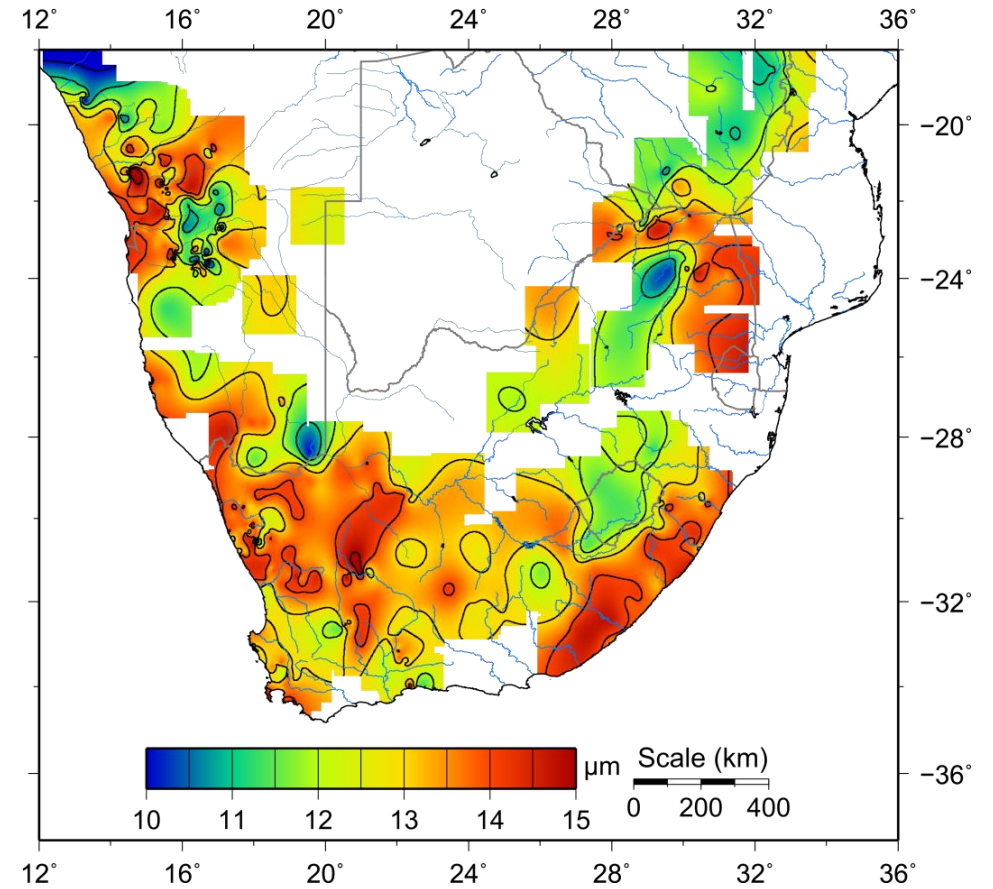


Figure 7-5: Map interpolating (a) AFT ages and (b) MTL across southern Africa using. The Interpolation was performed using a “spline in tension technique” in GMT (Smith and Wessel, 1990; Wessel et al., 2013). A mask of radius 1.5° latitude/longitude was used around each data point to hide the interpolation map where it is unconstrained due to an absence of data points.

data points, the transition is marked by a drop of c. 200 - 300 Ma in less than 100km. In northern Namibia, some samples record a similar drop in age over horizontal distances of 15 km.

The AFT age interpolation map (Fig. 7-5a) shows a clear asymmetry in the distribution of ages that are Jurassic in age or younger. Whereas in the south east corner of South Africa, post-Mid-Jurassic AFT ages are confined to the region (c. 150 - 300 km wide) between the continental margin and elevated plateau; along the south and western margins, post-Mid-Jurassic AFT ages extend at least 700 km inland from the continental margin. This implies that enhanced denudation of the crust occurred over both the present day continental margin and the interior plateau. This is an important observation as it indicates that the major escarpment zone, prominent in the present topography, does not represent a clear boundary between a deeply eroded coastal plain and an inland plateau characterised by minimal post break-up erosion; at least not on the southern and western margin of southern Africa.

The transition to Palaeozoic AFT ages which appear to characterise the cratonic interior regions of the plateau, is poorly defined due to a lack of data but it seems to be coincident with the southwestern tectonic boundary of the Kaapvaal craton. Along the continental margin of northern Namibia post-Mid-Jurassic ages are again confined to the c. 150 km wide coastal plain. The eastern margin of South Africa and Zimbabwe has a much wider coastal plain (c. 700 km) but again the younger ages are only found seaward of the escarpment zone in this region.

No easily definable trend in AFT ages is apparent moving inland from the western and southern South African margins. The majority of ages across the Cape Fold Belt are c. 110 - 140 Ma with only a few samples yielding ages  $\pm 30$  Myr older or younger than this interval. Along the western margin abrupt age variations occur between samples that yield ages greater than 100 Ma and ages that are c. 80 - 100 Ma. Moreover, the schematic age trend through the Kenhardt and Augrabies region presented in Chapter 6 - Figure 6-22, is seen more prominently in the interpolation map. In this region, the zone of ages c. 60 - 100 Ma trend NW - SE and are constrained by a fairly substantial number of samples.

A similar zone of young Mid - Late Cretaceous ages which extend anomalously far inland is present in northern Namibia and trends NE-SW. Much like the zone of young ages in southwest Africa, Cretaceous ages in Namibia appear to follow the major craton bounding structures present in the Namaqua mobile belt. A region of young ages in Namibia extended inland through the escarpment following the trend of the Damara mobile belt and has been attributed to reactivation of NE-SW trending faults (Raab et al., 2002; Brown et al., 2014).

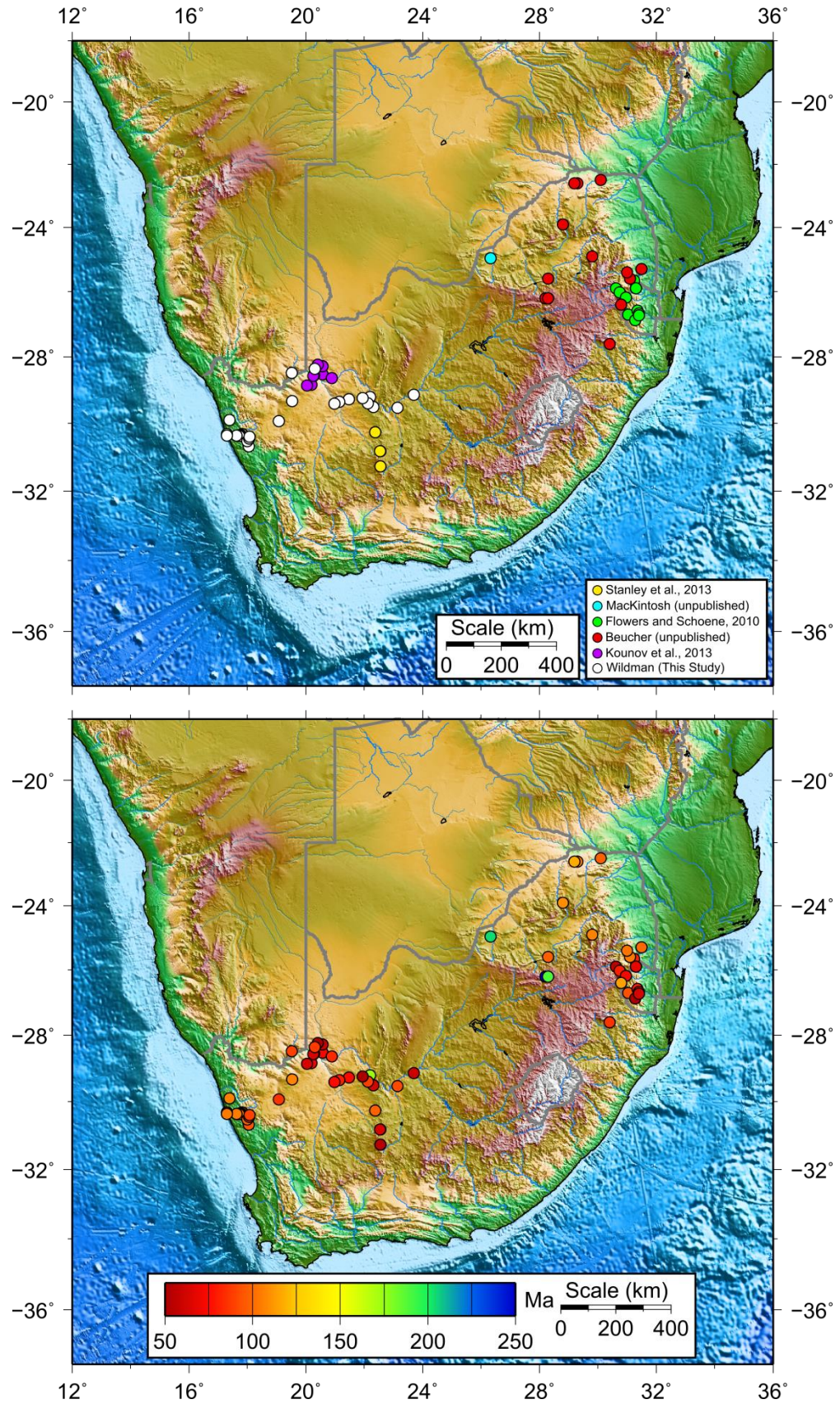
On a continental scale, simple conceptual models of passive margin evolution envisage, enhanced (rapid and large magnitude) denudation focused at the continental margins and minimal denudation occurs on the continental interior (Ollier and Pain, 1997; Gilchrist et al., 1994; Van der Beek et al., 2002). In the fission track record, this should result in old pre-rift AFT ages in the continental interior having short MTLs while younger syn or post-rift samples on the coastal plain have long MTLs. On the MTL interpolation map (Fig. 7-5b) it can be observed that in south east Africa and in northern Namibia zones of long MTL generally correlate with zones of young AFT ages. In keeping with the expected relationship at passive continental margins, most of the zones with short MTLs are found in the continental interior and correlate with older AFT ages. On the continental interior in south western interior MTLs are mainly 13.5 - 14.5  $\mu\text{m}$  indicative of fairly rapid cooling over the region at a time indicated by the AFT age. The long wavelength pattern in the South African data set is indeed consistent with these simple models. However, the very significant deviations to this simple expected pattern, as described above, indicate a more complex pattern of post break-up landscape evolution is superimposed on the continental scale response.

### **7.2.3 South African apatite (U-Th-Sm)/He data**

The coverage of apatite (U-Th-Sm)/He data in southern Africa is severely limited. At present only three studies have published AHe results from a small number of samples (Flowers and Schoene, 2010; Kounov et al., 2013; Stanley et al., 2013) and only one of these have presented the AHe data alongside complimentary AFT data from the same samples (Kounov et al., 2013).

Additional unpublished data (Beucher and Brown, pers. commun.) were available and are included in the regional database. Including all of these data, as well as new AHe data presented in this thesis, there are 70 samples which have been dated using a multiple single-grain approach. Details on the source of this data and the mean AHe age are summarised in Figure 7-6. However, following previous discussions on the significance of a mean AHe age, the value of each data point should be treated with caution and the full single grain age dataset should be inspected to investigate how much dispersion is present and what the main control on this dispersion may be (e.g. grain size, eU, fragmentation). In all of the published studies, only a limited number of single grain ages ( $n \leq 5$ ) were obtained. These datasets all show variable amounts of dispersion (approximated by the standard deviation of the mean AHe age) which can be significant (0 - 56%). The cause of this dispersion is often attributed to the effects of radiation damage based on positive eU correlations but it is often the case that these relationships are absent or inverted and, when only a limited number of grains are analysed, correlations are almost always poorly defined (e.g. Flowers and Schoene, 2010; Stanley et al., 2013). To provide a broad overview of the available AHe data, the dispersion on single grain ages is put to one side for now, as is the effect of alpha ejection which is influenced by the samples cooling history (Meesters and Dunai, 2002a,b; Gautheron et al., 2013).

Data from the south eastern margin has mainly focussed on the coastal plain and escarpment zone in and north of Swaziland. Mean AHe ages range between 50 and 120 Ma with no clear pattern emerging with distance from the coast or elevation. Further east, AHe ages from samples collected closer to the South Africa - Botswana border and likewise samples collected near to Johannesburg, are older (c. 190 - 300 Ma) than samples seaward of the escarpment. 11 samples from this region are from Flowers and Schoene (2010) study of the erosion history of the eastern Kaapvaal craton. Thermal history modelling of this data predicts rapid cooling initiating at c. 120 - 110 Ma which is attributed to a rapid erosional response to regional uplift. By identifying the coincident timing of enhanced cooling with kimberlite intrusive activity, emplacement of the Etendeka Lavas and continental rifting of the western margin Flowers and Schoene, (2010), suggest that uplift is driven by buoyancy in the deep mantle.



**Figure 7-6: Database of apatite (U-Th)/He data which shows (a) Sources of AHe data (b) Mean AHe age. DEM data is a combination of STRM30plus (1km data derived from the SRTM 3 arc sec (90m) global data) and the ETOPO2 global data (for ocean areas).**

However, rift-related uplift and erosion would have occurred during the break-up of Eastern Gondwanaland during the Early - Mid Jurassic. The thermal history models are also limited due to the small number of AHe grains. As evidenced by the data presented in this study there is a large degree of uncertainty in AHe measurements and many similar looking AHe datasets may agree with different thermal histories when complimentary AFT data are included.

Focussing more directly on the relationship between mantle processes and tectonic activity, Stanley et al. (2013) present AHe data from kimberlite xenoliths and adjacent basement rock. Mean uncorrected AHe ages from four samples range from c. 45 - 98 Ma. Thermal history inversion of this data interpreted alongside the emplacement age and preserved facies of the sampled kimberlites led to the conclusion that kilometre scale erosion of the plateau occurred during the period 120 - 90 Ma. The driving mechanism behind uplift is again attributed to dynamic processes in the mantle. However, like the data from the eastern South African margin from Flowers and Schoene (2010) AFT data is not available and this creates uncertainty in the thermal history models which have been produced by inverting AHe data only. Additional thermal history information may be available in eU - age relationships which are suggested by Stanley et al. (2013) to explain single grain age dispersion. However, as discussed in Chapter 4 - Section 4.4.5, there still exists considerable uncertainty in how radiation damage influences AHe diffusion and therefore how inverse modelling approaches treat radiation damage effects over a particular t-T history. AFT data would provide additional independent information to constrain the nature of cooling. An example of this is the AHe data collected next to the Markt kimberlite (Stanley et al., 2013). The AHe data is highly dispersed (20 - 60%) and is modelled using the radiation damage of Flowers et al. (2009) resulting in a model which predicts prolonged residence at temperatures between 40 and 50°C until after c. 30 Ma. The implications of this being that up to 1.5 km of Late Cenozoic erosion may have occurred at this location. Considering the large degree of single age dispersion insights from AFT data or modelling radiation damage after Gautheron et al. (2009) may help to support or cast doubt on this conclusion.

The remaining AHe data obtained by Kounov et al. (2013) have previously been discussed in Chapter 6. This data is integrated with AFT and, in short, supports erosion driven cooling initiating between 120 and 90 Ma driven by regional uplift with less than 1km of erosion occurring over the entire Cenozoic. However, no radiation damage model is included in this thermal history inversion despite age dispersion in some samples being 20% or greater.

The detail of Cenozoic erosion across southern Africa remains enigmatic. However, most studies that have employed AHe analysis have concluded that only minor amounts of Cenozoic erosion (<1km) are possible and only in rare circumstances is it greater than 1km. AHe analysis has been more successful, it appears, at refining the record of cooling during the time interval of 110 - 90 Ma constraining both the large magnitude of cooling and its regional occurrence. When there is no AFT data to compliment AHe analysis and the number of single grain AHe ages from a particular sample is low, the limitations of thermal history inversion should now be apparent. AHe data presented in this thesis corroborates the regional nature of cooling during 110 - 90 Ma but it also helps to constrain an early Cretaceous cooling episode, extending inland to the Kaapvaal craton, and early Cenozoic erosion which locally may exceed 1km.

### **7.3 Denudation of the SW African continental margin and interior plateau**

To better investigate the spatial and temporal variations in the denudation levels across all of southwestern Africa, the AFT data of Brown (1992) were inverted using the modelling approach described in Chapter 4 - Section 4.5.1, and denudation estimates were derived for each of these samples based on the expected thermal history path as described in Chapter 5 - Section 5.6.2. These estimates were combined with those made from the new data presented in Chapter 5 and Chapter 6 to provide greater coverage of the region. Using all these data points, separate interpolation maps were constructed over discrete time intervals from 150 Ma until present day (Fig. 7-7).



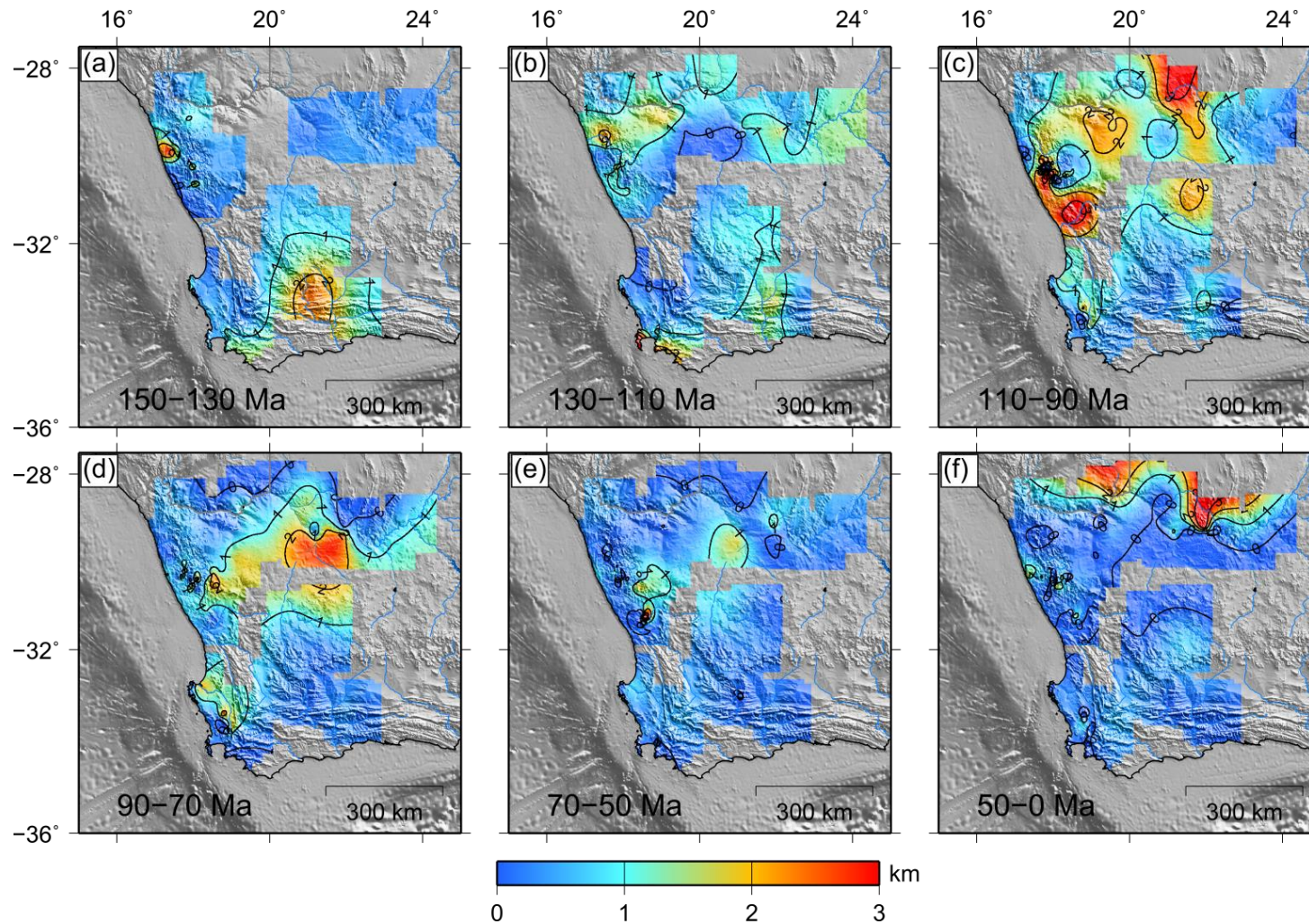


Figure 7-7: Interpolation maps based on denudation estimates extracted from thermal histories models. Estimates were made using a geothermal gradient of  $25^{\circ}\text{C}/\text{km}$  and the change in temperature of the expected thermal history model over the specified time interval. DEM data is taken from the ETOPO2 global dataset. The Interpolation was performed using a “spline in tension technique” in GMT (Smith and Wessel, 1990; Wessel et al., 2013). A mask of radius  $1.5^{\circ}$  was used around each data point to hide the interpolation map where it is unconstrained due to an absence of data points.

### 7.3.1 150 – 130 Ma

Estimates of denudation at this time (Fig. 7-7a) are based on fewer data points ( $n = 62$ ) than subsequent time intervals ( $n = 119$ ). This is due to almost 50% of thermal history models predicting that cooling initiated from temperatures greater than c.  $110 \pm 10^\circ\text{C}$  after 130 Ma. There is also a degree of uncertainty in the amount of denudation estimated at this time from samples which are both unconstrained prior to the onset of cooling and which begin to cool towards the younger end of the time interval (i.e. closer to c. 130 Ma). In these cases, cooling of the sample from 150 Ma through temperatures hotter than c.  $110 \pm 10^\circ\text{C}$  will be unresolved by the model and as such the amount of denudation calculated will be a minimum estimate. Across the entire region an average thickness of 700m has been eroded and removed from the surface. Peaks in denudation, where magnitudes are between 2 and 3 km, are found in isolated patches seaward of the present day western and southern margin escarpments. Inland of the Cape Fold Belt levels of denudation progressively decrease from c. 1.5 to 0.5 km northward. Along much of the western margin denudation amounts are between 0.5 and 1 km, In the Namaqualand region however, it is estimated that less than 1000m of denudation occurred across the margin but may have been  $> 2\text{km}$  in local zones. However, the low levels of margin denudation may be subject to the uncertainties mentioned above.

### 7.3.2 130 – 110 Ma

The average denudation thickness at this time (Fig. 7-7b) is slightly higher than the previous interval at c. 800m. At the most southerly point on the map rapid cooling recorded in a single sample (sample 8732-36) beginning at c. 130 Ma predicts denudation amounts of just less than 4km. Denudation of the surrounding area is estimated to be much lower than this (c. 250 - 700 m), increasing eastward. Further north, a large region of minimal denudation ( $< 500\text{m}$ ) is bound to the east and west by regions where denudation exceeds 750m. The eastern boundary of this zone of low denudation is fairly abrupt and coincides with the presence of the Hartbees River Fault (c.f. Chapter 6 - Figure 6-3). To the west, the transition from low denudation to high denudation is more

gradual. South of the Groothoek Thrust and Buffels River Shear Zone and south of the NQH, denudation is estimated to exceed 2km.

### **7.3.3 110 – 90 Ma**

The highest magnitudes of average denudation (1.15 km) occur during the 110 - 90 Ma time interval (Fig. 7-7c). However, this time interval is also characterised by much more variability both in the amount of denudation and spatial distribution. Low amounts of denudation (< 500m) occur behind the Cape Fold Belt and at the coast near to Cape Town. In the southwest Cape region denudation greater than 1km is found between NW - SE trending faults. Denudation is generally greater in the north of the study area than in the south. Denudation is commonly greater than 2 km and in places exceeds 3km. The zones of high denudation are found coincident with the NW-SE lineaments of the Bitterfontein region, in the heavily dissected NQH basement terrain and between the Hartbees and Doringberg faults on the Bushmanland plateau. In the NQH region, denudation varies abruptly by a kilometre or two. The lowest levels of denudation are found on the elevated plateau near Vaalputs; the low-lying coastal plain between Buffelsrivier and Kleinsee; and the valley at Garies.

### **7.3.4 90 – 70 Ma**

Following the episode of regionally enhanced denudation during 110 - 90 Ma (Fig. 7-7d), the average denudation thickness during 90 - 70 Ma falls to c. 800m. However, there still exists a high degree of spatial variability in the amount of denudation predicted. 1 - 2 km of denudation are still predicted to have occurred in fault bounded blocks in the south west; between the Hartbees and Doringberg faults in the north east; and in discrete locations in the NQH. While denudation in the surrounding area is generally less than 1 km, high levels of denudation (1 - 2.5 km) still persist inland of the present day escarpment in the north of the study area but do not further south. The highest levels of denudation on the continental interior are recorded by two samples (samples S-20 and SA12-15) on the southwestern side of the Hartbees fault.

### **7.3.5 70 – 50 Ma**

Major kilometre scale denudation across the SW Cape is largely complete by this time period (Fig. 7-7e) with a regional average of just under 400m. Areas where denudation is higher than the average and exceeds 1km are the southwestern side of the Hartbees Fault and within the NW - SE trending faults at Bitterfontein and Vanrhynsdorp. Interpolating denudation estimates between these two areas defines a NE - SW trending zone of c. 1 km of denudation however this feature is based on relatively few data points. Enhanced denudation perpendicular to the main structural trend may be an indication that ongoing activity on these structures was influential in maintaining erosion during the Late Cretaceous and earliest Cenozoic.

### **7.3.6 50 – 0 Ma**

From c. 50 Ma until present day, the average denudation across SW Africa is c. 200m and is fairly uniform across the region (Fig. 7-7f). Only occasional samples have thermal histories which suggest kilometre scale erosion in the Cenozoic and these mainly occur in the same structural zones that have appeared to control the location enhanced denudation during previous time periods. Models which suggest significant Cenozoic cooling are very much a minority within the dataset and are frequently obtained from samples which have limited track length data, single grain AFT ages, AHe data or a combination of all three. As such, any interpretations based on the inference of denudation estimated from these samples, needs to be done with a great deal of caution. The prevailing scenario based on all other available data is that erosion was minimal during the Cenozoic; limited to less than 1km.

## **7.4 Correlating onshore denudation with offshore accumulation: Insights from the Orange Basin**

### **7.4.1 The Orange Basin**

Offshore basins adjacent to the western and southern margins of southern Africa have been extensively studied using seismic reflection, seismic refraction and

borehole investigations in part due to their hydrocarbon potential (Emery et al., 1975; Dingle and Hendey, 1984; Brown et al., 1995; Paton et al., 2007; Rouby et al., 2009; Kuhlmann et al., 2010; Guillocheau et al., 2012). However, there still exists considerable uncertainty surrounding the deep crustal structure of the offshore margin (e.g. Hirsch et al., 2009, 2010); the distribution of post-rift sediment accumulation over time both along strike of the margin and in distal parts of the offshore domain (e.g. Guillocheau et al., 2012); the post-rift structural evolution of the margin (e.g. de Vera et al., 2010); and correlations between major offshore unconformities and periods of enhanced sediment accumulation with regional tectonic processes and denudation of material from the adjacent continent (e.g. Rouby et al., 2009).

The Orange Basin is a major sedimentary basin in the South Atlantic extending along the entire western margin of South Africa and southern Namibia (Fig. 7-1). Sediments have progressively accumulated in the Orange Basin from the Late Jurassic (i.e. onset of rifting) through to present day and cover an area of approximately  $1.3 \times 10^5 \text{ km}^2$  and achieve a thickness up to 7 - 8 km in the north and 3 km in the south (Gerrard and Smith, 1982; Dingle and Hendey, 1984; Séranne and Anka, 2005; Paton et al., 2008; de Vera et al., 2010; Kuhlmann et al., 2010). These sediments thin out further away (c. 800 - 1000 km) from the coastline and overly a 45 km thick pre-rift basement, which decreases to c. 25 km, 100 km oceanward of the margin (Séranne and Anka, 2005; Rouby et al., 2009).

The present day delivery of sediments from the continental interior to the Orange Basin is facilitated by the westward flowing Orange River which has a catchment area of 952, 200  $\text{km}^2$  (Goudie, 2005). While it is suggested that westward drainage of Southern Africa has persisted since continental break-up, internal reorganization may have altered the position of the major drainage outlet over this time (Dingle and Hendey, 1984).

It is suggested by de Wit (1999) that in the Early Cretaceous two major rivers existed: the Kalahari River, which drained southern Botswana and southern Namibia and had its outlet in a position similar to that of the present day Orange

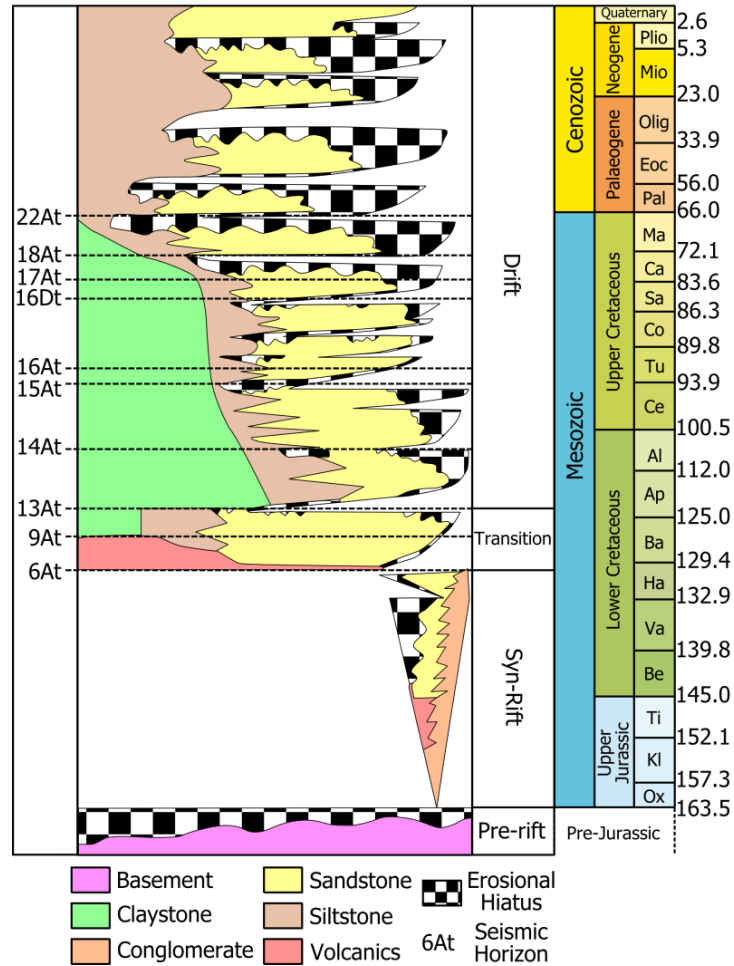
River or closer to the present day Buffels River (e.g. Stevenson and McMillan, 2004); and the Karoo River which drained the South African continental interior and entered the Atlantic at the mouth of the present day Olifants River. The establishment of the present day drainage network is suggested to have occurred by the end of the Miocene through progressive capture of smaller tributaries by the Orange River (Goudie, 2005). However, it has been suggested that during the Cretaceous and Early Cenozoic drainage reorganizations may have been episodic and related to periods of tectonic uplift of the continent in the Late Cretaceous and Oligocene (Dingle and Hendey, 1984; Partridge and Maud, 1987; Dollar, 1998; Goudie, 2005). These internal drainage reorganisations would not have greatly altered the total volume of sediment delivered to the entire Orange Basin (Rouby et al., 2009) but may influence the lag time between onshore erosion and offshore accumulation. Sediment would also have been supplied to the Orange Basin by smaller rivers along the coast which would have been influential in progressively eroding high elevation rift-flanks formed during continental break-up (e.g. Gilchrist et al., 1994; Kooi and Beaumont, 1994; Van der Beek et al., 2002). Because of the long-term stability of the southwest African drainage system, major episodes of denudation across the catchment should be reflected in the offshore record as periods of increased sediment accumulation (e.g. Gallagher and Brown, 1999b; Tinker et al., 2008b; Rouby et al., 2009).

## **7.4.2 Stratigraphy of the Orange Basin**

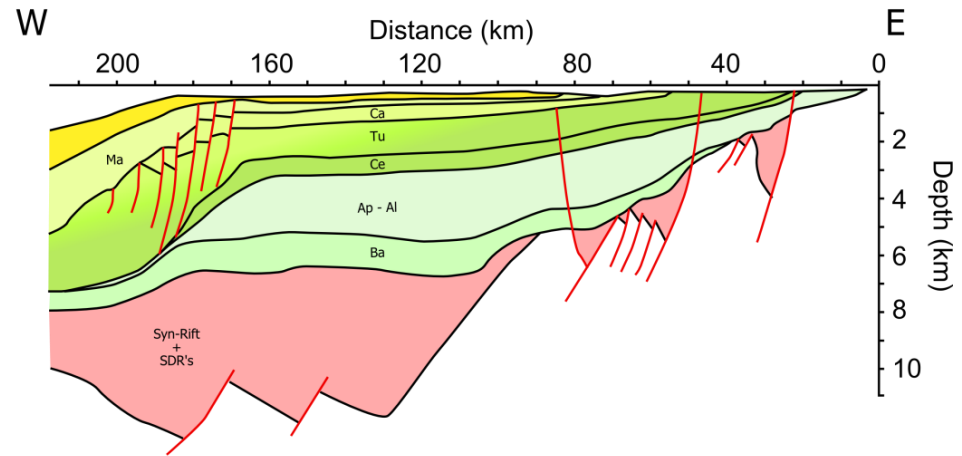
### ***7.4.2.1 Syn-rift sequence (c. 160 – 130 Ma)***

Extension of the western Gondwanan continental lithosphere at c. 160 Ma, initiated a complex, multi-phase, period of continental rifting involving thinning and subsidence of the lithosphere (Bauer et al., 2000; Eagles, 2007; Paton et al., 2008; Torsvik et al., 2009; Moulin et al., 2010). Syn-rift volcanic rocks and continental sediments were deposited unconformably over pre-Cambrian basement in graben and half-graben structures (Brown et al., 1995; McMillan, 2003; Hirsch et al., 2010; Franke et al., 2010) (Fig. 7-8). Wedges of volcanic rocks, possibly interbedded with sedimentary layers, are inferred by the presence of seaward dipping reflectors in seismic profiles (e.g. Franke et al.,

(a) Stratigraphic Column



(b) Orange Basin Section 1



Orange Basin Section 2

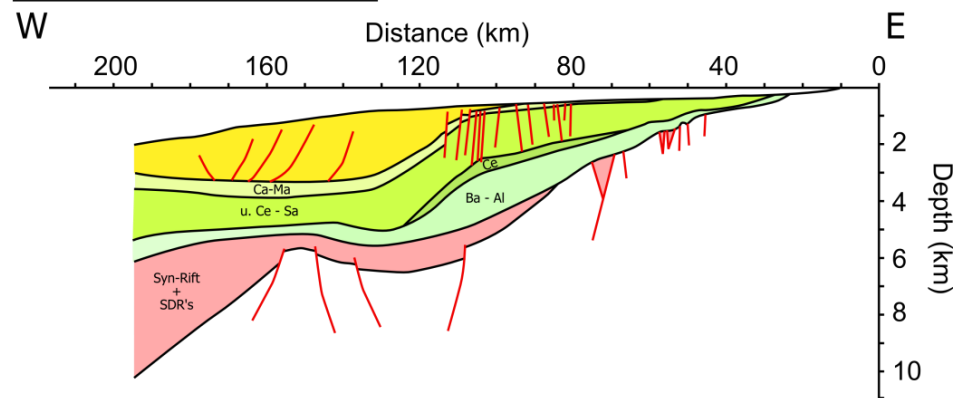


Figure 7-8: Summary of the stratigraphy of the Orange Basin. (a) Stratigraphic column showing major lithological units and timing of major erosional unconformities (after Kuhlmann et al., 2010). (b) Offshore cross sections through the Orange Basin (see Figure 7-1 for location) (after Guillocheau et al., 2012).

2007; de Vera et al., 2010; Koopmann et al., 2014). These volcanic rocks are thought to have been emplaced coevally with the Parana-Etendeka continental flood basalts at c. 135 - 130 Ma (Reid et al., 1990; Reid and Rex, 1994) and mark the onset of continental break up and sea floor spreading in the South Atlantic (Bauer et al., 2000; Hirsch et al., 2010; Koopmann et al., 2014).

Seismic interpretations and sporadic well data suggest the presence of several kilometres of volcanic, volcano-clastic and terrestrial sediments but the total volume, distribution and geometry of these deposits is still largely unknown (Jackson et al., 2000; Van der Spuy, 2003; Hirsch et al., 2010; Guillocheau et al., 2012). The timing for the development of the South Atlantic syn-rift succession is from the onset of rifting during the Late Jurassic (Oxfordian, 160 Ma) until the Late Hauterivian - Early Barremian (c. 130 Ma) which is marked by the well-defined break-up unconformity (Braun and Beaumont, 1989; Franke, 2013). This timing overlaps with the 150 - 130 Ma period of denudation predicted from LTT data from adjacent continent. A detailed chronology of the timing of deposition and thickness of overlying drift successions based on their biostratigraphy is given by McMillan (2003). The following section will discuss the Cenozoic - Cretaceous drift succession in terms of four key intervals which broadly overlap with the time periods used in discussions of denudation and which are bounded by major tectonically controlled unconformities (Broad et al., 2006; de Vera et al., 2010; Kuhlmann et al., 2010).

#### ***7.4.2.2 Late Hauterivian/Early Barremian – Early Aptian (c. 130 – 115 Ma)***

The first drift succession forms a ramp-like contact with the underlying syn-rift sediments and marks the rift to drift transition (Fig. 7-8) (Broad et al., 2006). The sediments are predominantly marine sandstone and shales and fluvial red beds (Gerrard and Smith, 1982; Broad et al., 2006; Kuhlmann et al., 2010). The succession is estimated to be up to 800 m thick but spatially variable based on borehole measurements with isopach maps suggesting a total thickness of up to 1500 m in the northwest of the basin (McMillan, 2003; Hirsch et al., 2010). The presence of a diverse assemblage of marine fossils within these sediments



suggests that distal parts of the Orange Basin were submerged under the developing Atlantic Ocean (McMillan, 2003).

#### **7.4.2.3 Early Aptian to Late Cenomanian/Early Turonian (115 – 90 Ma)**

The Early Aptian to Early Turonian sediments are deposited on the 13At1 unconformity, which defines the transition to full marine conditions of the margin, and represents the thickest succession in the Orange Basin (c. 2800m) (Fig. 7-8) (Muntingh and Brown, 1993; McMillan, 2003; Hirsch et al., 2010). Major progradation of the shelf occurred during the deposition of these sediments which was focused on the middle shelf rather than the inner shelf (Dingle and Robson, 1992; Brown et al., 1995; Broad et al., 2006; de Vera et al., 2010; Hirsch et al., 2010). The sediments are predominantly fluvial-deltaic sandstones interbedded with clays and shales (McMillan, 2003). The bulk of this interval accumulated through the Albian (c. 115 - 100 Ma) but the maximum thickness of c. 2000 - 2200 m is achieved only in the main depocentre of the Orange River and thins towards the continental shelf and southern reaches of the basin (McMillan, 2003; Hirsch et al., 2010). Up to 600m of Early Cenomanian successions are preserved in the middle shelf but erosion has occurred locally on the inner and outer shelves. The Late Cenomanian (c. 97.2 - 93.5 Ma) is characterised by a period of non-deposition offshore and the development of a regionally observed unconformity (15At1) at the base of the Turonian (McMillan, 2003).

#### **7.4.2.4 Early Turonian to Late Maastrichtian (c. 90 – 65 Ma)**

Aggradational sequences dominate the sedimentary succession above this unconformity (Fig. 7-8) (Broad et al., 2006). However, multiple unconformities and occasional prograding sequences suggest fluctuations in sea-level and/or uplift of the continent (McMillan, 2003; Séranne and Anka, 2005; de Vera et al., 2010). Sedimentary successions throughout the Turonian and Coniacian were deposited with a relatively uniform thickness (c. 200 - 500m) in the distal outer-shelf, thinning towards the inner shelf (McMillan, 2003; Hirsch et al., 2010). A thicker (1 - 2 km) Santonian to Early Campanian (c. 85 - 75 Ma) succession is present in the northern part of the Orange Basin which has experienced listric

faulting at the slope break (McMillan, 2003). These units are sandstones, grits, and interbedded shales that represent the last fluvially influenced Cretaceous sedimentary deposits (McMillan, 2003; Van der Spuy, 2003; Paton et al., 2008). During the Maastrichtian thin (>500m) chalks were deposited on the upper slope of the margin (McMillan, 2003). Two unconformities in the Maastrichtian mark the onset (17At1, 80 Ma) and termination (22At1, 65 Ma) of erosion of the proximal parts of the margin which have been attributed to uplift of the adjacent margin (Hirsch et al., 2010).

#### **7.4.2.5 Cenozoic sequences (c. 65 – 0 Ma)**

The depocentre shifts seaward during the Cenozoic and accumulates relatively limited terrestrial sediments (Fig. 7-8) (Broad et al., 2006). The maximum thickness of sediments accumulated during the Cenozoic is c. 1200m over the outer shelf and only a few hundred metres on the inner shelf (Hirsch et al., 2010). Lower Cenozoic sandstones and claystones and Oligocene - Early Miocene Carbonate sequences were eroded during periods of intervening sea-level regression and/or localised tectonic instability of the margin (Gerrard and Smith, 1982; McMillan, 2003; Wigley and Compton, 2006; de Vera et al., 2010; McMillan et al., 2010). Tectonically driven uplift and subsidence controlling the development of erosional unconformities are suggested to have occurred during the late Eocene/Early Oligocene, Mid-Miocene and possibly in the Pliocene (Partridge and Maud, 1987; McMillan, 2003; Wigley and Compton, 2006).

However, the thermochronology data presented in this study suggests that erosion onshore was relatively limited throughout the Cenozoic (total being <1km) and therefore any uplift event must have been of relatively low magnitude, or focused within the offshore regions rather than onshore. It should also be remembered that Cenozoic successions in the offshore basins are poorly understood due to a lack of equivalent onshore deposits, limited sampling from oil exploration wells, low sedimentation rates and restricted distribution (Wigley and Compton, 2006).

### 7.4.3 Structural features in the Orange Basin

During continental rifting, the shallow lithosphere thins by extensional faulting creating graben and half-graben structures in the pre-rift basement (Ziegler and Cloetingh, 2004; Lavier and Manatschal, 2006; Huismans and Beaumont, 2008). As discussed in Chapter 2, recent investigations of rifted margins have revealed that they experience a complex structural development involving inward migration of active faulting towards the main rift axis (e.g. Corti et al., 2013; Brune et al., 2014); extensional deformation far afield (c. 300km) from the main centre of rifting (Huismans and Beaumont, 2008, 2011; Autin et al., 2013); and prolonged or multi-phase rifting histories (Lundin and Doré, 2011; Péron-Pinvidic et al., 2013). In the offshore basin, the presence of overlying extrusive volcanic rocks hinders the identification of basement structures (Franke et al., 2013). The presence of syn-rift basins are inferred from modern day active rifts such as the East African rift zone (Ebinger and Scholz, 2011), analogue (Corti, 2012) and numerical modelling (Huismans and Beaumont, 2011) and the deposition of siliclastic sediments and volcanics (Gerrard and Smith, 1982; Light et al., 1992; Brown et al., 1995; Van der Spuy, 2003; Hirsch et al., 2010).

Within the drift successions gravitational tectonics is frequently described involving slumping driven extension in the proximal margin and toe-thrusting in the outer-shelf (Brown et al., 1995; Paton et al., 2008; de Vera et al., 2010, Hirsch et al., 2010). de Vera et al. (2010) describe in detail the 145 km long gravity driven system across the Orange Basin which occurs in the Upper Aptian - Santonian (c. 115 - 83 Ma) sequence. This structural system is comprised of three domains: (i) a 90 km long extensional domain up-dip of the major basin slope characterised by listric faults dipping east; (ii) a 10 km long transitional domain with both extensional and contractional structures; and (iii) a 55km long contractional domain with low-angle thrusts and folds dipping landward. There is a lack of correlation of these structures between adjacent seismic lines suggesting that they terminate abruptly along strike of the margin (Brown et al., 1995; de Vera et al., 2010). The major zone of extension and compression has a basal detachment in the marine shales of the Turonian-Cenomanian boundary (Muntingh and Brown, 1993; Séranne and Anka, 2005; de Vera et al., 2010).

Normal fault displacement involves steep vertical displacement and rotation of fault block promoting growth strata up to 2.5km thick to be deposited. Lower amounts of vertical displacement and structural relief (<1km) are observed on thrust faults in the compressional domain (de Vera et al., 2010).

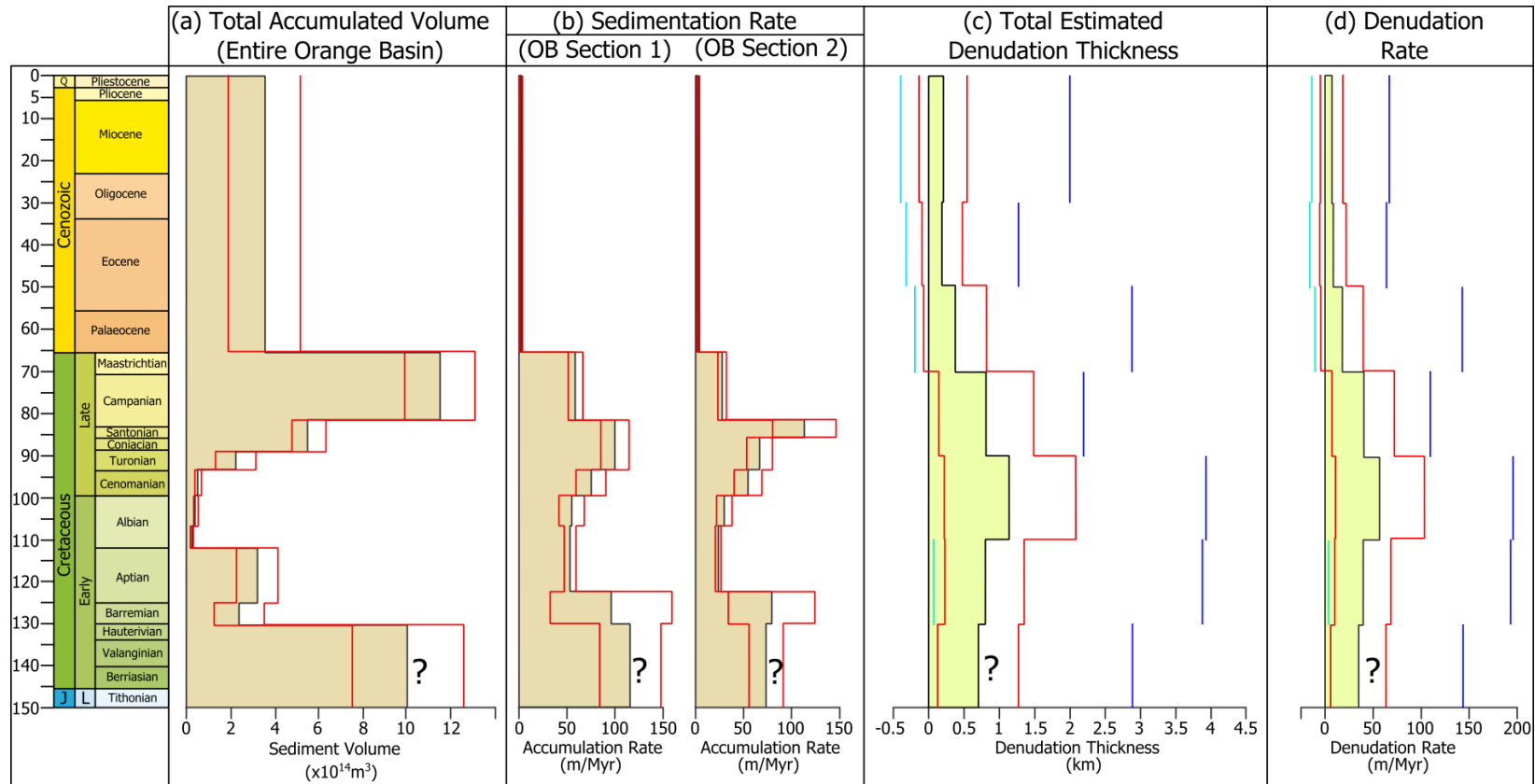
The development of growth strata and stratigraphic relationships led de Vera et al. (2010) to conclude that gravitational tectonics were periodically active in short-lived episodes. The wider mechanisms which trigger movement on these faults are still uncertain and has been related to the influx of high volumes of sediment to the basin (Jungslagger, 1999; Paton et al., 2007; Kuhlmann et al., 2010), basin inversion and the development of enhanced structural relief; or margin uplift (Séranne and Anka, 2005; Paton et al., 2008; de Vera et al., 2010). The timing of gravitational failure episodes (c. 100 - 80 Ma) overlaps with the timing of major denudation of the continental margin inferred from low temperature thermochronology. This period of denudation is interpreted here to be structurally controlled and involve the removal of several kilometres of material from the continental margin and interior. A combination of each of the three possible mechanisms triggering gravity sliding mentioned above may have occurred either in tandem or over different periods during the 100 - 80 Ma interval. Moreover, the regional in-plane, predominantly extensional, stress field across the margin at this time (e.g. Bird et al., 2006; Andreoli et al., 2009; Viola et al., 2012; Salomon et al., 2014) may have made the offshore sequences susceptible to faulting.

Towards the coast, faults in the extensional domain extend into and offset Cenozoic sequences suggesting later reactivation of pre-existing earlier faults (de Vera et al., 2010). A discrete shallower system of gravitational structures is also observed in Cenozoic successions, detaching at the Late Maastrichtian - Early Cenozoic unconformity (Jungslagger, 1999; Séranne and Anka, 2005). Further evidence for later Cenozoic (neotectonic) fault activity comes from the identification of inversion structures on normal faults and presence and alignment of mud volcanoes in the Orange Basin (Ben-Avraham et al., 2002; Viola et al., 2005).

#### 7.4.4 Linking onshore denudation with offshore accumulation

The timing and magnitude of offshore sediment accumulation has been used in previous studies to approximate the amount of material removed from the adjacent continental margin (e.g. Emery et al., 1975; Dingle et al., 1983; Rust and Summerfield, 1990; Rouby et al., 2009). However, many of these studies focused on sedimentation in the proximal part of the margin over broad time intervals. A recent study into the development of the offshore basin along the entire southwestern African margin, south of the Walvis Ridge has refined the major timings and magnitudes of sediment accumulation volumes and rates since 150 Ma (Guillocheau et al., 2012). This study also estimates the amount of sediments in the poorly constrained distal parts of the margin. The results from this study are compared with the denudation record estimated from LTT data presented in this thesis. The chart of total volume accumulation reflects the entire southwestern margin offshore basin and therefore is subject to uncertainties in the spatial distribution of sediments over time (Fig. 7-9a). Two charts of sedimentation rate correspond to the lines of section shown on Figure 7-8 and provide a more detailed account of the region of the Orange Basin relevant to the study area onshore (Fig. 7-9b).

High sediment volumes (c.  $1 \times 10^{15} \text{ km}^3$ ) are calculated for the syn-rift period until c. 130 Ma, with high sedimentation rates recorded in the Orange Basin. The amount of denudation and estimated denudation rate over the syn-rift period is consistent with the volumes and rates of offshore accumulation at this time (Fig. 7-9c and 7-9d). However, correlating both sources of data is subject to uncertainty inherited within them. The offshore record of syn-rift sediment accumulation is often difficult to resolve due to the presence of extrusive volcanics masking underlying sedimentary and structural features in seismic profiles. Moreover, sediments interbedded with volcanics may be underestimated during seismic interpretation. The denudation record is uncertain because denudation driving sample cooling through temperatures greater than  $110^\circ\text{C}$  prior to, or during, the 150 - 130 Ma interval is not quantified but would contribute to offshore sedimentation. Indeed some samples suggest that cooling has been ongoing since c. 170 - 160 Ma (e.g. JN2, FS-1605, KC 1/70).



**Figure 7-9: Histograms summarising the offshore clastic sediment accumulation history in the Orange Basin and the denudation history of the SW African margin. Total Accumulated Volume histogram (after Guillocheau et al., 2012) is based on five margin perpendicular sections from the Walvis Ridge to SW Cape (including OB Section 1 and OB Section 2) which are extrapolated linearly and interpolated laterally. Sedimentation Rates (after Guillocheau et al., 2012) for OB Section 1 and 2 correspond to Section 1 and Section 2 from Figure 7-1 and Figure 7-8. Red lines indicate the uncertainties on both accumulated volume and sedimentation rate estimates which propagate from uncertainties in interpolating and extrapolating the sections and from correcting sediment volumes for carbonate fraction. Denudation thicknesses are averages of all calculated values during each time interval. Denudation rate is calculated by the denudation thickness divided by the length of the time interval. Red lines are the uncertainty on denudation estimates and reflect  $1\sigma$  std. dev. Light blue and dark blue lines are the minimum and maximum denudation estimate, respectively, recorded by a sample during a particular time interval.**

Between c. 125 - 120 Ma there is a moderate decrease in sedimentation rate in the Orange Basin which persists for c. 15 Myr. The total sediment volume across the entire margin falls dramatically over this time but in two stages: first to c.  $3 \times 10^{14}$  km<sup>3</sup> through the Barremian and Aptian (130 - 112 Ma) and then to less than  $1 \times 10^{14}$  km<sup>3</sup> in the lower Albian (112 - 108 Ma). This period of decreasing sedimentation overlaps with the 130 - 110 Ma period of onshore denudation. Average denudation at this time is approximately the same as the previous interval but in reality may be considerably less than the amount of denudation which has occurred during the syn-rift phase that is simply unconstrained in the current thermochronology data. The estimates of denudation thickness and rates are therefore consistent with a decrease in sedimentation volume and rate.

During the Albian through to lower Campanian (c. 110 - 80 Ma) sedimentation rates progressively increase in the Orange Basin to near syn-rift levels before decreasing again through the Upper Campanian and Maastrichtian (c. 80 - 70 Ma). Sediment volumes across the margin increase almost exponentially for the Middle Albian to Upper Maastrichtian (c. 110 - 70 Ma). Average denudation is greatest over 110 - 90 Ma and is still moderately high through 90 - 70 Ma. Average denudation during the 110 - 90 Ma interval is also associated with a large standard deviation; high maximum denudation value and zero minimum denudation value. This is a reflection of the high spatial variability of the intensity of denudation across the margin which is here interpreted as being controlled by structural reactivation across discrete fault zones and blocks. Tectonic reactivation of major structures may have an interesting but as yet unclear relationship with regional tectonic uplift during this relatively short time interval. For example, fault block offsets may have occurred during the earliest drift phase inducing localised erosion but also disrupting the transportation of material to the offshore basin. Subsequent regional uplift of the entire SW margin and continental interior, possibly driven by dynamic uplift arising from deep mantle flow, with possible westward tilting (e.g. Partridge and Maud, 1987; McMillan, 2003; Braun et al., 2014a) would then have promoted enhanced sedimentation during the Late Cretaceous. The small volumes of sediment which accumulated during the Albian (c. 112 - 99 Ma) and Cenomanian (99 - 93.5 Ma)

may also reflect erosion of these sediments from the proximal margin and redistribution to distal parts in the Late Cretaceous (McMillan, 2003).

Extremely low sediment volumes are calculated for the entire Cenozoic and reflect low rates of sediment accumulation in the Orange over this time. Average denudation rate over the three Cenozoic time intervals discussed here (70 - 50 Ma; 50 - 30 Ma; and 30 - 0 Ma) progressively decreases, however local maximum values can still remain high. However, the detail of the offshore stratigraphic record over this time is poorly documented and, except for a handful of samples, no major Cenozoic cooling (particularly late Cenozoic cooling), is observed in thermal history models.

The correlation of offshore sediment accumulation and onshore denudation can only be used as a general overview of the relationship between erosion and sedimentation (e.g. Rouby et al., 2009). This is because the offshore domain and corresponding erosion domain (i.e. coverage of data points) is not entirely complimentary. For example, estimates of total accumulated volumes in the Orange Basin include sediment thickness observed further north along the Namibian margin and therefore may smooth out the absence or variable thickness of sedimentary sequences which may have significance in terms of the evolution of the margin (e.g. McMillan, 2003). Another example is that the onshore data set includes samples from the southern margin which may have recorded the removal of material that has been deposited in the southern Outeniqua Basin (Tinker et al., 2008a, b). However, the timing of peak sediment volume accumulation and sedimentation rate is comparable to that observed in the Orange Basin (Tinker et al., 2008b). Two peaks in volume accumulation are observed at c 120 - 140 Ma and c. 70 - 95 Ma with an intervening period of low accumulation and low sedimentation rates. This period of low accumulation during the Cretaceous still greatly exceeds that observed in the Cenozoic further supporting limited regional denudation during the Cenozoic.



## 7.5 The Cenozoic evolution of SW Africa

### 7.5.1 Cenozoic erosion as permitted by low temperature thermochronometry and cosmogenic nuclide analyses

The current AFT and AHe dataset largely supports the view that major cooling of the upper crust occurred during the Cretaceous, with most samples reaching temperatures equal to, or below, c. 60°C prior to the Cenozoic. At low temperatures such as these the AFT thermochronometer lacks sensitivity because rates of fission track annealing at temperatures lower than c. 60°C is exponentially reduced (Gleadow and Duddy, 1981; Gleadow et al., 1986b; Wagner et al., 1989; Gleadow and Fitzgerald, 1987). Studies which have combined AHe and AFT analysis potentially extend the temperature sensitivity of the dating approach to c. 35 - 40°C. However, as has been previously discussed, the temperature sensitivity of AHe analysis increases for larger grain sizes and greater amounts of accumulated radiation damage. Radiation damage has likely influenced AHe closure temperatures in samples analysed from the NQH study due to high concentrations of U and Th. For this reason, denudation throughout the Cenozoic remains poorly constrained across southern Africa. Despite these uncertainties, thermal history models inverting AFT and/or AHe data have been used to estimate the amounts and rates of Cenozoic denudation (Table 7-1). These studies generally conclude that Cenozoic denudation is limited to less than 1.5 km and, in many cases; hundreds of metres rather than kilometres of material have been removed over the last 30 - 50 Myr. The rate at which denudation has occurred as inferred from these models is at most 40 m/Myr but typically has been lower than 5 m/Myr.

Cosmogenic nuclide analysis involves the accumulation of daughter nuclides over time generated by the interaction of cosmic radiation and rock-forming minerals (Lal, 1991). As incoming cosmogenic particles cannot penetrate beyond the upper few metres of the Earth's surface, in-situ dating has been effectively used to constrain recent (c.  $10^3$  -  $10^7$  years) rates of erosion across South Africa (Fleming et al., 1999; Cockburn et al., 2000; Kounov et al., 2007; Decker et al., 2011; Erlanger et al., 2012; Scharf et al., 2013). These analyses are consistent with the main conclusions drawn from AFT and AHe analysis; that depths of

Method	Source	Region	Average Denudation Rate (m/Myr)	Time Interval
Apatite Fission Track	Brown (1992)	Namaqualand & SW Cape	8	70 - 0 Myr
	Raab et al. (2002, 2005)	Northern Namibia	1.5 - 30	52 - 0 Myr
	Cockburn et al. (2000)	Northern Namibia	10 - 40	150 - 36 Myr
	Brown et al. (2002)	SE Africa (Drakensberg)	10	64 - 0 Myr
	Kounov et al. (2009)	Namaqualand & Calvinia	9.8 - 37.3	45 - 0 Myr
	Brown et al. (2013)	Southern Namibia	15 - 25	65 - 0 Myr
Joint AFT and AHe	M. Wildman (This Study)	Namaqualand & Bushmanland Plateau	15	70 - 0 Myr
	Kounov et al., (2013)	Augrabies Falls, South Africa & Fish River Canyon, Namibia	6 - 18.7	60 - 0 Myr
Apatite (U-Th-Sm)/He	Stanley et al. (2013)	Western Karoo Basin	1 - 17	60 - 0 Myr
	Flowers and Schoene (2010)	Eastern Kaapvaal Craton	14	65 - 0 Myr
Cosmogenic Nuclide	Fleming et al. (1999)	SE Africa (Drakensberg Plateau)	1.4 - 10	1 - 0 Myr
	Fleming et al. (1999)	SE Africa (Drakensberg escarpment)	26.9 - 62.3	1 - 0 Myr
	Cockburn et al. (2000)	Northern Namibia	0.4 - 10	36 - 0 Myr
	Bierman and Caffee (2001)	Northern Namibia	5 - 16	3 - 0 Myr
	Van der Wateren and Dunai (2001)	Northern Namibia (Central Namib inselbergs)	0.5 - 1	15 - 0 Myr
	Van der Wateren and Dunai, (2001)	Northern Namibia (Kuseb River Valley)	40 - 160	5 - 0 Myr
	Bierman et al. (2014)	Cape Fold Belt	3.4 - 6	3 - 0 Myr
	Codilean et al. (2008, 2014)	Northern Central Namibia	8 - 18	3 - 0 Myr
	Decker et al. (2011)	Cape Fold Belt, SE Karoo Basin, NE KwaZulu-Natal	0.5 - 4	1 - 0 Myr
	Erlanger et al. (2012)	SE Africa (Port Elizabeth)	15 - 17	4 - 0 Myr
	Kounov et al. (2007)	Calvinia and Cape Fold Belt	1 - 3	1 - 0 Myr
	Scharf et al. (2013)	Cape Fold Belt	2 - 8	1 - 0 Myr

**Table 7-1: Denudation rates for southern Africa based on apatite fission track, apatite (U-Th-Sm)/He and cosmogenic nuclide studies.**

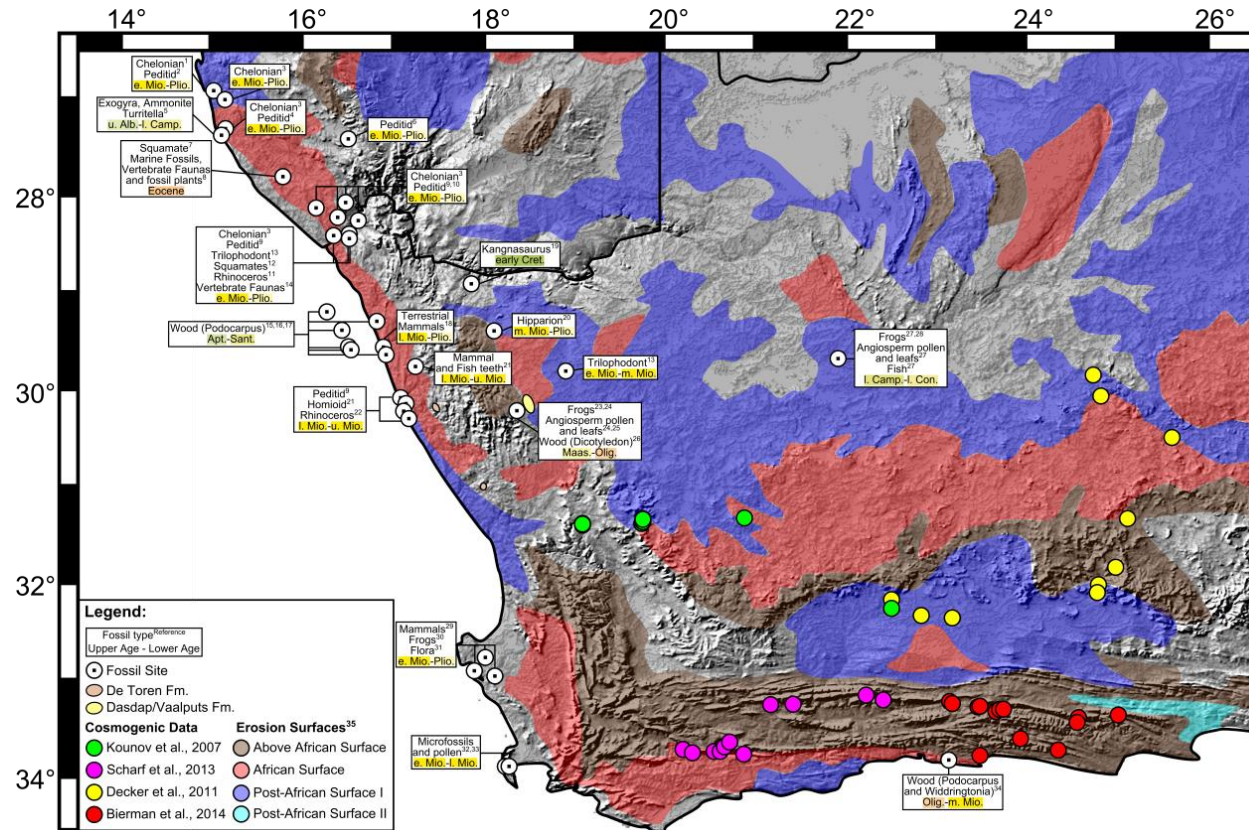
erosion have been relatively minor during the Cenozoic. Present day erosion rates are estimated to be as low as 0.4 m/Myr (Cockburn et al., 2000; Decker et al., 2011) and over the recent geological past (c. < 30 - 40 Ma) likely been less than 20 m/Myr. Extrapolating these values over the entire Cenozoic (c. 65 Myr) yields similar estimates (c. 1 - 1.5 km) of total vertical section being removed as obtained from AFT and AHe analysis. Where these studies have revealed much

higher rates of erosion (e.g. Fleming et al., 1999: 26.9 - 62.3 m/Myr; Van der Wateren and Dunai, 2001: 40 - 160 m/Myr) they have reflected incision of individual rivers channels or the escarpment face as opposed to the erosion of interfluves and flat surfaces.

### **7.5.2 Late Cretaceous to Cenozoic palaeontology**

Geological markers of Late Cretaceous or Cenozoic age are extremely rare across southwestern Africa and therefore resolving the geological history over this time period is extremely difficult. Fossil flora and fauna in southwestern African are found in thin Tertiary cover sediments; lacustrine sediments in palaeo-crater-lakes; and on the inner continental shelf. However, the fossil record is rather poor in terms of the abundance of preserved material and in its genealogical diversity which can be used to define a relative chronology (Rage et al., 2013). For this reason a single isolated and poorly dated fossil should not be used to infer a regional environment but can be used as an indicator of the local setting which can be used to provide some constraint to geological models. However, the fossil data set when viewed as a whole can be provide crucial insights into the erosion history of the region and the environment which prevailed at the time of fossil deposition (Fig. 7-10).

Cretaceous fauna is extremely rare and found only in three localities in the region of interest. Two of these sites, the Arnot pipe at Banke and the Stompoor pipe near Marydale have been briefly discussed in Chapter 5 and 6, respectively, as additional constraints for thermal history models. The third fossil site is located at Kangnas farm on the Koa River where dinosaur teeth and bones assigned to the Early Cretaceous (Haughton, 1915; Cooper, 1985) were described. These specimens include species of Pipidae (frogs) which were described by Haughton (1931) and Estes (1977) from the lacustrine mudstones in the Arnot pipe and by Smith (1986) and Trueb et al. (2005) in similar crater-lake sedimentary succession at Stompoor. The common occurrence of angiosperm pollen (Kirchheimer, 1934), fossil wood (Adamson, 1931) and fossil leaves (Rennie, 1931) at both localities developed in a similar manner (Smith, 1986). Haughton (1931) initially assigned a speculative Cretaceous - early Tertiary age



**Figure 7-10: Map collating various datasets used to infer Cenozoic landscape development in SW Africa. These datasets include: Palaeontological evidence, cosmogenic nuclide studies (c.f. Table 7-1), geological units (c.f. Chapter 5 – Section 5.2.7) and erosion surfaces (after Partridge, 1998). References for cosmogenic nuclide studies are in the figure legend. Other references are: 1 = Stromer, 1926; 2 = Mein and Pickford, 2008; 3 = de Broin, 2003; 4 = Hopwood, 1929; 5 = Haughton, 1930; 6 = Mein and Senut, 2003; 7 = Rage et al., 2013; 8 = Pickford, 2008; 9 = Pickford and Mein, 2011; 10 = Corbett, 1989; 11 = Guerin, 2000; 12 = Rage, 2003; 13 = Pickford, 2005; 14 = Corvinus and Hendey, 1978; 15 = Bamford and Corbett, 1994; 16 = Bamford and Corbett, 1995; 17 = Bamford and Stevenson, 2002; 18 = Cooke, 1968; 19 = Cooper, 1985; 20 = Pickford et al., 1999; 21 = Senut et al., 1997; 22 = Tankard, 1974; 23 = Haughton, 1931; 24 = Scholtz, 1985; 25 = Estes, 1977; 26 = Adamson, 1931; 27 = Smith, 1986; 28 = Trueb et al., 2005; 29 = Roberts et al., 2011; 30 = Hendey, 1970; 31 = Coetzee and Rodgers, 1982; 32 = Coetzee and Muller, 1984; 33 = Coetzee and Praglowski, 1986; 34 = Helgren and Butzer, 1977; 35 = Partridge, 1998.**

to the Pipidae and the host sediments. This age has been better constrained by radiometric dating of the underlying kimberlite and surrounding intrusions giving ages of c. 50 - 70 Ma (Davis, 1977; Moore and Verwoerd, 1975). The sediments in the surface depression at the intrusion are suggested to have been deposited fairly soon after emplacement (c. 0.3 - 4 Myr) (Scholtz et al., 1985) and therefore a Late Cretaceous - Early Cenozoic age for the lacustrine sediments and fossils is probable. The preservation of these fossils and the crater-lake sediments implies that the present day surface was established in the Late Cretaceous - Early Cenozoic with only very minor amounts of erosion since this time.

In-situ fossil wood in Pleistocene deposits were collected from the Namaqualand coastline and offshore in Late Cretaceous sediments on the inner continental shelf have been dated as Aptian to Coniacian in age (Bamford and Corbett, 1994, 1995; Bamford, 2000, 2004; Bamford and Stevenson, 2002). The presence of this fossil wood is suggested as evidence for an extensive forest on the palaeo-coastal plain which extended along the southern Namibian and western South African margin (Bamford and Corbett, 1994, 1995; Bamford, 2000, 2004; Bamford and Stevenson, 2002). Late Cretaceous palynological data from the same species of plant was identified in an offshore borehole 150km southwest of Cape Town (McLachlan, 1974) and in the lacustrine sediments of the Arnot pipe (Scholtz et al., 1985).

The early to mid Cenozoic fossil record is similarly poor; however recent fossil specimens have been obtained from the southwest Namibia margin. Vertebrate faunas, terrestrial and marine gastropods, terrestrial molluscs and plants have been identified in small limestone outcrops (Pickford et al., 2008 a, b). Rage et al. (2013) also reported amphibians and squamates (lizards and snakes) from the same localities. These studies concluded that the fossils are Eocene in age and are representative of a terrestrial environment with a long-lived freshwater source (Pickford et al., 2008 a, b; Rage et al., 2013).

A larger number of Late Cenozoic (post-Oligocene) fossils have been recovered from the coastal margin and continental interior. In southern Namibia early

Miocene to Pliocene abundant Pedetid (rodent) (Pickford and Mein, 2011) and Chelonian (turtle) (de Broin, 2003) fossils have been obtained suggesting a terrestrial environment with local freshwater sources or one close to the shoreline. On the Namaqualand coast, *Ceratotherium* (Rhino) (Tankard and Rodgers, 1978) and Hominoid (Gorilla) teeth have been used as evidence for a well-vegetated sub-tropical environment (Senut et al., 1997). The presence of shark teeth along the margin suggests that the coastline was close to its present day location in the Miocene (Senut et al., 1997). This environment is also postulated for the SW Cape with an assemblage of vertebrate faunas of Miocene to Pleistocene age being identified at Langebaanweg near Saldhana combined with palynological data from area (Coetzee and Rodgers, 1982; Coetzee and Muller, 1984; Coetzee and Praglowski, 1986). Evidence of larger mammals (Pickford, 2005), chelonians (de Broin, 2003) and squamates (Rage, 2003) of a similar age were identified at Arrisdrift on the Orange River and slightly younger (Pliocene) Hipparion (Horse) teeth at Areb (Pickford et al., 1999). This supports an environment which has been relatively stable in terms of erosion and the development of topography since the Miocene with limited erosion occurring across Southern Namibia and southwestern Africa.

### **7.5.3 The Cenozoic geomorphological development of southwestern Africa**

It is postulated here that much of the southwest African topography was created during the Cretaceous by a combination of syn-rift uplift of the continental margin, post-rift fault reactivation of pre-existing structures and possibly regional dynamic uplift. While insights from low temperature thermochronology and cosmogenic nuclide analysis do not imply significant rates or magnitudes of Cenozoic erosion, several geomorphological studies have advocated that the present day topography of South Africa is a young feature formed by a Cenozoic phase (or phases) of uplift and erosion (e.g. Partridge and Maud, 1987; Burke, 1996; Burke and Gunnell, 2008; Roberts and White, 2010). The notion that erosion or planation surfaces (previously discussed in Chapter 3 - Section 3.4) can be identified, assigned an age, correlated and mapped regionally has been a common but controversial (Chorley, 1965; Phillips, 2002) approach to resolving

large scale geomorphological development of the African continent. As stated by Burke and Gunnell (2008) resolving Africa's geomorphological history through the use of erosion surfaces is a "*well-trodden and treacherous path*". However, these authors still maintain that the approach has merit and strongly support the existence of the infamous African Surface.

Erosion surfaces are formed by the destruction of relief over time to a regional base level, typically but not exclusively sea level, leading to the development of a low-lying, low-relief planation surface, or "peneplain" (Partridge and Maud, 1987; Phillips, 2002; Watchman and Twidale, 2002; Burke and Gunnell, 2008). The development of such a surface is possible if tectonic stability persists over long timescales (Palmquist, 1975; Grimaud et al., 2014). If these surfaces are subsequently uplifted and dissected by incising rivers, the remnant surfaces (i.e. their present day form) can be correlated based their topographic concordance or similar weathering profiles (e.g. Partridge and Maud, 1987; Ollier and Pain, 2000; Burke and Gunnell, 2008; Japsen et al., 2012; Green et al., 2013; Lidmar-Bergström et al., 2013). By constraining an upper and lower limit on the development of this and successive surfaces using sedimentary or volcanic deposits then the timing of erosion, and intervening phases of uplift can be inferred.

The discussion on South African erosion surfaces has, for over half a century, been a source of much debate (e.g. Dixey, 1955; King, 1955; Wellington, 1955; de Swardt and Bennet, 1974; Ollier and Marker, 1985; Partridge and Maud, 1987), criticism (Van der Beek et al., 2002; Brown et al., 2002) and confusion (Burke and Gunnell, 2008). The occurrence and significance of erosion surfaces has been continually scrutinised due to advancements in our knowledge of plate tectonics, isostasy and mantle dynamics; the development of dating techniques to constrain the timing, magnitude and rates of erosion and; the surfaces themselves being reclassified and redefined to fit regional models of uplift and erosion (see Burke and Gunnell, 2008 pp. 13 - 19). The most recent synopses of South African erosion surfaces have been provided by Burke and Gunnell (2008) and Partridge et al. (2006), which summarises the work of Partridge and Maud (1987), Partridge (1998) and other works by these authors (Fig. 7-10). These

works describe the regionally extensive African erosion surface as a continent wide composite surface which developed over a time period of c. 150 - 20 Ma (Partridge and Maud, 1987) or 130 - 30 Ma (Burke and Gunnell, 2008). It is described as a composite surface as its development involved the amalgamation of smaller erosion surfaces which evolved separately due to local climatic or tectonic factors (Burke and Gunnell, 2008). Burke (1996) and Burke and Gunnell (2008) suggest that the African Surface was a regionally low-lying surface which was uplifted and incised due to mantle driven vertical uplift at c. 30 Ma. Partridge and Maud, (1987) alternatively suggest that several topographic features remained above the developing African Surface which was uplifted in the Early Miocene. They also advocate the existence of the undulating Post-African Surface I and II erosion surfaces; attributed to renewed river incision in response to Early Miocene uplift (150 - 300m) and Pliocene (100 - 900 m) uplift, with greater uplift on the eastern coast relative to the west.

The use of erosion surfaces to infer cyclic episodes of uplift and erosion is fraught with uncertainty concerning many aspects from the correlation of remnant surfaces (Summerfield, 1985; Van der Beek et al., 2002; Burke and Gunnell, 2008) to the more fundamental issue of whether or not it is plausible that an evolving landscape is permitted the time and tectonic stability to become a peneplain (e.g. Phillips, 2002). The uncertainty in topographic correlation of erosion surfaces induced by local climatic, tectonic and lithological factors was somewhat circumvented by both Burke and Gunnell (2008) and Partridge and Maud (1987) in their "composite" description of the African Surface. However, the development of local planar surfaces because of such environmental factors or as a result of marine planation, etchplanation or lateral stream erosion provides alternative explanations to the dissection of regionally extensive peneplanes (Phillips, 2002). As stated above the development of a large scale planation surface is dependent on long-periods of tectonic stability.

Numerical modelling has suggested that tectonic stability maintained over 50 Myr coupled with a sea level rise of at least 250m over this time would be required to form a peneplane (Pitman and Golovchenko, 1991). Discussions in



previous chapters highlight the important role structural reactivation and dynamic uplift may have had over South Africa's post-rift evolution. This combined with on-going isostatic fluctuations to onshore denudation and offshore accumulation, eustatic sea-level variations and climate shifts throughout the Cretaceous and Cenozoic suggests that it is unlikely that southern Africa has been afforded the stability over time to develop a single, extensive, flat and low-lying surface.

Recent numerical approaches have attempted to unravel the uplift history of Africa by inverting the physiography of drainage networks over time (e.g. Roberts and White, 2010; Paul et al., 2014). In this way, Africa's present day topography is suggested to have evolved during the Cenozoic, predominantly after c. 30 Ma. The physical model used in these studies is subject to important assumptions and uncertainties which are largely only qualitatively constrained. The underlying assumption is that when a tectonically stable and lithologically homogenous setting is uplifted dendritic drainage networks form and erode the surface to sea level (Roberts and White, 2010). In order to use present day drainage networks to infer the uplift, the extent to which erosion has modified the original form of the river profile needs to be constrained. However, this component is notoriously difficult to define due to variations in lithology, channel width, climate, discharge and upstream drainage area over time and space (Hovius, 1998; Whipple and Tucker, 1999; Peizhen et al., 2001; Sklar and Dietrich, 2001; Brocard and van der Beek, 2006). These uncertainties are addressed in these studies through forward modelling of synthetic river profiles or through mathematical inference to conclude that uplift is a primary control on the form of river profiles (Roberts and White, 2010; Paul et al., 2014). A more problematic assumption is that which is made on the initial conditions of the model: that Africa was a low-lying surface with no notable topography (i.e. peneplain) in the Early Cenozoic. This assumption is largely based on the work, discussed above, by Burke and Gunnell (2008) and Partridge and Maud (1987) and is therefore subject to the same degree of uncertainty.

## 7.6 Dynamic topography

Thermochronology and cosmogenic nuclide dating are used to investigate the evolution of landscapes by inferring the timing and magnitude of erosion from cooling histories cosmogenic nuclide concentrations; while many geomorphological studies use elevated landforms such as erosion surfaces, river terraces and raised beaches to infer timing and magnitudes of uplift. While enhanced erosion is often a direct consequence of a period of uplift (moderated by lithology and climate) identifying the mechanism which has driven uplift is more difficult, and relies on our understanding of the regional tectonic history of the study area. It is also important to note here that the link between uplift and erosion is a complex one, and it is not inevitable that a landscape experiences an immediate erosional response to an increase in elevation. The high Tibetan plateau, for example, is at a mean elevation of 5km and yet large parts of it are characterised by internal drainage and sediment accumulation, not erosion (e.g. Summerfield and Brown, 1998). The key to establishing a direct erosional response to regional uplift seems to require that major catchments are established, or evolve quickly, and scale spatially to the region of uplifted terrain (e.g. Braun et al., 2013b). In such cases the large size of the catchments compensates for the moderate slope increase in the channel and ensures that a significant erosional response is temporally and spatially correlated with the phase of uplift.

In South Africa, uplift of continental margins is believed to have occurred during lithospheric thinning and mantle upwelling during the breakup of Gondwana (Braun and Beaumont, 1989; Gilchrist and Summerfield, 1991; Van der Beek et al., 2002; Séranne and Anka, 2005). Uplift is suggested to have been maintained following continental break-up by the isostatic response to the erosion of rift-related topography (Tucker and Slingerland, 1994; Rouby et al., 2013) with additional support provided by underplating beneath the margin (Hirsch et al., 2010). However, discussion of viable mechanisms for regional uplift during South Africa's post-rift phase, particularly during the Cenozoic, have been more speculative or neglected entirely (King, 1955; Partridge and Maud, 1987; Moore et al., 2009).

Since the observation of a major zone a low seismic velocity beneath South Africa and the interpretation of this as an upwelling of hot buoyant material from the lower mantle, vertical stresses imposed at the base of the lithosphere has provided a convenient mechanism for generating long wavelength uplift (i.e. dynamic uplift) (Nyblade and Robinson, 1994; Lithgow-Bertelloni and Silver, 1998; Gurnis et al., 2000; Moucha et al., 2008; Forte et al., 2010a). In the past, mantle driven dynamic uplift has been used as a mechanism for explaining uplift in the Mid-Cretaceous (c. 115 - 90 Ma, Kounov et al., 2009); Late Cretaceous (c. 90 - 70 Ma, Braun et al., 2014a); Oligocene (c. 30 Ma, Burke, 1996; Burke and Gunnell, 2008) or Pliocene (c. 5 - 3 Ma, Partridge, 1998). Geophysicists debate the origin of the upwelling both in terms of its timing and source in the mantle and its longevity over geological timescales. The vertical stresses associated with dynamic uplift have been ascribed to convective flow in the lower mantle (Lithgow-Bertelloni and Silver, 1998; Ritsema et al., 1999) and driven by positive buoyancy in the mid-lower mantle beneath southern Africa (Gurnis et al., 2000).

Supporters of a youthful South African topography have suggested that the topography has been carved following Africa becoming stationary over a long-lived lower mantle superplume during the early Cenozoic (c. 60 - 30 Ma) (Burke and Wilson, 1972; Scotese et al., 1988; Garnero et al., 2007). Local upwellings in the upper mantle are proposed to have created a “basin and swell” topography over Africa since the late Eocene (Burke and Gunnell, 2008; Roberts and White, 2010; Paul et al., 2014).

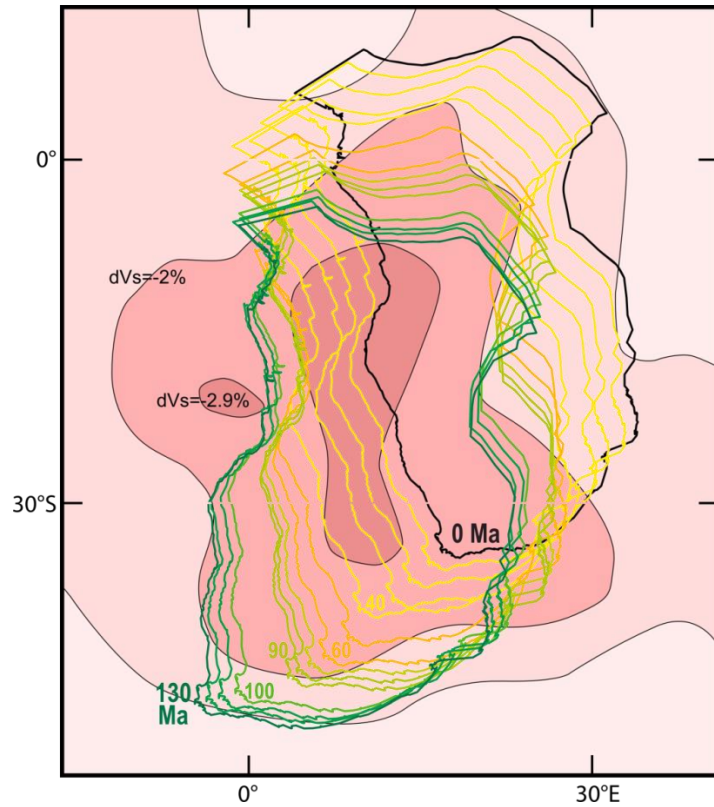
LTT and CN dating can provide constraints on erosion while surface uplift can only be inferred as a mechanism for triggering these erosion events. This therefore prompts the question: Does dynamic uplift produce an erosional response on the surface? For LTT to be effective this erosion would have to be of the order of several kilometres in magnitude. On one hand, because of the long wavelength, low amplitude and slow rate of dynamic uplift it should not trigger a large erosional response (Braun, 2010; Braun et al., 2013b). On the other hand, recent modelling by Braun et al., (2013b) has shown that dynamic topography may be efficiently eroded if uplift significantly increases the drainage areas, as this parameter has a control over fluvial erosion rate. These insights are only

obtained, however, when an initially flat topography is assumed therefore neglecting the effect of a pre-existing topographic relief and drainage network (Braun et al., 2013b). Estimates of erosion of dynamic topography are also severely influenced by the erosional parameter in the stream power law (see equation below) which varies depending on climate and lithology and are therefore poorly constrained over space and time:

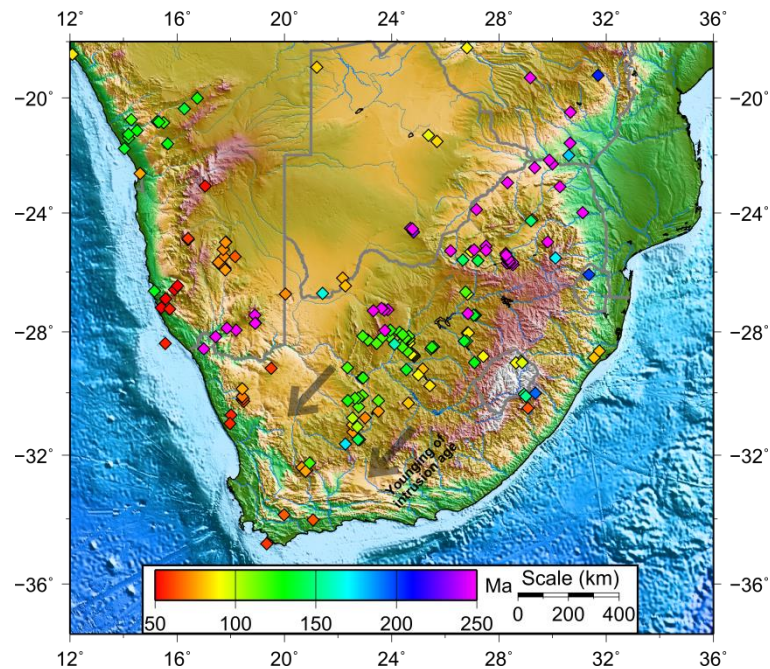
$$e = KA^mS^n$$

Where  $e$  = erosion rate (m/yr),  $A$  = upstream drainage area ( $m^2$ ),  $S$  = gradient of the channel slope,  $K$  = coefficient of erosion ( $m^{0.2}/yr$ ),  $m$  and  $n$  are positive parameters which depend on climate and lithology.

The surface process model outlined by Braun et al., (2013b) was used by Braun et al. (2014a) to propose a model for uplift of Southern Africa in the Late Cretaceous which involved westward tilting of the continent as it passed over a fixed mantle upwelling (Fig. 7-11) (e.g. Torsvik et al., 2010; Torsvik and Cocks, 2013). This model proposes a mechanism for the increased sediment influx in the Orange Basin during the Late Cretaceous and limited accumulation during the Cenozoic, while the pattern of kimberlite intrusion ages (Fig. 7-12) (Jelsma et al., 2004; Moore et al., 2008) is indicative of eastward plate movement over the mantle anomaly. The climate during this Late Cretaceous period of erosion is proposed to be predominantly humid and therefore promoting a more erosive environment (Smith, 1986; Bamford and Stevenson, 2002; Braun et al., 2014). While the regional prevalence of such a climate would be consistent with the episode of Late Cretaceous denudation advocated in this thesis, it should be acknowledged that the timing and regional extent of the continental climate is largely uncertain. As climate has an important influence on the erosion parameters in the stream power law, this uncertainty must be appreciated when considering the erosional response to dynamic uplift. Moreover, the model assumes an initial flat topography at sea-level, neglecting the influence of the pre-existing relief generated and eroded during rifting. While the magnitude and timing of erosion inferred by the model is consistent with previously published AFT and AHe studies it does not explain the detail of the spatial and temporal



**Figure 7-11: Passage of the African plate over the low seismic velocity region in the mantle, suggested to be evidence of a hot mantle upwelling, from 130 Ma to present day (after Braun et al., 2014a).**



**Figure 7-12: Map illustrating the age distribution of intrusive igneous bodies from the pre-Cambrian. Database of intrusion ages was taken from Jelsma et al. (2004). Age distribution shows a decrease towards the SW Cape and a general trend of older intrusion ages being found within the boundaries of the Kaapvaal craton relative to off-craton intrusions.**

complexity of the thermal histories obtained from joint AFT and AHe inversion presented in this thesis.

The major issue with this work and many previous models is that the lithosphere is often treated as a single coherent slab and therefore does not take account of the influence of heterogeneous rock erodability (e.g. Braun et al., 2014b), brittle lithospheric deformation (e.g. Burov, 2011) or complex crustal rheology (e.g. Armitage et al., 2013). At present, dynamic uplift appears to be an important element in the history of southern Africa's topographic evolution, but the exact role it has played in the formation of South Africa's topography is still enigmatic because its influence will be masked by the effects of in-plane lithospheric deformation and the isostatic response to complex surface process. To help understand the interplay of these processes high quality low temperature thermochronology datasets should be incorporated as explicit constraints to these numerical landscape models to help improve the robustness of predictions about patterns of uplift derived from them.

## 7.7 Conclusion

The inversion of two borehole profiles reinforces that a major cooling episode, driven by denudation, occurred during the Early Cretaceous. The regional AFT and AHe dataset shows that Late Jurassic (c. 180 Ma) to Early Cenozoic (c. 60 Ma) dominated the Namibian and SE African continental margins while similarly young ages in SW Africa extend 100s km inland to the SW margin of the Kaapvaal craton (see Fig. 7-7). Old pre-rift AFT and AHe ages are confined to the interior craton. This trend in LTT data is interpreted to have been produced by a combination of the erosion of topography generated during rifting and continental break-up followed by a phase or phases of tectonic reactivation during the middle and late Cretaceous caused by in-plane horizontal stresses possibly combined with an additional vertical dynamic forcing arising from flow within the deep mantle. Kilometre scale denudation at this time is in broad agreement with the timing of enhanced sediment accumulation in offshore basins.

The period of enhanced denudation which is proposed to have occurred at c. 110 - 90 Ma precedes a peak in offshore accumulation beginning at c. 80 Ma. This is a rather long lag-time for the transportation of eroded sediments however the creation of structural relief over c. 110 - 90 Ma may have disrupted the drainage network and resulted in material being deposited in interior basins or distal parts of the offshore domain. Cosmogenic nuclide data suggest that in the Cenozoic regional erosion was extremely low but higher rates of channel incision are recorded within some individual river valleys (e.g. Kuiseb River, Namibia; Sundays River, South Africa). The preservation of crater-lake deposits hosting a wide range of terrestrial fossils on the continental plateau and the preservation of terrestrial flora and fauna fossils at the continental margin are in good agreement with landscape characterised by low rates of regional erosion (c. < 5 - 10 m/Ma) throughout the Cenozoic.

# CHAPTER 8

## REASSESSING THE NAMAQUALAND SECTOR OF THE SOUTH AFRICAN CONTINENTAL MARGIN

### 8.1 The pre-rift setting of SW Africa: pre-Cretaceous (>150 Ma)

Before the onset of continental rifting, South Africa and South America formed the western remnant of the supercontinent Gondwana. During the Permo-Triassic, compression driving the development of the Cape Fold Belt promoted the deposition of the Karoo Supergroup unit. The deposition of these sediments marks the last time when the continental interior was unambiguously below sea-level (Gilchrist et al., 1994). Beyond this, the Early Mesozoic pre-rift topography is largely uncertain. Doucouré and de Wit, (2003) suggest that South Africa was low-lying (c. 100 - 400m) with low relief but that the first order bimodal structure of the continent was in place. The emplacement of Karoo flood basalts and associated dykes may have helped to produce a relatively flat topography. It has been suggested that thermal upwelling and underplating occurred during rifting of Eastern and Western Gondwana at this time causing magmatism and uplift (White and McKenzie, 1989).

However, remnant relief created during Carboniferous and Permian orogenies and isostatic readjustments to denudation of these features and the removal of Dwyka ice-sheets may have created perturbations in the flat topography. The Archean Kaapvaal craton has likely remained a positive topographic feature at this time due to the presence of underlying thick lithosphere and low density mantle root (Boyd, 1989; le Stunff and Ricard, 1995; Niu et al, 2004; Baptiste and Tommasi, 2013). Thermochronology data from the KC1/70 and QU1/65 boreholes predict that cooling initiates between c. 180 - 160 Ma and continues throughout the Cretaceous. It is difficult to define the initial trigger for the onset of cooling. Possibilities include thermal relaxation following Karoo



magmatism at c. 180, a denudational response to thermally driven uplift during the opening of the South Indian Ocean or tectonic uplift in related to the earliest phase of south Atlantic rifting.

## **8.2 Continental rifting and break-up in the Southern Atlantic: Late Jurassic – Hauterivian (150 – 130 Ma)**

Continental break-up and the separation of East and West Gondwana is suggested to have occurred by c. 160 - 150 Ma due to the presence of the M33 (159Ma), M25 (154.4 Ma) and M22 (150.2 Ma) magnetic anomalies (Chron) in the Somali and Mozambique basins (Coffin and Rabinowitz, 1987; Eagles and König, 2008; Leinweber and Jokat, 2012). Initial continental rifting predating break-up was likely underway at the time of Karoo magmatism (c. 180 Ma) (White and McKenzie, 1989; Maslanyj et al., 1992; Duncan et al., 1997; Elliot and Fleming, 2000). The detail of the rifting history of the South Atlantic margin is still unresolved but is proposed to have initiated in the south during the Late Jurassic - Early Cretaceous (c. 160 - 140 Ma) with break-up occurring at c. 135 Ma (chron M11) (Jackson et al., 2000; Eagles, 2007; Heine et al., 2013). The style of South Atlantic rifting was likely akin to simple shear rifting with the Southern Africa acting as the 'upper plate' (e.g. Unternehr et al., 2010; Blaich et al., 2013; Péron-Pinvidic et al., 2013).

The rifting history was likely prolonged and poly-phase leading to crustal thinning occurring over several hundreds of kilometres (e.g. Huisman and Beaumont, 2011). This poly-phase scenario involved initial extensive thinning during non-volcanic type rifting followed by volcanic type rifting involving interactions between the lithosphere and the Tristan de Cunha plume (Blaich et al., 2013; Franke, 2013; Koopmann et al., 2014). This latter phase resulted in the emplacement of the Parana-Etendeka lavas (Hawkesworth et al., 2000; Marsh et al., 2001). Moreover, the emplacement of low density crust beneath the margin (e.g. Hirsch et al., 2010) due to underplating or presence of metasomatised lithosphere (Franke, 2013) may have been coeval with rifting.

Rifting created significant relief across SW Africa due to tectonic and thermally driven uplift triggering an erosional response of the surface as rivers adjust to base level lowering. This erosion led to the removal of several kilometres of rock (most likely from an unknown thickness of Karoo Supergroup and Karoo Flood Basalts) (see Chapter 7 - Figure 7-7). This erosion is reflected in the thermochronology and offshore record with samples recording the onset of major cooling at c. 150 - 130 Ma across the entire study area and the presence of thick wedges of syn-rift deposits in fault-bounded graben, respectively (Jackson et al., 2000; Paton et al., 2008).

### **8.3 The post rift phase (i): Barremian – Albian (130 – 110 Ma)**

In the offshore sedimentary record, this period has been referred to as a transitional phase between the rift and drift phases where the sedimentary record changes from a terrestrial to marine depositional environment (de Vera et al., 2010; Kuhlmann et al., 2010) while the amount of sediment accumulating in the offshore basins is progressively decreasing (Guillocheau et al., 2012). Also occurring during this period is continental break-up at the Central and Equatorial Atlantic rift (Heine et al., 2013) and a global climatic shift from ice-house to hot house conditions (Scotese et al., 1999). Thermal history models suggest that denudation of SW Africa continued through this period but with the rates being highly variable across the margin in space and time due to the extent of relief reduction which occurred during the syn-rift phase, lithology of the substrate, onset of a more erosive climate and the surface response to vertical motions such as thermal subsidence and isostatic uplift.

### **8.4 The post rift phase (ii): Albian – Santonian (c. 110 – 80 Ma)**

At the beginning of this time interval, referred to as the Mid-Cretaceous in previous chapters, break-up in the southern Atlantic had completed and Africa resided in its “drift” phase (Kuhlmann et al., 2010; Heine et al., 2013). This is traditionally seen as a time when major fault activity ceased and the margin becomes “passive” (White and McKenzie, 1989; Gladchenko et al., 1997; Jackson

et al., 2000). However, the LTT presented here has been used to infer rapid, km-scale denudation in discrete locations, controlled by reactivation of pre-existing basement structures. This is consistent with recent structural evidence obtained from the continental margin (see Chapter 5) (Brandt et al., 2005; Viola et al., 2012; Salomon et al., 2014) and offshore basins (See Chapter 7) (Paton et al., 2008; de Vera et al., 2010). Denudation at this time is manifested at both the continental margin and in the interior plateau at the craton boundary.

Increases in relative plate velocity (Torsvik et al., 2009; Heine et al., 2013) and the relative westward passage of the Falkland-Agulhas Fracture Zone south of southern Africa (Uenzelmann-Neben et al., 1999; Parsiegla et al., 2008) imposed an extensional stress regime across SW Africa similar to the present day (Bird et al., 2006; Andreoli et al., 2009; Viola et al., 2012; Gaina et al., 2013). Despite being subjected to the same lateral stress-field, the manner of lithospheric deformation at the continental margin and craton margin may have been quite different due to the contribution of vertical motions to in-plane stresses, the orientation and geometry of pre-existing structures and differences in mantle-lithosphere rheology (See Chapter 5 and 6).

Over this time offshore sedimentation rates and accumulation volumes progressively increase to a maximum at c. 80 Ma which may reflect an initial period of relief generation perturbing drainage networks followed by rapid removal of the relief by erosion. The humid climate prevailing over much of SW Africa (Fawcett and Barron, 1998; Scotese et al., 1999; Bamford and Stevenson, 2002) at this time would have encouraged more intense weathering and faster rates of erosion. The role of mantle convection at this time is still unclear but lateral convection beneath the margin (e.g. Huisman and Beaumont, 2011; Beaumont and Ings, 2012) and/or the onset of dynamic uplift driven by plate movement over a region of upwelling mantle (e.g. Gurnis et al., 2000; Moucha et al., 2008; Forte et al., 2010a; Braun et al., 2014a) could enhance the in-plane stress field. Dynamic uplift, in particular, may have played a major control on the regional nature of denudation at this time (e.g. Flowers and Schoene, 2010; Stanley et al., 2013) and the timing of sediment transport to the Orange basin (Braun et al., 2014a). Significant uncertainty still remains with the predictions of

both the spatial and temporal pattern of dynamic uplift across Africa. The empirical constraints on surface evolution such as those derived in this thesis will hopefully enable progress to be made in resolving some of the outstanding problems facing the theoretical aspects of understanding mantle convection models and improve predictions of dynamic uplift.

### **8.5 The post rift phase (iii): Campanian to Maastrichtian (80 – 65 Ma)**

Determining whether or not there has been a discrete episode of intracontinental deformation during the Late Cretaceous which is separate from that which occurred in the Mid-Cretaceous (e.g. Viola et al., 2012) is difficult with the current spatial and temporal resolution of LTT data. Estimates of denudation suggest that hundreds of metres of erosion continued to occur in the Late Cretaceous and Early Cenozoic with only a few samples suggesting km-scale denudation at this time. A stress regime of regional compression is suggested to have been in place at this time causing deformation in northern and western Africa (Guiraud and Bosworth, 1997; Raab et al., 2002, 2005). A combination of far-field stresses linked to plate kinematic changes in the Atlantic and Indian oceans and the ongoing passage of the African plate over a large mantle upwelling may have prolonged deformation at the southwestern craton boundary and in other discrete locations. By this time South Africa had attained much of its present elevation and major topographic features (i.e. low-lying coastal plain, broad escarpment zone, low-relief plateau) as supported by the preservation of crater-lake sediments, terrestrial fossils and in-situ cosmogenic nuclide studies (see Chapter 7). The major drainage network of southwestern Africa, dominated by the Orange River and its tributaries, was established by this time (Partridge and Maud, 1987; Dollar, 1998; de Wit, 1999).

### **8.6 The post rift phase (iv): Paleogene (65 – 25 Ma)**

The Early Palaeogene, in comparison to the Cretaceous, appears to be a relatively stable period in South Africa's history. African plate velocities rapidly decreased (Torsvik et al., 2009, Nürnberg and Müller, 1991), the Indian Ocean mid-ocean ridge became extinct (Ganerød et al., 2011) and strike-slip motion

along the Agulhas-Falkland Plateau ceased (Gaina et al., 2013). A major decrease in sediment accumulation volumes and rates in tandem with decreasing magnitudes of denudation suggests that kilometre scale erosion was completed by the end of the Cretaceous. The lower erosion rates during the Early Cenozoic likely reflect the change to a less tectonically active period as well as additional moderation by the exposure of more resistant basement rock (e.g. Cockburn et al., 2000) and the onset of a more arid climate (e.g. de Wit, 1999) following the Cretaceous. A warm, very humid climate likely prevailed during the Palaeocene-Eocene thermal maximum (c. 55 Ma) (Zachos et al., 2001) until becoming semi-arid in the middle Eocene (Gutzmer and Beukes, 2000; Bamford, 2000). During this time thick weathering profiles may have developed across Southern Africa. By the late Palaeogene (Oligocene) the African plate became fixed in its present position and the volcanic rifting in the East African Rift Zone initiated (Berhe et al., 1987; Baker et al., 1996; Hofmann et al., 1997; Chorowicz, 2005). Extension propagated southward and may have contributed significantly to the regional stress field and stability of the southern continent however its influence on lithospheric deformation in SW Africa was probably minor (Ebinger et al., 2000; Bird et al., 2006).

## **8.7 The post rift phase (v): Neogene (25 – 0 Ma)**

The late Cenozoic has frequently been quoted by geomorphologists as a period when a phase or phases of major uplift and erosion have occurred. This uplift is proposed to have formed major features of the South African landscape from deep river valleys such as the Orange River Valley (Bluck et al., 2007) and the Koa River Valley (Dollar, 1998, de Wit, 1999) to the entire great escarpment (Partridge and Maud, 1987; Burke and Gunnell, 2008). Thermochronology data, including that presented in this thesis, suggests that, regionally, there has been less than 1km of erosion during the Late Cenozoic. While it can be argued that AFT and even AHe analysis do not have the temporal resolution to resolve late Cenozoic erosion, insights from cosmogenic nuclide analysis and the preservation of river terraces and in-situ terrestrial fossils supports the inference made from LTT.

To be clear, the available evidence does not support major *erosion* during the Cenozoic and so excludes the possibility that the large scale topography (i.e. escarpment zone separating a coastal plain from an elevated interior) was created during this time, but this does not exclude the possibility of Cenozoic changes in elevation. The data in this thesis and the literature indicates that any Cenozoic uplift of southern Africa was not accompanied by major, regional erosion and any geomorphic response must be restricted to moderate, local channel incision. Dated river terrace sequences on both the lower Orange river (west coast) and from the Sundays river (south east coast) provide the likely scale of Cenozoic rock uplift during the Neogene (c. 4.4 - 16 m/Ma) (Erlanger et al., 2012; Bierman et al., 2014; Dauteuil et al., 2014).

Prior to the onset of the present day semi-arid climate (Pickford and Senut, 1997), a humid climate prevailed during the Early - Middle Miocene. This erosive climate may have intensified river incision; enhancing relief on the scale of tens to hundreds of metres (Mvondo et al., 2011; Dauteuil et al., 2014). However, late Cenozoic erosion cannot be completely ascribed to major climate changes alone because sea level fluctuations (Roberts et al., 2011), neotectonic fault activity (de Beer, 2012) and small-scale mantle convection (e.g. Moucha et al., 2008) could have contributed to uplift and erosion of the surface. Improvements in quantitative dating techniques combined with a better resolution of the Cenozoic offshore sedimentary record will help to resolve how the South African landscape has evolved during this time.

## **8.8 Wider implications of this work**

This study of the South African Atlantic margin uses two low temperature thermochronometry techniques to derive crustal cooling histories across the continental margin. By interpreting these thermal histories alongside independent geological information from both the on and offshore domain new insights into the syn and post-rift topographic development of the continental margin and interior are obtained. The laterally extensive phase of denudation during the syn-rift phase and occurrence of at least one phase of tectonically controlled, kilometre scale, denudation during the post-rift phase can be

compared and contrasted to other high elevation continental margins traditionally viewed as “passive” margins. These include the continental margins of western Norway, eastern Greenland, SW India and southwestern Australia. For example recent work along the North Atlantic margins have also invoked a post-rift origin for topography. Post-rift surface uplift is suggested to have been driven by mantle upwellings or in-plane stresses induced by lithospheric resistance to plate motions or convection in the upper mantle; particularly at settings such as craton margins where large crustal thicknesses exist (Japsen et al., 2014). While similar mechanisms are cited in this thesis, the model proposed here for the development of the South African margin differs in two main ways to that proposed by recent studies in Scandanavia: (i) geological and thermochronological data do not require a landscape evolution model involving multiple phases of regional planation, burial and re-exhumation (e.g. Japsen et al., 2009; Green et al., 2013; Lidmar-Bergström et al., 2013) and (ii) involves more localised vertical movements on discrete fault blocks due to a combination of the pre-existing tectonic fabric of the margin, isostatic adjustments to the removal of rift-related topography and regional tectonic stresses (e.g. Redfield et al., 2004, 2005 a, b). A more direct comparison is ready to be made with the continental margin further north of this study area (i.e. Namibia and Angola) and on the composite margin along eastern South America. Recent LTT from the Brazilian passive margin has also invoked reactivation of basement structures in the post-rift phase of a margins evolution (e.g. Cogné et al., 2012; Karl et al., 2013). It is likely that most “passive” continental margins are inherently prone to post-rift deformation however the timing, style and magnitude of deformation will be determined by the margins pre-existing tectonic fabric and regional tectonic setting. The data will also be of interest to future studies of interior cratonic areas far from active plate boundaries which have long been considered stable and the effect mantle upwelling may have on the deformation of these platforms and their margins.

More locally to the study area, the revised model for the long-term geomorphic development of SW Africa proposed in this thesis suggests that considerable topography and relief has existed to various extents throughout the Cretaceous. Reconstructing this palaeotopography based on quantitative data will have major

implications for reconstructing palaeoclimates, palaeodrainage networks and well as providing constraints for surface, tectonic and mantle convection models.

From an industrial point of view, the timing, magnitude and regional distribution of denudation the continental margin and interior plateau will help to refine our understanding of offshore sedimentary record in the Orange Basin and the nature of hydrocarbon generation and trapping (e.g. Paton et al. 2008, de Vera et al., 2010, Hartwig et al., 2010, Kuhlmann et al., 2010). Additionally, the interpretation that the Mid - Late Cretaceous phase of denudation was controlled by structural reactivation has implications for studies which are attempting to understand the long-term stability of the South African upper crust for the purposes of radioactive waste storage (e.g. Andersen et al., 1986, Andreoli et al., 1990); seismic monitoring (e.g. Scheepers and Andreoli, 2004; Malephane et al., 2013) and shale-gas exploration (Geel et al., 2013; Scheiber-Enslin et al., 2013). Finally, recent interest in dry-rock geothermal energy in the apparent elevated heat-flow region of the Namaqualand basement (Dhansay et al., 2014; Tshibalo et al., 2015) would benefit from the temperature-time (T-t) insights obtained on the region by the high density thermochronology dataset presented here.

This work will also find relevance to future low temperature thermochronology studies, particularly those wishing to apply LTT techniques to geologically old (c. >100 Myr) geological settings or who wish to combine AHe and AFT datasets. This new data presented here highlights the importance of directly measuring Sm content for AHe dating; the uncertainty surrounding the influence of radiation damage on fission track annealing and helium diffusion and thus closure temperature and the importance of modelling LTT data in a manner which best treats the large uncertainty on individual measurements. Future studies should acknowledge the large degree of single grain AHe age dispersion which is evident in many samples but also lack simple correlations with eU or grain size. The need for larger datasets of single grain AHe ages for individual samples should be apparent and adopted.



## 8.9 Future Work

In order to continually improve our knowledge of the SW African rifted continental margin and rifted continental margins and continental interiors worldwide, several avenues of further study are available. This future work could include additional low temperature thermochronology work to resolve variations in margin development along strike of the coast and the location of the inland boundary between young (syn-rift or younger) AFT ages and old (Karoo) AFT ages. More effort should be made to quantitatively date the development of the Cenozoic landscape of Southern Africa. Due to the high uranium content of many samples the closure temperature of the AHe system is elevated and therefore, in many cases, there is only a minor improvement on the minimum amount of denudation that can be recorded beyond AFT analysis alone. A significant period in time is either unresolved or poorly constrained before cosmogenic nuclide analysis provides more recent insights on erosion rates. Obtaining additional thermochronometry data from borehole profiles across southern Africa will also provide much needed information on geothermal gradients today and in the past. New quantitative data can then be integrated with numerical modelling studies attempting to link surface processes to models of continental rifting and dynamic uplift. Further field-based studies in NQH and BMP should aim to improve our knowledge of the post-rift structural history of both the continental margin and margin of the Kaapvaal craton while geomorphic studies should interpret landforms in the framework of short-term landscape stability and consider the variability of climate, lithology and tectonics over space and time.

There also remains much scope for improving low temperature thermochronometry techniques. Our understanding in how radiation damage enhances helium retention and possibly fission track annealing is still limited and as such creates uncertainty when interpreting and modelling AFT and AHe data. Improving our understanding of how radiation damage effects helium diffusion will help thermochronologists decipher the cause of highly dispersed single grain AHe ages. Other aspects which promote dispersion in AHe single grain ages such as zonation, variations in chemical composition and the effect of analysing

fragmented apatites also warrant further investigation. As many single grains analysed in this study are 1 termination fragments a future study using the HelFrag modelling approach (Beucher et al., 2013) is a logical next step.

## 8.10 Conclusions

The impetus behind this study was to investigate the long-term landscape evolution of the western continental margin and interior plateau of South Africa. In particular, the study was designed to address whether the present day topography was formed during phases of Cenozoic uplift and erosion or whether the topography is a remnant of Cretaceous topography formed shortly after the break-up of Gondwana.

Insights on the cooling history of the upper crust from AFT and AHe analysis were interpreted alongside onshore structural, geological and geomorphological data and the offshore sedimentary record in the Orange Basin to infer the timing and magnitude of major phases of onshore denudation. The following geological conclusions were drawn:

- (i) A major phase of erosion (causing up to 3km of denudation) prevailed across the developing continental margin and inland to the SW margin of the Kaapvaal craton during the Early Cretaceous rift-phase (c. 150 - 130 Ma).
- (ii) Average erosion rates remained relatively high during the late Early Cretaceous (c. 130 - 110 Ma;  $42 \pm 8$  m/Ma) but may have decreased with time and the removal of rift-related topography.
- (iii) A second phase of kilometre scale erosion was induced by regional uplift of southern Africa during the Mid - Late Cretaceous (c. 110 - 70 Ma). Average erosion rates of c.  $36 \pm 3$  -  $57 \pm 4$  m/Myr over this period caused c. 1800m of regional denudation. However, this regional uplift was coupled with localised reactivation of basement structures at the continental margin and craton boundary and, therefore, large fluctuations in the amount of denudation recorded by samples is observed. The maximum amount of denudation is estimated to be c.

3.9 km, recorded in samples from the Namaqualand Highlands (see Chapter 5, Figure 5-20).

- (iv) Despite integrating AHe analysis with AFT analysis to improve the T-t resolution of the LTT approach, no clear evidence has been obtained for significant Cenozoic erosion of the margin or plateau. Estimates of Cenozoic erosion rates based on thermochronology data from this study, and previous thermochronology studies, are consistent with the extrapolation of erosion rates estimated by cosmogenic nuclide data (c. 1 - 5m/Ma) through the Cenozoic. Moreover, this quantitative data is consistent with offshore sediment volumes and the carbonate and mud dominated sedimentary facies (i.e. limited terrestrial input) in the Orange Basin at this time. This does not preclude surface uplift causing changes in elevation throughout the Cenozoic but signifies that this did not trigger deep erosion.

By adopting a low temperature thermochronometry approach that combined AFT and AHe analysis (including large numbers of single grain analysis), it was possible to draw the following conclusions on AFT and AHe analysis:

- (i) Samples that yield single grain AHe ages older than their corresponding AFT age are common in geological settings where AFT ages are typically “old” (i.e. older than c. >100 Myr) and/or rocks with high concentrations of U and Th.
- (ii) Highly dispersed single grain AHe ages are also common in such settings because of the combined effects of radiation damage, grain size, grain fragmentation and zonation of parent nuclides. However, resolving the dominant cause of dispersion from simple correlations with age are likely to be fruitless due to each effect acting to decouple the expected simple 2D graphical relationships. The severity of dispersion is also linked to the true thermal history of the sample and therefore analytical protocols should aim to maximise the observed dispersion.
- (iii) In order to extract useful information from complex AHe datasets a large number of analyses of single grains (c. 10 to 20) should be

performed. More importantly, however, AFT analysis should also be performed on the *same* sample to provide independent empirical constraints on the thermal history of the sample.

Across the Namaqualand continental margin and Bushmanland Plateau there is limited geological information to help constrain the geological history over the past 100 - 150 Myr. In settings such as these, low temperature thermochronology is a powerful tool which provides unique insights into the timing and evolution of large-scale topography. Being able to resolve long-term landscape evolution is a crucial step in refining tectonic models responsible for driving major changes to the landscape. Over the last 150 Ma, the South African landscape has responded to an assortment of drivers including regional uplift and local tectonic deformation driven by in-plane stresses, associated with the initial break-up of Gondwana and subsequent African plate motions, and vertical stresses imposed at the base of the lithosphere by buoyant mantle flow. In conclusion, the South African continental margin does not adhere to the traditional “passive” classification of a continental margin. Other passive continental margins around the world are beginning to be interpreted in this vein with many researchers working towards the ultimate conclusion that passive continental margins should be considered much more dynamic and interesting geological settings.

# **A1 LOW TEMPERATURE THERMOCHRONOLOGY - METHODOLOGY**

## **A1.1 Sample Preparation**

### **A1.1.1 Mineral Separation**

To extract apatite crystals from host rock samples a five stage process is applied which involves (i) crushing, (ii) washing, (iii) vertical magnetic separation, (iv) heavy liquid separation and (v) horizontal magnetic separation. A percussion pulveriser was used to break c. 2 kg samples of the host rock into hand sized blocks which were then passed through a jaw crusher. This material was then sieved to separate out suitably sized material (90 - 500  $\mu\text{m}$ ) and the process repeated for material  $>500 \mu\text{m}$ . The range of acceptable grain size was chosen to give a large range of possible grain radius and fragment lengths to allow the maximisation of age dispersion if required. Only material that was  $> 500 \mu\text{m}$  but  $< \text{c. } 2 - 3 \text{ mm}$  was passed through the disk mill for final separation. The samples were then washed using a Gemini shaking table which separated out minerals of different densities. Apatite has a reasonably high density of c.  $3.2\text{g.cm}^{-3}$  and so the mineral separates containing the heavier minerals were taken for further processing. Samples were then passed through a Frantz magnetic separator orientated vertically allowing strongly magnetic minerals to be extracted, apatite is non-magnetic. Heavy liquid separation was performed using the inorganic LST solution at a density of  $2.80\text{g.cm}^{-3}$  which allows apatite crystals (along with other heavy minerals) to sink. This material was then carefully decanted and washed thoroughly using de-ionized water and dried under a hot lamp for a short time before horizontal magnetic separation. During horizontal magnetic separation the sample was passed through a magnet inclined to a user defined slope allowing specific minerals which are weakly magnetic to be extracted. This process can be customised by altering the inclination and current of the magnet to allow specific minerals to be extracted. The approach used here was to maintain a side slope of  $20^\circ$  and use three stages of separation using a current of 0.5 A, 0.9 A, and 1.5 A. This produced satisfactory yields of apatite from the mineral separate.

### A1.1.2 AFT Sample Preparation

Following mineral separation procedures, a polished grain mount is created using a small amount of the apatite separate. The amount of mineral separate used was sufficient so that enough apatite is present for multiple single grain analysis but is distributed with enough space between the grains such that they are easily distinguished from one another. The mount was polished to reveal flat internal surfaces of individual grains. The apatite grains were mounted in a small amount of epoxy resin, placed on a 50.8 mm by 25.4 mm slide and the mineral separate distributed evenly in the resin. Once dry, the grain mount was polished using a three step process. The first step used a coarse (26  $\mu\text{m}$ ) grinding paper to produce a flat surface with exposed apatite grains. This first stage produces severe scratching of the grain mount that can be removed in the second stage using a finer grinding paper (15  $\mu\text{m}$ ). The third stage used a soft rotating surface with covered with a 1  $\mu\text{m}$  micro-polish solution of aluminium oxide and was designed to remove small divots and chipped marks on the apatite grains. Following polishing, slides containing the grain mount were cut to a size that allowed the glass to fit in a standard irradiation tubes.

Before fission tracks could be observed under an optical microscope the grain mounts underwent a chemical etching (e.g. Green et al., 1986). The grain mount was submersed in 5.5 Molar  $\text{HNO}_3$  for  $20 \pm 1^\circ\text{C}$  allowing the etchant to reveal spontaneous tracks that intersect the polished grain mount. Strict adherence to etching procedures is important as the recipe used to etch the grain mounts has an effect on the annealing calibrations used during thermal history modelling.

A mica external detector (see Appendix 1.2.1) was placed flat over the grain mount. Grain mount and mica were then wrapped in plastic film which was slightly heated and melted to produce a tight seal where the mica is flush against the grain mount. The sample packages were then loaded into an irradiation tube with standard glasses placed at the top, middle and bottom of the sample stack. Irradiation tubes were sent to the Oregon State University Radiation Centre, USA, where a low energy neutron flux was passed through the samples inducing fission of  $^{235}\text{U}$ . These induced tracks are picked up in the

external detector and can be counted in a similar manner to spontaneous tracks in the grain mount. As with the grain mount, the mica was then etched to reveal the etch pits of the induced tracks. After the irradiation only the mica is etched to reveal induced tracks. The grain mount and external detector are then mounted onto a slide such that the grain mount is a mirror image of the mica detector.

### **A1.1.3 Apatite (U-Th-Sm)/He Sample Preparation**

Following mineral separation, samples are observed under a Zeiss Stemi 2000-C optical microscope and assessed in terms of their shape, size and clarity (i.e. devoid of large inclusions and fractures). Suitable individual crystals were then handpicked from the mineral separate and photographed using image capturing software. As well as selecting crystals based on their quality, the selection process also involved selecting a range of varying grain radius and a mixture of 2T, 1T and 0T grains. Each selected grain was then observed under a petrographic microscope at higher magnification to identify small fluid and mineral inclusions which may be present in the apatite crystal and should be avoided. Following this assessment the crystals with the best quality were chosen for (U-Th-Sm)/He analysis and were measured using ImageJ image processing and analysis software.

Prior to degassing apatite crystals during apatite (U-Th-Sm)/He analysis, the crystal is placed inside a platinum capsule. It is this capsule that is heated by a laser during analysis. Before these platinum capsules can be used they must first be leached to remove any contaminants that may be present. This process involves placing the capsules in 10% HNO<sub>3</sub> acid for 48 hours at 60°C. The capsules are then washed with deionised water and are ready to be packed. Each Pt capsule is a cylinder which is manually closed at one end; a single apatite crystal is then placed inside the half closed capsule. The capsule is then closed at the second end.

## A1.2 Apatite Fission Track Analysis

### A1.2.1 Apatite fission track ages – External Detector Method

As with all radiometric dating techniques, AFT analysis requires an estimate of the relative abundance of the parent to daughter product. However, unlike conventional radiometric dating methods the daughter product is not a particle but the physical damage to the crystal lattice (i.e. the spontaneous fission tracks). This daughter product is readily quantified by counting tracks which intersect the polished surface under an optical microscope within a defined area. To determine the abundance of parent isotopes (i.e.  $^{238}\text{U}$ ), a mica external detector is used. The external detector method (EDM) (Hurford and Green, 1982) permits individual grains to be dated, even in the presence of heterogeneous uranium distribution (Fig. A1-1). The external detector picks up induced fission tracks in the grain produced during the irradiation of the  $^{235}\text{U}$ . As the neutron flux during irradiation is monitored using the standard glasses within the sample stack, the number of induced tracks in the mica can be counted and is representative of the  $^{235}\text{U}$  content of the grain.  $^{238}\text{U}$  can then be estimated as the ratio of  $^{235}\text{U}/^{238}\text{U}$  is constant in nature (1/137.88). Using the relative track densities in the AFT age can be measured using the following equation:

$$t = \frac{1}{\lambda_d} \ln \left( \lambda_d \frac{\rho_s}{\rho_i} \rho_d \zeta g + 1 \right)$$

Where  $t$  = age;  $\rho_s$  = spontaneous track density;  $\rho_i$  = induced track density;  $\rho_d$  = track density in a dosimeter (a standard glass of known uranium concentration);  $g$  = geometry factor which defines the relationship between spontaneous tracks that intersect the polished surface and induced tracks; and  $\zeta$  = a constant of proportionality which includes the fission decay constant. The value of  $\zeta$  is calculated by each fission track analyst and provides a means of standardising the counting process. Details of the  $\zeta$  value calculated for this study are detailed in Appendix 2.



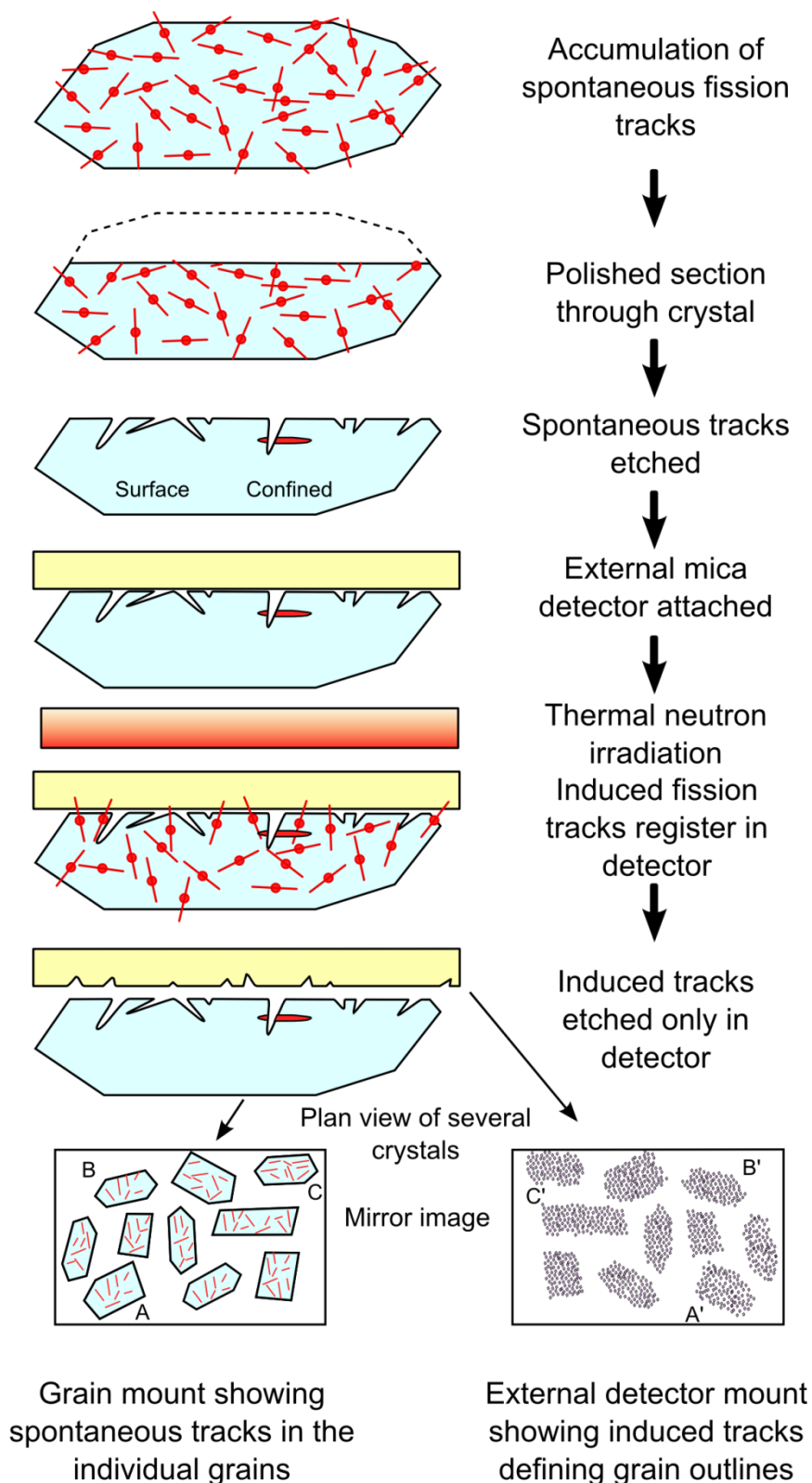


Figure A1-1: External Detector Method after Gallagher et al. (1998). The apatite crystal is polished and etched as described in the text revealing spontaneous tracks which intersect the polished surface. Confined tracks are also revealed if the etchant has infiltrated the crystal via a surface track, cleavage plane or fracture. A uranium free external detector is placed over the crystal and the package irradiated inducing fission of  $^{235}\text{U}$ . Fission tracks induced in the crystal cross into the external detector which is then etched, revealing the tracks.

### **A1.2.2 Apatite fission track length data**

Fission tracks initially form with the same etchable length (c.  $16.3 \pm 1 \mu\text{m}$ ) (Gleadow et al., 1986a). However, once a fission track forms the unetched damage trail gradually begins to repair itself at a rate primarily governed by temperature and to a lesser extent the chemical composition of the apatite. This process is referred to as thermal annealing and provides crucial thermal history information on a sample. The extent of fission track annealing over geological timescales increases rapidly at temperatures greater than c.  $60^\circ\text{C}$  up to  $110 \pm 10^\circ\text{C}$  at which point tracks are completely annealed after they are formed. Track length data is essential information required for accurate interpretation of an AFT age due to apparent fission track ages decreasing with increasing thermal annealing. For example, as mean track lengths decrease, fission tracks are less likely to intersect the polished surface and be visible to count; this effectively lowers  $\rho_s$  and, therefore, the apparent age.

An estimation of the distribution of track lengths within the apatite is made by measuring c. 100 tracks that are entirely below the surface (i.e. confined tracks). Confined tracks are etched by the etchant infiltrating the crystal via conduits such as cracks, cleavage planes and other surface tracks. It is best practice to measure tracks that are horizontal so that the length is a true representation. Horizontal confined tracks have a prominent appearance in reflected light and should be simultaneously in focus along the track and are therefore readily identifiable under a high magnification microscope. The angle of tracks relative to the c-axis of the crystal is also measured to correct for anisotropic etching and annealing.

Over geological time, at temperatures colder than  $110 \pm 10^\circ\text{C}$ , fission tracks are continually produced and retained within the crystal lattice. Therefore, a sample residing at the present day surface will retain fission tracks that have formed at different points in the samples thermal history. Typically the preserved track lengths will be a combination of relatively long tracks that have formed since the sample has cooled and remained below c.  $60^\circ\text{C}$  and a proportion of shorter tracks that have formed early and have been subjected to

thermal annealing. A 'true' apatite fission track (i.e. one which records the time the sample cooled below c.  $110 \pm 10^\circ\text{C}$ ) is only obtained if the sample has cooled rapidly, yielding long track lengths, and has then not been reheated. More complex patterns of cooling will produce more complex track length distributions and therefore measuring track lengths can help to infer denudational cooling histories.

### **A1.2.3 Practical approach to AFT analysis**

Fission Track analysis was performed using a Zeiss HAL 100 microscope at a magnification of 1250x. Referencing information and track length data were recorded using FTStage software developed by Dumitru (1993). First, the apatite grain mount and external detector are fixed to a 50.8 mm x 25.4 mm slide in a manner such that the external detector and grain mount are mirror images of one another. This is aided by holes being punctured into the external detector and grain mount while they are still sandwiched together. The slide is then referenced using a central reference point, pinholes and individual grains.

The grain mount was then scanned systematically for samples that have a polished surface which is parallel to the c-axis. This can be identified by a uniform orientation of etch pits within the crystal. Using a measured grid, an area over the grain was defined and the number of spontaneous tracks was counted. The field of view was then switched to the corresponding print on the external detector where the number of induced etch pits were counted over the same area and location as the crystal. This is done for as many grains as possible to obtain a suitable statistical average age. 20 grains per sample are typically reported in most studies. For each grain 3 to 5  $D_{\text{par}}$  measurements were made to constrain compositional variation within the individual apatite crystals.

A systematic search was also adopted for track length measurements with measurements only taken on grains polished parallel to the c-axis of the crystal. If a confined track is identified it is assessed in terms of its horizontal orientation and structure. The orientation of the c-axis is then measured followed by the length of the confined track. 100 confined tracks, or as many

available, were measured to generate a robust distribution of track lengths. Tracks lengths are measured using a digitizing tablet which is calibrated against a stage micrometer.

## **A1.3 Apatite (U-Th-Sm)/He Analysis\***

### **A1.3.1 Helium Extraction**

The aliquots of single crystals within Pt foil capsules were placed in 2 mm deep holes in a Cu planchet that sits within a stainless steel chamber. This chamber is closed, securely tightened and moved into position under the laser. As the chamber was open to atmospheric contamination the chamber and flexible steel tube connecting it to the extraction line must be pumped clean. This process uses a combination of turbo molecular and ion pumps which cleans the line of atmospheric H and He and generates a vacuum of pressure  $<10^{-9}$  torr. To remove background CH<sub>4</sub> and H<sub>2</sub>O, heating tape was placed around both the chamber and flexi-tube for at least 24 hours. During and following the cleaning procedure of the extraction system, tests are routinely carried out to ensure there is no leak in the system.

Samples were heated using a diode laser system ( $\lambda = 808$  nm) at c. 800°C for 60 seconds. This method heats the crystal indirectly to a temperature which will allow diffusive loss of He but will not melt the crystal itself. The temperature of the capsule was estimated visually using the colour of the Pt tube. Ensuring the apatite is not heated at too high a temperature or for too long is important as this could lead to volatilisation of U and Th from the crystal (Foeken et al., 2006). After the initial heating, the extracted gas is left for 5 minutes to accumulate. The extraction system is then opened to the mass spectrometer with the gases

---

\* A total of 247 single grain AHe analyses were performed during this study. 175 were analysed at SUERC, Glasgow, and 72 analysed at UCL, London. The analytical procedure outlined is specifically that undertaken at SUERC. The analytical procedure followed at UCL was almost identical with minor variations in certain aspects such as laser heating time, dissolution time and spike concentration. However, similar ages of the Durango apatite standard were obtained from both facilities and therefore it is assumed that regardless of where the analysis was performed, reliable AHe ages were obtained.

becoming purified as they passed through two liquid nitrogen cooled charcoal traps. The gas is allowed to accumulate in a HidenHAL3F quadrupole mass spectrometer for 60 seconds where H,  $^3\text{He}$ ,  $^4\text{He}$  and  $\text{CH}_4$  were measured. To ensure complete extraction of He, each sample is reheated using the same approach with reheat values ideally being close to or at blank level. Failure for a sample to reach blank level could be due to high volumes of He within the crystal or an indication that U-Th rich inclusions are present and are not being fully degassed at the applied temperature. He concentrations from samples are calculated against a calibration standard of  $^4\text{He}$  which is obtained by repeat measurements of the  $^4\text{He}$  standard throughout the analysis, typically with a reproducibility of (1 - 2%). Cold blanks were frequently run to ensure that no contamination of the extraction system had taken place. Hot blanks involved heating of an empty Pt capsule to ensure the capsule itself is not a significant source of He.

### **A1.3.2 U, Th and Sm analysis**

Following helium extraction the chamber is opened and aliquots are removed from the Cu planchet and placed into Teflon beakers. The aliquots were then spiked with 0.03 ml of calibrated solution with a known concentration of  $^{235}\text{U}$ ,  $^{230}\text{Th}$  and  $^{149}\text{Sm}$  which allowed the relative abundances of  $^{238}\text{U}$ ,  $^{232}\text{Th}$  and  $^{147}\text{Sm}$  to be determined. To the spike solution, 2 ml of  $\text{HNO}_3$  was added and placed on the hot plate for c. 48 hours to completely dissolve the apatite. Samples were then analysed using inductively coupled plasma mass spectrometry (ICP-MS). A blank vial of  $\text{HNO}_3$  was added to the ICP-MS run as were vials, placed after every third sample, with a known  $^{238}\text{U}$  concentration so that sample measurements can be calibrated.

### **A1.3.3 Apatite (U-Th-Sm)/He age calculation**

Once the concentrations of He, U, Th and Sm have been measured, the (U-Th-Sm)/He age can be calculated using the following equation:

$$[\text{He}] = 8 \left( \frac{137.88}{1+137.88} \right) [\text{U}] (e^{\lambda_{238}t} - 1) + 7 \left( \frac{1}{1+137.88} \right) [\text{U}] (e^{\lambda_{235}t} - 1) + 6[\text{Th}] (e^{\lambda_{232}t} - 1) + 0.1499[\text{Sm}] (e^{\lambda_{147}t} - 1)$$

Where [U], [Th] and [Sm] are the concentrations of uranium, thorium and samarium respectively;  $\lambda$  is the relevant U and Th decay constant ( $\lambda_{238} = 1.55 \times 10^{-10} \text{ yr}^{-1}$ ;  $\lambda_{235} = 9.85 \times 10^{-10} \text{ yr}^{-1}$ ;  $\lambda_{232} = 4.95 \times 10^{-11} \text{ yr}^{-1}$ ,  $\lambda_{147} = 6.54 \times 10^{-12} \text{ yr}^{-1}$  and t is the age. The value of 137.88 is determined from the ratio of  $U^{238}$  to  $U^{235}$ , assumed to be constant in nature.

## A2 APATITE FISSION TRACK AND APATITE (U-Th-Sm)/He STANDARDS

### A2.1 Zeta Calibration

The zeta calibration factor used in the AFT age calculation is determined for an analyst by counting multiple apatite samples of known age (see Hurford and Green, 1983): Durango ( $31.4 \pm 0.5 \text{ Ma}$ ; 9 measurements), Mount Dromedary ( $98.7 \pm 1.1 \text{ Ma}$ ; 12 measurements) and Fish Canyon Tuff ( $27.9 \pm 0.7 \text{ Ma}$ ; 12 measurements). The zeta value will vary depending on the standard glass used during irradiation and is also designed to account for systematic errors in counting tracks by different operators. The following equation is used to obtain the zeta value:

$$\zeta = \frac{(e^{\lambda t} - 1)}{\lambda \left( \frac{\rho_s}{\rho_i} \right) \rho_d}$$

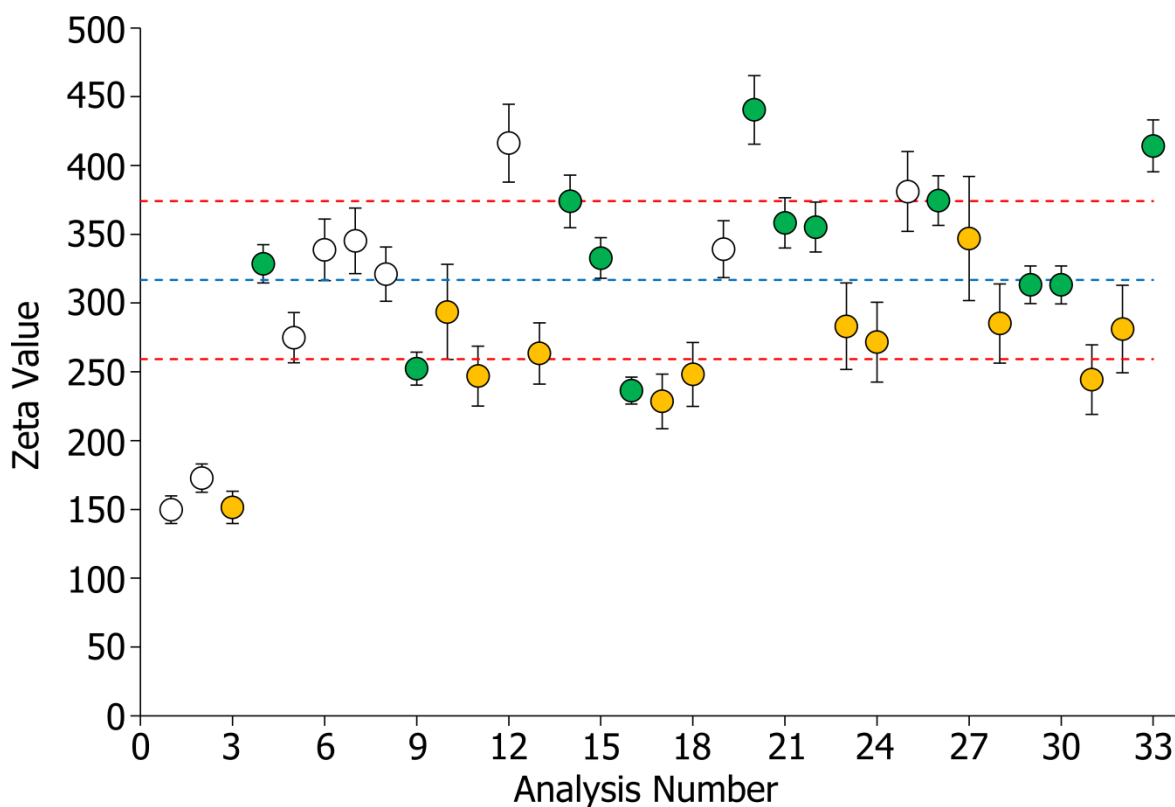
Where  $\lambda$  = the total decay rate of  $^{238}\text{U}$ ,  $1.55 \times 10^{-4} \text{ Ma}^{-1}$ ;  $\rho_d$  = track density in a standard glass dosimeter;  $\rho_s$  = spontaneous track density in standard sample,  $\rho_i$  = induced track density in standard sample and t = the age of the standard sample (i.e. Durango, Fish Canyon or Mount Dromedary).

Full details of individual zeta measurements are presented in Table A2-1 with their variation of over time shown in Figure A2-1. After discounting the first three zeta values based on the lack of counting experience of the analyst at the time, the mean zeta value obtained was  $316.7 \pm 10.5$ . This value will likely change, albeit very slightly, as additional standards will be counted with future sample analysis. Continually adding to and refining the zeta calibration factor is

Analysis	Date	Standard	N <sub>s</sub>	N <sub>i</sub>	N <sub>s</sub> /N <sub>i</sub>	N <sub>d</sub>	ρ <sub>d</sub> (10 <sup>5</sup> cm <sup>2</sup> )	ζ	St. Dev.
1	22/5/12	Durango A	288	1412	0.204	14137	20.6	149.8	10.1
2	7/6/12	Durango B	365	2054	0.178	14137	20.5	172.8	10.3
3	18/6/12	FCT E	212	1119	0.189	13142	19.5	151.4	11.7
4	24/6/12	Mt. Drom. C	789	2449	0.322	12993	18.8	328.4	13.9
5	8/1/13	Durango A	272	2446	0.111	14137	20.6	274.8	18.3
6	11/1/13	Durango 1	282	2493	0.113	10272	14.6	338.6	22.4
7	21/1/13	Durango 1	250	2399	0.104	11381	17.5	345.2	23.8
8	22/1/13	Durango 2	321	2869	0.112	11381	16.5	321.0	19.8
9	29/1/13	Mt. Drom. 2	709	1448	0.490	11381	16.1	252.3	11.9
10	30/1/13	FCT 4	96	932	0.103	16703	18.5	293.5	34.6
11	22/2/13	FCT D	156	1102	0.142	13142	16.0	246.9	21.7
12	25/2/13	Durango 2	257	2713	0.095	10272	15.7	416.3	28.3
13	26/2/13	FCT B	168	1250	0.134	12993	15.8	263.3	22.3
14	26/2/13	Mt. Drom. 1	544	1843	0.295	11381	17.4	373.9	19.2
15	27/2/13	Mt. Drom. B	695	2615	0.266	9308	22.5	332.7	14.8
16	27/2/13	Mt. Drom. A	873	2354	0.371	9308	22.7	236.3	9.8
17	27/2/13	FCT C	160	1301	0.123	9308	19.9	228.5	19.7
18	27/2/13	FCT F	132	1312	0.101	9308	22.4	248.1	23.2
19	27/2/13	Durango B	324	3579	0.091	14137	20.5	339.2	20.7
20	27/2/13	Mt. Drom. 2A	423	1461	0.290	10272	15.6	440.4	24.9
21	27/2/13	Mt. Drom. B	506	2051	0.247	9308	22.5	358.4	18.3
22	28/2/13	Mt. Drom. A	562	1956	0.287	9308	22.7	355.2	18.1
23	1/3/13	FCT C	92	927	0.099	9308	19.9	283.1	31.5
24	4/3/13	FCT F	99	1053	0.094	9308	22.4	271.6	29.1
25	5/3/13	Durango 2	204	1939	0.105	10272	15.7	381.1	29.0
26	6/3/13	Mt. Drom. 2A	616	1809	0.341	10272	15.6	374.5	18.0
27	7/3/13	FCT D	67	665	0.101	13142	16.0	346.9	45.0
28	15/3/13	FCT 1	113	1037	0.109	16703	18.0	285.1	28.8
29	16/4/13	Mt. Drom. C	740	2191	0.338	12993	18.8	313.3	13.7
30	2/7/13	MtDrom2	742	2126	0.349	16527	18.2	313.2	13.7
31	3/7/13	FCT1	110	846	0.130	16527	17.6	244.4	25.2
32	3/7/13	FCT2	92	666	0.138	16527	14.4	281.1	31.8
33	5/7/13	MtDrom1	670	2065	0.324	16527	14.8	414.3	18.9
<b>Mean ζ 316.7 St. Dev. 57.4</b>								<b>N 30</b>	
<b>s.e. 10.5</b>									

**Table A2-1: Results of zeta calibration for apatite fission track analysis (Hurford and Green, 1983). Shaded analyses were excluded from the calculation of the mean zeta value as they were anomalously low. The reason for this error is likely due to the inexperience of the user during the first few analyses.**

important as it can reduce the error of the obtained zeta value and hence the error on the age. Samples JN2, JN3, FS1605, GGO2 and PRU 106 were counted



**Figure A2-1: Plot of zeta calibration values over time. Error bars on individual zeta value measurements are 1 st. dev. derived from the individual single grain ages of the sample that was counted. Red dashed lines indicate  $\pm 1$  st. dev. of the mean zeta value (blue dashed line). Apatite standards analysed: Durango (white circles); Fish Canyon Tuff (yellow circles) and Mount Dromedary (green circles).**

prior to zeta calibration analysis number 30. As such AFT ages for these samples were obtained using  $\zeta = 317.3 \pm 11.1$ .

## A2.2 Apatite (U-Th-Sm)/He analysis of Durango apatite

As with AFT analysis, the AHe system is calibrated against a standard of known age, most commonly, Durango fluoroapatite. The near gem quality Durango apatite occurs in hydrothermal or volcanogenic deposits at Cerro de Mercado, Mexico, and has a certified composition (Young et al., 1969). The surrounding volcanic rocks of the Durango apatite deposits have an age of  $30.3 - 30.9 \pm 0.4$  Ma obtained from K/Ar dating on sanidine (Naeser and Fleischer, 1975) and an age of  $31.4 \pm 0.5$  Ma from K/Ar dating of feldspars while direct fission track dating of Durango apatite yielded an age of  $31.4 \pm 0.5$  Ma (McDowell and Keizer, 1977, Green, 1985). Table A2-2 shows the Durango ages obtained routinely during



Anaylsis	Durango Sample	<sup>4</sup> He (cc)	<sup>238</sup> U (ng)	<sup>235</sup> U (ng)	<sup>232</sup> Th (ng)	<sup>147</sup> Sm (ng)	Th/U	Age (Ma)	err.	Mean Age (Ma)	St. Dev
1	DUR1	1.3E-08	0.41	0.0029	11.9	10.8	29.4	31.5	0.4	31.0	3.1
2	DUR2	1.9E-09	0.06	0.0004	1.8	1.8	31.0	32.3	0.4		
3	DUR3	5.4E-09	0.16	0.0012	5.1	5.1	31.2	31.4	0.4		
4	DUR4	2.3E-09	0.08	0.0006	2.3	2.1	28.5	30.6	0.4		
5	DUR5	2.0E-09	0.06	0.0005	1.9	1.8	29.2	31.2	0.4		
6	DUR6	2.1E-09	0.07	0.0005	1.9	1.8	27.2	32.2	0.4		
7	DUR7	2.9E-09	0.10	0.0007	3.1	3.1	30.2	28.2	0.3		
8	DUR8	2.0E-09	0.07	0.0005	2.0	1.9	28.3	30.5	0.4		
9	DUR9	2.3E-09	0.08	0.0006	2.2	2.2	29.5	30.0	0.3		
10	DUR10	1.3E-09	0.05	0.0003	1.3	1.3	28.6	30.5	0.4		
11	DUR11	3.1E-09	0.10	0.0007	3.0	2.9	29.6	30.4	0.4		
12	DUR12	1.5E-09	0.05	0.0004	1.4	1.4	28.2	29.6	0.3		
13	DUR13	8.2E-09	0.35	0.0026	7.9	7.5	22.4	29.6	0.3		
14	DUR14	2.3E-09	0.07	0.0005	2.2	2.2	29.8	31.1	0.4		
15	DUR15	5.5E-09	0.17	0.0012	5.2	4.9	30.1	31.4	0.4		
16	DUR16	3.0E-09	0.18	0.0013	2.8	2.5	15.4	28.7	0.3		
17	DUR17	3.4E-09	0.20	0.0014	4.4	5.4	22.3	21.7	0.2		
18	DUR18	4.3E-09	0.13	0.0009	4.1	4.1	31.2	31.6	0.4		
19	DUR19	4.4E-09	0.14	0.0010	4.3	4.0	31.1	30.5	0.4		
20	DUR20	9.9E-09	0.31	0.0022	9.6	9.0	31.3	30.6	0.4		
21	DUR21	5.5E-09	0.19	0.0014	4.8	4.4	25.4	33.3	0.4		
22	DUR22	3.8E-09	0.12	0.0009	3.7	3.6	30.1	29.9	0.3		
23	DUR24	7.7E-09	0.24	0.0017	7.3	6.1	31.0	31.4	0.4		
24	DUR25	8.0E-09	0.21	0.0015	5.9	4.8	27.8	39.7	0.5		
25	DUR27	4.7E-09	0.16	0.0011	4.8	4.7	30.2	29.1	0.3		
26	DUR28	1.1E-08	0.32	0.0024	10.8	9.8	33.2	30.4	0.4		
27	DUR30	8.4E-09	0.26	0.0019	8.1	7.7	31.2	31.0	0.4		
28	DUR31	4.6E-09	0.18	0.0013	4.4	4.3	25.0	30.3	0.3		
29	DUR32	4.9E-09	0.23	0.0017	6.3	5.5	27.2	22.8	0.3		
30	DUR33	3.9E-09	0.10	0.0008	2.8	2.6	26.5	40.6	0.5		
31	DUR34	3.8E-09	0.16	0.0012	4.0	3.9	24.7	27.2	0.3		
32	DUR35	1.3E-08	0.41	0.0030	12.0	11.9	29.1	30.9	0.4		
33	DUR38	1.7E-09	0.07	0.0005	1.7	1.6	24.1	29.8	0.3		
34	DUR39	2.4E-09	0.08	0.0005	2.4	2.2	31.6	30.8	0.4		
35	DUR40	1.5E-09	0.05	0.0004	1.4	1.4	27.8	30.7	0.4		
36	DUR41	5.9E-09	0.18	0.0013	5.7	5.5	31.5	31.0	0.4		
37	DUR42	5.0E-09	0.21	0.0015	4.7		22.2	30.7	0.3		
38	DUR43	4.7E-09	0.19	0.0014	5.0		25.8	28.0	0.3		
39	DUR44	9.6E-10	0.09	0.0006	1.9		22.3	14.8	0.2		
40	DUR45	2.4E-09	0.08	0.0006	2.3		27.8	31.1	0.4		
41	DUR46	2.0E-09	0.08	0.0006	2.1		26.5	28.4	0.4		
42	DUR47	6.3E-09	0.21	0.0015	5.7		27.2	33.2	0.4		
43	DUR48	2.3E-09	0.14	0.0010	3.7		26.7	19.0	0.2		
44	DUR49	3.0E-10	0.16	0.0012	4.0		24.8	2.2	0.0		
45	DUR50	4.2E-10	0.24	0.0017	5.0		21.1	2.5	0.0		

Analysis	Durango Sample	<sup>4</sup> He (cc)	<sup>238</sup> U (ng)	<sup>235</sup> U (ng)	<sup>232</sup> Th (ng)	<sup>147</sup> Sm (ng)	Th/U	Age (Ma)	err.	Mean Age (Ma)	St. Dev
46	UCL DUR 2	2.2E-09	0.10	0.0007	1.9		19.3	32.8	1.6	31.0	3.1
47	UCL DUR 3	1.9E-09	0.09	0.0006	1.7		19.2	32.1	1.5		
48	UCL DUR 4	2.0E-09	0.09	0.0007	1.7		19.0	33.0	1.6		
49	UCL DUR 5	3.2E-09	0.13	0.0010	3.0		22.0	31.2	1.5		
50	UCL DUR 6	5.1E-09	0.21	0.0015	4.6		22.0	33.1	1.6		
51	UCL DUR 7	5.9E-09	0.25	0.0018	5.6		22.7	31.1	1.5		
52	UCL DUR 8	4.5E-09	0.18	0.0013	4.0		21.9	32.9	1.6		
53	UCL DUR 9	7.6E-10	0.03	0.0002	0.7		20.7	30.9	1.5		
54	UCL DUR 10	6.1E-10	0.03	0.0002	0.6		22.0	32.2	1.5		
55	UCL DUR 11	9.5E-10	0.04	0.0003	0.8		20.4	32.4	1.5		
56	UCL DUR 12	3.0E-09	0.13	0.0009	2.6		20.6	32.9	1.6		
57	UCL DUR 13	3.8E-09	0.16	0.0012	3.4		21.0	32.4	1.5		
58	UCL DUR 14	5.0E-09	0.21	0.0016	4.5		20.9	32.5	1.6		
59	UCL DUR 15	1.0E-08	0.48	0.0035	9.0		18.6	32.5	1.5		
60	UCL DUR 16	8.5E-09	0.36	0.0026	7.7		21.4	32.0	1.5		
61	UCL DUR 17	8.2E-09	0.37	0.0027	7.3		19.8	32.1	1.5		
62	DUR51	1.2E-09	0.04	0.0003	0.9		22.3	37.4	1.8		
63	DUR52	2.3E-09	0.08	0.0006	2.2		28.0	31.8	1.5		
64	DUR53	7.3E-09	0.24	0.0018	6.6		27.1	33.1	1.6		
65	DUR54	1.2E-09	0.05	0.0004	1.2		23.0	29.8	1.4		
66	DUR55	3.4E-09	0.13	0.0009	3.2		24.4	31.6	1.5		
67	DUR56	2.5E-09	0.10	0.0007	2.4		23.4	31.1	1.5		

**Table A2-2: Apatite (U-Th-Sm)/He data generated for Durango apatite standards during sample analysis. Shaded samples yielded ages that were considerably younger than the standard Durango age ( $31.4 \pm 0.5$  Ma) and were not included when calculating the mean age and standard deviation.**

sample analysis throughout the entire study. These results yielded a mean age of 31.0 Ma (number of grains = 67) and a standard deviation of 3.1. This is in good agreement with the Durango ages from earlier studies (e.g. 32.2 Ma - Zeitler et al., 1987, 34 Ma - Wolf et al., 1996, 32.1 Ma - Farley, 2000, 32.8 Ma - Persano, 2003) and with independent age estimates described above. Three samples (shaded in Table A2-2) have been discounted as they have extremely low ages. This problem has likely been caused by an analytical error during the degassing stage.

## **A3 DATA QUALITY ASSESSMENT**

### **A3.1 AFT single grain ages**

Each sample was assessed in terms of its  $P(\chi^2)$  and single grain age variance. The  $\chi^2$ , or Chi-Sq, test is a statistical test for homogeneity within a sample set. More specifically, this test is used to assess whether the observed data (i.e. single grain fission track counts) are consistent with a Poisson variation with a common mean value. In cases where the p-value of the  $\chi^2$  test is less than 0.05, there is statistical evidence against the data being consistent with Poisson variation and therefore may be more consistent with more than one population of ages. However, this latter point cannot be inferred directly from a low  $\chi^2$  value. For samples where  $P(\chi^2) < 0.05$  and/or a variance  $> c. 10\%$ , radial plots were used to identify any “extreme” outliers which were dominating the results of these statistical tests. The threshold for defining outlier grains was arbitrarily set as grains which lie out with  $2.5\sigma$  of the central AFT age. This allows for some “natural” over dispersion in the sample which may occur due to naturally occurring phenomena. Once “outlier” grains were identified, both the polished grain and grain print were reassessed for their suitability for fission track dating and excluded if there were grounds to do so (Table A3-1). This process, in most cases, improved both the  $P(\chi^2)$  and dispersion values of samples without resorting to a ruthless elimination of data purely on statistical grounds.

### **A3.2 AHe single grain ages**

A similar data quality assessment was performed for single grain AHe ages. Outliers were first identified and then investigated on a grain by grain basis to justify whether or not the data should be excluded. The majority of excluded single grain ages can be justified based on problems encountered during the analytical stage (Table A3-2). Such problems include incomplete degassing of the apatite crystal resulting in an anomalously young single grain age. A second common problem is the analysis of excess He relative to the measured U and Th of the grain. This problem can occur if there is an inclusion within the apatite

crystal which releases He during the degassing stage but does not dissolve with the apatite crystal prior to ICP-MS analysis.

Sample Name	No. of Grains removed	Reason for exclusion
NQ12-04	1	Age > 2.5 $\sigma$ ; Large min. inclusion, lots of small fluid inclusions in grain mount; etch pits not completely parallel to c-axis; heterogenous track distribution in mica print.
NQ12-08	1	Age > 3 $\sigma$ ; Etch pits are not clear on the mica print, possibly due to poor contact with grain mount during irradiation.
NQ12-12	2	Age > 3 $\sigma$ ; Poor polish and dirty looking grain mount, patches of high track density. Age > 2.5 $\sigma$ ; thick fracture running through grain mount.
NQ12-20	1	Age > 2.5 $\sigma$ ; Lots of divets on grain mount, many fluid inclusions present.
NQ12-21	3	Age > 4 $\sigma$ ; Two possible inclusions, fluid inclusions, small area available to count; small chip on mica print. Age > 3.5 $\sigma$ ; Two inclusions in grain. Age > 3 $\sigma$ ; Lots of small fluid inclusions, etch pits may be entirely c-axis parallel.
NQ12-23	1	Age > 2.5 $\sigma$ ; Inclusion in grain; patchy distribution of etch pits in mica print.
NQ12-27	2	Age > 2.5 $\sigma$ ; poor polish, fractures in grain mount; etch pits on mica print have an uneven distribution. Age > 2.5 $\sigma$ ; Inclusion in grain, some etch pits not c-axis parallel, poor polish; scratches on mica.
SA12-06B	1	Age > 2.5 $\sigma$ ; Grain has two large mineral inclusions and small fluid inclusions; Mica print has large scratch.
SA12-14	3	Age > 3 $\sigma$ ; Large mineral inclusion in centre of grain. Age > 3 $\sigma$ ; Poor polish of grain mount and possible inclusions; patchy appearance in mica print. Age > 3 $\sigma$ ; Orange staining, poor polish on grain mount; scratches and patchy appearance on mica print.
SA12-27	1	Age > 2.5 $\sigma$ ; Poor polishing, heterogenous distribution of tracks in grain mount.

**Table A3-1: Details of single grain apatite fission track ages excluded from further analysis.**

Sample Name	Grains removed	Reason for exclusion
NQ12-04	3	Age > 4 $\sigma$ ; Possible analytical error during the degassing stage.
NQ12-06	10	No measurement of U, Th or Sm
	11	Age > 5 $\sigma$ , excluded as statistical outlier, possible degassing problem
NQ12-07	23	Age > 4 $\sigma$ , excluded as statistical outlier, possible degassing problem
NQ12-09	4	No measurement of He
	13	Extreme outlier, incomplete degassing of crystal
NQ12-10	19	Extreme outlier, excess helium relative to U and Th, possible inclusion.
NQ12-11	1	Ages obtained during an analysis were Durango standards were anomalously young. These sample ages are also anomalously young relative to other grains from the same sample.
	2	Ages obtained during an analysis were Durango standards were anomalously young. These sample ages are also anomalously young relative to other grains from the same sample.
	3	Ages obtained during an analysis were Durango standards were anomalously young. These sample ages are also anomalously young relative to other grains from the same sample.
	4	Ages obtained during an analysis were Durango standards were anomalously young. These sample ages are also anomalously young relative to other grains from the same sample.
	9	Incomplete degassing of apatite crystal
NQ12-13	17	Age > 6 $\sigma$ , excess helium relative to U and Th, possible inclusion.
NQ12-15	1	Incomplete degassing of apatite crystal
	4	Ages obtained during an analysis were Durango standards were anomalously young. These sample ages are also anomalously young relative to other grains from the same sample.
	5	Incomplete degassing of apatite crystal
NQ12-17	3	No measurement of U, Th or Sm
	14	Age > 2 $\sigma$ , Ages obtained during an analysis were Durango standards were anomalously young.
SA12-05	3	Extreme outlier, excess helium relative to U and Th, possible inclusion.
	4	Age > 3 $\sigma$ , excluded as statistical outlier, possible degassing problem, Ages obtained during an analysis were Durango standards were anomalously young.
SA12-06B	10	No He measurement
	12	Extreme outlier, excess helium relative to U and Th, possible inclusion.
	13	Age > 4 $\sigma$ ; Incomplete degassing of apatite crystal
SA12-14	27	No He measurement
	4	Extreme outlier, excess helium relative to U and Th, possible inclusion.
SA12-30	4	Extreme outlier, excess helium relative to U and Th, possible inclusion.
SA12-35	3	Incomplete degassing of apatite crystal
	8	Incomplete degassing of apatite crystal
SA12-36	2	No He measurement
	8	Age > 3 $\sigma$ , Ages obtained during an analysis were Durango standards were anomalously young.
	12	Age > 3 $\sigma$ , Ages obtained during an analysis were Durango standards were anomalously young.
	14	Age > 2 $\sigma$ , Ages obtained during an analysis were Durango standards were anomalously young.
GGO2	6	Age > 3 $\sigma$ ; Incomplete degassing of apatite crystal
	9	Extreme outlier, excess helium relative to U and Th, possible inclusion.
	13	Age > 4 $\sigma$ ; Incomplete degassing of apatite crystal
	15	No He measurement
	18	No He measurement
JN2	24	No He measurement
	16	Age > 5 $\sigma$ , excluded as statistical outlier.
	22	Age > 7 $\sigma$ , excluded as statistical outliers.

Table A3-2: Details of single grain apatite (U-Th-Sm)/He ages excluded from further analysis.

## A4 SAMPLE DETAILS

Long (°)	Lat (°)	Sample	Elev. (m)	Lithology	Strat. Age
22.20	-29.22	<b>FS1605</b>	843	Granite Breccia	NMP
20.30	-28.36	<b>GGO2</b>	846	Granite	NMP
18.05	-30.68	<b>JN2</b>	376	Nabeep Gneiss	NMP
17.38	-29.90	<b>JN3</b>	418	Streak Gneiss	NMP
17.99	-30.55	<b>NQ12-01</b>	238	VCg Qtz-fdsp granite	NMP
17.95	-30.46	<b>NQ12-03</b>	582	Cg. porphyritic bt-granite	NMP
17.93	-30.40	<b>NQ12-04</b>	720	Cg. Porphyritic bt-hbl-granite gneiss.	NMP
17.86	-30.34	<b>NQ12-06</b>	690	Mg.-Cg. Qtz-fdsp-bt gneiss.	NMP
17.82	-30.32	<b>NQ12-07</b>	688	Mg.-Cg. Qtz-fdsp-bt gneiss.	NMP
17.80	-30.34	<b>NQ12-08</b>	598	Mg. Bt-gneiss	NMP
17.77	-30.34	<b>NQ12-09</b>	355	Mg. Banded Qtz-fdsp-bt gneiss.	NMP
17.75	-30.36	<b>NQ12-10</b>	239	Fg-Mg banded Qtz-fdsp-bt gneiss	NMP
17.72	-30.37	<b>NQ12-11</b>	416	F-Mg. Qtz-fdsp-bt gneiss	NMP
17.68	-30.36	<b>NQ12-12</b>	388	Mg. Qtz-fdsp-bt "Tiger" gneiss	NMP
17.62	-30.36	<b>NQ12-13</b>	354	Mg. Qtz-fdsp-bt "Tiger" gneiss	NMP
17.30	-30.32	<b>NQ12-15</b>	38	Banded pelitic Mg. Bt-qtz-fdsp paragneiss	NMP
17.27	-30.29	<b>NQ12-16</b>	11	Mg. Qtz-fdsp-bt "tiger" gneiss	NMP
17.29	-30.36	<b>NQ12-17</b>	5	Mg. Pelitic qtz-fdsp-bt gneiss.	NMP
17.28	-30.34	<b>NQ12-18</b>	5	Vcg. Bt-augen gneiss	NMP
17.64	-30.28	<b>NQ12-19</b>	250	Mg. Qtz-fdsp "Tiger" gneiss	NMP
17.72	-30.20	<b>NQ12-20</b>	473	Vcg. Bt-augen gneiss	NMP
17.77	-30.21	<b>NQ12-21</b>	665	Mg-Cg. "Tiger" gneiss (qtz-fdsp-bt)	NMP
18.52	-31.23	<b>NQ12-23</b>	300	Cg. Porphyritic bt-gneiss	NMP
18.35	-31.13	<b>NQ12-24</b>	400	Granite gneiss	NMP
17.93	-30.21	<b>NQ12-25</b>	740	mg. Qtz-fdsp-bt gneiss	NMP
17.93	-30.13	<b>NQ12-26</b>	850	Mg qtz-fdsp-bt-orthogneiss	NMP
17.88	-30.03	<b>NQ12-27</b>	600	mg-fg banded qtz-fdsp-bt gneiss	NMP
17.90	-30.17	<b>NQ12-28</b>	650	Mg. Qtz-fdsp gneiss +/- bt	NMP
17.78	-30.09	<b>NQ12-29</b>	720	Mg. Qtz-feldspar-bt "tiger" gneiss	NMP
17.83	-30.15	<b>NQ12-30</b>	550	Mg felsic bt-gneiss	NMP
18.08	-30.17	<b>NQ12-33</b>	1050	Mg-bt granite gneiss	NMP
18.16	-30.18	<b>NQ12-34</b>	1000	Gneiss dome	NMP
19.52	-28.48	<b>PRU 106</b>	783	Navos Granite (Vioolsdrif)	NMP
23.70	-29.15	<b>SA12-05</b>	1007	Granite dropstone (weathered cream coloured matrix Dwyka)	Dwyka Group
23.14	-29.54	<b>SA12-06b</b>	1068	Bt. Gneiss ( weathered cream coloured matrix Dwyka)	Dwyka Group
22.31	-29.52	<b>SA12-08</b>	1039	hbl-bt-granite-augengneiss	NMP
22.12	-29.40	<b>SA12-09</b>	995	Qtz-fdsp-bt Gneiss	NMP
21.94	-29.36	<b>SA12-10</b>	1075	Porphyroblastic Qtz-fdsp-bt gneiss	NMP
21.94	-29.24	<b>SA12-11</b>	1057	Cg. Porphyritic bt Granite	NMP
21.63	-29.30	<b>SA12-12</b>	981	Bt-Qtz-Fsdp orthogneiss	NMP
21.47	-29.28	<b>SA12-13a</b>	962	Paragneiss	NMP
21.15	-29.35	<b>SA12-14</b>	797	Banded pelitic gneiss	NMP
20.98	-29.42	<b>SA12-15</b>	884	Cg. Felsic Bt-Gneiss	NMP
19.53	-29.34	<b>SA12-19b</b>	1034	Felsic qtz-fdsp-bt gneiss	NMP
19.08	-29.93	<b>SA12-22</b>	922	bt-hbl-augengneiss	NMP
18.70	-30.23	<b>SA12-27</b>	987	Granite dropstone (Dwyka)	Dwyka Group
18.00	-30.53	<b>SA12-30</b>	258	bt-qtz-fdsp orthogneiss	NMP
18.06	-30.53	<b>SA12-32</b>	351	Granite	NMP
18.06	-30.49	<b>SA12-33</b>	400	Granite	NMP
18.06	-30.45	<b>SA12-35</b>	605	granite/granodiorite	NMP
18.06	-30.45	<b>SA12-36</b>	707	granite/granodiorite	NMP
18.06	-30.43	<b>SA12-37</b>	807	granite/granodiorite	NMP
18.07	-30.40	<b>SA12-38</b>	959	granite/granodiorite	NMP
18.23	-30.39	<b>SA12-47</b>	1064	granite/granodiorite	NMP
18.42	-30.32	<b>SA12-51</b>	1066	bt-qtz-fdsp grantic gneiss	NMP
18.46	-30.32	<b>SA12-52</b>	1065	Granodiorite	NMP

Table A4-1: Details on sample location and lithology

## A5 APATITE FISSION TRACK DATA

### A5.1 Radial plots

Single grain apatite fission track data are presented using radial plots as this method provides a means to display single grain age dispersion, taking into account the precision of each measurement (Galbraith, 2010). The plots were created using the Java application RadialPlotter (Vermeesch, 2009) by plotting a point, for each single grain measurement, where:

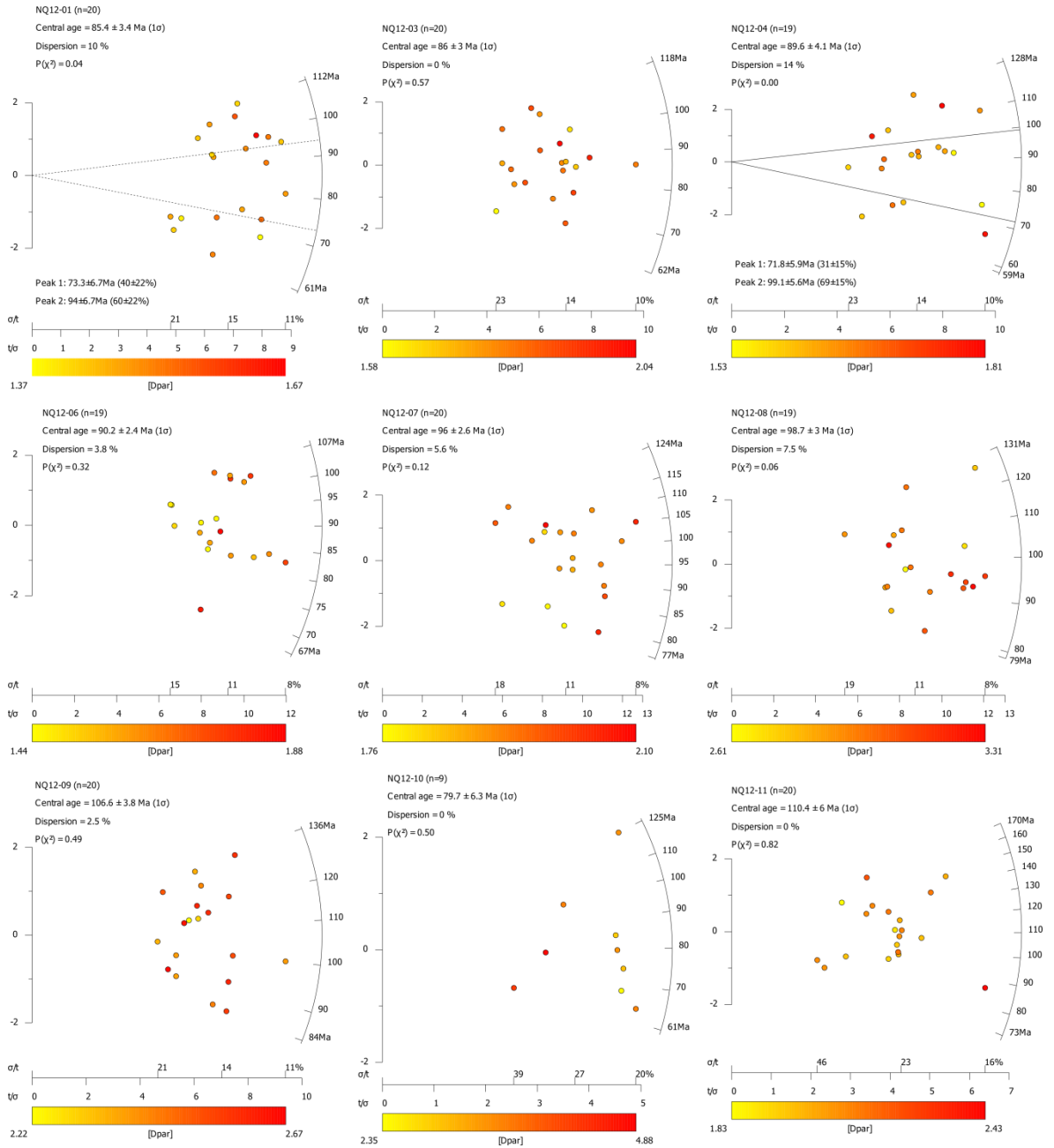
$$x_j = \frac{1}{\sigma(z_j)} \text{ and } y_j = \frac{(z_j - z_0)}{\sigma(z_j)}, \text{ for } 1 < j < n.$$

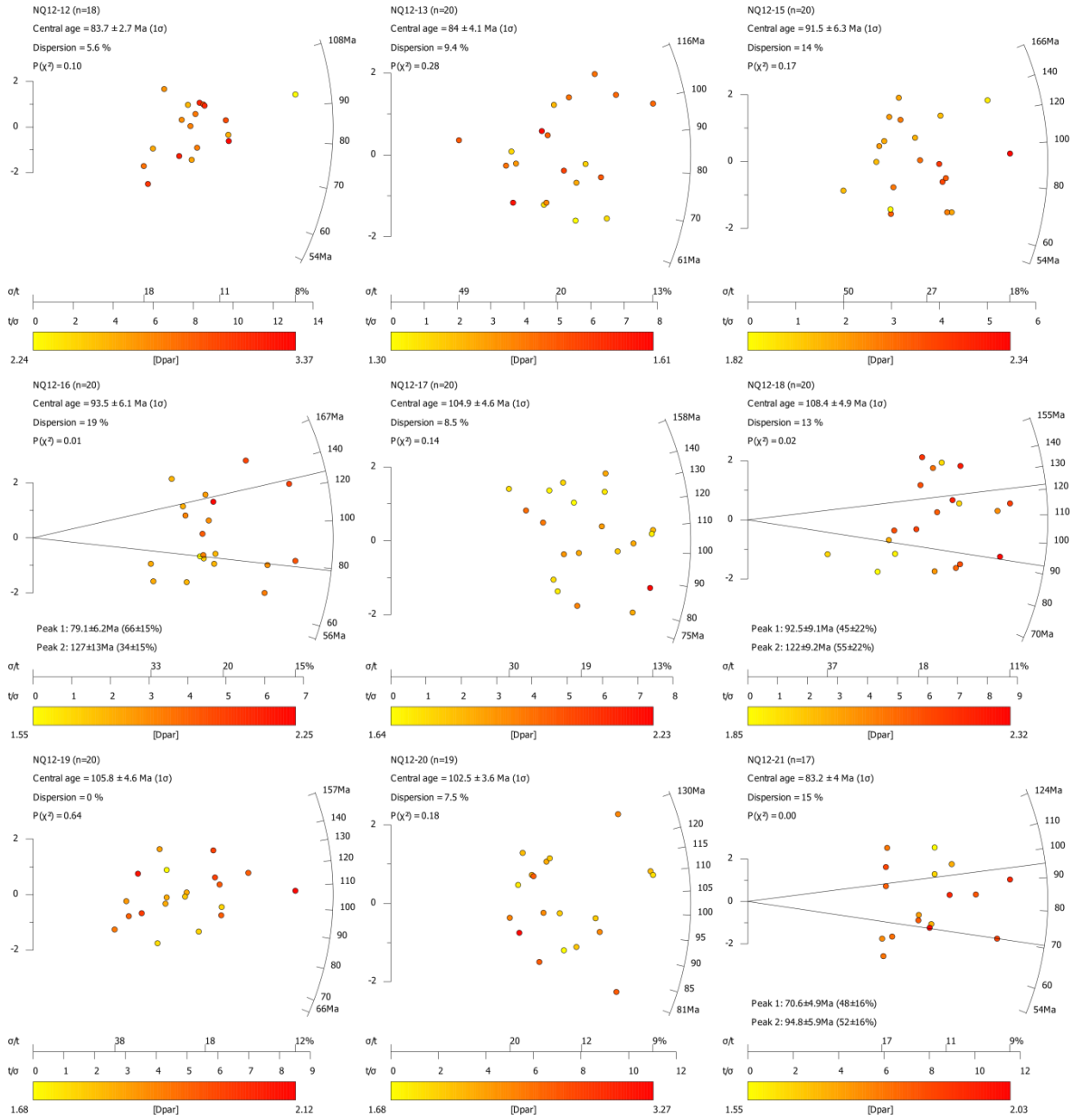
Where  $z_j$  is a transformation of the age data (in this case a logarithmic transformation) and  $\sigma(z_j)$  being the corresponding measurement of uncertainty of the age measurement;  $z_0$  is the transformation of central AFT age. Less precise data will plot closer to the origin than more precise data. Each single grain age can be determined using a line which cuts through the origin and the corresponding data point.

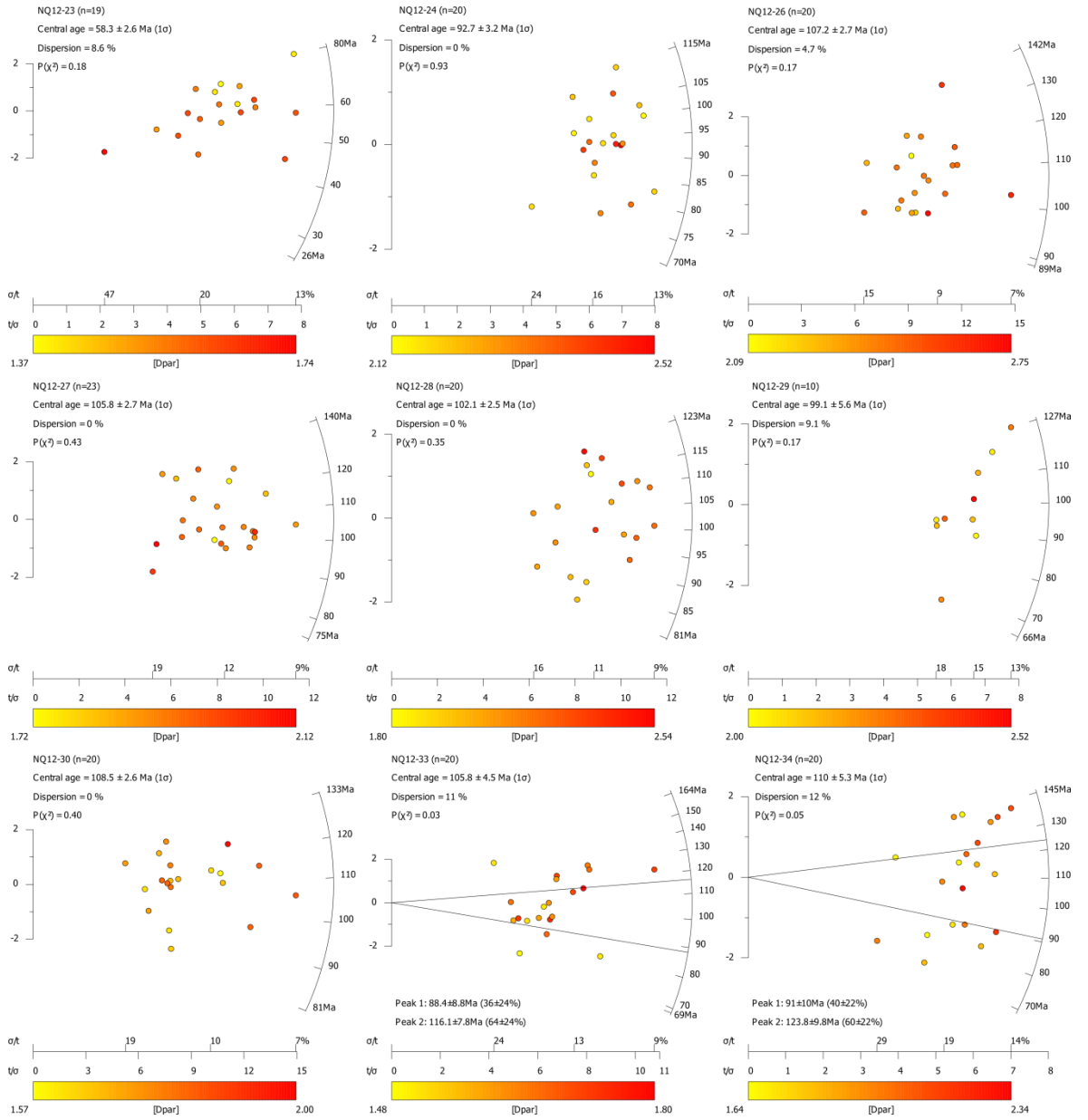
A  $\chi^2$  test for statistical homogeneity was performed on every sample with the corresponding p-value shown each radial plot. When the p-value is  $< 0.05$ , there is the possibility that the sample set contains more than one population. In these cases a mixture model (Galbraith and Green, 1990) was used to investigate whether the single grain age distributions better represent more than one population of ages. Radial lines on the radial plot indicate peak centres and the age of the peaks and proportions of grains belonging to that population are beneath the radial plot. Details of the algorithm used for the mixture modelling can be found in Vermeesch, (2009).

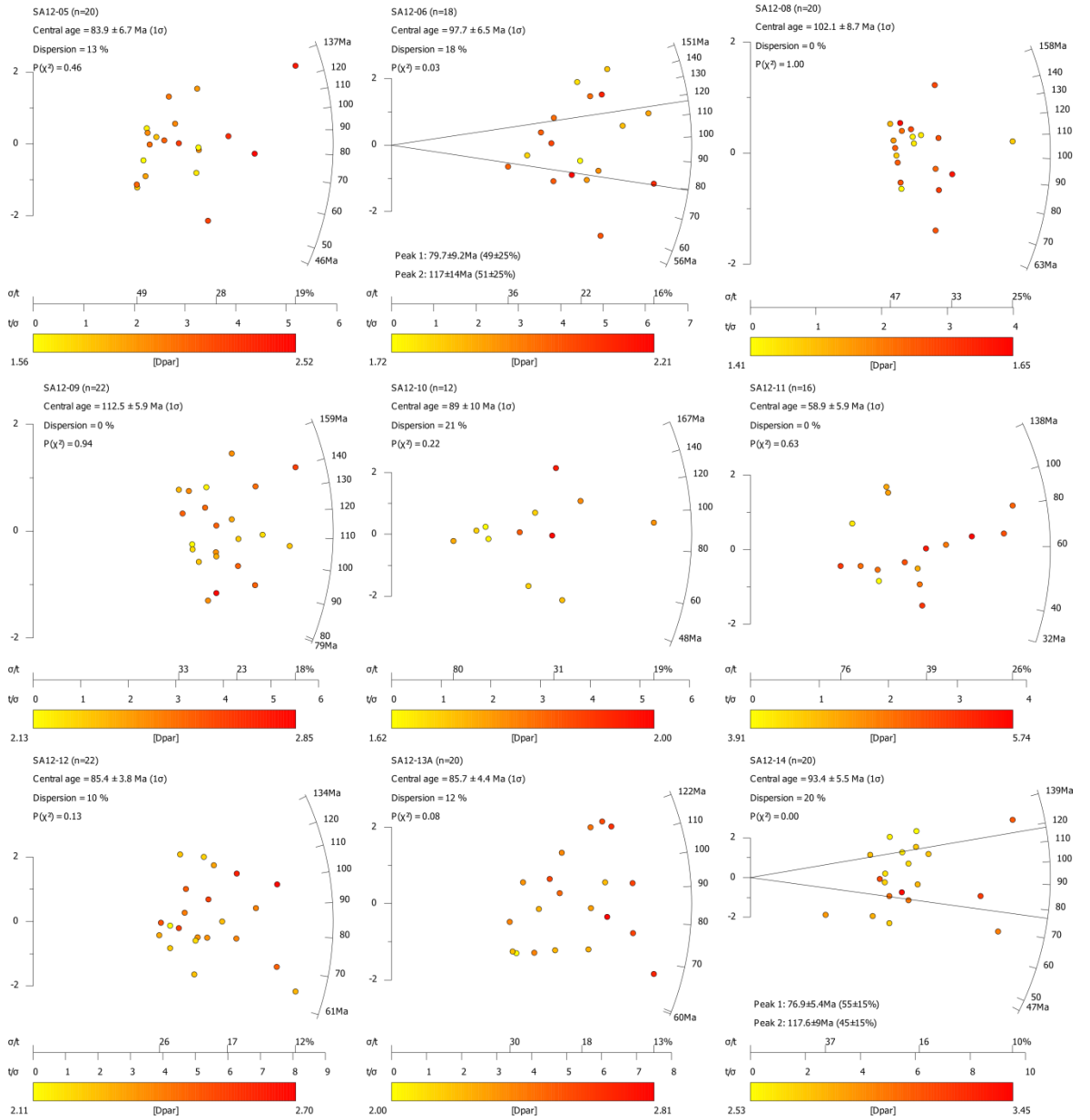
Single grain data for all apatite fission track samples can be found in the electronic supplementary material.

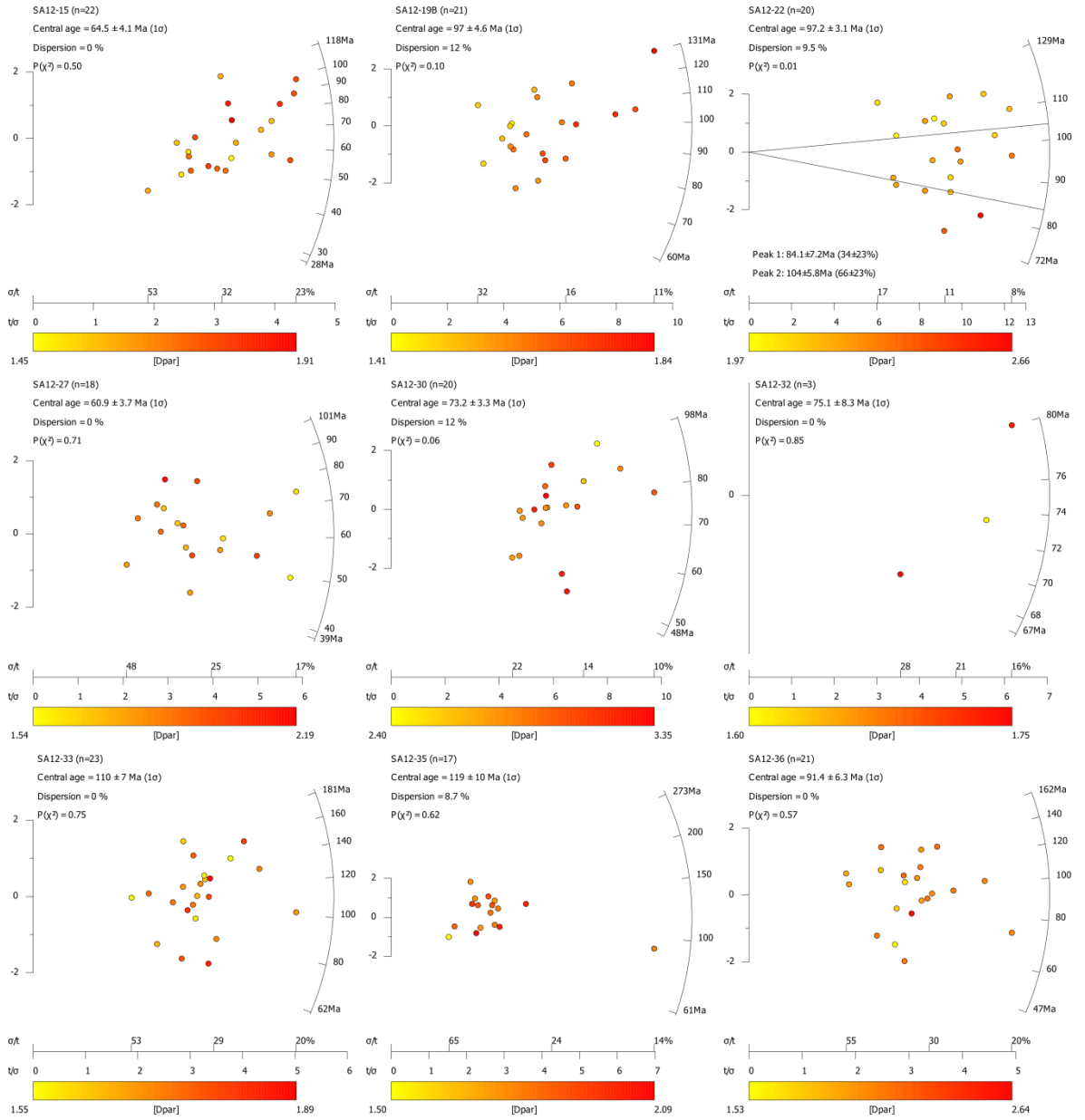


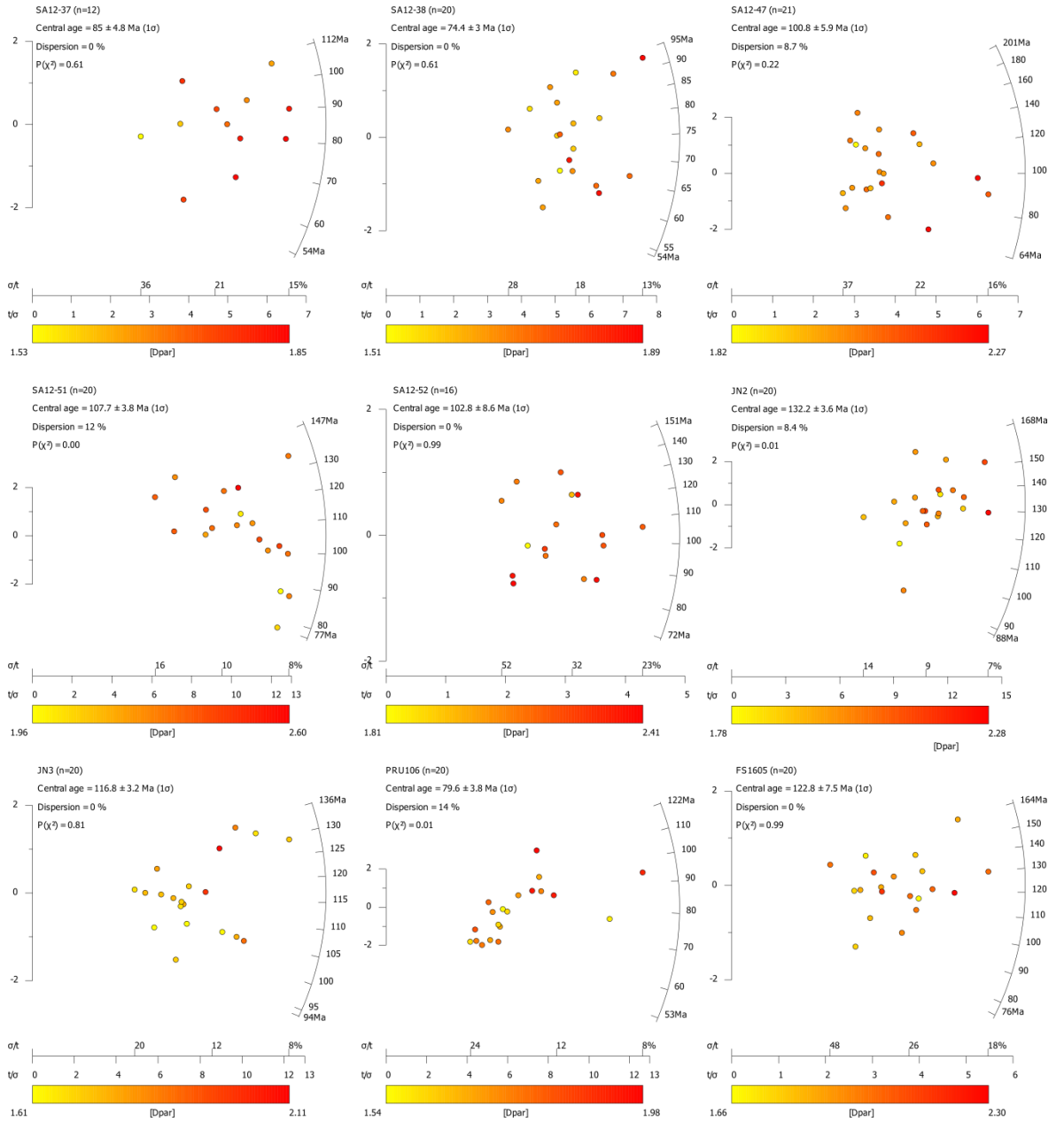


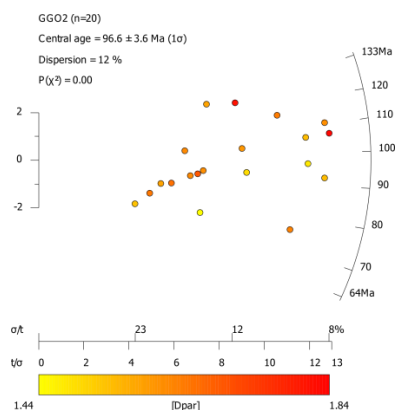












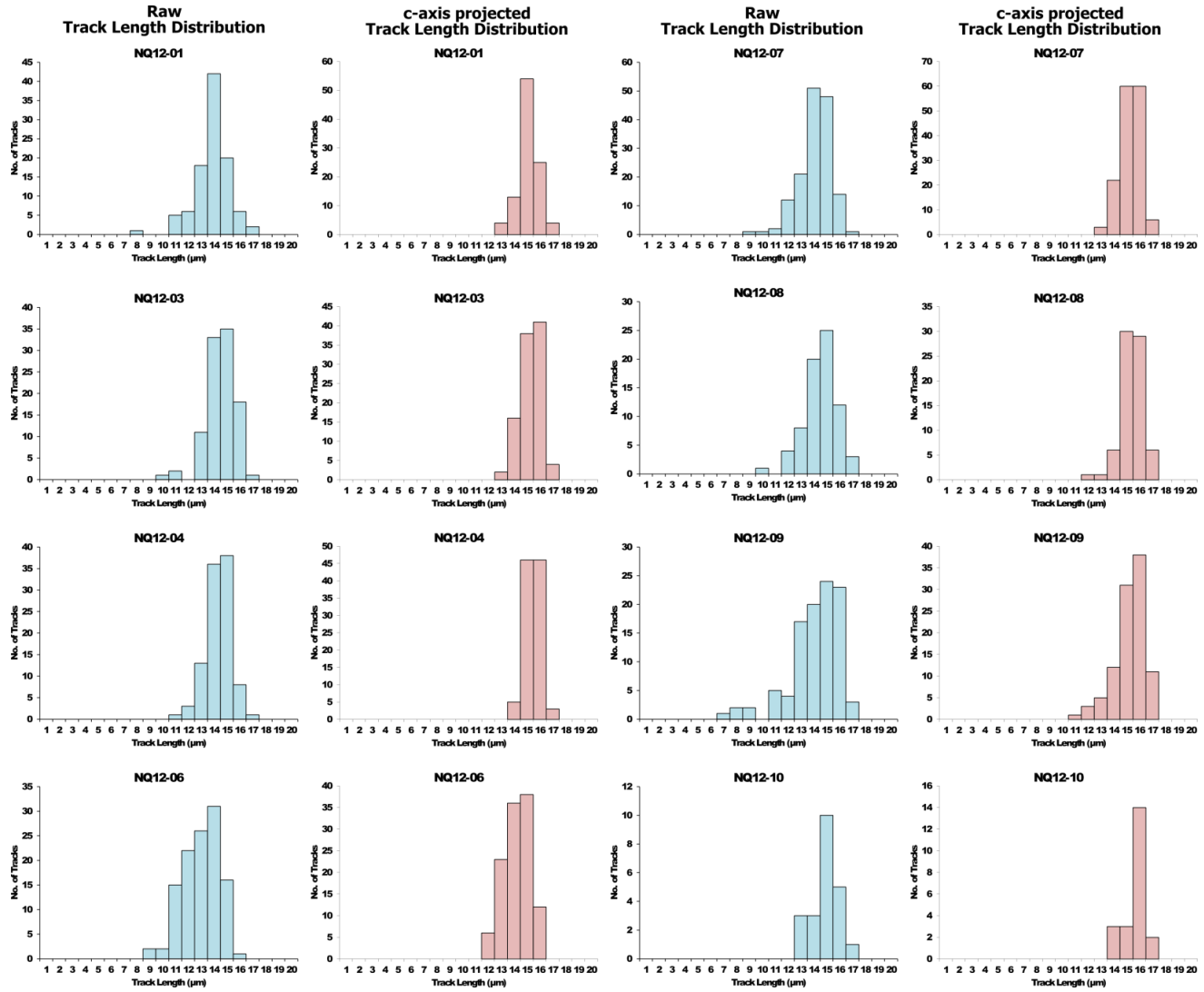
**Figure A5-1: Radial plots of single grain apatite fission track analysis after (Galbraith, 2010). Radial plots were drawn using the Java application RadialPlotter (Vermeesch, 2009).**

## A5.2 Track length distribution

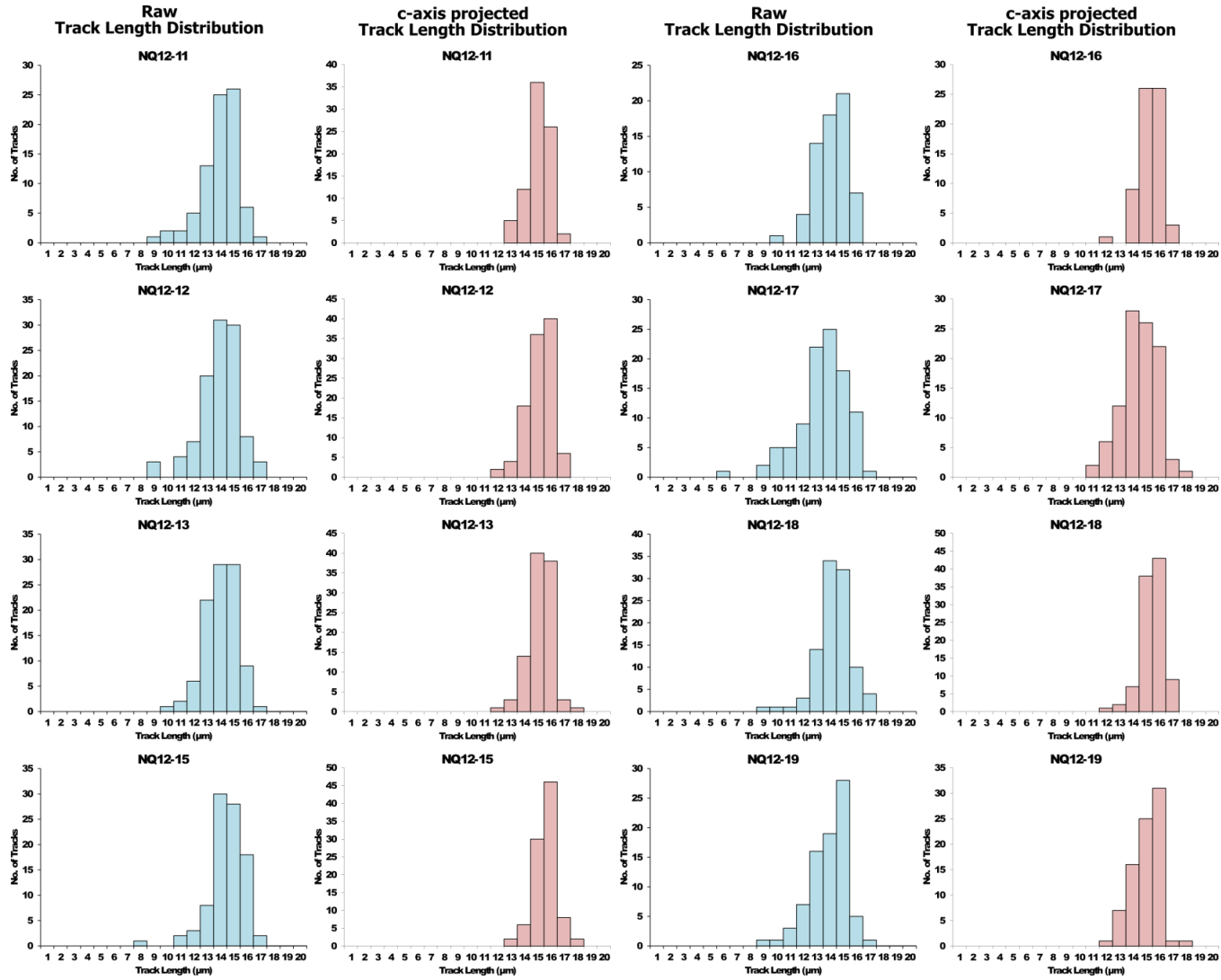
Track length distributions for all samples are presented below (Figure A5-2). Two histograms are presented for each sample. The first illustrates the raw measured track length distribution and the second illustrates the length distribution after measured tracks have been corrected for their orientation to the crystallographic c-axis (see Ketcham et al., 2007).

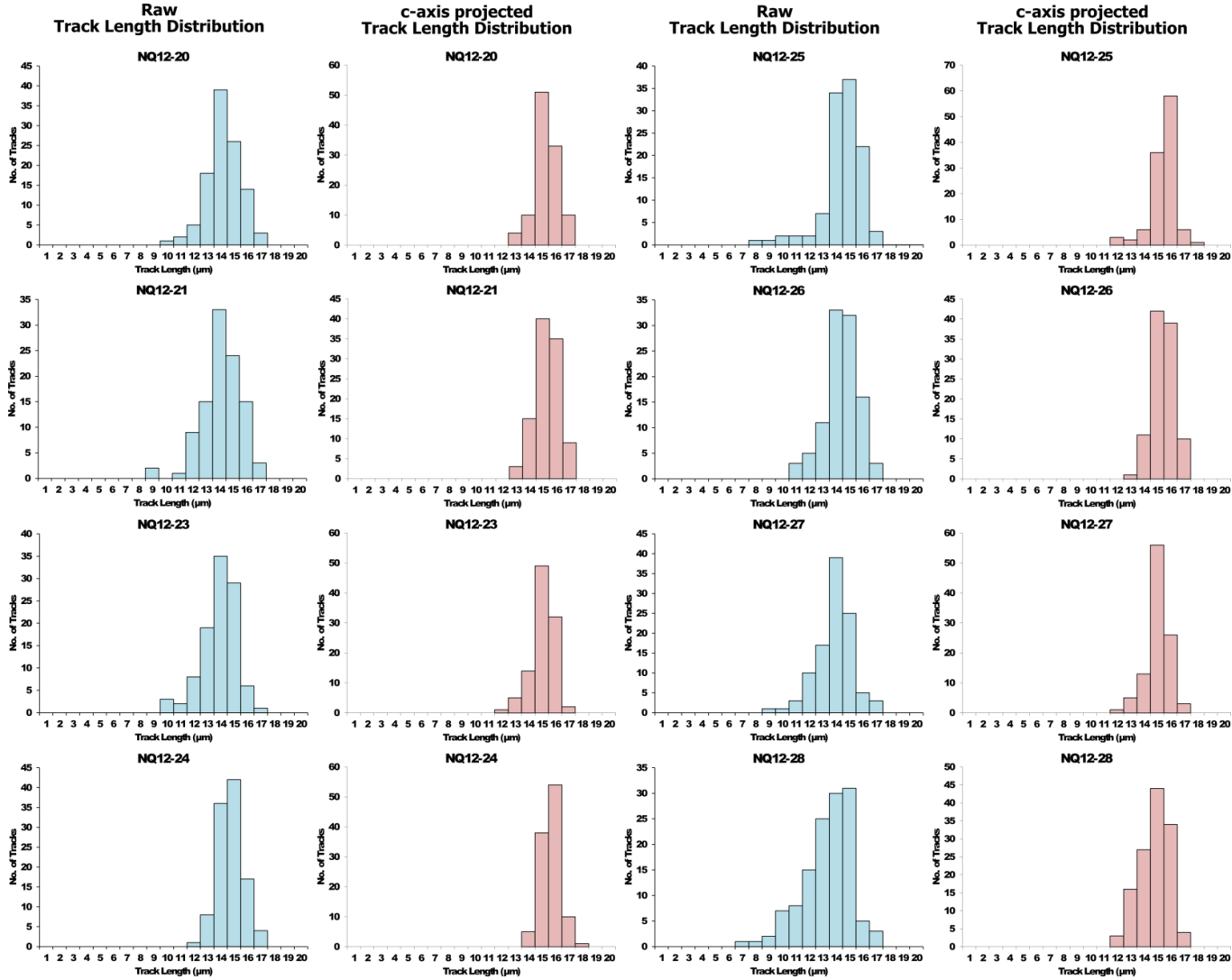
A complete list of individual track length measurements can be found in the relevant section of the QTQt input file (see Appendix 7).

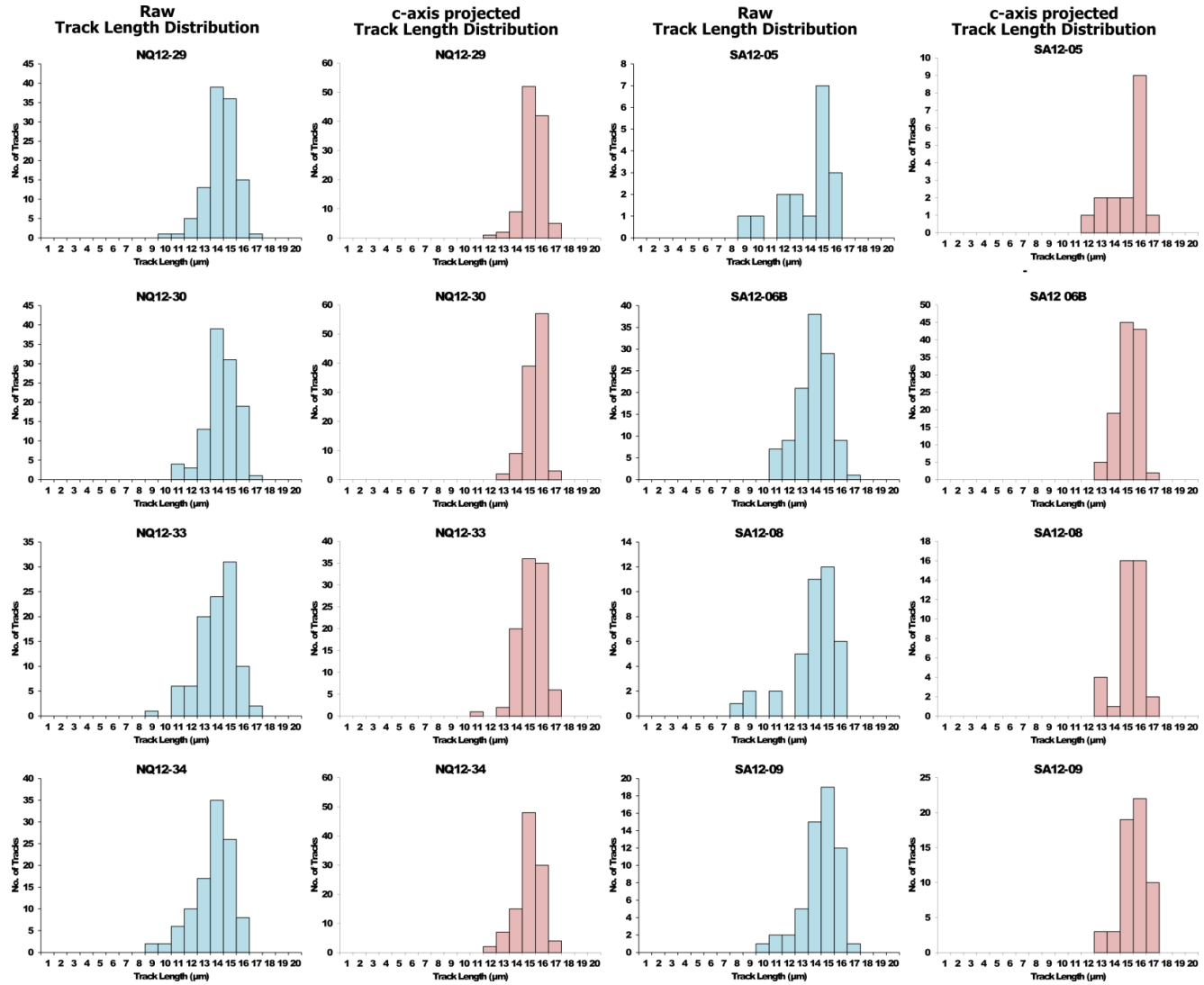
**Figure A5-2: (overleaf) Fission track length distributions for all analysed samples. Both raw track length distributions and track length distributions corrected for orientation to c-axis are shown.**

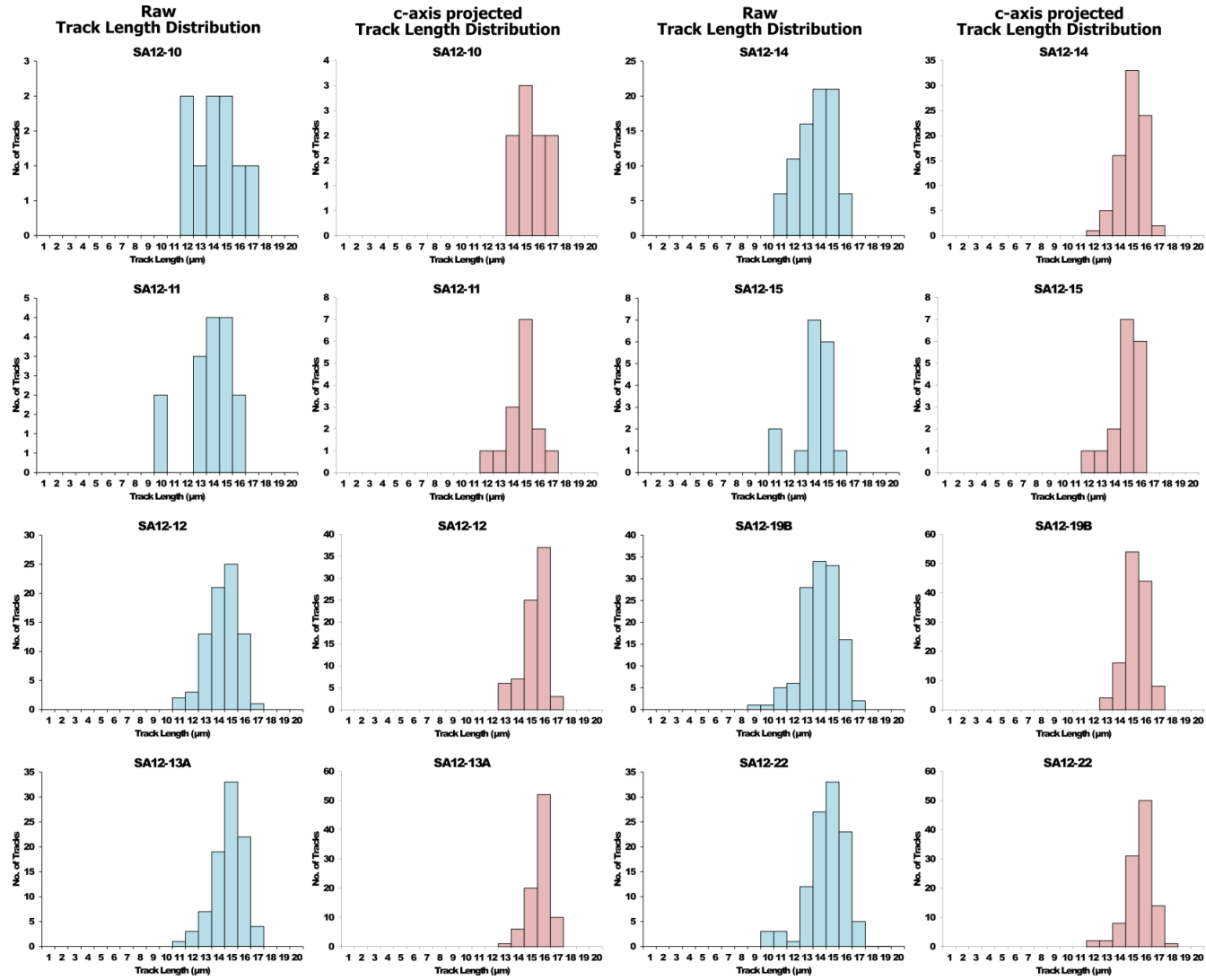


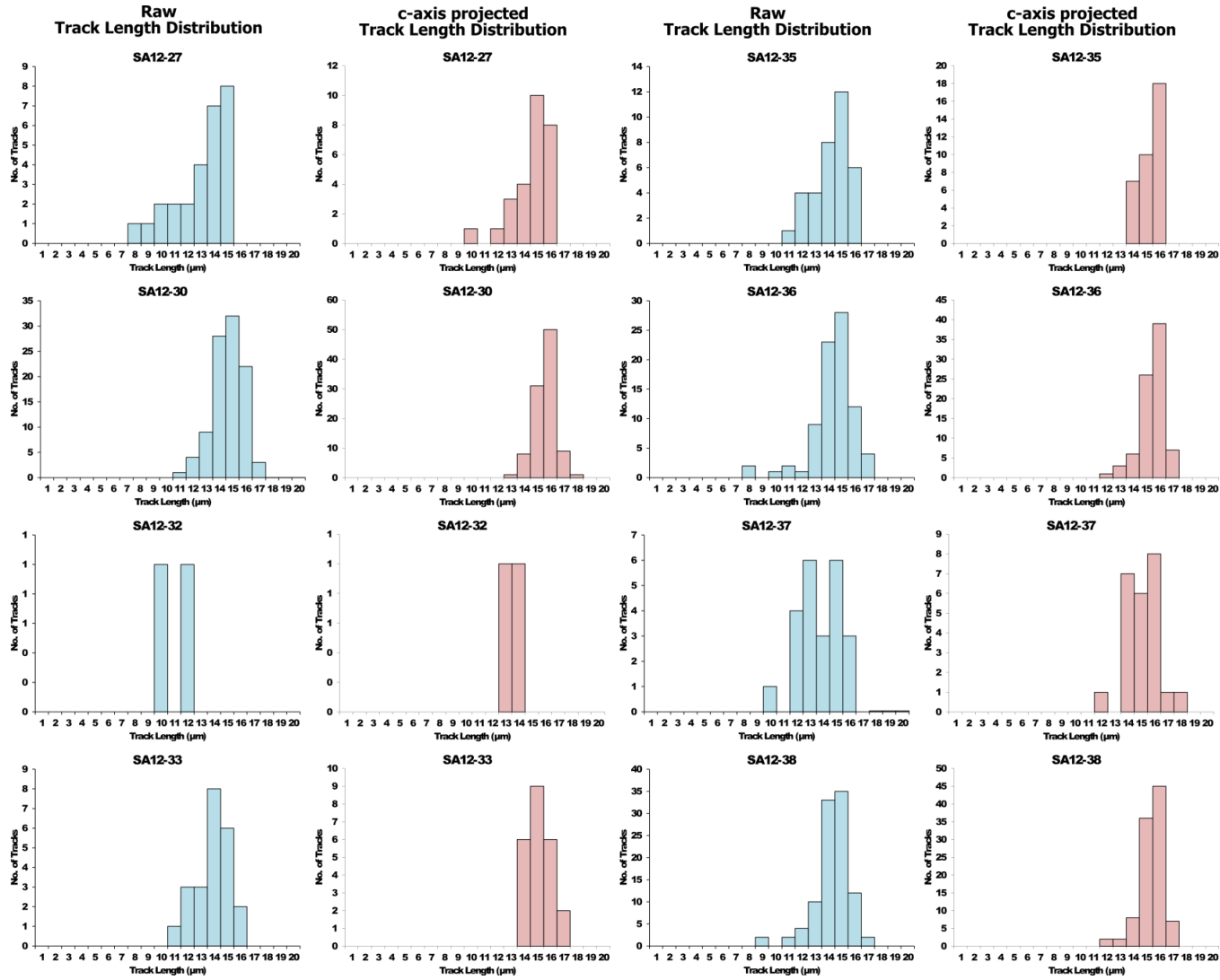


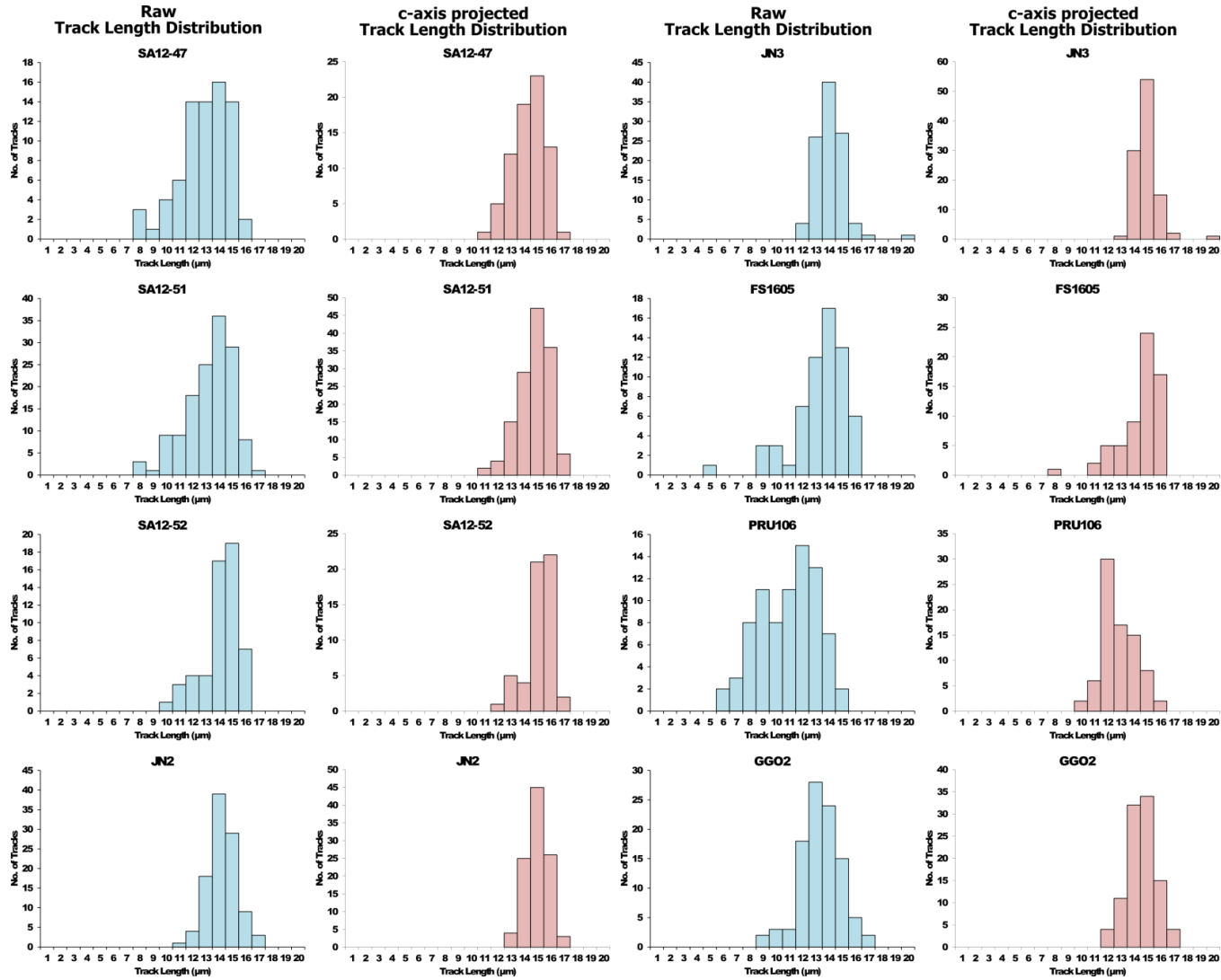












# A6 ADDITIONAL AFT DATA

Sample	Long. (°)	Lat. (°)	Elev. (m)	$\rho_s^a$ ( $10^6\text{cm}^{-2}$ )	$N_s^b$	$\rho_i^a$ ( $10^6\text{cm}^{-2}$ )	$N_i^b$	$\rho_d^a$ ( $10^6\text{cm}^{-2}$ )	$N_d^b$	$P(\chi^2)^c$ (%)	AFT Age <sup>d</sup> $\pm 1\sigma$ (Ma)	#XtIs	Measured			#HCT <sup>f</sup>
													MTL ( $\mu\text{m}$ )	$\pm 1\sigma$	Sde	
8732-50	17.5	-29.7	50	0.7	756	1.3	1478	1.3	5435	80.7	115 6	15	14.08	0.2	1.0	36
8732-51*	17.8	-29.2	970	1.3	1824	4.7	6466	2.3	9958	0.3	117 6	20	13.70	0.2	1.5	63
8732-52*	17.7	-28.8	190	0.5	734	2.3	3052	2.3	9958	0	108 7	20	12.93	0.5	1.9	14
8732-86	19.3	-28.8	420	1.1	1573	4.1	6148	2.3	9958	0	114 7	22	13.47	0.2	1.4	85
8732-87	19.1	-29.2	870	0.6	551	1.4	1183	1.3	5435	23.6	105 6	15	14.07	0.2	1.2	44
8732-88	19.4	-29.1	900	1.9	1326	4.1	2856	1.3	5435	22.6	104 4	15	13.73	0.1	1.3	100
8732-93	21.1	-28.6	700	0.8	852	2.0	2111	1.3	5435	28.4	91 4	20	13.97	0.1	1.1	94
NF-008	19.8	-29.3	-950	0.3	680	0.7	1611	1.3	7331	25	92 9	26	13.17	0.3	2.2	54
S-20	21.1	-29.5	900	1.8	1989	3.9	4235	1.1	5309	0	99 5	20	13.82	0.3	2.0	57
S-21	21.1	-29.5	1010	0.3	214	0.6	411	1.2	5309	75.1	104 9	20	13.97	0.4	1.7	20
8732-42*	18.5	-31.2	370	1.1	1741	2.5	3732	1.3	12343	0	105 4	20	13.36	0.3	2.5	100
8732-43*	18.1	-30.8	300	0.5	899	1.8	3027	2.3	9958	65.2	121 5	20	13.44	0.2	1.4	37
8732-44*	17.8	-30.8	100	1.7	2144	6.2	7990	2.3	9958	17.9	109 3	20	13.34	0.1	1.4	115
8732-45*	17.6	-30.9	0	1.3	652	2.7	1324	1.3	12343	92.3	111 6	19	12.75	0.3	2.5	100
8732-46*	17.9	-30.3	750	1.2	2094	3.1	5434	2.3	9958	0	154 7	21	13.30	0.2	1.6	116
8832-72	18.4	-30.5	1335	0.4	221	0.8	425	1.0	4441	68.2	88 3	20	13.68	0.5	1.6	11
8832-73	18.4	-30.5	1180	1.3	1082	2.6	2207	1.0	4441	9.1	83 4	20	13.62	0.2	2.1	102
8832-74	18.3	-30.5	1000	1.0	802	1.4	1148	1.0	4441	25.5	118 6	20	13.66	0.3	2.1	47
8832-75	18.5	-30.3	1030	1.4	1731	2.7	3278	1.0	4441	5.2	95 4	20	13.46	0.3	2.0	39
8832-78	18.1	-30.5	1620	1.7	1228	3.3	2349	1.0	4441	20.2	89 4	20	13.14	0.2	2.0	104
8832-79	18.1	-30.5	1500	0.8	1078	1.5	2048	1.0	4441	64.8	90 4	20	13.99	0.4	1.6	19
8732-34*	19.1	-33.8	450	2.7	3102	3.8	4442	1.3	12343	77.6	157 5	25	12.93	0.2	2.4	125
8732-35*	18.4	-33.8	300	1.7	1121	2.9	1934	1.3	12343	57	130 5	22	12.82	0.2	2.0	100
8732-36*	18.4	-34.1	150	4.3	4529	7.9	8365	1.3	12343	0.2	126 4	20	14.20	0.2	1.0	100
8732-37*	17.9	-32.8	0	0.6	746	1.0	1163	1.3	12343	87.7	144 7	25	13.38	0.2	2.0	75
8832-61	19.4	-33.6	290	0.4	332	0.9	694	0.1	4423	75.6	104 7	20	13.04	0.4	1.7	15
8832-71	18.1	-32.8	0	0.4	456	0.7	753	1.0	4441	61.9	102 6	20	13.60	0.3	2.4	65
DR3/86	21.0	-33.0	900	1.8	924	3.1	1608	1.4	7635	59.9	138 6	20	14.12	0.3	2.0	35
S-19	21.5	-31.2	1270	0.8	729	1.0	882	1.1	5309	20.9	163 9	20	13.37	0.3	3.0	100
FTCG 04	18.9	-33.7	670	0.6	1.5	1145	1.4	9637	30	119 9	20	12.53	0.4	1.6	18	
FTCG 05	18.9	-34.0	130	2.4	2043	4.4	3763	1.4	9637	30	130 4	20	13.67	0.4	1.4	100
FTCG 06	18.8	-34.0	100	1.5	945	2.3	1502	1.4	9637	15	151 6	15	13.33	0.4	1.6	85
FTCG 08	18.5	-33.6	90	1.3	818	2.0	1225	1.4	9637	10	160 7	20	13.57	0.4	1.3	69
FTCG 09	18.0	-33.1	20	4.0	1391	6.6	2289	1.4	9637	< 1	147 10	10	12.90	0.4	1.5	100
FTCG 11	17.9	-33.0	10	2.8	1605	4.5	2615	1.4	9637	60	147 5	20	13.32	0.4	1.3	100
FTCG 14	18.0	-32.8	10	1.0	267	1.5	405	1.4	9637	80	157 12	7	13.61	0.4	1.3	100
FTCG 16	18.8	-33.5	210	1.1	952	2.2	1908	1.4	9637	15	120 5	20	12.86	0.4	1.6	100
FTCG 17	18.7	-33.5	300	2.2	2616	4.0	4732	1.4	9637	15	132 4	20	13.00	0.4	1.8	100
FTCG 18	18.4	-33.5	150	4.6	3554	7.8	6020	1.4	9637	<1	142 4	20	13.12	0.4	1.5	100
8832-62	18.9	-33.7	729	0.6	421	1.1	812	1.3	4423	9.2	119 9	20	13.46	0.4	1.7	18
8832-63	18.9	-33.7	630	0.8	426	1.9	1031	1.3	4423	72.4	93 6	20	14.63	0.2	0.6	7
8832-65	18.9	-33.7	450	0.5	369	1.4	945	1.3	4423	65.9	89 6	20	14.13	0.2	1.0	35
8832-66	19.0	-33.7	320	0.5	206	1.4	558	1.3	4423	82.5	86 7	15	13.32	0.4	0.5	2
8832-68	18.8	-33.5	125	0.4	324	1.0	845	1.4	4423	87.1	90 6	20	13.62	0.4	1.3	11
8832-54	20.6	-32.6	1658	1.0	848	1.6	1296	1.1	4423	25.3	126 6	20	13.73	0.3	1.6	55
8732-41*	20.6	-32.5	1550	0.9	1495	1.5	2534	1.3	12343	3.3	141 6	30	13.56	0.1	1.8	170
8832-55	20.6	-32.5	1430	1.3	786	2.0	1215	1.1	4423	93	127 6	20	13.02	0.3	2.1	48
8832-56	20.6	-32.5	1290	1.1	719	1.6	1013	1.2	4423	53.4	142 8	20	13.55	0.2	1.7	100
8832-57	20.6	-32.6	1190	1.8	966	3.0	1612	1.2	4423	0.5	131 8	20	13.18	0.3	1.6	32
8832-58	20.6	-32.6	1090	1.4	567	2.5	1057	1.2	4423	37.7	111 7	20	12.81	0.3	2.1	64
8832-59	20.5	-32.6	980	0.7	515	1.2	859	1.2	4423	77.5	126 8	20	13.30	0.3	1.8	35
8732-39*	20.2	-32.9	880	1.0	681	3.0	2098	2.3	9958	93.4	132 6	32	13.38	0.2	1.5	88
8832-60	20.5	-32.6	850	0.7	525	1.2	934	1.2	4423	84.1	120 7	20	13.10	0.3	2.2	65
8732-40*	20.5	-32.6	730	0.9	940	2.8	3086	2.3	9958	88	124 5	28	13.48	0.1	1.9	170
<b>Borehole Samples</b>													<b>Depth (m)</b>			
<i>QU 1/65 Quagga's Fontein</i>																
8732-95	21.4	-31.8	11	0.7	751	1.0	1030	1.0	3427	23.8	130 7	20	13.78	0.2	1.8	100
QU 335	21.4	-31.8	103	0.6	483	0.9	799	1.1	3427	25.4	112 7	20	13.48	0.2	1.9	100
QU 741	21.4	-31.8	228	0.5	186	0.9	304	1.1	3427	16.9	114 11	11				
8732-96*	21.4	-31.8	397	1.1	520	1.2	872	1.3	7331	91.3	130 8	20	13.18	0.3	2.1	50
8732-98*	21.4	-31.8	925	1.5	685	2.9	1329	1.3	12343	29.0	116 6	22	13.03	0.3	2.1	52
8732-97	21.4	-31.8	1358	0.7	255	1.5	555	1.0	3427	27.2	83 7	17	13.00	0.4	1.8	21
8732-100	21.4	-31.8	1942	0.4	601	1.4	2246	1.0	3427	0.0	45 4	20	11.23	0.6	3.6	42
8732-101	21.4	-31.8	2148	0.2	231	0.9	1326	1.1	3427	0.0	30 8	20	9.64	0.4	2.8	56
8732-102	21.4	-31.8	2318	0.1	113	0.4	474	1.1	3427	65.3	44 5	20	10.72	0.5	2.8	27
8732-103	21.4	-31.8	2435	0.3	264	4.4	3650	1.3	5435	0.0	16 2	15	9.93	0.4	2.6	53
8732-105*	21.4	-31.8	2545	0.2	333	4.5	6602	1.3	7331	0.5	11 1	20	9.83	0.4	2.7	41
<i>KC 1/70 Leeuweriet (Klip Cypher)</i>																
KC-1	20.6	-31.4	222	0.1	162	0.2	209	1.1	3427	97.9	146 16	18	13.77	0.4	2.3	35
KC-3	20.6	-31.4	838	0.3	262	0.4	348	1.1	3427	95.5	142 12	18	13.90	0.4	1.5	15
KC-6	20.6	-31.4	1608	0.3	246	0.6	579	1.1	3427	70.1	81 6	19	12.58	0.2	1.7	53
KC-8	20.6	-31.4	2178	0.5	846	1.6	2742	1.1	3427	18.1	60 3	20	11.94	0.1	1.4	101
KC-21	20.6	-31.4	6190	0.0	0	2.4	1125	1.1	3427		0	4				

**Table A6-1: Results of apatite fission track analysis from Brown (1992).** a:  $\rho_i, s, d$  are track density of induced, spontaneous, dosimeter tracks. b:  $N_i, s, d$  are the number of induced, spontaneous and dosimeter tracks counted. c: p-value of the chi-sq age homogeneity test (Galbraith, 2010; see appendix 3.1). d: Ages were calculated using a  $\zeta = 350.2 \pm 5$  for a NBS glass SRM 612. e: SD is the standard deviation of measured horizontal confined track lengths. f: HCT = Horizontal Confined Track.

## A7 ADDITIONAL THERMAL HISTORY MODELS

Additional thermal history models and the original QTQt data files for all outcrop samples can be found in the supplementary electronic appendix. The models can be accessed by following the simple path:

*Appendix7 > SAMPLE NAME/PROFILE NAME > AFT/NoRD/RDF/RDG > Plots > #####.svg*

*e.g. > Appendix 7 > NQ12-04 > RDF > Plots > NQ12-04\_AFT\_AHe\_RDF\_NoFrag\_4\_ExpectedTt.svg*

Plots are saved as unedited .svg or .pdf files generated by QTQt.

The QTQt files were created using the following template:

NQ12-04	sample name
17.929 -30.403 720	longitude, latitude, Elevation (m)
0 100 19 316.7 1660000 16348	no. of T-t points <sup>1</sup> , N <sub>lengths</sub> , N <sub>counts</sub> , Zeta, ρ <sub>d</sub> , N <sub>d</sub>
105	code for annealing model <sup>2</sup>
0 1.643 0.15	code for composition <sup>3</sup> , Value, error on value
1 16.3	code for initial track length <sup>4</sup>
1	code for project track data <sup>5</sup>
0	code for Cf tracks <sup>6</sup>
0	code for etchant <sup>7</sup>
#### # # # #	Time, δTime, Temp, δTemp <sup>8</sup>
#### # # # #	Present Temp, δTemp <sup>8</sup>
89.6 4.1	FT age, error on FT age (Ma)
13.85 0.1	MTL, error on MTL (µm)
0.98 0.098	MTL Std Dev, error on MTL Std Dev (µm)
92 207	Ns, Ni
" "	
16.21 56.618	Individual track length, angle to c-axis
" "	
9	No. of AHe ages
0	code for radiation damage model <sup>9</sup>
1.36E+11 1.01E+12 3.32E+11 0 -96.42 10.58 328.62 106.08 0	He, U, Th, Sm <sup>10</sup> , Age (Ma) <sup>11</sup> , error on age, grain length, width, height <sup>12</sup>
20 0.005 138000	α-ejection distance, Do (m2/s), activation energy (Jmol/K)
" " " " " " " " " "	
" " " " " " " " " "	

1 When this value = 0 no temperature-time constraints are set.

2 105 = Ketcham, 2007, multikinetic annealing model.

3 0 = D<sub>par</sub>

4 1 = calculate compositionally dependent initial length

5 1 = use projected length model

6 0 = No Cf tracks

7 0 = 5.5 Molar

8 These values represent T-t constant points and are only present if no. of T-t points (see comment 1) does not equal 0.

9 0 – no Radiation Damage, 1 – Gautheron et al (2009), 2 – Flowers et al (2009)

10 He, U, Th, Sm are entered as atoms.

11 age set to a negative value to triggers sampling from a distribution centred on the observed age/input error.

12 grain dimensions are in µm, when height is set to 0, it is assumed height = width.

**Table A 7-1: QTQt input file example and template guide.**



## REFERENCES

- Adamson, R. S. (1931). Note on some petrified wood from Banke, Namaqualand. *Transactions of the Royal Society of South Africa*, 19(3), 255-258.
- Aitken, A. R. A., Raimondo, T., & Capitanio, F. A. (2013). The intraplate character of supercontinent tectonics. *Gondwana Research*, 24(3), 807-814.
- Altermann, W., & Hälbich, I. W. (1990). Thrusting, folding and stratigraphy of the Ghaap Group along the southwestern margin of the Kaapvaal Craton. *South African Journal of Geology*, 93(4), 553-566.
- Altermann, W., & Hälbich, I. W. (1991). Structural history of the southwestern corner of the Kaapvaal Craton and the adjacent Namaqua realm: new observations and a reappraisal. *Precambrian Research*, 52(1), 133-166.
- Altermann, W., & Nelson, D. R. (1998). Sedimentation rates, basin analysis and regional correlations of three Neoproterozoic and Palaeoproterozoic sub-basins of the Kaapvaal craton as inferred from precise U-Pb zircon ages from volcanoclastic sediments. *Sedimentary Geology*, 120(1), 225-256.
- Andersen, N. J. B., Faurie, J. N., & Fernandez, L. M. (1986). Geophysical investigations on the Vaalputs radioactive waste disposal site in the Republic of South Africa. In Ainslie, L. C. (ed.), *Radwaste '86: proceedings volume*, Nuclear Development Corp. of South Africa (Pty.) Ltd., Pelindaba, Pretoria, p. 1048.
- Andersen, T. B., Corfu, F., Labrousse, L., & Osmundsen, P. T. (2012). Evidence for hyperextension along the pre-Caledonian margin of Baltica. *Journal of the Geological Society*, 169(5), 601-612.
- Anderson, D. L., & Natland, J. H. (2005). A brief history of the plume hypothesis and its competitors: concept and controversy. *Geological Society of America Special Papers*, 388, 119-145.
- Anderson, L., Ferraccioli, F., Eagles, G., Steinberger, B., & Ritsema, J. (2012, April). Spatial and Temporal variability in Dynamic Topography in East Antarctica. In EGU General Assembly Conference Abstracts, 14, 10926).
- Andreoli, M. A. G., Brynard, H. J., Anderson, N. J. B., Hart, R. J., Moore, J. M., Smith, C., Price, B., Ashwal, L. D. & Welke, H. (1990). The geology of the Vaalputs radioactive waste disposal site, with implications for granite-charnockite relationships and crustal evolution in western Namaqualand. *Geological Society of South Africa*, 787, 16-19.
- Andreoli, M. A. G., Doucouré, M., Van Bever Donker, J., Brandt, D., & Andersen, N. J. B. (1996). Neotectonics of southern Africa. *Africa Geoscience Review*, 3, 1-16.
- Andreoli, M. A., Hart, R. J., Ashwal, L. D., & Coetzee, H. (2006). Correlations between U, Th content and metamorphic grade in the western Namaqualand Belt, South Africa, with implications for radioactive heating of the crust. *Journal of Petrology*, 47(6), 1095-1118.
- Andreoli, M. A., Viola, G., Kounov, A., Scheepers, J., Heidbach, O., & Stengel, I. (2009). History of stress at Vaalputs, Namaqualand, South Africa: evidence for a Mid-Cretaceous "Wegener-type Orogeny" in western southern Africa. 11th SAGA Biennial Technical Meeting and Exhibition.
- Armitage, J. J., Collier, J. S., & Minshull, T. A. (2010). The importance of rift history for volcanic margin formation. *Nature*, 465(7300), 913-917.
- Armitage, J. J., Jaupart, C., Fourel, L., & Allen, P. A. (2013). The instability of continental passive margins and its effect on continental topography and heat flow. *Journal of Geophysical Research: Solid Earth*, 118(4), 1817-1836.
- Aslanian, D., & Moulin, M. (2013). Palaeogeographic consequences of conservative models in the South Atlantic Ocean. *Geological Society, London, Special Publications*, 369(1), 75-90.
- Aslanian, D., Moulin, M., Olivet, J. L., Unternehr, P., Matias, L., Bache, F., Rabineau, M., Nouzé, M., Klingelhoefer, F., Contrucci, I. & Labails, C. (2009). Brazilian and African passive margins of the Central Segment of the South Atlantic Ocean: Kinematic constraints. *Tectonophysics*, 468(1), 98-112.
- Ault, A. K., & Flowers, R. M. (2012). Is apatite U-Th zonation information necessary for accurate interpretation of apatite (U-Th)/He thermochronometry data?. *Geochimica et Cosmochimica Acta*, 79, 60-78.

- Ault, A. K., Flowers, R. M., & Bowring, S. A. (2009). Phanerozoic burial and unroofing history of the western Slave craton and Wopmay orogen from apatite (U-Th)/He thermochronometry. *Earth and Planetary Science Letters*, 284(1), 1-11.
- Autin, J., Bellahsen, N., Leroy, S., Husson, L., Beslier, M. O., & d'Acremont, E. (2013). The role of structural inheritance in oblique rifting: insights from analogue models and application to the Gulf of Aden. *Tectonophysics*, 607, 51-64.
- Baker, J. A., Thirlwall, M. F., & Menzies, M. A. (1996). Sr- Nd- Pb isotopic and trace element evidence for crustal contamination of plume-derived flood basalts: Oligocene flood volcanism in western Yemen. *Geochimica et Cosmochimica Acta*, 60(14), 2559-2581.
- Balestrieri, M. L., Stuart, F. M., Persano, C., Abbate, E., & Bigazzi, G. (2005). Geomorphic development of the escarpment of the Eritrean margin, southern Red Sea from combined apatite fission-track and (U-Th)/He thermochronometry. *Earth and Planetary Science Letters*, 231(1), 97-110.
- Ballard, S., & Pollack, H. N. (1987). Diversion of heat by Archean cratons: a model for southern Africa. *Earth and Planetary Science Letters*, 85(1), 253-264.
- Bamford, M. K. (2000). Fossil woods of Karoo age deposits in South Africa and Namibia as an aid to biostratigraphical correlation. *Journal of African Earth Sciences*, 31(1), 119-132.
- Bamford, M. K. (2004). Diversity of the woody vegetation of Gondwanan southern Africa. *Gondwana Research*, 7(1), 153-164.
- Bamford, M. K., & Corbett, I. B. (1994). Fossil wood of Cretaceous age from the Namaqualand continental shelf, South Africa. *Palaeontologia africana*, 31, 83-95.
- Bamford, M. K., & Corbett, I. B. (1995). More fossil wood from the Namaqualand coast, South Africa; onshore material. *Palaeontologia africana*, 32, 67-74.
- Bamford, M. K., & Stevenson, I. R. (2002). A submerged Late Cretaceous podocarpaceous forest, west coast, South Africa: research letter. *South African journal of science*, 98(3 & 4), 181-185.
- Baptiste, V., & Tommasi, A. (2013). Petrophysical constraints on the seismic properties of the Kaapvaal craton mantle root. *Solid Earth Discussions*, 5, 963-1005.
- Baptiste, V., Tommasi, A., & Demouchy, S. (2012). Deformation and hydration of the lithospheric mantle beneath the Kaapvaal craton, South Africa. *Lithos*, 149, 31-50.
- Barbarand, J., Carter, A., Wood, I., & Hurford, T. (2003). Compositional and structural control of fission-track annealing in apatite. *Chemical Geology*, 198(1), 107-137.
- Bauer, K., Neben, S., Schreckenberger, B., Emmermann, R., Hinz, K., Fechner, N., Gohl, K., Schulze, A., Trumbull, R. B. & Weber, K. (2000). Deep structure of the Namibia continental margin as derived from integrated geophysical studies. *Journal of Geophysical Research: Solid Earth (1978-2012)*, 105(B11), 25829-25853.
- Beaumont, C., & Ings, S. J. (2012). Effect of depleted continental lithosphere counterflow and inherited crustal weakness on rifting of the continental lithosphere: General results. *Journal of Geophysical Research: Solid Earth (1978-2012)*, 117, B08407
- Beaumont, C., Fullsack, P., & Hamilton, J. (1992). Erosional control of active compressional orogens. In McClay, K. R. (ed.), *Thrust tectonics* (pp. 1-18). Netherlands: Springer.
- Beaumont, C., Kooi, H., & Willett, S. (2000). Coupled tectonic-surface process models with applications to rifted margins and collisional orogens. In Summerfield, M. A. (ed.), *Geomorphology and global tectonics*, p. 29-55. Chichester, UK: Wiley
- Becker, K., Franke, D., Trumbull, R., Schnabel, M., Heyde, I., Schreckenberger, B., Koopmann, H., Bauer, K., Jokat, W. & Krawczyk, C. M. (2014). Asymmetry of high-velocity lower crust on the South Atlantic rifted margins and implications for the interplay of magmatism and tectonics in continental breakup. *Solid Earth*, 5, 1011-1026.
- Begg, G. C., Griffin, W. L., Natapov, L. M., O'Reilly, S. Y., Grand, S. P., O'Neill, C. J., Hronsky, J. M. A., Djomani, Y. P., Swain, C. J., Deen, T., & Bowden, P. (2009). The lithospheric architecture of Africa: Seismic tomography, mantle petrology, and tectonic evolution. *Geosphere*, 5(1), 23-50.
- Belton, D. X., Lorencak, M., Carter, T. J., Norman, M., Kohn, B. P., & Gleadow, A. J. W. (2004). Samarium in apatite: contributions to radiogenic helium and the effect on (U-Th)/He thermochronology. In 10th International Fission track Dating Conference. Amsterdam (p. 40).
- Ben-Avraham, Z., Smith, G., Reshef, M., & Jungslager, E. (2002). Gas hydrate and mud volcanoes on the southwest African continental margin off South Africa. *Geology*, 30(10), 927-930.

- Berhe, S. M., Desta, B., Nicoletti, M., & Teferra, M. (1987). Geology, geochronology and geodynamic implications of the Cenozoic magmatic province in W and SE Ethiopia. *Journal of the Geological Society*, 144(2), 213-226.
- Beucher, R., Brown, R. W., Roper, S., Stuart, F., & Persano, C. (2013). Natural age dispersion arising from the analysis of broken crystals: Part II. Practical application to apatite (U-Th)/He thermochronometry. *Geochimica et Cosmochimica Acta*, 120, 395-416.
- Beukes, N. J., & Gutzmer, J. E. N. S. (2008). Origin and paleoenvironmental significance of major iron formations at the Archean-Paleoproterozoic boundary. *Reviews in Economic Geology*, 15, 5-47.
- Bezerra, F. H. R., Rossetti, D. F., Oliveira, R. G., Medeiros, W. E., Neves, B. B., Balsamo, F., Nogueira, F. C. C., Dantas, E. L., Andrades Filho, C. & Góes, A. M. (2014). Neotectonic reactivation of shear zones and implications for faulting style and geometry in the continental margin of NE Brazil. *Tectonophysics*, 614, 78-90
- Bierman, P. R., & Caffee, M. (2001). Slow rates of rock surface erosion and sediment production across the Namib Desert and escarpment, southern Africa. *American Journal of Science*, 301(4-5), 326-358.
- Bierman, P. R., Coppersmith, R., Hanson, K., Neveling, J., Portenga, E. W., & Rood, D. H. (2014). A cosmogenic view of erosion, relief generation, and the age of faulting in southern Africa. *GSA Today*, 24(9), 4-11.
- Bird, P., Ben-Avraham, Z., Schubert, G., Andreoli, M., & Viola, G. (2006). Patterns of stress and strain rate in southern Africa. *Journal of Geophysical Research: Solid Earth* (1978-2012), 111, B08402.
- Bishop, P. (2007). Long-term landscape evolution: linking tectonics and surface processes. *Earth Surface Processes and Landforms*, 32(3), 329-365.
- Bishop, P., & Goldrick, G. (2010). Lithology and the evolution of bedrock rivers in post-orogenic settings: constraints from the high-elevation passive continental margin of SE Australia. *Geological Society, London, Special Publications*, 346(1), 267-287.
- Blaich, O. A., Faleide, J. I., & Tsikalas, F. (2011). Crustal breakup and continent-ocean transition at South Atlantic conjugate margins. *Journal of Geophysical Research: Solid Earth* (1978-2012), 116, B01402
- Blaich, O. A., Faleide, J. I., Tsikalas, F., Gordon, A. C., & Mohriak, W. (2013). Crustal-scale architecture and segmentation of the South Atlantic volcanic margin. *Geological Society, London, Special Publications*, 369(1), 167-183.
- Blenkinsop, T., and Moore, A., (2013), Tectonic geomorphology of passive margins and continental hinterlands. In: Shroder, John F., (ed.) *Treatise on Geomorphology*, p. 71-92. London, UK: Elsevier.
- Bluck, B. J., Ward, J. D., Cartwright, J., & Swart, R. (2007). The Orange River, southern Africa: an extreme example of a wave-dominated sediment dispersal system in the South Atlantic Ocean. *Journal of the Geological Society*, 164(2), 341-351.
- Bonini, M., Sani, F., & Antonielli, B. (2012). Basin inversion and contractional reactivation of inherited normal faults: A review based on previous and new experimental models. *Tectonophysics*, 522, 55-88.
- Bonow, J. M., Japsen, P., & Nielsen, T. F. (2014). High-level landscapes along the margin of southern East Greenland—A record of tectonic uplift and incision after breakup in the NE Atlantic. *Global and Planetary Change*, 116, 10-29.
- Boschi, L., Faccenna, C., and Becker, T. W., (2010). Mantle structure and dynamic topography in the Mediterranean Basin. *Geophysical Research Letters*, 37, L20303
- Bosworth, W., Guiraud, R., & Kessler, L. G. (1999). Late Cretaceous (ca. 84 Ma) compressive deformation of the stable platform of northeast Africa (Egypt): Far-field stress effects of the “Santonian event” and origin of the Syrian arc deformation belt. *Geology*, 27(7), 633-636.
- Bott, M. H. P. (1981). Crustal doming and the mechanism of continental rifting. *Tectonophysics*, 73(1), 1-8.
- Bott, M. H. P., & Kusznir, N. J. (1979). Stress distributions associated with compensated plateau uplift structures with application to the continental splitting mechanism. *Geophysical Journal International*, 56(3), 451-459.
- Bown, J. W., & White, R. S. (1995). Effect of finite extension rate on melt generation at rifted continental margins. *Journal of Geophysical Research: Solid Earth* (1978-2012), 100(B9), 18011-18029.

- Boyd, F. R. (1989). Compositional distinction between oceanic and cratonic lithosphere. *Earth and Planetary Science Letters*, 96(1), 15-26.
- Brandt, D., Andreoli, M. A. G., & McCarthy, T. S. (2003). Mesozoic fluvial deposits on a rifted continental margin near Vaalputs, Namaqualand, South Africa. *South African Journal of Geology*, 106(1), 11-16.
- Brandt, D., Andreoli, M. A. G., & McCarthy, T. S. (2005). The late Mesozoic palaeosoils and Cenozoic fluvial deposits at Vaalputs, Namaqualand, South Africa: Possible depositional mechanisms and their bearing on the evolution of the continental margin. *South African Journal of Geology*, 108(2), 271-284.
- Brandt, M. B., Grand, S. P., Nyblade, A. A., & Dirks, P. H. (2012). Upper mantle seismic structure beneath Southern Africa: constraints on the buoyancy supporting the African superswell. *Pure and applied geophysics*, 169(4), 595-614.
- Braun, J., & Beaumont, C. (1989). A physical explanation of the relation between flank uplifts and the breakup unconformity at rifted continental margins. *Geology*, 17(8), 760-764.
- Braun, J., & Van Der Beek, P. (2004). Evolution of passive margin escarpments: What can we learn from low-temperature thermochronology?. *Journal of Geophysical Research: Earth Surface* (2003-2012), 109, F04009
- Braun, J., 2010, The many surface expressions of mantle dynamics. *Nature Geoscience*. 3, 12, 825-833.
- Braun, J., Deschamps, F., Rouby, D., & Dauteuil, O. (2013a). Flexure of the lithosphere and the geodynamical evolution of non-cylindrical rifted passive margins: Results from a numerical model incorporating variable elastic thickness, surface processes and 3D thermal subsidence. *Tectonophysics*, 604, 72-82.
- Braun, J., Robert, X., & Simon-Labric, T., (2013b), Eroding dynamic topography. *Geophysical Research Letters*. 40, 8, 1494-1499
- Braun, J., Guillocheau, F., Robin, C., Baby, G., & Jelsma, H. (2014a). Rapid erosion of the Southern African Plateau as it climbs over a mantle superswell. *Journal of Geophysical Research: Solid Earth*, 119(7), 6093-6112.
- Braun, J., Simon-Labric, T., Murray, K. E., & Reiners, P. W. (2014b). Topographic relief driven by variations in surface rock density. *Nature Geoscience*.
- Braun, J., van der Beek, P., & Batt, G. (2006). Quantitative thermochronology. *Quantitative Thermochronology*, pp. 270. UK: Cambridge University Press.
- Broad, D. S., Jungslager, E. H. A., McLachlan, I. R., & Roux, J. (2006). Offshore mesozoic basins. In Johnson, M. R., Anhaeusser, C. R., and Thomas, R. J. (eds.), *The Geology of South Africa*, p. 553-571. Pretoria, South Africa: Geological Society of South Africa/Council for GeoScience.
- Brocard, G. Y., & Van der Beek, P. A. (2006). Influence of incision rate, rock strength, and bedload supply on bedrock river gradients and valley-flat widths: Field-based evidence and calibrations from western Alpine rivers (southeast France). *Geological Society of America Special Papers*, 398, 101-126.
- Brown, L. F. (Ed.). (1995). *Sequence Stratigraphy in Offshore South African Divergent Basins: An Atlas on Exploration for Cretaceous Lowstand Traps* by Soekor (Pty) Ltd, AAPG Studies in Geology 41 (No. 41). AAPG.
- Brown, R.W., 1992. A fission track thermochronology study of the tectonic and geomorphic development of the sub-aerial continental margins of southern Africa. PhD thesis, La Trobe University, Bundoora, Australia, 407 pp.
- Brown, R. W., Rust, D. J., Summerfield, M. A., Gleadow, A. J., & De Wit, M. C. (1990). An Early Cretaceous phase of accelerated erosion on the south-western margin of Africa: Evidence from apatite fission track analysis and the offshore sedimentary record. *International Journal of Radiation Applications and Instrumentation. Part D. Nuclear Tracks and Radiation Measurements*, 17(3), 339-350.
- Brown, R. W., Summerfield, M. A., & Gleadow, A. J. W. (1994). Apatite fission track analysis: Its potential for the estimation of denudation rates and implications for models of long-term landscape development. In Kirby, M. J. (ed.), *Process Models and Theoretical Geomorphology*, p. 23-53. UK: Wiley.
- Brown, R. W., Summerfield, M. A., & Gleadow, A. J. (2002). Denudational history along a transect across the Drakensberg Escarpment of southern Africa derived from apatite fission track thermochronology. *Journal of Geophysical Research: Solid Earth* (1978-2012), 107 (B12), 2350

- Brown, R. W., Beucher, R., Roper, S., Persano, C., Stuart, F., & Fitzgerald, P. (2013). Natural age dispersion arising from the analysis of broken crystals. Part I: Theoretical basis and implications for the apatite (U-Th)/He thermochronometer. *Geochimica et Cosmochimica Acta*, 122, 478-497.
- Brown, R., Summerfield, M., Gleadow, A., Gallagher, K., Carter, A., Beucher, R., & Wildman, M. (2014). Intracontinental deformation in southern Africa during the Late Cretaceous. *Journal of African Earth Sciences*, 100, 20-41.
- Brune, S., Heine, C., Pérez-Gussinyé, M., & Sobolev, S. V. (2014). Rift migration explains continental margin asymmetry and crustal hyper-extension. *Nature Communications*, 5, 1-9.
- Buck, W. R., Martinez, F., Steckler, M. S., & Cochran, J. R. (1988). Thermal consequences of lithospheric extension: pure and simple. *Tectonics*, 7(2), 213-234.
- Burbank, D. W., Blythe, A. E., Putkonen, J., Pratt-Sitaula, B. G. A. B. E. T., Gabet, E., Oskin, M., Barros, A. & Ojha, T. P. (2003). Decoupling of erosion and precipitation in the Himalayas. *Nature*, 426(6967), 652-655.
- Burke, K. (1996). The African plate. *South African Journal of Geology*, 99(4), 341-409.
- Burke, K., & Gunnell, Y. (2008). The African erosion surface: a continental-scale synthesis of geomorphology, tectonics, and environmental change over the past 180 million years. *Geological Society of America Memoirs*, 201, 1-66.
- Burke, K., & Wilson, J. T. (1972). Is the African plate stationary?. *Nature*, 239, 387 - 390
- Burov, E. B. (2011). Rheology and strength of the lithosphere. *Marine and Petroleum Geology*, 28(8), 1402-1443.
- Burov, E. B., & Watts, A. B. (2006). The long-term strength of continental lithosphere: "jelly sandwich" or "crème brûlée"?. *GSA today*, 16(1), 4.
- Burov, E., & Cloetingh, S. (2009). Controls of mantle plumes and lithospheric folding on modes of intraplate continental tectonics: differences and similarities. *Geophysical Journal International*, 178(3), 1691-1722.
- Burov, E., & Cloetingh, S. A. P. L. (1997). Erosion and rift dynamics: new thermomechanical aspects of post-rift evolution of extensional basins. *Earth and Planetary Science Letters*, 150(1), 7-26.
- Burov, E., & Guillou-Frottier, L. (2005). The plume head-continental lithosphere interaction using a tectonically realistic formulation for the lithosphere. *Geophysical Journal International*, 161(2), 469-490.
- Burov, E., Guillou-Frottier, L., d'Acromont, E., Le Pourhiet, L., & Cloetingh, S. A. P. L. (2007). Plume head-lithosphere interactions near intra-continental plate boundaries. *Tectonophysics*, 434(1), 15-38.
- Burov, E., Watts, T., Podladchikov, Y., & Evans, B. (2014). Observational and modeling perspectives on the mechanical properties of the lithosphere. *Tectonophysics*, 631, 1-3.
- Burov, E., & Gerya, T. (2014). Asymmetric three-dimensional topography over mantle plumes. *Nature*, 513(7516), 85-89.
- Burtner, R. L., Nigrini, A., & Donelick, R. A. (1994). Thermochronology of Lower Cretaceous source rocks in the Idaho-Wyoming thrust belt. *AAPG bulletin*, 78(10), 1613-1636.
- Carlson, W. D., Donelick, R. A., & Ketcham, R. A. (1999). Variability of apatite fission-track annealing kinetics: I. Experimental results. *American mineralogist*, 84, 1213-1223.
- Catuneanu, O., Hancox, P. J., & Rubidge, B. S. (1998). Reciprocal flexural behaviour and contrasting stratigraphies: a new basin development model for the Karoo retroarc foreland system, South Africa. *Basin Research*, 10(4), 417-439.
- Cayley, A., (1859), On contour lines and slope lines. *Philosophical Magazine*, 18, 264-268.
- Champagnac, J. D., Molnar, P., Sue, C., & Herman, F. (2012). Tectonics, climate, and mountain topography. *Journal of Geophysical Research: Solid Earth* (1978-2012), 117(B2).
- Chaumont, J., Soulet, S., Krupa, J. C., & Carpena, J. (2002). Competition between disorder creation and annealing in fluoroapatite nuclear waste forms. *Journal of nuclear materials*, 301(2), 122-128.
- Chen, Y., Zhang, Z., Sun, C., & Badal, J. (2013). Crustal anisotropy from Moho converted Ps wave splitting analysis and geodynamic implications beneath the eastern margin of Tibet and surrounding regions. *Gondwana Research*, 24(3), 946-957.
- Cherniak, D. J., Watson, E. B., & Thomas, J. B. (2009). Diffusion of helium in zircon and apatite. *Chemical Geology*, 268(1), 155-166.
- Chorley, R. J. (1965). The application of quantitative methods to geomorphology. *Frontiers in Geographic Teaching*, 147-163.

- Chorowicz, J. (2005). The East African rift system. *Journal of African Earth Sciences*, 43(1), 379-410.
- Clemson, J., Cartwright, J., & Booth, J. (1997). Structural segmentation and the influence of basement structure on the Namibian passive margin. *Journal of the Geological Society*, 154(3), 477-482.
- Clifford, T. N., Barton, E. S., Stern, R. A., & Duchesne, J. C. (2004). U-Pb zircon calendar for Namaquan (Grenville) crustal events in the granulite-facies terrane of the O'okiep Copper District of South Africa. *Journal of Petrology*, 45(4), 669-691.
- Cloetingh, S., & Burov, E. (2011). Lithospheric folding and sedimentary basin evolution: a review and analysis of formation mechanisms. *Basin Research*, 23(3), 257-290.
- Cloetingh, S., Burov, E., & Francois, T. (2013). Thermo-mechanical controls on intra-plate deformation and the role of plume-folding interactions in continental topography. *Gondwana Research*, 24(3), 815-837.
- Cloetingh, S., McQueen, H., & Lambeck, K. (1985). On a tectonic mechanism for regional sealevel variations. *Earth and Planetary Science Letters*, 75(2), 157-166.
- Cockburn, H. A. P., Brown, R. W., Summerfield, M. A., & Seidl, M. A. (2000). Quantifying passive margin denudation and landscape development using a combined fission-track thermochronology and cosmogenic isotope analysis approach. *Earth and Planetary Science Letters*, 179(3), 429-435.
- Cocks, L. R. M., & Torsvik, T. H. (2011). The Palaeozoic geography of Laurentia and western Laurussia: a stable craton with mobile margins. *Earth-Science Reviews*, 106(1), 1-51.
- Coetzee, J. A., & Muller, J. (1984). The phytogeographic significance of some extinct Gondwana pollen types from the Tertiary of the southwestern Cape (South Africa). *Annals of the Missouri Botanical Garden*, 71(4), 1088-1099.
- Coetzee, J. A., & Praglowski, J. (1986). Pollen evidence for the occurrence of *Casuarina* and *Myrica* in the Tertiary of South Africa. *Grana*, 23(1), 23-41.
- Coetzee, J. A., & Rogers, J. (1982). Palynological and lithological evidence for the Miocene palaeoenvironment in the Saldanha region (South Africa). *Palaeogeography, Palaeoclimatology, Palaeoecology*, 39(1), 71-85.
- Coffin, M. F., & Rabinowitz, P. D. (1987). Reconstruction of Madagascar and Africa: evidence from the Davie fracture zone and western Somali basin. *Journal of Geophysical Research: Solid Earth* (1978-2012), 92(B9), 9385-9406.
- Cogné, N., Gallagher, K., & Cobbold, P. R. (2011). Post-rift reactivation of the onshore margin of southeast Brazil: Evidence from apatite (U-Th)/He and fission-track data. *Earth and Planetary Science Letters*, 309(1), 118-130.
- Cogné, N., Gallagher, K., Cobbold, P. R., Riccomini, C., & Gautheron, C. (2012). Post-breakup tectonics in southeast Brazil from thermochronological data and combined inverse-forward thermal history modeling. *Journal of Geophysical Research: Solid Earth* (1978-2012), 117(B11).
- Colberg, J. S., & Anders, A. M. (2014). Numerical modeling of spatially-variable precipitation and passive margin escarpment evolution. *Geomorphology*, 207, 203-212.
- Colliston, W. P., Schoch, A. E., & Cole, J. (2014). The Grenvillian Namaqua-Natal fold belt adjacent to the Kaapvaal Craton: 1. Distribution of Mesoproterozoic collisional terranes deduced from results of regional surveys and selected profiles in the western and southern parts of the fold belt. *Journal of African Earth Sciences*, 100, 7-19.
- Conrad, C. P., & Gurnis, M. (2003). Seismic tomography, surface uplift, and the breakup of Gondwanaland: Integrating mantle convection backwards in time. *Geochemistry, Geophysics, Geosystems*, 4(3).
- Conrad, C. P., & Husson, L. (2009). Influence of dynamic topography on sea level and its rate of change. *Lithosphere*, 1(2), 110-120.
- Cooke, H. B. S. (1968). The fossil mammal fauna of Africa. *Quarterly Review of Biology*, 234-264.
- Cooper, C. M., & Miller, M. S. (2014). Craton formation: Internal structure inherited from closing of the early oceans. *Lithosphere*, 6(1), 35-42.
- Cooper, M. R. (1985). A revision of the ornithischian dinosaur *Kangnasaurus coetzeei* Haughton, with a classification of the Ornithischia. *South African Museum*.
- Corbett, I. B. (1989). The sedimentology of diamondiferous deflation deposits within the Sperrgebiet, Namibia (Doctoral dissertation, University of Cape Town).
- Cornelissen, A. K., & Verwoerd, W. J. (1975). The Bushmanland kimberlites and related rocks. *Physics and Chemistry of the Earth*, 9, 71-80.

- Cornell, D. H., Thomas, R. J., Gibson, R., Moen, H. F. G., Reid, D. L., Moore, J. M., & Gibson, R. L. (2006). The Namaqua-Natal Province. In Johnson, M. R., Anhaeusser, C. R., and Thomas, R. J. (eds.), *The Geology of South Africa*. Pretoria, South Africa: Geological Society of South Africa/Council for GeoScience.
- Corner, B., Cartwright, J., & Swart, R. (2002). Volcanic passive margin of Namibia: A potential fields perspective. *Geological Society of America, Special Papers*, 362, 203-220.
- Corti, G. (2012). Evolution and characteristics of continental rifting: Analog modeling-inspired view and comparison with examples from the East African Rift System. *Tectonophysics*, 522, 1-33.
- Corti, G., Ranalli, G., Agostini, A., & Sokoutis, D. (2013). Inward migration of faulting during continental rifting: Effects of pre-existing lithospheric structure and extension rate. *Tectonophysics*, 594, 137-148.
- Corti, G., van Wijk, J., Cloetingh, S., & Morley, C. K. (2007). Tectonic inheritance and continental rift architecture: Numerical and analogue models of the East African Rift system. *Tectonics*, 26(6).
- Corvinus, G., & Hendey, Q. B. (1978). A new Miocene vertebrate locality at Arrisdrift in South West Africa (Namibia). *Jb. Geol. Paläont. Mh*, 4, 193-205.
- Cowie, P. A., Attal, M., Tucker, G. E., Whittaker, A. C., Naylor, M., Ganas, A., & Roberts, G. P. (2006). Investigating the surface process response to fault interaction and linkage using a numerical modelling approach. *Basin Research*, 18(3), 231-266.
- Cox, K. G. (1992). Karoo igneous activity, and the early stages of the break-up of Gondwanaland. *Geological Society, London, Special Publications*, 68(1), 137-148.
- Cox, K. G. (1993). Continental magmatic underplating. *Philosophical Transactions of the Royal Society of London. Series A: Physical and Engineering Sciences*, 342(1663), 155-166.
- Crowley, K., Cameron, M., & McPherson, B. (1990). Annealing of etchable fission-track damage in F-, OH-, Cl- and Sr-apatite: 1. Systematics and preliminary interpretations. *International Journal of Radiation Applications and Instrumentation. Part D. Nuclear Tracks and Radiation Measurements*, 17(3), 409-410.
- Crowley, K. D., Cameron, M., & Schaefer, R. L. (1991). Experimental studies of annealing of etched fission tracks in fluorapatite. *Geochimica et Cosmochimica Acta*, 55(5), 1449-1465.
- Curtis, C. G., Trumbull, R. B., de Beer, C. H., Harris, C., Reid, D. L., & Romer, R. L. (2011). Geochemistry of the early Cretaceous Koegel Fontein anorogenic igneous complex, South Africa. *South African Journal of Geology*, 114(3-4), 353-378.
- Curtis, C. G., Harris, C., Trumbull, R. B., de Beer, C., & Mudzanani, L. (2013). Oxygen Isotope Diversity in the Anorogenic Koegel Fontein Complex of South Africa: a Case for Basement Control and Selective Melting for the Production of Low- $\delta^{18}\text{O}$  Magmas. *Journal of Petrology*, 54(7), 1259-1283.
- Czarnota, K., Hoggard, M. J., White, N., & Winterbourne, J. (2013). Spatial and temporal patterns of Cenozoic dynamic topography around Australia. *Geochemistry, Geophysics, Geosystems*, 14(3), 634-658.
- Daly, M. C., Chorowicz, J., & Fairhead, J. D. (1989). Rift basin evolution in Africa: the influence of reactivated steep basement shear zones. *Geological Society, London, Special Publications*, 44(1), 309-334.
- Danišík, M., Štěpančíková, P., & Evans, N. J. (2012). Constraining long-term denudation and faulting history in intraplate regions by multisystem thermochronology: An example of the Sudetic Marginal Fault (Bohemian Massif, central Europe). *Tectonics*, 31(2), TC2003.
- Dauteuil, O., Bessin, P., & Guillocheau, F. (2014). Topographic growth around the Orange River valley, southern Africa: a Cenozoic record of crustal deformation and climatic change. *Geomorphology*, *in press*.
- Dauteuil, O., Deschamps, F., Bourgeois, O., Mocquet, A., & Guillocheau, F. (2013). Post-breakup evolution and palaeotopography of the North Namibian Margin during the Meso-Cenozoic. *Tectonophysics*, 589, 103-115.
- Dávila, F. M., and Lithgow-Bertelloni, C. (2013). Dynamic topography in South America, *Journal of South American Earth Sciences*, 43, 127 - 144.
- Davis, G. L. (1977). The ages and uranium contents of zircons from kimberlites and associated rocks. *Carnegie Institution of Washington Yearbook*, 76, 631-654.
- Davis, M., & Kusznir, N. J. (2004). Depth-dependent lithospheric stretching at rifted continental margins. *Proceedings of NSF Rifted Margins Theoretical Institute*, 92-136.
- Davis, W. M. (1899). The geomorphological cycle. *Geographical Journal*, 14, 481-504.

- Day, R. W. (1987). False Bay dolerites. *Annals Geological Survey of South Africa*, 21, 1-7.
- de Beer, C. H. (2010). The geology of the Garies area: Explanation of 1:250 000-scale Sheet 3017 Garies. South Africa: Council for Geoscience
- de Beer, C. H. (2012). Evidence of Neogene to Quaternary faulting and seismogenic deformation along the Namaqualand coast, South Africa. *South African Journal of Geology*, 115(2), 117-136.
- de Beer, C. H., & Council for geoscience. (2002). The Geology of the Calvinia Area: Explanation of 1: 250 000-scale Sheet 3118 Calvinia. South Africa: Council for Geoscience.
- de Broin, F. D. L. (2003). The Miocene chelonians from the southern Namibia, Faunas from the southern Namibia. *Memoir of the Geological Survey of Namibia*, 19, 67-102.
- de Swardt, A. M. J., & Bennet, G. (1974). Structural and physiographic development of Natal since the late Jurassic. *Transactions of the Geological Society of South Africa*, 77, 309-322.
- de Vera, J., Granado, P., & McClay, K. (2010). Structural evolution of the Orange Basin gravity-driven system, offshore Namibia. *Marine and Petroleum Geology*, 27(1), 223-237.
- de Wit, M. C. J. (1988). Aspects of the geomorphology of the north-western Cape, South Africa. In Dardis, G. F. and Moon, B. P. (eds.), *Geomorphological studies in southern Africa*, p. 57-69, Rotterdam, Netherlands: CRC Press.
- de Wit, M. C. J. (1999). Post-Gondwana drainage and the development of diamond placers in western South Africa. *Economic Geology*, 94(5), 721-740.
- de Wit, M. C. J., Ward, J. D., Bamford, M. K., & Roberts, M. J. (2009). The significance of the Cretaceous diamondiferous gravel deposit at Mahura Muthla, Northern Cape province, South Africa. *South African Journal of Geology*, 112(2), 89-108.
- Decker, J. E., Niedermann, S., & de Wit, M. J. (2011). Soil erosion rates in South Africa compared with cosmogenic <sup>3</sup>He-based rates of soil production. *South African Journal of Geology*, 114(3-4), 475-488.
- Dewey, J. F., & Burke, K. (1975). Hot spots and continental break-up: implications for collisional orogeny. *Geology*, 2(2), 57-60.
- Dewey, J. F., Robb, L., & Van Schalkwyk, L. (2006). Did Bushmanland extensionally unroof Namaqualand?. *Precambrian Research*, 150(3), 173-182.
- Dhansay, T., de Wit, M., & Patt, A. (2014). An evaluation for harnessing low-enthalpy geothermal energy in the Limpopo Province, South Africa. *South African Journal of Science*, 110(3-4), 1-10.
- Di Caprio, L., Gurnis, M., Muller, R. D., and Tan, E., Mantle dynamics of continentwide Cenozoic subsidence and tilting of Australia, *Lithosphere*, 3(5), 311 - 316
- Dingle, R. V., & Hendry, Q. B. (1984). Late Mesozoic and Tertiary sediment supply to the eastern Cape Basin (SE Atlantic) and palaeo-drainage systems in southwestern Africa. *Marine Geology*, 56(1), 13-26.
- Dingle, R. V., & Robson, S. H. (1992). Southwestern Africa continental rise: structural and sedimentary evolution, In Poag, W. and de Graciansky, P. C. (eds.), *Geologic evolution of Atlantic continental rifts*, p. 62-75. New York: Van Nostrand Reinhold.
- Dingle, R. V., Siesser, W. G., & Newton, A. R. (1983). *Mesozoic and Tertiary geology of southern Africa: A Global Approach to Geology*, pp. 375, Taylor Francis.
- Dixey, F. (1955). Erosion surfaces in Africa; some considerations of age and origin. *Transactions Geological Society South Africa*, 58, 265-280.
- Dobson, K. J., Stuart, F. M., & Dempster, T. J. (2008). U and Th zonation in Fish Canyon Tuff zircons: Implications for a zircon (U-Th)/He standard. *Geochimica et Cosmochimica Acta*, 72(19), 4745-4755.
- Dodson, M. H. (1973). Closure temperature in cooling geochronological and petrological systems. *Contributions to Mineralogy and Petrology*, 40(3), 259-274.
- Dollar, E. S. (1998). Palaeofluvial geomorphology in southern Africa: a review. *Progress in physical geography*, 22(3), 325-349.
- Donelick, R. A. (1991). Crystallographic orientation dependence of mean etchable fission track length in apatite: An empirical model and experimental observations. *American Mineralogist*, 76, 83-91.
- Donelick, R. A., Ketcham, R. A., & Carlson, W. D. (1999). Variability of apatite fission-track annealing kinetics: II. Crystallographic orientation effects. *American Mineralogist*, 84, 1224-1234.
- Donelick, R. A., O'Sullivan, P. B., & Ketcham, R. A. (2005). Apatite fission-track analysis. *Reviews in Mineralogy and Geochemistry*, 58(1), 49-94.



- Donelick, R. A., Roden, M. K., Mooers, J. D., Carpenter, B. S., & Miller, D. S. (1990). Etchable length reduction of induced fission tracks in apatite at room temperature ( $\approx 23^\circ \text{C}$ ): Crystallographic orientation effects and "initial" mean lengths. *International Journal of Radiation Applications and Instrumentation. Part D. Nuclear Tracks and Radiation Measurements*, 17(3), 261-265.
- Donelick, R., Farley, K., Asimow, P. D., & O'Sullivan, P. (2003). Pressure dependence of He diffusion and fission-track annealing kinetics in apatite?: Experimental results. *Geochimica et Cosmochimica Acta*, 67(18), A82.
- Doucouré, C. M., & de Wit, M. J. (2003). Old inherited origin for the present near-bimodal topography of Africa. *Journal of African Earth Sciences*, 36(4), 371-388.
- Du Toit A. L. (1937) Our wandering continents. A hypothesis of continental drifting. London, UK: Oliver and Boyd.
- Du Toit A. L. (1954) The geology of South Africa. pp. 611, Edinburgh, UK: Oliver and Boyd.
- Duddy, I. R., Green, P. F., & Laslett, G. M. (1988). Thermal annealing of fission tracks in apatite 3. Variable temperature behaviour. *Chemical Geology: Isotope Geoscience section*, 73(1), 25-38.
- Duddy, I. R., Green, P. F., Hegarty, K. A., Bray, R. J., & O'Brien, G. W. (1998). Dating and duration of hot fluid flow events determined using AFTA and vitrinite reflectance-based thermal history reconstruction. *Geological Society, London, Special Publications*, 144(1), 41-51.
- Dumitru, T. A. (1993). A new computer-automated microscope stage system for fission-track analysis. *Nuclear Tracks and Radiation Measurements*, 21(4), 575-580.
- Dunai, T. J. (2005). Forward modeling and interpretation of (U-Th)/He ages. *Reviews in mineralogy and geochemistry*, 58(1), 259-274.
- Duncan, A. R., & Marsh, J. S. (2006). The Karoo igneous province. In Johnson, M. R., Anhaeusser, C. R., and Thomas, R. J. (eds.), *The Geology of South Africa*, p. 501-520. Pretoria, South Africa: Geological Society of South Africa/Council for GeoScience.
- Duncan, R. A., Hooper, P. R., Rehacek, J., Marsh, J. S., & Duncan, A. R. (1997). The timing and duration of the Karoo igneous event, southern Gondwana. *Journal of Geophysical Research: Solid Earth (1978-2012)*, 102(B8), 18127-18138.
- Eagles, G. (2007). New angles on South Atlantic opening. *Geophysical Journal International*, 168(1), 353-361.
- Eagles, G., & König, M. (2008). A model of plate kinematics in Gondwana breakup. *Geophysical Journal International*, 173(2), 703-717.
- Ebbing, J., Lundin, E., Olesen, O., & Hansen, E. K. (2006). The mid-Norwegian margin: a discussion of crustal lineaments, mafic intrusions, and remnants of the Caledonian root by 3D density modelling and structural interpretation. *Journal of the Geological Society*, 163(1), 47-59.
- Ebinger, C. J., Yemane, T., Harding, D. J., Tesfaye, S., Kelley, S., & Rex, D. C. (2000). Rift deflection, migration, and propagation: Linkage of the Ethiopian and Eastern rifts, Africa. *Geological Society of America Bulletin*, 112(2), 163-176.
- Ebinger, C., & Scholz, C. A. (2011). Continental rift basins: the East African perspective. In Busby, C., & Azor Perez, A., *Tectonics of Sedimentary Basins: Recent Advances*. p. 183-208. Wiley-Blackwell
- Egholm, D.L., Knudsen, M.F. & Sandiford, M. (2013). Lifespan of mountain ranges scaled by feedbacks between landsliding and erosion by rivers. *Nature*, 498, 475-478.
- Eglington, B. M. (2006). Evolution of the Namaqua-Natal Belt, southern Africa-A geochronological and isotope geochemical review. *Journal of African Earth Sciences*, 46(1), 93-111.
- Ehlers, T. A., & Farley, K. A. (2003). Apatite (U-Th)/He thermochronometry: methods and applications to problems in tectonic and surface processes. *Earth and Planetary Science Letters*, 206(1), 1-14.
- Ehlers, T. A., Armstrong, P. A., & Chapman, D. S. (2001). Normal fault thermal regimes and the interpretation of low-temperature thermochronometers. *Physics of the Earth and Planetary Interiors*, 126(3), 179-194.
- Elliot, D. H., & Fleming, T. H. (2000). Weddell triple junction: The principal focus of Ferrar and Karoo magmatism during initial breakup of Gondwana. *Geology*, 28(6), 539-542.
- Emery, K. O., Uchupi, E., Bowin, C. O., Phillips, J., & Simpson, E. S. W. (1975). Continental margin off western Africa: Cape St. Francis (South Africa) to Walvis Ridge (South-West Africa). *AAPG Bulletin*, 59(1), 3-59.

- Emmel, B., Lisker, F., & Hewawasam, T. (2012). Thermochronological dating of brittle structures in basement rocks: A case study from the onshore passive margin of SW Sri Lanka. *Journal of Geophysical Research: Solid Earth* (1978-2012), 117(B10).
- England, P., & Molnar, P. (1990). Surface uplift, uplift of rocks, and exhumation of rocks. *Geology*, 18(12), 1173-1177.
- Eriksson, P. G., Altermann, W., & Hartzler, F. J. (2006). The Transvaal Supergroup and its precursors. In Johnson, M. R., Anhaeusser, C. R., and Thomas, R. J. (eds.), *The Geology of South Africa*, p. 237-260. Pretoria, South Africa: Geological Society of South Africa/Council for GeoScience.
- Eriksson, P. G., Banerjee, S., Nelson, D. R., Rigby, M. J., Catuneanu, O., Sarkar, S., Roberts, R. J., Ruban, D., Mtinkulu, M. N. & Sunder Raju, P. V. (2009). A Kaapvaal craton debate: nucleus of an early small supercontinent or affected by an enhanced accretion event?. *Gondwana Research*, 15(3), 354-372.
- Erlanger, E. D., Granger, D. E., & Gibbon, R. J. (2012). Rock uplift rates in South Africa from isochron burial dating of fluvial and marine terraces. *Geology*, 40(11), 1019-1022.
- Estes, R. (1977). Relationships of the South African fossil frog *Eoxenopoides reuningi* (Anura, Pipidae). *South African Museum, Annals*. 73(2), 1-36.
- Farley, K. A. (2000). Helium diffusion from apatite: General behavior as illustrated by Durango fluorapatite. *Journal of Geophysical Research: Solid Earth* (1978-2012), 105(B2), 2903-2914.
- Farley, K. A. (2002). (U-Th)/He dating: Techniques, calibrations, and applications. *Reviews in Mineralogy and Geochemistry*, 47(1), 819-844.
- Farley, K. A., & Stockli, D. F. (2002). (U-Th)/He dating of phosphates: Apatite, monazite, and xenotime. *Reviews in mineralogy and geochemistry*, 48(1), 559-577.
- Farley, K. A., Shuster, D. L., & Ketcham, R. A. (2011). U and Th zonation in apatite observed by laser ablation ICPMS, and implications for the (U-Th)/He system. *Geochimica et Cosmochimica Acta*, 75(16), 4515-4530.
- Farley, K. A., Wolf, R. A., & Silver, L. T. (1996). The effects of long alpha-stopping distances on (U-Th)/He ages. *Geochimica et Cosmochimica Acta*, 60(21), 4223-4229.
- Fawcett, P. J., & Barron, E. J. (1998). The role of geography and atmospheric CO<sub>2</sub> in long-term climate change: Results from model simulations for the Late Permian to the Present. *Oxford Monographs on Geology and Geophysics*, 39, 21-38.
- Fishwick, S., & Bastow, I. D. (2011). Towards a better understanding of African topography: a review of passive-source seismic studies of the African crust and upper mantle. *Geological Society, London, Special Publications*, 357(1), 343-371.
- Fishwick, S., Kennett, B. L. N., & Reading, A. M. (2005). Contrasts in lithospheric structure within the Australian craton—insights from surface wave tomography. *Earth and Planetary Science Letters*, 231(3), 163-176.
- Fitzgerald, P. G., Baldwin, S. L., Webb, L. E., & O'sullivan, P. B. (2006). Interpretation of (U-Th)/He single grain ages from slowly cooled crustal terranes: a case study from the Transantarctic Mountains of southern Victoria Land. *Chemical Geology*, 225(1), 91-120.
- Flament, N., Gurnis, M., & Müller, R. D. (2013). A review of observations and models of dynamic topography. *Lithosphere*, 5(2), 189-210.
- Fleischer, R. L., Price, P. B., & Walker, R. M. (1965). Effects of temperature, pressure, and ionization of the formation and stability of fission tracks in minerals and glasses. *Journal of Geophysical Research*, 70(6), 1497-1502.
- Fleisher, R. L., Price, P. B., & Walker, R. M. (1975). *Nuclear tracks in solids: Principles and applications*. p. 626. Berkeley, California: University of California Press.
- Fleming, A., Summerfield, M. A., Stone, J. O., Fifield, L. K., & Cresswell, R. G. (1999). Denudation rates for the southern Drakensberg escarpment, SE Africa, derived from in-situ-produced cosmogenic <sup>36</sup>C1: initial results. *Journal of the Geological Society*, 156(2), 209-212.
- Flowers, R. M. (2009). Exploiting radiation damage control on apatite (U-Th)/He dates in cratonic regions. *Earth and Planetary Science Letters*, 277(1), 148-155.
- Flowers, R. M. (2014). Geomorphology: Tales of topography, *Nature Geoscience*, 7, 483-485.
- Flowers, R. M., & Kelley, S. A. (2011). Interpreting data dispersion and “inverted” dates in apatite (U-Th)/He and fission-track datasets: an example from the US midcontinent. *Geochimica et Cosmochimica Acta*, 75(18), 5169-5186.

- Flowers, R. M., & Schoene, B. (2010). (U-Th)/He thermochronometry constraints on unroofing of the eastern Kaapvaal craton and significance for uplift of the southern African Plateau. *Geology*, 38(9), 827-830.
- Flowers, R. M., Ault, A. K., Kelley, S. A., Zhang, N., & Zhong, S. (2012). Epeirogeny or eustasy? Paleozoic-Mesozoic vertical motion of the North American continental interior from thermochronometry and implications for mantle dynamics. *Earth and Planetary Science Letters*, 317, 436-445.
- Flowers, R. M., Ketcham, R. A., Shuster, D. L., & Farley, K. A. (2009). Apatite (U-Th)/He thermochronometry using a radiation damage accumulation and annealing model. *Geochimica et Cosmochimica Acta*, 73(8), 2347-2365.
- Foeken, J., Stuart, F. M., Dobson, K. J., Persano, C., & Vilbert, D. (2006). A diode laser system for heating minerals for (U-Th)/He chronometry. *Geochemistry, Geophysics, Geosystems*, 7(4).
- Foley, S. F. (2008). Rejuvenation and erosion of the cratonic lithosphere. *Nature Geoscience*, 1(8), 503-510.
- Forte, A. M., Quéré, S., Moucha, R., Simmons, N. A., Grand, S. P., Mitrovica, J. X., & Rowley, D. B. (2010a). Joint seismic-geodynamic-mineral physical modelling of African geodynamics: A reconciliation of deep-mantle convection with surface geophysical constraints. *Earth and Planetary Science Letters*, 295(3), 329-341.
- Forte, A. M., Moucha, R., Simmons, N. A., Grand, S. P., & Mitrovica, J. X. (2010b). Deep-mantle contributions to the surface dynamics of the North American continent. *Tectonophysics*, 481(1), 3-15.
- Foulger, G. R. (2007). The “plate” model for the genesis of melting anomalies. *Geological Society of America Special Papers*, 430, 1-28.
- Fourie, C. J. S., & Cole, P., Council for Geoscience (South Africa), (1997). *Geological Map of the Republic of South Africa and the Kingdoms of Lesotho and Swaziland 1997*. Council for Geoscience.
- Fowler, C. M. R. (2005). *The solid earth: an introduction to global geophysics*. Cambridge University Press.
- Franco-Magalhaes, A. O. B., Cuglieri, M. A. A., Hackspacher, P. C., & Saad, A. R. (2014). Long-term landscape evolution and post-rift reactivation in the southeastern Brazilian passive continental margin: Taubaté basin. *International Journal of Earth Sciences*, 103(2), 441-453.
- Franke, D. (2013). Rifting, lithosphere breakup and volcanism: Comparison of magma-poor and volcanic rifted margins. *Marine and Petroleum Geology*, 43, 63-87.
- Franke, D., Ladage, S., Schnabel, M., Schreckenberger, B., Reichert, C., Hinz, K., Paterlini, M., de Abelleira, J. & Siciliano, M. (2010). Birth of a volcanic margin off Argentina, South Atlantic. *Geochemistry, Geophysics, Geosystems*, 11(2), Q0AB04.
- Franke, D., Neben, S., Ladage, S., Schreckenberger, B., & Hinz, K. (2007). Margin segmentation and volcano-tectonic architecture along the volcanic margin off Argentina/Uruguay, South Atlantic. *Marine Geology*, 244(1), 46-67.
- Gaina, C., Torsvik, T. H., van Hinsbergen, D. J., Medvedev, S., Werner, S. C., & Labails, C. (2013). The African Plate: A history of oceanic crust accretion and subduction since the Jurassic. *Tectonophysics*, 604, 4-25.
- Galbraith, R. F. (2010). *Statistics for fission track analysis*. CRC Press.
- Galbraith, R. F., & Green, P. F. (1990). Estimating the component ages in a finite mixture. *International Journal of Radiation Applications and Instrumentation. Part D. Nuclear Tracks and Radiation Measurements*, 17(3), 197-206.
- Gallagher, K. (2012). Transdimensional inverse thermal history modeling for quantitative thermochronology. *Journal of Geophysical Research: Solid Earth (1978-2012)*, 117(B2).
- Gallagher, K., & Brown, R. (1999a). Denudation and uplift at passive margins: the record on the Atlantic Margin of southern Africa. *Philosophical Transactions of the Royal Society of London. Series A: Mathematical, Physical and Engineering Sciences*, 357(1753), 835-859.
- Gallagher, K., & Brown, R. (1999b). The Mesozoic denudation history of the Atlantic margins of southern Africa and southeast Brazil and the relationship to offshore sedimentation. *Geological Society, London, Special Publications*, 153(1), 41-53.
- Gallagher, K., and Brown, R., (1997), The onshore record of passive margin evolution. *Journal of the Geological Society*, 154(3), 451-457.
- Gallagher, K., Brown, R., & Johnson, C. (1998). Fission track analysis and its applications to geological problems. *Annual Review of Earth and Planetary Sciences*, 26(1), 519-572.

- Gallagher, K., Charvin, K., Nielsen, S., Sambridge, M., & Stephenson, J. (2009). Markov chain Monte Carlo (MCMC) sampling methods to determine optimal models, model resolution and model choice for Earth Science problems. *Marine and Petroleum Geology*, 26(4), 525-535.
- Ganerød, M., Torsvik, T. H., Van Hinsbergen, D. J. J., Gaina, C., Corfu, F., Werner, S., Owen-Smith, T. M., Ashwal, L. D., Webb, S. J. & Hendriks, B. W. H. (2011). Palaeoposition of the Seychelles microcontinent in relation to the Deccan Traps and the Plume Generation Zone in Late Cretaceous-Early Palaeogene time. Geological Society, London, Special Publications, 357(1), 229-252.
- Garnero, E. J., Lay, T., & McNamara, A. (2007). Implications of lower-mantle structural heterogeneity for the existence and nature of whole-mantle plumes. *Geological Society of America Special Papers*, 430, 79-101.
- Gautheron, C., & Tassan-Got, L. (2010). A Monte Carlo approach to diffusion applied to noble gas/helium thermochronology. *Chemical Geology*, 273(3), 212-224.
- Gautheron, C., Tassan-Got, L., Barbarand, J., & Pagel, M. (2009). Effect of alpha-damage annealing on apatite (U-Th)/He thermochronology. *Chemical Geology*, 266(3), 157-170.
- Gautheron, C., Barbarand, J., Ketcham, R. A., Tassan-Got, L., van der Beek, P., Pagel, M., Pinna-Jamme, R., Couffignal, F. & Fialin, M. (2013). Chemical influence on  $\alpha$ -recoil damage annealing in apatite: Implications for (U-Th)/He dating. *Chemical Geology*, 351, 257-267.
- Gautheron, C., Tassan-Got, L., Ketcham, R. A., & Dobson, K. J. (2012). Accounting for long alpha-particle stopping distances in (U-Th-Sm)/He geochronology: 3D modeling of diffusion, zoning, implantation, and abrasion. *Geochimica et Cosmochimica Acta*, 96, 44-56.
- Geel, C., Schulz, H. M., Booth, P., de Wit, M., & Horsfield, B. (2013). Shale gas characteristics of Permian black shales in South Africa: results from recent drilling in the Ecca Group (Eastern Cape). *Energy Procedia*, 40, 256-265.
- Gernigon, L., Lucazeau, F., Brigaud, F., Ringenbach, J. C., Planke, S., & Le Gall, B. (2006). A moderate melting model for the Vøring margin (Norway) based on structural observations and a thermo-kinematical modelling: Implication for the meaning of the lower crustal bodies. *Tectonophysics*, 412(3), 255-278.
- Gerrard, I., & Smith, G. C. (1982). Post-Paleozoic succession and structure of the southwestern African continental margin. *Studies in continental margin geology: AAPG Memoir*, 34, 49-74.
- Giachetta, E., Refice, A., Capolongo, D., Gasparini, N. M., & Pazzaglia, F. J. (2014). Orogen-scale drainage network evolution and response to erodibility changes: insights from numerical experiments. *Earth Surface Processes and Landforms*.
- Gilchrist, A. R., & Summerfield, M. A. (1990). Differential denudation and flexural isostasy in formation of rifted-margin upwarps, *Nature* 346, 739 - 742
- Gilchrist, A. R., & Summerfield, M. A. (1991). Denudation, isostasy and landscape evolution. *Earth Surface Processes and Landforms*, 16(6), 555-562.
- Gilchrist, A. R., & Summerfield, M. A. (1994). Tectonic models of passive margin evolution and their implications for theories of long-term landscape development. In Kirby, M. J. (ed.), *Process models and theoretical geomorphology*, p. 55-84, Chichester, UK: Wiley.
- Gilchrist, A. R., Kooi, H., & Beaumont, C. (1994). Post-Gondwana geomorphic evolution of southwestern Africa: Implications for the controls on landscape development from observations and numerical experiments. *Journal of Geophysical Research: Solid Earth* (1978-2012), 99(B6), 12211-12228.
- Gilks, W. R. (2005). *Markov chain monte carlo*. John Wiley & Sons, Ltd.
- Gładczenko, T. P., Hinz, K., Eldholm, O., Meyer, H., Neben, S., & Skogseid, J. (1997). South Atlantic volcanic margins. *Journal of the Geological Society*, 154(3), 465-470.
- Gleadow, A. J. W., & Duddy, I. R. (1981). A natural long-term track annealing experiment for apatite. *Nuclear Tracks*, 5(1), 169-174.
- Gleadow, A. J. W., Duddy, I. R., & Lovering, J. F. (1983). Fission track analysis: a new tool for the evaluation of thermal histories and hydrocarbon potential. *APEA Journal*, 23(2), 93-102.
- Gleadow, A. J. W., Duddy, I. R., Green, P. F., & Lovering, J. F. (1986a). Confined fission track lengths in apatite: a diagnostic tool for thermal history analysis. *Contributions to Mineralogy and Petrology*, 94(4), 405-415.

- Gleadow, A. J., Duddy, I. R., Green, P. F., & Hegarty, K. A. (1986b). Fission track lengths in the apatite annealing zone and the interpretation of mixed ages. *Earth and Planetary Science Letters*, 78(2), 245-254.
- Gleadow, A. J. W., & Fitzgerald, P. G. (1987). Uplift history and structure of the Transantarctic Mountains: new evidence from fission track dating of basement apatites in the Dry Valleys area, southern Victoria Land. *Earth and Planetary Science Letters*, 82(1), 1-14.
- Goldrick, G., & Bishop, P. (1995). Differentiating the roles of lithology and uplift in the steepening of bedrock river long profiles: an example from southeastern Australia. *The Journal of Geology*, 103(2), 227-231.
- Goren, L., Willett, S. D., Herman, F., & Braun, J. (2014). Coupled numerical-analytical approach to landscape evolution modeling. *Earth Surface Processes and Landforms*, 39(4), 522-545.
- Goudie, A. S. (2005). The drainage of Africa since the Cretaceous. *Geomorphology*, 67(3), 437-456.
- Govers, R., & Wortel, M. J. R. (1993). Initiation of asymmetric extension in continental lithosphere. *Tectonophysics*, 223(1), 75-96.
- Graveleau, F., & Dominguez, S. (2008). Analogue modelling of the interaction between tectonics, erosion and sedimentation in foreland thrust belts. *Comptes Rendus Geoscience*, 340(5), 324-333.
- Green, P. F. (1986). On the thermo-tectonic evolution of Northern England: evidence from fission track analysis. *Geological Magazine*, 123(5), 493-506.
- Green, P. F. (1988). The relationship between track shortening and fission track age reduction in apatite: combined influences of inherent instability, annealing anisotropy, length bias and system calibration. *Earth and Planetary Science Letters*, 89(3), 335-352.
- Green, P. F., & Duddy, I. R. (2006). Interpretation of apatite (U-Th)/He ages and fission track ages from cratons. *Earth and Planetary Science Letters*, 244(3), 541-547.
- Green, P. F., & Durrani, S. A. (1977). Annealing studies of tracks in crystals. *Nuclear Track Detection*, 1(1), 33-39.
- Green, P. F., Crowhurst, P. V., & Duddy, I. R. (2004). Integration of AFTA and (U-Th)/He thermochronology to enhance the resolution and precision of thermal history reconstruction in the Anglesea-1 well, Otway Basin, SE Australia. In *Eastern Australian Basins Symposium II* (pp. 117-131). Petroleum Exploration Society of Australia, Special Publication. Petroleum Exploration Society of Australia: West Perth.
- Green, P. F., Crowhurst, P. V., Duddy, I. R., Japsen, P., & Holford, S. P. (2006). Conflicting (U-Th)/He and fission track ages in apatite: enhanced He retention, not anomalous annealing behaviour. *Earth and Planetary Science Letters*, 250(3), 407-427.
- Green, P. F., Duddy, I. R., Gleadow, A. J. W., Tingate, P. R., & Laslett, G. M. (1986). Thermal annealing of fission tracks in apatite: 1. A qualitative description. *Chemical Geology: Isotope Geoscience section*, 59, 237-253.
- Green, P. F., Duddy, I. R., Laslett, G. M., Hegarty, K. A., Gleadow, A. W., & Lovering, J. F. (1989). Thermal annealing of fission tracks in apatite 4. Quantitative modelling techniques and extension to geological timescales. *Chemical Geology: Isotope Geoscience Section*, 79(2), 155-182.
- Green, P. F., Lidmar-Bergström, K., Japsen, P., Bonow, J. M., & Chalmers, J. A. (2013). Stratigraphic landscape analysis, thermochronology and the episodic development of elevated, passive continental margins. *Geological Survey of Denmark and Greenland*
- Gresse, P. G., & Germs, G. J. B. (1993). The Nama foreland basin: sedimentation, major unconformity bounded sequences and multisided active margin advance. *Precambrian Research*, 63(3), 247-272.
- Gresse, P. G., Von Veh, M. W., & Frimmel, H. E. (2006). Namibian (Neoproterozoic) to early Cambrian successions. In Johnson, M. R., Anhaeusser, C. R., and Thomas, R. J. (eds.), *The Geology of South Africa*, p. 395-420. Pretoria, South Africa: Geological Society of South Africa/Council for GeoScience.
- Griffin, W. L., O'Reilly, S. Y., Natapov, L. M., & Ryan, C. G. (2003). The evolution of lithospheric mantle beneath the Kalahari Craton and its margins. *Lithos*, 71(2), 215-241.
- Grimaud, J. L., Chardon, D., & Beauvais, A. (2014). Very long-term incision dynamics of big rivers. *Earth and Planetary Science Letters*, 405, 74-84.
- Grist, A. M., & Zentilli, M. (2005). The thermal history of the Nares Strait, Kane Basin, and Smith Sound region in Canada and Greenland: constraints from apatite fission-track and (U Th Sm)/He dating. *Canadian Journal of Earth Sciences*, 42(9), 1547-1569.

- Groenewald, P. B., Grantham, G. H., and Watkeys, M. K., (1991), Geological evidence for a Proterozoic to Mesozoic link between southeastern Africa and Dronning Maud Land, Antarctica, *Journal of the Geological Society*, 148(6), 1115-1123.
- Guenther, W. R., Reiners, P. W., & Tian, Y. (2014). Interpreting date-eU correlations in zircon (U-Th)/He datasets: A case study from the Longmen Shan, China. *Earth and Planetary Science Letters*, 403, 328-339.
- Guenther, W. R., Reiners, P. W., Ketcham, R. A., Nasdala, L., & Giester, G. (2013). Helium diffusion in natural zircon: Radiation damage, anisotropy, and the interpretation of zircon (U-Th)/He thermochronology. *American Journal of Science*, 313(3), 145-198.
- Guérin, C., (2000). The neogene rhinoceroses of Namibia. *Palaeontologia Africana*, 36, 119-138.
- Guillocheau, F., Rouby, D., Robin, C., Helm, C., Rolland, N., Le Carlier de Veslud, C., & Braun, J. (2012). Quantification and causes of the terrigenous sediment budget at the scale of a continental margin: a new method applied to the Namibia-South Africa margin. *Basin Research*, 24(1), 3-30.
- Guillou-Frottier, L., Burov, E., Cloetingh, S., Le Goff, E., Deschamps, Y., Huet, B., & Bouchot, V. (2012). Plume-induced dynamic instabilities near cratonic blocks: Implications for P-T-t paths and metallogeny. *Global and Planetary Change*, 90, 37-50.
- Guiraud, R., & Bosworth, W. (1997). Senonian basin inversion and rejuvenation of rifting in Africa and Arabia: synthesis and implications to plate-scale tectonics. *Tectonophysics*, 282(1), 39-82.
- Gurnis, M., Mitrovica, J. X., Ritsema, J., & van Heijst, H. J. (2000). Constraining mantle density structure using geological evidence of surface uplift rates: The case of the African superplume. *Geochemistry, Geophysics, Geosystems*, 1(7), 1020.
- Gutzmer, J., & Beukes, N. J. (2000). Asbestiform manjiroite and todorokite from the Kalahari manganese field, South Africa. *South African Journal of Geology*, 103(3-4), 163-174.
- Haack, U. (1983). Reconstruction of the cooling history of the Damara Orogen by correlation of radiometric ages with geography and altitude. In Martin, H. & Eder, F. W., *Intracontinental Fold Belts*, pp. 873-884. Berlin Heidelberg, Germany: Springer.
- Hack, J. T. (1960). Interpretation of erosional topography in humid temperate regions. *Bobbs-Merrill*.
- Haddon, I. G., & McCarthy, T. S. (2005). The Mesozoic-Cenozoic interior sag basins of Central Africa: The Late-Cretaceous-Cenozoic Kalahari and Okavango basins. *Journal of African Earth Sciences*, 43(1), 316-333.
- Hager, B. H., Clayton, R. W., Richards, M. A., Comer, R. P., & Dziewonski, A. M. (1985). Lower mantle heterogeneity, dynamic topography and the geoid. *Nature*, 313(6003), 541-545.
- Hansen, K., & Reiners, P. W. (2006). Low temperature thermochronology of the southern East Greenland continental margin: evidence from apatite (U-Th)/He and fission track analysis and implications for intermethod calibration. *Lithos*, 92(1), 117-136.
- Hardy, S., & Gawthorpe, R. (2002). Normal fault control on bedrock channel incision and sediment supply: Insights from numerical modeling. *Journal of Geophysical Research: Solid Earth* (1978-2012), 107(B10).
- Harry, D. L., & Sawyer, D. S. (1992). Basaltic volcanism, mantle plumes, and the mechanics of rifting: The Paraná flood basalt province of South America. *Geology*, 20(3), 207-210.
- Hartley, R. A., Roberts, G. G., White, N., Richardson, C., 2011, Transient convective uplift of an ancient buried landscape, *Nature Geoscience*, 4(8), 562-565.
- Hartwig, A., Boyd, D., Kuhlmann, G., Adams, S. G., Campher, C., Anka, Z., di Primo, R. & Albrecht, T. (2010). Characterization of hydrocarbon generation and migration dynamics based on seismic interpretation and basin modeling: an integrated study of the Orange Basin, South Africa. *AAPG Search and Discovery Article*, 90108.
- Haughton, S. H. (1915). On some dinosaur remains from Bushmanland. *Transactions of the Royal Society of South Africa*, 5(1), 259-264.
- Haughton, S. H. (1930). On the occurrence of Upper Cretaceous marine fossils near Bogenfels, SW Africa. *Transactions of the Royal Society of South Africa*, 18(4), 361-365.
- Haughton, S. H. (1931). On a collection of fossil frogs from the clays at Banke. *Transactions of the Royal Society of South Africa*, 19(3), 233-249.
- Hawkesworth, C. J., Gallagher, K., Kirstein, L., Mantovani, M. S. M., Peate, D. W., & Turner, S. P. (2000). Tectonic controls on magmatism associated with continental break-up: an example from the Paraná-Etendeka Province. *Earth and Planetary Science Letters*, 179(2), 335-349.

- Hawthorne, F. C., Groat, L. A., Raudsepp, M., Ball, N. A., Kimata, M., Spike, F. D., Ball, N. A., Kimata, M., Spike, F. D., Gaba, R., Halden, N. M., Lumpkin, G. R., Ewing, R., Gregor, R. B., Lytle, F. W., Ercit, T. S., Rossman, G. R., Wicks, F. J., Ramik, R. A., Sherriff, B. L., Fleet, M. E. & McCammon, C. (1991). Alpha-decay damage in titanite. *American Mineralogist*, 76(3-4), 370-396.
- Heimsath, A. M., & Ehlers, T. A. (2005). Quantifying rates and timescales of geomorphic processes. *Earth Surface Processes and Landforms*, 30(8), 917-921.
- Heimsath, A. M., Chappell, J., Finkel, R. C., Fifield, K., & Alimanovic, A. (2006). Escarpment erosion and landscape evolution in southeastern Australia. *Geological Society of America Special Papers*, 398, 173-190.
- Heine, C., Müller, R. D., Steinberger, B., & Torsvik, T. H. (2008). Subsidence in intracontinental basins due to dynamic topography. *Physics of the Earth and Planetary Interiors*, 171(1), 252-264.
- Heine, C., Zoethout, J., and Müller, R. D., (2013), Kinematics of the South Atlantic rift, *Solid Earth*, 4, 215-253.
- Helgren, D. M., & Butzer, K. W. (1977). Paleosols of the southern Cape Coast, South Africa: implications for laterite definition, genesis, and age. *Geographical review*, 430-445.
- Hendey, Q. B. (1970). The age of the fossiliferous deposits at Langebaanweg, Cape Province. *Annals of the South African Museum*, 56(3), 119-131.
- Hendriks, B. W. H., & Redfield, T. F. (2005). Apatite fission track and (U-Th)/He data from Fennoscandia: An example of underestimation of fission track annealing in apatite. *Earth and Planetary Science Letters*, 236(1), 443-458.
- Hendriks, B. W. H., & Redfield, T. F. (2006). Reply to: Comment on “Apatite Fission Track and (U-Th)/He data from Fennoscandia: An example of underestimation of fission track annealing in apatite” by BWH Hendriks and TF Redfield. *Earth and Planetary Science Letters*, 248(1), 569-577.
- Hendriks, B. W. H., Osmundsen, P. T., & Redfield, T. F. (2010). Normal faulting and block tilting in Lofoten and Vesterålen constrained by Apatite Fission Track data. *Tectonophysics*, 485(1), 154-163.
- Herbert, C. T., & Compton, J. S. (2007). Depositional environments of the lower Permian Dwyka diamictite and Prince Albert shale inferred from the geochemistry of early diagenetic concretions, southwest Karoo Basin, South Africa. *Sedimentary Geology*, 194(3), 263-277.
- Hillis, R. R., Holford, S. P., Green, P. F., Doré, A. G., Gatliff, R. W., Stoker, M. S., Thomson, K., Turner, J. P., Underhill, J. P. & Williams, G. A. (2008). Cenozoic exhumation of the southern British Isles. *Geology*, 36(5), 371-374.
- Hirsch, K. K., Bauer, K., & Scheck-Wenderoth, M. (2009). Deep structure of the western South African passive margin—Results of a combined approach of seismic, gravity and isostatic investigations. *Tectonophysics*, 470(1), 57-70.
- Hirsch, K. K., Scheck-Wenderoth, M., van Wees, J. D., Kuhlmann, G., & Paton, D. A. (2010). Tectonic subsidence history and thermal evolution of the Orange Basin. *Marine and Petroleum Geology*, 27(3), 565-584.
- Hofmann, C., Courtillot, V., Feraud, G., Rochette, P., Yirgu, G., Ketefo, E., & Pik, R. (1997). Timing of the Ethiopian flood basalt event and implications for plume birth and global change. *Nature*, 389(6653), 838-841.
- Holford, S. P., Green, P. F., Duddy, I. R., Turner, J. P., Hillis, R. R., & Stoker, M. S. (2009). Regional intraplate exhumation episodes related to plate-boundary deformation. *Geological Society of America Bulletin*, 121(11-12), 1611-1628.
- Holford, S. P., Green, P. F., Hillis, R. R., Underhill, J. R., Stoker, M. S., & Duddy, I. R. (2010). Multiple post-Caledonian exhumation episodes across NW Scotland revealed by apatite fission-track analysis. *Journal of the Geological Society*, 167(4), 675-694.
- Holford, S. P., Hillis, R. R., Hand, M., & Sandiford, M. (2011). Thermal weakening localizes intraplate deformation along the southern Australian continental margin. *Earth and Planetary Science Letters*, 305(1), 207-214.
- Holford, S. P., Tuitt, A. K., Hillis, R. R., Green, P. F., Stoker, M. S., Duddy, I. R., Sandiford, M. & Tassone, D. R. (2014). Cenozoic deformation in the Otway Basin, southern Australian margin: implications for the origin and nature of post-breakup compression at rifted margins. *Basin Research*, 26(1), 10-37.
- Hopwood, A. T. (1929). A review of fossil mammals of Central Africa. *American Journal of Science*, (98), 101-118.

- Hourigan, J. K., Reiners, P. W., & Brandon, M. T. (2005). U-Th zonation-dependent alpha-ejection in (U-Th)/He chronometry. *Geochimica et Cosmochimica Acta*, 69(13), 3349-3365.
- House, M. A., Wernicke, B. P., Farley, K. A., & Dumitru, T. A. (1997). Cenozoic thermal evolution of the central Sierra Nevada, California, from (U-Th)/He thermochronometry. *Earth and Planetary Science Letters*, 151(3), 167-179.
- Hovius, N. (1998). Controls on sediment supply by large rivers. *Special Publications of SEPM*
- Huismans, R. S., & Beaumont, C. (2008). Complex rifted continental margins explained by dynamical models of depth-dependent lithospheric extension. *Geology*, 36(2), 163-166.
- Huismans, R. S., Podladchikov, Y. Y., & Cloetingh, S. (2001). Transition from passive to active rifting: Relative importance of asthenospheric doming and passive extension of the lithosphere. *Journal of Geophysical Research: Solid Earth (1978-2012)*, 106(B6), 11271-11291.
- Huismans, R., & Beaumont, C. (2011). Depth-dependent extension, two-stage breakup and cratonic underplating at rifted margins. *Nature*, 473(7345), 74-78.
- Hurford, A. J., & Green, P. F. (1982). A users' guide to fission track dating calibration. *Earth and Planetary Science Letters*, 59(2), 343-354.
- Hurford, A. J., & Green, P. F. (1983). The zeta age calibration of fission-track dating. *Chemical Geology*, 41, 285-317.
- Hutton, J. (1788). *Theory of the Earth; or an Investigation of the Laws observable in the Composition, Dissolution, and Restoration of Land upon the Globe*. *Transactions of the Royal Society of Edinburgh*, 1(02), 209-304.
- Inkpen, R. 2005: *Science, philosophy and physical geography*, 176 pp. London and New York: Routledge.
- Issler, D., McQueen, H., & Beaumont, C. (1989). Thermal and isostatic consequences of simple shear extension of the continental lithosphere. *Earth and planetary science letters*, 91(3), 341-358.
- Jackson, M., Cramez, C., & Fonck, J. M. (2000). Role of subaerial volcanic rocks and mantle plumes in creation of South Atlantic margins: implications for salt tectonics and source rocks. *Marine and Petroleum Geology*, 17(4), 477-498.
- Jacobs, J., Thomas, R. J., & Weber, K. (1993). Accretion and indentation tectonics at the southern edge of the Kaapvaal craton during the Kibaran (Grenville) orogeny. *Geology*, 21(3), 203-206.
- Jakica, S., Quigley, M. C., Sandiford, M., Clark, D., Fifield, L. K., & Alimanovic, A. (2011). Geomorphic and cosmogenic nuclide constraints on escarpment evolution in an intraplate setting, Darling Escarpment, Western Australia. *Earth Surface Processes and Landforms*, 36(4), 449-459.
- Janney, P. E., Shirey, S. B., Carlson, R. W., Pearson, D. G., Bell, D. R., Le Roex, A. P., Ishikawa, A., Nixon, P. H. & Boyd, F. R. (2010). Age, composition and thermal characteristics of South African off-craton mantle lithosphere: Evidence for a multi-stage history. *Journal of Petrology*, 51(9), 1849-1890.
- Janssen, M. E., Stephenson, R. A., & Cloetingh, S. A. P. L. (1995). Temporal and spatial correlations between changes in plate motions and the evolution of rifted basins in Africa. *Geological Society of America Bulletin*, 107(11), 1317-1332.
- Japsen, P., Green, P. F., Bonow, J. M., Nielsen, T. F., & Chalmers, J. A. (2014). From volcanic plains to glaciated peaks: Burial, uplift and exhumation history of southern East Greenland after opening of the NE Atlantic. *Global and Planetary Change*, 116, 91-114.
- Japsen, P., Bonow, J. M., Green, P. F., Chalmers, J. A., & Lidmar-Bergström, K. (2006). Elevated, passive continental margins: Long-term highs or Neogene uplifts? New evidence from West Greenland. *Earth and Planetary Science Letters*, 248(1), 330-339.
- Japsen, P., Bonow, J. M., Green, P. F., Chalmers, J. A., & Lidmar-Bergström, K. (2009). Formation, uplift and dissection of planation surfaces at passive continental margins—a new approach. *Earth Surface Processes and Landforms*, 34(5), 683-699.
- Japsen, P., Chalmers, J. A., Green, P. F., & Bonow, J. M. (2012). Elevated, passive continental margins: Not rift shoulders, but expressions of episodic, post-rift burial and exhumation. *Global and Planetary Change*, 90, 73-86.
- Jelsma, H. A., de Wit, M. J., Thiart, C., Dirks, P. H., Viola, G., Basson, I. J., & Anckar, E. (2004). Preferential distribution along transcontinental corridors of kimberlites and related rocks of Southern Africa. *South African Journal of Geology*, 107(1-2), 301-324.



- Jelsma, H., Barnett, W., Richards, S., & Lister, G. (2009). Tectonic setting of kimberlites. *Lithos*, 112, 155-165.
- Johnson, M. R., Van Vuuren, C. J., Visser, J. N. J., Cole, D. I., Wickens, H. D. V., Christie, A. D. M. & Brandl, G. (2006). Sedimentary rocks of the Karoo Supergroup. In Johnson, M. R., Anhaeusser, C. R., and Thomas, R. J. (eds.), *The Geology of South Africa*, p. 461-499. Pretoria, South Africa: Geological Society of South Africa/Council for GeoScience.
- Jones, M. Q. W. (1987). Heat flow and heat production in the Namaqua mobile belt, South Africa. *Journal of Geophysical Research: Solid Earth* (1978-2012), 92(B7), 6273-6289.
- Jourdan, F., Féraud, G., Bertrand, H., & Watkeys, M. K. (2007). From flood basalts to the inception of oceanization: Example from the  $^{40}\text{Ar}/^{39}\text{Ar}$  high-resolution picture of the Karoo large igneous province. *Geochemistry, Geophysics, Geosystems*, 8(2).
- Jourdan, F., Féraud, G., Bertrand, H., Kampunzu, A. B., Tshoso, G., Watkeys, M. K., & Le Gall, B. (2005). Karoo large igneous province: Brevity, origin, and relation to mass extinction questioned by new  $^{40}\text{Ar}/^{39}\text{Ar}$  age data. *Geology*, 33(9), 745-748.
- Jungslager, E. H. (1999). Petroleum habitats of the Atlantic margin of South Africa. *Geological Society, London, Special Publications*, 153(1), 153-168.
- Karl, M., Glasmacher, U. A., Kollenz, S., Franco-Magalhaes, A. O., Stockli, D. F., & Hackspacher, P. C. (2013). Evolution of the South Atlantic passive continental margin in southern Brazil derived from zircon and apatite (U-Th-Sm)/He and fission-track data. *Tectonophysics*, 604, 224-244.
- Karlstrom, K. E., & Humphreys, E. D. (1998). Persistent influence of Proterozoic accretionary boundaries in the tectonic evolution of southwestern North America Interaction of cratonic grain and mantle modification events. *Rocky Mountain Geology*, 33(2), 161-179.
- Karlstrom, K. E., Coblenz, D., Dueker, K., and CREST Working Group. (2012). Mantle-driven dynamic uplift of the Rocky Mountains and Colorado Plateau and its surface response: Toward a unified hypothesis, *Lithosphere*, 4(1), 3-22.
- Karner, G. D., & Watts, A. B. (1982). On isostasy at Atlantic-type continental margins. *Journal of Geophysical Research: Solid Earth* (1978-2012), 87(B4), 2923-2948.
- Keen, C. E., & Boutilier, R. R. (2000). Interaction of rifting and hot horizontal plume sheets at volcanic margins. *Journal of Geophysical Research: Solid Earth* (1978-2012), 105(B6), 13375-13387.
- Kendall, B., van Acken, D., & Creaser, R. A. (2013). Depositional age of the early Paleoproterozoic Klippits Member, Nelani Formation (Ghaap Group, Transvaal Supergroup, South Africa) and implications for low-level Re-Os geochronology and Paleoproterozoic global correlations. *Precambrian Research*, 237, 1-12.
- Kennett, B. L. N., & Iaffaldano, G. (2013). Role of lithosphere in intra-continental deformation: Central Australia. *Gondwana Research*, 24(3), 958-968.
- Ketcham, R. A. (2005). The role of crystallographic angle in characterizing and modeling apatite fission-track length data. *Radiation measurements*, 39(6), 595-601.
- Ketcham, R. A., Carter, A., Donelick, R. A., Barbarand, J., & Hurford, A. J. (2007). Improved modeling of fission-track annealing in apatite. *American Mineralogist*, 92(5-6), 799-810.
- Ketcham, R. A., Donelick, R. A., Balestrieri, M. L., & Zattin, M. (2009). Reproducibility of apatite fission-track length data and thermal history reconstruction. *Earth and Planetary Science Letters*, 284(3), 504-515.
- Ketcham, R. A., Gautheron, C., & Tassan-Got, L. (2011). Accounting for long alpha-particle stopping distances in (U-Th-Sm)/He geochronology: refinement of the baseline case. *Geochimica et Cosmochimica Acta*, 75(24), 7779-7791.
- Ketcham, R. A., Guenther, W. R., & Reiners, P. W. (2013). Geometric analysis of radiation damage connectivity in zircon, and its implications for helium diffusion. *American Mineralogist*, 98(2-3), 350-360.
- King, L.C. (1942). *South African Scenery*. pp. 308. Edinburgh, UK: Oliver and Boyd.
- King, L.C. (1950). The cyclic land surfaces of Australia. *Proc. R. Soc. Vict.*, 62: 79-95.
- King, L. C. (1953a). Canons of landscape evolution, *Geological Society of America Bulletin*, 64, 721 - 752.
- King, L. C. (1953b). Necessity for continental drift. *Bulletin of the American Association of Petroleum Geology*. 37, 2163-77.
- King, L. C. (1955). Pediplanation and isostasy: an example from South Africa. *Quarterly Journal of the Geological Society*, 111(1-4), 353-359.
- King, L.C. (1956). Drakensberg Scarp of South Africa: a clarification. *Geographical Society of America Bulletin*, 67, 121-122.

- King, L. C. (1962). *Morphology of the Earth*. pp. 699. Edinburgh, UK: Oliver and Boyd.
- King, L.C., (1976). Planation remnants upon high lands. *Zeitschrift für Geomorphologie*, 20, 133-148.
- King, S. D. (2005). Archean cratons and mantle dynamics. *Earth and Planetary Science Letters*, 234(1), 1-14.
- King, S. D., & Ritsema, J. (2000). African hot spot volcanism: small-scale convection in the upper mantle beneath cratons. *Science*, 290(5494), 1137-1140.
- Kirby, E., & Whipple, K. X. (2012). Expression of active tectonics in erosional landscapes. *Journal of Structural Geology*, 44, 54-75.
- Kirchheimer, F. (1934). Über Tsuga-Pollen aus dem Tertiär. *Planta*, 22(2), 171-179.
- Kohn, B. P., Belton, D. X., Brown, R. W., Gleadow, A. J. W., Green, P. F., & Lovering, J. F. (2003). Comment on: "Experimental evidence for the pressure dependence of fission track annealing in apatite" by AS Wendt et al. [*Earth Planet. Sci. Lett.* 201 (2002) 593-607]. *Earth and Planetary Science Letters*, 215(1), 299-306.
- Kohn, B. P., Gleadow, A. J. W., Raza, A., Kohlmann, F., & Brown, R. W. (2006). Re-evaluating low temperature apatite thermochronology in slowly cooled terranes. *Geochimica et Cosmochimica Acta*, 70(18), A328.
- Kohn, B. P., Lorencak, M., Gleadow, A. J., Kohlmann, F., Raza, A., Osadetz, K. G., & Sorjonen-Ward, P. (2009). A reappraisal of low-temperature thermochronology of the eastern Fennoscandia Shield and radiation-enhanced apatite fission-track annealing. *Geological Society, London, Special Publications*, 324(1), 193-216.
- Kooi, H., & Beaumont, C. (1994). Escarpment evolution on high-elevation rifted margins: Insights derived from a surface processes model that combines diffusion, advection, and reaction. *Journal of Geophysical Research: Solid Earth* (1978-2012), 99(B6), 12191-12209.
- Koons, P. O., Upton, P., & Barker, A. D. (2012). The influence of mechanical properties on the link between tectonic and topographic evolution. *Geomorphology*, 137(1), 168-180.
- Koopmann, H., Franke, D., Schreckenberger, B., Schulz, H., Hartwig, A., Stollhofen, H., & di Primio, R. (2014). Segmentation and volcano-tectonic characteristics along the SW African continental margin, South Atlantic, as derived from multichannel seismic and potential field data. *Marine and Petroleum Geology*, 50, 22-39.
- Kounov, A., Niedermann, S., de Wit, M. J., Viola, G., Andreoli, M., & Erzinger, J. (2007). Present denudation rates at selected sections of the South African escarpment and the elevated continental interior based on cosmogenic  $^3\text{He}$  and  $^{21}\text{Ne}$ . *South African Journal of Geology*, 110(2-3), 235-248.
- Kounov, A., Viola, G., de Wit, M., & Andreoli, M. A. G. (2009). Denudation along the Atlantic passive margin: new insights from apatite fission-track analysis on the western coast of South Africa. *Geological Society, London, Special Publications*, 324(1), 287-306.
- Kounov, A., Viola, G., Dunkl, I., & Frimmel, H. E. (2013). Southern African perspectives on the long-term morpho-tectonic evolution of cratonic interiors. *Tectonophysics*, 601, 177-191.
- Ksienzyk, A. K., Dunkl, I., Jacobs, J., Fossen, H., & Kohlmann, F. (2014). From orogen to passive margin: constraints from fission track and (U-Th)/He analyses on Mesozoic uplift and fault reactivation in SW Norway. *Geological Society, London, Special Publications*, 390, SP390-27.
- Kuhlmann, G., Adams, S., Campher, C., van der Spuy, D., di Primio, R., & Horsfield, B. (2010). Passive margin evolution and its controls on natural gas leakage in the southern Orange Basin, blocks 3/4, offshore South Africa. *Marine and Petroleum Geology*, 27(4), 973-992.
- Kusznir, N. J., & Karner, G. D. (2007). Continental lithospheric thinning and breakup in response to upwelling divergent mantle flow: application to the Woodlark, Newfoundland and Iberia margins. *Geological Society, London, Special Publications*, 282(1), 389-419.
- Kusznir, N. J., & Ziegler, P. A. (1992). The mechanics of continental extension and sedimentary basin formation: a simple-shear/pure-shear flexural cantilever model. *Tectonophysics*, 215(1), 117-131.
- Lal, D. (1991). Cosmic ray labeling of erosion surfaces: "in situ" nuclide production rates and erosion models. *Earth and Planetary Science Letters*, 104(2), 424-439.
- Larson, S. Å., Cederbom, C. E., Tullborg, E. L., & Stiberg, J. P. (2006). Comment on "Apatite fission track and (U-Th)/He data from Fennoscandia: An example of underestimation of fission track annealing in apatite" by Hendriks and Redfield [*Earth Planet. Sci. Lett.* 236 (443-458)]. *Earth and Planetary Science Letters*, 248(1), 561-568.

- Laslett, G. M., Green, P. F., Duddy, I. R., & Gleadow, A. J. W. (1987). Thermal annealing of fission tracks in apatite 2. A quantitative analysis. *Chemical Geology: Isotope Geoscience Section*, 65(1), 1-13.
- Latin, D., & White, N. (1990). Generating melt during lithospheric extension: Pure shear vs. simple shear. *Geology*, 18(4), 327-331.
- Lavier, L. L., & Manatschal, G. (2006). A mechanism to thin the continental lithosphere at magma-poor margins. *Nature*, 440(7082), 324-328.
- Le Stunff, Y., & Ricard, Y. (1995). Topography and geoid due to lithospheric mass anomalies. *Geophysical Journal International*, 122(3), 982-990.
- Lee, C. T. A., Luffi, P., Höink, T., Li, Z. X. A., & Lenardic, A. (2008). The role of serpentine in preferential craton formation in the late Archean by lithosphere underthrusting. *Earth and Planetary Science Letters*, 269(1), 96-104.
- Leinweber, V. T., & Jokat, W. (2012). The Jurassic history of the Africa-Antarctica corridor—new constraints from magnetic data on the conjugate continental margins. *Tectonophysics*, 530, 87-101.
- Lenardic, A., Moresi, L. N., & Mühlhaus, H. (2003). Longevity and stability of cratonic lithosphere: insights from numerical simulations of coupled mantle convection and continental tectonics. *Journal of Geophysical Research: Solid Earth (1978-2012)*, 108(B6).
- Lenardic, A., Moresi, L., & Mühlhaus, H. (2000). The role of mobile belts for the longevity of deep cratonic lithosphere: the crumple zone model. *Geophysical Research Letters*, 27(8), 1235-1238.
- Levell, B., Argent, J., Doré, A. G., & Fraser, S. (2010, January). Passive margins: overview. In *Geological Society, London, Petroleum Geology Conference series*, 7, 823-830.
- Lidmar-Bergström, K., Bonow, J. M., & Japsen, P. (2013). Stratigraphic Landscape Analysis and geomorphological paradigms: Scandinavia as an example of Phanerozoic uplift and subsidence. *Global and Planetary Change*, 100, 153-171.
- Light, M. P. R., Maslanyj, M. P., & Banks, N. L. (1992). New geophysical evidence for extensional tectonics on the divergent margin offshore Namibia. *Geological Society, London, Special Publications*, 68(1), 257-270.
- Lisker, F., Ventura, B., & Glasmacher, U. A. (2009). Apatite thermochronology in modern geology. *Geological Society, London, Special Publications*, 324(1), 1-23.
- Lister, G. S., Etheridge, M. A., & Symonds, P. A. (1986). Detachment faulting and the evolution of passive continental margins. *Geology*, 14(3), 246-250.
- Lister, G. S., Etheridge, M. A., & Symonds, P. A. (1991). Detachment models for the formation of passive continental margins. *Tectonics*, 10(5), 1038-1064.
- Lithgow-Bertelloni, C., & Silver, P. G. (1998). Dynamic topography, plate driving forces and the African superswell. *Nature*, 395(6699), 269-272.
- Liu, L., & Gurnis, M. (2010). Dynamic subsidence and uplift of the Colorado Plateau. *Geology*, 38(7), 663-666.
- Lock, J., & Willett, S. (2008). Low-temperature thermochronometric ages in fold-and-thrust belts. *Tectonophysics*, 456(3), 147-162.
- Lovell, B., 2010, A pulse in the planet: regional control of high-frequency changes in relative sea level by mantle convection, *Journal of the Geological Society*, 167(4), 637-648.
- Lovera, O. M., Grove, M., & Harrison, T. M. (2002). Systematic analysis of K-feldspar <sup>40</sup>Ar/<sup>39</sup>Ar step heating results II: relevance of laboratory argon diffusion properties to nature. *Geochimica et Cosmochimica Acta*, 66(7), 1237-1255.
- Luft, F. F., Luft Jr, J. L., Chemale Jr, F., Lelarge, M. L. M. V., & Ávila, J. N. (2005). Post-Gondwana break-up record constraints from apatite fission track thermochronology in NW Namibia. *Radiation measurements*, 39(6), 675-679.
- Lundin, E. R., & Doré, A. G. (2002). Mid-Cenozoic post-breakup deformation in the 'passive' margins bordering the Norwegian-Greenland Sea. *Marine and Petroleum Geology*, 19(1), 79-93.
- Lundin, E. R., & Doré, A. G. (2011). Hyperextension, serpentinization, and weakening: A new paradigm for rifted margin compressional deformation. *Geology*, 39(4), 347-350.
- Lyell, C. (1833). *Principles of Geology: Being an Attempt to Explain the Former Changes of the Earth's Surface, by Reference to Causes Now in Operation (Vol. 3)*.
- Macey, P. H., Siegfried, H. P., Minnaar, H., Almond, J., & Botha, P. M. W. (2011). The geology of the Loeriesfontein area. Explanation of 1:250 000-scale Loeriesfontein. South Africa: Council for Geoscience

- MacLennan, J., & Lovell, B. (2002). Control of regional sea level by surface uplift and subsidence caused by magmatic underplating of Earth's crust. *Geology*, 30(8), 675-678.
- Magee, C., Jackson, C. A. L., & Schofield, N. (2013). The influence of normal fault geometry on igneous sill emplacement and morphology. *Geology*, 41(4), 407-410.
- Maggi, A., Jackson, J. A., McKenzie, D., & Priestley, K. (2000). Earthquake focal depths, effective elastic thickness, and the strength of the continental lithosphere. *Geology*, 28(6), 495-498.
- Malephane, H., Durrheim, R. J., & Andreoli, M. A. G. (2013). Seismic monitoring in Namaqualand/Bushmanland region. In 13th SAGA Biennial Conference & Exhibition.
- Manatschal, G., & Müntener, O. (2009). A type sequence across an ancient magma-poor ocean-continent transition: the example of the western Alpine Tethys ophiolites. *Tectonophysics*, 473(1), 4-19.
- Marais, J. A. H., Agenbacht, A. L. D., Prinsloo, M., & Basson, W. A. (2001). The geology of the Springbok area. Explanation of 1:250 000-scale 2916 Loriesfontein. South Africa: Council for Geoscience
- Mareschal, J. C., & Jaupart, C. (2013). Radiogenic heat production, thermal regime and evolution of continental crust. *Tectonophysics*, 609, 524-534.
- Marsh, J. S., Ewart, A., Milner, S. C., Duncan, A. R., & Miller, R. M. (2001). The Etendeka Igneous Province: magma types and their stratigraphic distribution with implications for the evolution of the Paraná-Etendeka flood basalt province. *Bulletin of Volcanology*, 62(6-7), 464-486.
- Maslanyj, M. P., Light, M. P. R., Greenwood, R. J., & Banks, N. L. (1992). Extension tectonics offshore Namibia and evidence for passive rifting in the South Atlantic. *Marine and Petroleum Geology*, 9(6), 590-601.
- Matthews, K. J., Hale, A. J., Gurnis, M., Muller, R. D., DiCaprio, L., 2011, Dynamic subsidence of Eastern Australia during the Cretaceous, *Gondwana Research*, 19(2), 372-383.
- Maus, S., Barckhausen, U., Berkenbosch, H., Bournas, N., Brozena, J., Childers, V., Dostaler, F., Fairhead, J. D., Finn, C., von Frese, R. R. B., Gaina, C., Golynsky, S., Kucks, R., Luhr, H., Milligan, P., Morgen, S., Muller, R. D., Olesen, O., Pilkington, M., Saltus, R., Schreckenberger, B., Thebault, E., & Caratori Tontini, F. (2009). EMAG2: A 2-arc min resolution Earth Magnetic Anomaly Grid compiled from satellite, airborne, and marine magnetic measurements. *Geochemistry, Geophysics, Geosystems*, 10(8), Q08005.
- Maxwell, J. C., 1870, On hills and dales: *Philosophical Magazine*, 40, 421-427.
- Maystrenko, Y. P., Scheck-Wenderoth, M., Hartwig, A., Anka, Z., Watts, A. B., Hirsch, K. K., & Fishwick, S. (2013). Structural features of the Southwest African continental margin according to results of lithosphere-scale 3D gravity and thermal modelling. *Tectonophysics*, 604, 104-121.
- McKenzie, D. (1978). Some remarks on the development of sedimentary basins. *Earth and planetary science letters*, 40(1), 25-32.
- McKenzie, D. 1984. A possible mechanism for epeirogenic uplift. *Nature*, 307, 616-618.
- McKenzie, D., & Bickle, M. J. (1988). The volume and composition of melt generated by extension of the lithosphere. *Journal of petrology*, 29(3), 625-679.
- McKeon, R. E., Zeitler, P. K., Pazzaglia, F. J., Idleman, B. D., & Enkelmann, E. (2014). Decay of an old orogen: Inferences about Appalachian landscape evolution from low-temperature thermochronology. *Geological Society of America Bulletin*, 126(1-2), 31-46.
- McLachlan, A. J. (1974). Development of some lake ecosystems in tropical Africa, with special reference to the invertebrates. *Biological Reviews*, 49(3), 365-397.
- McMillan, I. K. (2003). Foraminiferally defined biostratigraphic episodes and sedimentation pattern of the Cretaceous drift succession (Early Barremian to Late Maastrichtian) in seven basins on the South African and southern Namibian continental margin. *South African Journal of Science*, 99(11-12), 537-576.
- McPherson, A., Clark, D., Macphail, M., & Cupper, M. (2014). Episodic post-rift deformation in the south-eastern Australian passive margin: evidence from the Lapstone Structural Complex. *Earth Surface Processes and Landforms*, 39, 1449-1466.
- Meesters, A. G. C. A., & Dunai, T. J. (2002a). Solving the production-diffusion equation for finite diffusion domains of various shapes: Part I. Implications for low-temperature (U-Th)/He thermochronology. *Chemical Geology*, 186(3), 333-344.
- Meesters, A. G. C. A., & Dunai, T. J. (2002b). Solving the production-diffusion equation for finite diffusion domains of various shapes: Part II. Application to cases with  $\alpha$ -ejection and nonhomogeneous distribution of the source. *Chemical Geology*, 186(3), 347-363.

- Mein, P. & Pickford, M. (2008), Early Miocene Rodentia from the Northern Sperrgebiet, Namibia. *Memoir of the Geological Survey of Namibia*, 20, 235-290.
- Mein, P., & Senut, B. (2003). The Pedetidae from the Miocene site of Arrisdrift (Namibia). *Memoir of the Geological Survey of Namibia*, 19, 161-170.
- Meldrum, A., Boatner, L. A., Weber, W. J., & Ewing, R. C. (1998). Radiation damage in zircon and monazite. *Geochimica et Cosmochimica Acta*, 62(14), 2509-2520.
- Menzies, M. A., Klemperer, S. L., Ebinger, C. J., & Baker, J. (2002). Characteristics of volcanic rifted margins. *Geological Society of America, Special Papers*, 362, 1-14.
- Miller, D. S., Crowley, K. D., Dokka, R. K., Galbraith, R. F., Kowallis, B. J., & Naeser, C. W. (1993). Results of interlaboratory comparison of fission track ages for 1992 Fission Track Workshop. *Nuclear Tracks and Radiation Measurements*, 21(4), 565-573.
- Miro, S., Grebille, D., Chateigner, D., Pelloquin, D., Stoquert, J. P., Grob, J. J., Constantini, J. M. & Studer, F. (2005). X-ray diffraction study of damage induced by swift heavy ion irradiation in fluorapatite. *Nuclear Instruments and Methods in Physics Research Section B: Beam Interactions with Materials and Atoms*, 227(3), 306-318.
- Mitchell, S.G. & Montgomery, D.R. 2006: Influence of a glacial buzzsaw on the height and morphology of the Cascade Range in central Washington State, USA. *Quaternary Research* 65, 96-107.
- Mitrovica, J. X., Beuamont, C., and Jarvis, G. T., (1989), Tilting of continental interiors by the dynamical effects of subduction, *Tectonics*, 8(5), 1079-1094.
- Molnar, P., & England, P. (1990). Late Cenozoic uplift of mountain ranges and global climate change: chicken or egg?. *Nature*, 346(6279), 29-34.
- Moore, A. E., & Verwoerd, W. J. (1985). The olivine melilitite-"kimberlite"-carbonatite suite of Namaqualand and Bushmanland, South Africa. *South African Journal of Geology*, 88(2), 281-294.
- Moore, A., Blenkinsop, T., & Cotterill, F. W. (2008). Controls on post-Gondwana alkaline volcanism in Southern Africa. *Earth and Planetary Science Letters*, 268(1), 151-164.
- Moore, A., Blenkinsop, T., & Cotterill, F. W. (2009). Southern African topography and erosion history: plumes or plate tectonics? *Terra Nova*, 21(4), 310-315.
- Moucha, R., & Forte, A. M. (2011). Changes in African topography driven by mantle convection. *Nature Geoscience*, 4(10), 707-712.
- Moucha, R., Forte, A. M., Mitrovica, J. X., Rowley, D. B., Quéré, S., Simmons, N. A., & Grand, S. P. (2008). Dynamic topography and long-term sea-level variations: There is no such thing as a stable continental platform. *Earth and Planetary Science Letters*, 271(1), 101-108.
- Moulin, M., Aslanian, D., & Unternehr, P. (2010). A new starting point for the South and Equatorial Atlantic Ocean. *Earth-Science Reviews*, 98(1), 1-37.
- Moulin, M., Fluteau, F., Courtillot, V., Marsh, J., Delpéch, G., Quidelleur, X., Gerard, M. & Jay, A. E. (2011). An attempt to constrain the age, duration, and eruptive history of the Karoo flood basalt: Naude's Nek section (South Africa). *Journal of Geophysical Research: Solid Earth* (1978-2012), 116(B7).
- Muller, M. R., Jones, A. G., Evans, R. L., Grütter, H. S., Hatton, C., Garcia, X., Hamilton, M. P., Meinsopust, M. P., Cole, P., Ngwisanyi, T., Hitchins, D., Fourie, C. J., Jelsma, H. A., Evans, S. F., Aravanis, T., Pettit, W., Webb, S. J. & Wasborg, J. (2009). Lithospheric structure, evolution and diamond prospectivity of the Rehoboth Terrane and western Kaapvaal Craton, southern Africa: Constraints from broadband magnetotellurics. *Lithos*, 112, 93-105.
- Müller, R. D., Dyksterhuis, S., & Rey, P. (2012). Australian paleo-stress fields and tectonic reactivation over the past 100 Ma. *Australian Journal of Earth Sciences*, 59(1), 13-28.
- Müller, R. D., Sdrolias, M., Gaina, C., Steinberger, B., & Heine, C. (2008). Long-term sea-level fluctuations driven by ocean basin dynamics. *science*, 319(5868), 1357-1362.
- Müntener, O., & Manatschal, G. (2006). High degrees of melt extraction recorded by spinel harzburgite of the Newfoundland margin: The role of inheritance and consequences for the evolution of the southern North Atlantic. *Earth and Planetary Science Letters*, 252(3), 437-452.
- Muntingh, A., & Brown Jr, L. F. (1993). Sequence Stratigraphy of Petroleum Plays, Post-Rift Cretaceous Rocks (Lower Aptian to Upper Maastrichtian), Orange Basin, Western Offshore, South Africa: Chapter 4: Recent Applications of Siliciclastic Sequence Stratigraphy.
- Mvondo, F., Dauteuil, O., & Guillocheau, F. (2011). The Fish River canyon (Southern Namibia): a record of Cenozoic mantle dynamics?. *Comptes Rendus Geoscience*, 343(7), 478-485.

- Naeser, C. W., & Faul, H. (1969). Fission track annealing in apatite and sphene. *Journal of Geophysical Research*, 74(2), 705-710.
- Nasdala, L., Wenzel, M., Vavra, G., Irmer, G., Wenzel, T., & Kober, B. (2001). Metamictisation of natural zircon: accumulation versus thermal annealing of radioactivity-induced damage. *Contributions to Mineralogy and Petrology*, 141(2), 125-144.
- Newton, A. R., Shone, R. W., & Booth, P. W. K. (2006). The Cape fold belt. *The Geology of South Africa*. In Johnson, M. R., Anhaeusser, C. R., and Thomas, R. J. (eds.), *The Geology of South Africa*, p. 521-530. Pretoria, South Africa: Geological Society of South Africa/Council for GeoScience.
- Nguuri, T. K., Gore, J., James, D. E., Webb, S. J., Wright, C., Zengeni, T. G., Gwavava, J. & Snoke, J. A. (2001). Crustal structure beneath southern Africa and its implications for the formation and evolution of the Kaapvaal and Zimbabwe cratons. *Geophysical Research Letters*, 28(13), 2501-2504.
- Niu, F., Levander, A., Cooper, C. M., Lee, C. T. A., Lenardic, A., & James, D. E. (2004). Seismic constraints on the depth and composition of the mantle keel beneath the Kaapvaal craton. *Earth and Planetary Science Letters*, 224(3), 337-346.
- Nürnberg, D., & Müller, R. D. (1991). The tectonic evolution of the South Atlantic from Late Jurassic to present. *Tectonophysics*, 191(1), 27-53
- Nyblade, A. A., & Robinson, S. W. (1994). The African superswell. *Geophysical Research Letters*, 21(9), 765-768.
- Oldroyd, D. R., & Grapes, R. H. (2008). Contributions to the history of geomorphology and Quaternary geology: an introduction. Geological Society, London, Special Publications, 301(1), 1-17.
- Ollier, C. D. (1982). The Great Escarpment of eastern Australia: tectonic and geomorphic significance. *Journal of the Geological Society of Australia*, 29(1-2), 13-23.
- Ollier, C. D. (1985). Morphotectonics of continental margins with great escarpments. *Tectonic geomorphology*, 3-25.
- Ollier, C. (2014). Some Principles in the Study of Planation Surfaces. In Rabassa, J. & Ollier, C. (eds.), *Gondwana Landscapes in southern South America*, p. 47-59. Netherlands: Springer.
- Ollier, C. D., & Marker, M. E. (1985). The great escarpment of southern Africa. *Z. Geomorph. Suppl*, 54, 37-56.
- Ollier, C. D., & Pain, C. F. (1997). Equating the basal unconformity with the palaeoplain: a model for passive margins. *Geomorphology*, 19(1), 1-15.
- Ollier, C., & Pain, C. F. (2000). *The origin of mountains*. Psychology Press.
- O'Reilly, B. M., Hauser, F., Jacob, A. W., & Shannon, P. M. (1996). The lithosphere below the Rockall Trough: wide-angle seismic evidence for extensive serpentinisation. *Tectonophysics*, 255(1), 1-23.
- O'Sullivan, P. B., & Parrish, R. R. (1995). The importance of apatite composition and single-grain ages when interpreting fission track data from plutonic rocks: a case study from the Coast Ranges, British Columbia. *Earth and Planetary Science Letters*, 132(1), 213-224.
- Palmquist, R. C. (1975). The compatibility of structure, lithology, and geomorphic models. *Theories of landform development*, 6, 145.
- Parsiegla, N., Gohl, K., & Uenzelmann-Neben, G. (2008). The Agulhas Plateau: Structure and evolution of a large igneous province. *Geophysical Journal International*, 174(1), 336-350.
- Partridge, T. C. (1998). Of diamonds, dinosaurs and diastrophism; 150 million years of landscape evolution in southern Africa. *South African Journal of Geology*, 101(3), 167-184.
- Partridge, T. C., & Maud, R. R. (1987). Geomorphic evolution of southern Africa since the Mesozoic. *South African Journal of Geology*, 90(2), 179-208.
- Partridge, T. C., & Maud, R. R. (2000). Macro-scale geomorphic evolution of southern Africa. *Oxford Monographs on Geology and Geophysics*, 40, 3-18.
- Partridge, T. C., Botha, G. A., & Haddon, I. G. (2006). Cenozoic deposits of the interior. *The geology of South Africa*, 585-604.
- Paton, D. (2012). Post-Rift Deformation of the North East and South Atlantic Margins: Are "Passive Margins" Really Passive?. In Busby, C., & Azor Perez, A., *Tectonics of Sedimentary Basins: Recent Advances*. p. 249-269. Wiley-Blackwell.
- Paton, D. A., Macdonald, D. I., & Underhill, J. R. (2006a). Applicability of thin or thick skinned structural models in a region of multiple inversion episodes; southern South Africa. *Journal of structural geology*, 28(11), 1933-1947.

- Paton, D. A. (2006b). Influence of crustal heterogeneity on normal fault dimensions and evolution: southern South Africa extensional system. *Journal of structural geology*, 28(5), 868-886.
- Paton, D. A., Di Primio, R., Kuhlmann, G., Van Der Spuy, D., & Horsfield, B. (2007). Insights into the petroleum system evolution of the southern Orange Basin, South Africa. *South African Journal of Geology*, 110(2-3), 261-274.
- Paton, D. A., van der Spuy, D., di Primio, R., & Horsfield, B. (2008). Tectonically induced adjustment of passive-margin accommodation space; influence on the hydrocarbon potential of the Orange Basin, South Africa. *AAPG bulletin*, 92(5), 589-609.
- Paul, J. D., Roberts, G. G., & White, N. (2014). The African landscape through space and time. *Tectonics*, 32, 898-935
- Peizhen, Z., Molnar, P., & Downs, W. R. (2001). Increased sedimentation rates and grain sizes 2-4 Myr ago due to the influence of climate change on erosion rates. *Nature*, 410(6831), 891-897.
- Pekeris, C. L. (1935). Thermal convection in the interior of the Earth. *Geophysical Supplements to the Monthly Notices of the Royal Astronomical Society*, 3(8), 343-367.
- Penck, W., 1924, *Die Morphologische Analyse: Ein Kapitel der physikalischen Geologie*. J. Engelhorns, Stuttgart.
- Péron-Pinvidic, G., & Manatschal, G. (2009). The final rifting evolution at deep magma-poor passive margins from Iberia-Newfoundland: a new point of view. *International Journal of Earth Sciences*, 98(7), 1581-1597.
- Péron-Pinvidic, G., Manatschal, G., & Osmundsen, P. T. (2013). Structural comparison of archetypal Atlantic rifted margins: a review of observations and concepts. *Marine and Petroleum Geology*, 43, 21-47.
- Persano, C., Stuart, F. M., Bishop, P., & Barfod, D. N. (2002). Apatite (U-Th)/He age constraints on the development of the Great Escarpment on the southeastern Australian passive margin. *Earth and Planetary Science Letters*, 200(1), 79-90.
- Persano, C. (2003). A combination of apatite fission track and (U-Th)/He thermochronometers to constrain the escarpment evolution in south eastern Australia: a case study of high elevation passive margins (Doctoral dissertation, University of Glasgow).
- Persano, C., Stuart, F. M., Bishop, P., & Dempster, T. J. (2005). Deciphering continental breakup in eastern Australia using low-temperature thermochronometers. *Journal of Geophysical Research: Solid Earth* (1978-2012), 110(B12).
- Peslier, A. H., Woodland, A. B., Bell, D. R., & Lazarov, M. (2010). Olivine water contents in the continental lithosphere and the longevity of cratons. *Nature*, 467(7311), 78-81.
- Petersen, K. D., Nielsen, S. B., Clausen, O. R., Stephenson, R., & Gerya, T. (2010). Small-scale mantle convection produces stratigraphic sequences in sedimentary basins. *Science*, 329(5993), 827-830.
- Petit, C., & Ebinger, C. (2000). Flexure and mechanical behavior of cratonic lithosphere: Gravity models of the East African and Baikal rifts. *Journal of Geophysical Research: Solid Earth* (1978-2012), 105(B8), 19151-19162.
- Peulvast, J. P., & de Claudino Sales, V. (2004). Stepped surfaces and palaeolandforms in the northern Brazilian "Nordeste": constraints on models of morphotectonic evolution. *Geomorphology*, 62(1), 89-122.
- Phillips, D., Kiviets, G.B., Biddulph, M.G., Madav, M.K., 2000. Cenozoic volcanism. In: Partridge, T.C., Maud, R.R. (Eds.), *The Cenozoic of Southern Africa*, p. 182-197. Oxford University Press.
- Phillips, J. D. (2002). Erosion, isostatic response, and the missing peneplains. *Geomorphology*, 45(3), 225-241.
- Pickford, M. (2005). *Choerolophodon pygmaeus* (Proboscidea: Mammalia) from the Middle Miocene of southern Africa: research letter. *South African journal of science*, 101(3-4), 175-177.
- Pickford, M. (2008). Freshwater and terrestrial Mollusca from Early Miocene deposits of the northern Sperrgebiet, Namibia. *Memoir of the Geological Survey of Namibia*, 20, 65-74.
- Pickford, M., & Mein, P. (2011). Nuevos Pedetidae (Rodentia: Mammalia) del Mio-Plioceno de Africa. *Estudios Geológicos*, 67(2), 455-469.
- Pickford, M., Eisenmann, V., & Senut, B. (1999). Timing of landscape development and calcrete genesis in northern Namaqualand, South Africa. *South African Journal of Science*, 95, 357-358.

- Pickford, M., Senut, B., Morales, J., & Sanchez, I.M. (2008a). Fossiliferous Cainozoic carbonates of the Northern Sperrgebiet. In Pickford, M. & Senut, B. (Eds.), *Geology and Palaeobiology of the Northern Sperrgebiet, Namibia*. Memoir of the Geological Survey of Namibia 20, 25-42.
- Pickford, M., Senut, B., Morales, J., Mein, P., & Sanchez, I.M. (2008b). Mammalia from the Lutetian of Namibia. In Pickford, M. & Senut, B. (Eds.), *Geology and Palaeobiology of the Northern Sperrgebiet, Namibia*. Memoir of the Geological Survey of Namibia 20, 465-514.
- Pidgeon, R. T. (2014). Zircon radiation damage ages. *Chemical Geology*, 367, 13-22.
- Pitman, W. C., & Golovchenko, X. (1991). The effect of sea level changes on the morphology of mountain belts. *Journal of Geophysical Research: Solid Earth* (1978-2012), 96(B4), 6879-6891.
- Praeg, D., Stoker, M. S., Shannon, P. M., Ceramicola, S., Hjelstuen, B., Laberg, J. S., & Mathiesen, A. (2005). Episodic Cenozoic tectonism and the development of the NW European 'passive' continental margin. *Marine and Petroleum Geology*, 22(9), 1007-1030.
- Priestley, K., McKenzie, D., Debayle, E., & Pilidou, S. (2008). The African upper mantle and its relationship to tectonics and surface geology. *Geophysical Journal International*, 175(3), 1108-1126.
- Pugh, J. C. (1955). Isostatic readjustment in the theory of pediplanation. *Quarterly Journal of the Geological Society*, 111(1-4), 361-374.
- Pysklywec, R. N., & Beaumont, C. (2004). Intraplate tectonics: feedback between radioactive thermal weakening and crustal deformation driven by mantle lithosphere instabilities. *Earth and Planetary Science Letters*, 221(1), 275-292.
- Raab, M. J., Brown, R. W., Gallagher, K., Carter, A., & Weber, K. (2002). Late Cretaceous reactivation of major crustal shear zones in northern Namibia: constraints from apatite fission track analysis. *Tectonophysics*, 349(1), 75-92.
- Raab, M. J., Brown, R. W., Gallagher, K., Weber, K., & Gleadow, A. J. W. (2005). Denudational and thermal history of the Early Cretaceous Brandberg and Okenyenya igneous complexes on Namibia's Atlantic passive margin. *Tectonics*, 24(3), TC3006.
- Rabassa, J., & Ollier, C. (Eds.). (2014). *Gondwana Landscapes in Southern South America: Argentina, Uruguay and Southern Brazil*.
- Rabassa, J. (2014). Some concepts on Gondwana landscapes: long-term landscape evolution, genesis, distribution and age. In Rabassa, J. & Ollier, C. (eds.), *Gondwana Landscapes in southern South America*, p. 9-46. Netherlands: Springer.
- Rage, J. C. (2003). Squamate reptiles from the early Miocene of Arrisdrift (Namibia). *Geology and Palaeobiology of the central and southern Namib*, 2, 43-50.
- Rage, J. C., Pickford, M., & Senut, B. (2013). Amphibians and squamates from the middle Eocene of Namibia, with comments on pre-Miocene anurans from Africa. *Annales de Paléontologie*, 99(3), 217-242.
- Ravenhurst, C. E., Roden, M. K., Willett, S. D., & Miller, D. S. (1993). Dependence of fission track annealing kinetics on apatite crystal chemistry. *Nuclear Tracks and Radiation Measurements*, 21(4), 622.
- Raymo, M. E., & Ruddiman, W. F. (1992). Tectonic forcing of late Cenozoic climate. *Nature*, 359(6391), 117-122.
- Redfield, T. F., Torsvik, T. H., Andriessen, P. A. M., & Gabrielsen, R. H. (2004). Mesozoic and Cenozoic tectonics of the Møre Trøndelag Fault Complex, central Norway: constraints from new apatite fission track data. *Physics and Chemistry of the Earth, Parts A/B/C*, 29(10), 673-682.
- Redfield, T. F., Braathen, A., Gabrielsen, R. H., Osmundsen, P. T., Torsvik, T. H., & Andriessen, P. A. M. (2005a). Late Mesozoic to Early Cenozoic components of vertical separation across the Møre-Trøndelag fault complex, Norway. *Tectonophysics*, 395(3), 233-249.
- Redfield, T. F., Osmundsen, P. T., & Hendriks, B. W. H. (2005b). The role of fault reactivation and growth in the uplift of western Fennoscandia. *Journal of the Geological Society*, 162(6), 1013-1030.
- Reech, M., 1858, *Propriété générale des surfaces fermées*: Ecole Polytech. Jour. Paris, 37, 169 - 178.
- Reemst, P., & Cloetingh, S. (2000). Polyphase rift evolution of the Vøring margin (mid-Norway): Constraints from forward tectonostratigraphic modeling. *Tectonics*, 19(2), 225-240.
- Reeves, C., & De Wit, M. (2000). Making ends meet in Gondwana: retracing the transforms of the Indian Ocean and reconnecting continental shear zones. *Terra Nova*, 12(6), 272-280.



- Reid, D. L. (1990). The Cape Peninsula dolerite dyke swarm, South Africa: Mafic Dikes and Emplacement Mechanisms. p. 325-334. Rotterdam, The Netherlands: Balkema.
- Reid, D. L., & Rex, D. C. (1994). Cretaceous dykes associated with the opening of the South Atlantic; the Mehlberg Dyke, northern Richtersveld. *South African Journal of Geology*, 97(2), 135-145.
- Reid, D. L., Cooper, A. F., Rex, D. C., & Harmer, R. E. (1990). Timing of post-Karoo alkaline volcanism in southern Namibia. *Geological Magazine*, 127(5), 427-433.
- Reid, D. L., Erlank, A. J., & Rex, D. C. (1991). Age and correlation of the False Bay dolerite dyke swarm, south-western Cape, Cape Province. *South African Journal of Geology*, 94(2-3), 155-158.
- Reinecker, J., O. Heidbach, M. Tingay, P. Connolly, and B. Muller (2004), The 2004 release of the World Stress Map, World Stress Map Proj. (Available online at [www.world-stress-map.org](http://www.world-stress-map.org))
- Reiners, P. W., & Farley, K. A. (2001). Influence of crystal size on apatite (U-Th)/He thermochronology: an example from the Bighorn Mountains, Wyoming. *Earth and Planetary Science Letters*, 188(3), 413-420.
- Reiners, P. W., Zhou, Z., Ehlers, T. A., Xu, C., Brandon, M. T., Donelick, R. A., & Nicolescu, S. (2003). Post-orogenic evolution of the Dabie Shan, eastern China, from (U-Th)/He and fission-track thermochronology. *American Journal of Science*, 303(6), 489-518.
- Rennie, J. V. (1931). Note on fossil leaves from the Banke clays. *Transactions of the Royal Society of South Africa*, 19(3), 251-253.
- Reston, T. J. (2007). The formation of non-volcanic rifted margins by the progressive extension of the lithosphere: the example of the West Iberian margin. *Geological Society, London, Special Publications*, 282(1), 77-110.
- Reston, T. J. (2009). The structure, evolution and symmetry of the magma-poor rifted margins of the North and Central Atlantic: a synthesis. *Tectonophysics*, 468(1), 6-27.
- Reston, T., & McDermott, K. (2014). An assessment of the cause of the 'extension discrepancy' with reference to the west Galicia margin. *Basin Research*, 26(1), 135-153.
- Reusch, A. M., Nyblade, A. A., Wiens, D. A., Shore, P. J., Ateba, B., Tabod, C. T., & Nnange, J. M. (2010). Upper mantle structure beneath Cameroon from body wave tomography and the origin of the Cameroon Volcanic Line. *Geochemistry, Geophysics, Geosystems*, 11(10).
- Reynisson, R. F., Ebbing, J., Lundin, E., & Osmundsen, P. T. (2010). Properties and distribution of lower crustal bodies on the mid-Norwegian margin. *Geological Society of London, Petroleum Geology Conference series*, 7, 843-854.
- Ritsema, J., van Heijst, H. J., & Woodhouse, J. H. (1999). Complex shear wave velocity structure imaged beneath Africa and Iceland. *Science*, 286(5446), 1925-1928.
- Roberts, D. L., Botha, G. A., Maud, R. R., & Pether, J. (2006). Coastal cenozoic deposits. In Johnson, M. R., Anhaeusser, C. R., and Thomas, R. J. (eds.), *The Geology of South Africa*, p. 605-628. Pretoria, South Africa: Geological Society of South Africa/Council for GeoScience.
- Roberts, D. L., Matthews, T., Herries, A. I., Boulter, C., Scott, L., Dondo, C., Mtembi, P., Browning, C., Smith, R. M. H., Haarhoff, P. & Bateman, M. D. (2011). Regional and global context of the Late Cenozoic Langebaanweg (LBW) palaeontological site: West Coast of South Africa. *Earth-Science Reviews*, 106(3), 191-214.
- Roberts, G. G., & White, N. (2010). Estimating uplift rate histories from river profiles using African examples. *Journal of Geophysical Research: Solid Earth* (1978-2012), 115(B2).
- Roe, G. H., Stolar, D. B., & Willett, S. D. (2006). Response of a steady-state critical wedge orogen to changes in climate and tectonic forcing. *Geological Society of America Special Papers*, 398, 227-239.
- Römer, W. (2010). Multiple planation surfaces in basement regions: Implications for the reconstruction of periods of denudation and uplift in southern Zimbabwe. *Geomorphology*, 114(3), 199-212.
- Rouby, D., Bonnet, S., Guillocheau, F., Gallagher, K., Robin, C., Biancotto, F., Dauteuil, O. & Braun, J. (2009). Sediment supply to the Orange sedimentary system over the last 150My: An evaluation from sedimentation/denudation balance. *Marine and Petroleum Geology*, 26(6), 782-794.
- Rouby, D., Braun, J., Robin, C., Dauteuil, O., & Deschamps, F. (2013). Long-term stratigraphic evolution of Atlantic-type passive margins: A numerical approach of interactions between surface processes, flexural isostasy and 3D thermal subsidence. *Tectonophysics*, 604, 83-103.

- Rowley, D. B., Forte, A. M., Moucha, R., Mitrovica, J. X., Simmons, N. A., Grand, S. P., (2013), Dynamic topography change of the eastern United States since 3 million years ago, *Science*, 340, 6140, 1560-1563
- Rust, D. J., & Summerfield, M. A. (1990). Isopach and borehole data as indicators of rifted margin evolution in southwestern Africa. *Marine and Petroleum Geology*, 7(3), 277-287.
- Sacek, V., Braun, J., & Beek, P. (2012). The influence of rifting on escarpment migration on high elevation passive continental margins. *Journal of Geophysical Research: Solid Earth* (1978-2012), 117(B4).
- Saintot, A., Stephens, M. B., Viola, G., & Nordgulen, Ø. (2011). Brittle tectonic evolution and paleostress field reconstruction in the southwestern part of the Fennoscandian Shield, Forsmark, Sweden. *Tectonics*, 30(4).
- Salomon, E., Koehn, D., Passchier, C., Hackspacher, P. C., & Glasmacher, U. A. (2014). Contrasting stress fields on correlating margins of the South Atlantic. *Gondwana Research*, *in press*.
- Sambridge, M., Gallagher, K., Jackson, A., & Rickwood, P. (2006). Trans-dimensional inverse problems, model comparison and the evidence. *Geophysical Journal International*, 167(2), 528-542.
- Scharf, T. E., Codilean, A. T., de Wit, M., Jansen, J. D., & Kubik, P. W. (2013). Strong rocks sustain ancient postorogenic topography in southern Africa. *Geology*, 41(3), 331-334.
- Scheepers, J. and Andreoli, M.A.G, 2004, The seismological record of Vaalputs up to 31st December 2003: Necca Open File Report GEA-1650, 99 pp
- Scheepers, R., & Schoch, A. E. (2006). The Cape Granite Suite. In Johnson, M. R., Anhaeusser, C. R., and Thomas, R. J. (eds.), *The Geology of South Africa*, p. 421-432. Pretoria, South Africa: Geological Society of South Africa/Council for GeoScience.
- Scheffler, K., Buehmann, D., & Schwark, L. (2006). Analysis of late Palaeozoic glacial to postglacial sedimentary successions in South Africa by geochemical proxies-response to climate evolution and sedimentary environment. *Palaeogeography, Palaeoclimatology, Palaeoecology*, 240(1), 184-203.
- Scheiber-Enslin, S., Webb, S., Ebbing, J., & Eberle, D. (2013, January). Integrated interpretation of potential field and seismic data for shale gas potential in the Karoo Basin, South Africa. In 2013 SEG Annual Meeting. Society of Exploration Geophysicists.
- Schettino, A., & Scotese, C. R. (2005). Apparent polar wander paths for the major continents (200 Ma to the present day): a palaeomagnetic reference frame for global plate tectonic reconstructions. *Geophysical Journal International*, 163(2), 727-759.
- Schlüter, T. (2008). *Geological Atlas of Africa: With Notes on Stratigraphy, Tectonics, Economic Geology, Geohazards, Geosites and Geoscientific Education of Each Country*. pp. 307, Berlin Heidelberg: Springer.
- Schmidt, J. S., Lelarge, M. L. M. V., Conceicao, R. V., & Balzaretto, N. M. (2014). Experimental evidence regarding the pressure dependence of fission track annealing in apatite. *Earth and Planetary Science Letters*, 390, 1-7.
- Scholtz, A. (1985). The palynology of the upper lacustrine sediments of the Arnot Pipe, Banke, Namaqualand, The South African Museum, 95
- Schröder, S., Bedorf, D., Beukes, N. J., & Gutzmer, J. (2011). From BIF to red beds: Sedimentology and sequence stratigraphy of the Paleoproterozoic Koegas Subgroup (South Africa). *Sedimentary Geology*, 236(1), 25-44.
- Scotese, C. R., Boucot, A. J., & McKerrow, W. S. (1999). Gondwanan palaeogeography and palaeoclimatology. *Journal of African Earth Sciences*, 28(1), 99-114.
- Scotese, C. R., Gahagan, L. M., & Larson, R. L. (1988). Plate tectonic reconstructions of the Cretaceous and Cenozoic ocean basins. *Tectonophysics*, 155(1), 27-48.
- Seidl, M. A., Weissel, J. K., & Pratson, L. F. (1996). The kinematics and pattern of escarpment retreat across the rifted continental margin of SE Australia. *Basin Research*, 8(3), 301-316.
- Senut, B., Pickford, M., & Wessels, D. (1997). Panafrican distribution of lower Miocene Hominoidea. *Comptes Rendus de l'Académie des Sciences-Series IIA-Earth and Planetary Science*, 325(9), 741-746.
- Séranne, M., & Anka, Z. (2005). South Atlantic continental margins of Africa: a comparison of the tectonic vs climate interplay on the evolution of equatorial west Africa and SW Africa margins. *Journal of African Earth Sciences*, 43(1), 283-300.
- Shephard, G. E., Liu, L., Müller, R. D., & Gurnis, M. (2012). Dynamic topography and anomalously negative residual depth of the Argentine Basin. *Gondwana Research*, 22(2), 658-663.

- Shephard, G. E., Muller, R. D., Liu, L., and Gurnis, M., 2010, Miocene drainage reversal of the Amazon River driven by plate-mantle interaction, *Nature Geoscience*, 3(12), 870-875.
- Shirey, S. B., Carlson, R. W., Richardson, S. H., Menzies, A., Gurney, J. J., Pearson, D. G., Harris, J. & Wiechert, U. (2001). Archean emplacement of eclogitic components into the lithospheric mantle during formation of the Kaapvaal Craton. *Geophysical Research Letters*, 28(13), 2509-2512.
- Shuster, D. L., & Farley, K. A. (2009). The influence of artificial radiation damage and thermal annealing on helium diffusion kinetics in apatite. *Geochimica et Cosmochimica Acta*, 73(1), 183-196.
- Shuster, D. L., Flowers, R. M., & Farley, K. A. (2006). The influence of natural radiation damage on helium diffusion kinetics in apatite. *Earth and Planetary Science Letters*, 249(3), 148-161.
- Sibson, R. H. (1985). A note on fault reactivation. *Journal of Structural Geology*, 7(6), 751-754.
- Simmons, N. A., Forte, A. M., & Grand, S. P. (2007). Thermochemical structure and dynamics of the African superplume. *Geophysical Research Letters*, 34(2), L02301.
- Sinclair, H. D., Coakley, B. J., Allen, P. A., & Watts, A. B. (1991). Simulation of foreland basin stratigraphy using a diffusion model of mountain belt uplift and erosion: an example from the central Alps, Switzerland. *Tectonics*, 10(3), 599-620.
- Sklar, L. S., & Dietrich, W. E. (2001). Sediment and rock strength controls on river incision into bedrock. *Geology*, 29(12), 1087-1090.
- Smith, R. M. H. (1986). Sedimentation and palaeoenvironments of Late Cretaceous crater-lake deposits in Bushmanland, South Africa. *Sedimentology*, 33(3), 369-386.
- Smith, W. H. F., & Wessel, P. (1990). Gridding with continuous curvature splines in tension. *Geophysics*, 55(3), 293-305.
- Sobel, E. R., & Seward, D. (2010). Influence of etching conditions on apatite fission-track etch pit diameter. *Chemical Geology*, 271(1), 59-69.
- Soudouji, F., Yuan, X., Kind, R., Lebedev, S., Adam, J. M. C., Kästle, E., & Tilmann, F. (2013). Seismic evidence for stratification in composition and anisotropic fabric within the thick lithosphere of Kalahari Craton. *Geochemistry, Geophysics, Geosystems*, 14(12), 5393-5412.
- Spiegel, C., Kohn, B., Belton, D., Berner, Z., & Gleadow, A. (2009). Apatite (U-Th-Sm)/He thermochronology of rapidly cooled samples: the effect of He implantation. *Earth and Planetary Science Letters*, 285(1), 105-114.
- Spiegel, C., Kohn, B., Raza, A., Rainer, T., & Gleadow, A. (2007). The effect of long-term low-temperature exposure on apatite fission track stability: a natural annealing experiment in the deep ocean. *Geochimica et Cosmochimica Acta*, 71(18), 4512-4537.
- Stankiewicz, J., Parsiegla, N., Ryberg, T., Gohl, K., Weckmann, U., Trumbull, R., & Weber, M. (2008). Crustal structure of the southern margin of the African continent: Results from geophysical experiments. *Journal of Geophysical Research: Solid Earth* (1978-2012), 113(B10).
- Stanley, J. R., Flowers, R. M., & Bell, D. R. (2013). Kimberlite (U-Th)/He dating links surface erosion with lithospheric heating, thinning, and metasomatism in the southern African Plateau. *Geology*, 41(12), 1243-1246.
- Steckler, M. S., & Watts, A. B. (1982). Subsidence history and tectonic evolution of Atlantic-type continental margins. *Geodynamics Series*, 6, 184-196.
- Steer, P., Huisman, R.S., Valla, P.G., Gac, S. & Herman, F. (2012). Bimodal Plio-Quaternary glacial erosion of fjords and low-relief surfaces in Scandinavia. *Nature Geoscience*, 5, 635-639.
- Stevenson, I. R., & McMillan, I. K. (2004). Incised valley fill stratigraphy of the Upper Cretaceous succession, proximal Orange Basin, Atlantic margin of southern Africa. *Journal of the Geological Society*, 161(2), 185-208.
- Stockli, D. F., Farley, K. A., & Dumitru, T. A. (2000). Calibration of the apatite (U-Th)/He thermochronometer on an exhumed fault block, White Mountains, California. *Geology*, 28(11), 983-986.
- Stracke, K. J., Ferguson, J., & Black, L. P. (1979). Structural setting of kimberlites in south-eastern Australia. *Kimberlites, Diatremes, and Diamonds: Their Geology, Petrology, and Geochemistry*, 71-91.
- Strak, V., Dominguez, S., Petit, C., Meyer, B., & Loget, N. (2011). Interaction between normal fault slip and erosion on relief evolution: Insights from experimental modelling. *Tectonophysics*, 513(1), 1-19.

- Stromer, E. (1926). Reste Land- und Süßwasser bewohnender Wirbeltiere aus den Diamantfeldern
- Summerfield, M. A. (1985). Plate tectonics and landscape development on the African continent. In Morisawa, M., and Hack, J. T., *Tectonic Geomorphology*, 27-51. Boston: Allan and Unwin.
- Summerfield, M. A., & Brown, R. W. (1998). Geomorphic factors in the interpretation of fission-track data. In van den Haute, P. & De Corte, F., *Advances in fission-track geochronology*, p. 269-284, Netherlands: Springer.
- Summerfield, M. A. (1991). *Global geomorphology: An introduction to the study of landforms* (pp. 1-537). London/New York: Longman Scientific & Technical.
- Summerfield, M. A., (2000). *Geomorphology and global tectonics*. John Wiley & Sons Inc.
- Svensen, H., Corfu, F., Polteau, S., Hammer, Ø., & Planke, S. (2012). Rapid magma emplacement in the Karoo large igneous province. *Earth and Planetary Science Letters*, 325, 1-9.
- Sykes, L. R. (1978). Intraplate seismicity, reactivation of preexisting zones of weakness, alkaline magmatism, and other tectonism postdating continental fragmentation. *Reviews of Geophysics*, 16(4), 621-688.
- Szatmari, P. (2000). Chapter 6: Habitat of Petroleum Along the South Atlantic Margins. In Mello, M. R. & Katz, B. J. (eds.), *Petroleum Systems of South Atlantic Margins*, AAPG Memoir, 73, 69-75.
- Tankard, A. J., & Rogers, J. (1978). Late Cenozoic palaeoenvironments on the west coast of southern Africa. *Journal of Biogeography*, 319-337.
- Tankard, A. J., Eriksson, S. C., Hunter, D. R., Jackson, M. P. A., Hobday, D. K., and Minter, W. E. L. (1982). Crustal evolution of southern Africa: 3.8 billion years of Earth history (p. 523). New York: Springer-Verlag.
- Tankard, A. J., Ultiana, M. A., Welsink, H. J., Ramos, V. A., Turic, M., Milani, A. F. E., de Brito Neves, B. B., Eyles, N, & Miller, R. M. (1995). Structural and tectonic controls of basin evolution in southwestern Gondwana during the Phanerozoic.
- Tankard, A., Welsink, H., Aukes, P., Newton, R., & Stettler, E. (2009). Tectonic evolution of the Cape and Karoo basins of South Africa. *Marine and Petroleum Geology*, 26(8), 1379-1412.
- Tankard, A.J. (1974) Varswater Formation of the Langebaanweg-Saldanha area, Cape Province. *Transactions of the Geological Society of South Africa*. 77, 265-283.
- ten Brink, U., & Stern, T. (1992). Rift flank uplifts and hinterland basins: comparison of the Transantarctic Mountains with the Great Escarpment of southern Africa. *Journal of Geophysical Research: Solid Earth* (1978-2012), 97(B1), 569-585.
- ter Voorde, M., De Bruijne, C. H., Cloetingh, S. A. P. L., & Andriessen, P. A. M. (2004). Thermal consequences of thrust faulting: simultaneous versus successive fault activation and exhumation. *Earth and Planetary Science Letters*, 223(3), 395-413.
- Thiede, R. C., Arrowsmith, J. R., Bookhagen, B., McWilliams, M. O., Sobel, E. R., & Strecker, M. R. (2005). From tectonically to erosionally controlled development of the Himalayan orogen. *Geology*, 33(8), 689-692.
- Thomas, D. S. G., & Shaw, P. A. (1990). The deposition and development of the Kalahari Group sediments, central southern Africa. *Journal of African Earth Sciences (and the Middle East)*, 10(1), 187-197.
- Thomas, M. F. (1995). Models for landform development on passive margins. Some implications for relief development in glaciated areas. *Geomorphology*, 12(1), 3-15.
- Thomas, R. J., Agenbacht, A. L. D., Cornell, D. H., & Moore, J. M. (1994a). The Kibaran of southern Africa: tectonic evolution and metallogeny. *Ore Geology Reviews*, 9(2), 131-160.
- Thomas, R. J., Cornell, D. H., Moore, J. M., & Jacobs, J. (1994b). Crustal evolution of the Namaqua-Natal Metamorphic province, southern Africa. *South African Journal of Geology*, 97(1), 8-14.
- Thybo, H., & Artemieva, I. M. (2013). Moho and magmatic underplating in continental lithosphere. *Tectonophysics*, 609, 605-619.
- Tinker, J., de Wit, M., & Brown, R. (2008a). Mesozoic exhumation of the southern Cape, South Africa, quantified using apatite fission track thermochronology. *Tectonophysics*, 455(1), 77-93.
- Tinker, J., de Wit, M., & Brown, R. (2008b). Linking source and sink: evaluating the balance between onshore erosion and offshore sediment accumulation since Gondwana break-up, South Africa. *Tectonophysics*, 455(1), 94-103.

- Torsvik, T. H., & Cocks, L. R. M. (2013). Gondwana from top to base in space and time. *Gondwana Research*, 24(3), 999-1030.
- Torsvik, T. H., Burke, K., Steinberger, B., Webb, S. J., & Ashwal, L. D. (2010). Diamonds sampled by plumes from the core-mantle boundary. *Nature*, 466(7304), 352-355.
- Torsvik, T. H., Rousse, S., Labails, C., & Smethurst, M. A. (2009). A new scheme for the opening of the South Atlantic Ocean and the dissection of an Aptian salt basin. *Geophysical Journal International*, 177(3), 1315-1333.
- Trueb, L., Ross, C. F., & Smith, R. (2005). A new pipoid anuran from the Late Cretaceous of South Africa. *Journal of Vertebrate Paleontology*, 25(3), 533-547.
- Trumbull, R. B., Reid, D. L., de Beer, C., Van Acken, D., & Romer, R. L. (2007). Magmatism and continental breakup at the west margin of southern Africa: A geochemical comparison of dolerite dikes from northwestern Namibia and the Western Cape. *South African Journal of Geology*, 110(2-3), 477-502.
- Tshibalo, A. E., Dhansay, T., Nyabeze, P., Chevallerier, L., Musekiwa, C., & Olivier, J. (2015). Evaluation of the Geothermal Energy Potential for South Africa. 19 - 25.
- Tucker, G. E., & Slingerland, R. L. (1994). Erosional dynamics, flexural isostasy, and long-lived escarpments: A numerical modeling study. *Journal of Geophysical Research: Solid Earth* (1978-2012), 99(B6), 12229-12243.
- Tucker, G. E., & Slingerland, R. (1996). Predicting sediment flux from fold and thrust belts. *Basin Research*, 8(3), 329-349.
- Tucker, G. E., & van der Beek, P. (2013). A model for post-orogenic development of a mountain range and its foreland. *Basin Research*, 25(3), 241-259.
- Turcotte, D. L., & Schubert, G. (2002). *Geodynamics*, 456 pp. New York: Cambridge University Press.
- Turner, J. P., & Williams, G. A. (2004). Sedimentary basin inversion and intra-plate shortening. *Earth-Science Reviews*, 65(3), 277-304.
- Twidale, C. R. (1968). *Geomorphology: with special reference to Australia*. pp. 406. California: Nelson.
- Twidale, C. R. (1992). King of the plains: Lester King's contributions to geomorphology. *Geomorphology*, 5(6), 491-509.
- Twidale, C. R. (2007). *Ancient Australian landscapes*. Rosenberg Pub Pty Limited.
- Twidale, C. R. (2014). Pediments and platforms: problems and solutions. *Géomorphologie: relief, processus, environnement*, 1, 43-56.
- Uenzelmann-Neben, G., Gohl, K., Ehrhardt, A., & Seargent, M. (1999). Agulhas Plateau, SW Indian Ocean: new evidence for excessive volcanism. *Geophysical Research Letters*, 26(13), 1941-1944.
- Unternehr, P., Curie, D., Olivet, J. L., Goslin, J., & Beuzart, P. (1988). South Atlantic fits and intraplate boundaries in Africa and South America. *Tectonophysics*, 155(1), 169-179.
- Unternehr, P., Péron-Pinvidic, G., Manatschal, G., & Sutra, E. (2010). Hyper-extended crust in the South Atlantic: in search of a model. *Petroleum Geoscience*, 16(3), 207-215.
- van der Beek, P., & Braun, J. (1998). Numerical modelling of landscape evolution on geological time-scales: A parameter analysis and comparison with the south-eastern highlands of Australia. *Basin Research*, 10(1), 49-68.
- van der Beek, P., Braun, J., Summerfield, M., & Brown, R. (1998). Morphotectonic evolution of rifted margins: not just flank uplift and escarpment retreat. In *Annales Geophysicae*, 16.
- van der Beek, P., Summerfield, M. A., Braun, J., Brown, R. W., & Fleming, A. (2002). Modeling post-breakup landscape development and denudational history across the southeast African (Drakensberg Escarpment) margin. *Journal of Geophysical Research: Solid Earth* (1978-2012), 107(B12).
- Van der Spuy, D. (2003). Aptian source rocks in some South African Cretaceous basins. *Geological Society, London, Special Publications*, 207(1), 185-202.
- Van der Wateren, F. M., & Dunai, T. J. (2001). Late Neogene passive margin denudation history—cosmogenic isotope measurements from the central Namib desert. *Global and Planetary Change*, 30(3), 271-307.
- Van Soest, M. C., Monteleone, B. D., Hodges, K. V., & Boyce, J. W. (2011). Laser depth profiling studies of helium diffusion in Durango fluorapatite. *Geochimica et Cosmochimica Acta*, 75(9), 2409-2419.
- Van Wijk, J. W., Baldrige, W. S., Van Hunen, J., Goes, S., Aster, R., Coblenz, D. D., Grand, S. P., & Ni, J. (2010). Small-scale convection at the edge of the Colorado Plateau:

- Implications for topography, magmatism, and evolution of Proterozoic lithosphere. *Geology*, 38(7), 611-614.
- Vanacker, V., Von Blanckenburg, F., Hewawasam, T., & Kubik, P. W. (2007). Constraining landscape development of the Sri Lankan escarpment with cosmogenic nuclides in river sediment. *Earth and Planetary Science Letters*, 253(3), 402-414.
- Vermeesch, P. (2008). Three new ways to calculate average (U-Th)/He ages. *Chemical Geology*, 249(3), 339-347.
- Vermeesch, P. (2009). RadialPlotter: A Java application for fission track, luminescence and other radial plots. *Radiation Measurements*, 44(4), 409-410.
- Vermeesch, P., Seward, D., Latkoczy, C., Wipf, M., Günther, D., & Baur, H. (2007).  $\alpha$ -Emitting mineral inclusions in apatite, their effect on (U-Th)/He ages, and how to reduce it. *Geochimica et Cosmochimica Acta*, 71(7), 1737-1746.
- Vidal, O., Wendt, A. S., & Chadderton, L. T. (2003). Further discussion on the pressure dependence of fission track annealing in apatite: reply to the critical comment of Kohn et al. *Earth and Planetary Science Letters*, 215(1-2), 307-316.
- Vink, G. E. (1982). Continental rifting and the implications for plate tectonic reconstructions. *Journal of Geophysical Research: Solid Earth (1978-2012)*, 87(B13), 10677-10688.
- Viola, G., Andreoli, M., Ben-Avraham, Z., Stengel, I., & Reshef, M. (2005). Offshore mud volcanoes and onland faulting in southwestern Africa: neotectonic implications and constraints on the regional stress field. *Earth and Planetary Science Letters*, 231(1), 147-160.
- Viola, G., Kounov, A., Andreoli, M. A. G., & Mattila, J. (2012). Brittle tectonic evolution along the western margin of South Africa: More than 500Myr of continued reactivation. *Tectonophysics*, 514, 93-114.
- Visser, J. N. J. (1989). The Permo-Carboniferous Dwyka Formation of southern Africa: deposition by a predominantly subpolar marine ice sheet. *Palaeogeography, Palaeoclimatology, Palaeoecology*, 70(4), 377-391.
- Visser, J. N. J. (1990). Glacial bedforms at the base of the Permo-Carboniferous Dwyka Formation along the western margin of the Karoo Basin, South Africa. *Sedimentology*, 37(2), 231-245.
- Visser, J. N., & Young, G. M. (1990). Major element geochemistry and paleoclimatology of the Permo-Carboniferous glaciogenic Dwyka Formation and postglacial mudrocks in southern Africa. *Palaeogeography, Palaeoclimatology, Palaeoecology*, 81(1), 49-57.
- Voordouw, R. J., & Rajesh, H. M. (2012). Granitoids from the Margate terrane and their implications for tectono-magmatic models of the Natal Metamorphic Province (South Africa). *South African Journal of Geology*, 115(1), 47-64.
- Voorhoeve, H. (1988). The thermal evolution of lithosphere extending on a low-angle detachment zone. *Basin research*, 1(1), 1-9.
- Wagner, G. A., Gleadow, A. J. W., & Fitzgerald, P. G. (1989). The significance of the partial annealing zone in apatite fission-track analysis: Projected track length measurements and uplift chronology of the Transantarctic Mountains. *Chemical Geology: Isotope Geoscience section*, 79(4), 295-305.
- Wallner, H., & Schmeling, H. (2010). Rift induced delamination of mantle lithosphere and crustal uplift: a new mechanism for explaining Rwenzori Mountains' extreme elevation?. *International Journal of Earth Sciences*, 99(7), 1511-1524.
- Wang, H., van Hunen, J., Pearson, D. G., & Allen, M. B. (2014). Craton stability and longevity: The roles of composition-dependent rheology and buoyancy. *Earth and Planetary Science Letters*, 391, 224-233.
- Ward, J. D., & Martin, H. (1987). A terrestrial conglomerate of Cretaceous age: a new record from the Skeleton Coast, Namib Desert. *Communications of the Geological Survey of Namibia*, 3, 57-58.
- Warnock, A. C., Zeitler, P. K., Wolf, R. A., & Bergman, S. C. (1997). An evaluation of low-temperature apatite U-Th/He thermochronometry. *Geochimica et Cosmochimica Acta*, 61(24), 5371-5377.
- Watchman, A. L., & Twidale, C. R. (2002). Relative and 'absolute' dating of land surfaces. *Earth-Science Reviews*, 58(1), 1-49.
- Waters, D. J. (1989). Metamorphic evidence for the heating and cooling path of Namaqualand granulites. *Geological Society, London, Special Publications*, 43(1), 357-363.
- Watts, A. B. (2001). *Isostasy and Flexure of the Lithosphere*. pp. 451. Cambridge University Press.

- Wegener, A. (1915). Die Entstehung der Kontinente und Ozeane, 23, pp. 94, Friedrich Vieweg & Sohn, Braunschweig
- Weissel, J. K., & Karner, G. D. (1989). Flexural uplift of rift flanks due to mechanical unloading of the lithosphere during extension. *Journal of Geophysical Research: Solid Earth* (1978-2012), 94(B10), 13919-13950.
- Weissel, J. K., & Seidl, M. A. (1998). Inland propagation of erosional escarpments and river profile evolution across the southeast Australian passive continental margin. *Rivers over rock: fluvial processes in bedrock channels*, 189-206.
- Wellington, J. H. (1955). *Southern Africa: a geographical study*. pp. 528. Cambridge: University Press.
- Wendt, A. S., Vidal, O., & Chadderton, L. T. (2002). Experimental evidence for the pressure dependence of fission track annealing in apatite. *Earth and Planetary Science Letters*, 201(3), 593-607.
- Wendt, A. S., Vidal, O., & Chadderton, L. T. (2003). The effect of simultaneous temperature, pressure and stress on the experimental annealing of spontaneous fission tracks in apatite: a brief overview. *Radiation measurements*, 36(1), 339-342.
- Wernicke, B. (1981). Low-angle normal faults in the Basin and Range province: Nappe tectonics in an extending orogen. *Nature*, 291(5817), 645-648.
- Wernicke, B. (1985). Uniform-sense normal simple shear of the continental lithosphere. *Canadian Journal of Earth Sciences*, 22(1), 108-125.
- Wessel, P., Smith, W. H., Scharroo, R., Luis, J., & Wobbe, F. (2013). Generic mapping tools: improved version released. *Eos, Transactions American Geophysical Union*, 94(45), 409-410.
- Whipple, K. X. (2009). The influence of climate on the tectonic evolution of mountain belts. *Nature Geoscience*, 2(2), 97-104.
- Whipple, K. X., & Meade, B. J. (2004). Controls on the strength of coupling among climate, erosion, and deformation in two-sided, frictional orogenic wedges at steady state. *Journal of Geophysical Research: Earth Surface* (2003-2012), 109(F1).
- Whipple, K. X., & Tucker, G. E. (1999). Dynamics of the stream-power river incision model: Implications for height limits of mountain ranges, landscape response timescales, and research needs. *Journal of Geophysical Research: Solid Earth* (1978-2012), 104(B8), 17661-17674.
- Whipple, K. X., Kirby, E., & Brocklehurst, S. H. (1999). Geomorphic limits to climate-induced increases in topographic relief. *Nature*, 401(6748), 39-43.
- White, R. S., & McKenzie, D. (1995). Mantle plumes and flood basalts. *Journal of Geophysical Research: Solid Earth* (1978-2012), 100(B9), 17543-17585.
- White, R. S., Smith, L. K., Roberts, A. W., Christie, P. A. F., Kuszniir, N. J., Roberts, A. M., Christie, P. A. F., Kuszniir, N. J. & Tymms, V. J. (2008). Lower-crustal intrusion on the North Atlantic continental margin. *Nature*, 452(7186), 460-464.
- White, R., & McKenzie, D. (1989). Magmatism at rift zones: the generation of volcanic continental margins and flood basalts. *Journal of Geophysical Research: Solid Earth* (1978-2012), 94(B6), 7685-7729.
- White, S. H., De Boorder, H., & Smith, C. B. (1995). Structural controls of kimberlite and lamproite emplacement. *Journal of Geochemical Exploration*, 53(1), 245-264.
- White, S., Stollhofen, H., Stanistreet, I. G., & Lorenz, V. (2009). Pleistocene to recent rejuvenation of the Hebron Fault, SW Namibia. *Geological Society, London, Special Publications*, 316(1), 293-317.
- Whitmarsh, R. B., Manatschal, G., & Minshull, T. A. (2001). Evolution of magma-poor continental margins from rifting to seafloor spreading. *Nature*, 413(6852), 150-154.
- Wigley, R. A., & Compton, J. S. (2006). Late Cenozoic evolution of the outer continental shelf at the head of the Cape Canyon, South Africa. *Marine Geology*, 226(1), 1-23.
- Will, T. M., & Frimmel, H. E. (2013). The Influence of Inherited Structures on Dike Emplacement during Gondwana Breakup in Southwestern Africa. *The Journal of Geology*, 121(5), 455-474.
- Willett, S. D., & Brandon, M. T. (2002). On steady states in mountain belts. *Geology*, 30(2), 175-178.
- Willett, S. D., Slingerland, R., & Hovius, N. (2001). Uplift, shortening, and steady state topography in active mountain belts. *American journal of Science*, 301(4-5), 455-485.
- Wilson, M. (1993). Magmatism and the geodynamics of basin formation. *Sedimentary Geology*, 86(1), 5-29.

- Wolf, R. A., Farley, K. A., & Kass, D. M. (1998). Modeling of the temperature sensitivity of the apatite (U-Th)/He thermochronometer. *Chemical Geology*, 148(1), 105-114.
- Wolf, R. A., Farley, K. A., & Silver, L. T. (1996). Helium diffusion and low-temperature thermochronometry of apatite. *Geochimica et Cosmochimica Acta*, 60(21), 4231-4240.
- Woolley, A. R., & Bailey, D. K. (2012). The crucial role of lithospheric structure in the generation and release of carbonatites: geological evidence. *Mineralogical Magazine*, 76(2), 259-270.
- Young, E. J., Myers, A. T., Munson, E. L., & Conklin, N. M. (1969). Mineralogy and geochemistry of fluorapatite from Cerro de Mercado, Durango, Mexico. US Geological Survey Professional Paper, 650(D), D84-D93.
- Zachos, J., Pagani, M., Sloan, L., Thomas, E., & Billups, K. (2001). Trends, rhythms, and aberrations in global climate 65 Ma to present. *Science*, 292(5517), 686-693.
- Zalán, P. V., & Oliveira, J. (2005). Origin and structural evolution of the Cenozoic Rift System of Southeastern Brasil. *B. Geoci. Petrobras, Rio de Janeiro*, 13(2), 269-300.
- Zeh, A., Gerdes, A., & Barton, J. M. (2009). Archean accretion and crustal evolution of the Kalahari Craton—the zircon age and Hf isotope record of granitic rocks from Barberton/Swaziland to the Francistown Arc. *Journal of Petrology*, egp 027.
- Zeitler, P. K., Herczeg, A. L., McDougall, I., & Honda, M. (1987). U-Th-He dating of apatite: A potential thermochronometer. *Geochimica et Cosmochimica Acta*, 51(10), 2865-2868.
- Zhang, N., Zhong, S. J., and Flowers, R. M., 2012, Predicting and testing continental vertical motion histories since the Paleozoic, *Earth and Planetary Science Letters*, 317, 426 - 435.
- Zhao, G., Wilde, S. A., Cawood, P. A., & Sun, M. (2001). Archean blocks and their boundaries in the North China Craton: lithological, geochemical, structural and P-T path constraints and tectonic evolution. *Precambrian Research*, 107(1), 45-73.
- Ziegler, P. A., & Cloetingh, S. (2004). Dynamic processes controlling evolution of rifted basins. *Earth-Science Reviews*, 64(1), 1-50.
- Ziegler, P. A., Cloetingh, S., & van Wees, J. D. (1995). Dynamics of intra-plate compressional deformation: the Alpine foreland and other examples. *Tectonophysics*, 252(1), 7-59
- Ziegler, P.A., (1996). Geodynamic processes governing development of rifted basins. In Roure, F., Ellouz, N., Shein, V.S., Skvortsov, I. (Eds.), *Geodynamic Evolution of Sedimentary Basins*. Technip, Paris, pp. 19- 67.